UNIVERSITY CARLOS III OF MADRID

DOCTORAL THESIS

ADVANCED CONSTITUTIVE RELATIONS FOR MODELING THERMO-VISCOPLASTIC BEHAVIOUR OF METALLIC ALLOYS SUBJECTED TO IMPACT LOADING

Author:
José Antonio Rodríguez Martínez

Directors:
Ángel Arias Hernández
Alexis Rusinek

DEPARTMENT OF CONTINUUM MECHANICS AND STRUCTURAL ANALYSIS

Leganés, February 2010

DOCTORAL THESIS

ADVANCED CONSTITUTIVE RELATIONS FOR MODELING THERMO-VISCOPLASTIC BEHAVIOUR OF METALLIC ALLOYS SUBJECTED TO IMPACT LOADING

Author: José Antonio Rodríguez Martínez

Directors: Ángel Arias Hernández
Alexis Rusinek

Firma del Tribunal Calificador:

Firma

Presidente:

Vocal:

Vocal:

Vocal:

Secretario:

Calificación:

Leganés, de de

THÈSE

Présentée par

José Antonio Rodríguez Martínez

Pour obtenir le grade de

DOCTEUR

De l'Université Paul Verlaine de Metz

(Spécialité : Mécanique des matériaux)

(Option : Sciences des matériaux)

Advanced constitutive relations for modeling thermo-viscoplastic behaviour of metallic alloys subjected to impact loading

Soutenue à Madrid le 19 Février 2010

Composition du jury:

A. MOLINARI	Professeur des Universités à l'Université Paul Verlaine de Metz	Président
T. LODYGOWSKI	Professeur des Universités Université Polytechnique de Poznań	Rapporteur
R. PĘCHERSKI	Professeur des Universités à l'Institut de recherche Technologique Fondamentale. Académie Polonaise de las Sciences	Rapporteur
R. ZAERA	Professeur des Universités à l'Université Carlos III de Madrid	Examinateur
J. FERNÁNDEZ	Professeur des Universités à l'Université Carlos III de Madrid	Examinateur
P. CHEVRIER	Professeur des Universités à l'école nationale d'ingénieurs de Metz	Examinateur
A. RUSINEK	Professeur des Universités à l'école nationale d'ingénieurs de Metz	Directeur de thèse
A. ARIAS	Maitre de conférences à l'Université Carlos III de Madrid	Directeur de thèse

Laboratoire de **M**écanique **B**iomécanique **S**tructures (**LaBPS**)
Ecole **N**ationale d'**I**ngénieurs de **M**etz (**ENIM**)
Université **P**aul **V**erlaine de **M**etz (**UPVM**)

To Janusz Roman Klepaczko

Agradecimientos

En primer lugar quiero agradecer a mis padres y a mis hermanos…por todo! Sin ellos no hubiera sido posible llevar a cabo este trabajo.

A Alexis y Ángel por la enorme dedicación que han tenido y por su confianza, pero sobre todo por su amistad. La relación personal que nos une desde hace ya varios años es sin lugar a dudas el mayor y más importante logro conseguido durante el desarrollo de esta Tesis.

A Ramón Zaera, tener la oportunidad de trabajar con una persona de su talla personal y profesional ha supuesto un aliciente fundamental para la consecución de este trabajo.

A José Fernández Sáez, por acogerme en el seno del grupo de investigación Dinámica y Fractura de Elementos Estructurales. Quiero agradecerele de manera muy especial su manifiesta responsabilidad en el buen devenir de esta Tesis.

A Raphaël Pesci cuya contribución a esta Tesis doctoral ha sido de vital importancia. Por su inestimable ayuda y ante todo por los buenos ratos que hemos pasado juntos en este tiempo.

A Carlos Navarro cuyo apoyo e interés han sido constantes durante este tiempo. Le agradezco de manera muy especial sus valiosos consejos y haberme animado a formar parte de este departamento.

A los de aquí, Guadalupe y Rolando y a los de allá David, Jorge y Karlos por los buenos ratos, por su apoyo y amistad y por las tardes de tertulia.

A José Puerta, a Sergio Puerta y a David Arias cuya contribución a la realización de esta Tesis ha resultado determinante.

A mis compañeros de departamento por su ayuda, apoyo, amistad y sobre todo por generar un ambiente de trabajo tan magnífico.

A Tomasz Łodygowski y Ryszard Pęcherski por toda la ayuda que me han prestado durante este tiempo. Por la confianza que depositaron en mí, trabajar con ellos ha supuesto una enorme satisfacción personal.

A Pierre Chevrier, responsable de la calurosa acogida que siempre encontré en el ENIM.

A Richard Bernier y Edgar Dossou por la inestimable y desinteresada ayuda.

Al personal del ENIN por las facilidades prestadas durante los periodos que estuve en Metz.

Al personal del ENSAM por su colaboración desinteresada.

A toda la familia Jankowiak y de manera muy especial a Agata por acogerme tantas veces durante mis estancias en Francia y Polonia. Por hacerme sentir como en casa.

A toda la familia Rusinek por acogerme durante mis estancias en Metz.

A mis amigos por su apoyo y de manera especial a Luis y a Ramón por mantenerme de buen humor, siempre!

A Carlos Vela por su inestimable ayuda.

Special mention

A special mention is required for ***Janusz Roman Klepaczko*** *who passed away on August 15, 2008 at the age of 73.*

Graduated from Warsaw University of Technology in 1959, began the research work in 1960 at IPPT – Institute of Fundamental Technological Research, Polish Academy of Sciences, Warsaw, Poland and continued it until 1984, becoming full professor in 1983. Since 1985 he was working in LPMM (Laboratory of Physic and Mechanic of Materials), Paul Verlaine University of Metz, France, where he was founder of the experimental laboratory. He was well known in the field of dynamic behaviour of materials; he was the author of over 200 publications and supervised 30 doctors in several research centres around the world. Janusz was involved in research until the end of his life. He was a great researcher and had a passion for Science.

This doctoral Thesis gave me the incredible opportunity of learning from him. He was for me a source of motivation and inspiration.

The contents presented in this work are based on the research he conducted during his life. His contributions to this Thesis are patently clear in every page of the manuscript.

Professor Klepaczko thanks!

Abstract

In this doctoral Thesis the thermo-viscoplastic behaviour of metallic alloys used for structural protection purposes has been analyzed. The study includes the proposition of advanced constitutive relations and their integration into numerical models. These numerical models are validated for impact problems within the low-intermediate range of impact velocities *(until 85 m/s)*.

The advanced constitutive relations derived are based on the **Rusinek-Klepaczko** model whose validity is extended to metallic alloys showing dependence on plastic strain on the volume thermally activated. In addition the constitutive relations developped allow describing macroscopically viscous drag effects at high strain rates, negative strain rate sensitivity and *martensitic* transformation phenomena.

Implementation of previous constitutive relations has been conducted into the **FE** code **ABAQUS/Explicit**. Thus, development of numerical models for the simulation of ring expansion test and conventional dynamic tension test has allowed analyzing the formation of plastic instabilities. In this analysis the effects of strain rate sensitivity, strain hardening and plastic wave propagation have been considered.

Finally, it has been examined the impact behaviour of metallic alloys widely used for structural protection purposes: the mild steel **ES**, the aluminium alloy **2024-T3**, the steel **AISI 304** and the steel **TRIP 1000**. For that goal conventional characterization tests as well as impact tests have been conducted. Numerical models based on the constitutive relations derived have been developped in order to simulate the impact tests. These numerical models offered a suitable description of the perforation process in terms of ballistic limit and the associated failure mode of the target.

Resumen

En esta tesis doctoral se ha analizado el comportamiento termo-viscoplástico de aleaciones metálicas de aplicación en la protección frente a impacto. El estudio incluye la proposición de ecuaciones constitutivas avanzadas, su implementación en modelos numéricos y la validación de los mismos con aplicación en problemas de impacto en el rango de velocidades bajo-medio *(hasta 85 m/s)*.

Las ecuaciones constitutivas avanzadas que se plantean toman como base la ley de endurecimiento de Rusinek-Klepaczko y extiende su validez a metales que presentan sensibilidad a la velocidad de deformación dependiente de la deformación plástica. Las ecuaciones constitutivas consideradas permiten describir macroscópicamente los efectos viscosos a altas velocidades de deformación, la sensibilidad negativa a la velocidad de deformación y los fenómenos de transformación *martensítica*.

La implementación de las ecuaciones constitutivas anteriores se ha llevado a cabo en el código de elementos finitos **ABAQUS/Explicit**. Así, el desarrollo de modelos numéricos para las configuraciones del ensayo convencional de tracción dinámica y del ensayo de expansión de anillo ha permitido analizar las causas que residen detrás de la formación de inestabilidades plásticas. En el análisis se ha considerado la influencia de la sensibilidad a la velocidad de deformación, el endurecimiento por deformación y el efecto de la propagación de ondas.

Finalmente se ha examinado el comportamiento frente a impacto de metales de amplia aplicación como estructuras de protección: el acero suave **ES**, la aleación de aluminio **2024-T3**, el acero **AISI 304** y el acero **TRIP 1000**. Para ello, se han llevado a cabo ensayos experimentales de caracterización mecánica convencional y ensayos experimentales de impacto mediante proyectil indeformable. La utilización de modelos numéricos que implementan las ecuaciones constitutivas desarrolladas proporciona una adecuada descripción del proceso de impacto en términos del límite de velocidad de perforación y del modo de fallo asociado.

Résumé

Dans cette thèse certains problèmes liés au comportement thermo-viscoplastiques des alliages métalliques sont analysés. Ainsi, la réponse des métaux pour un large spectre en vitesses de déformation et en températures a été étudiée. Ceci est d'un intérêt majeur dans de nombreuses applications industrielles. L'optimisation des matériaux dans le but de supporter de plus en plus de sollicitations extrêmes est un problème très actuel.

Au niveau modélisation la validation du modèle Rusinek-Klepaczko (**RK**) a été étendue à différents alliages sans dépendance avec la déformation plastique dans la définition du volume thermiquement activé. De plus, Une extension du modèle **MRK** a été faite dans le but de décrire le comportement des matériaux présentant une dépendance en déformation dans le description de la sensibilité à la vitesse de déformation. Ce modèle a été utilisé pour décrire les matériaux avec une sensibilité négative à la vitesse de déformation et présentant un fort effet du drainage visqueux. En complément une loi de comportement a été développée pour décrire le comportement des matériaux avec une transformation de phase de type martensitique.

Ces lois de comportement ont été implémentées dans un code éléments finis. Grâce à ces outils des études précises et fines on été menées au niveau des instabilités thermo-viscoplastiques notamment sous chargement dynamique. Deux études particulières ont été faites, l'une sur le processus d'expansion des anneaux et une seconde sur la traction dynamique. Une étude complète a été menée sur le couplage entre la plasticité locale et le phénomène lié à la propagation des ondes élastiques générées par l'impact du chargement.

En complément des essais **3D** de type perforation ont été réalisés dans le but de valider les approches analytiques. Divers matériaux ont été utilisés comme : l'acier **ES**, un alliage d'aluminium **2024-T3**, un acier **AISI 304** et un acier de type **TRIP 1000**. L'ensemble des matériaux ayant été caractérisé au préalable via des essais simples. Le but de ces études de perforation étant d'étudier leur réponse sous impact dynamique et de valider les outils analytiques et numériques.

INDEX

CHAPTER 1

INTRODUCTION AND OBJECTIVES

Abstract

Exhaustive analysis of metals deformation behaviour answers to the necessity of proving to industrial sectors of materials suitable for bearing hard mechanical and thermo-mechanical loadings. For design purposes, many engineering fields are required of an accurate knowledge of the thermo-viscoplastic behaviour of metallic alloys. Particularly, high loading rate events have become increasingly relevant for the modern industry. Thus, in this chapter of the Thesis are set the objectives of the present investigation. The main goal is to go further in the understanding of the thermo-viscoplastic behaviour of metallic alloys subjected to impact loading. It must be must provided an integrated view of the processes which reside behind the formation of plastic instabilities, which are the main responsible for failure in metals subjected to impact.

1 CHAPTER 1. INTRODUCTION AND OBJECTIVES

1.1 Motivation

Exhaustive analysis of metals deformation and failure behaviours answers to the necessity of proving to industrial sectors of materials suitable for bearing hard mechanical and thermo-mechanical loadings. For design purposes, engineering fields like aeronautical, automotive, oil and naval industries, machining processes, military applications or civil engineering are required of an accurate knowledge of the thermo-viscoplastic behaviour of metals, Fig. 1.1. Particularly, high loading rate events have become increasingly relevant for the modern industry [Borvik et al. 2003a]. In design of offshore structures, account is taken of accidental loads such as dropped objects collisions, explosions and penetration by fragments [Rusinek and Zaera 2007]. Impact loads are also pertinent in design of fortification structures as protection against terrorist attacks. In the transport industry, energy absorption and crashworthiness are now critical issues in the design process of vehicles, vessels and aircrafts [Abramowicz and Jones 1984, Abramowicz and Jones 1984, Rusinek et al. 2008a]. In addition, many of the problems found in structural impact are also relevant in machining processes and metal forming operations.

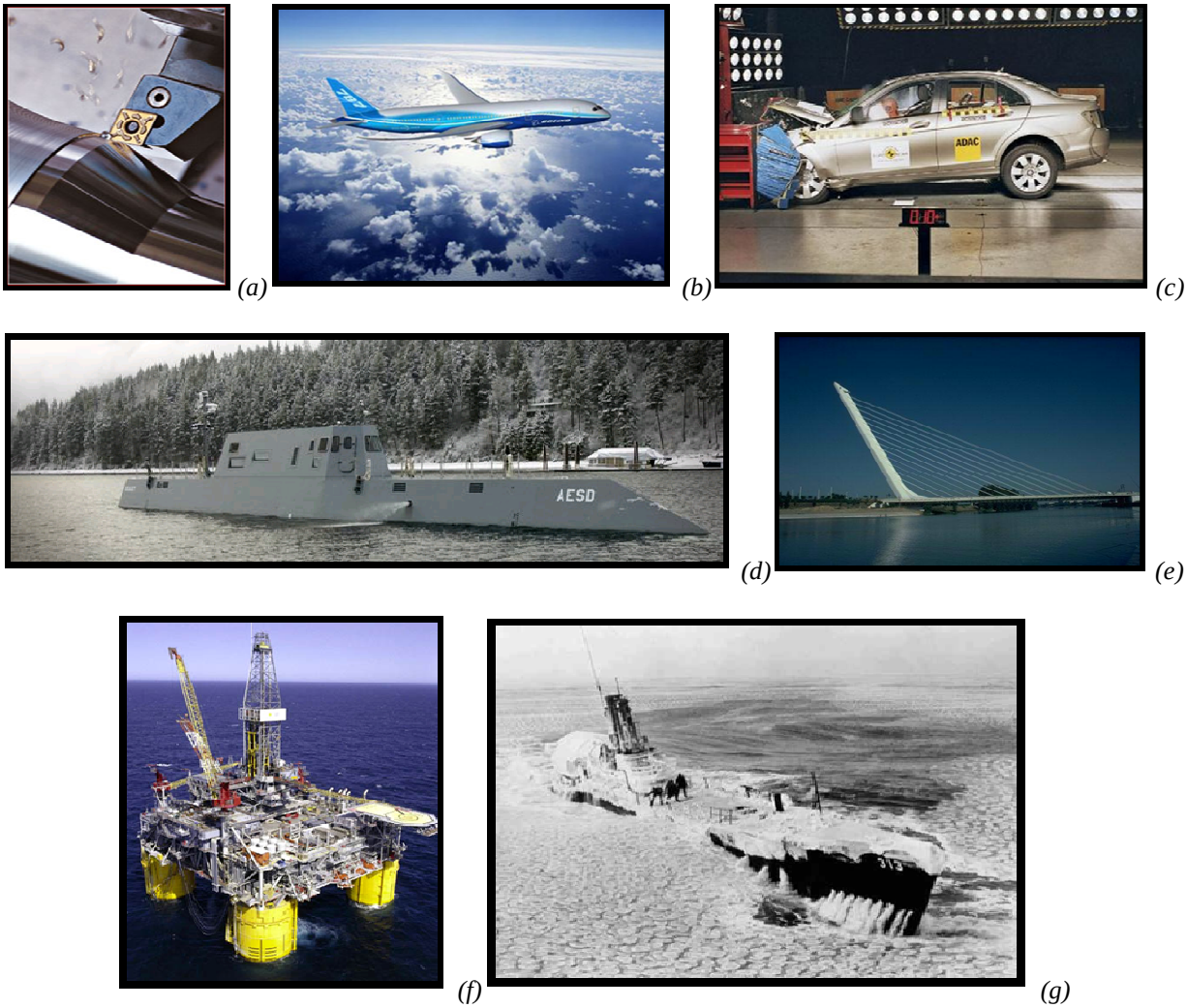

(a) (b) (c) (d) (e) (f) (g)

Fig. 1.1. Engineering applications where metallic alloys may be subjected to wide ranges of strain rate and temperature during their service life. (a) Machining processes, (b) Aeronautical industry, (c) Automotive industry, (d) Military applications, (e) Civil engineering, (f) Oil industry, (g) Naval industry.

Metal plasticity has been extensively studied over the last decades. Pioneer works of Orowan and Taylor were suitable to describe deformation of metals in terms of theory of dislocations. Later on, the seminal works of Perzyna [Perzyna 1966], Campbell and Fergusson [Campbell and Fergusson 1970] and Kocks et al. [Kocks et al. 1975] among others allowed a better understanding of the thermo-viscoplastic behaviour of metals. Deformation mechanisms which reside behind metals plasticity were investigated [Campbell 1954, Seeger 1957, Basinski 1959, Conrad 1961, Klepaczko and Duffy 1982, Zerilli and Armstrong 1987, Klepaczko 1991, Taylor 1992, Tanner and McDowell 1999, Kocks 2001, Kocks and Mecking 2003, Lennon and Ramesh 2004].

Based on these contributions, several authors [Kumar et al. 1968, Hirth and Lothe 1982, Clifton 1983, Follansbee 1986, Regazzoni et al. 1987, Follansbee and Kocks 1988, Zerilli and Armstrong 1992, Huang et al. 2009] focused their interest in the high rate deformation behaviour of metallic alloys. From such investigations, it was stated that plastic instabilities play a prominent role in the deformation and failure of engineering materials under dynamic solicitations [Papirno et al. 1990, Couque 1998, Molinari et al. 2002]. High strain rates lead to material temperature increase due to adiabatic heating. It slows down plastic wave propagation inducing flow localization and subsequent failure. Understanding formation and propagation of instabilities in metals offers significant steps towards optimizing material's behavior at high strain-rates. Susceptibility of metals for instabilities formation determines their suitability for absorbing energy under dynamic solicitations.

The relation between thermo-viscoplastic material behaviour, plastic wave propagation and instabilities formation is observable in impact-perforation problems. From such an integrated point of view, the understanding of the materials response under impact has still not been reached. Perforation events are characterized by the complex mechanical and thermo-mechanical processes which take place in the target-material during loading. Target failure is preceded by instabilities formation like shear banding, Fig. 1.2, necking Fig. 1.2 or petalling Fig. 1.2 [Borvik et al. 1999, Borvik et al. 2003b, Dey et al. 2004, Odeshi et al. 2006, Arias et al. 2008, Rusinek et al. 2009a]. Impact processes are interesting from themselves as well as from the extreme conditions taking place in the material during loading.

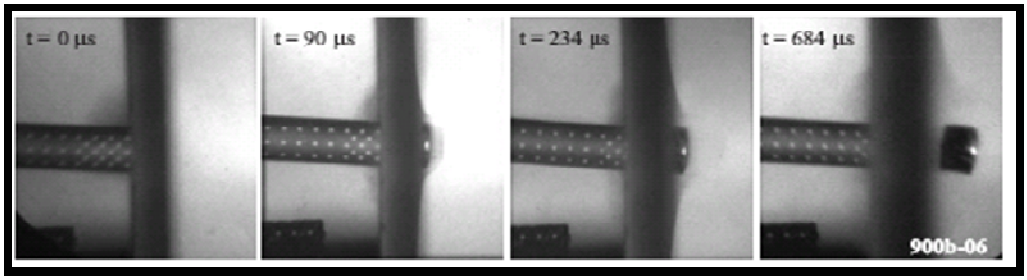

(a)

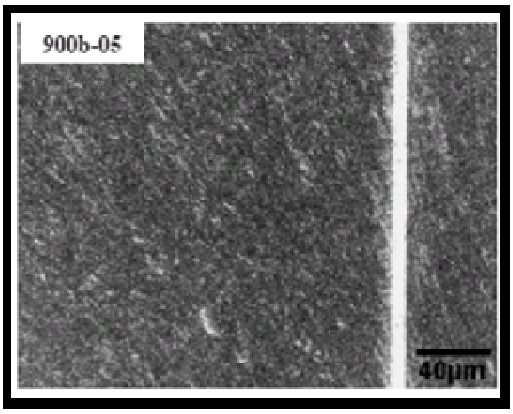

(b)

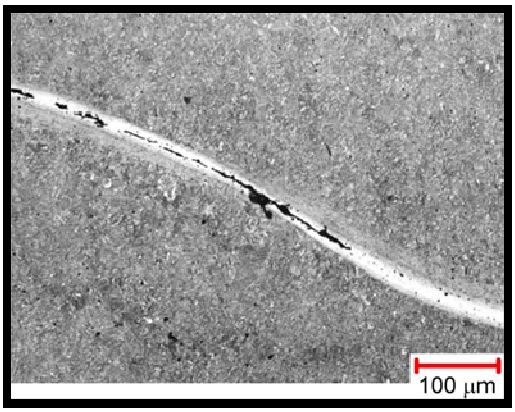

(c)

*Fig. 1.2. Failure mechanisms taking place under impact. (a) Sequence of images of the perforation process of **Weldox 460-E** steel plate by a non-deformable blunt projectile with flat faces [Dey et al. 2004]. (b) Adiabatic shear band in a plate of steel **Weldox 460-E** impacted by a non-deformable blunt projectile with flat faces [Dey et al. 2004]. (c) Adiabatic shear band induced by a ballistic impact in a steel plate [Odeshi et al. 2006].*

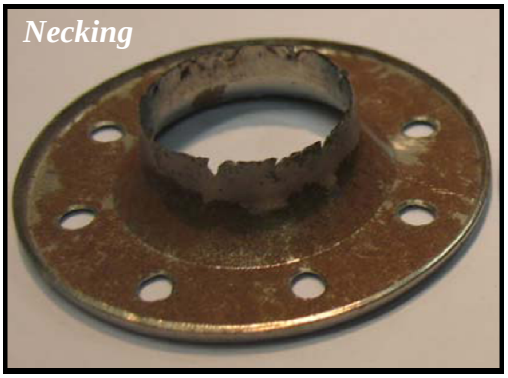

(a)

(b)

(c)

Fig. 1.3. Failure mechanisms taking place under impact. (a) Necking failure mode [Rusinek et al. 2009a]. (b)-(c) Petalling failure mode [Rusinek et al. 2009a].

Many experimental, analytical and numerical investigations dealing with impact-perforation of projectiles on metallic plates are nowadays available in the open literature. Comprehensive reviews on the research into the penetration and perforation of structures by free-flying projectiles can be found in the works due to Goldsmith [Goldsmith 1999], Corbett et al. [Corbet et al. 1996], and Zukas et al. [Zukas et al. 1982, Zukas et al. 1990]. The effect of target materials and thicknesses, [Borvik et al. 2003b], impact velocity [Borvik et al. 2002a, Arias et al. 2008, Rusinek et al. 2008b] and projectile nose shape [Borvik et al. 2002a, Arias et al. 2008] on the perforation process has been examined. In those works it is empirically analyzed the strong dependence existing between thermo-viscoplastic materials behaviour and instabilities formation [Dey et al. 2004].

It is therefore well proven the relation existing between deformation behaviour of metals, formation of plastic instabilities and perforation problems. This relation is intrinsically tied to the thermo-viscoplastic behaviour of the material and it can be illustrated by the thermo-viscoplastic yield function defined by Eq. 1.1.

$$f\left(\sigma_{ij},\bar{\varepsilon}^{p},\dot{\bar{\varepsilon}}^{p},T\right)=\bar{\sigma}-\sigma_{y}\left(\bar{\varepsilon}^{p},\dot{\bar{\varepsilon}}^{p},T\right)=0 \qquad (1.1\text{-}a)$$

$$\bar{\sigma}=\sqrt{\frac{3}{2}\cdot s_{ij}:s_{ij}} \qquad (1.1\text{-}b)$$

Where, assuming Huber-Misses plasticity, $\bar{\sigma}$ is the equivalent stress $\bar{\varepsilon}^{p}$ is the equivalent plastic strain, $\dot{\bar{\varepsilon}}^{p}$ is the equivalent plastic strain rate, T is the temperature and s_{ij} is the deviatoric part of the stress tensor σ_{ij}. Then, the yield function evolution reads as follows, Eq. 1.2.

$$\dot{f}\left(\sigma_{ij},\bar{\varepsilon}^{p},\dot{\bar{\varepsilon}}^{p},T\right)=\frac{\partial f}{\partial\sigma_{ij}}\dot{\sigma}_{ij}+\frac{\partial f}{\partial\bar{\varepsilon}}\dot{\bar{\varepsilon}}^{p}+\frac{\partial f}{\partial\dot{\bar{\varepsilon}}^{p}}\ddot{\bar{\varepsilon}}^{p}+\frac{\partial f}{\partial T}\dot{T}=0 \qquad (1.2)$$

where $\ddot{\bar{\varepsilon}}^{p}$ is the equivalent plastic acceleration.

From Eq. 1.2. we can gather that the derivatives of the yield function with respect to strain *(so strain hardening* $\theta=\partial\sigma/\partial\varepsilon^{p}$*)*, strain rate *(so strain rate sensitivity* $m=\partial\sigma/\partial\log(\dot{\varepsilon}^{p})$*)* and temperature *(so temperature sensitivity* $\upsilon=\partial\sigma/\partial T$*)* are determining plastic behaviour of metals under transient loadings. It is therefore necessary to provide suitable analytical definitions of those rate-dependent terms of the material behaviour. In particular, certain unconventional deformation modes exhibited by some metals which involve sudden variations of such rate-dependent terms are of main relevance in impact problems. These are, for example, dislocations drag at high strain rates, negative strain rate sensitivity or *martensitic* transformation.

Unfortunately deformation behaviour of metals, formation of plastic instabilities and perforation problems are usually treated separately in the framework of the continuum mechanics.

In this doctoral Thesis the efforts are gathered on an attempt for offering a complete approach of the high rate behaviour of metallic alloys. From the advance constitutive description of metals within wide ranges of loading conditions until the deformation mechanisms which reside behind the absorption of energy in metallic alloys subjected to impact/perforation. The key is the determination of the causes which control instabilities formation under dynamic solicitations.

1.2 Objectives

With the problem expressed in such terms, the objectives of this doctoral Thesis are set:

The goal is to go further in the understanding of the thermo-viscoplastic behaviour of metallic alloys subjected to impact loading. It must be provided an integrated view of the processes which reside behind the formation of plastic instabilities, which are the main responsible for failure in metals subjected to impact. In order to achieve this task the following procedure is applied

- Constitutive modelling of metallic alloys has to be examined. Study and derivation of analytical constitutive descriptions suitable for describing the thermo-viscoplastic behaviour of metallic alloys under wide ranges of strain rate and temperature. A constitutive description has to be proposed in order to complement the **Rusinek-Klepaczko** (**RK**) model [Rusinek and Klepaczko 2001]. The **RK** formulation is suitable for describing the behaviour of metals whose rate sensitivity is independent of plastic strain. The former, the **Modified Rusinek-Klepaczko** (**MRK**) model, has to be suitable for defining the behaviour of metals showing dependence of strain on the volume thermally activated.

- Particular attention must be focused on determined unconventional deformation mechanisms that may take place in metals under dynamic loading; viscous drag effect at high strain rates, negative strain rate sensitivity and *martensitic* transformation. Extensions of the **RK** and **MRK** models to describe such phenomena have to be derived.

- Implementation of the constitutive relations developed into a **FE** code. It will allow developing a numerical methodology in order to analyze the influence that strain hardening, strain rate sensitivity and temperature sensitivity have on the formation of instabilities under dynamic loading.

- Development of an experimental methodology for perforation of metallic sheets under wide ranges of impact velocity at different initial temperatures. Then, the constitutive models developed will be applied to simulate the perforation tests. The understanding of the thermo-mechanical response of metallic alloys under impact-perforation is pursued. The causes which reside behind suitability of metals for absorbing energy under dynamic events are examined.

1.3 Methodology

Thus, the methodology developed in this doctoral Thesis is set:

1. Derivation and validation of constitutive relations for modelling the thermo-viscoplastic behaviour of metallic alloys under wide ranges of strain rate and temperature. These constitutive relations have to gather physical foundations as well as simple formulation and easy calibration procedure.

2. Implementation of the constitutive descriptions into **FE** code. Based on the constitutive relations developed a numerical analysis to determine the causes which reside behind instabilities formation under dynamic loading is conducted. The roles played by strain hardening and strain rate sensitivity are examined.

3. Thermo-mechanical characterization of the behaviour of metals under wide ranges of strain rate and temperature and study of their deformation mechanisms. Then, it will be conducted the modelling of their thermo-viscoplastic behaviour by means of the constitutive descriptions developed. In addition, it will be determined their potential application for withstanding extreme loading conditions. For that task, an experimental methodology has to be developed in order to understand the mechanisms which reside behind the absorption of energy of metals subjected to impact-perforation.

1.4 Original contributions

The original contributions carried out in this Thesis are outlined in the following points:

- Constitutive modeling of several metallic alloys using the **RK** model. Proposition of an original constitutive relation (**MRK**) for describing the thermo-viscoplastic behaviour of metals with the volume thermally activated dependent on plastic strain.

- Extensions to viscous drag at high strain rates, negative strain rate sensitivity and *martensitic* transformation are derived for both, **RK** and **MRK** models. The constitutive descriptions developed have been validated for modeling different metallic alloys of relevance for protection applications.

- The constitutive relations developed have been implemented into the **FE** code **ABAQUS/Explicit**. Both, ring expansion test and conventional dynamic tension test have been numerically examined under wide ranges of impact velocities. The main role played by strain hardening and strain rate sensitivity on the formation of instabilities has been highlighted.

- It has been analyzed the thermo-viscoplastic behaviour of steel **ES** under impact/perforation. Perforation tests were recorded using high speed infrared camera. An original methodology is proposed for determining the critical failure strain which induces material failure during the tests. It has been estimated that the localization process which leads to target-failure involves local plasticity values close to $\overline{\varepsilon}^{p} \approx 1$. Numerical simulations of the impact tests were conducted. The numerical model developed allowed for a proper description of the perforation process in terms of ballistic limit prediction and failure mode. Instabilities formation has been identified as the mechanism leading to the collapse of the target.

- The thermo-viscoplastic behaviour of **AA 2024-T3** has been characterized in tension under wide ranges of strain rate and temperature. The material possesses high strain hardening and elevated ductility. A remarkable characteristic of this alloy is the strong increase of the strain hardening with the temperature decrease. The temperature sensitivity has been found dependent on plastic strain. The thermo-viscoplastic behaviour of **AA 2024-T3** has been modeled using the extended **MRK** model to viscous drag effects. Numerical simulations of the high velocity impact tests were conducted. The numerical model developed allowed for a proper description of the perforation process in terms of ballistic limit prediction and failure mode.

- The thermo-viscoplastic behaviour of the steel **AISI 304** is characterized and examined. The *martensitic* volume fraction was determined in the post mortem specimens. It was revealed that the phase transformation occurs in this material even under a temperature increase above $\Delta T > 140$ K. Such finding is reported for the first time in the open literature. The thermo-viscoplastic behaviour of the material has been defined using the extended **RK** model to viscous drag effects. Moreover perforation tests of **AISI 304** sheets are conducted. It has been detected *martensite* formation during perforation. Numerical simulations of the impact process were conducted. The numerical model developed allowed for a proper description of the perforation process in terms of ballistic limit prediction and failure mode.

- The thermo-mechanical behaviour of the steel **TRIP 1000** under wide ranges of strain rate and temperature has been examined. In order to study the material behaviour under fast loading, perforation tests on **TRIP 1000** sheets have been performed. No *martensitic* transformation was found during perforation. Under dynamic solicitation the steel **TRIP 1000** seems to behave as a regular **H**igh **S**trength **S**teel with an absence of *martensitic* transformation.

1.5 Contents

This introduction is the first chapter of the six into which the Thesis is divided.

The second chapter is devoted to the constitutive modeling of metallic alloys. The **RK** formulation is introduced. Applicability of this constitutive description is extended to different metallic alloys. Complementary to the **RK** model, the **MRK** model is proposed. The latter will allow for describing the thermo-viscoplastic behaviour of metals with the volume thermally activated dependent on plastic strain. Extension to viscous drag effects, negative strain rate sensitivity and phase transformation phenomena are derived for both, **RK** and **MRK** models.

The third chapter has advantage of numerical simulations in order to analyze the causes which reside behind formation of instabilities under dynamic loading. Two different numerical configurations are used for that task; ring expansion test and conventional dynamic tension test. Wave propagation, strain hardening and strain rate effects on the formation of plastic instabilities are examined. Optimization of materials for absorbing energy under impact loading is pursued.

The fourth and fifth chapters deal with the impact-perforation behaviour of four metallic alloys, **ES** steel, aluminium alloy **2024-T3**, steel **AISI 304** and steel **TRIP 1000**. These materials are thermo-mechanically characterized, analytically modeled and subjected to perforation by non-deformable projectiles. Their deformation mechanisms are tied to their answer under impact-perforation.

In the sixth chapter are collected the main conclusions derived from this work. In addition, the required forthcoming works are sketched.

Moreover, different appendixes are attached where determined aspects of this doctoral Thesis are detailed.

Finally, the bibliography used to conduct this work is reported.

CHAPTER 2

ADVANCED CONSTITUTIVE RELATIONS FOR METALLIC ALLOYS BASED ON THE RUSINEK-KLEPACZKO MODEL

Abstract

In this chapter of the Thesis the constitutive modeling of metallic alloys is examined. In order to complement the **Rusinek Klepaczko** model, the **Modified Rusinek-Klepaczko** constitutive description has been proposed. The former is suitable for describing the behaviour of metals whose rate sensitivity in independent of plastic strain. The latter is suitable for defining the behaviour of metals showing dependence of strain on the volume thermally activated. Extensions to viscous drag effects, negative strain rate sensitivity and *martensitic* transformation phenomena are derived for both, **Rusinek Klepaczko** and **Modified Rusinek-Klepaczko** models. It has been proven the suitability of the constitutive relations developed for defining the thermo-viscoplastic behaviour of both **BCC** and **FCC** metallic alloys.

2 CHAPTER 2. ADVANCED CONSTITUTIVE RELATIONS FOR METALLIC ALLOYS BASED ON THE RUSINEK-KLEPACZKO MODEL

2.1 Introduction

Over the last decades, deformation of metals has been subjected to intensive study since it is of fundamental interest to analyze loading processes. Accurate knowledge of the response of metallic alloys under loading is required to optimize materials used to build mechanical elements in charge of bearing demanding solicitations. In order to understand the thermo-viscoplastic behavior of metals, a constitutive description is required. Driven by economic sectors like automotive, aeronautical or military industries, the research conducted to derive theoretical descriptions of the deformation behaviour of metallic alloys has gathered substantial efforts.

Macroscopic constitutive descriptions proposed over the years may be primarily split into two groups:

- **Phenomenological constitutive relations**: They provide a definition of the material flow stress based on empirical observations. They consist on mathematical functions with lack of physical background which fit experimental observations. Phenomenological models are characterized by reduced number of material constants and easy calibration. Some examples are those models proposed in [Cowper and Symonds 1952, Litonski 1977, Steinberg et al. 1980, Johnson and Cook 1983, Klepaczko 1987, El-Magd 1994]. Due to their empirical character, they use to exhibit restricted application fields *(covering limited ranges of strain rate and temperature)* and reduced flexibility *(specific formulation for determined materials)*.

- **Physical-based constitutive relations**: They account for physical aspects of the material behaviour. Most of them are founded on the theory of thermodynamics and kinetics of slip developed in [Kocks et al. 1975, Kocks and Mecking 2003] ***(Appendix A)***. Some examples are those models proposed in [Zerilli and Armstrong 1987, Nemat-Nasser and Li 1998, Rusinek and Klepaczko 2001, Nemat-Nasser and Guo 2003, Molinari and Ravichandran 2005, Voyiadjis and Abed 2005, Abed and Voyiadjis 2005, Durrenberger et al. 2007, Durrenberger et al. 2008, Voyiadjis and Almasri 2008]. In comparison with phenomenological descriptions they use to have larger number of material constants and their determination procedure follows physical assumptions. In contrast, they allow for accurate definition of the material behaviour under wide ranges of loading conditions. It must be pointed out that the physical-based approach lack on the definition of the microstructure evolution *(purely physical models should be taking into account for that goal, however they are not considered in this Thesis)*. The effect that potential microstructural changes may have on the material straining is not gathered by this kind of approach. It limits the application of this type of constitutive relations to the description of the instantaneous rate sensitivity of materials. However, it simplifies the implementation of this kind of constitutive descriptions into **FE** codes *(simplifying their mathematical formulation and reducing their material constants)*.

Thus in the present work, the attention will be focused on the second sort of constitutive relations previously mentioned. Due to their flexibility, physical-based models are of increasing interest for engineering applications like high speed machining (**HSM**), perforation, blast loading or crash-test [Rusinek et al. 2009a]. During such processes, the material work-piece is subjected to wide ranges of strain rate and temperature as well as large deformation [Rusinek et al. 2009a].

Macroscopic plasticity in metals is the result of dislocations moving through the crystal lattice. Two types of obstacles are encountered that try to prevent dislocation movements through the lattice; long-range and short-range barriers [Kocks et al. 1975, Kocks 2001, Kocks and Mecking 2003, Bonora and Milella 2001, Voyiadjis and Abed 2005, Voyiadjis and Almasri 2008]. The long-range obstacles are due to the structure of the material and cannot be overcome by introducing thermal energy through the crystal [Zerilli and Armstrong 1987, Nemat-Nasser and Isaacs 1997, Nemat-Nasser and Li 1998]. They contribute to the flow stress with a component that is non-thermally activated *(athermal stress).* The short-range barriers can be overcome assisted by thermal energy [Zerilli and Armstrong 1987, Nemat-Nasser and Isaacs 1997, Nemat-Nasser and Li 1998, Bonora and Milella 2001, Voyiadjis and Almasri 2008]. Thermal activation aids dislocation gliding, decreasing the intrinsic lattice friction in the case of most **BCC** metals *(overcoming Peierls stress)* or decreasing the strength of obstacles in the case of many **FCC** metals *(overcoming forests of dislocations).* In both cases, thermal activation reduces the applied stress required to force the dislocation past obstacle [Lennon and Ramesh 2004].

Thus, flow stress of a material *(using **J2** theory)* can be decomposed into equivalent athermal stress $\bar{\sigma}_{\mu}$ and equivalent thermal stress $\bar{\sigma}^{*}$, Eq. 2.1. [Seeger 1953, Klepaczko 1975, Zerilli and Armstrong 1987, Follansbee and Kocks 1988, Nasser and Isaacs 1997, Kocks 2001, Abed and Voyiadjis 2005, Voyiadjis and Almasri 2008]

$$\bar{\sigma} = \bar{\sigma}_{\mu} + \bar{\sigma}^{*} \tag{2.1}$$

A scheme of the evolution of the stress components as a function of temperature is depicted in Fig. 2.1. At low temperature, flow stress decreases with temperature. This region is influenced by thermal and athermal stress components. Next region with increasing temperature is basically athermal. At very high temperature, flow stress decreases again with increasing temperature. According to the considerations reported for example in [Voyiadjis and Almasri 2008], it must be pointed out that is not necessary for all metals to have the three regions here described.

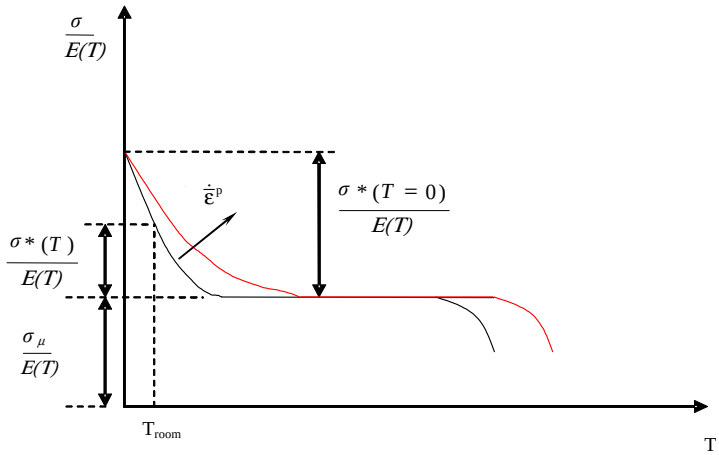

Fig. 2.1. Decomposition of normalized macroscopic stress versus temperature

Definition *(and contribution to the overall flow stress)* of thermal and athermal terms is dependent on the crystal structure of the material. The causes are related to the available symmetries of the lattice, the nature of the dislocation cores and the available slip systems as it is reported in [Lennon and Ramesh 2004].

In most **BCC** metals, overcoming Peierls stress resistance uses to be the main phenomenon involved in the thermally activated processes [Conrad 1961]. Consequently, the thermal component of the flow stress $\bar{\sigma}^* = \bar{\sigma}^*\left(\dot{\bar{\varepsilon}}^p, T\right)$ can be defined independent of plastic strain [Zerilli and Armstrong 1987, Rusinek and Klepaczko 2001, Nemat-Nasser and Guo 2003]. Initial yield stress of **BCC** metals is strongly temperature and rate dependent [Zerilli and Armstrong 1987, Voyiadjis and Abed 2005, Rusinek et al. 2005, Rusinek et al. 2007]. Strain hardening is primarily accomplished through long-range barriers [Kocks et al. 1975] such as grain boundaries, far field forest of dislocations and other micro-structural elements with far-field influence [Nemat-Nasser and Li 1998]. Temperature and deformation rate have relatively small effect on strain hardening, Fig. 2.2.

Moreover, Peierls stress in certain **FCC** metals is relatively unimportant [Voyiadjis and Abed 2005, Lennon and Ramesh 2004]. *(Determined exceptions to these observations can be found. For example many austenitic steels and certain aluminium alloys hardly show influence of strain on the rate sensitivity as it will be discussed later in this document).* The rate-controlling mechanism uses to be the overcoming of dislocation forests by individual dislocations [Voyiadjis and Abed 2005]. Thermal activation behaviour may become dependent on the plastic strain $\bar{\sigma}^* = \bar{\sigma}^*\left(\bar{\varepsilon}^p, \dot{\bar{\varepsilon}}^p, T\right)$ [Zerilli and Armstrong 1987, Nemat-Nasser and Li 1998, Voyiadjis and Abed 2005, Lennon and Ramesh 2004]. Such **FCC** metals use to exhibit large strain hardening due to an increase in the amount of dislocation interactions with increasing strain [Seeger 1957]. Strain hardening tends to be highly temperature and strain rate dependent, while the yield stress uses to have reduced dependence to such effects [Lennon and Ramesh 2004], Fig. 2.2.

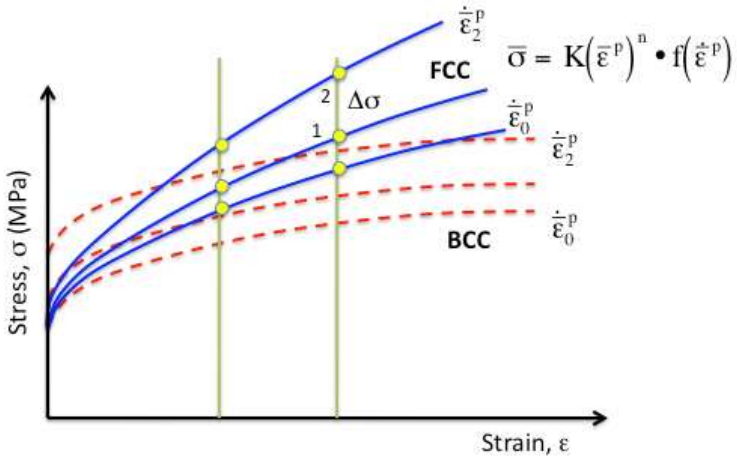

*Fig. 2.2. Strain rate sensitivity definition for **BCC** and **FCC** metals (the general case).*

In agreement with the previous considerations, the **V**olume **T**hermally **A**ctivated (**VTA**) defined by Eq. 2.2 [Taylor 1992, Uenishi and Teodosiu 2004, Klepaczko et al. 2009], decreases with plastic strain for such **FCC** metals *(rate sensitivity dependent on plastic strain)* [Basinski 1959, Zerilli and Armstrong 1987, Voyiadjis and Almasri 2008] while it is independent of deformation level for **BCC** metals [Armstrong and Campbell 1973, Voyiadjis and Almasri 2008].

$$V^* \approx k \cdot T \cdot \left. \frac{\partial \ln\left(\dot{\bar{\varepsilon}}^p\right)}{\partial \bar{\sigma}^*} \right|_T = k \cdot T \cdot \Psi\big|_T \quad \text{where} \quad \begin{cases} \Psi\left(\dot{\bar{\varepsilon}}^p\right)\big|_T & \text{rate sensitivity independent of platic strain} \\ \Psi\left(\bar{\varepsilon}^p, \dot{\bar{\varepsilon}}^p\right)\big|_T & \text{rate sensitivity dependent on platic strain} \end{cases} \tag{2.2}$$

In the previous expression, Eq. 2.2, *k* is the Boltzmann constant and T is the absolute temperature.

It is clear that different formulations are required in order to describe properly these two different behaviors. Such behaviours must be indentified analyzing experiments within wide ranges of strain and stain rate. In the present work two different constitutive descriptions are used depending on the effect that plastic strain may have on the rate sensitivity of the material. Furthermore, certain unconventional deformation behaviors of metals like dislocations drag at high strain rates, negative rate sensitivity or *martensitic* transformation have to be modeled if it is required an accurate description of the thermo-viscoplastic behaviour of metallic alloys under wide ranges of strain rate and temperature.

2.2 The Rusinek-Klepaczko constitutive relation

In order to model the behaviour of metallic alloys without effect of strain on the **VTA**, Rusinek and Klepaczko [Rusinek and Klepaczko 2001] proposed the constitutive relation which is reported in this section of the document, Eq. 2.2'.

$$V^* \approx k \cdot T \cdot \left. \frac{\partial \ln\left(\dot{\bar{\varepsilon}}^p\right)}{\partial \bar{\sigma}^*} \right|_T = k \cdot T \cdot \Psi\big|_T \quad \text{where} \quad \begin{cases} \Psi\left(\dot{\bar{\varepsilon}}^p\right)\big|_T & \text{(RK model)} \\ \Psi\left(\bar{\varepsilon}^p, \dot{\bar{\varepsilon}}^p\right)\big|_T & \text{(MRK model)} \end{cases} \tag{2.2'}$$

This constitutive description is the base of the models developed in this doctoral Thesis. Its strengths lie on a favourable macroscopic definition of the material behaviour under different types of solicitation and a formulation suitable for its implementation into **FE** codes. **RK** model is noted for its versatility and easy calibration procedure.

2.2.1 Literature review

The formulation of the **RK** model is based on the additive decomposition of the total stress, Eq. 2.3. The term acting as multiplicative factor of the stresses addition $E(T)/E_0$ defines the Young's modulus evolution with temperature [Klepaczko 1998], Eq. 2.4.

$$\bar{\sigma}\left(\bar{\varepsilon}^p, \dot{\bar{\varepsilon}}^p, T\right) = \frac{E(T)}{E_0}\left[\bar{\sigma}_\mu\left(\bar{\varepsilon}^p, \dot{\bar{\varepsilon}}^p, T\right) + \bar{\sigma}^*\left(\dot{\bar{\varepsilon}}^p, T\right)\right] \tag{2.3}$$

$$E\left(T\right) = E_0\left\{1 - \frac{T}{T_m}\exp\left[\theta^*\left(1 - \frac{T_m}{T}\right)\right]\right\} \qquad T>0 \tag{2.4}$$

Where E_0, T_m and θ^* denote respectively the Young's modulus at $T = 0\,K$, the melting temperature and the characteristic homologous temperature. This expression allows for defining the thermal softening depending on the crystal lattice [Rusinek et al. 2009b], Fig. 2.3. In the case of **BCC** metals

$\theta^* \approx 0.6$ and in the case of **FCC** metals $\theta^* \approx 0.9$ as reported in Rusinek at al. [Rusinek et al. 2009b].

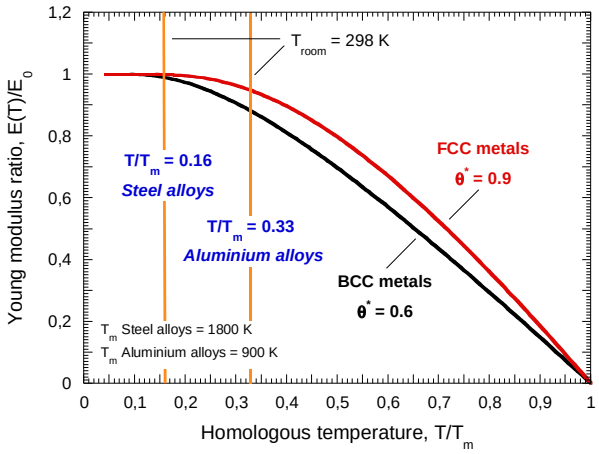

Fig. 2.3. Evolution of Young's modulus ratio for different θ values.*

The athermal stress is defined by Eq. 2.5.

$$\overline{\sigma}_{\mu}\left(\overline{\varepsilon}^{p},\dot{\overline{\varepsilon}}^{p},T\right)=B(\dot{\overline{\varepsilon}}^{p},T)(\varepsilon_0+\overline{\varepsilon}^{p})^{n(\dot{\overline{\varepsilon}}^{p},T)} \tag{2.5}$$

Where the modulus of plasticity $B\left(\dot{\overline{\varepsilon}}^{p},T\right)$ defines rate and temperature sensitivities of strain hardening, $n\left(\dot{\overline{\varepsilon}}^{p},T\right)$ is the strain hardening exponent depending on strain rate and temperature and ε_0 is the strain level which defines the yield stress at specific strain rate and temperature.

The explicit formulations describing the modulus of plasticity and the strain hardening exponent are given by Eqs. 2.6-2.7.

$$B\left(\dot{\overline{\varepsilon}}^{p},T\right)=B_0\left(\left(\frac{T}{T_m}\right)\log\left(\frac{\dot{\varepsilon}_{max}}{\dot{\overline{\varepsilon}}^{p}}\right)\right)^{-v} \qquad T>0 \tag{2.6}$$

$$n\left(\dot{\overline{\varepsilon}}^{p},T\right)=n_0\left\langle 1-D_2\left(\frac{T}{T_m}\right)\log\left(\frac{\dot{\overline{\varepsilon}}^{p}}{\dot{\varepsilon}_{min}}\right)\right\rangle \tag{2.7}$$

Where B_0 is the material constant, v is the temperature sensitivity, n_0 is the strain hardening exponent at T = 0 K, D_2 is the material constant, $\dot{\varepsilon}_{max}$ is the maximum strain rate accepted for a particular material and $\dot{\varepsilon}_{min}$ is the lower limit of the model. The McCauley operator is defined as $\langle\bullet\rangle=\bullet$ if $\langle\bullet\rangle\geq 0$ or $\langle\bullet\rangle=0$ if $\langle\bullet\rangle\leq 0$.

The effective stress $\overline{\sigma}^{*}\left(\dot{\overline{\varepsilon}}^{p},T\right)$ is the flow stress component which defines the rate dependent interactions with short range obstacles. It denotes the rate controlling deformation mechanism from thermal activation. At temperatures T > 0 K, thermal activation assists the applied stress.

The theory of thermodynamics and kinetics of slip ***(Appendix A)*** [Kocks et al. 1975] is founded on a set of equations which relate activation energy ΔG, mechanical threshold stress $\hat{\sigma}$ (**MTS**), applied stress $\overline{\sigma}$, strain rate $\dot{\overline{\varepsilon}}^{p}$, temperature T and determined physical material parameters. Based on such understanding of the material behaviour, Rusinek and Klepaczko [Rusinek and Klepaczko 2001] derived the following expression, Eq. 2.8. This formulation gathers the reciprocity between strain rate and temperature by means of an Arrhénius type equation.

$$\overline{\sigma}^{*}\left(\dot{\overline{\varepsilon}}^{p},T\right)=\sigma_{0}^{*}\left\langle 1-D_{1}\left(\frac{T}{T_{m}}\right)\log\left(\frac{\dot{\varepsilon}_{max}}{\dot{\overline{\varepsilon}}^{p}}\right)\right\rangle^{m^{*}} \tag{2.8}$$

Where σ_{0}^{*} is the effective stress at T = 0 K which is related to the **MTS**, D_1 is the material constant and m^{*} is the constant allowing to define the strain rate/temperature dependence [Klepaczko 1987].

In the case of adiabatic conditions of deformation the constitutive relation is combined with the energy balance principle, Eq. 2.9. Such relation allows for an approximation of the thermal softening of the material by means of the adiabatic heating.

$$\Delta T\left(\overline{\varepsilon}^{p},\overline{\sigma}\right)=\frac{\beta}{\rho C_{p}}\int_{0}^{\overline{\varepsilon}_{max}^{p}}\overline{\sigma}\left(\overline{\varepsilon}^{p},\dot{\overline{\varepsilon}}^{p},T\right)d\overline{\varepsilon}^{p} \tag{2.9}$$

where β is the Taylor-Quinney coefficient, ρ is the material density and C_p is the specific heat at constant pressure. Transition from isothermal to adiabatic conditions is assumed at $\dot{\overline{\varepsilon}}^{p}=10\ s^{-1}$ in agreement with experimental observations and numerical estimations reported for example in [Oussouaddi and Klepaczko 1991, Berbenni et al. 2004, Rusinek et al. 2005].

Subsequently is reported the straightforward method proposed by [Rusinek and Klepaczko 2001, Klepaczko et al. 2009] for the model calibration. It allows defining step by step the model-parameters. Contrary to other constitutive descriptions, the procedure does not involve a global fitting. It must be noticed that the constants are defined using physical assumptions [Rusinek and Klepaczko 2001, Klepaczko et al. 2009].

The main steps necessary for defining the model parameters are:

1. It is assumed that at low strain rate $\dot{\overline{\varepsilon}}^{p}\leq 0.001\ s^{-1}$ the stress contribution due to thermal activation is reduced and in this case the following relation is imposed, Eq. 2.10. Thus, it is possible to define the constant D_1 depending on the melting temperature T_m.

$$\begin{cases}\sigma^{*}\left(\dot{\overline{\varepsilon}}^{p},T\right)\Big|_{300\ K,0.001\ s^{-1}}=0\\ D_{1}=\left[\left(\frac{300}{T_{m}}\right)\log\left(\frac{\dot{\varepsilon}_{max}}{0.001}\right)\right]^{-1}\end{cases} \tag{2.10}$$

2. Therefore, at room temperature and under quasi-static loading the contribution of the thermal stress component to the total stress is zero, Eq. 2.11. The overall stress level is defined by Eq. 2.11. Fitting this equation to experiments a first estimation of B and n can be found.

$$\begin{cases} \bar{\sigma}\left(\bar{\varepsilon}^{p}, 0.001, 300\right) = \dfrac{E\left(300\right)}{E_0}\left[B(\varepsilon_0 + \bar{\varepsilon}^{p})^{n} + 0\right] \\ B, n \ \text{first approximation for next fitting} \end{cases} \qquad (2.11)$$

3. Next, it is assumed that the increase of the flow stress caused by the strain rate augment is due to the thermal stress $\bar{\sigma}^{*}\left(\dot{\bar{\varepsilon}}^{p}, T\right)$.Thus, the stress increase is defined as follows, Eq. 2.12. Fitting of Eq. 2.12. to experimental results for an imposed strain level makes possible to determine the material constants m^{*} and σ_0^{*}. The strain level should be assumed $\bar{\varepsilon}^{p} \leq 0.1$ in order to guarantee isothermal condition of deformation. For larger strain values, adiabatic condition may induce a thermal softening on the material and in such a case a decrease of the strain hardening.

$$\begin{cases} \Delta\bar{\sigma}\Big|_{0.001\,s^{-1}\rightarrow\dot{\bar{\varepsilon}}^{p}}^{\bar{\varepsilon}^{p}} = \bar{\sigma}\Big|_{\dot{\bar{\varepsilon}}^{p}}^{\bar{\varepsilon}^{p}} - \bar{\sigma}\Big|_{0.001\,s^{-1}}^{\bar{\varepsilon}^{p}} = \bar{\sigma}^{*}\left(\dot{\bar{\varepsilon}}^{p}, T\right)\Big|^{\bar{\varepsilon}^{p}} \\ \sigma_0^{*}, m^{*} \end{cases} \qquad (2.12)$$

4. Finally, it is applied the complete equation for the total stress, Eq. 2.3 combined with experimental results, $\bar{\sigma} - \bar{\varepsilon}^{p}\Big|_{\dot{\bar{\varepsilon}}^{p}}$. The stress dependency upon temperature and strain rate for the modulus of plasticity $B\left(\dot{\bar{\varepsilon}}^{p}, T\right)$ and the strain hardening exponent $n\left(\dot{\bar{\varepsilon}}^{p}, T\right)$ can be defined.

This model has proven capacity to describe the thermo-viscoplastic behaviour of the **ES** steel for wide ranges of strain rate and temperature as reported in [Rusinek and Klepaczko 2001, Rusinek et al. 2005, Rusinek and Zaera 2007, Rusinek et al. 2009a].

2.2.2 Applied method for modeling reference metallic alloys

Next, in order to demonstrate the versatility of this constitutive description, the **RK** model has been used to analyze the behaviour of other metallic alloys *(with **BCC** and **FCC** crystal lattices)* without dependence of plastic strain on the **VTA**. Thus, using the calibration procedure described previously, the behaviour of four different steel alloys has been modeled and compared with experimental results available in the international literature. The reference materials analyzed in this section of the document *(steel **DH-36**, steel **HSLA-65**, steel alloy **AL-6XN** and steel alloy **Uranus-B66**)* have particular interest for different industrial applications. Modeling of their thermo-viscoplastic behaviour will be assumed as representative of the capabilities of the **RK** model to describe macroscopically the deformation behaviour of metallic alloys. Strain, strain rate and temperature effects on the material flow stress are examined.

2.2.2.1 Ferritic steels (BBC structure)

The *ferritic* steels analyzed in this work consist of *ferrite–pearlitic* structure, where layers of *pearlite* lie between whole grains of *ferrite*. It is known that *ferrite* have lower strength and hardness, but higher plasticity and toughness, whereas *pearlite* has reversed properties. The added elements as

Ti, **Mn**, **Al** and **Cr** allow for carbon compatibility. These additive elements generate carbides which increases strength of steels.

2.2.2.1.1 Steel DH-36

Steel **DH-36** is a high strength structural steel used in marine applications as reported in [Nemat-Nasser and Guo, 2003]. The chemical composition of this steel is given in Table 2.1. The high strength is due to the carbon content which is relatively high 0.14%.

C	Mn	Cu	Si	Cr	Mo	V	Ti	Al	Nb	P	S
0.14	1.37	0.14	0.22	0.08	0.03	0.001	0.003	0.017	0.03	0.007	0.001

*Table 2.1. Chemical composition of the steel **DH-36** (% weight) [Nemat-Nasser and Guo, 2003].*

Although this steel is commonly used in shipbuilding, low attention has been focused on its thermo-viscoplastic behaviour. For this reason the work published by Nemat-Nasser and Guo [Nemat-Nasser and Guo, 2003], where an extensive analysis of the dynamic behaviour of this metal for different temperatures and strain rates is reported, has considerable interest.

The following set of material constants for calibration of the **RK** model has been found, Table 2.2.

B_0 (MPa)	ν (-)	n_0 (-)	D_2 (-)	ε_0 (-)	σ_0^* (MPa)	m^* (-)	D_1 (-)	T_m (K)	$\dot{\varepsilon}_{min}$ (s^{-1})	$\dot{\varepsilon}_{max}$ (s^{-1})	θ^* (-)
906.7	0.02	0.2	0.085	0.018	491.11	2.127	0.49	1600	10^{-5}	10^{7}	0.59

*Table 2.2. Constants determined for the steel **DH-36** for the **RK** model.*

Conventional physical constants of steel can be obtained from material handbooks, Table 2.3.

E_0 (GPa)	C_p ($Jkg^{-1}K^{-1}$)	β (-)	ρ (kgm^{-3})
200	470	0.9	7800

Table 2.3. Physical constants for steel.

The first comparisons of the analytical predictions of the model with experiments are performed via analysis of strain rate effect within the range $0.001\ s^{-1} \le \dot{\bar{\varepsilon}}^p \le 3000\ s^{-1}$, Fig. 2.4. It must be noticed that the flow stress level and the strain hardening of the material are well defined by the model predictions, Fig. 2.4. In addition, the material rate sensitivity is well described by the analytical predictions of the **RK** model, Fig. 2.5.

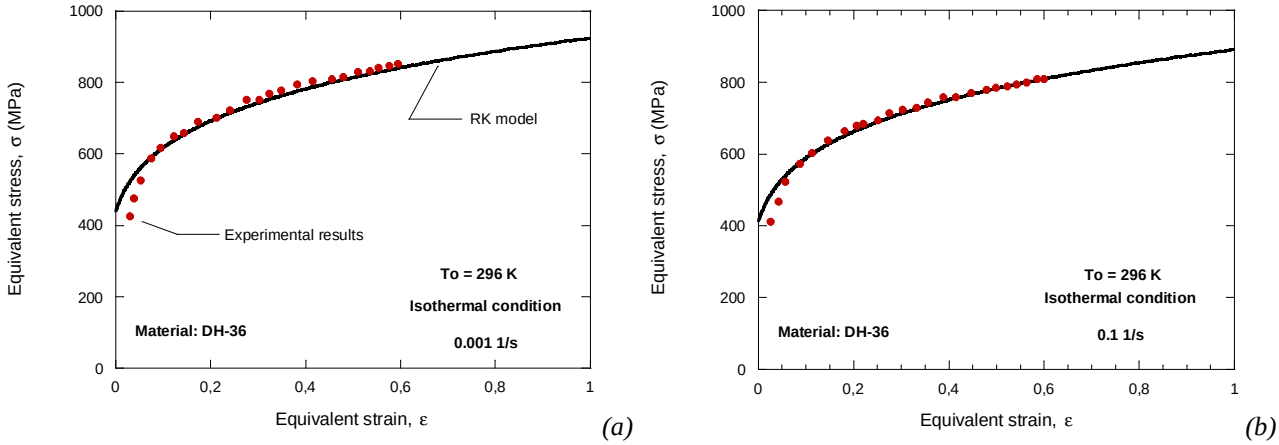

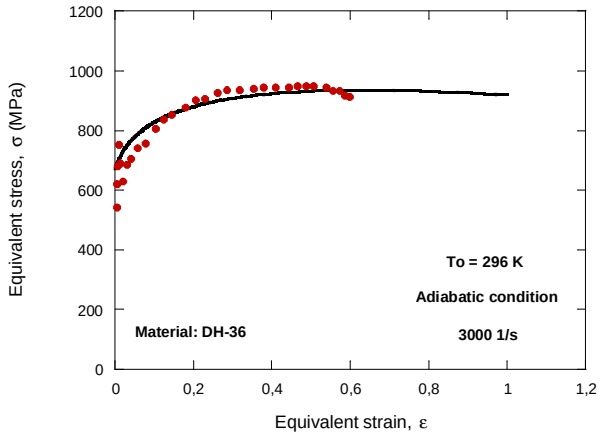

(c)

*Fig. 2.4. Comparison between analytical predictions (this Thesis) and experimental results for the steel **DH-36** [Nemat-Nasser and Guo, 2003] for different strain rate levels at room temperature. (a) 0.001 s^{-1}, (b) 0.1 s^{-1}(c) 3000 s^{-1}.*

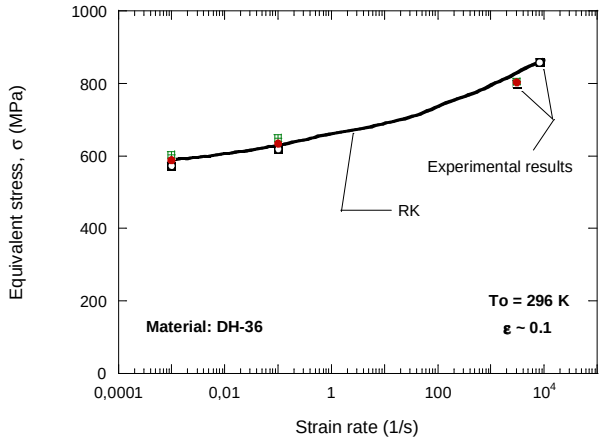

*Fig. 2.5. Comparison between modelling (this Thesis) and experiments [Nemat-Nasser and Guo, 2003] for the steel **DH-36**, ε_p=0.1 and room temperature.*

Next, analytical predictions of the model are compared with experiments for different initial temperatures. Satisfactory matching between model and experiments is observed, Fig. 2.6. The difference takes place only within the domain of the **D**ynamic **S**train **A**ging (**DSA**) temperatures, Fig. 2.6. The **RK** model cannot describe such effect and the predictions are limited to the adiabatic temperature increase without definition of the **DSA**, Fig. 2.6. The **DSA** appearance depends on the strain rate level [Nemat-Nasser and Guo 2003, Klepaczko et al. 2009], Fig. 2.6. If $\dot{\bar{\varepsilon}}^{p} \geq 3000\ \ s^{-1}$, the **DSA** effect vanishes and the analytical predictions are in agreement with experiments for the whole range of initial temperatures considered, Fig. 2.6-d.

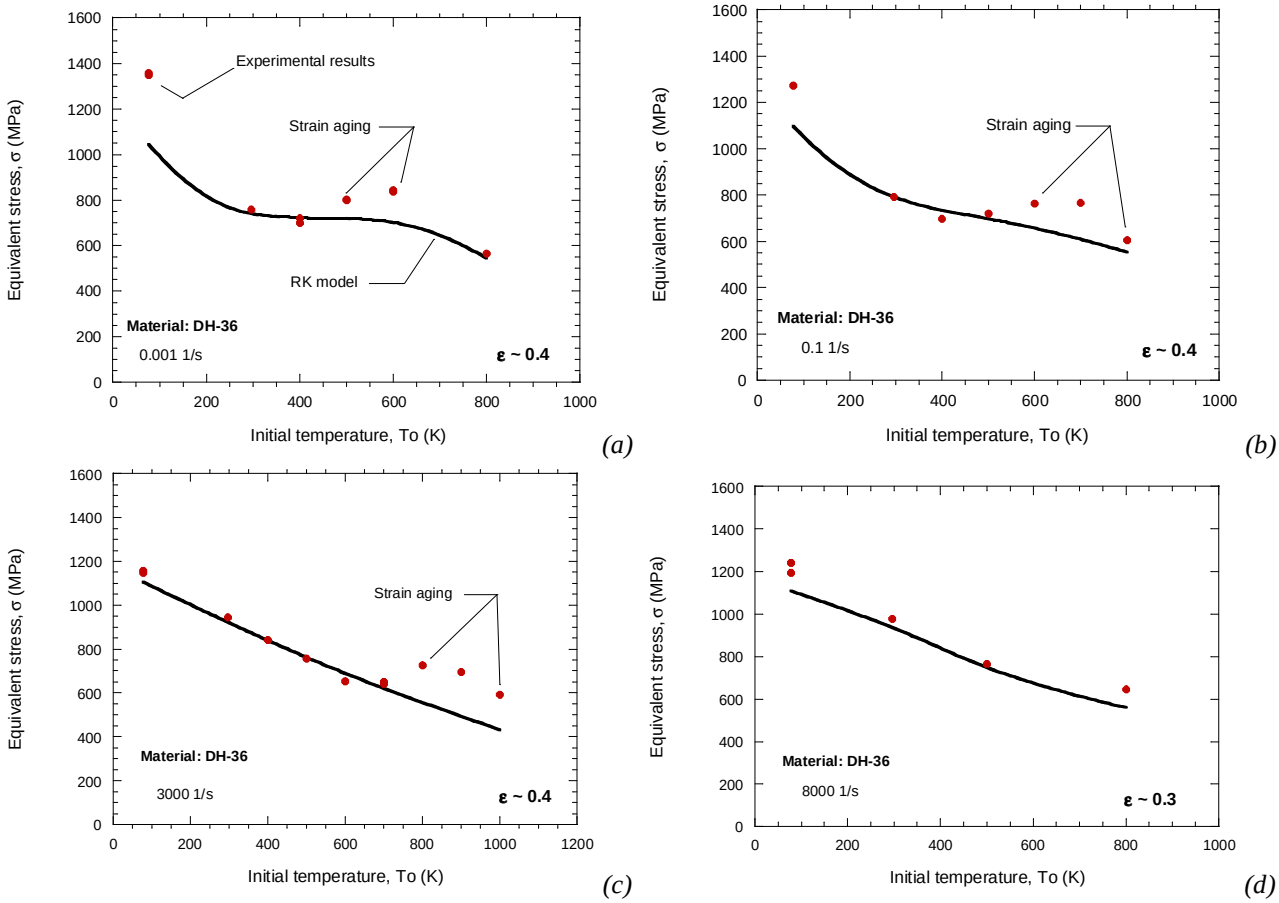

*Fig. 2.6. Temperature sensitivity description of the steel **DH-36** by the **RK** model, comparison with experimental results for ε_p=0.4 [Nemat-Nasser and Guo, 2003]. (a) 0.001 s^{-1}, (b) 0.1 s^{-1}, (c) 3000 s^{-1}, (d) 8000 s^{-1}.*

It must be pointed out that the definition of the thermo-viscoplastic behaviour of the steel **DH-36** provided by the **RK** model is better than that provided by other constitutive descriptions *(both those physical-based as well as those phenomenological)* as it was reported by Klepaczko et al. [Klepaczko et al. 2009].

Finally it is shown the description of the flow stress of the steel **DH-36** provided by the **RK** model within wide ranges of strain and strain rate, Fig. 2.7.

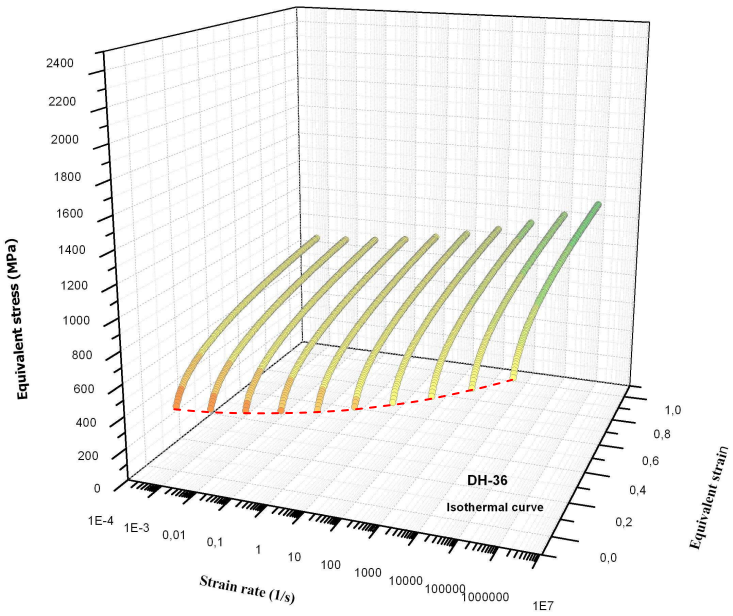

*Fig. 2.7. Description of the flow stress of the steel **DH-36** provided by the **RK** model within wide ranges of strain and strain rate.*

Next it is analyzed the thermo-viscoplastic behavior of the steel **HSLA-65**.

2.2.2.1.2 Steel HSLA-65

High-**S**trength **L**ow-**A**lloy steels (**HSLA**s) were initially developed in the 1960's. **HSLA** steels are also referred to as "micro alloyed", since they are indeed alloyed in extremely small amounts of alloying elements in comparison with other commercial steel alloys. The chemical composition in weight of the steel **HSLA-65** is reported in Table 2.4, [Nemat-Nasser and Guo 2005].

C	Mn	Cu	Si	Cr	Mo	V	Ti	Al	Nb	P	Ni	S
0.08	1.4	<0.01	0.24	0.01	0.02	0.07	0.01	0.03	0.04	0.005	<0.01	0.005

*Table 2.4. Chemical composition of the steel **HSLA-65** (% weight) [Nemat-Nasser and Guo 2005].*

The main advantages of **HSLA** steels are good combination of strength and toughness, coupled to good weldability. In particular, **HSLA-65** is suitable for use in the naval surface vessels and submarines.

The following set of material constants for the calibration of the **RK** model has been found, Table 2. 5.

B_0 (MPa)	ν (-)	n_0 (-)	D_2 (-)	ε_0 (-)	σ_0^* (MPa)	m^* (-)	D_1 (-)	T_m (K)	$\dot{\varepsilon}_{min}$ (s^{-1})	$\dot{\varepsilon}_{max}$ (s^{-1})	θ^* (-)
940	0.2	0.14	0.19	0.018	120	2.8	0.49	1600	10^{-5}	10^{7}	0.59

*Table 2.5. Constants determined for the steel **HSLA-65** for the **RK** model.*

In Fig. 2.8. the analytical predictions of the constitutive description are compared with experimental results for different strain rates and temperatures. In the tests performed by [Nemat-Nasser and Guo 2005], strain rate and temperature varied within the ranges $0.001\ s^{-1} \le \dot{\bar{\varepsilon}}^p \le 8500\ s^{-1}$ and $77\ K \le T_0 \le 700\ K$ respectively. It is shown in Fig. 2.8. that the **RK** model predicts correctly the strain rate effect on the plastic behaviour of the material. In addition the flow stress level and the

strain hardening of this steel are properly defined. It must be noticed that the material thermal softening due to adiabatic heating at high strain rates is well described, Fig. 2.8.

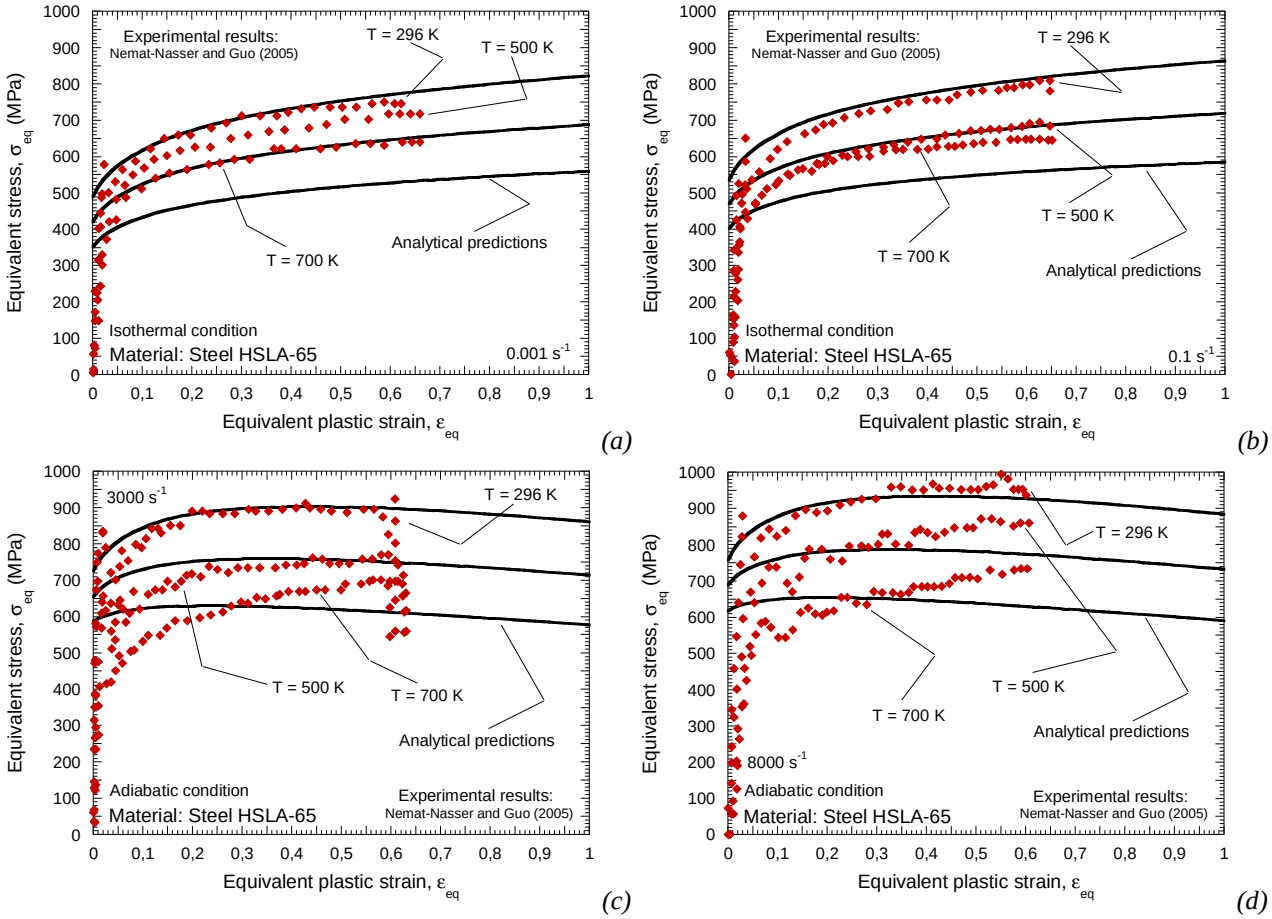

*Fig. 2.8. Comparison between analytical predictions of the **RK** model and experimental results [Nemat-Nasser and Guo 2005] for the steel **HSLA-65**.*

Concerning the temperature sensitivity, the model allows for a correct approximation of the experimental results for a wide range of initial temperatures, Fig. 2.9. As it was pointed out for the steel **DH-36**, in the case of the **HSLA-65** the difference between analytical predictions and experiments only takes place within the domain of the **DSA** effect, Fig. 2.9.

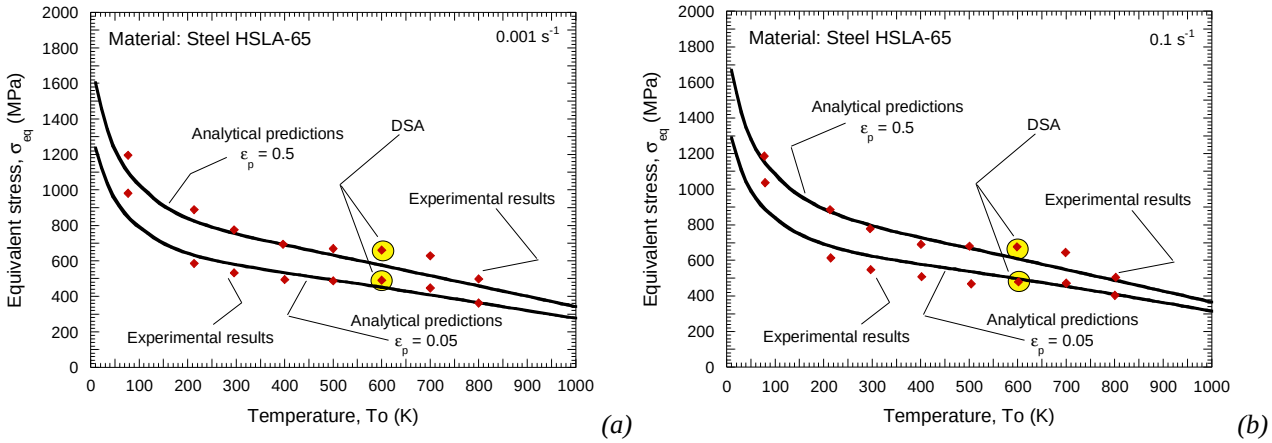

*Fig. 2.9. Temperature sensitivity description of the steel **HSLA-65** by the **RK** model, comparison with experimental results for ε_p=0.05 and ε_p=0.5 [Nemat-Nasser and Guo 2005]. (a) 0.001 s^{-1}, (b) 0.1 s^{-1}.*

Next, the flow stress definition provided by the **RK** model for wide ranges of strain and strain rate is illustrated, Fig. 2.10.

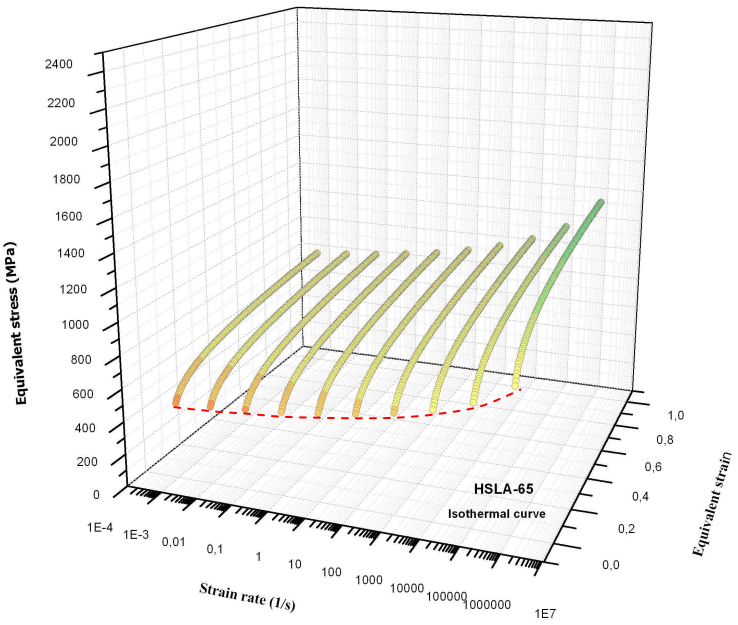

*Fig. 2.10. Description of the flow stress of the steel **HSLA-65** provided by the **RK** model within wide ranges of strain and strain rate.*

In the following section of the document is examined the thermo-viscoplastic behaviour of *austenitic* steels without dependence of plastic strain on the strain rate sensitivity.

2.2.2.2 Austenitic steels (FCC structure)

Austenitic steels generally have a relatively low initial yield stress and they are characterized by a high work hardening. The formation of twins may occur enhanced by the low **S**tacking **F**ault **E**nergy (**SFE)** of these steels *(**TWIP** steels)*. This causes high dislocation accumulation leading to great strain hardening rate, Fig. 2.11. The strength of *austenitic* steels increases with **C** content, **N** and, to a certain extent, also **Mo**. These steels use to exhibit very high ductility and toughness. The yield stress increases in the case of presence of *ferrite (duplex steels)*, which makes the material stronger, but it reduces work hardening and ductility. Opposite mechanical properties than those exhibited by the *austenitic* steels are shown by the *martensitic* steels, which are characterized by very high initial yield stress and reduced failure strain level, Fig. 2.11.

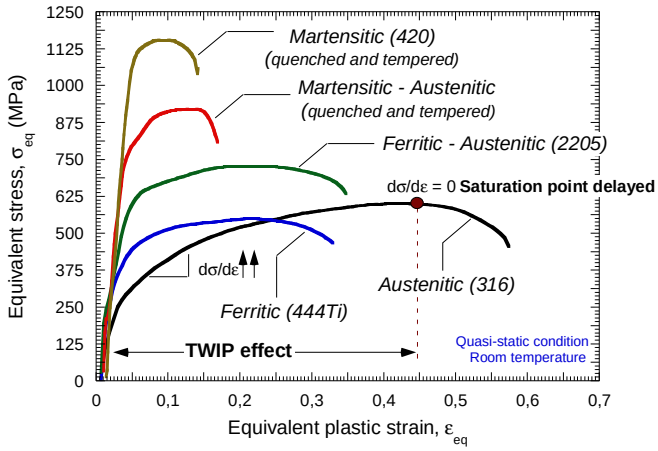

Fig. 2.11. Comparison between different types of stainless steels [Rusinek et al. 2009b].

In the following sections of this document two different *austenitic* steel alloys are analyzed and modeled using the **RK** constitutive description.

2.2.2.2.1 Steel alloy AL-6XN

AL-6XN is a relatively new nitrogen-strengthened *austenitic* steel alloy. This alloy combines high strength and good fabricability with excellent corrosion and pitting resistance to a wide variety of applications. The chemical composition of the steel alloy **AL-6XN** is reported in Table 2.6. [Nemat-Nasser et al. 2001]. As reported by [Nemat-Nasser et al. 2001] the main difference between this alloy and other *austenitic* steel alloys, as for example the **Nitronic-50** [Guo and Nemat-Nasser 2006], is that the **AL-6XN** contains higher level of **Ni** and **Mo**, which stabilizes *austenite (reducing the potential martensitic transformation caused by material straining)*, [Denhard and Espy 1972] and improves pitting and corrosion resistance [Brooks and Lippold 1990].

C	**Mn**	**Cu**	**Ni**	**Si**	**Cr**	**Mo**	**N**
0.024	0.41	0.2	23.84	0.36	20.56	6.21	0.213

*Table 2.6. Chemical composition of the steel alloy **AL-6XN** (% weight) [Nemat-Nasser et al. 2001].*

This steel alloy is currently used in production of nuts, bolts and other fasteners, tube and pipe systems for pulp and paper, distillation and other industrial equipment.

The following set of material constants for calibration of the **RK** model has been found, Table 2.7.

B_0 (MPa)	ν (-)	n_0 (-)	D_2 (-)	ε_0 (-)	σ_0^* (MPa)	m^* (-)	D_1 (-)	T_m (K)	$\dot{\varepsilon}_{min}$ (s^{-1})	$\dot{\varepsilon}_{max}$ (s^{-1})	θ^* (-)
1627.4	0.012	0.438	0.05	0.018	802.25	2.471	0.49	1600	10^{-5}	10^{7}	0.9

*Table 2.7. Constants determined for the steel alloy **AL-6XN** for the **RK** model.*

The analysis of the strain rate effect on the plastic behaviour of this material is reported in the form of stress-strain curves, Fig. 2.12. The comparison of analytical predictions with experiments is conducted within the range $10^{-3}\ s^{-1} \le \dot{\bar{\varepsilon}}^p \le 8.3 \cdot 10^{3}\ s^{-1}$ at room temperature. High work hardening and large ductility are shown by this material. It is observed for the whole range of strain rates considered a proper agreement between experiments and modeling, Fig. 2.12.

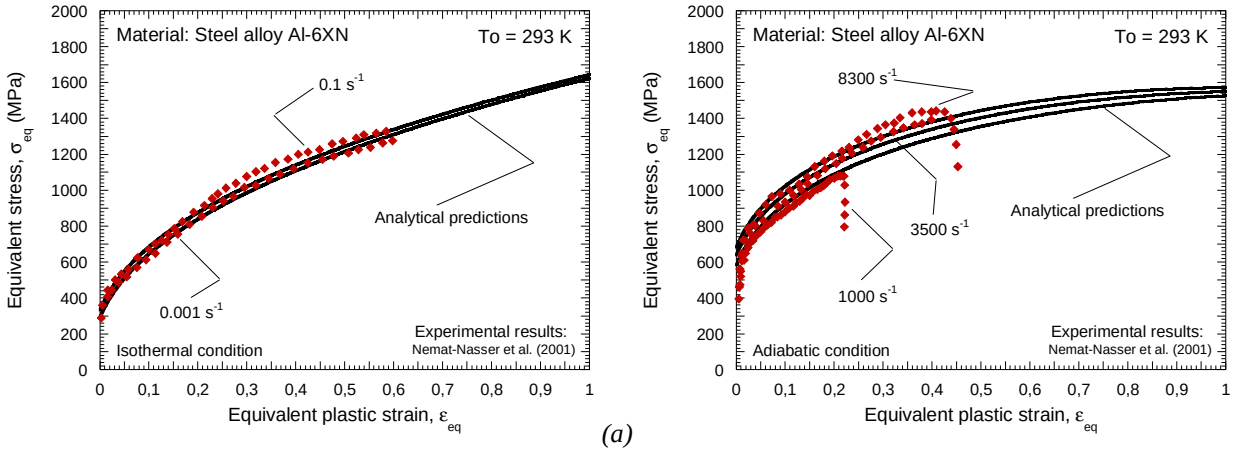

*Fig. 2.12. Strain rate effect on the plastic behaviour of the steel alloy **AL-6XN**, comparison between **RK** model and experimental results [Nemat-Nasser et al. 2001]. (a) Isothermal conditions of deformation. (b) Adiabatic conditions of deformation.*

The second comparison concerns the high strain rate behaviour for different initial temperatures, Fig. 2.13. The range of initial temperatures covered is 77 K $\leq T_0 \leq$ 1000 K. Good matching is observed between experimental results and model predictions.

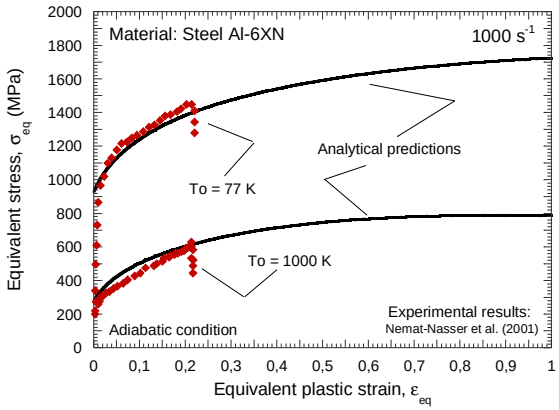

*Fig. 2.13. Temperature effect on the plastic behaviour of the steel alloy **AL-6XN**. Comparison between **RK** model and experiments [Nemat-Nasser et al. 2001].*

Next it is shown the description of the flow stress of the steel alloy **AL-6XN** predicted by the **RK** model within wide ranges of strain and strain rate, Fig. 2.14.

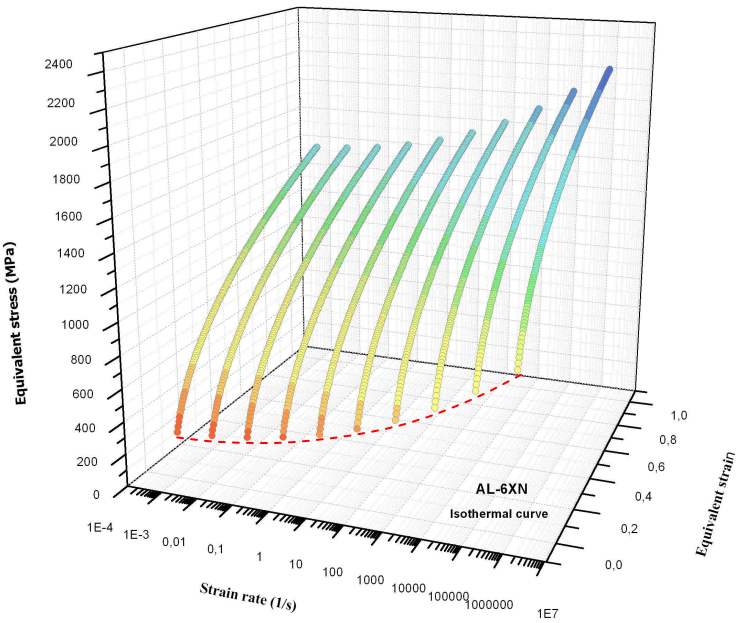

*Fig. 2.14. Description of the flow stress of the steel alloy **AL-6XN** predicted by the **RK** model within wide ranges of strain and strain rate.*

Subsequently is analyzed the thermo-viscoplastic behavior of the steel alloy **Uranus-B66**.

2.2.2.2.2 Steel alloy Uranus-B66

The **Uranus-B66** is a recently developed nitrogen-strengthened *austenitic* steel alloy. This alloy has improved corrosion resistance, particularly in sea water. Moreover, the **Uranus-B66** presents attractive mechanical properties like high strength, ductility and toughness. This notable behaviour is enhanced by the presence of **N** in solid solution, [Frechard et al. 2008, Frechard et al. 2006]. The chemical composition of the **Uranus-B66** steel alloy is reported in Table 2.8., [Frechard et al. 2008].

C	Mn	Cu	Cr	Ni	Mo	N	W
0.02	3.7	1.4	23.8	21.2	5.5	0.47	2.4

*Table 2.8. Chemical composition of the steel alloy **Uranus-B66** (% weight) [Frechard et al. 2008].*

Thus, this material presents a great interest in several engineering fields like marine structures, nuclear and chemical industries or ballistic applications, [Magness 1994, Couque et al. 2000]. In the present work, the experimental data provided by [Frechard et al. 2008] are used to obtain the values of the material constants of the **RK** formulation. The following set of constants has been found, Table 2.9.

B_0 (MPa)	ν (-)	n_0 (-)	D_2 (-)	ε_0 (-)	σ_0^* (MPa)	m^* (-)	D_1 (-)	T_m (K)	$\dot{\varepsilon}_{min}$ (s^{-1})	$\dot{\varepsilon}_{max}$ (s^{-1})	θ^* (-)
2100.4	0.003	0.455	0.012	0.018	874.61	1.648	0.49	1600	10^{-5}	10^{7}	0.9

*Table 2.9. Constants determined for the steel alloy **Uranus-B66** for the **RK** model.*

As discussed before, in the case of the steel alloy **AL-6XN**, the **Uranus-B66** presents high work hardening and large ductility *(enhanced by **TWIP** effect)*. The notorious strength level showed by this steel is enhanced by the additive elements **N** and **Mb**, Fig. 2.15. Satisfactory agreement is obtained between **RK** model predictions and experiments for different strain rates at room temperature, Fig. 2.15.

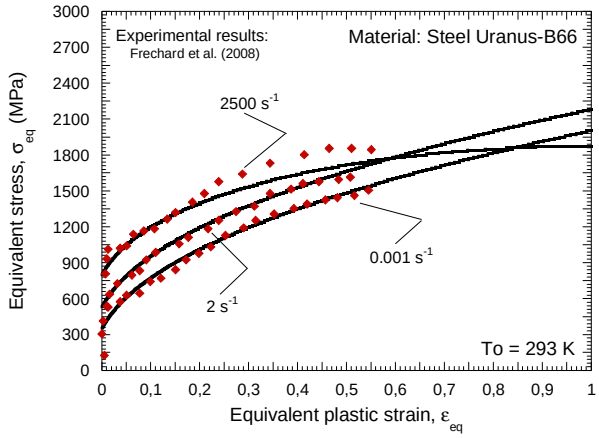

Fig. 2.15. Flow stress evolution as a function of plastic strain for different strain rates. Comparison between modelling and experiments [Frechard et al. 2008].

Moreover, it is shown in Fig. 2.16. that the **RK** constitutive relation is suitable for describing the strain rate sensitivity of this material. Good matching between experiments and analytical predictions is observed from static to dynamic loading, $0.01\ s^{-1} \le \dot{\varepsilon}^p \le 10^3\ s^{-1}$.

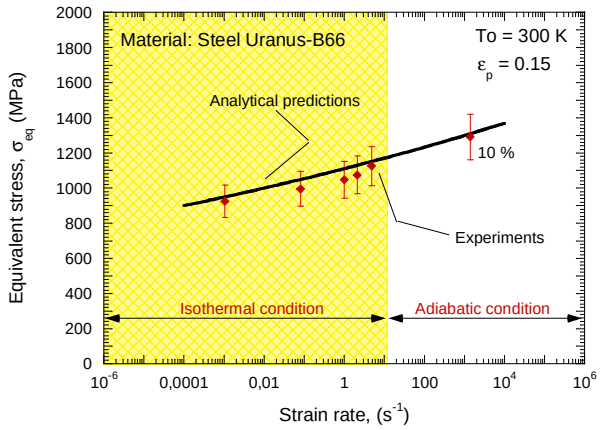

*Fig. 2.16. Strain rate sensitivity of the **Uranus-B66**. Comparison between modelling and experiments [Frechard et al. 2008].*

In addition in Fig. 2.17. is illustrated the flow stress evolution as a function of plastic strain for different initial temperatures under static and dynamic solicitations. The model describes satisfactorily the flow stress level and the strain hardening of the material for wide ranges of temperatures, Fig. 2.17.

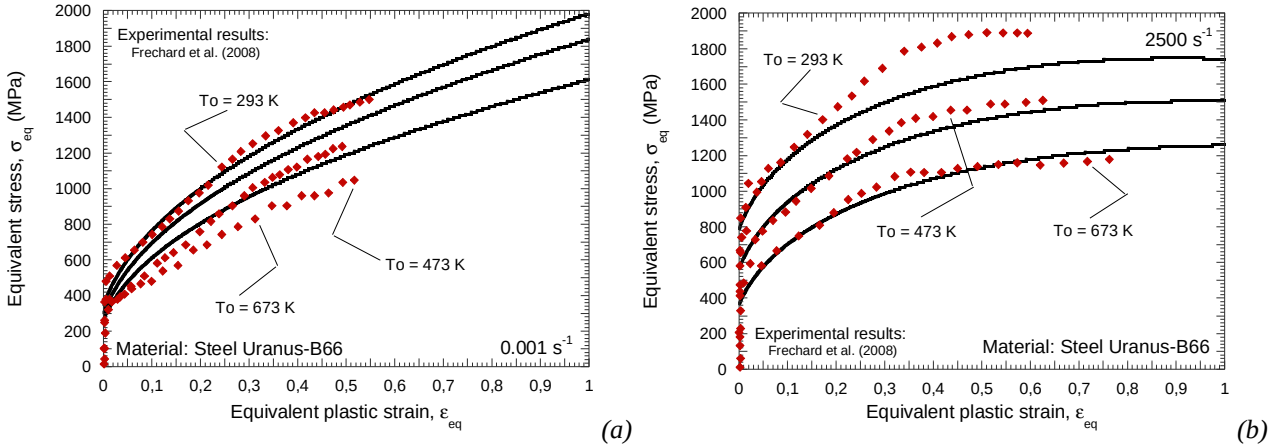

Fig. 2.17. Flow stress evolution as a function of plastic strain for different initial temperatures. Comparison between modelling and experiments [Frechard et al. 2008]. (a) 10^{-3} s^{-1}, (b) $2.5 \cdot 10^{3}$ s^{-1}.

The absence of an athermal region in the material behaviour is well described by the constitutive relation, Fig. 2.18. The difference between analytical predictions and experiments is less than 10 %.

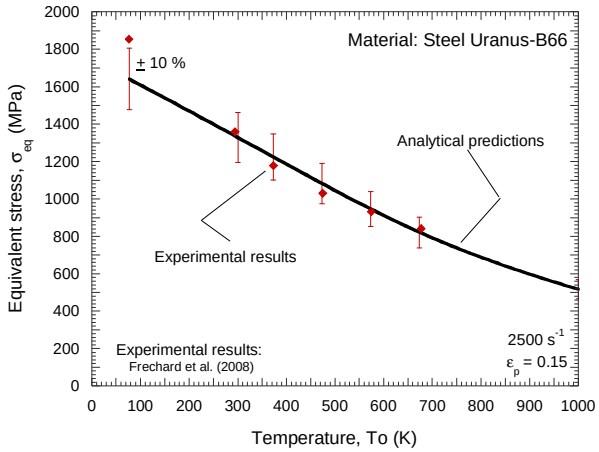

Fig. 2.18. Flow stress evolution as a function of the initial temperature. Comparison between analytical predictions and experiments [Frechard et al. 2008]. Strain rate 0.1 s^{-1} and ε_p= 0.15.

Finally is shown the description of the flow stress of the steel **Uranus-B66** predicted by the **RK** model within wide ranges of strain and strain rate, Fig. 2.19.

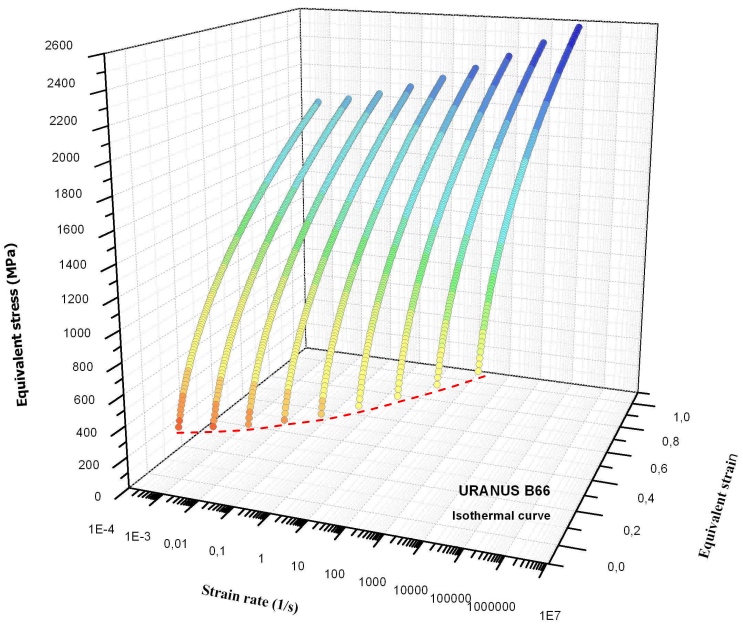

*Fig. 2.19. Description of the flow stress of the steel alloy **Uranus-B66** predicted by the **RK** model within wide ranges of strain and strain rate.*

Thus, in this section of the document has been modeled and studied the deformation behaviors of four reference metallic alloys by means of the **RK** constitutive description. Satisfactory agreement between analytical predictions and experiments has been found for the whole ranges of strain rate and temperature analyzed.

Next, an original constitutive description for modeling the thermo-viscoplastic behaviour of metallic alloys with dependence of strain on the **VTA** is proposed.

2.3 The Modified Rusinek-Klepaczko constitutive relation

The new model (**MRK**), based on the original **RK** formulation, is described below. It is suitable for defining the behaviour of metals with dependence of plastic strain on the strain rate sensitivity, Eq. 2.2''.

$$V^{*} \approx k \cdot T \cdot \left. \frac{\partial \ln\left(\dot{\bar{\varepsilon}}^{p}\right)}{\partial \bar{\sigma}^{*}} \right|_{T} = k \cdot T \cdot \Psi\big|_{T} \quad \text{where} \quad \begin{cases} \Psi\left(\dot{\bar{\varepsilon}}^{p}\right)\big|_{T} & \text{(RK model)} \\ \Psi\left(\bar{\varepsilon}^{p}, \dot{\bar{\varepsilon}}^{p}\right)\big|_{T} & \text{(MRK model)} \end{cases} \tag{2.2''}$$

2.3.1 Formulation developed

As for the original **RK** constitutive description, the formulation of the model is based on the additive decomposition of the total stress, Eq. 2.13.

$$\bar{\sigma} = \frac{E(T)}{E_0} \cdot \left[\bar{\sigma}_{\mu} + \bar{\sigma}^{*} \right] \tag{2.13}$$

Where the Young's modulus evolution with temperature is defined as in the **RK** model, Eq. 2.4.

According to the considerations reported for example in [Zerilli and Armstrong 1987, Voyiadjis and Almasri 2008, Voyiadjis and Abed 2005, Follansbee and Kocks 1988] let us assume the athermal stress $\overline{\sigma}_{\mu}$ independent of plastic strain. As it was previously discussed, the initial yield stress of such kind of metals *(with dependence of plastic strain on the **VTA**)* may show reduced rate and temperature dependences *(certain temperature effect is taken into account by the Young's modulus temperature dependent)*. In agreement with [Voyiadjis and Almasri 2008] the athermal stress will be just tied to the initial yield stress in the form, Eq. 2.14.

$$\overline{\sigma}_{\mu} = Y \tag{2.14}$$

Where Y is the flow stress on plastically undeformed material.

The definition of the thermal stress is based on the formulation proposed by Rusinek and Klepaczko [Rusinek and Klepaczko 2001]. However, now it is necessary to include the effect of the plastic strain on the rate sensitivity of the material, Eq. 2.15.

$$\overline{\sigma}^{*}\left(\overline{\varepsilon}^{p},\dot{\overline{\varepsilon}}^{p},T\right)=\sigma_{0}^{*}\left(\overline{\varepsilon}^{p}\right)\cdot\left\langle 1-\xi_{1}\left(\frac{T}{T_{m}}\right)\log\left(\frac{\dot{\varepsilon}_{max}}{\dot{\overline{\varepsilon}}^{p}}\right)\right\rangle^{1/\xi_{2}} \tag{2.15}$$

In agreement with the considerations reported in [Zerilli and Armstrong 1987, Voyiadjis and Abed 2005] such dependence may be formulated by Eq. 2.16.

$$\overline{\sigma}_{0}^{*}\left(\overline{\varepsilon}^{p}\right)=B\cdot\left(\overline{\varepsilon}^{p}\right)^{n} \tag{2.16}$$

However, strain hardening is intrinsically dependent on strain rate and temperature. Based on the formulation derived in [Rusinek and Klepaczko 2001], a more suitable expression *(in comparison with Eq. 2.16.)* is proposed Eq. 2.17.

$$\overline{\sigma}_{0}^{*}\left(\overline{\varepsilon}^{p},\dot{\overline{\varepsilon}}^{p},T\right)=B\left(\dot{\overline{\varepsilon}}^{p},T\right)\cdot\left(\overline{\varepsilon}^{p}\right)^{n\left(\dot{\overline{\varepsilon}}^{p},T\right)} \tag{2.17}$$

Therefore, Eq. 2.16. becomes rate and temperature dependent, Eq. 2.17. Thus, the model considers the dependences on strain and on strain rate exhibited by the **MTS** [Follansbee and Kocks 1988]. This definition is consistent with the dominance of the dislocation-obstacle interactions in the plastic deformation of polycrystalline metals [Follansbee and Kocks 1988, Lennon and Ramesh 2004]. The modulus of plasticity $B\left(\dot{\overline{\varepsilon}}^{p},T\right)$, defines rate and temperature sensitivities on strain hardening, Eq. 2.6. Moreover $n\left(\dot{\overline{\varepsilon}}^{p},T\right)$ is the strain hardening exponent dependent on strain rate and temperature Eq. 2.7.

Next, a systematic procedure for the model calibration is proposed

2.3.2 Systematic procedure for calculation of the model parameters

As for the original **RK** model, the constants of the **MRK** relation are defined using physical assumptions.

The main steps necessary for defining the model parameters are:

1. The athermal component of the flow stress, *Y*, is estimated as the initial yield stress [Follansbee and Kocks 1988].

2. Subsequently, resorting on experimental data at different initial temperatures, is plotted the flow stress level evolution as a function of temperature for different plastic strain levels under quasi-static loading [Voyiadjis and Almasri 2008], Fig. 2.20-a. For each plastic strain level, let us assume, as first approximation, that the experimental data follow a linear trend [Voyiadjis and Almasri 2008], Fig. 2.20-a. The intersection of the fitting curves with T = 0 K are represented as a function of the plastic deformation *(**MTS** evolution as a function of the plastic deformation)*. Those points are fitted with Eq. 2.17, Fig. 2.20-b. A first estimation for *B* and *n* is obtained.

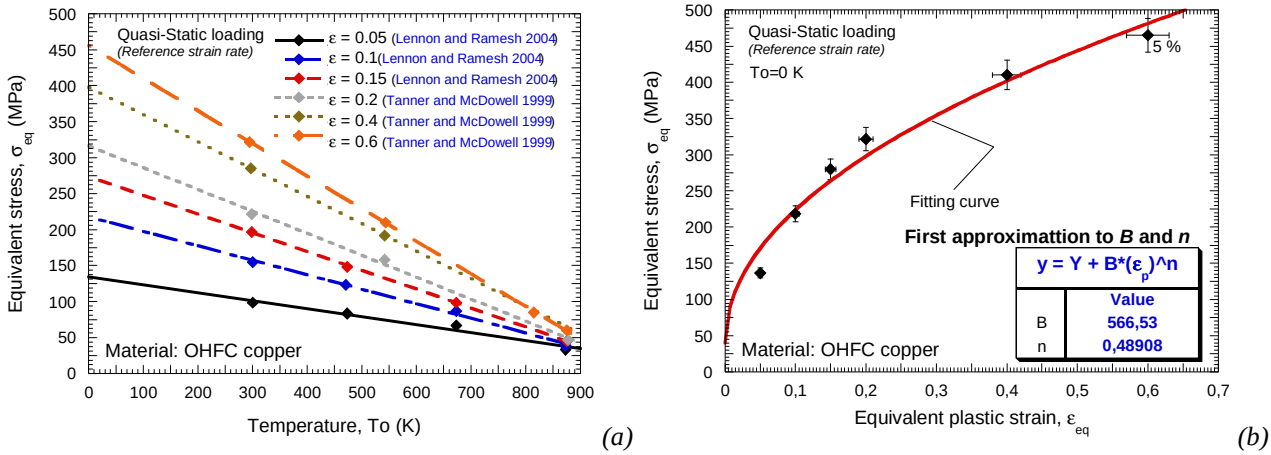

*Fig. 2.20. (a) Evolution of the flow stress as a function of the initial temperature for different deformation levels [Lennon and Ramesh 2004, Tanner and McDowell 1999] and fitting following a linear trend. (b) Flow stress evolution at T=0 K (**MTS**) as a function of plastic deformation, and fitting using the strain hardening function.*

3. It is assumed that the increase of the total stress with the strain rate is caused by the thermal stress $\bar{\sigma}^*\left(\bar{\varepsilon}^p, \dot{\bar{\varepsilon}}^p, T\right)$.Thus, the stress increase is defined as follows, Eq. 2.18.

$$\Delta\bar{\sigma}\left(\dot{\bar{\varepsilon}}^p_{reference} \rightarrow \dot{\bar{\varepsilon}}^p\right)\Big|_{\bar{\varepsilon}^p} = \bar{\sigma}\left(\dot{\bar{\varepsilon}}^p\right)\Big|_{\bar{\varepsilon}^p} - \bar{\sigma}\left(\dot{\bar{\varepsilon}}^p_{reference}\right)\Big|_{\bar{\varepsilon}^p} = \bar{\sigma}^*\left(\dot{\bar{\varepsilon}}^p, T\right)\Big|_{\bar{\varepsilon}^p} \qquad (2.18)$$

By combination of Eq. 2.15 with experimental results for an imposed strain level, $\bar{\varepsilon}^p$, it is possible to determine the material constants ξ_1 and ξ_2. The strain level should be assumed $\bar{\varepsilon}^p \leq 0.1$ as previously discussed.

4. The last step is equivalent to that defined in the original **RK** model, **Section 2.2.1**.

2.3.3 Applied method for modeling reference metallic alloys

The model is applied to describe the behaviour of annealed **OFHC** copper. This material shows high dependence of plastic strain on the **VTA**, strain hardening strongly varies with strain rate and temperature [Nemat-Nasser and Li 1998] *(such characteristic is common to most annealed **FCC***

metals). Such behaviour makes this material propitious for validation of the **Modified Rusinek-Klepaczko** formulation. By means of the procedure reported in the previous section, the model has been calibrated using the experimental data collected from [Nemat-Nasser and Li 1998, Follansbee 1986, Lennon and Ramesh 2004, Tanner and McDowell 1999]. The following set of constants has been found, Table 2.10.

Y (MPa)	B_0 (MPa)	ν (-)	n_0 (-)	D_2 (-)	ξ_2 (-)	ξ_1 (-)	T_m (K)	$\dot{\varepsilon}_{min}$ (s^{-1})	$\dot{\varepsilon}_{max}$ (s^{-1})	θ^* (-)
40	560.28	0.30447	0.492	0.0553	0.0131	0.0011932	1340	10^{-5}	10^{7}	0.9

*Table 2.10. Constants determined for annealed **OFHC** copper for thermal and athermal components of the **MRK** model.*

Conventional physical constants of **OFHC** copper can be obtained from material handbooks, Table 2.11.

E_0 (GPa)	C_p ($Jkg^{-1}K^{-1}$)	β (-)	ρ (kgm^{-3})
130	385	0.9	8960

*Table 2.11. Physical constants for annealed **OFHC** copper.*

Copper is a ductile metal with very high thermal and electrical conductivity. Such properties make it attractive in electrical applications, piping, manufacture of semiconductors and super conductor components. It also finds application for shaped-charges liner. This part of shaped charges is responsible for forming the jet which penetrates the target [Rosenberg et al. 2009, Ayisit 2008]. Liner-material is required of excellent ductility and high density in order to avoid fragmentation of the jet during penetration. This problem of instabilities formation and subsequent fragmentation is of main interest for industrial applications and it will be approached in the following chapter of this Thesis. Particularly, shaped charges are frequently used for military applications, although the most extensive use today of shaped charges is in the oil and gas industry to pierce metal, concrete, and other solid materials [Rosenberg et al. 2009, Ayisit 2008]. Next, the predictions of the **MRK** model are compared with experiments.

The first step is to evaluate the predictions of the **MRK** model for different strain rate levels at room temperature, Fig. 2.21. At low strain rate the model predicts properly the material behaviour in terms of flow stress level and strain hardening rate up to a plastic strain level close to $\bar{\varepsilon}^p \approx 1$, Fig. 2.21-a-b. However, at high strain rates Fig. 2.21-c, the difference takes place. The model underestimates the material flow stress although the hardening rate is well described.

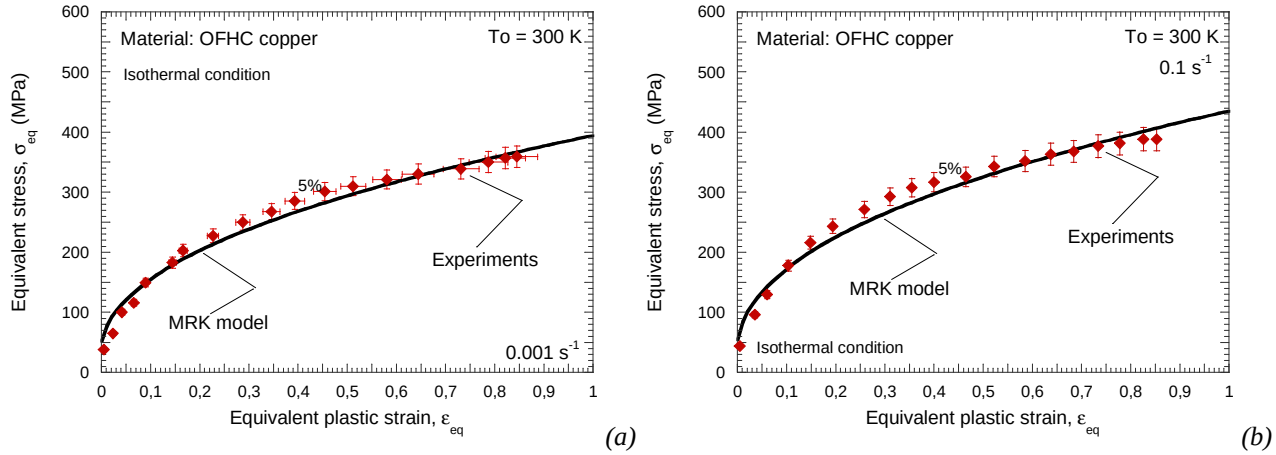

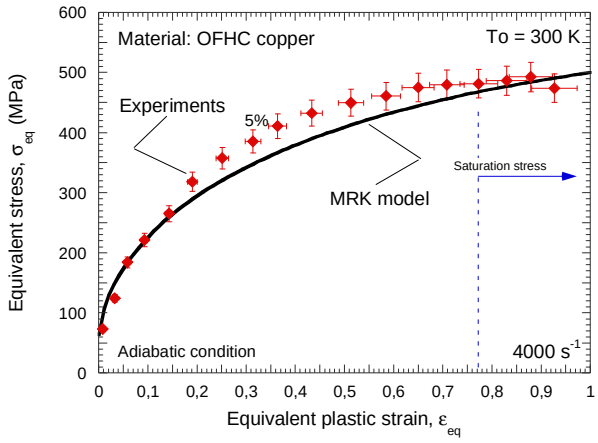

*Fig. 2.21. Description of the flow stress evolution as a function of the plastic strain by the **MRK** model and comparison with experiments at room temperature [Nemat-Nasser and Li 1998]. (a) 0.001 s^{-1}, (b) 0.1 s^{-1}, (c) 4000 s^{-1}.*

In order to examine the disagreement between model predictions and experiments at high strain rates the following analysis is conducted.

First, it is noticed that thanks to the dependence of the **VTA** on plastic strain included into the model formulation, the **MRK** constitutive relation is able to describe the material behaviour within the range of strain rates $10^{-3}\ s^{-1} \le \dot{\bar{\varepsilon}}^{p} \le 10^{3}\ s^{-1}$. The model defines properly the changes in the rate sensitivity that the material exhibits due to variations in the plastic deformation, Fig. 2.22. However, in the case of $\dot{\bar{\varepsilon}}^{p} \ge 10^{3}\ s^{-1}$ the rate sensitivity of the material drastically changes, the flow stress suddenly increases. The Arrhenius-type equation used to derive the thermal stress component of the model *(an Arrhenius-type equation was also used to derive the thermal stress component of the **RK** model)* cannot reproduce such behaviour [Rusinek et al. 2010].

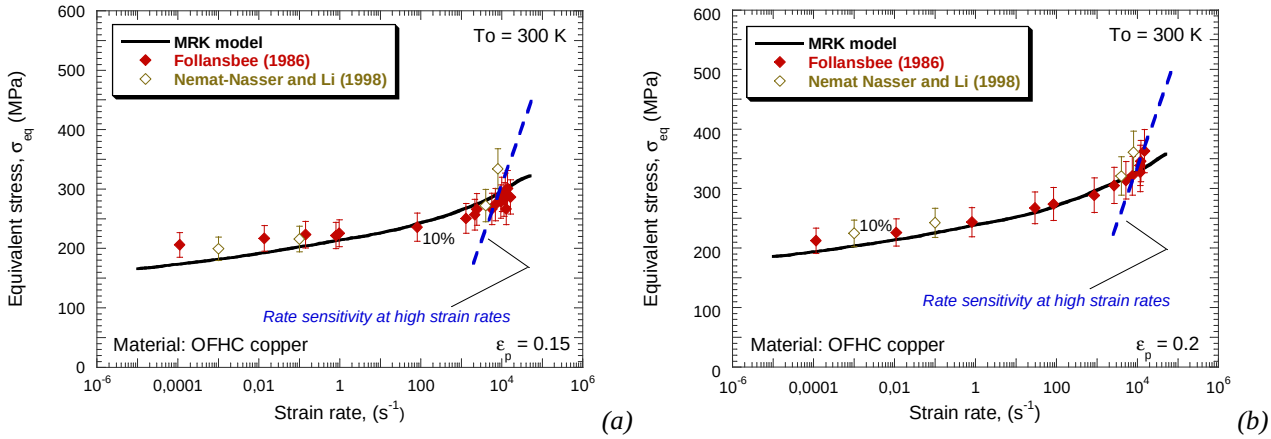

*Fig. 2.22. Description of the flow stress evolution as a function of strain rate by the **MRK** model and comparison with experiments at room temperature, ε_p=0.2 [Nemat-Nasser and Li 1998].*

The difference between model predictions and experiments taking place at high strain rates is extended to the whole range of initial temperatures evaluated, Fig. 2.23.

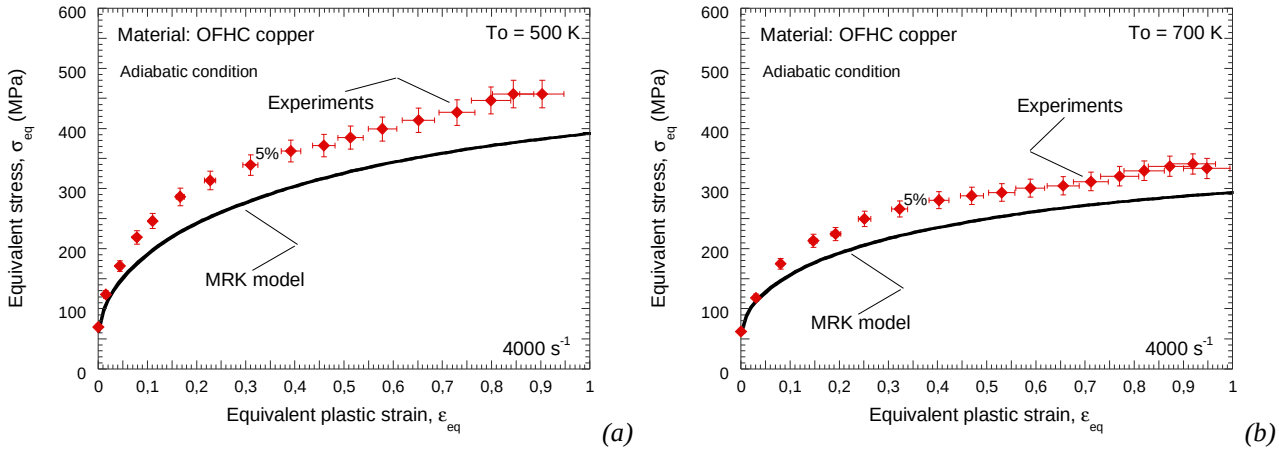

*Fig. 2.23. Description of the flow stress evolution as a function of plastic strain by the **MRK** model and comparison with experiments at 4000 s^{-1} [Nemat-Nasser and Li 1998]. (a) T_0=500 K, (b) T_0=700 K.*

So, for determined metallic alloys, previous **RK** and **MRK** formulations cannot offer a proper description of the material within wide ranges of loading conditions because of underestimation of the flow stress at high strain rates and temperatures. Thus, in the following section of the document it is introduced an extension of these models in order to convert them in suitable for defining the materials behaviour under such loading cases.

2.4 Extended constitutive relations for the macroscopic modeling of viscous drag effect at high strain rates

2.4.1 Literature review

Determined metals show a viscous drag component of the flow stress at high rate of deformation, $\dot{\varepsilon}^p \geq 10^3\ s^{-1}$ [Campbell and Fergusson 1970, Follansbee 1986, Regazzoni et al. 1987, Huang et al. 2009]. The characteristic flow stress augment caused by this stress contribution is shown in Fig. 2.24.

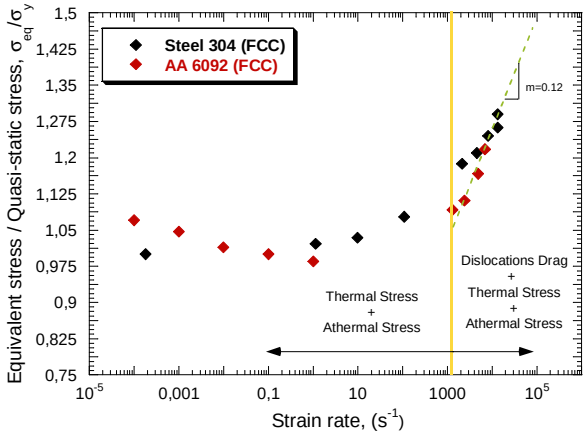

Fig. 2.24 Evolution of the normalized equivalent stress as a function of strain rate for two metallic alloys [Follansbee 1986, Zhang et al. 2001].

Several explanations of this phenomenon have been proposed over the years. Many of them based on a transition in rate controlling deformation mechanism from thermal activation at low strain rates to some form of dislocations' drag [Kumar et al. 1968, Campbell and Ferguson 1970].

According to Campbell and Ferguson [Campbell and Ferguson 1970], when viscous drag effect takes place, the equivalent stress may be defined as follows [Nemat-Nasser et al. 2001, Guo and Nemat-Nasser 2006, Rusinek et al. 2010], Eq. 2.19.

$$\bar{\sigma} = \bar{\sigma}_{\mu} + \bar{\sigma}^{*} + \bar{\sigma}_{vs} \tag{2.19}$$

Where the equivalent stress is decomposed into athermal component $\bar{\sigma}_{\mu}$, thermal component $\bar{\sigma}^{*}$ and viscous drag component $\bar{\sigma}_{vs}$.

For pure drag deformation mechanisms a simple description of the material behaviour can be derived. The deformation rate $\dot{\bar{\varepsilon}}^{p}$ *(equivalent strain rate assuming **J2** plasticity)* is tied to the dislocations' velocity by the Orowan relationship, Eq. 2.20.

$$\dot{\bar{\varepsilon}}^{p} = \frac{\rho_m \cdot b \cdot v}{\bar{M}} \tag{2.20}$$

Where ρ_m is the mobile dislocations density, b is the Burgers vector, $\bar{M}$ is the Taylor factor and v is the mean dislocations velocity.

Moreover, Eq. 2.21. describes the relation between dislocations velocity and flow stress.

$$v = \frac{\bar{\sigma} \cdot b}{\bar{M} \cdot B} \tag{2.21}$$

Where B is the drag coefficient.

Combination of Eq. 2.20. and Eq. 2.21. leads to the linear relation between flow stress and strain rate commonly reported in the literature for defining the deformation drag mechanisms, Eq. 2.22.

$$\bar{\sigma} = \dot{\bar{\varepsilon}}^{p} \cdot \frac{B \cdot \bar{M}^2}{\rho_m \cdot b^2} \tag{2.22}$$

It is assumed that the linear dependence of applied stress on strain rate occurs because of a corresponding increase in the average dislocation velocity [Kumar et al. 1968, Regazzoni et al. 1987, Kapoor and Nemat-Nasser 1999]. However, it has been reported in [Regazzoni et al. 1987, Kapoor and Nemat-Nasser 1999] that beyond a certain point the dislocations velocity no longer increases with strain rate, Fig. 2.25. The maximum velocity at which dislocations move, v_s is limited by the elastic shear waves velocity, $v_s = S_0 = \sqrt{G/\rho}$ where G is the shear modulus. It was suggested in [Weertman 1973, Regazzoni et al. 1987] that the relation between dislocations velocity and stress is no longer linear at $v > v_s/3$ *(relativistic effects)*, Fig. 2.25.

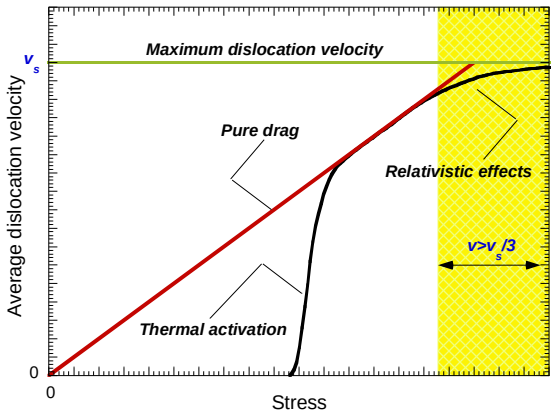

Fig. 2.25. Typical deviations of the average dislocations velocity expected from relativistic effects [Regazzoni et al. 1987].

When the relativistic effects take place, the increasing strain rate seems to be accommodated by an augment of the dislocations density; the material flow stress level remains constant [Kapoor and Nemat-Nasser 1999], Fig. 2.26.

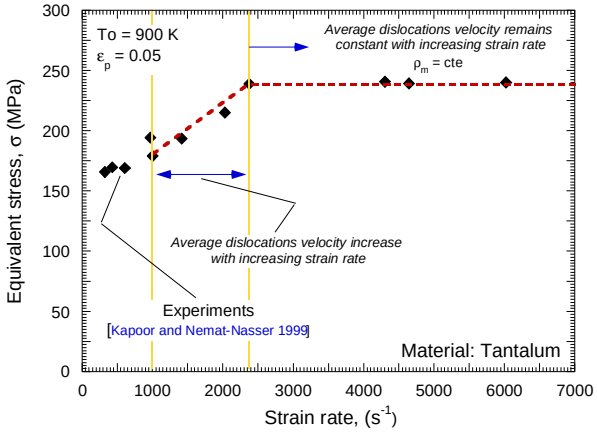

Fig. 2.26. Experimental data of the flow stress evolution as a function of strain rate for Tantalum for ε_p=0.05 at To=900K. Definition of the stages of the viscous drag process [Kapoor and Nemat-Nasser 1999].

In addition, it is necessary to take into account that the dislocations drag is not the only one mechanism controlling deformation at high strain rates, but it is superposed to the thermally controlled mechanisms [Follansbee 1986, Regazzoni et al. 1987], Fig. 2.27. In the presence of thermal activation only, the stress increases slowly with the logarithm of strain rate, whereas in the presence of dislocation drag only, the curve is steep and reaches the strain rate for the applied stress. The curve obtained when both thermally activated and drag mechanisms are operative follows the thermal activation curve at low stresses and the drag curve at high stresses [Regazzoni et al. 1987], Fig. 2.27.

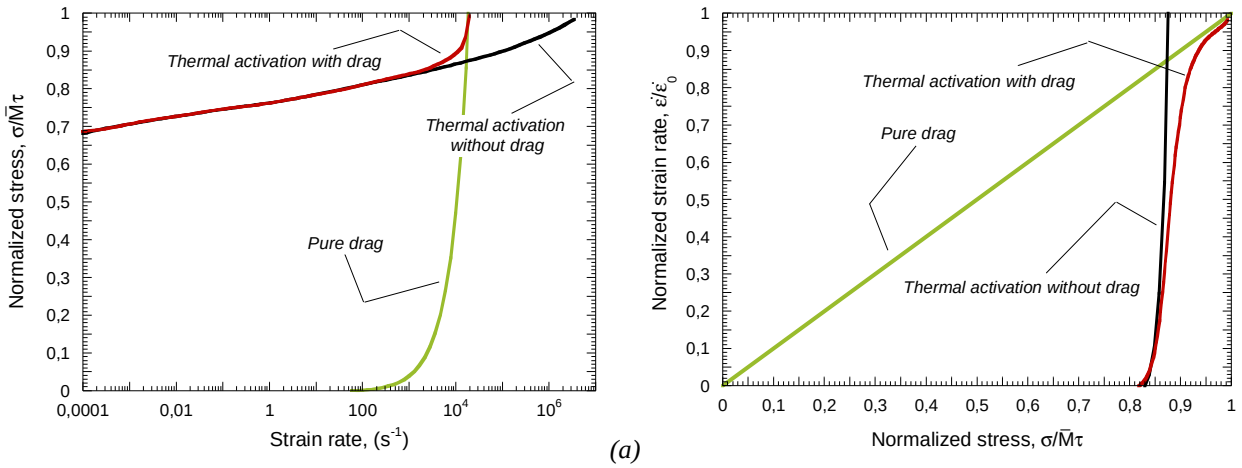

Fig. 2.27. Description of the flow stress evolution for thermal activation only, drag only and superposition of thermal activation with drag [Regazzoni et al. 1987].

Previous considerations are of fundamental relevance when deriving physical-based constitutive relations suitable for defining the thermo-viscoplastic behaviour of metallic alloys under wide ranges of strain rate. According to these considerations, for metallic alloys showing deformation drag mechanisms, their strain rate sensitivity cannot be defined using the constitutive descriptions only based on an Arrhénius-type equation [Nemat-Nasser et al. 2001, Guo and Nemat-Nasser 2006, Rusinek et al. 2010].

Based on the previous considerations the extension of **RK** and **MRK** models for defining dislocations drag at high strain rates is conducted.

2.4.2 Applied method for modeling reference metallic alloys

2.4.2.1 Formulation developed

It is added a new term to the equivalent Huber-Misses stress $\overline{\sigma}$. The updated formulation of the models is reported in Eq. 2.23:

$$\overline{\sigma}\left(\overline{\varepsilon}^{p},\dot{\overline{\varepsilon}}^{p},T\right)=\frac{E(T)}{E_0}\left[\overline{\sigma}_{\mu}+\overline{\sigma}^{*}\right]+\overline{\sigma}_{vs}\left(\dot{\overline{\varepsilon}}^{p}\right) \qquad (2.23)$$

Where $\overline{\sigma}_{vs}\left(\dot{\overline{\varepsilon}}^{p}\right)$ is the stress component describing the viscous drag effects.

Based on experimental observations, Kapoor and Nemat-Nasser [Kapoor and Nemat-Nasser 1999] proposed the following macroscopic definition for the viscous drag stress, Eq. 2.24.

$$\overline{\sigma}_{vs}\left(\dot{\overline{\varepsilon}}^{p}\right)=\chi\cdot\left[1-\exp\left(-\alpha\cdot\dot{\overline{\varepsilon}}^{p}\right)\right] \qquad (2.24\text{-}a)$$

$$\alpha=\left(\frac{\overline{M}^{2}\cdot B}{\rho_{m}\cdot b^{2}\cdot\tau_{y}}\right) \qquad (2.24\text{-}b)$$

Where χ is a material constant, α represents an effective damping coefficient affecting the dislocation motion and τ_y is the athermal yield stress [Nemat-Nasser et al. 2001]. This expression enables to define both stages of dislocations drag behaviour. First stage of flow stress linearly increasing with strain rate and subsequent stage of rate sensitivity no longer active.

In the following curves is illustrated the evolution of the viscous drag component as a function of χ and α for different strain rate levels, Fig. 2.28. Under a certain level of deformation rate $\dot{\varepsilon}^p \leq 100\ s^{-1}$ the viscous drag component is negligible no matter the value of the constants χ and α, Fig. 2.28. In that case, the rate sensitivity is governed by the thermal activation mechanisms.

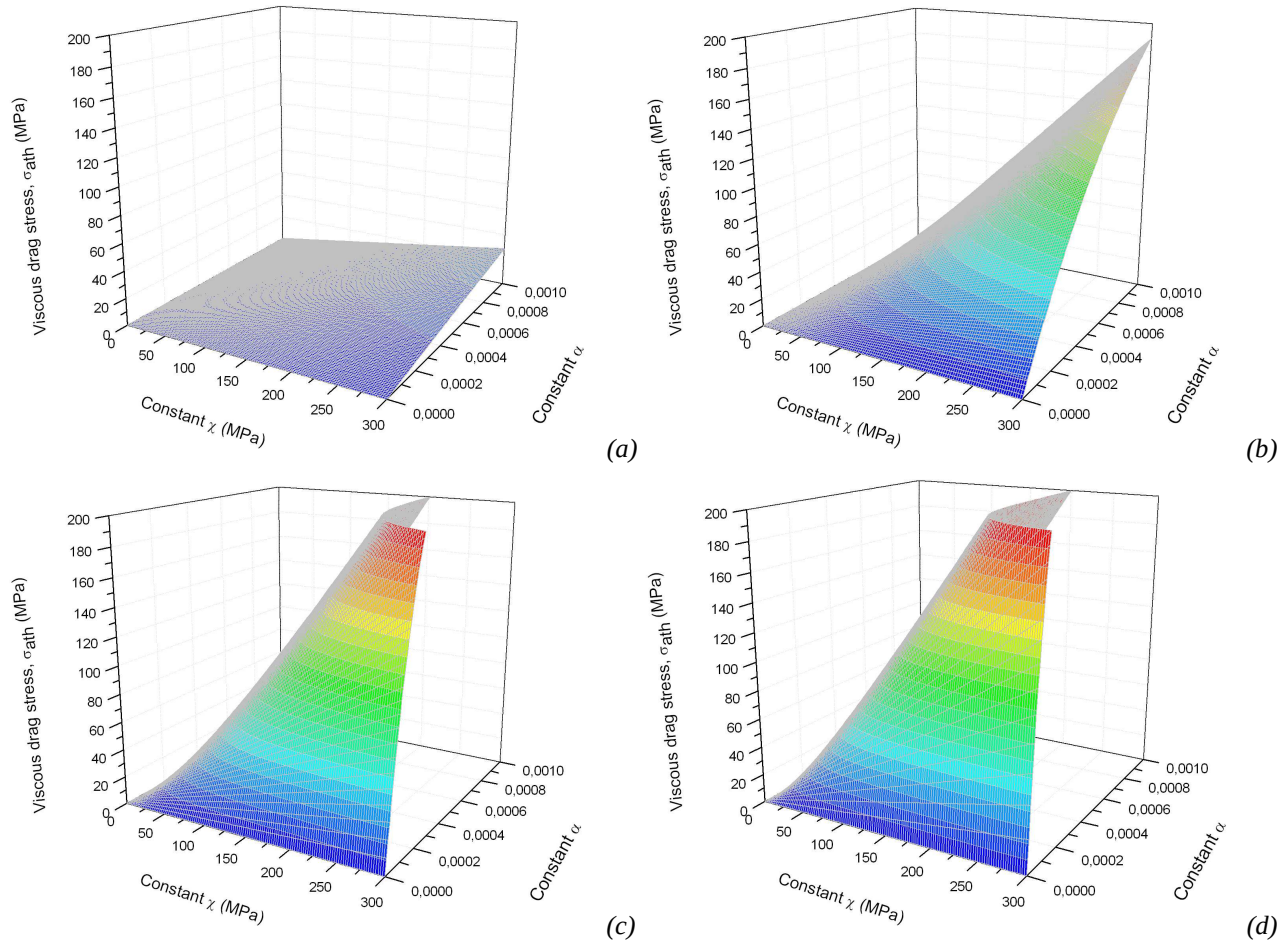

Fig. 2.28. Evolution of the viscous drag component as a function of χ and α for different strain rate levels. (a) 100 s^{-1}, (b) 1000 s^{-1}, (c) 5000 s^{-1}, (d) 10000 s^{-1}.

At higher strain rate level $\dot{\varepsilon}^p \geq 100\ s^{-1}$ the flow stress due to viscous drag becomes relevant and it quickly increases with the rate of deformation, Fig. 2.28. The increase of both material constants χ and α leads to an augment on the flow stress.

Subsequently is proposed a method for the drag stress term calibration.

2.4.2.2 Systematic procedure for calculation of the model parameters

The steps are described below.

1. Once the model ***(RK or MRK)*** is already calibrated for a particular material, the analytical predictions of the constitutive description are compared with experiments. Then, the difference at room temperature on the flow stress level at high strain rates between analytical predictions and experiments is obtained.

2. This difference is fitted to Eq. 2.24. Thus it is possible to determine the material constants χ and α, Fig. 2.29.

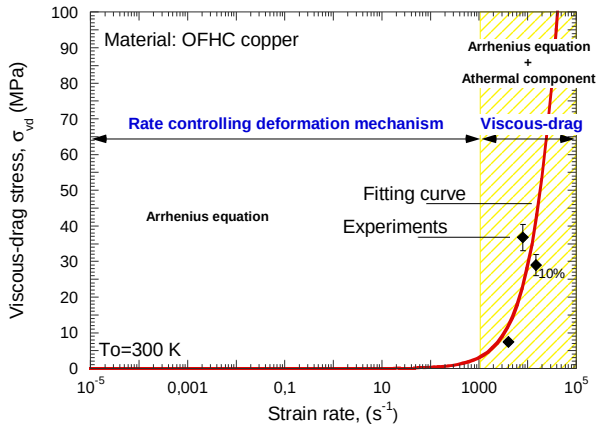

*Fig. 2.29. Calibration of the viscous drag stress component for annealed **OFHC** copper using experimental data reported in [Nemat-Nasser and Li 1998].*

The dependence of the viscous drag term only on strain rate facilitates considerably the calibration procedure.

2.4.2.3 Application to annealed OFHC copper

Thus, the extension to viscous drag effects has been calibrated for annealed **OFHC** copper. The following material constants have been found, Table. 2.12.

χ (MPa)	α (-)
249	0.0000122

*Table 2.12. Constants determined for the annealed **OFHC** copper for the viscous drag component of the extended **MRK** model.*

Using the extension to viscous drag effects is possible to describe the behaviour of annealed **OFHC** copper within the whole range of strain rates as it is described in this section of the document.

In Fig. 2.30. is shown the description of the flow stress evolution as a function of plastic strain obtained using original and extended **MRK** models. The analytical predictions are compared with experiments at room temperature for $\dot{\bar{\varepsilon}}^{p} = 8000\ s^{-1}$ [Nemat-Nasser and Li 1998]. It can be observed that in the case of the extended **MRK** model the strain hardening of the material, as well as its flow stress level, is well defined, Fig. 2.30. However, the underestimation of the material stress level is visible in the case of the original **MRK** constitutive relation.

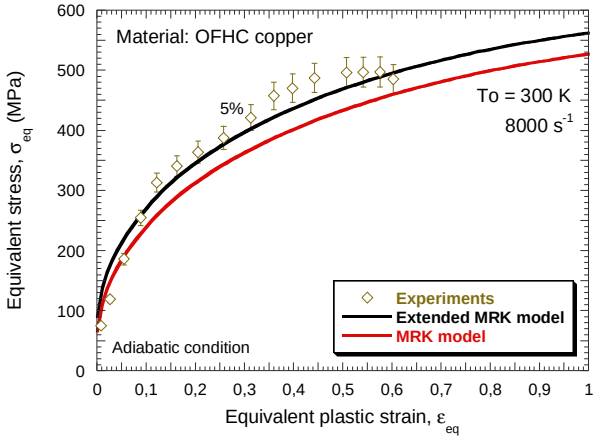

*Fig. 2.30. Description of the flow stress evolution as a function of plastic strain by original and extended **MRK** models and comparison with experiments at room temperature for 8000 s^{-1} [Nemat-Nasser and Li 1998].*

The relevance of adding the viscous drag stress term to the **MRK** model is illustrated in Fig. 2.31. The extended **MRK** model provides a proper definition of the material rate sensitivity for $\dot{\bar{\varepsilon}}^{p} \geq 1000\ s^{-1}$. At high strain rate level a considerable difference between original and extended **MRK** models takes place.

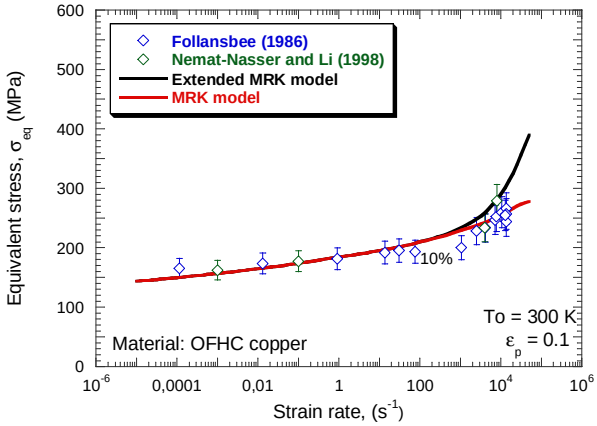

*Fig. 2.31. Description of the flow stress evolution as a function of strain rate by original and extended **MRK** models and comparison with experiments at room temperature for ε_p=0.1 [Nemat-Nasser and Li 1998].*

In addition, definition of the dislocations drag effect at high strain rate allows for a correct description of the material temperature sensitivity, Fig. 2.32. The athermal character of the viscous drag term makes it fundamental for the description of the temperature sensitivity of the material.

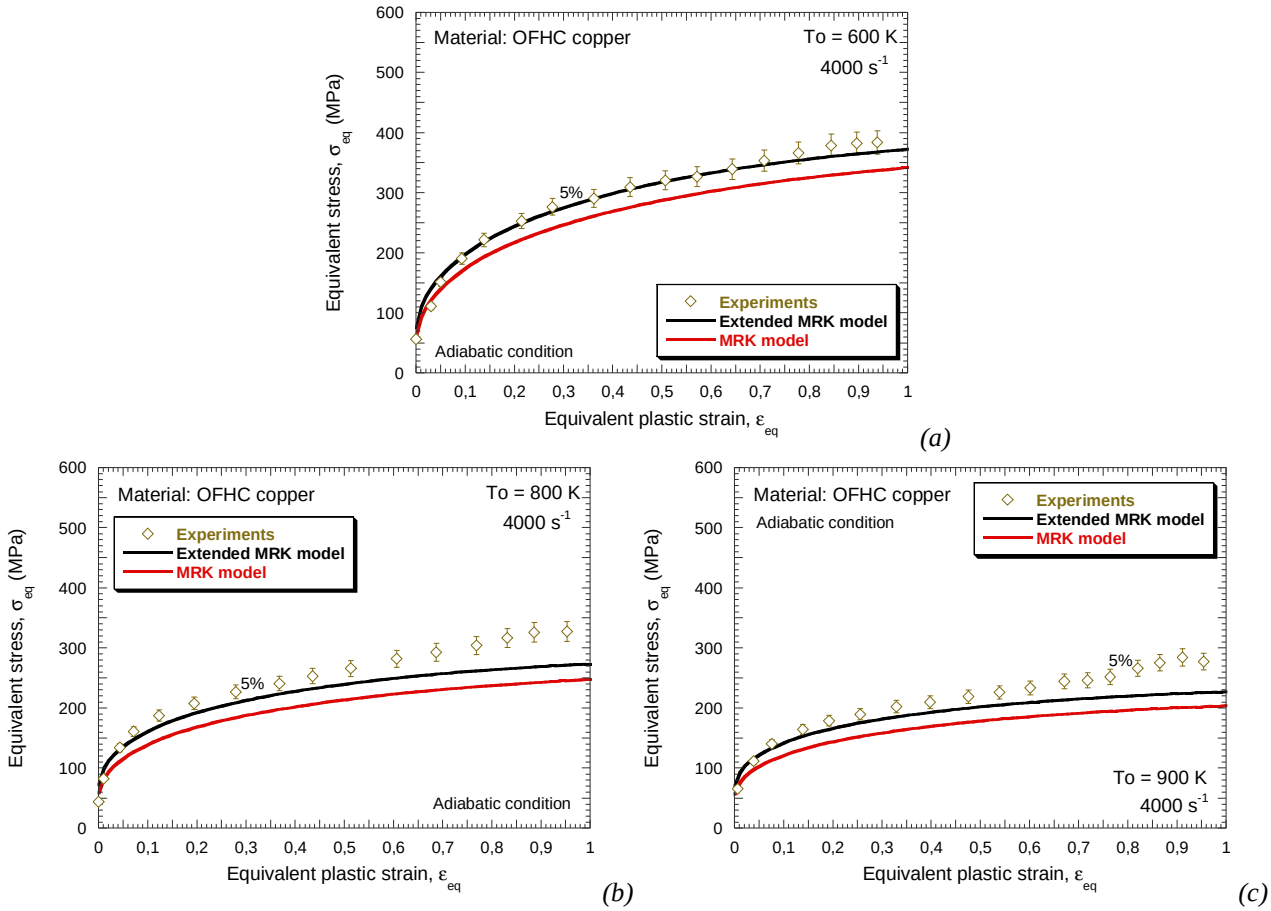

*Fig. 2.32. Description of the flow stress evolution as a function of plastic strain by original and extended **MRK** models and comparison with experiments at 4000 s^{-1}. (a) T_0=600 K, (b) T_0=800 K, (c) T_0=900 K [Nemat-Nasser and Li 1998].*

Such considerations are revealed in the following graphs, Fig. 2.33. The extended **MRK** constitutive model describes accurately the temperature sensitivity of annealed **OFHC** copper. The absence of athermal flow stress for the whole range of initial temperatures analyzed is properly defined, Fig. 2.33.

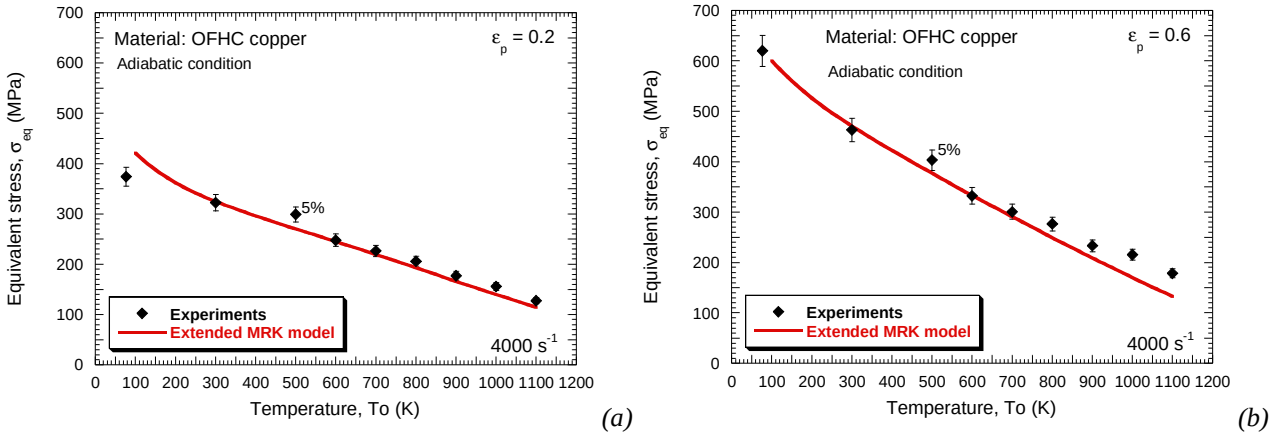

*Fig. 2.33. Temperature sensitivity description using the extended **MRK** model and comparison with experiments at 4000 s^{-1}. (a) ε_p=0.2, (b) ε_p=0.6 [Nemat-Nasser and Li 1998].*

Finally is necessary to notice that the extended **MRK** relation provides a better analytical description of the thermo-viscoplastic behaviour of annealed **OFHC** copper than other physical-based models as reported in [Rusinek et al. 2010].

The viscous drag formulation can be also added to the original **RK** formulation allowing the definition of, for example, the thermo-viscoplastic behaviour of the **AA 7075** *(it is assumed that this material does not exhibit dependence of plastic strain on the **VTA** since its strain hardening remains approximately constant for different temperatures and strain rates)* within wide ranges of strain rate and temperature as it will be discussed in the following section of the manuscript.

2.4.2.4 Application to aluminium alloy 7075

The **AA 7075** shows a remarkable effect of the drag regime on its deformation behaviour at high strain rates. In addition, the material response under high loading rate has been precisely analyzed in [El-Magd and Abouridouane 2006] facilitating comprehension of its deformation mechanisms.

The **AA** 7xxx series are alloyed with **Zn**, and can be hardened to the highest strengths of any **AA**. Thus, the **AA 7075** notable for its strength, with good fatigue strength and average machinability, but it is not weldable and has less resistance to corrosion than many other **AA**. It is widely used in aeronautical industry for construction of aircraft structures, such as wings and fuselages. Its main alloying elements are listed in Table 2.13.

Mn	**Si**	**Cr**	**Ti**	**Fe**	**Mg**	**Zn**	**Ti**	**Cu**
0.3	0.4	0.23	0.2	0.5	2.5	5.5	0.2	1.6

*Table 2.13. Chemical composition of the **AA 7075** (% of weight) [El-Magd and Abouridouane 2006].*

The model has been calibrated for the **AA 7075** using the experimental data reported in [El-Magd and Abouridouane 2006]. The following set of constants has been found, Tables 2.14-2.15.

B_0 (MPa)	ν (-)	n_0 (-)	D_2 (-)	ε_0 (-)	σ_0^* (MPa)	m^* (-)	D_1 (-)	T_m (K)	$\dot{\varepsilon}_{min}$ (s^{-1})	$\dot{\varepsilon}_{max}$ (s^{-1})	θ^* (-)
790.3	-0.0002	0.1966	0.0555	0.018	196.57	1.2857	0.3	900	10^{-5}	10^{7}	0.9

*Table 2.14. Constants determined for the **AA 7075** for the **RK** model.*

χ (MPa)	α (-)
286.7	0.00005368

*Table 2.15. Constants determined for the **AA 7075** for the viscous drag component of the extended **RK** model.*

Conventional physical constants of **AA** can be obtained from material handbooks, Table 2.16.

E_0 (GPa)	C_p ($Jkg^{-1}K^{-1}$)	β (-)	ρ (kgm^{-3})
70	900	0.9	2700

*Table 2.16. Physical constants for **AA.***

In the following section, the predictions of the extended **RK** model are compared with experiments.

The first step is to evaluate the predictions of the extended **RK** model for different strain rate levels. It is reported in Fig. 2.34. a satisfactory agreement between model predictions and experiments from quasi-static loading to high strain rate $0.001\,s^{-1} \le \dot{\bar{\varepsilon}}^p \le 2529\,s^{-1}$. The difference only takes place after saturation stress stage $d\bar{\sigma}/d\bar{\varepsilon}^p = 0$ which corresponds to non-homogeneous behaviour *(open symbols in Figs 2.34 – 2.35).* In such a case nucleation and growth of micro voids sharply decreases the flow stress, Fig. 2.34 [El-Magd and Abouridouane 2006]. It must be noticed

that the viscous drag component added to the **RK** model allows for a correct definition of the material behaviour under high rate of deformation, Fig. 2.34-d.

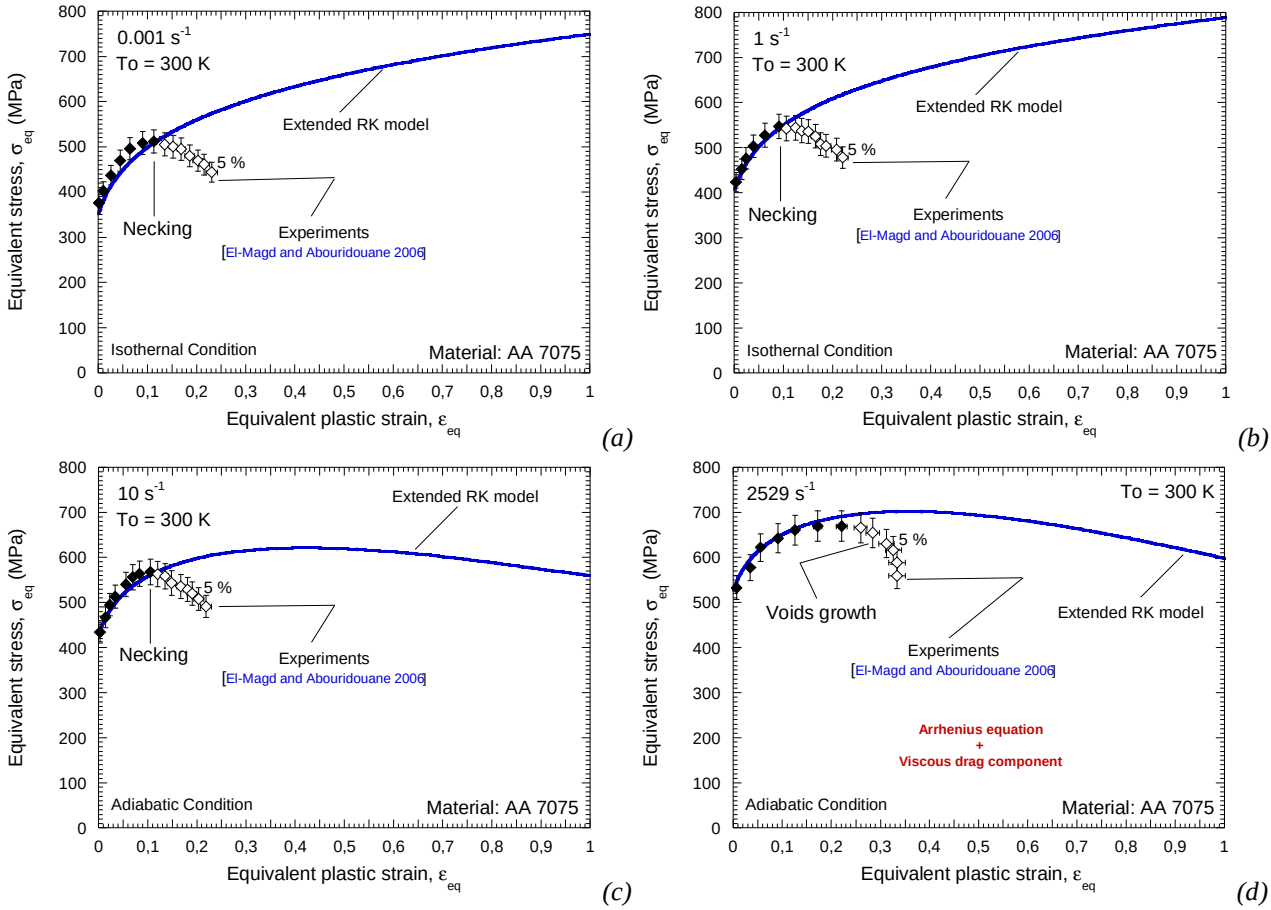

*Fig. 2.34. Description of the flow stress evolution versus plastic strain by the extended **RK** model and comparison with experiments at room temperature [El-Magd and Abouridouane 2006]. (a) 0.001 s^{-1}, (b) 1 s^{-1}, (c) 10 s^{-1}, (d) 2529 s^{-1}.*

As it was pointed out before, the viscous drag component exhibits great relevance on the description of the material behaviour when subjected to elevated initial temperature and high rate of deformation. It compensates the underestimation on the flow stress at high strain rate that would be obtained using only the Arrhénius equation as the mechanism to describe the rate sensitivity of the material, Fig. 2.35. That point is confirmed in Fig. 2.35. where the analytical predictions of the original formulation of the **RK** model are compared with those corresponding to the extension to dislocation drag effects.

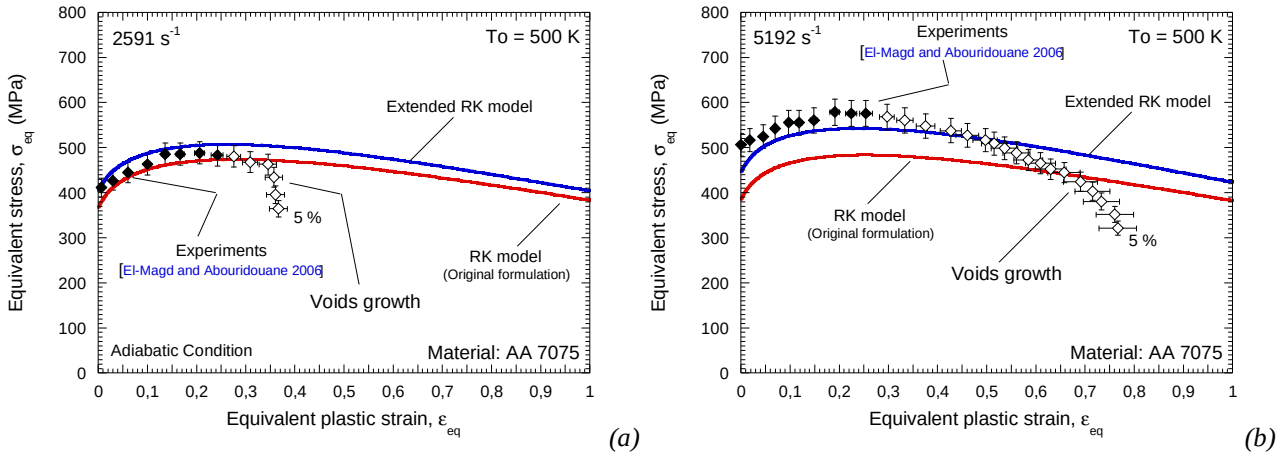

*Fig. 2.35. Description of the flow stress evolution versus plastic strain by original and extended **RK** models and comparison with experiments at T_0 = 500 K [El-Magd and Abouridouane 2006]. (a) 2591 s^{-1}, (b) 5192 s^{-1}.*

Finally is necessary to notice that the extended **RK** relation provides a better analytical description of the thermo-viscoplastic behaviour of the **AA 7075** than other constitutive models as reported in [Rusinek and Rodríguez-Martínez 2009].

2.5 Extended constitutive relations for the macroscopic modeling of negative strain rate sensitivity

Previous formulations may not be enough to define the macroscopic behavior of certain alloys. It is known that some aluminium and steel alloys exhibit **N**egative **S**train **R**ate **S**ensitivity (**NSRS**) under certain loading conditions [Clausen et al. 2004, Allain et al. 2008]. Thus, in order to make suitable previous constitutive descriptions to define such behaviour an original formulation is reported in the following section of the document.

2.5.1 Literature review

Some metallic alloys exhibit macroscopic **NSRS**, Eq. 2.25., from quasi-static to intermediate strain rates $10^{-4}\ s^{-1} \le \dot{\bar{\varepsilon}}^{p} \le 100\ s^{-1}$, Fig. 2.36.

$$m = \left.\frac{d(\bar{\sigma})}{d\log(\dot{\bar{\varepsilon}}^{p})}\right|_{\bar{\varepsilon}^{p},T} < 0 \qquad \text{for} \quad \dot{\bar{\varepsilon}}^{p} < \dot{\bar{\varepsilon}}^{p}_{trans-NSRS} \tag{2.25}$$

Such behaviour has considerable relevance in industrial applications since it may reduce the ductility of the material [Higashi et al. 1991, Mukai et al. 1994, Dorward and Hasse 1995] and therefore affects to its formability and machinability.

This effect was traditionally explained due to the solute–dislocation interaction at the microscopic level [Cottrell 1953, Cottrell 1953, Sleeswijk 1958, Kubin and Estrin 1985]. An alternative explanation has been proposed by Picu [Picu 2004] and other authors based on the strength variation of dislocation junctions due to the presence of solute clusters on forest dislocations *(so, **NSRS** is basically shown by **FCC** metals).* At low strain rate, the solute has sufficient mobility to induce a clustering effect stopping mobile dislocations. At high rate of deformation, the increase of dislocations' velocity avoids appearance of clustering effect. Thus, after certain strain rate level

$\dot{\bar{\varepsilon}}^{p}_{trans-NSRS}$, the strain rate sensitivity becomes positive, Fig. 2.36. Moreover, since **NSRS** is related to diffusion of solute, it is thermally activated [Abbadi et al. 2002, Klose et al. 2004]. The **NSRS** effect tends to disappear with decreasing temperature. Interesting studies concerning the effect of temperature on this phenomenon are reported for example in [Abbadi et al. 2002, Klose et al. 2004].

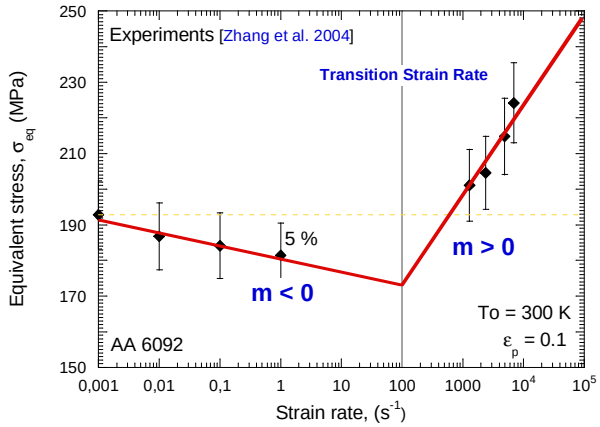

*Fig. 2.36. Description of the negative and the positive strain rate sensitivities taking place in **AA 6092** [Zhang et al. 2004].*

Some attempts to model the **NSRS** are reported in the open literature, for example in [Brechet and Estrin 1995, Hähner 1997, Zhang et al. 2001]. The most relevant seems to be the approach due to McCormick [McCormick 1971].

However, such micromechanical descriptions of the **NSRS** lead to complex mathematical formulations difficult to implement into **FE** codes. Moreover they use to have large number of material constants and difficult calibration-procedures. In addition, those models only define the material behaviour within the range of strain rate in which this effect takes place. They do not provide a formulation for the whole range of strain rates detected in many engineering applications, $10^{-4}\ s^{-1} \le \dot{\bar{\varepsilon}}^{p} \le 10^{4}\ s^{-1}$.

In this section of the document an extension of the **RK** and **MRK** models to define macroscopically the **NSRS** is reported.

2.5.2 Applied method for modeling reference metallic alloys

2.5.2.1 Formulation developed

The extension is conducted by adding a new term to the equivalent Huber-Misses stress $\bar{\sigma}$. The updated formulation of the model is reported in Eq. 2.26.

$$\bar{\sigma}\left(\bar{\varepsilon}^{p}, \dot{\bar{\varepsilon}}^{p}, T\right) = \frac{E(T)}{E_0}\left[\bar{\sigma}_{\mu} + \bar{\sigma}^{*} + \bar{\sigma}_{ns}\left(\dot{\bar{\varepsilon}}^{p}, T\right)\right] \qquad (2.26)$$

Where $\bar{\sigma}_{ns}\left(\dot{\bar{\varepsilon}}^{p}, T\right)$ is the stress component taking into account the **NSRS** which is dependent on strain rate and temperature. This formulation has a semi-physical character and it is based on the experimental observations reported for example in [Higashi et al. 1991, Abbadi et al. 2002, Klose et al. 2004]. The original expression proposed is defined by Eq. 2.27.

$$\bar{\sigma}_{ns}\left(\dot{\bar{\varepsilon}}^{p},T\right)=\sigma_0^{ns}\cdot\left\langle\log\left(\frac{\dot{\bar{\varepsilon}}_{trans-NSRS}}{\dot{\bar{\varepsilon}}^{p}}\right)\right\rangle\cdot\left\langle 1-D_3\left(\frac{T_m}{T}\right)\log\left(\frac{\dot{\bar{\varepsilon}}^{p}}{\dot{\varepsilon}_{max}}\right)\right\rangle \qquad (2.27)$$

Where σ_0^{ns} and D_3 are material constants describing respectively the stress decrease due to **NSRS** and the reciprocity between strain rate and temperature. Such reciprocity is obtained using an Arrhénius-type equation. The influence of plastic strain on the **NSRS** effect is assumed negligible. Such assumption is based, for example, on the experimental data reported in [Clausen et al. 2004]. Thus, in comparison with the original formulation of the **RK** and **MRK** relations only two new material constants are added. The transition between positive and negative strain rate sensitivity is denoted by $\dot{\bar{\varepsilon}}^{p}_{trans-NSRS}$ and it can be obtained from experiments.

In the following curves is shown the evolution of the **NSRS** component, $\bar{\sigma}_{ns}\left(\dot{\bar{\varepsilon}}^{p},T\right)$ as a function of σ_0^{ns} and D_3 for different strain rate levels at room temperature, Fig. 2.37. The value of the new stress component decreases with the strain rate increase, Fig. 2.37. until the transition strain rate level is reached *(It is considered* $\dot{\bar{\varepsilon}}^{p}_{trans-NSRS}=76.58\ s^{-1}$*)*. The increase of both material constants σ_0^{ns} and D_3 leads to an augment of the **NSRS** of the material, Fig. 2.37.

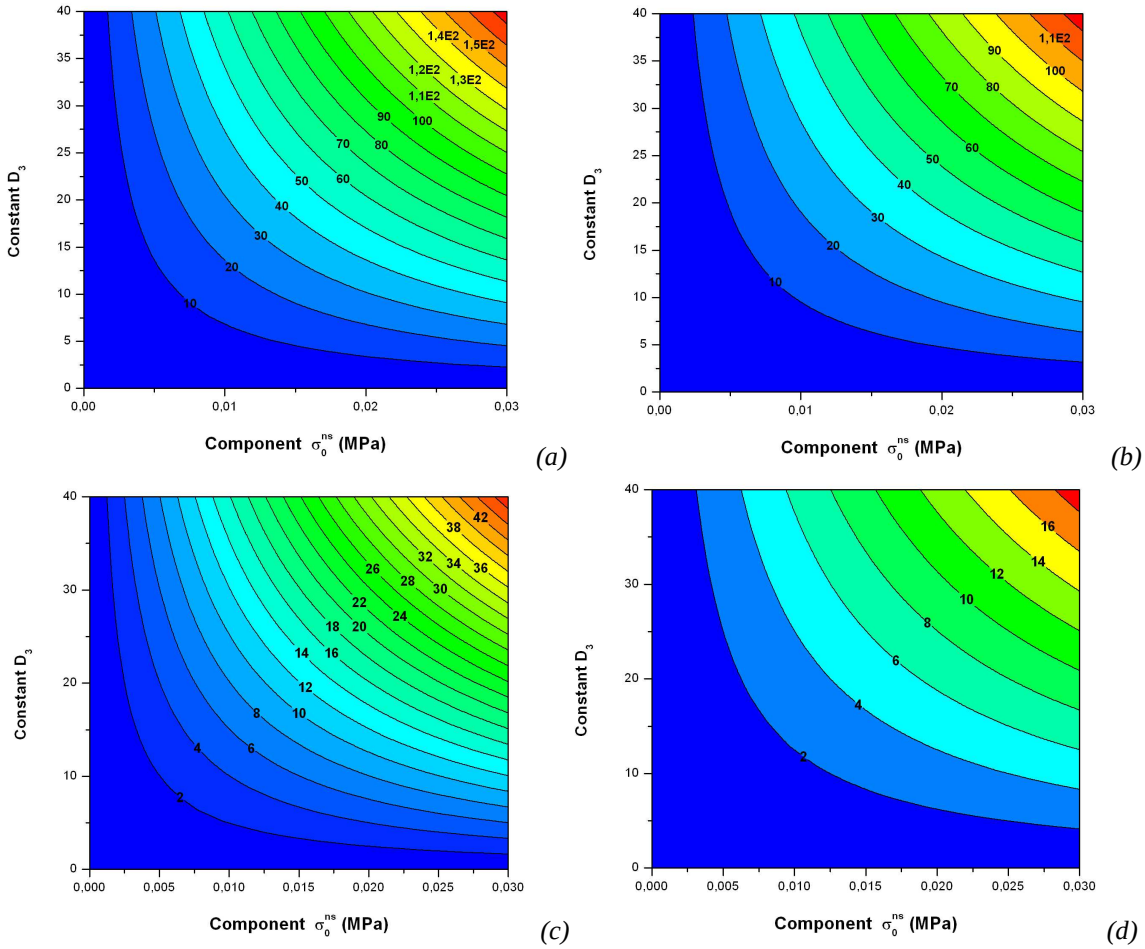

*Fig. 2.37. Evolution of the **NSRS** stress component as a function of σ_0^{ns} and D_3 for different strain rate levels at room temperature. (a) 0.001 s^{-1}, (b) 0.01 s^{-1}, (c) 1 s^{-1}, (d) 10 s^{-1}.*

Next, it is defined a method for the model calibration.

2.5.2.2 Systematic procedure for calculation of the model parameters

The main steps necessary for the definition of the model parameters are:

1. The transition strain rate $\dot{\bar{\varepsilon}}^{p}_{trans-NSRS}$ at room temperature is identified for a given plastic strain value. For the range of strain rates $\dot{\bar{\varepsilon}}^{p} \le \dot{\bar{\varepsilon}}^{p}_{trans-NSRS}$ the value of stress corresponding to $\dot{\bar{\varepsilon}}^{p}_{trans-NSRS}$ is subtracted from the real flow stress, Fig. 2.38. The stress difference is the flow stress decrease due to the **NSRS** and it is fitted to Eq. 2.27. using the least square method. Thus, the material constants σ_0^{ns} and D_3 can be obtained.

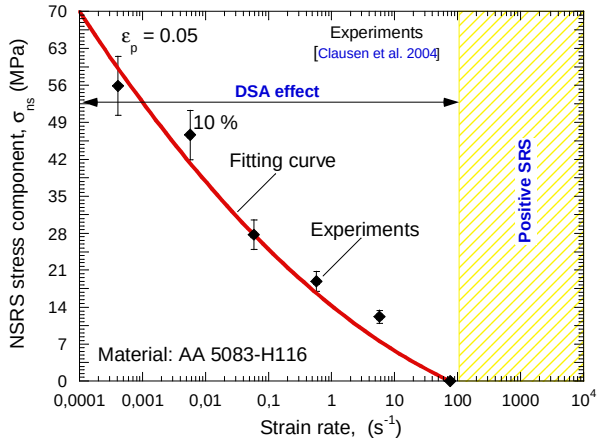

*Fig. 2.38. Calibration of the **NSRS** stress term for the **AA 5083-H116** using the experimental data reported in [Clausen et al. 2004].*

2. Subtracting the **NSRS** stress component from the real flow stress of the material, the **RK** or the **MRK** models can be calibrated following the procedure reported in previous sections of this document.

Next, the extended **RK** model to **NSRS** is applied to describe the thermo-viscoplastic behaviour of the **AA 5083-H116**.

2.5.2.3 Application to aluminium alloy 5083-H116

This material is found propitious for validation of the model proposed since it exhibits remarkable **NSRS** within wide ranges of strain rate. It has been frequently chosen in the literature for the analysis of such phenomenon [Clausen et al. 2004, Benallal et al. 2008]. Its deformation behaviour has been subjected to intensive study by several laboratories.

The **AA** 5xxx series are alloyed with **Mg**, derive most of their strength from solution hardening, and can also be work hardened to strengths comparable to steel alloys. The **AA 5083-H116** is one of the strongest aluminium–magnesium alloys. It is widely used in naval structures as ship hulls and offshore topsides due to its high strength and good corrosion resistance. The main alloying elements are listed in Table 2.17.

Mn	Si	Cr	Ti	Fe	Mg	Zn	Ti	Cu
0.5	0.4	0.17	0.15	0.5	4.5	0.25	0.2	0.1

*Table 2.17. Chemical composition of the **AA 5083-H116** (% of weight) [Clausen et al. 2004].*

The high content of **Mg** is responsible for the **NSRS** showed by this **AA** as discussed in [Clausen et al. 2004, Benallal et al. 2008].

Using the procedure reported in the previous section, the extended **RK** model to **NSRS** has been calibrated for the **AA 5083-H116** *(it is assumed that this material does not exhibit dependence of plastic strain on the **VTA** since its strain hardening remains approximately constant for different temperatures and strain rates)* using the experimental data reported in [Clausen et al. 2004]. The following set of constants has been found, Tables 2.18.

B_0 (MPa)	ν (-)	n_0 (-)	D_2 (-)	ε_0 (-)	σ_0^* (MPa)	m^* (-)	D_1 (-)	T_m (K)	$\dot{\varepsilon}_{min}$ (s^{-1})	$\dot{\varepsilon}_{max}$ (s^{-1})	θ^* (-)
666	0.01	0.35	0.04	0.0118	1536.3	8.37	0.3	900	10^{-5}	10^{7}	0.9

*Table 2.18. Constants determined for the **AA 5083-H116** for the **RK** model.*

σ_0^{ns} (MPa)	D_3 (-)	$\dot{\bar{\varepsilon}}_{trans-NSRS}$ (s^{-1})
0.01	36	76.58

*Table 2.19. Constants determined for the **AA 5083-H116** for the extension of the **RK** model to **NSRS**.*

Since the maximum strain rate reported in the experiments taken as reference is $\dot{\bar{\varepsilon}}^p \approx 1000\ s^{-1}$ [Clausen et al. 2004] it is assumed that the drag mechanisms are not active [Rusinek and Rodríguez-Martínez 2009]. Thus, the contribution of an eventual dislocations drag component to the flow stress for the range of strain rates considered can be neglected *(at least for the purposes of this section of the document).*

Then, the predictions of the extended **RK** model are validated with experiments.

The first step is to evaluate the definition of the **NSRS** provided by the extended **RK** model. In Fig. 2.39. is illustrated the agreement between analytical predictions and experiments for different strain rates $0.00041\ s^{-1} \le \dot{\bar{\varepsilon}}^p \le 122\ s^{-1}$. The lower limit $\dot{\bar{\varepsilon}}^p = 0.00041\ s^{-1}$ corresponds to the minimum value of strain rate for which there is experimental data available. The upper limit is approximately the strain rate value corresponding to the transition between the negative and the positive strain rate sensitivities $\dot{\bar{\varepsilon}}^p = 122\ s^{-1} \approx \dot{\bar{\varepsilon}}^p_{trans-NSRS} = 76.58\ s^{-1}$. Thus, the flow stress level in the case of $\dot{\bar{\varepsilon}}^p = 122\ s^{-1} \approx \dot{\bar{\varepsilon}}^p_{trans-NSRS}$ is lower than in the case of $\dot{\bar{\varepsilon}}^p = 0.00041\ s^{-1}$. The relevance of defining properly the **NSRS** component of the flow stress is illustrated in Fig. 2.39-a where predictions of the extended **RK** model are compared with those obtained from the original **RK** relation. Relevant differences between the flow stress level predicted by both models are observed. Moreover, it must be noticed that the constitutive description predicts properly the strain hardening of the material.

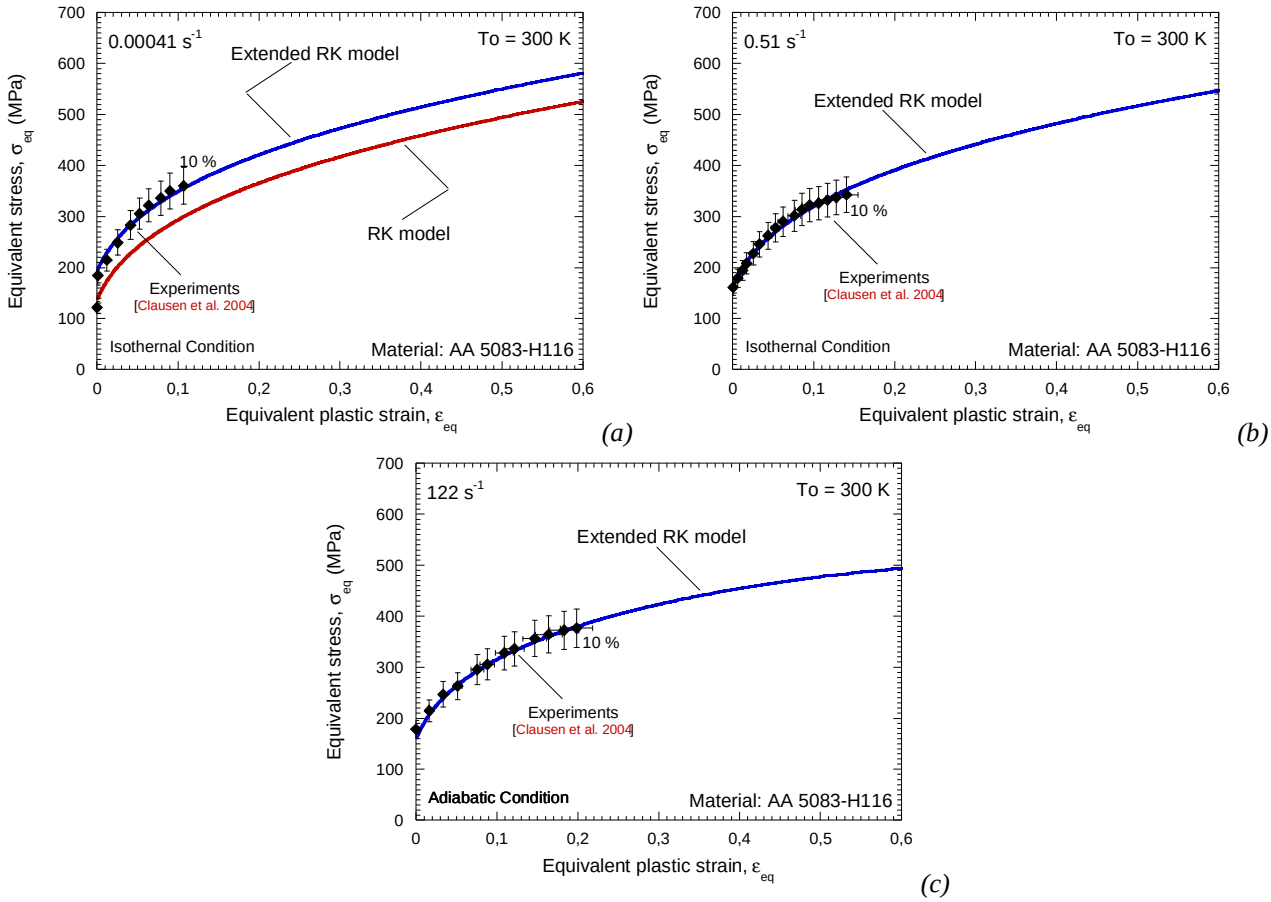

*Fig. 2.39. Description of the flow stress evolution as a function of the plastic strain by the extended **RK** model and comparison with experiments at room temperature [Clausen et al. 2004]. (a) 0.00041 s^{-1}, (b) 0.51 s^{-1}, (c) 122 s^{-1}.*

Next it is depicted the rate sensitivity of the material within wide ranges of strain rate and the comparison with the predictions of the extended **RK** model, Fig. 2.40. Good matching for the whole range of strain rates is observed between model and experiments.

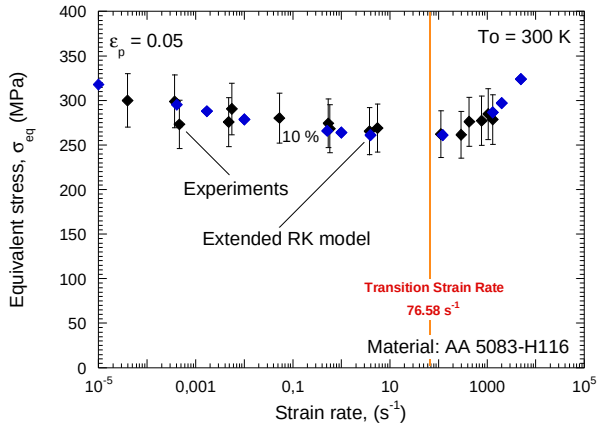

*Fig. 2.40. Description of the flow stress evolution as a function of strain rate by the extended **RK** model and comparison with experiments at room temperature and ε_p=0.05 [Clausen et al. 2004].*

Concerning the temperature sensitivity, the experimental data available only allow for evaluating the model in the case of $T \geq T_{room}$, Fig. 2.41. The model describes accurately the decrease of the flow stress with temperature Fig. 2.41. The difference only takes place in the case of T_0 = 600 K.

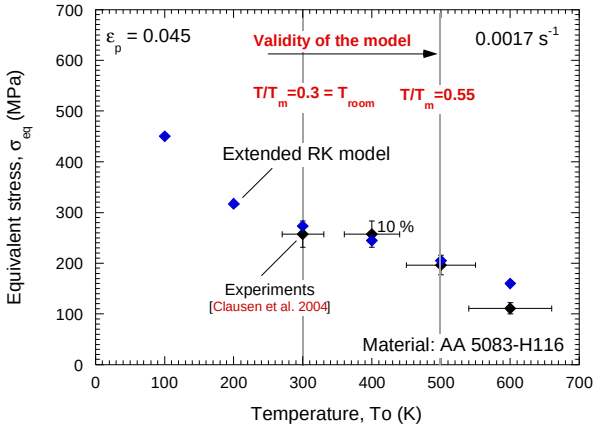

*Fig. 2.41. Description of the temperature sensitivity by the extended **RK** model and comparison with experiments for ε_p=0.045 and 0.00017 s^{-1} [Clausen et al. 2004].*

Finally is necessary to notice that the extended **RK** relation provides a better analytical description of the thermo-viscoplastic behaviour of the **AA 5083-H116** than other constitutive models as reported in [Rusinek and Rodríguez-Martínez 2009].

But dislocations drag and **NSRS** are not the only effects that cannot be defined using the original formulations of the **RK** and **MRK** models.

2.6 Extended constitutive relations for the macroscopic modeling of martensitic transformation

In *austenitic* steels the *martensitic* transformation may strongly modify the strain hardening of the material. Such type of steel alloys has become of relevance because of their widespread use, for example, in the automotive industry. Thus, it is necessary to extend the applicability of these constitutive descriptions to the macroscopic modeling of such phenomenon. For that task, an original formulation is presented in the following section of the document.

2.6.1 Literature review

Martensitic transformation from **FCC** *austenite (γ)* to **BCC** *martensite (α')* provides to steel alloys of high work-hardening and improved ductility and toughness [Angel 1954, Olson and Cohen 1972, Delannay et al. 2008, Curtze et al. 2009, Curtze et al. 2009, Da Rocha and Silva de Oliveira 2009, Fischer et al. 2000, Jiménez et al. 2009]. Such mechanical properties are required for metals in charge of absorbing energy under dynamic loading, Fig. 2.42.

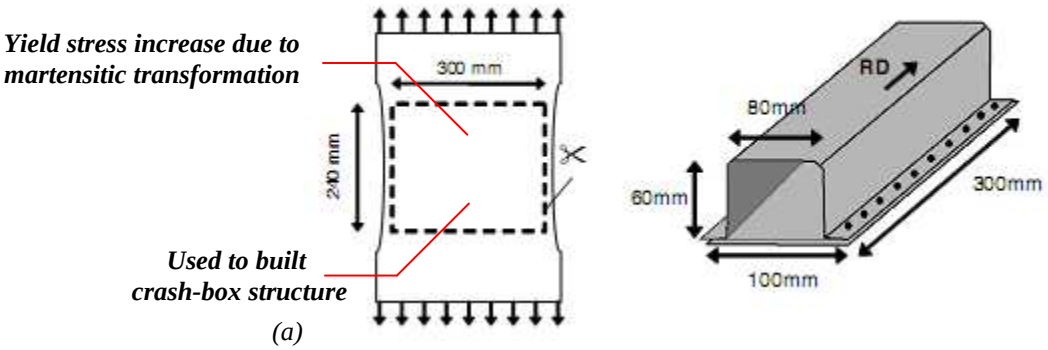

Fig. 2.42. Pre-strain history of a crash box structure (a) Specimen dimensions after pre-strain process. (b) Omega box after bending [Durrenberger et al. 2006].

Two effects are responsible for the deformation process taking place in *austenitic* steels during and after the *martensitic* transformation [Leblond et al. 1989, Fischer et al. 2000, Delannay et al. 2008]

- The "Magee effect" [Magee 1966] related to orientation process due to transformation of preferred variants.

- The "Greenwood-Johnson effect" [Greenwood and Johnson 1965] related to the displacive character of the *austenite-martensite* transformation [Leblond et al. 1989]. It corresponds to the plastic strain induced in the parent phase because of the volume difference between two coexisting phases.

The controlling factor for the kinetics of *martensitic* transformation is the supply of free energy. The free-energy variation of the system must be large enough to enable the reaction to mount the activation barrier between *austenite* and *martensite* [Angel 1954, Olson and Cohen 1972, Curtze et al. 2009], Fig. 2.43.

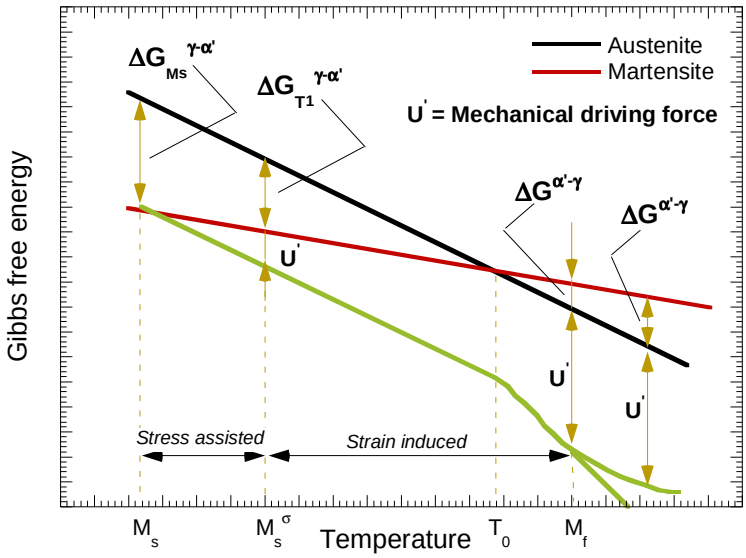

Fig. 2.43. Free energy of martensite and austenite as a function of temperature [Olson and Cohen 1972, Curtze et al. 2009].

In Fig. 2.43. M_s is the temperature at which *martensite* forms without assistance of external driving force because of the difference between the free energy of both phases, $\Delta G_{T_1}^{\gamma\rightarrow\alpha'}$. Within the range $M_s \leq T \leq T_0$ a mechanical driving force has to be supplied to the system to induce the *martensitic* transformation. Transformation occurs if the mechanical driving force makes the system to fulfill Eq. 2.28.

$$\Delta G_{T_1}^{\gamma\rightarrow\alpha'} + U^{'} = \Delta G_{M_s}^{\gamma\rightarrow\alpha'} \tag{2.28}$$

If $M_s^{\sigma} \leq T \leq T_0$ the stress required for the transformation exceeds the yield stress of the *austenite* and strain is required for the transformation, Fig. 2.44.

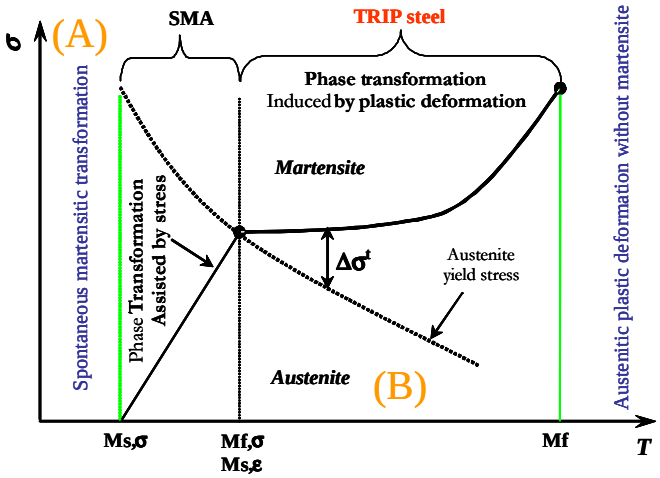

Fig. 2.44. Schematic description of the effect of temperature on the martensitic transformation.

At higher temperatures $T_0 < T < M_f$ the chemical driving force opposes to the transformation and the mechanical work applied to the system must be higher than the difference in the free energy between both phases, $U^{'} \geq \Delta G_{T_0 \leq T \leq M_d}^{\gamma\rightarrow\alpha'}$. Finally, M_f represents the temperature at which no *martensitic* transformation takes place, no matter the plastic deformation of the parent phase [Lebedev and Kosarchuk 2000].

Due to the relation existing between deformation and temperature in the material behaviour, the strain rate also plays a crucial role in the *martensitic* transformation. For high strain rates, the *martensitic* transformation could not exist; Fig. 2.45. Thermal softening of the material due to adiabatic heating under dynamic loading prevents the phase transformation.

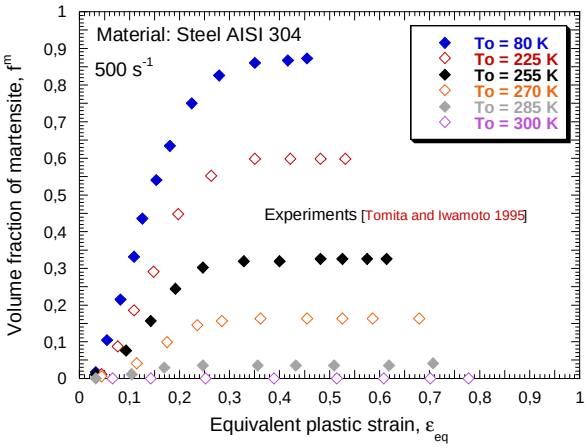

Fig. 2.45. Volume fraction of martensite as a function of plastic deformation for different initial temperatures. Strain rate = 500 s^{-1} [Tomita and Iwamoto 1995].

The influence of plastic deformation, loading rate and initial temperature on the transformation kinetics has been analyzed for example in [Iwamoto et al. 1998, Iwamoto and Tsuta 2000, Bouaziz and Guelton 2001, Al-Abbasi and Nemes 2003, Papatriantafillou et al. 2006, Taleb and Petit 2006, Larour et al. 2006, Meftah et al. 2007, Bouaziz et al. 2008, Curtze et al. 2009, Huh et al. 2009, Jiménez et al. 2009].

In order to model the *martensitic* transformation phenomena, several constitutive relations can be found in the international literature [Leblond et al. 1986a, Leblond et al. 1986b, Fischer 1990, Fischer 1992, Fischer et al. 1996, Cherkaoui et al. 1998, Cherkaoui et al. 2000, Delannay et al. 2008, Mahnken et al. 2009]. The most relevant seems to be the approach by Olson and Cohen [Olson and Cohen 1975]. This model called **OC** was later generalized to take into account the stress state effect [Stringfellow et al. 1992], strain rate [Tomita and Iwamoto 1995] and stress state for stacking fault energy [Iwamoto et al. 1998]. A use of these kind of physical models in **FE** codes results in long computational time causing limiting industrial applications since these constitutive relations are coupled with a homogenization method as proposed by Aravas [Aravas 1987].

Thus, in the following section of this manuscript is proposed a simplified formulation to describe the macroscopic effect that the *martensitic* transformation may have on the material flow stress. It takes into account the influence of strain, strain rate and temperature on such process. Short computational time and simple formulation makes the formulation developed attractive for numerical applications in industry, where the phase transformation in *austenitic* steels might be dominant, for example in perforation, crash box behaviour or high speed machining processes. However, the application of this approach does not provide information about microstructure evolution during plastic deformation.

2.6.2 Applied method for modeling reference metallic alloys

2.6.2.1 Formulation developed

A third stress component $\bar{\sigma}_T\left(\bar{\varepsilon}_p, \dot{\bar{\varepsilon}}_p, T\right)$ is added to the **RK** or to the **MRK** models *(depending on the influence that the plastic strain may have on the rate sensitivity of the material)*, which allows approximation of the macroscopic effect of the *martensitic* transformation *(drastic increase of the material strain hardening).*

Thus, the general form of the extended model is given by Eq. 2.29

$$\bar{\sigma}\left(\bar{\varepsilon}^{p},\dot{\bar{\varepsilon}}^{p},T\right)=\frac{E(T)}{E_0}\left[\bar{\sigma}_{\mu}+\bar{\sigma}^{*}\right]+\bar{\sigma}_{T}\left(\bar{\varepsilon}^{p},\dot{\bar{\varepsilon}}^{p},T\right) \tag{2.29}$$

In order to define macroscopically the phase transformation effect observed in experiments the following expression is introduced, Eq. 2.30.

$$\bar{\sigma}_{T}\left(\bar{\varepsilon}^{p},\dot{\bar{\varepsilon}}^{p},T\right)=\sigma_0\cdot f\left(\bar{\varepsilon}^{p},\dot{\bar{\varepsilon}}^{p}\right)\cdot g\left(T\right) \tag{2.30}$$

The first multiplier σ_0 is a fitting parameter which allows defining the maximum stress increase due to *martensitic* transformation. The multiplier can be estimated by mechanical testing. The value of σ_0 must be identified at the lowest temperature of interest or the lowest temperature of experimental data available. The best solution is performing mechanical testing at $T_0 < M_s$ .Thus, it corresponds to the maximum effect of the *martensitic* transformation. The stress component $\bar{\sigma}_{T}\left(\bar{\varepsilon}^{p},\dot{\bar{\varepsilon}}^{p},T\right)$ is split into two independent functions, the effect of plastic strain and strain rate during the phase transformation, $f\left(\bar{\varepsilon}^{p},\dot{\bar{\varepsilon}}^{p}\right)$ and the thermal reduction of the rate of the *martensitic* transformation, $g(T)$.

To define the influence of strain and strain rate in the phase transformation, the following function $f\left(\bar{\varepsilon}^{p},\dot{\bar{\varepsilon}}^{p}\right)$ is applied, Eq. 2.31. This expression is similar to the relation called *logistic function* derived in [Pecherski 1998, Pecherski 1998] to describe phenomenologically the plastic softening of the material during the development of multi-scale shear banding. The proposed probabilistic description of the plasticity and strain rate effects on the *martensitic* transformation is given by Eq. 2.31.

$$f\left(\bar{\varepsilon}^{p},\dot{\bar{\varepsilon}}^{p}\right)=\left[1-\exp\left(-h\left(\dot{\bar{\varepsilon}}^{p}\right)\cdot\bar{\varepsilon}^{p}\right)\right]^{\xi} \tag{2.31}$$

One function, $h\left(\dot{\bar{\varepsilon}}^{p}\right)$, and one material parameter, ξ , are introduced to approximate the behaviour of an *austenitic* steel during *martensitic* transformation. Thus, $h\left(\dot{\bar{\varepsilon}}^{p}\right)$ is defined as being strain-rate dependent in agreement with experimental observations.

A decrease of $h\left(\dot{\bar{\varepsilon}}^{p}\right)$ allows decreasing the rate of the *martensitic* transformation by diminishing its intensity and delaying its starting point, Fig. 2.46-a. Concerning the coefficient ξ, it controls the strain level where the *martensitic* transformation starts on the macroscopic scale *(the extra strain hardening induced by the martensitic transformation)*. The macroscopic phase transformation effect starts at determined level of strain, Fig. 2.46-b.

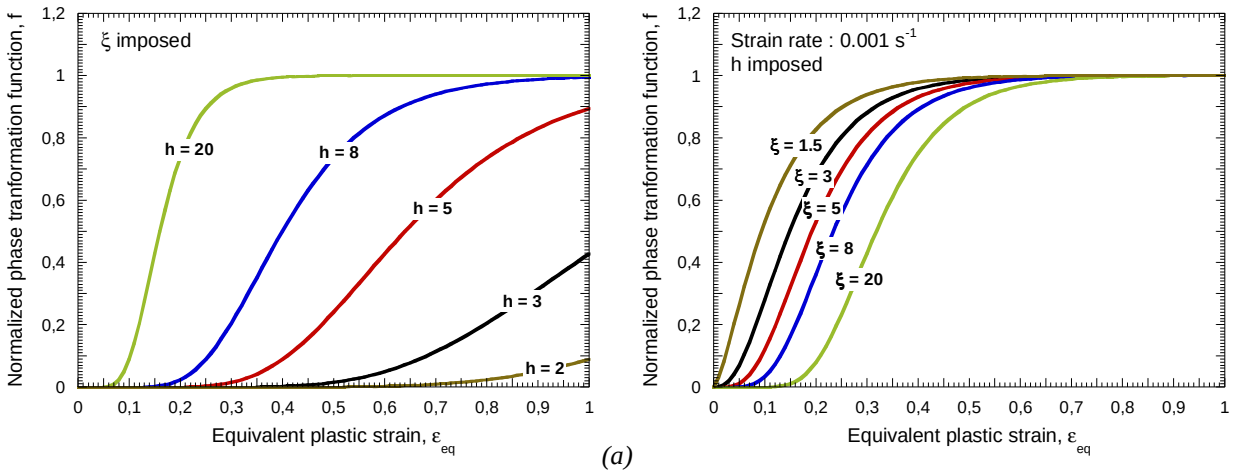

Fig. 2.46. Evolution of phase transformation function $f\left(\dot{\bar{\varepsilon}}^{p},\bar{\varepsilon}^{p}\right)$ as a function of plastic strain, (a) for different values of λ, (b) for different values of ξ.

In order to define the influence of strain rate in the *martensitic* transformation process, the following relation is proposed, Eq. 2.32.

$$h\left(\dot{\bar{\varepsilon}}^{p}\right)=\lambda_{0}\cdot\exp\left(-\lambda\cdot\dot{\bar{\varepsilon}}^{p}\right) \qquad (2.32)$$

Where λ_0 and λ are two shape fitting parameters which define the strain and strain rate dependences on the phase transformation.

It is observed that an increase of λ, Fig. 2.47, decreases the strain rate level where the phase transformation is annihilated. This coefficient can be identified using experiments obtained from the macroscopic behaviour of the material.

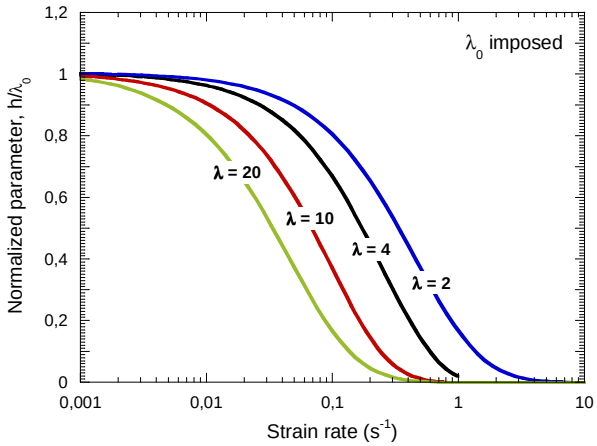

Fig. 2.47. Evolution of normalized parameter λ / λ_0 as a function of strain rate.

In the following section the relation which defines the effect of temperature on the kinetics of the *martensitic* transformation is discussed. Two formulations are proposed for that task.

2.6.2.1.1 Temperature function based on M_s and M_f values

The first expression proposed $g_1(T)$, Eq. 2.33., is based on the relation derived by Johnson and Cook [Johnson and Cook 1983] and similar to the formulation used by Papatriantafillou et al.

[Papatriantafillou et al. 2006] to describe the temperature sensitivity of the *martensitic* transformation.

$$\begin{cases} g_1(T) = 1 - \Theta^{\eta} \\ \Theta = \left(\dfrac{T - M_s}{M_f - M_s} \right) \end{cases} \quad \begin{array}{l} \text{if} \quad T \le M_s \rightarrow g_1(T) = 1 \\ \text{if} \quad T \ge M_f \rightarrow g_1(T) = 0 \end{array} \tag{2.33}$$

Where $\Theta = (T - M_s)/(M_f - M_s)$ is the normalised temperature. The values of M_s and M_f must be obtained from experiments. Moreover, η is the temperature sensitivity of the phase transformation.

A parametric study concerning η has been conducted in order to show the effect it has on the kinetics of the *martensitic* transformation, Fig. 2.48-a. As it is shown in Fig. 2.48-a, it allows for the description of the intensity and level of the *martensitic* transformation depending on the initial temperature, in qualitative agreement with experimental observations, Fig. 2.48-b [Tomita and Iwamoto 1995].

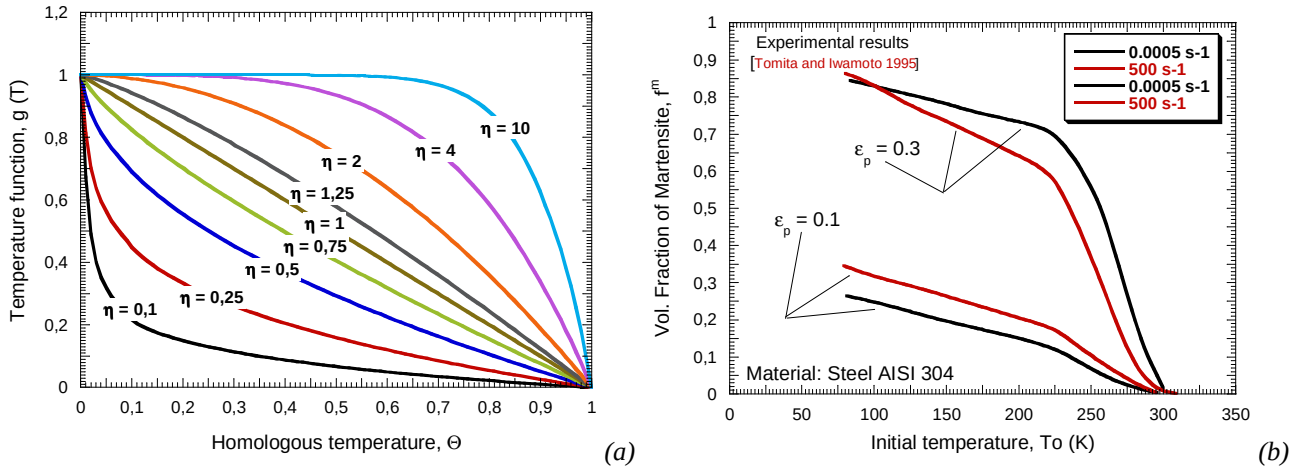

Fig. 2.48. (a) Evolution of the temperature function $g_1(T)$ as a function of the initial temperature for different values of η. (b) Evolution of the volume fraction of martensite as a function of temperature [Tomita and Iwamoto 1995].

2.6.2.1.2 Temperature function based on exponential function

The second expression proposed $g_2(T)$, Eq. 2.34, is an exponential type equation similar to that reported by Mahnken et al. [Mahnken et al. 2009] and originally proposed in [Koistinen and Marburger 1959].

$$g_2(T) = \exp\left[-\left(\frac{T}{M_f - T_0} \right)^{\alpha} \right] \tag{2.34}$$

Where T is the current temperature, T_0 and α are material constants. The expression proposed is depending on M_f but not on M_s as previously, Eq. 2.33. The M_f value must be obtained from experiments in quasi-static condition. For a given M_f there is only one possible combination of T_0 and α values which fit the requirements of the *martensitic* transformation process,

$\left(\text{if} \quad T \geq M_f \rightarrow g_2(T) = 0\right)$. For example in the case of M_f = 300 K, the parameters T_0 and α take the values 80 K and 5 respectively, Fig. 2.49.

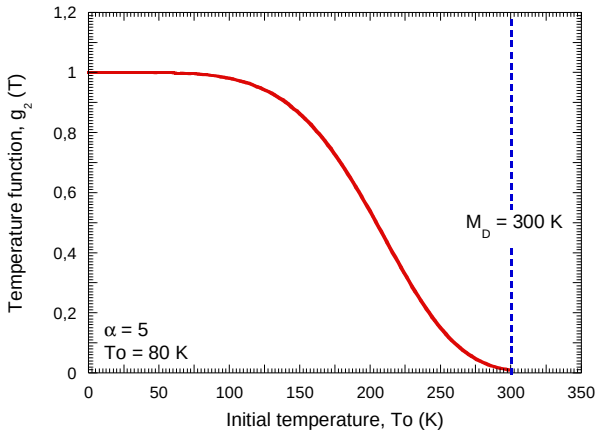

Fig. 2.49. Evolution of the function g_2 (T) with temperature.

Thus, this type of function $g_2(T)$ is less flexible in comparison with $g_1(T)$. However, it allows defining the effect of temperature within the whole range of initial temperatures without imposing any restriction. It facilitates the calibration procedure.

Next a systematic procedure for the model calibration is reported.

2.6.2.2 Systematic procedure for calculation of the model parameters

The procedure consists of the following steps:

1. First, at room temperature and low strain rate, it must be identified the plastic strain value where the *martensitic* transformation starts *(the macroscopic increase of strain hardening)*. Next, the stress level is artificially increased with plastic deformation step by step after the point of initiation of the phase transformation effect, Fig. 2.50, by using a strain hardening initial curve obtained in quasi-static loading. The stress increase due to the macroscopic effect of the *martensitic* transformation is subtracted from the material flow stress.

2. After subtraction of the macroscopic phase transformation effect, is possible to define the material constants for the original **RK** and **MRK** models using the procedure described in previous sections of the document.

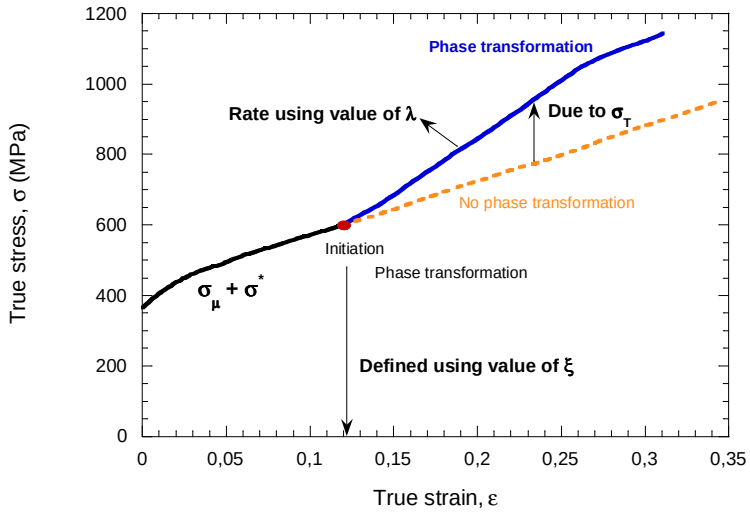

*Fig. 2.50. Schematic representation of the method used to determine the values of the material constants of the extended **RK** and **MRK** models to martensitic transformation effect.*

3. The phase transformation term is calibrated by a quantitative analysis of the stress component subtracted from the original material flow stress, Fig. 2.50. Experiments at different loading rates are fitted to Eq. 2.31. in order to obtain the material constants defining the strain and strain rate sensitivities of the *martensitic* transformation. Finally, using experimental data at different initial temperatures is possible to determine the material constants related to the temperature sensitivity of the *martensitic* transformation, Eqs. 2.33-2.34.

Next, the extended **RK** model to *martensitic* transformation is applied to define the thermo-viscoplastic behaviour of the **AISI 301 Ln2B** *(it is assumed that this material does not exhibit dependence of plastic strain on the **VTA** since its strain hardening in absence of martensitic transformation remains approximately constant for different temperatures and strain rates).*

2.6.2.3 Application to steel 301 Ln2B

Among the commercial *austenitic* steels, the **AISI 301** is noted by exhibiting strong work hardening increase caused by *martensitic* transformation. This fact and the precise study conducted in [Larour et al. 2006] of its deformation behaviours makes this material propitious for validation of the model proposed.

Grade **301** and its low carbon variants are used where a high strength stainless steel is required. Variant **301 Ln** has higher **N** content inducing work hardening increase and large ductility. Its chemical composition is listed in Table 2.20.

C	Mn	Si	Cr	Ni	N	P	S
0.0 3	2.0	1.0	18.5	8.0	0.20	0.045	0.015

*Table 2.20. Chemical composition of the steel **AISI 301Ln2B** (% weight).*

Typical applications of this material include rail car structural components, airframe structures and highway trailer components.

By application of the calibration procedure reported in the previous section, the following set of material constants has been obtained, Tables 2.21-2.22.

B_0 (MPa)	ν (-)	n_0 (-)	D_2 (-)	ε_0 (-)	σ_0^* (MPa)	m^* (-)	D_1 (-)	T_m (K)	$\dot{\varepsilon}_{min}$ (s^{-1})	$\dot{\varepsilon}_{max}$ (s^{-1})	θ^* (-)
1380	*0.1*	*0.41*	*0.05*	*0.018*	*488.33*	*1.66*	*0.52*	1600	10^{-5}	10^{7}	0.9

*Table 2.21. Values of material constants for the original **RK** constitutive relation for the steel **301 Ln2B**.*

σ_0 (MPa)	ξ	λ_0	λ
500	*17*	*10*	*4*

*Table 2.22. Material constants defining the martensitic transformation stress term for the steel **301 Ln2B**.*

Analytical results of the extended model are compared with experiments, [Larour et al. 2006]. The macroscopic effect of the *martensitic* transformation is well exposed by $\sigma-\varepsilon$ curves for different initial strain rates at room temperature, Fig. 2.51. In Fig. 2.51. is observed a satisfactory agreement between experimental results and analytical predictions of the model within a wide range of strain rates $0.006\ s^{-1} \le \dot{\bar{\varepsilon}}^p \le 920\ s^{-1}$.

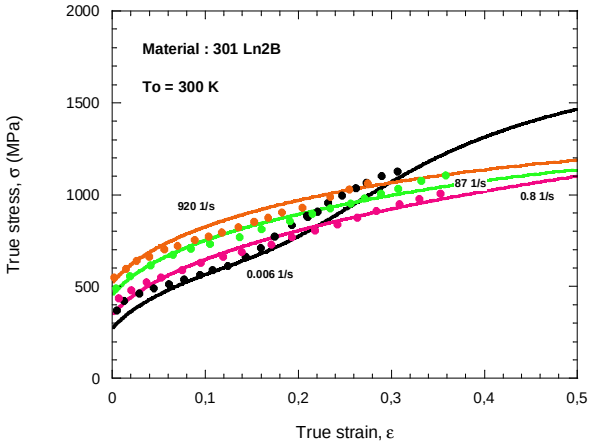

Fig. 2.51. Analytical predictions of the constitutive relation (solid lines) and comparison with experimental results [Larour et al. 2006].

The comparison between the analytical predictions obtained by means of original and extended **RK** formulations is shown in Fig. 2.52. The analytical prediction by the extended formulation demonstrate the annihilation of the phase transformation with the strain rate increase, Fig. 2.52-b.

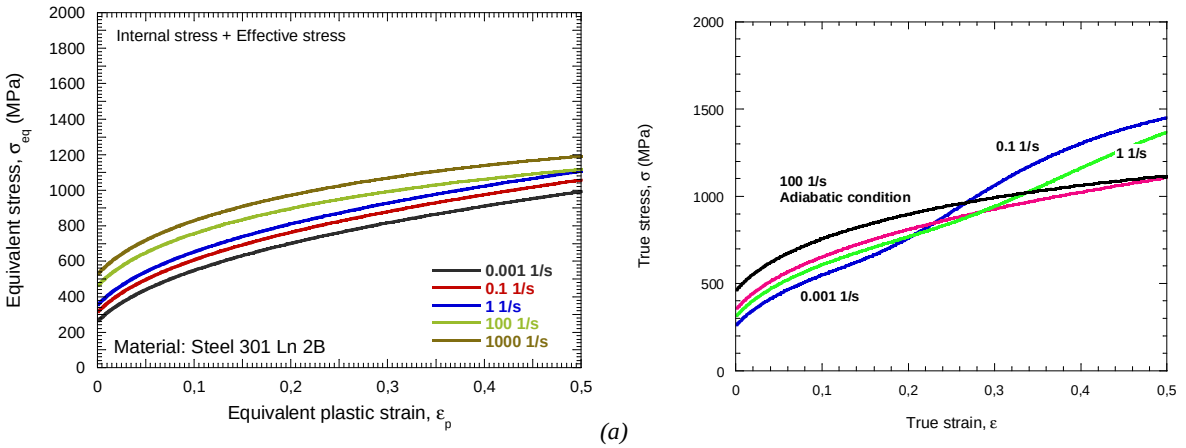

*Fig. 2.52. Analytical predictions of the constitutive relations (a) original **RK** formulation, (b) extended **RK** formulation, $g_i(T) = 1$*

In the following plot, Fig. 2.53., are illustrated the predictions of the constitutive relation when a jump of strain rate is imposed at room temperature. In the case of a jump of strain rate from quasi-

static to dynamic loading the model predicts correctly the annihilation of the *martensitic* transformation effect. In the opposite case, if the strain rate jump is conducted from dynamic to quasi-static loading, the model predicts the appearance of *martensitic* transformation macroscopic effect, Fig. 2.53.

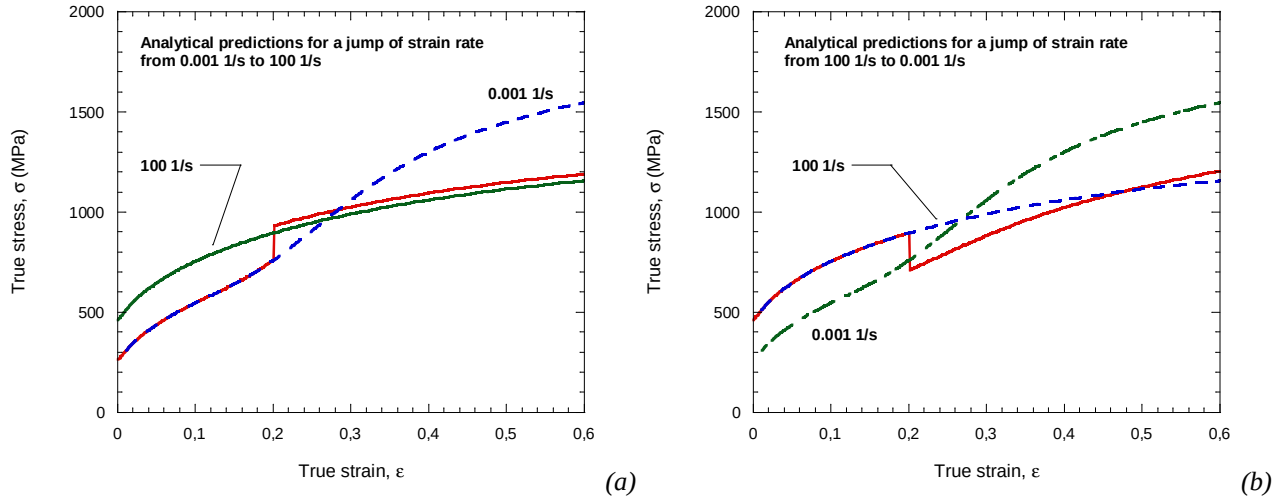

*Fig. 2.53. Analytical predictions of the extended **RK** model in the case of (a) positive and (b) negative jump of strain rate for g(T) = 1.*

The analytical predictions of the model under quasi-static conditions of deformation for several initial temperatures in the case of $g_1(T)$ using $\eta = 1$, and $g_2(T)$ using $T_0 = 80$ K and $\alpha = 5$ are shown in Fig. 2.54-a-b. A qualitative agreement was found with the experimental observations for several *austenitic* steels reported in [Tomita and Iwamoto 2001], Fig. 2.54-c. When the initial temperature is high enough, the *martensitic* transformation is annihilated, Fig. 2.54-a. The intensity of the phase transformation strongly increases when the temperature is close to the M_S, Fig. 2.54-a-b.

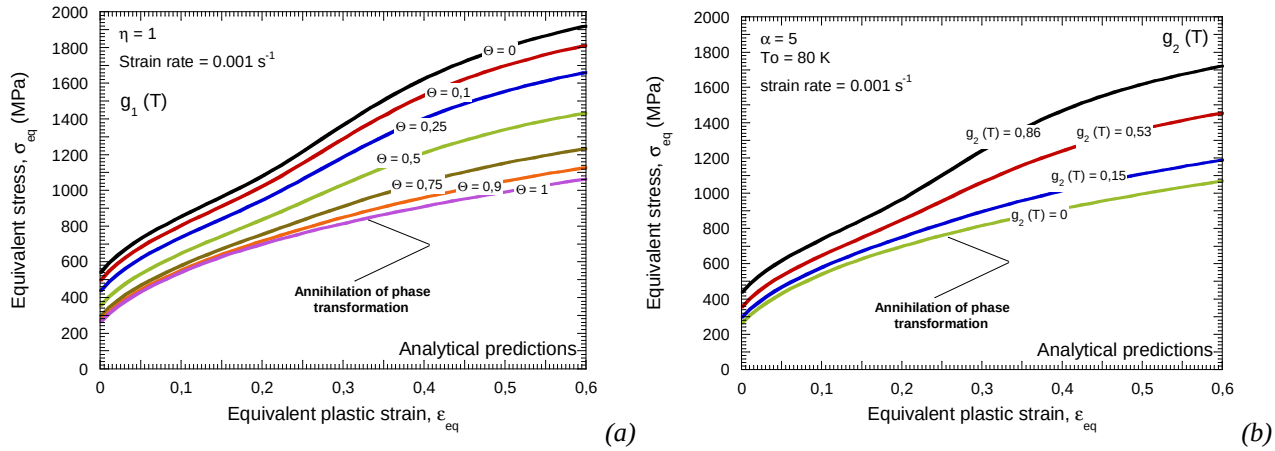

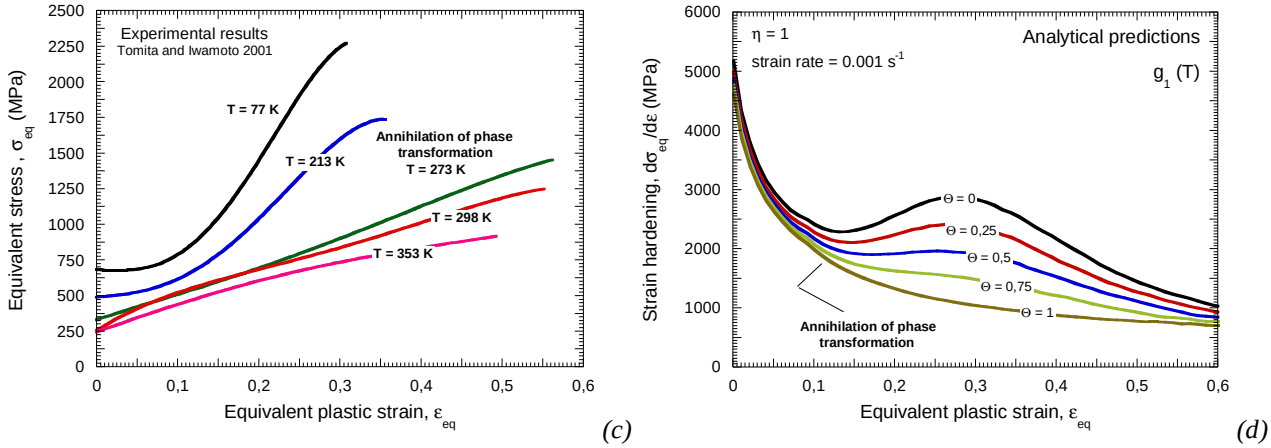

*Fig. 2.54. Analytical predictions of the extended **RK** model (a) in the case of g_1 (T) and (b) in the case of g_2 (T). (c) Evolution of the flow stress versus the plastic strain for steel **AISI 304** [Tomita and Iwamoto 2001]. (d) Description of the strain hardening evolution as a function of plastic strain by the extended **RK** model for different homologous temperatures.*

For $g_1(T)$ using $\eta = 1$, the evolution of the strain hardening rate as a function of the plastic deformation for different normalised temperatures Θ is shown in Fig. 2.54-d. An increase of strain hardening rate is observed during the *martensitic* transformation effect until saturation condition is reached. This maximum is lower with the initial temperature increase. When the maximum is exceeded, the strain hardening rate starts to decrease monotonically. Finally, it reaches a value close to the one corresponding to strain hardening curves which previously have not shown the *martensitic* transformation.

The constitutive descriptions reported in this document may be implemented into **FE** code. Details of the procedure for such implementation are given in **Appendix B** and **Appendix C**.

In this chapter of the document it has been examined the mechanisms which reside behind deformation of metals. Advanced constitutive relations have been developed in order to provide a macroscopic description of the thermo-viscoplastic behaviour of metallic alloys within wide ranges of strain rate and temperature. Such procedure must be the starting point in order to analyze loading processes. Such understanding of metals behaviour is applied in the following chapters of this Thesis in order to define the mechanisms responsible for absorbing energy under dynamic solicitation. For that task, the constitutive descriptions developed are implemented into **FE** code. Numerical simulations of ring expansion test and conventional dynamic tension test are conducted in order to determine the role played by rate sensitivity and strain hardening on the formation of instabilities.

CHAPTER 3

NUMERICAL ANALYSIS OF PLASTIC INSTABILITIES FORMATION UNDER DYNAMIC TENSION

Abstract

In this chapter of the Thesis is conducted a numerical study in order to examine the causes which reside behind the formation of plastic instabilities under dynamic loading. Two different configurations are used for that task; ring expansion and conventional dynamic tension. Wave propagation, strain hardening and strain rate effect on the formation of plastic instabilities are examined. The influence of rate sensitivity on plastic instabilities formation is analyzed by application of the extended **MRK** model to dislocations drag. The influence of strain hardening is analyzed by application o the extended **RK** model to *martensitic* transformation. A complete parametric study of the material constants involved in both extensions applied to **RK** and **MRK** models is carried out. From the analysis conducted is concluded that strain rate sensitivity and strain hardening rate are the main parameters involved in controlling plastic localization.

3 CHAPTER 3. NUMERICAL ANALYSIS OF PLASTIC INSTABILITIES FORMATION UNDER DYNAMIC TENSION

3.1 Introduction

The study of materials subjected to extreme loading conditions like crash, impact or explosion, has considerable interest for different industrial fields. A relevant amount of publications can be found in the international literature dealing with the high strain rate behaviour of metallic materials related to different engineering applications [Mann 1936, Klepaczko 1968, Kocks et al. 1975, Follansbee 1986, Regazzoni et al. 1987, Zerilli and Armstrong 1992, El-Magd 1994, Nemat-Nasser and Li 1998, Nemat-Nasser and Guo 2003].

Dynamic processes are strongly dependent on strain hardening, temperature sensitivity and strain rate sensitivity of the material. Locally, plastic strain values larger than $\bar{\varepsilon}_f^p > 1$ may be reached for some metals under dynamic loading conditions [Hu and Daehn 1996, Pandolfi et al. 1999, Triantafyllidis and Waldenmyer 2004]. High temperature level inducing thermal softening of the material is usually observed in such processes. It comes from an irreversible thermodynamic process which converts the plastic energy into heat. Adiabatic temperature increase is precursor of plastic instabilities [Batra and Chen 2001, Kuroda et al. 2006, Batra and Wei 2007, Alos et al. 2007] and subsequent failure.

Thus, advancing on understanding instabilities formation is of main relevance for certain engineering sectors like automotive, aeronautical or military industries where fast loading processes are of fundamental interest. Accurate knowledge of the causes leading to plastic instabilities formation is required for construction of mechanical elements responsible for absorbing energy under crash or impact perforation.

Formation of plastic instabilities under dynamic loading has been studied over the last decades [Mann 1936, Klepaczko 1968, Rajendran and Fyfe 1982, Grady 1982, Clifton et al. 1984, Batra and Kim 1990, Duszek and Perzyna 1991, Łodygowski et al. 1994, Perzyna 1994, Klepaczko 1998, Glema et al. 2000, Zhou et al. 2006, Rittel et al. 2006]. Special interest is found in the early works of Hutchinson and Neale [Hutchinson and Neale 1977], Ghosh [Ghosh 1977] and Fressengeas and Molinari [Fressengeas and Molinari 1987, Fressengeas and Molinari 1992] in which the mechanisms responsible of plastic localization and instabilities progression are analyzed.

Traditionally, it has been resorted to experimental procedures to approach the localization problem under high rate of loading [Mann 1936, Rajendran and Fyfe 1982, Grady 1982]. However, highly instrumented tests are required of complex devices with elevated cost. In addition, the information that can be obtained from the material behaviour is, many times, limited.

More recently the localization problem has attempted to be analytically described [Fressengeas and Molinari 1987, Fressengeas and Molinari 1992, Mercier and Molinari 2004, Zhou et al. 2006]. In these publications a perturbation analysis is conducted in order to analyze the mechanisms which reside behind plastic localization and instabilities progression. For this type of analytical studies, due to complications in the mathematical formulation of the problem, the definition of the homogeneous material behaviour uses to be given by a simplified power-type equation [Fressengeas and Molinari

1987, Fressengeas and Molinari 1992, Mercier and Molinari 2004, Zhou et al. 2006]. The accurate definition of the material behaviour is subordinated to a fast derivation of the problem solution. The evaluation of particular effects of the material behaviour, as viscous drag or *martensitic* transformation, on the formation of instabilities cannot be approached by such mathematical modelling of the problem.

If advanced constitutive relations want to be used for defining the material behaviour, numerical methods are a suitable alternative [Łodygowski and Perzyna 1997, Sørensen and Freund 2000, Glema et al. 2000, Guduru and Freund 2002, Rusinek and Zaera 2007].

In the mentioned works was glimpsed that rate sensitivity and strain hardening are playing a main role on controlling the instabilities formation. It is assumed that they act homogenizing materials behaviour [Mercier and Molinari 2004], increasing their ductility [Rajendran and Fyfe 1982, Hu and Daehn 1996, Altynova et al. 1996] and retarding plastic localization [Hu and Daehn 1996].

According to the methodology set for conducting this Thesis, in this chapter previous statements are evaluated by conducting numerical simulations of ring expansion test and conventional dynamic tension test. Application of advanced strain hardening laws for an accurate description of the plastic localization process is required. Thus, the influence of rate sensitivity on plastic instabilities formation is analyzed by application of the extended **MRK** model to dislocations drag [Rusinek et al. 2010]. The influence of strain hardening is analyzed by application of the extended **RK** model to *martensitic* transformation. A complete parametric study of the material constants involved in both extensions applied to **RK** and **MRK** models is carried out.

3.2 Dynamic tension tests

Among the dynamic characterization tests developed over the years, uniaxial tension has been the most common stress state used for analyzing instabilities formation. In particular conventional dynamic tension test and ring expansion test have been widely studied during the last decades [Mann 1936, Klepaczko 1968, Rajendran and Fyfe 1982, Grady 1982, Łodygowski and Perzyna 1997, Sørensen and Freund 2000, Glema et al. 2000, Guduru and Freund 2002, Rusinek and Zaera 2007].

3.2.1 Literature review

Thus, in this section of the document both testing configurations are introduced.

3.2.1.1 The ring expansion test

Rapid expansion of metallic rings is a non-conventional experiment developed to test materials at high strain rates under uniaxial tension state [Niordson 1965, Grady and Benson 1983, Hu and Daehn 1996]. The experiment consists of loading a ring of radius R at a roughly constant velocity V_0 varying within the range $25 \text{ m/s} \leq V_0 \leq 300 \text{ m/s}$. The strain rate applied to the material during the expansion is given by Eq. 3.1.

$$\dot{\bar{\varepsilon}}^{p} = \frac{V_0}{R(t)} \qquad (3.1)$$

Where $R(t)$ is the ring radius as function of time during the expansion.

Several experimental setups have been proposed for these tests, Fig. 3.1. [Diep et al. 2004, Triantafyllidis and Waldenmyer 2004]. The dynamic loading may be procured by a magnetic field or by the use of explosives, Fig. 3.1., the former providing a more uniform impact velocity in time.

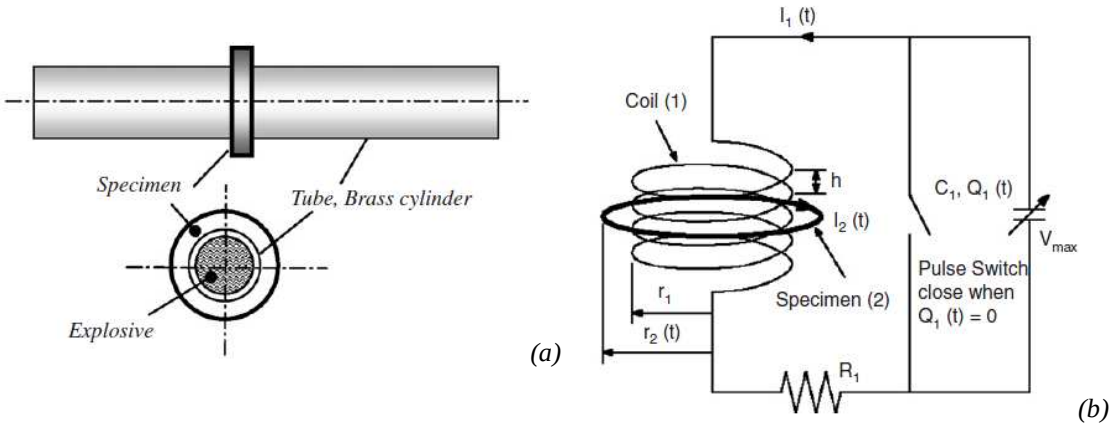

Fig. 3.1. Configuration of the loading conditions by explosive or by magnetic field in the ring expansion test [Diep et al. 2004, Triantafyllidis and Waldenmyer 2004].

The sample is subjected to uniform radial expansion until the development of neckings along the circumference of the ring takes place. Some of these necks are arrested before failure and the others lead to fracture of the specimen, resulting in a number of fragments. Physical phenomena occurring during the test are complex, and the resulting fragmentation pattern is the consequence of the competition between failure modes related to dynamic loading such as shear banding, and those characteristic of static loading such as void growth or fracture nucleation [Rusinek and Zaera 2007].

It is important to notice that complications resulting from wave propagation are eliminated due to the symmetry of the problem [Hu and Daehn 1996, Mercier and Molinari 2004, Rusinek and Zaera 2007]. Thus, ductility is expected to increase with expansion velocity, virtually without limits in velocity *(relativistic effects at very high impact velocities are expected to not make possible to fulfill previous statement)*, Fig. 3.2.

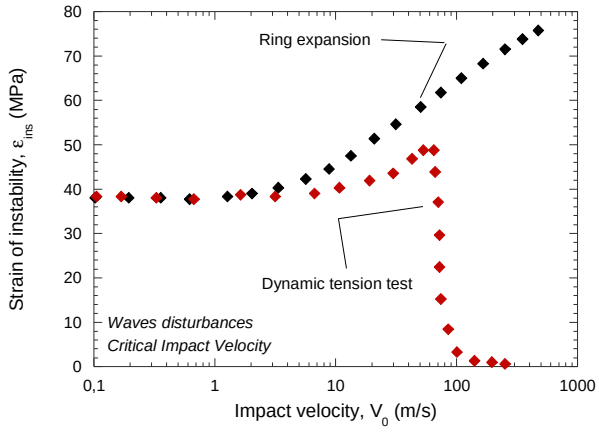

Fig. 3.2. Strain of instability as a function of impact velocity for ring expansion problem and dynamic tension test [Hu and Daehn 1996].

Due to the complex experimental devices required for performing this type of test and the limitations of the analytical modeling, numerical methods are positioned as a suitable tool to solve the localization problem [Sørensen and Freund 2000, Guduru and Freund 2002, Rusinek and Zaera 2007].

Next the main features of the conventional dynamic tension test are presented.

3.2.1.2 The conventional dynamic tension test

Analysis of the conventional dynamic tension test presents notable interest since disturbances coming from wave propagation take place in many engineering applications like for example fast cutting, crash-box test or impact-perforation. The effect that these disturbances have on the material response has to be carefully examined. The comparison with the results obtained for the ring expansion problem *(free of wave propagation)* is expected indispensable for that goal.

Let us consider a case analogous to a tension test that may be performed using hydraulic machine or Hopkinson bar, Fig. 3.3. The strain rate applied to the material during testing is defined by Eq. 3.2.

$$\dot{\varepsilon}^{p} = \frac{V_0}{L_t(t)} \tag{3.2}$$

Where L_t (t) is the active part of the specimen as function of time during the test.

In such tests, the specimen has a free end which is impacted. The second end is fixed. Thus, as consequence of the impact on the specimen, an incident tensile wave $\sigma_I(t)$ is generated. The stress wave reaches the opposite side of the specimen and it is reflected. The reflected stress wave is of the same sign than the incident wave due to the embedded boundary condition of the opposite impact side, Fig. 3.3.

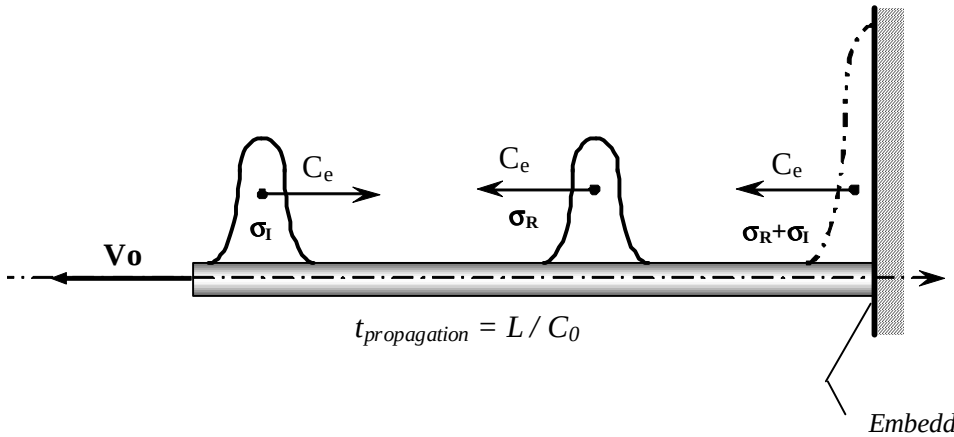

Fig. 3.3. Schematic representation of wave propagation along an elastic bar. Reflection of a longitudinal wave from the fixed end.

Considering the specimen as purely elastic, the wave speed is defined as follows, Eq. 3.3:

$$C_e(T) = \left(\frac{E(T)}{\rho(T)} \right)^{1/2} \tag{3.3}$$

Where E(T) is the Young's modulus and ρ(T) is the material density that in a general case can be considered dependent on temperature. In such an elastic case, it is known that the intensity of the reflected wave is equal to the intensity of the incident wave, Fig. 3.3. Thus, after reflection of the incident wave, the specimen is subjected to a solicitation whose value is double of the stress level induced into the material due to the incident stress wave.

Thus, it is possible to predict analytically the place where the deformation will be localized in the case of ideal plasticity as it was reported by Rusinek et al. [Rusinek et al 2008]. In that work the authors analyzed the crash-box problem, and they defined where the localization of deformation was taking place depending on the impact velocity and on the yield stress of the material.

However, if a material showing thermo-viscoplastic behaviour is considered, the wave propagation problem becomes more complex. The plastic wave propagation *(which is adiabatic by nature [Klepaczko 2005])* must be taken into account. The plastic wave speed is defined as follows, Eq. 3.4:

$$C_p\left(\bar{\varepsilon}^p,\dot{\bar{\varepsilon}}^p,T\right)=\left(\frac{1}{\rho}\cdot\frac{d\bar{\sigma}\left(\bar{\varepsilon}^p,\dot{\bar{\varepsilon}}^p,T\left(\bar{\varepsilon}^p\right)\right)}{d\bar{\varepsilon}^p}\right)^{1/2} \tag{3.4}$$

It depends on plastic strain $\bar{\varepsilon}^p$, strain rate $\dot{\bar{\varepsilon}}^p$ and temperature T. Moreover, the adiabatic condition of the process when considering dynamic problems must be taken into account, $\Delta T\left(\bar{\varepsilon}^p\right)$. In such a thermo-viscoplastic case is not possible to get analytical solution for the flow localization. Then, it is necessary to resort to experimental procedures to define where instability will take place.

In the particular configuration of impact tension test, Clark and Wood [Clark and Wood 1957] reported the following cases of localization depending on the impact velocity, Fig. 3.4.

a. In quasi-static condition, the stress wave induced in the specimen during a tensile test is much lower than that corresponding to the yield stress of the material. The plastic flow is homogeneously spread along the active part of the specimen. The instability in form of necking finally appears in the middle of the specimen having advantage of the smaller section of the sample in this zone *(geometrical instability).*

b. As the impact velocity is increased the necking moves to the opposite impact side. When the incident wave is reflected in the embedded side, its intensity is increased inducing flow localization.

c. In the following step double necking situation takes place. The impact velocity is high enough to induce plasticity in the impact end but the effect of reflection of the wave leads to faster trapping of plastic deformation and subsequent failure in the opposite impact side.

d. Next, double necking appears but failure occurs in the impacted end. The effect of the reflected wave induces plastic deformation in the opposite side end. However, the stress intensity due to the impact is high enough to induce fast localization in the impacted end, precursor of failure.

e. The final stage is the formation of a single necking leading to failure of the specimen in the impacted end. The stress wave induced by the impact involves fast trapping of plastic deformation. The velocity of the impacted end reaches the velocity of the plastic waves. Then, the **C**ritical **I**mpact **V**elocity (**CIV**) is reached. The sample behaviour becomes unstable. There is not equilibrium between the input force and the force measured on the embedded side [Hu and Daehn 1996, Rusinek et al. 2005]. The **CIV** acts as a limiting factor for material testing. The **CIV** is considered as a mechanical property of materials, Fig. 3.4.

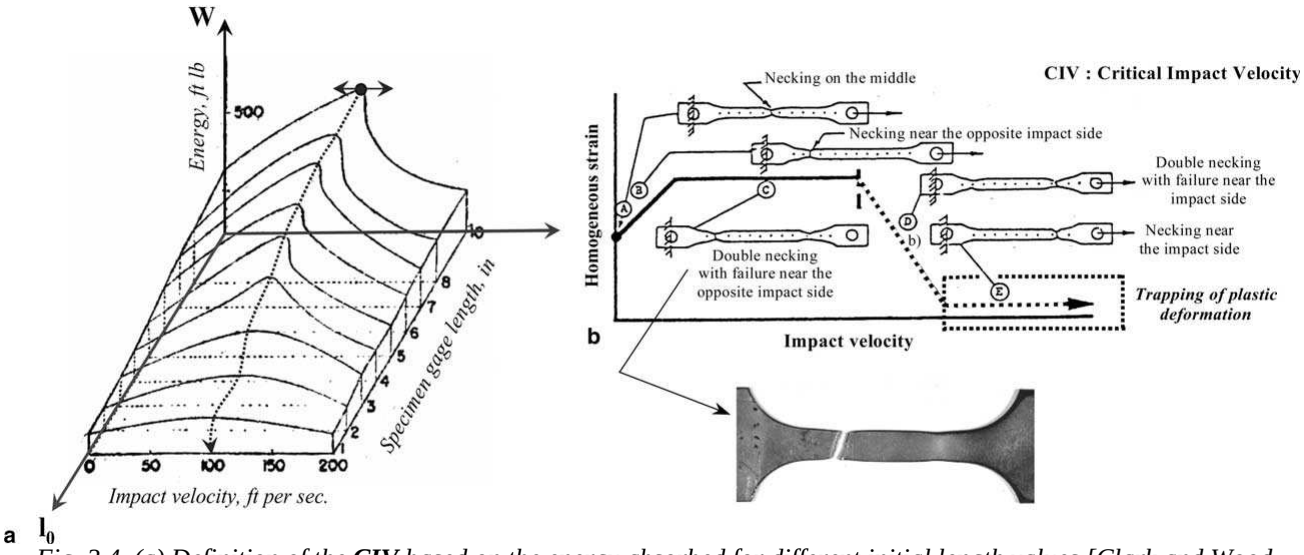

*Fig. 3.4. (a) Definition of the **CIV** based on the energy absorbed for different initial length values [Clark and Wood 1957]. (b) Schematic representation of the impact velocity effect on the process of dynamic necking [Clark and Wood 1957, Rusinek et al. 2005].*

Based on the early works of Rakhmatulin [Rakhmatulin 1945], Von Karman and Duwez [Von Karman and Duwez 1950] and Taylor [Taylor 1958], and according to Klepaczko [Klepaczko 2005], an analytical solution for the **CIV** can be obtained integrating the wave celerity along strain ***(Appendix D)***. The expression is split into two parts, Eq. 3.5.

$$\mathrm{CIV} = \int_0^{\varepsilon_e} \mathrm{C_e}\left(\mathrm{T}\right)\cdot \mathrm{d}\varepsilon + \int_{\varepsilon_e}^{\varepsilon_{pm}} \mathrm{C_p}\left(\overline{\varepsilon}^{\,p}, \dot{\overline{\varepsilon}}^{\,p}, \mathrm{T}\left(\overline{\varepsilon}^{\,p}\right)\right)\cdot \mathrm{d}\overline{\varepsilon}^{\,p} \qquad (3.5)$$

The first term of Eq. 3.5 corresponds to the elastic range, where ε_e is the elastic deformation corresponding to the initial yield stress, $\varepsilon_e = \varepsilon_e\big|_{\overline{\varepsilon}^{\,p}=0}$.

The second term corresponds to the plastic range. In that term ε_{pm} is the upper limit of integration defined as the plastic strain value for which the mass velocity *(in the plastic range)* equals the plastic wave speed [Klepaczko 2005].

However the uncertainty on defining the upper limit of integration for the plastic range $\varepsilon_{pm} = \varepsilon_{pm}\left(\overline{\varepsilon}^{\,p}, \dot{\overline{\varepsilon}}^{\,p}, \mathrm{T}\left(\overline{\varepsilon}^{\,p}\right)\right)$, Fig. 3.5, and the difficulties tied to the accurate estimation of the strain rate level in the necking zone *(it may be variable in time $\dot{\overline{\varepsilon}}_{necking}\left(t\right)$)*, make difficult to obtain a precise calculation of the **CIV** value using Eq. 3.5.

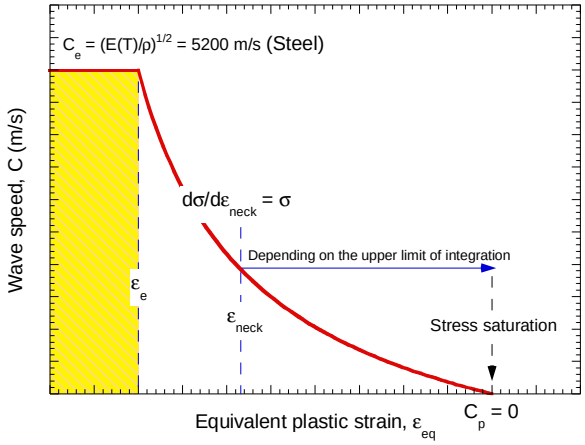

*Fig. 3.5. Schematic representation of the wave speed as a function of plastic strain for determined strain rate and temperature levels. Influence of the upper limit of integration ε_{pm} on the **CIV** value.*

Due to the complex experimental devices required for performing this type of test and the limitations of the analytical modeling, numerical methods are positioned as a suitable tool to solve the localization problem [Glema et al. 2000, Rusinek et al. 2005].

3.2.2 Numerical configurations

In the following sections of the document are described the numerical configurations used for both ring expansion and conventional dynamic tension.

3.2.2.1 The ring expansion configuration

The geometry and dimensions of the ring are depicted in Fig. 3.6. The inner diameter of the ring is φ=30 mm, with a thickness of e=1 mm and a width of t=1 mm *(1 mm^2 square cross section)* [Rusinek and Zaera 2007]. The impact velocity is applied in the inner surface of the ring and remains constant during loading [Rusinek and Zaera 2007].

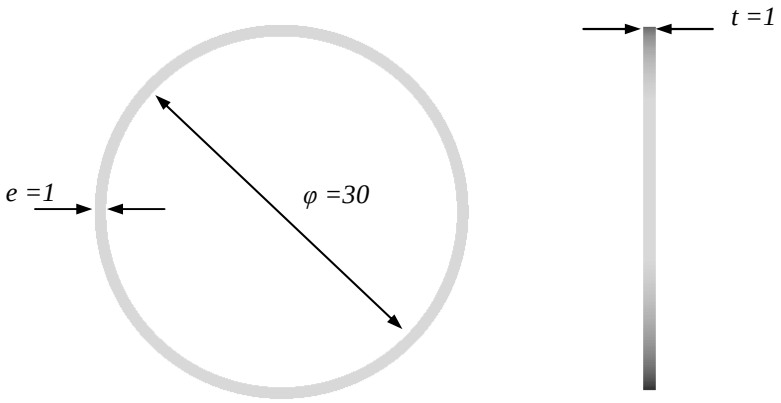

Fig. 3.6. Geometry and dimensions (mm) of the specimen used in the simulations [Rusinek and Zaera 2007].

The mesh used in the simulations is shown in Fig. 3.7. Three elements are placed along the thickness and width of the sample. Thus, the ring has been meshed using hexahedral elements whose aspect ratio is close to 1:1:1 *(≈0.33 × 0.33 × 0.33 mm^3)*. This definition is in agreement with the considerations reported by Zukas and Scheffler [Zukas and Scheffler 2000]. No geometrical or

material imperfections were introduced in the model [Larson et al. 1981] since they could change the necking problem *(and generate spurious wave propagation)* [Han and Tvergaard 1995, Sørensen and Freund 2000], the numerical uncertainties through the integration process being enough to trigger instability [Rusinek and Zaera 2007].

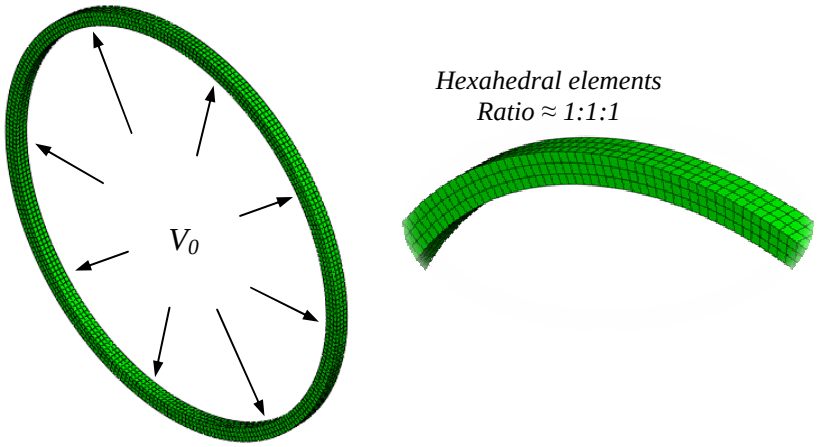

Fig. 3.7. Mesh configuration used in the numerical simulations.

The boundary conditions applied to the simulations must guarantee the uniaxial tensile state in the specimen during loading. In Fig. 3.8. can be observed that the triaxiality value during testing is that corresponding to uniaxial tension, $\sigma_{triaxiality} = 0.33$.

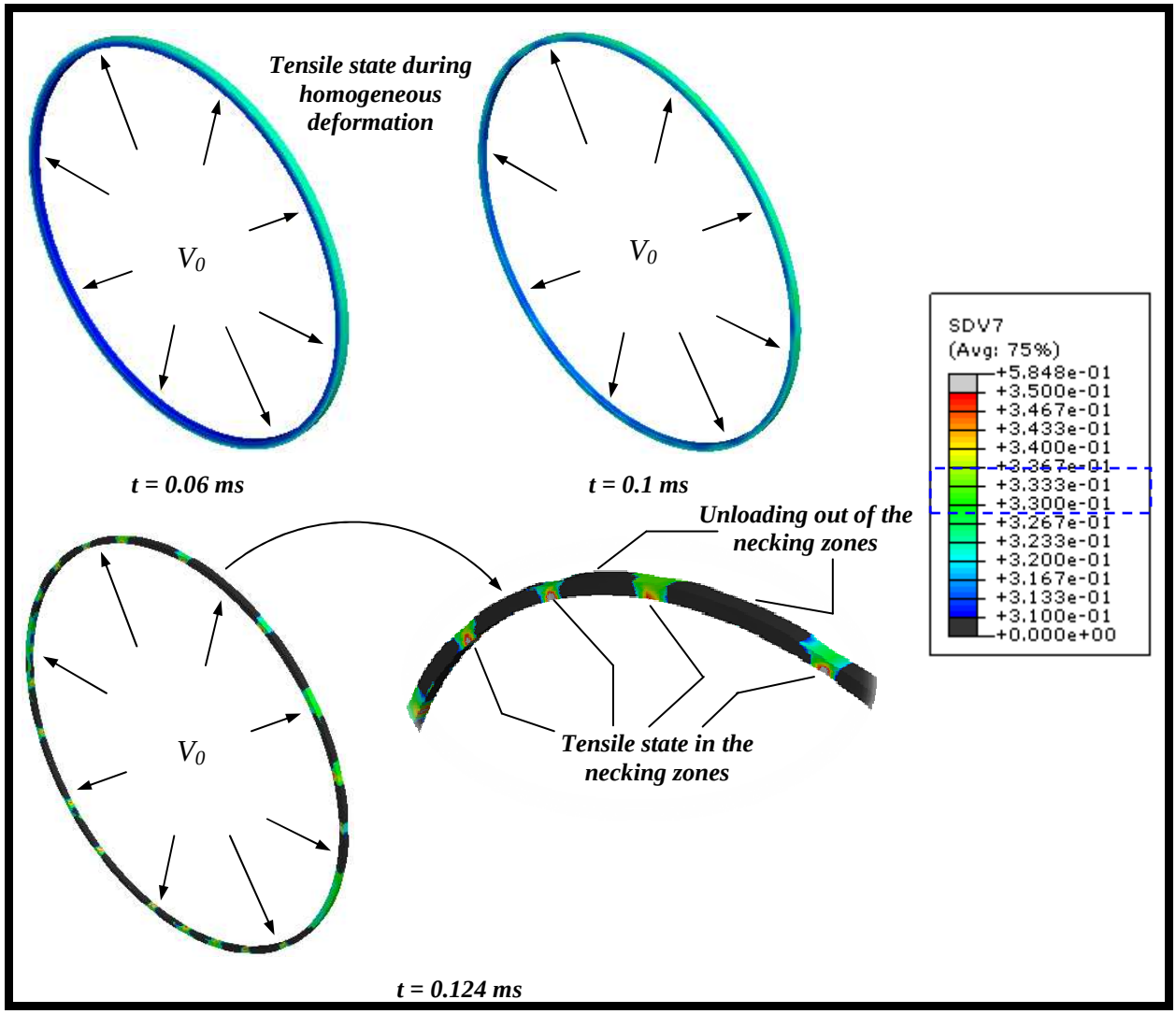

Fig. 3.8. Numerical estimation of the triaxiality contours during loading.

It must be noticed that the strain of instability is intrinsically given by the definition of the homogenous material behaviour *(constitutive description used to define the material behavior)*. Thus, in agreement with [Rusinek and Zaera 2007], a constant critical failure strain has been used in the simulations. Failure criterions based on critical values of strain are widely used in the literature [Johnson and Cook 1985, Bao and Wierzbicki 2004, Wierzbicki et al. 2005, Barsoum and Faleskog 2007], they are consistent with the theories of cracks propagation in ductile materials founded on energetic assumptions [Drucker 1959, Becker 2002]. In this particular case, the condition that must be imposed to the failure strain is to be large enough to not disturb plastic localization and necking progression.

3.2.2.2 The conventional dynamic tension configuration

The geometry and dimensions of the specimen used are based on previous works [Rusinek et al. 2008c, Rodríguez-Martínez et al. 2009]. Such geometry of specimen allows for observing well developed necking [Rodríguez-Martínez et al. 2009]. A scheme of the specimen is shown in Fig. 3.9. The thickness of the sample is t_s = 1.65 mm. Its impacted side is subjected to a constant velocity during the simulation. The movements are restricted to the axial direction. The opposite impact side is embedded. Such configuration idealizes the boundary conditions required for the test.

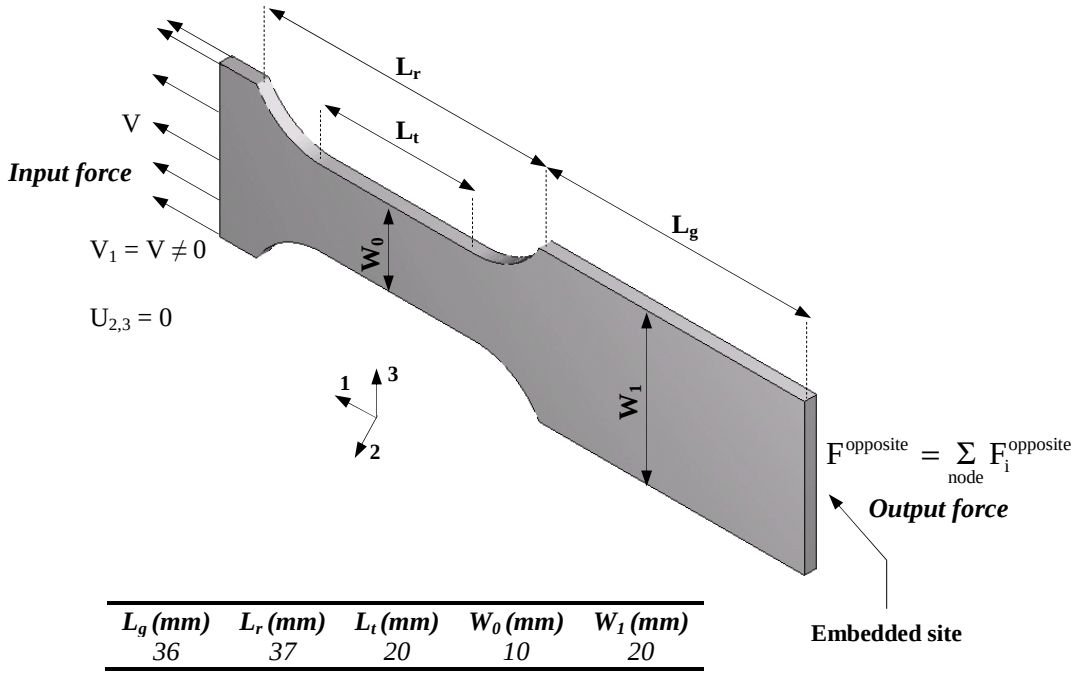

L_g (mm)	L_r (mm)	L_t (mm)	W_0 (mm)	W_1 (mm)
36	37	20	10	20

Fig. 3.9. Geometry and dimensions of the specimen used in the numerical simulations.

The active part of the specimen has been meshed using hexahedral elements whose aspect ratio is close to 1:1:1 *(≈0.55 × 0.55 × 0.55 mm^3)*. Beside the active part of the specimen two transition zones are defined. These zones are meshed with tetrahedral elements, Fig. 3.10-a. Such transition zones allow for increasing the number of elements along the 3 axis of the specimen, Fig. 3.10-a. This technique is used to get hexahedral elements in the outer sides of the sample maintaining the desired aspect ratio 1:1:1.

As it was reported for the ring expansion case, the boundary conditions applied to the simulations must guarantee the uniaxial tensile state in the active part of the specimen during loading. It can be observed in Fig. 3.10-b that the triaxiality value in the active part of the specimen is that corresponding to uniaxial tension, $\sigma_{triaxiality} = 0.33$.

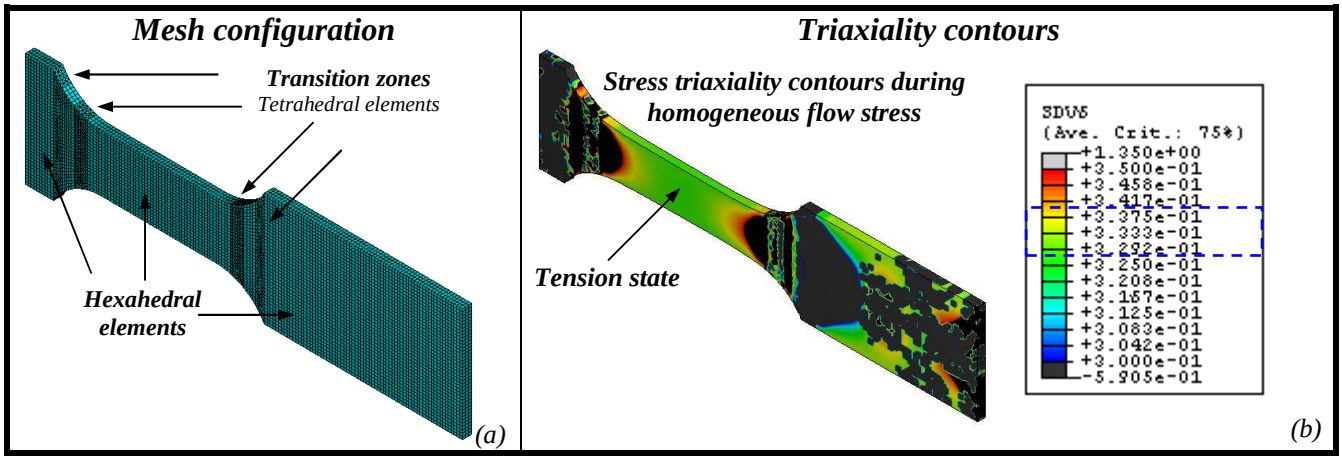

Fig. 3.10. (a) Mesh configuration used in the numerical simulations. (b) Numerical estimation of the triaxiality contours during loading.

A failure criterion has been used in the simulations based on the same considerations reported for the ring expansion case. Thus, as previously mentioned, a constant critical failure strain has been used in the simulations.

Next, the influence of rate sensitivity and strain hardening on flow localization under dynamic tension is analyzed using both numerical models previously introduced.

3.3 Influence of strain rate sensitivity on flow localization under dynamic tension

Let us go through the effect that rate sensitivity has on flow localization. For it, the extended **MRK** model to phonon drag effects is applied. The first step concerns to the methodology developped to examine the influence of strain rate sensitivity on the formation of plastic instabilities under dynamic tension

3.3.1 Methodology

The steps followed are described below:

1. The viscous drag formulation introduced in **Section 2.4.** is applied. Its strengths lie on a simple formulation only dependent on strain rate. It allows to isolate the effect that deformation rate has on the localization of plastic deformation.

2. The **OFHC** copper is choosen as reference material to analyze the effect that the stain rate sensitivity has on the formation of plastic instabilities. This material shows well described viscous drag effect at high strain rates allowing for a proper analysis of the problem.

3. Next, the numerical models developed are validated for the ring expansion case and for the conventional dynamic tension case.

4. An analysis of the influence of the rate sensitivity on the formation of instabilities is conducted using both, the ring expansion configuration and the conventional dynamic tension configuration. Comparison between both configurations is indispensable in order to determine the effect of the boundary conditions on the flow localization. The analysis is expressed in the following terms:

    a. Ring expansion test
        i. Influence of the strain rate sensitivity on the strain of instability.
        ii. Influence of the strain rate sensitivity on the number of pieces into which the ring is fragmented.
        iii. Influence of the strain rate sensitivity on the failure time.

    b. Conventional dynamic tension test
        i. Influence of the strain rate sensitivity on the strain of instability.
        ii. Influence of the strain hardening on the **CIV**.
        iii. Influence of the strain rate sensitivity on the input and output forces registered in the sample.

iv. Influence of the strain rate sensitivity on the position where the necking takes place
v. Influence of the strain rate sensitivity on the specimen elongation at failure

5. In order to provide of generality to the analysis, it is conducted a parametric study on the influence of the viscous drag formulation parameters on the flow localization.

3.3.2 Theoretical considerations

Viscous drag formulation used in the present work, Eq. 2.24-a', (**Section 2.4**) [Kapoor and Nemat-Nasser 1999] is revealed propitious in order to evaluate the influence of the rate sensitivity on the formation of instabilities. It exclusively depends on strain rate. As it will be discussed next, it enables to isolate the rate sensitivity effect on the material response.

$$\bar{\sigma}_{vs}\left(\dot{\bar{\varepsilon}}^{p}\right)=\chi\cdot\left[1-\exp\left(-\alpha\cdot\dot{\bar{\varepsilon}}^{p}\right)\right] \qquad (2.24\text{-}a')$$

The material constants corresponding to annealed **OFHC** copper have been chosen. In Fig. 3.11. the overall stress is decomposed into its respective stress components. It is observed that the viscous drag term starts to contribute to the material stress level in the case of $\dot{\bar{\varepsilon}}^{p}\geq 2000\ s^{-1}$. For $\dot{\bar{\varepsilon}}^{p}\geq 6000\ s^{-1}$ the drag mechanisms have a contribution of approximately 10 % to the overall flow stress, Fig. 3.11-b. At first sight, such contribution may not look so important in the description of the material behaviour, however it plays a fundamental role.

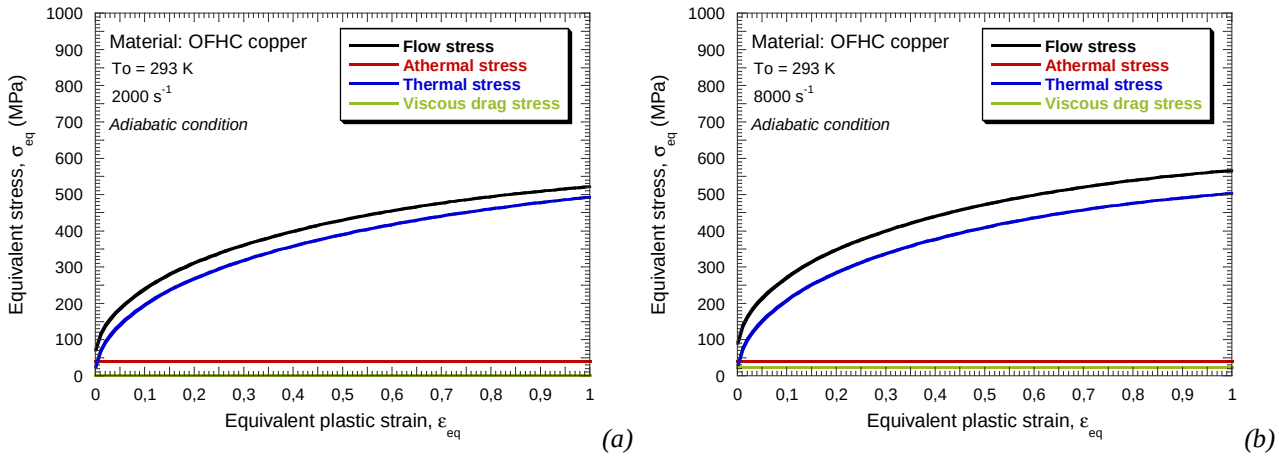

Fig. 3.11. Decomposition of the overall flow stress into its respective stress components.

The rate sensitivity of the material predicted by **MRK** and extended **MRK** models is shown in Fig. 3.12. Macroscopic effect of the dislocations drag process drastically changes the material strain rate sensitivity in the case of $\dot{\bar{\varepsilon}}^{p}\geq 1000\ s^{-1}$, Fig. 3.12. If only the thermally activated deformation mechanisms are taken into account, the rate sensitivity remains approximately constant, Fig. 3.12. Moreover, if the drag mechanisms are considered too, the rate sensitivity is subjected to a sudden increase for $\dot{\bar{\varepsilon}}^{p}\geq 1000\ s^{-1}$, Fig. 3.12. Both behaviors are radically different and the implications that this fact may have on the response of the material under dynamic loading will be extensively investigated in the present document.

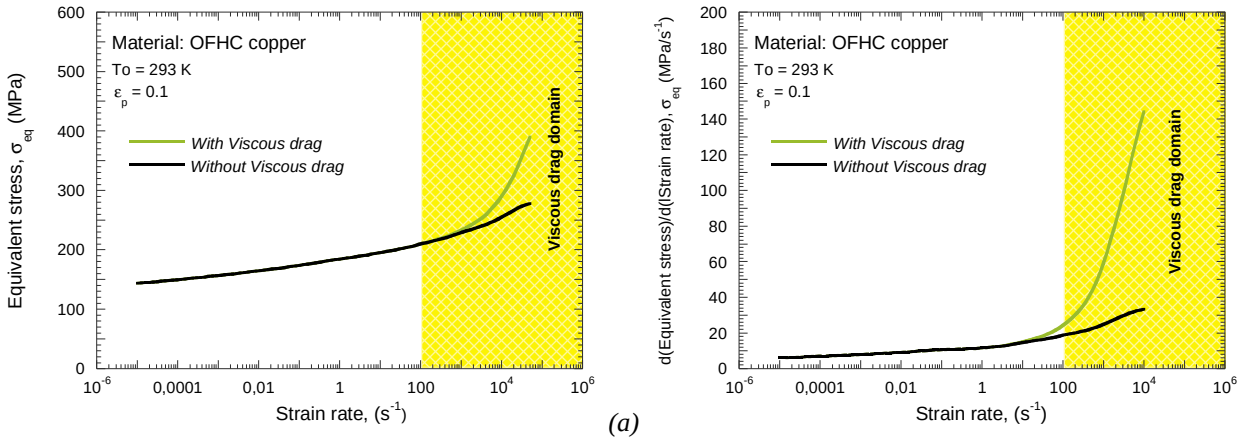

*Fig. 3.12. (a) Flow stress evolution versus strain rate of annealed **OFHC** copper predicted by **MRK** and extended **MRK** models. (b) Rate sensitivity of annealed **OFHC** copper predicted by **MRK** and extended **MRK** models.*

Moreover, it must be checked that the potential secondary effects induced by the addition of this stress term to the overall flow stress could be neglected. Such secondary effects refer to the increase of flow stress which leads to the elevation of material temperature *(due to adiabatic heating)* and to the subsequent potential modification of the material strain hardening.

Thus, in Fig. 3.13. is depicted the increase of temperature for **MRK** and extended **MRK** formulations for different strain rate levels. In the case of $\dot{\bar{\varepsilon}}^{p} = 3000\ s^{-1}$, Fig. 3.13-a, since the drag term is hardly influencing the overall flow stress, the increase of temperature caused by this stress component can be neglected. But even for much higher strain rate level, Fig. 3.13-b, the increase of temperature related to the viscous stress seems to be irrelevant.

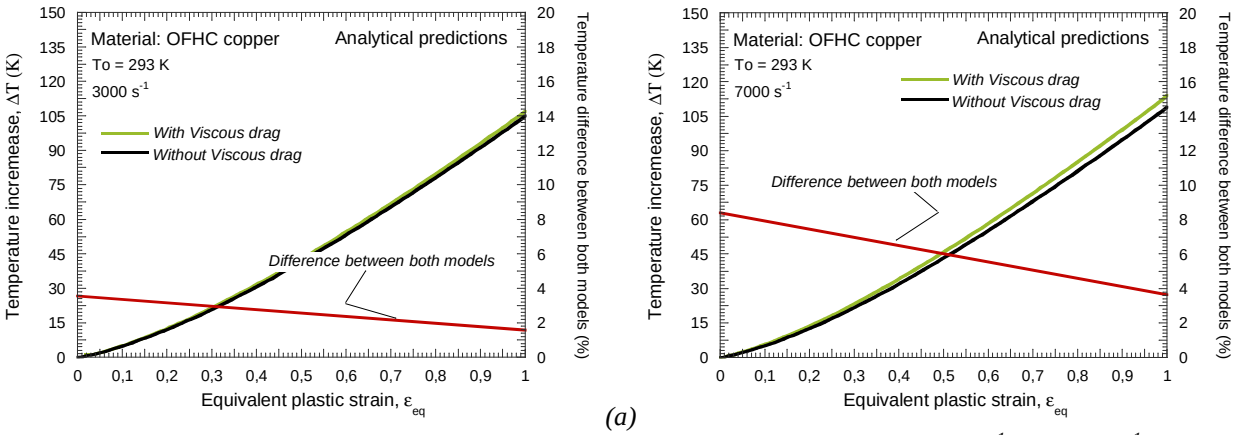

*Fig. 3.13. Temperature increase for **MRK** and extended **MRK** models. (a) 3000 s^{-1}, (b) 7000 s^{-1}.*

Analyzing Fig. 3.14. is observed that the viscous drag term is not affecting the material strain hardening but only when instability occurs. It can be concluded that any change that may be observed in the material behaviour caused by application of the viscous drag stress will be basically due to the increase of the rate sensitivity.

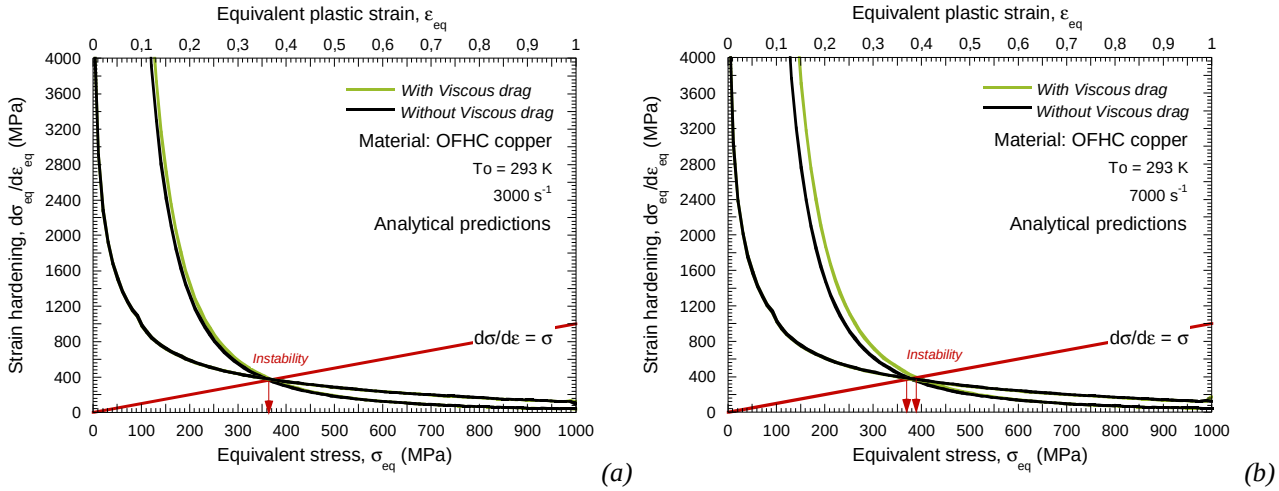

*Fig. 3.14. Strain hardening evolution versus plastic strain and versus flow stress for **MRK** and extended **MRK** models. (a) 1000 s^{-1}, (b) 5000 s^{-1}.*

3.3.3 Implementation of the extended MRK model to viscous drag effects into FE code and validation of the numerical model

Both **MRK** and extended **MRK** models have been used in the numerical simulations. Their implementation into **ABAQUS/Explicit FE** code has been conducted using the thermo-viscoplastic integration scheme for **J2** plasticity proposed by Zaera and Fernández-Sáez [Zaera and Fernández-Sáez 2006] ***(see Appendix B** and **Appendix C)***. The integration process is conducted under adiabatic conditions of deformation.

Stress – strain curves obtained from simulations at different impact velocities are compared with the analytical predictions of the constitutive relation. During the simulations, the measurement is conducted on an integration point belonging to an element out of necking zone *(placed in the active part of the specimen in the case of dynamic tension test)*, Fig. 3.15. There, the flow stress can be considered homogeneous.

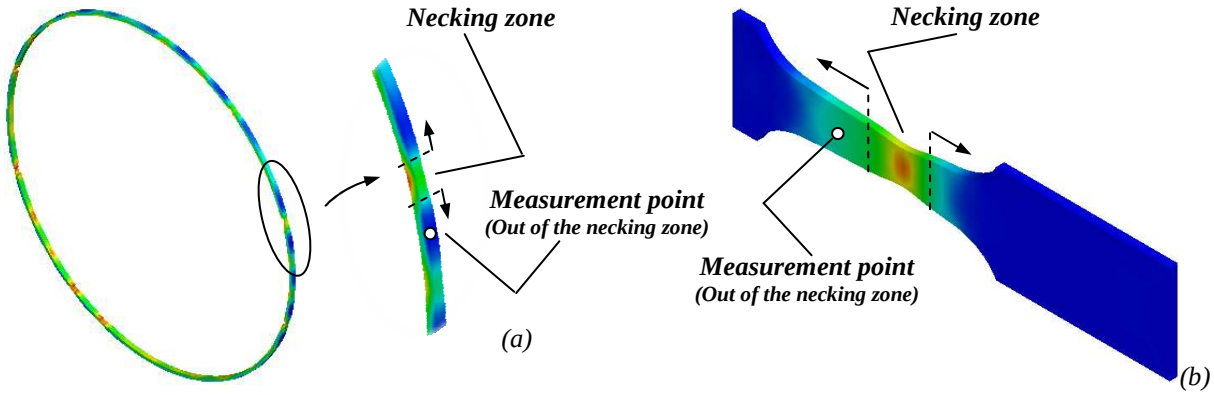

Fig. 3.15. Measurement point of strain-stress curves for the model validation. (a) Ring expansion. (b) Dynamic tension.

It has been already mentioned that the strain rate is not constant along both ring expansion and dynamic tension test. However, since the decrease of the strain rate during loading will be quite reduced, let us assume that a satisfactory comparison between analytical predictions and simulations can be conducted. The analytical predictions will be obtained using the initial strain rate applied to the test.

Perfect matching is observed between analytical predictions and simulation results for both numerical configurations, Fig. 3.16-3.17. It validates the numerical models developed.

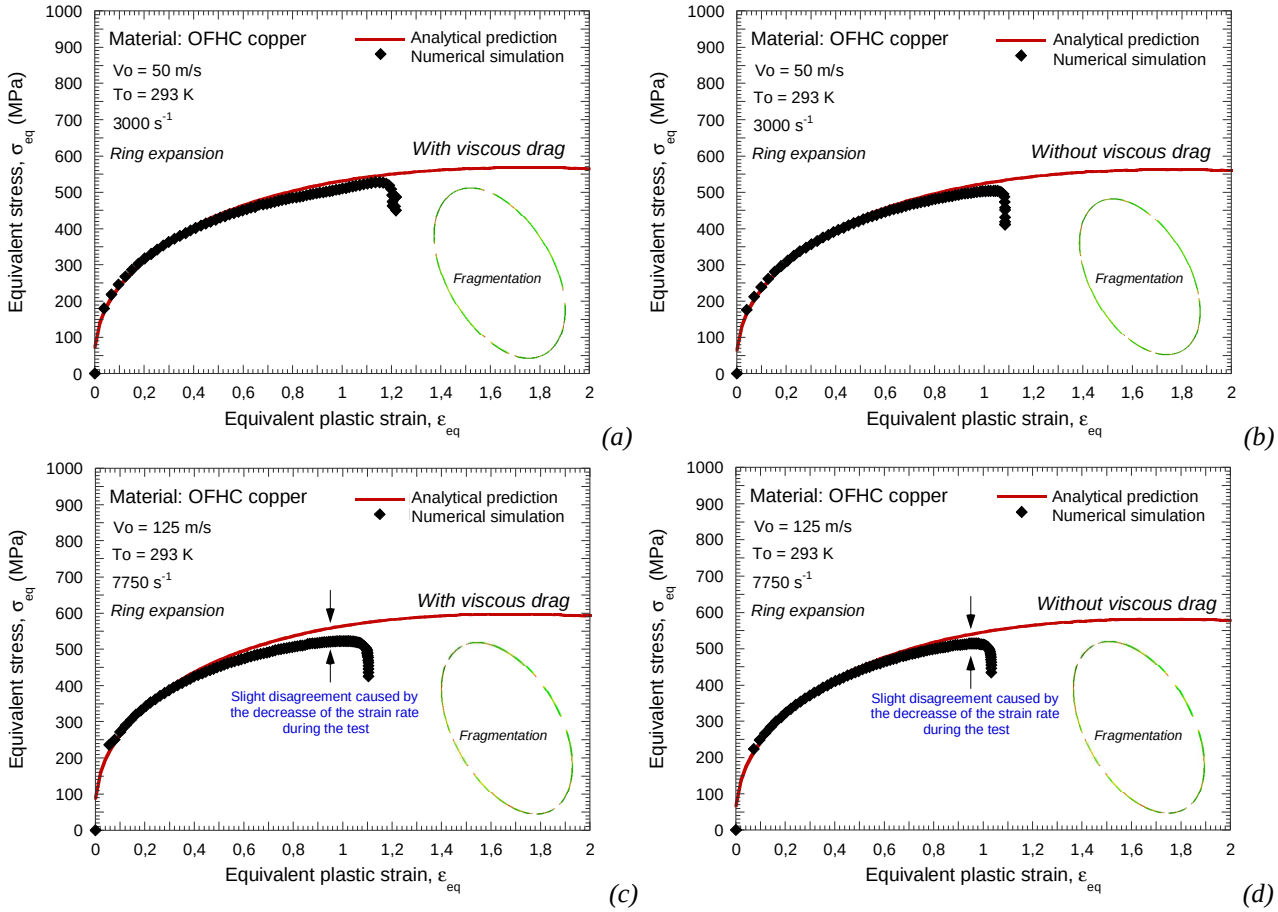

*Fig. 3.16. Comparison between numerical results and analytical predictions for **MRK** and extended **MRK** models at different impact velocities, V_0= 50 m/s and V_0= 125 m/s.*

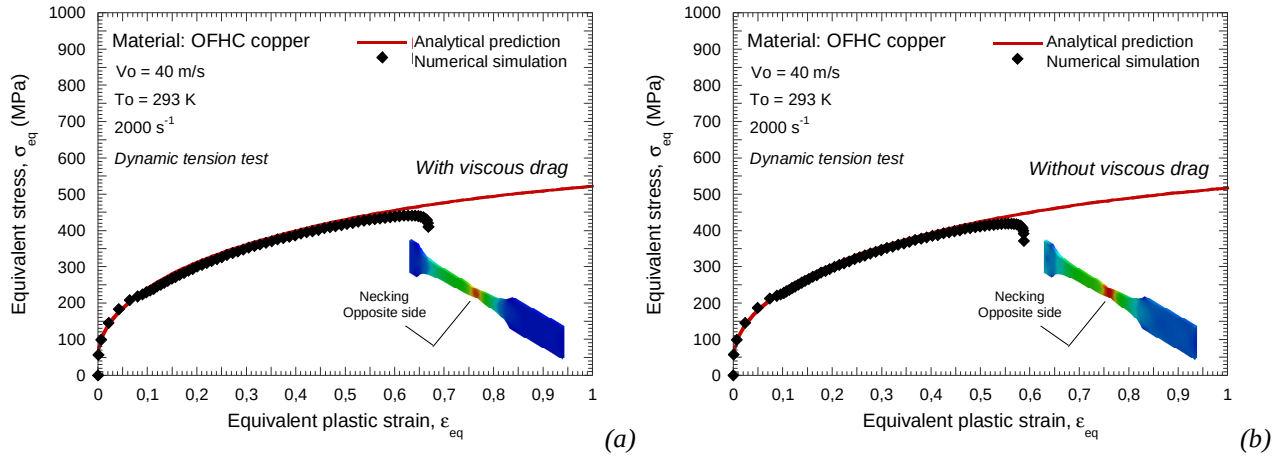

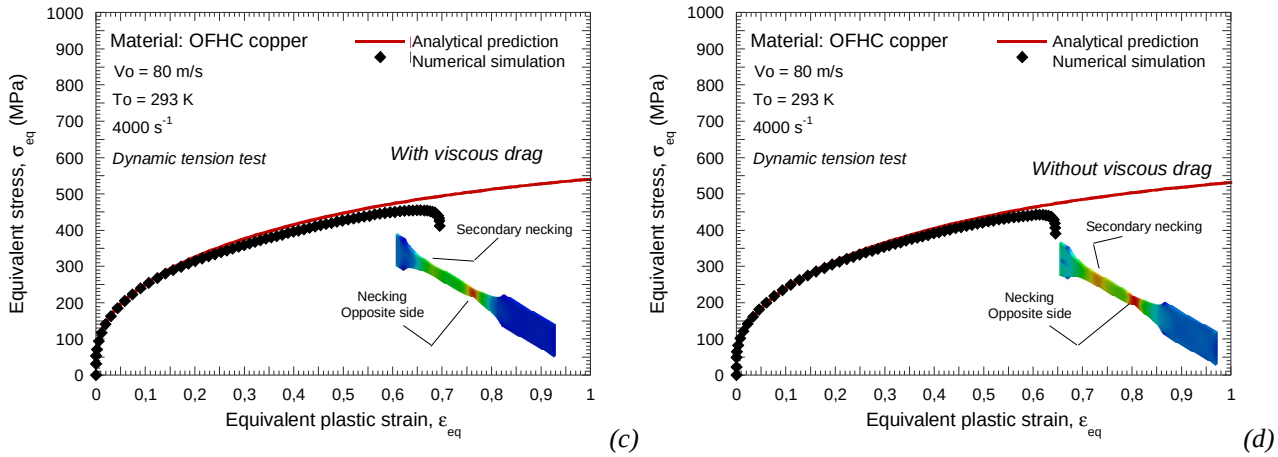

*Fig. 3.17. Comparison between numerical results and analytical predictions for **MRK** and extended **MRK** models at different impact velocities, V_0 = 40 m/s and V_0 = 80 m/s.*

3.3.4 Analysis and results for reference material

Next, is examined the influence of the viscous drag stress term *(material rate sensitivity)* on the formation of plastic instabilities under tensile state of loading.

3.3.4.1 The ring expansion test

In the ring expansion case numerical simulations within the range of impact velocities 10 m/s $\leq V_0 \leq$ 150 m/s have been carried out.

The first step is to analyze the evolution of the local plastic strain as a function of the global one *(theoretical deformation corresponding to homogeneous behaviour)* for both constitutive descriptions and different impact velocities. The measurement of the local plastic strain evolution is conducted as depicted in Fig. 3.18.

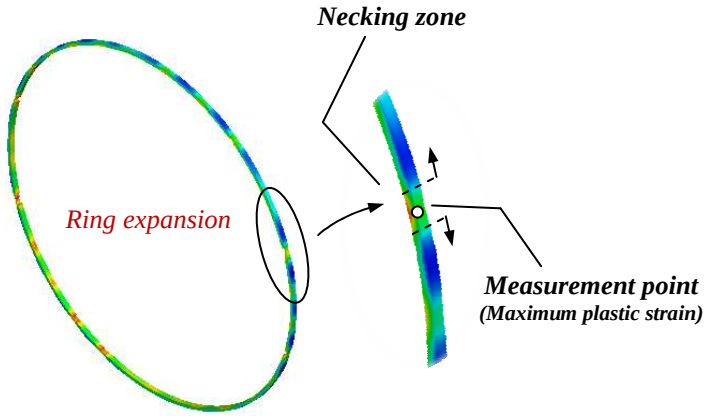

Fig. 3.18. Measurement point of local plastic strain in the ring expansion configuration.

By application of this procedure the following graphs are obtained for both, **MRK** and extended **MRK** models, Fig. 3.19. Until necking takes place the local plastic strain agrees with the theoretical one. Once instability is formed, the local plastic strain drastically deviates from the global specimen deformation [Triantafyllidis and Waldenmyer 2004], Fig. 3.19. The bifurcation point *(strain of instability)* is highly dependent on impact velocity as well as on viscous drag application.

At low impact velocities since the viscous drag term is not operative, Fig. 3.19-a, the strain of instability for **MRK** and extended **MRK** constitutive descriptions matches. Beyond a certain impact velocity *(when the viscous drag term becomes active)* the strain of instability in the case of the extended **MRK** equation becomes considerably larger than in the case of the original **MRK** formulation, Fig. 3.19. In addition, the instability progression seems to be slowed down with increasing rate sensitivity *(such consideration only can be postulated carefully since instability progression is controlled also by damage mechanics [Perzyna 2008], which are not taken into account in the numerical model).*

Such considerations are of fundamental relevance. It is proven that the rate sensitivity stabilizes the material behaviour and plays a fundamental role on the capability of metals for absorbing energy under dynamic loading.

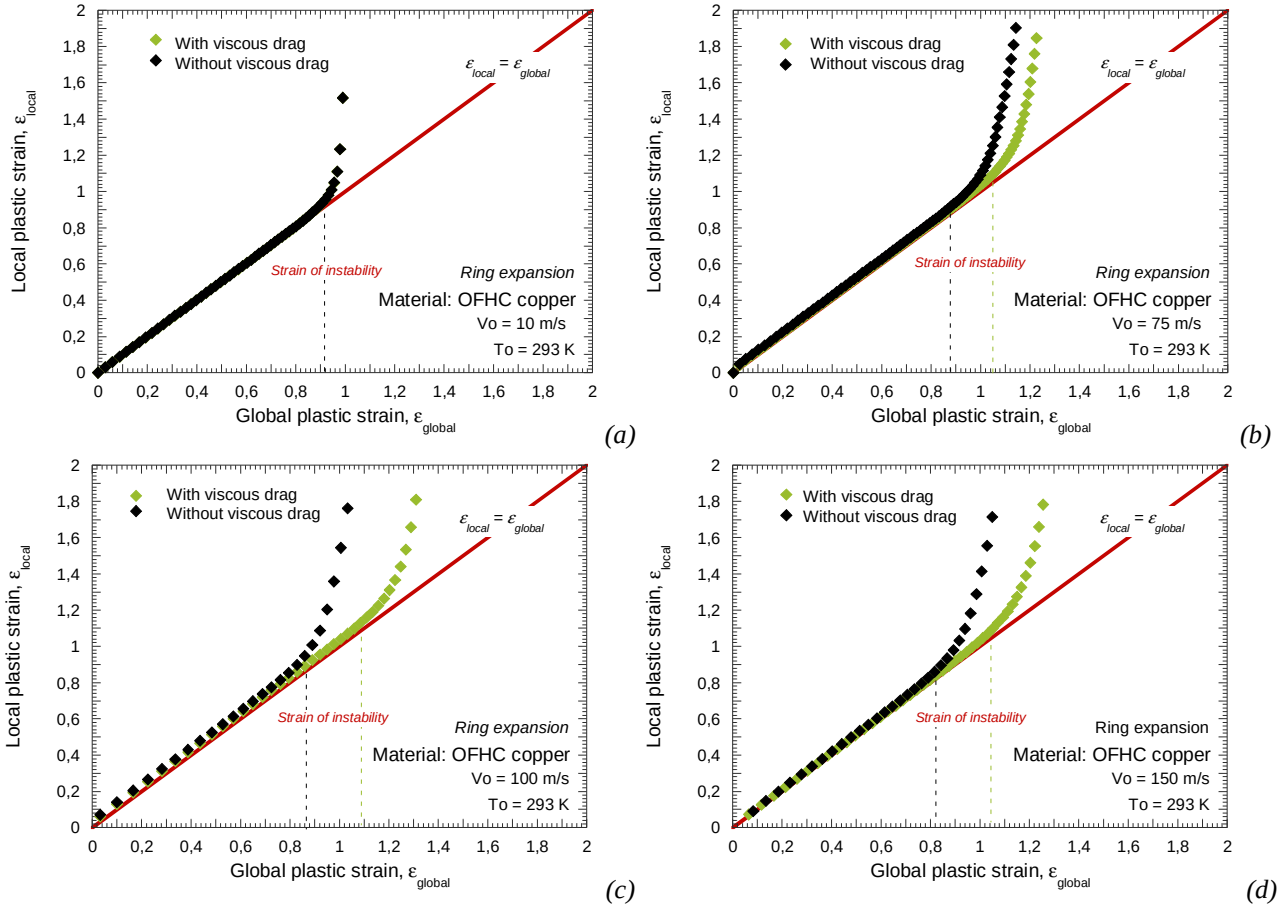

*Fig. 3.19. Evolution of the local plastic strain as a function of the global plastic strain for **MRK** and extended **MRK** models. (a) V_0=10 m/s, (b) V_0=75 m/s, (c) V_0=100 m/s, (d) V_0=150 m/s.*

In Fig. 3.20. is depicted the evolution of the strain of instability as a function of the impact velocity. For both models the strain of instability increases with impact velocity in agreement with the observations reported in [Hu and Daehn 1996], but the instability level for the extended **MRK** model is moved up in comparison with the original **MRK** model.

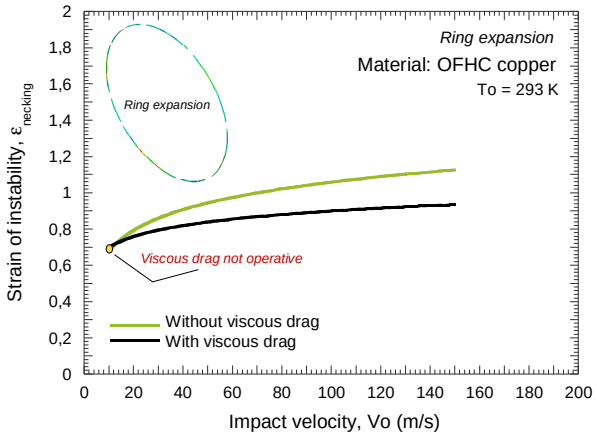

*Fig. 3.20. Strain of instability versus impact velocity for **MRK** and extended **MRK** models.*

Thus, the failure time is delayed *(a critical failure strain $\bar{\varepsilon}_f^p = 2$ has been imposed for this particular problem)* if the viscous drag term is operative, Fig. 3.21. In such a case, the number of pieces into which the ring is fragmented is larger, Fig. 3.21. Stabilization of the material and retardation of fragmentation lead to the increase in the number of fragments. All the plastic instabilities taking place during the ring expansion occur in a very short interval of time.

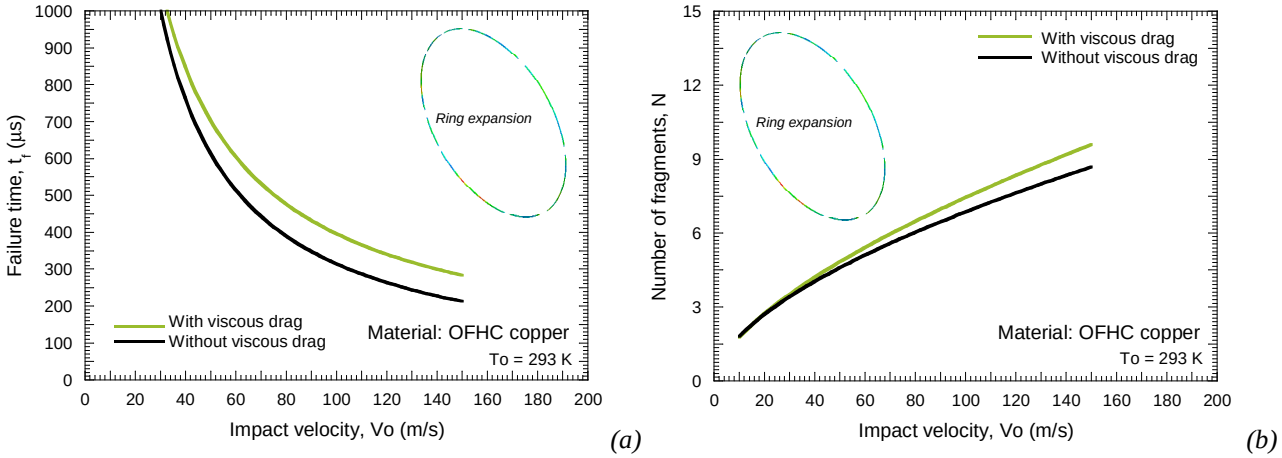

*Fig. 3.21. (a) Failure time and (b) number of fragments as a function of impact velocity for **MRK** and extended **MRK** models.*

These considerations can be clearly observed in the following plot, Fig. 3.22. where the plastic strain contours of the ring are shown just after failure for two different impact velocities. Viscous drag application spreads plasticity along the specimen, Fig. 3.22. Deformation before failure is quite uniform along the ring leading to larger number of fragments as previously mentioned.

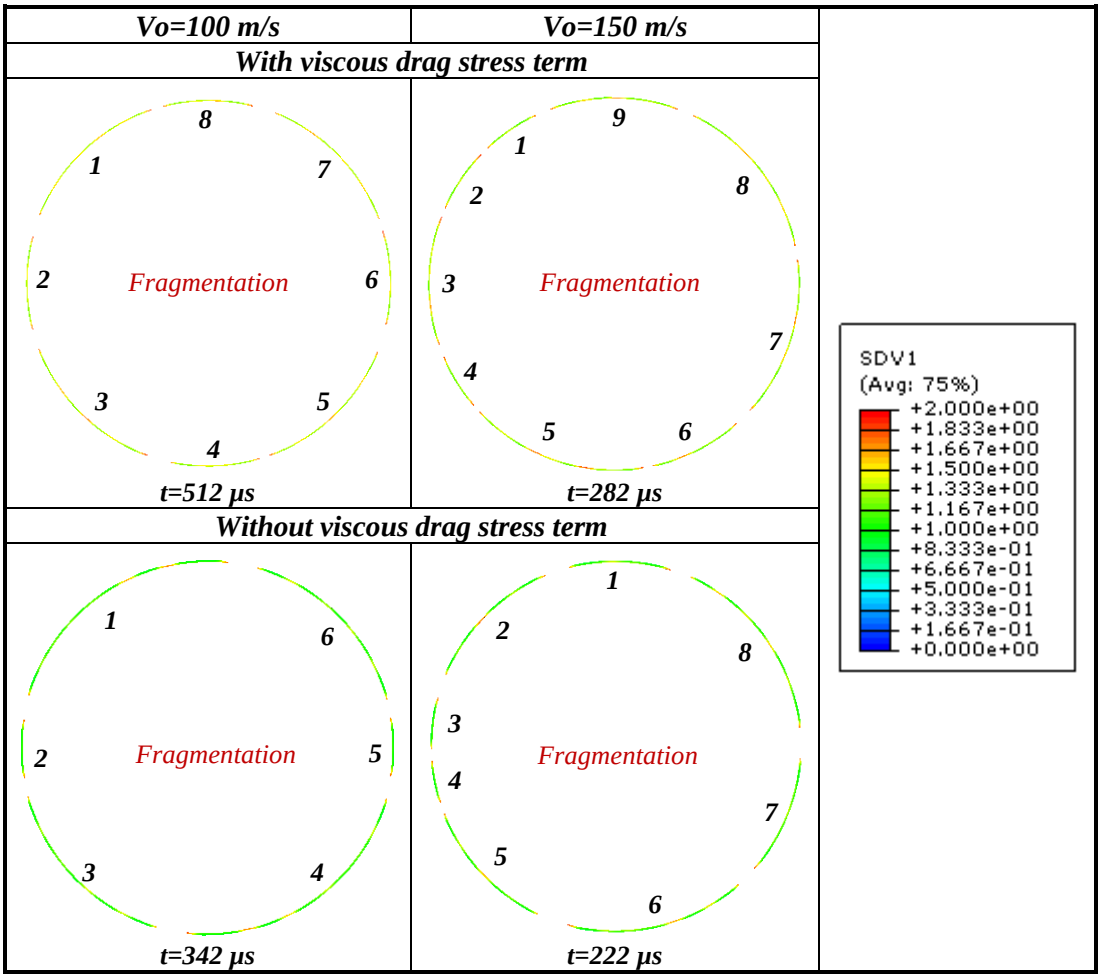

Fig. 3.22. Plastic strain contours at failure time and ring fragmentation for both models analyzed and two different impact velocities, V_0=100 m/s and V_0=150 m/s.

Next the conventional dynamic tension test is analyzed.

3.3.4.2 The conventional dynamic tension test

In the case of conventional dynamic tension test numerical simulations within the range of impact velocities 5 m/s $\leq V_0 \leq$ 160 m/s have been conducted.

As it was reported for the ring expansion case, the first step is to analyze the evolution of the local plastic strain with the global one for both constitutive descriptions and different impact velocities. The measurement technique for the local plastic strain is depicted in Fig. 3.23.

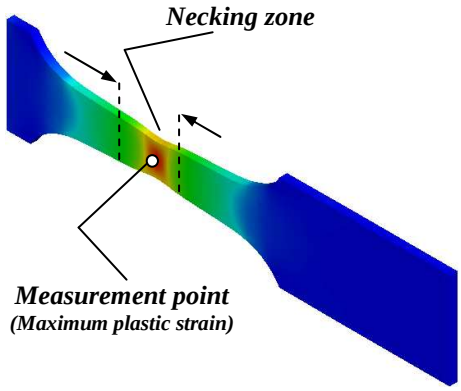

Fig. 3.23. Measurement point of local plastic strain in the conventional dynamic tension test configuration.

In Fig. 3.24-a can be observed that for such impact velocity, V_0 = 40 m/s, the viscous drag term is hardly active. No difference in the strain of instability between **MRK** and extended **MRK** models is observed. At larger impact velocity values, Fig. 3.24-b-c-d, the strain of instability is considerably delayed in the case of viscous drag application.

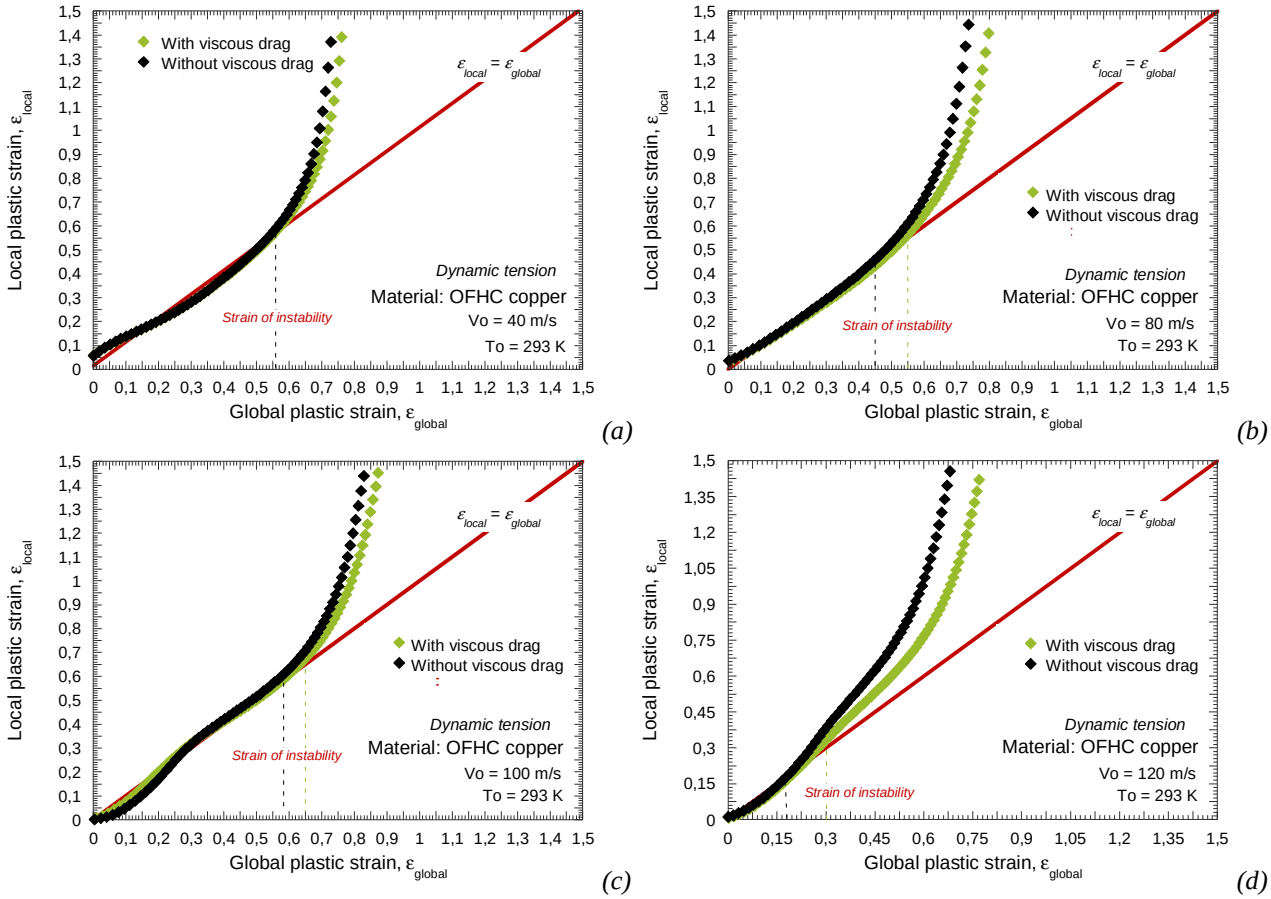

*Fig. 3.24. Evolution of the local plastic strain versus the global plastic strain for **MRK** and extended **MRK** models. (a) V_0=40 m/s, (b) V_0=80 m/s, (c) V_0=100 m/s, (d) V_0=120 m/s.*

It must be noticed that the strain of instability for the conventional dynamic tension tests is much more reduced than that observed for the ring expansion case. The interaction of waves during loading is responsible for such behaviour [Glema et al. 2000, Hill 1962, Rice 1976].

Next, it is shown the evolution of the strain of instability as a function of impact velocity for **MRK** and extended **MRK** models. Until the impact velocity V_0 = 60 m/s is achieved no differences

are found between both models, Fig. 3.25. Beyond that impact velocity the viscous drag plays an important role stabilizing material behaviour and increasing its ductility, Fig. 3.25. Up to this point the analysis is analogous to the ring expansion configuration.

However in the conventional dynamic tension test, as previously reported, the **CIV** phenomenon takes place, Fig. 3.25. It involves the drastic reduction on material ductility shown in Fig. 3.25.

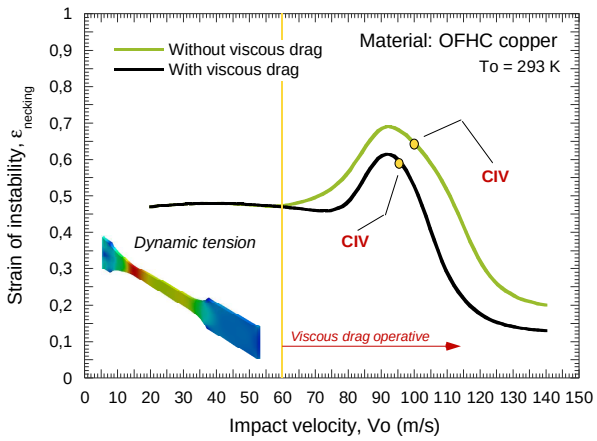

*Fig. 3.25. Strain of instability as a function of impact velocity for **MRK** and extended **MRK** models.*

By comparison of input *(at the impacted site, Fig. 3.9.)* and output *(at the clamped site, Fig. 3.9.)* forces the **CIV** value has been estimated, Fig. 3.26. It corresponds to the impact velocity for which both forces do not reach equilibrium [Hu and Daehn 1996, Rusinek et al. 2005, Rodríguez-Martínez et al. 2009], Eq. 3.6.

$$\mathrm{CIV} = \min\left\{ V_0 \,/\, F_{input}(t) \neq F_{output}(t) \right\} \tag{3.6}$$

For both cases analyzed the specimen seems to become unstable for similar impact velocity, **CIV** = $V_0 \approx 100$ m/s, Fig. 3.26. The potential influence of the rate sensitivity on the **CIV** will be taking up again later along this document. A larger contribution of the viscous drag term to the overall flow stress is expected to reveal the role that the rate sensitivity may have on the **CIV** in tension.

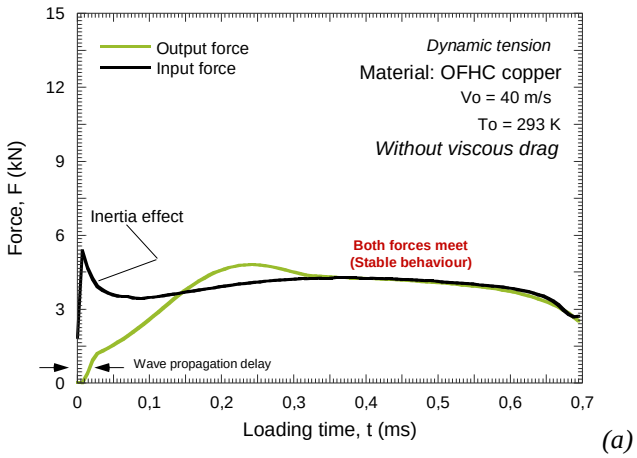

(a)

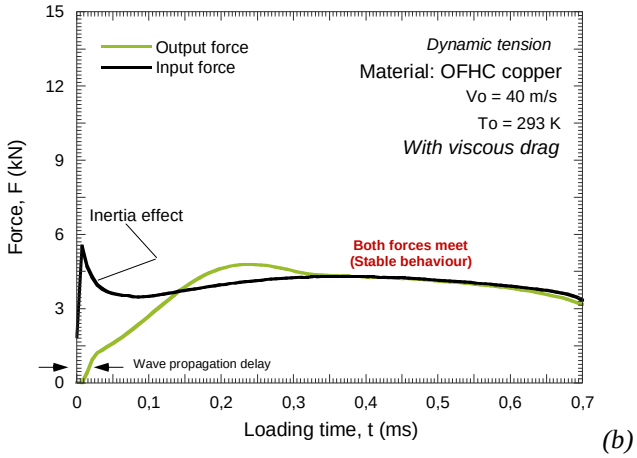

(b)

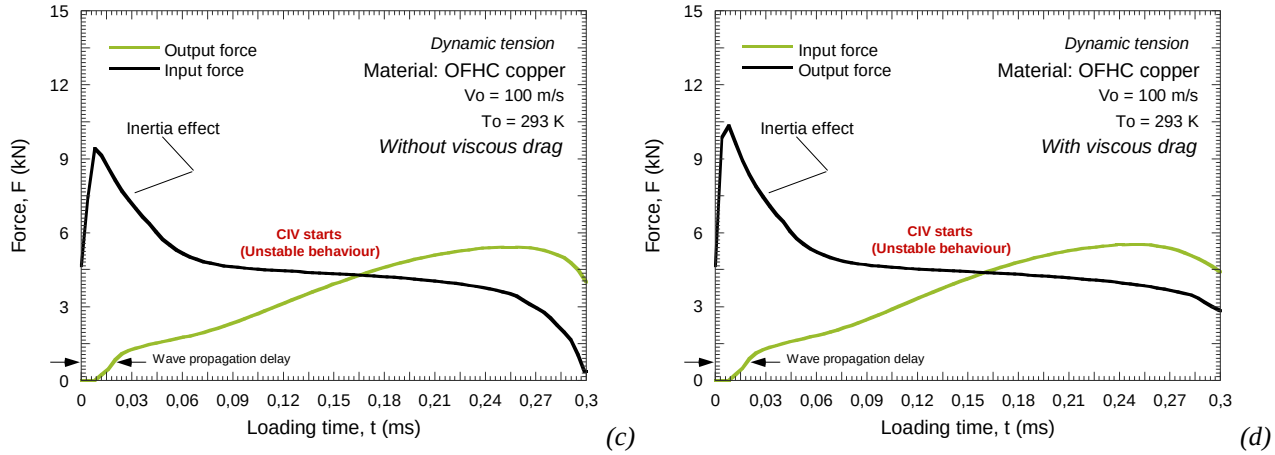

*Fig. 3.26. Output and input forces at V_0=40 and V_0=100 m/s for **MRK** and extended **MRK** models.*

But not only the local plastic behaviour of the material is affected by the viscous drag stress term, the specimen elongation at failure *(an imposed critical failure strain $\bar{\varepsilon}_f^p = 1.5$ has been used for this particular problem)* is strongly influenced too, Fig. 3.27. By application of the viscous drag component plasticity is spread along the active part of the sample, Fig. 3.27. These considerations agree with previous observations conducted for the ring expansion case.

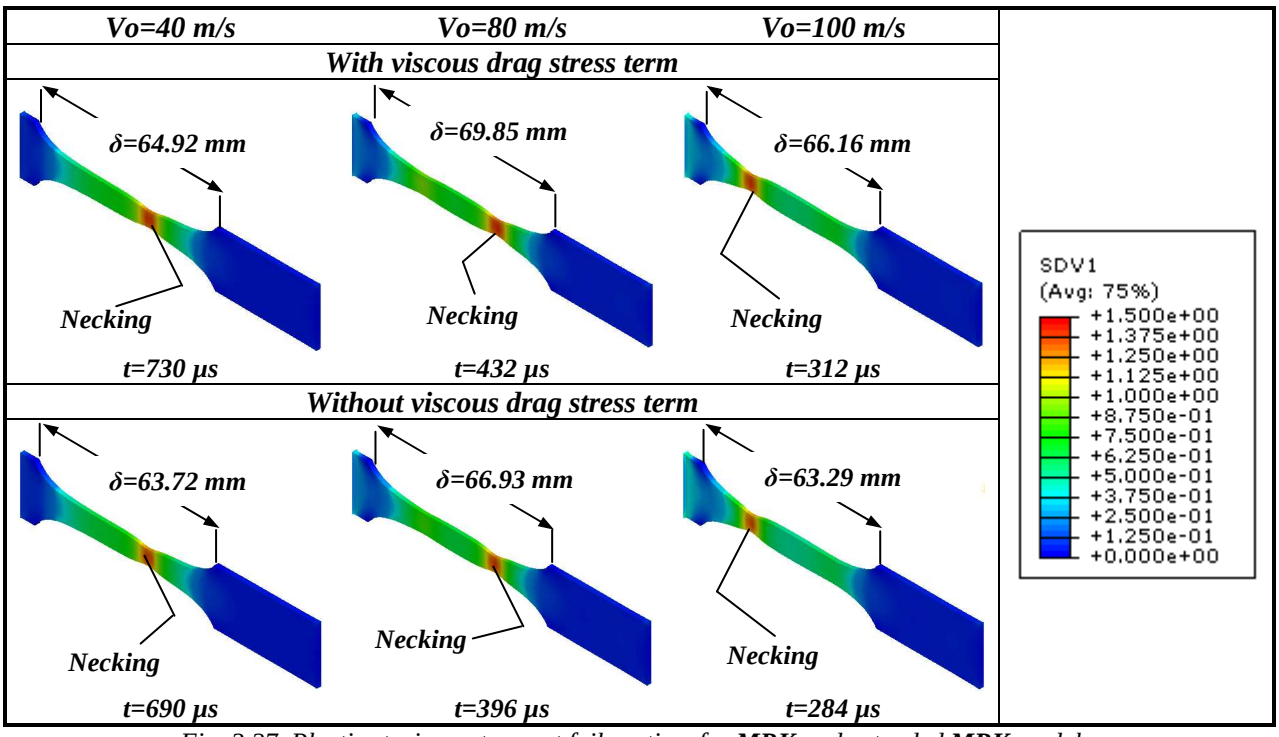

*Fig. 3.27. Plastic strain contours at failure time for **MRK** and extended **MRK** models.*

Because of the increasing rate sensitivity, the transversal displacement of the specimen at failure is larger in the case of viscous drag application. It delays necking formation, especially for high impact velocities, Fig. 3.28-c. However, the place where necking is formed is hardly influenced by the phonon drag stress term, Fig. 3.28-a-b.

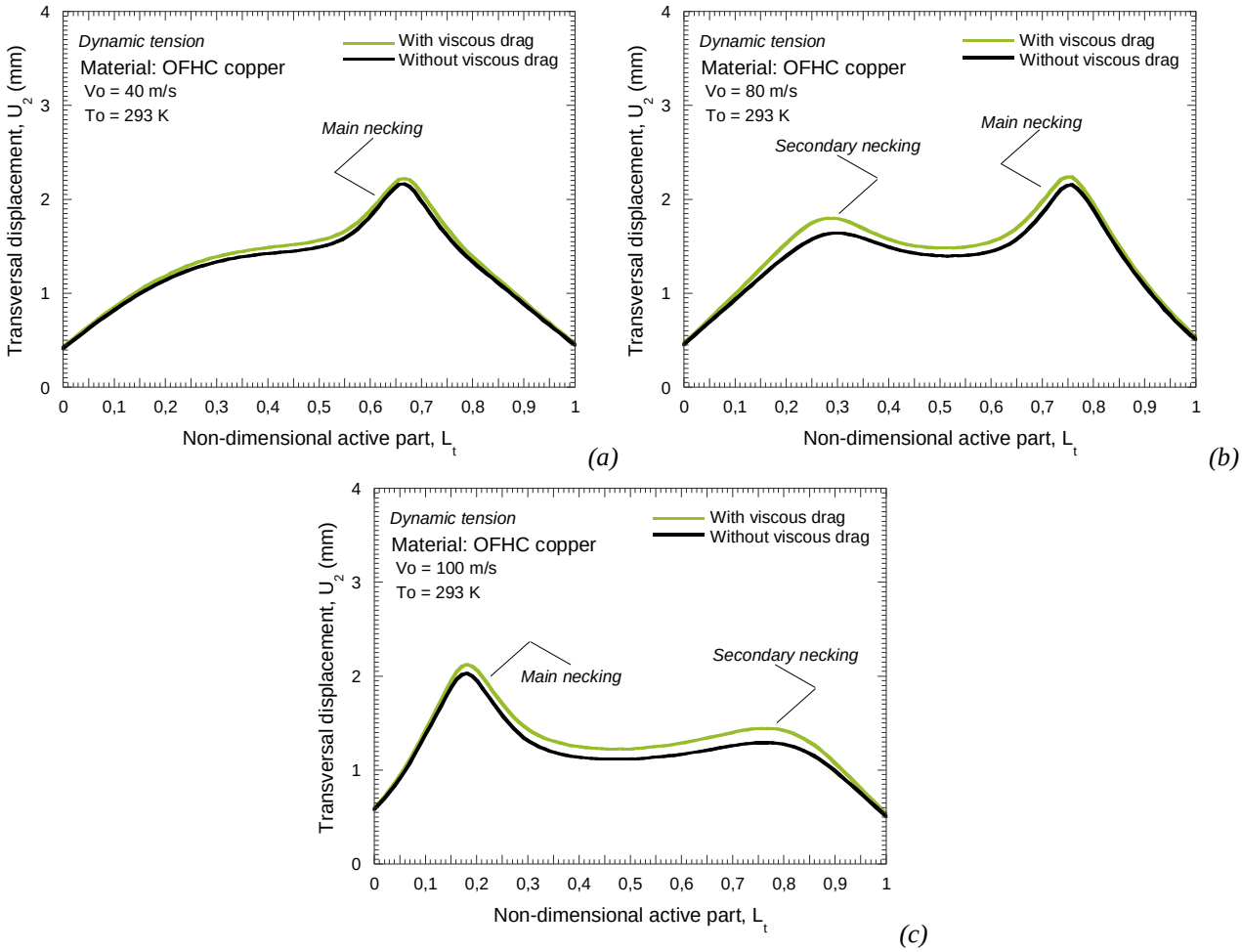

*Fig. 3.28. Transversal displacement of the active part of the specimen for **MRK** and extended **MRK** models. (a) V_0=40 m/s, (b) V_0=80 m/s, (c) V_0=100 m/s.*

Such behaviour was expected since during homogeneous deformation the material strain hardening *(plastic wave speed)* is not appreciably affected by the viscous drag application, Fig. 3.29. Out of the instability, the deformation rate is approximately the same for **MRK** and extended **MRK** constitutive descriptions, Fig. 3.29. Due to the reduced contribution of the viscous drag component to the overall flow stress of the material, the stress pulse propagation does not suffer appreciable variations.

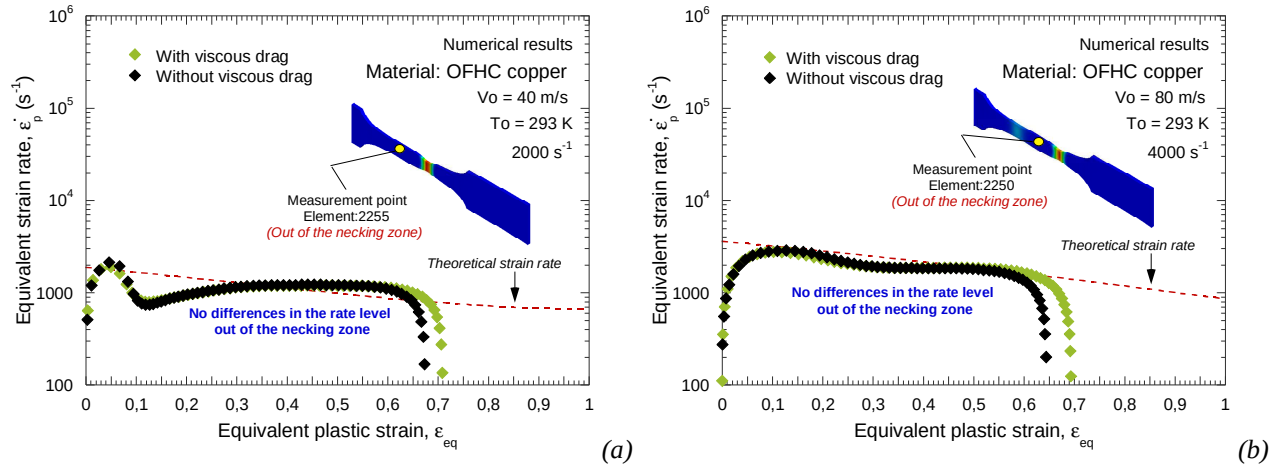

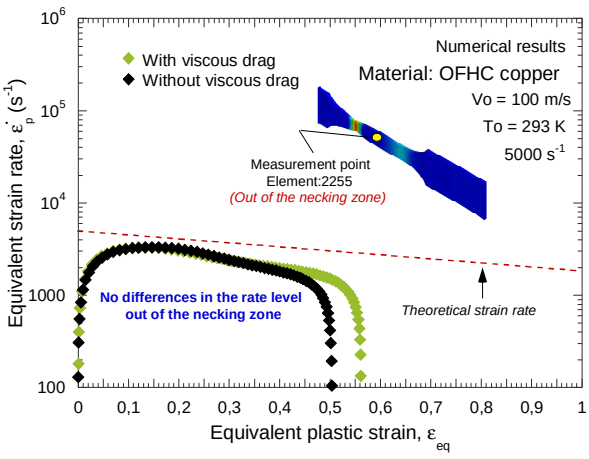

*Fig. 3.29. Evolution of strain rate as a function of plastic deformation out of the necking zone for **MRK** and extended **MRK** models. (a) V_0=40 m/s, (b) V_0=80 m/s, (c) V_0=100 m/s.*

When describing the constitutive behaviour of metallic alloys at high strain rates the dislocations drag phenomenon plays a fundamental role. A proper description of the rate sensitivity of metallic materials is indispensable in order to evaluate its suitability for absorbing energy under dynamic solicitations. From an overview of the considerations reported in this section of the document it can be concluded that the rate sensitivity of metals determine their ductility by homogenizing their behaviour under high loading rates.

In order to go further in this investigation, a parametric study on the influence of viscous drag formulation parameters on the material response when it is subjected to dynamic tension is conducted.

3.3.5 Influence of viscous drag formulation parameters on the flow localization

Let us maintain the constants of the original **MRK** formulation as those corresponding to **OFHC** copper, Table 3.1. The constants of the viscous drag term will be varied using the values listed in Table 3.1. The variations are conducted within the typical range of values reported for these constants [Nemat-Nasser et al. 2001, Guo and Nemat-Nasser 2006, Rusinek and Rodríguez-Martínez 2009, Rusinek et al. 2010] for different materials. The values in bold will be kept as the reference values *(when varying one parameter the other one will take the value in bold).*

χ (MPa)				α (-)			
100	*200*	***300***	*400*	*0.00001*	***0.00005***	*0.0001*	*0.0005*

Table 3.1. Value of the viscous drag stress term constants used for the parametric study.

Next, it is analyzed the effect of parameter χ on the flow localization under dynamic tension.

3.3.5.1 Influence of parameter χ

In Fig. 3.30-a. is depicted the evolution of the viscous drag stress component as a function of strain rate for different values of χ. The increase of χ elevates the flow stress of the material but also the rate sensitivity provided by the dislocations drag stress component, Fig. 3.30. However, the maximum rate sensitivity takes place at the same strain rate level, Fig. 3.30-b. The starting point of

the viscous drag effect remains invariable. The strain rate value where the plateau regime *(no increase of flow stress with strain rate)* is reached does it too, Fig. 3.30.

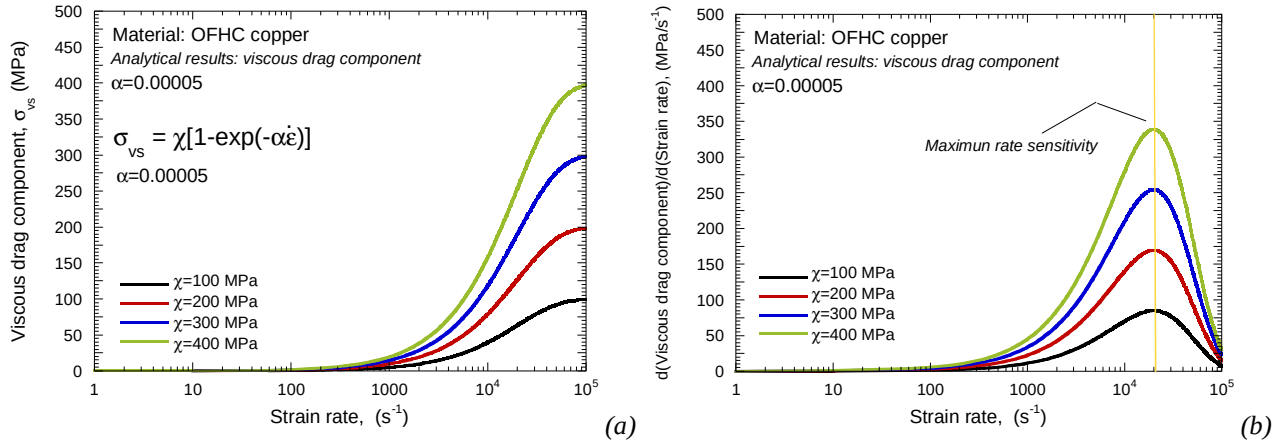

Fig. 3.30. (a) Viscous drag stress component versus strain rate. (b) Derivative of the viscous drag stress component versus strain rate.

The flow stress evolution versus the plastic strain is shown in Fig. 3.31-a-b. for different values of χ and two strain rate levels. The temperature increase caused by the augment on the flow stress with χ does not affect in a relevant way the material strain hardening *(plastic waves speed)*, Fig. 3.31. This observation has particular relevance since an important decrease of strain hardening may annihilate the expected beneficial effect on ductility caused by the rate sensitivity increase [Rodríguez-Martínez et al. 2009].

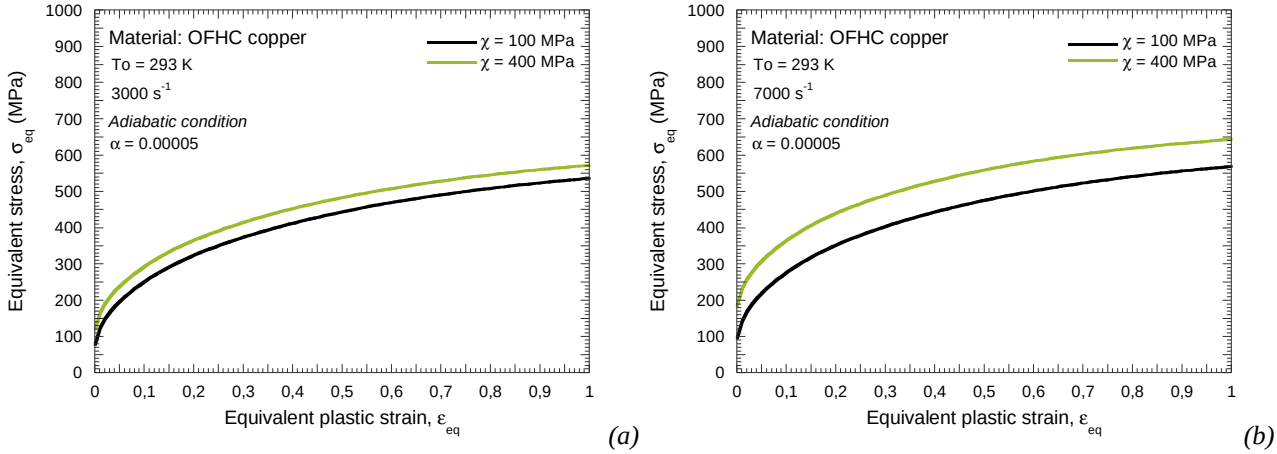

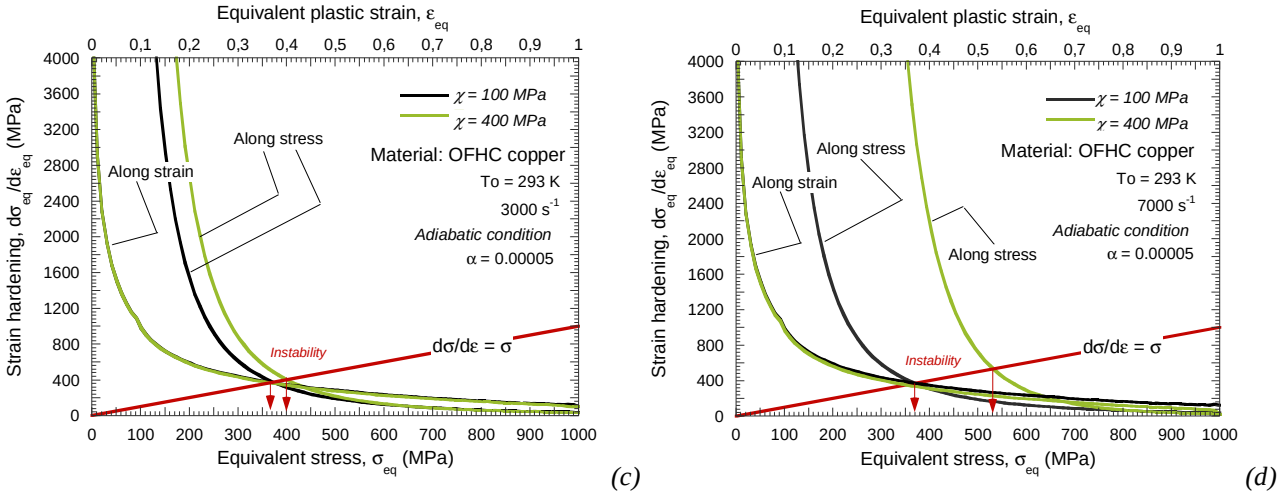

Fig. 3.31. (a)-(b) Flow stress evolution as a function of the plastic strain for different values of χ. (c)-(d) Strain hardening evolution versus plastic strain and stress for different values of χ.

Next, the effect of parameter χ on flow localization for the ring expansion configuration is analyzed.

3.3.5.1.1 The ring expansion test

In Fig. 3.32. is shown the evolution of the local plastic strain versus the global plastic strain for different values of χ and two impact velocities. The strain of instability augments with impact velocity and with increasing χ, Figs. 3.32-3.33.

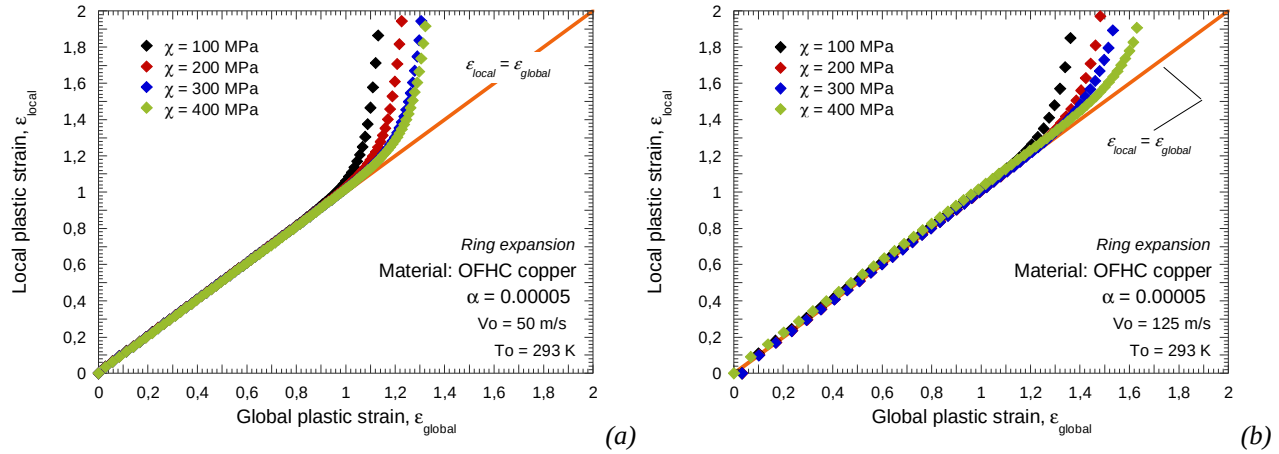

Fig. 3.32. Evolution of the local plastic strain versus the global plastic strain for different values of χ. (a) V_0=50 m/s, (b) V_0=125 m/s.

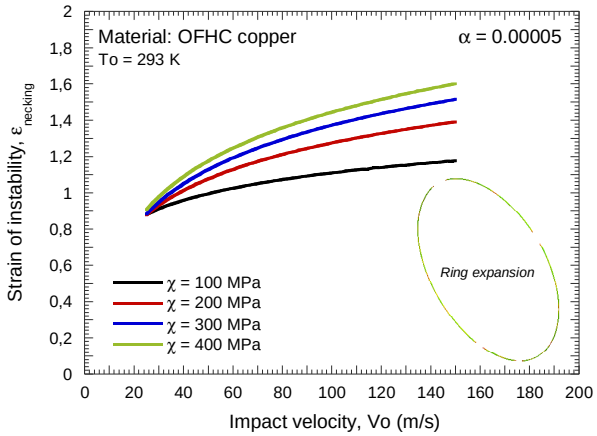

Fig. 3.33. Strain of instability as a function of the impact velocity for different values of χ.

In Fig. 3.34. is observed that the sudden increase in the rate sensitivity induced by the instability formation is delayed with the increase of χ. This phenomenon has reflect on the flow stress evolution and therefore on the strain hardening of the material. It proves that the rate sensitivity by itself modifies the local material response.

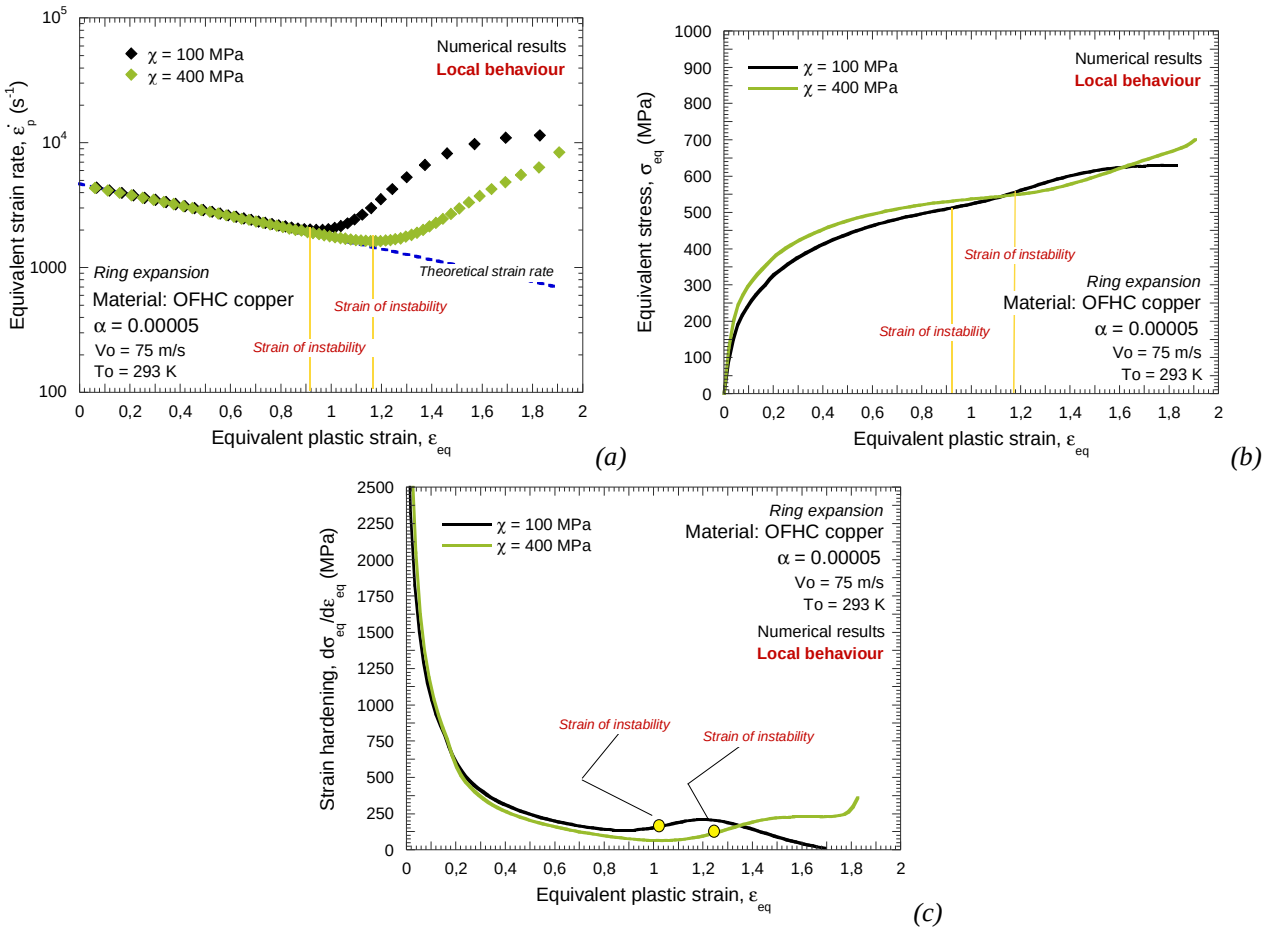

Fig. 3.34. Evolution of (a) strain rate, (b) flow stress and (c) strain hardening as a function of plastic strain in the necking for χ=100 MPa and χ=400 MPa at V_0=75 m/s.

Since with increasing χ the rate sensitivity of the material is augmented, the number of fragments also does it monotonically for the range of impact velocities analyzed in this study, Fig. 3.35.

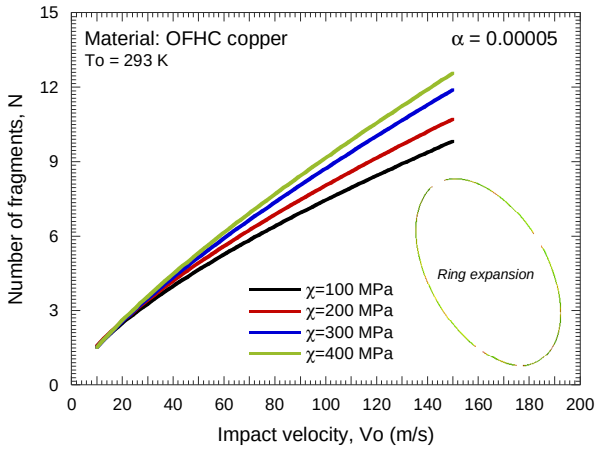

Fig. 3.35. Number of fragments as a function of the impact velocity for different values of χ

Thus, for large values of χ plasticity is spread along the ring, delaying the failure time and increasing the number of pieces into which the sample is fragmented, Figs. 3.35-3.36.

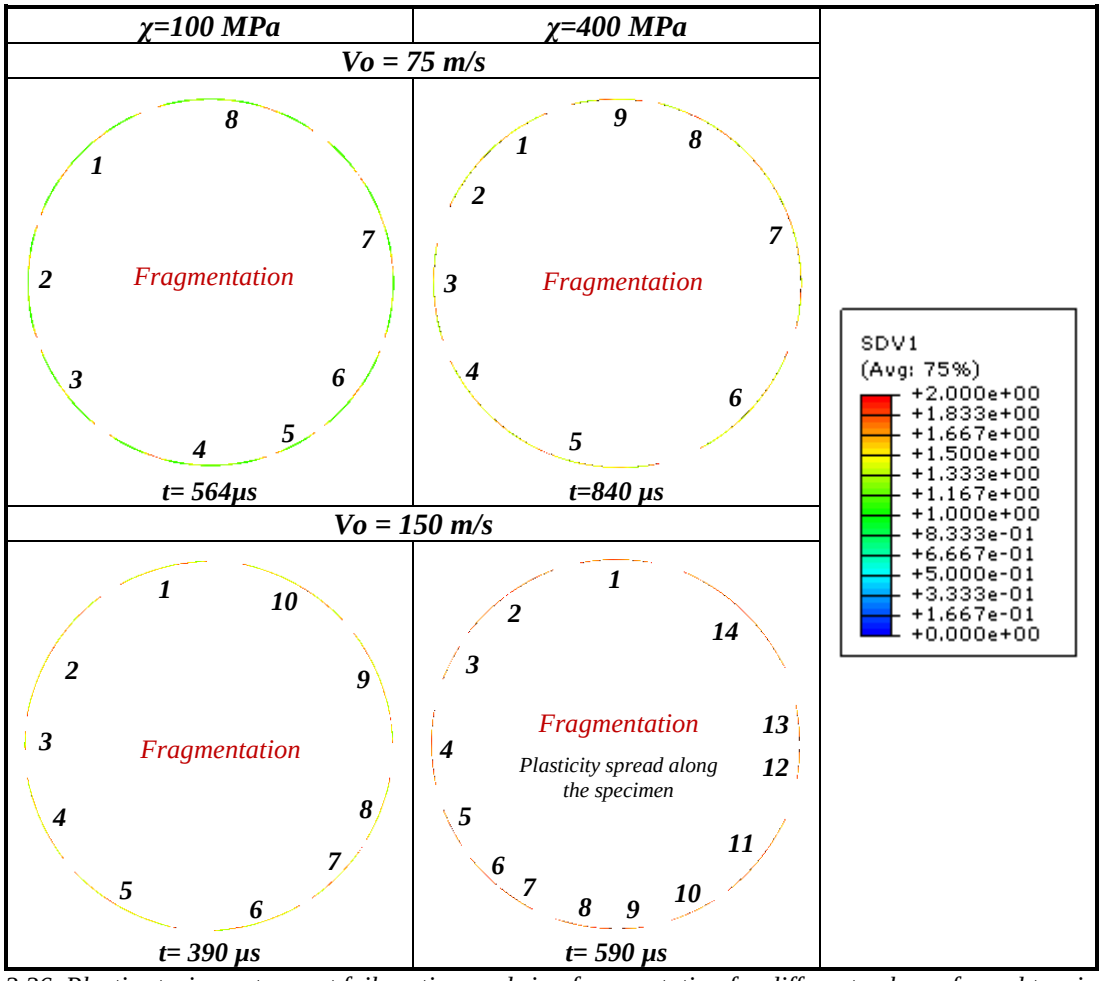

Fig. 3.36. Plastic strain contours at failure time and ring fragmentation for different values of χ and two impact velocities.

Subsequently, the effect of parameter χ on the strain localization for the conventional dynamic tension test configuration is analyzed.

3.3.5.1.2 The conventional dynamic tension test

As reported for the ring expansion configuration, increasing χ augments the strain of instability for the whole range of impact velocities analyzed, Fig. 3.37. Such effect is more remarkable as the impact velocity increases since the rate sensitivity of the material is strongly influenced by the value of χ, Fig. 3.37.

It has to be noted that in determined cases, due to waves disturbances, the heterogeneity in the strain field of the active part of the specimen occurs at the beginning of loading. It causes that $\varepsilon_{local}/\varepsilon_{global} \neq 1$ at the first stages of the test, Fig. 3.37-b. Such effect vanishes with deformation increase.

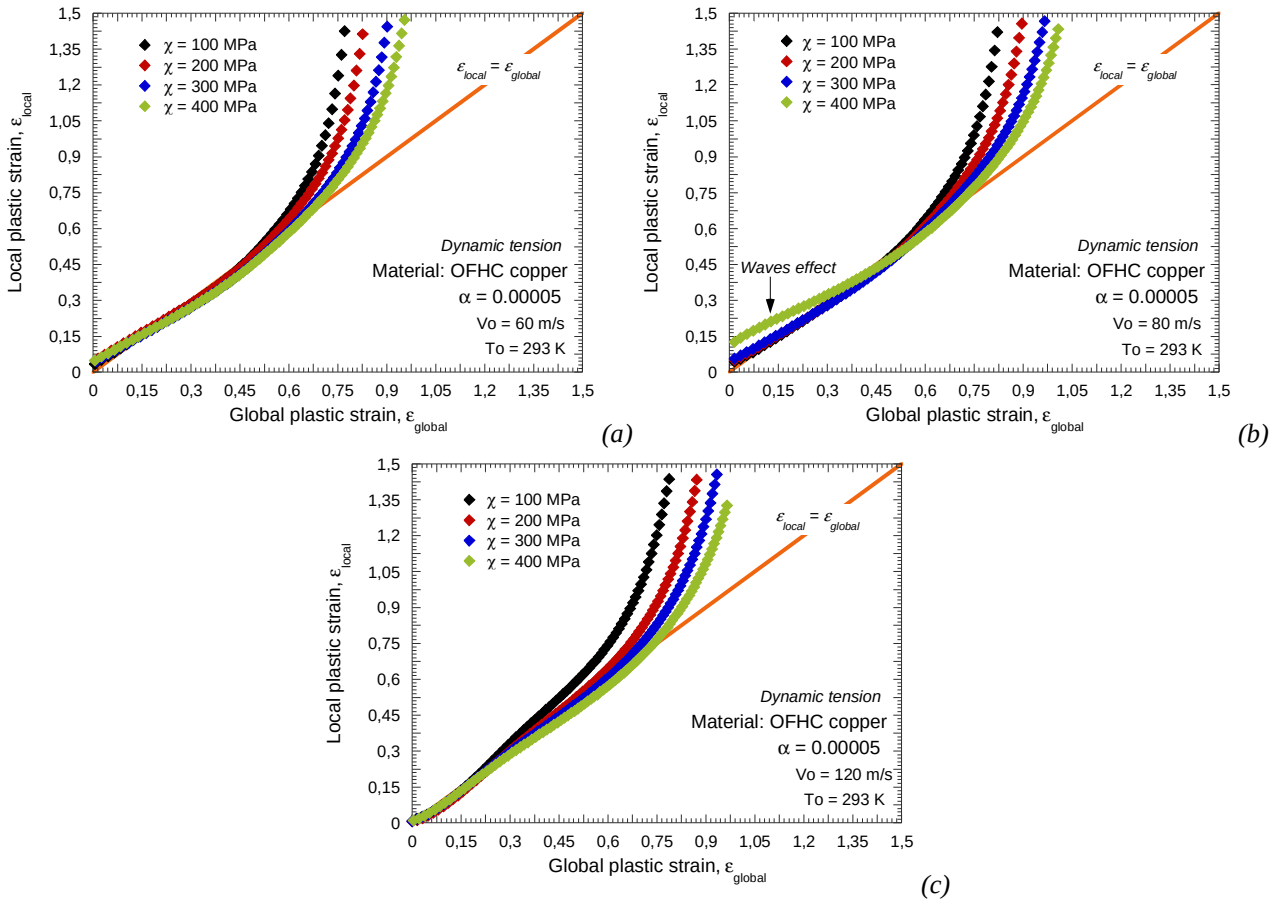

Fig. 3.37. Evolution of the local plastic strain as a function of the global plastic strain for different values of χ. (a) V_0=60 m/s, (b) V_0=80 m/s, (c) V_0=120 m/s.

Thus, variation of χ allows for observing properly the influence that viscous drag term has on the **CIV** value, Fig. 3.38.

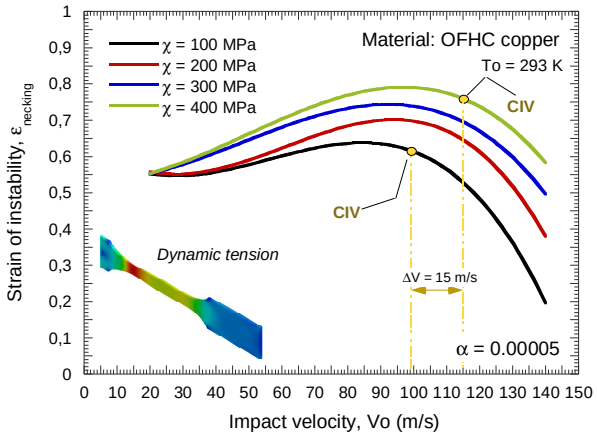

Fig. 3.38. Strain of instability versus impact velocity for different values of χ.

Let us analyze the evolution of the input and output forces as a function of time at V_0 = 100 m/s and V_0 = 110 m/s, Fig. 3.39. In the case of χ=100 MPa both forces do not find equilibrium, the sample behaviour is unstable, the **CIV** starts. However, for χ=400 MPa input and output forces meet in time, the specimen failure is delayed, the **CIV** has not been reached.

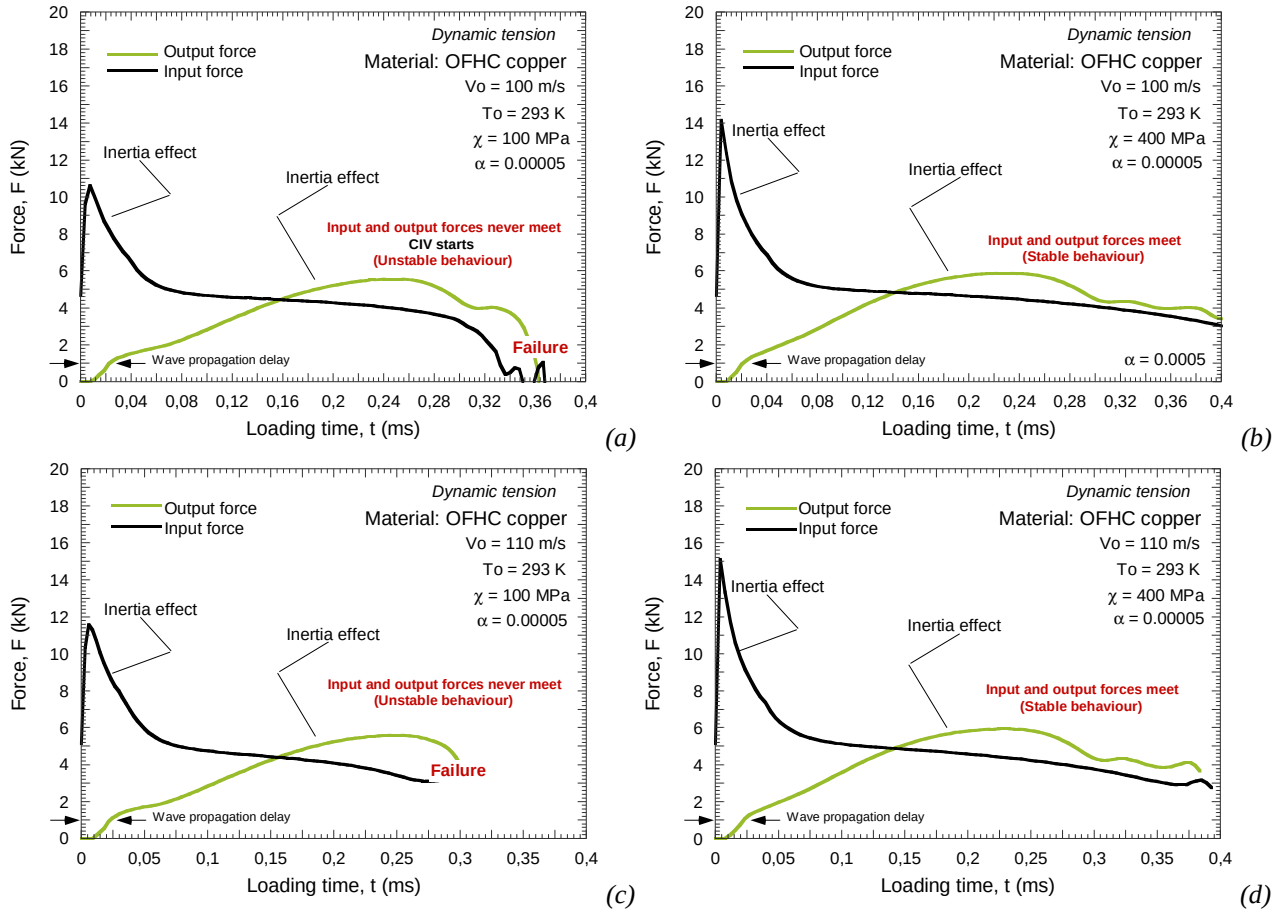

Fig. 3.39. Output and input forces at V_0=100 m/s and V_0=110 m/s for (a)-(c) χ=100 MPa and (b)-(d) χ=400 MPa.

This observation has main relevance. In order to understand how the viscous drag term may affect the **CIV** value let us conduct the following analysis.

From Eq. 3.5. is concluded that the **CIV** is only dependent on elastic and plastic wave speed. For the cases of χ=100 MPa and χ=400 MPa it has been reported in Fig. 3.38. a difference in the **CIV**

value $\Delta(\mathrm{CIV})\big|_{\chi=400\,\mathrm{MPa}\rightarrow\chi=100\,\mathrm{MPa}}^{\text{elastic range + plastic range}} \approx 15\,\mathrm{m/s}$. However the contribution of the elastic range to such difference is only $\Delta(\mathrm{CIV})\big|_{\chi=400\,\mathrm{MPa}\rightarrow\chi=100\,\mathrm{MPa}}^{\text{elastic range}} \approx 0.6\,\mathrm{m/s}$. In fact, due to the reduced initial yield stress of annealed **OFHC** copper the **CIV** value is basically controlled by the plastic range. Therefore, the addition of the viscous drag term influences the material strain hardening *(plastic wave speed)* in the necking zone. Since for an imposed strain rate value the strain hardening is not affected by the value of χ *(as previously demonstrated, Fig. 3.31)*, then in the necking zone the strain rate level must be influenced by the value of χ.

Previous expectations are confirmed in Fig. 3.40 where the evolution of strain rate in the necking is depicted as a function of strain for different values of χ. In the case of χ=100 MPa the strain rate is clearly larger at the beginning of loading, the material reaches early instability. Increasing rate sensitivity reduces the strain rate level in the necking at the beginning of loading, plasticity is spread along the specimen. In addition, relevant differences are observed in the stress level taking place in the necking, Fig. 3.40.

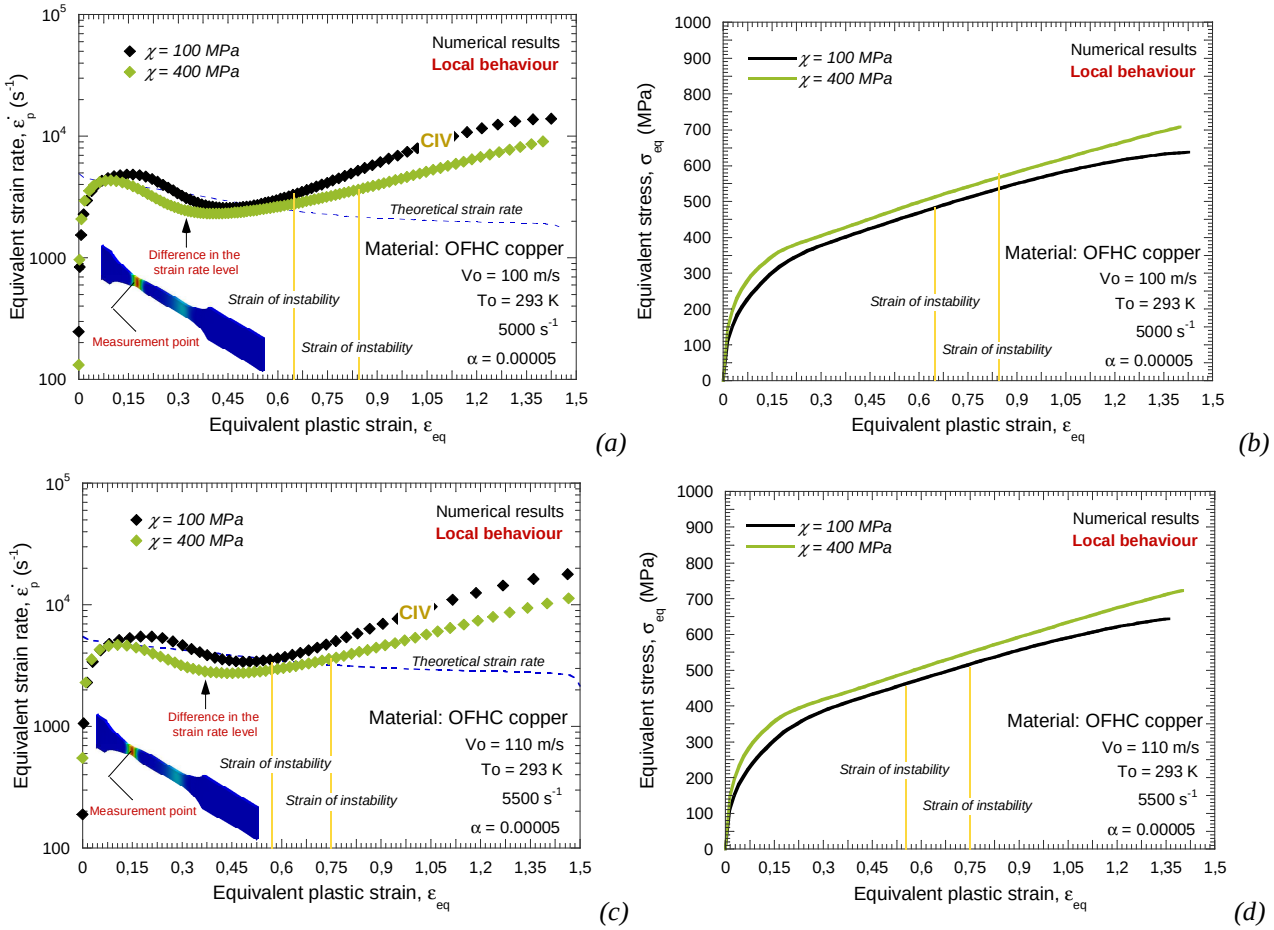

Fig. 3.40. Evolution (a) of strain rate and (b) stress as a function of plastic deformation in the necking zone for χ=100 MPa and χ=400 MPa at V_0=100 m/s and V_0=110 m/s.

Thus, in the necking, the strain hardening is modified by increasing the value of χ, Fig. 3.41. The celerity of the plastic waves is affected, Fig. 3.41. This behaviour is a plausible explanation for the **CIV** variation when different values of χ are applied.

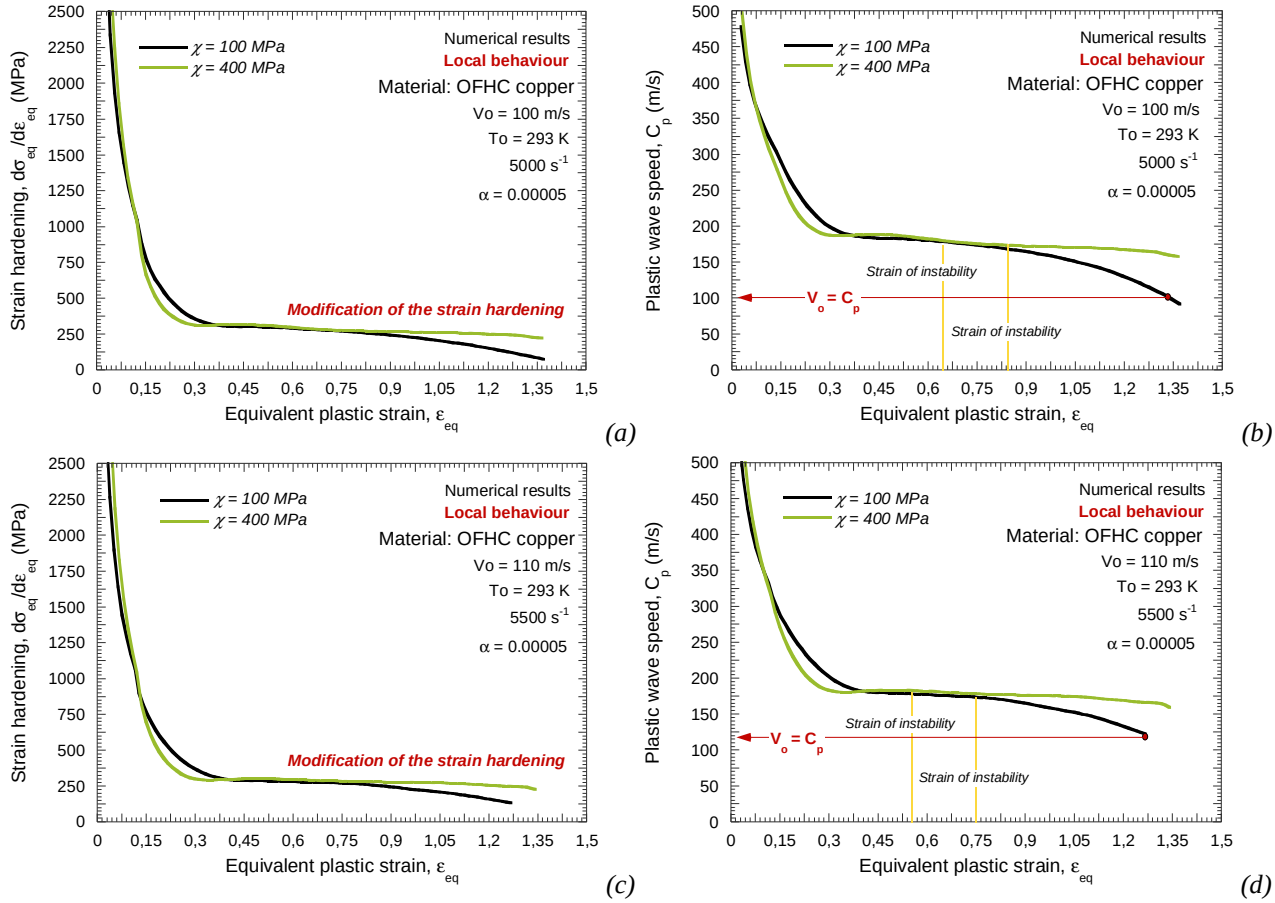

Fig. 3.41. (a) Strain hardening and (b) plastic wave celerity evolution as a function of plastic deformation in the necking zone for χ=100 MPa and χ=400 MPa at V_0=100 m/s.

It is observed that increasing χ spreads plasticity along the active part of the specimen, Fig. 3.42. It considerably delays the strain localization process. The transversal displacement of the specimen at failure time is clearly increased with χ, Fig. 3.42. The material augments its capability for absorbing energy.

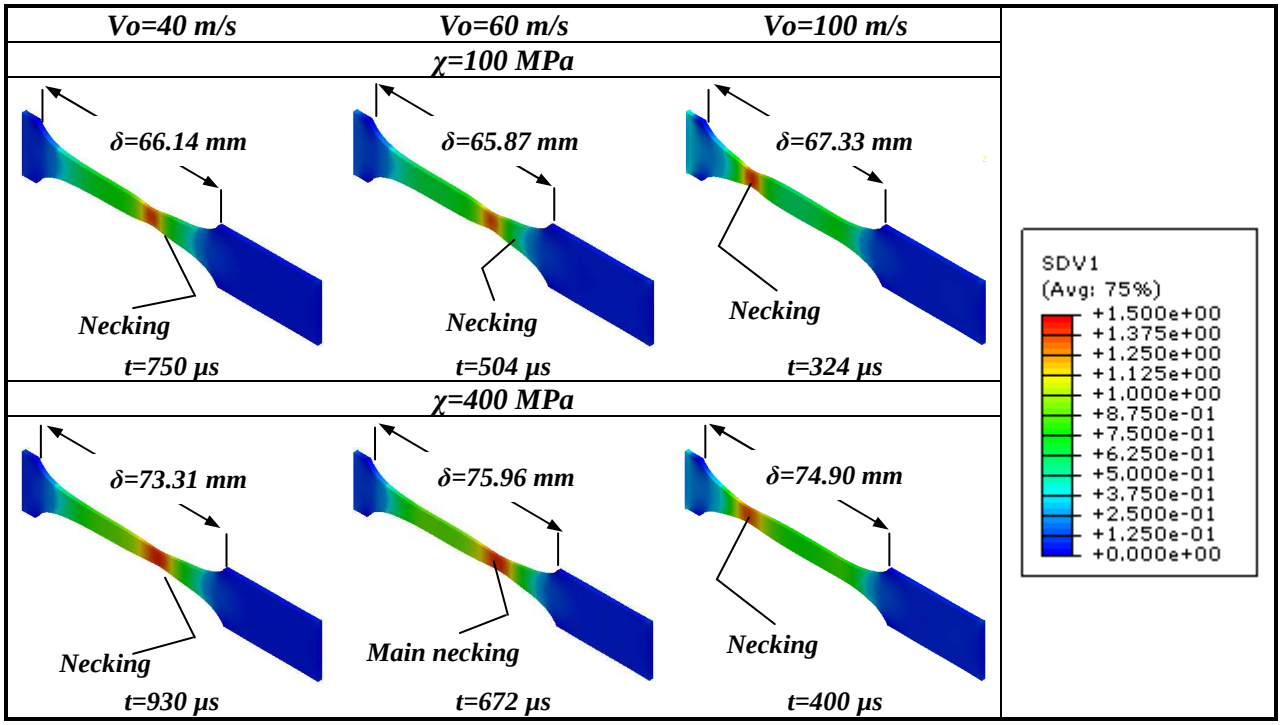

Fig. 3.42. Plastic strain contours at failure time for χ=100 MPa and χ=400 MPa and different impact velocities.

However, the place where necking appears is hardly influenced by the phonon drag stress term, Fig. 3.43. Such behaviour was expected since during homogeneous deformation the material strain hardening is not appreciably affected by the value of χ, Fig. 3.43. Outside the instability the deformation rate is the quite similar for different values of χ. The wave propagation is not altered, nor the necking position. *(Only in the necking the value of χ causes substantial differences in the deformation rate level).*

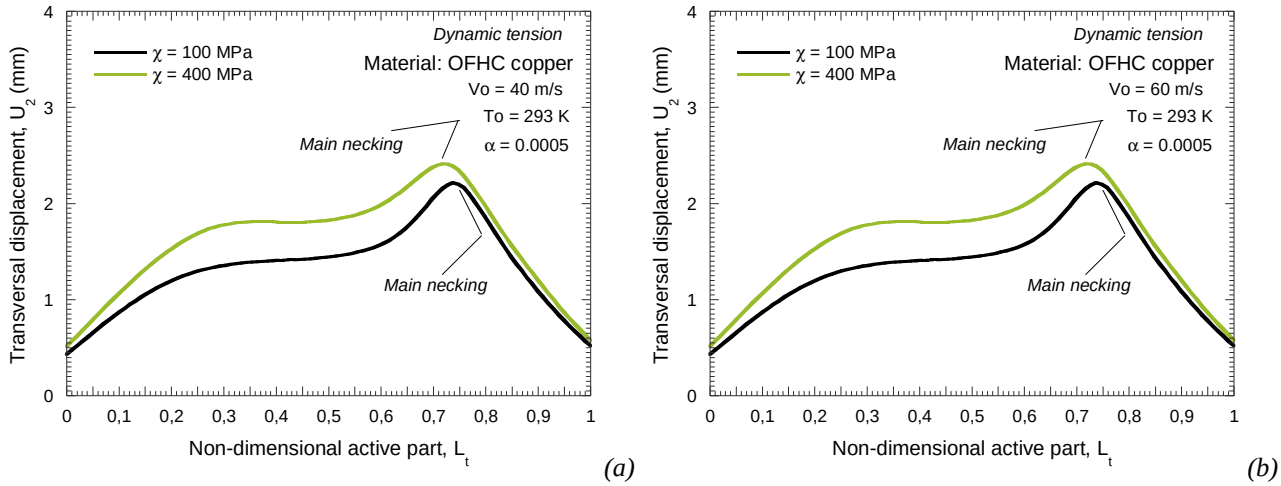

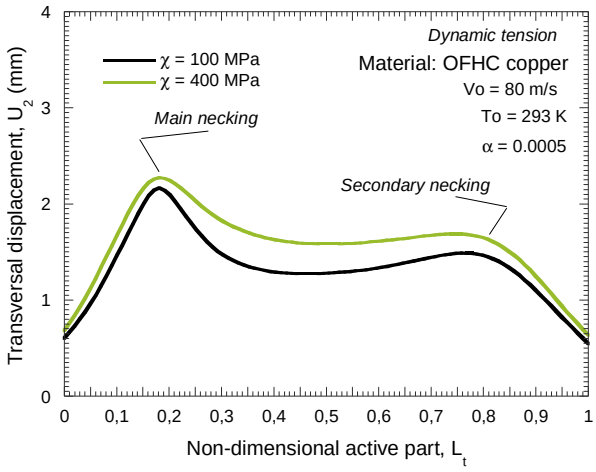

(c)

Fig. 3.43. Transversal displacement of the active part of the specimen for different values of χ. (a) V_0=40 m/s, (b) V_0=60 m/s, (c) V_0=120 m/s.

The transversal displacement of the specimen at failure time is clearly increased with χ, Fig. 3.44. Stronger plasticity gradients are found around the necking with the decrease of χ, Fig. 3.44.

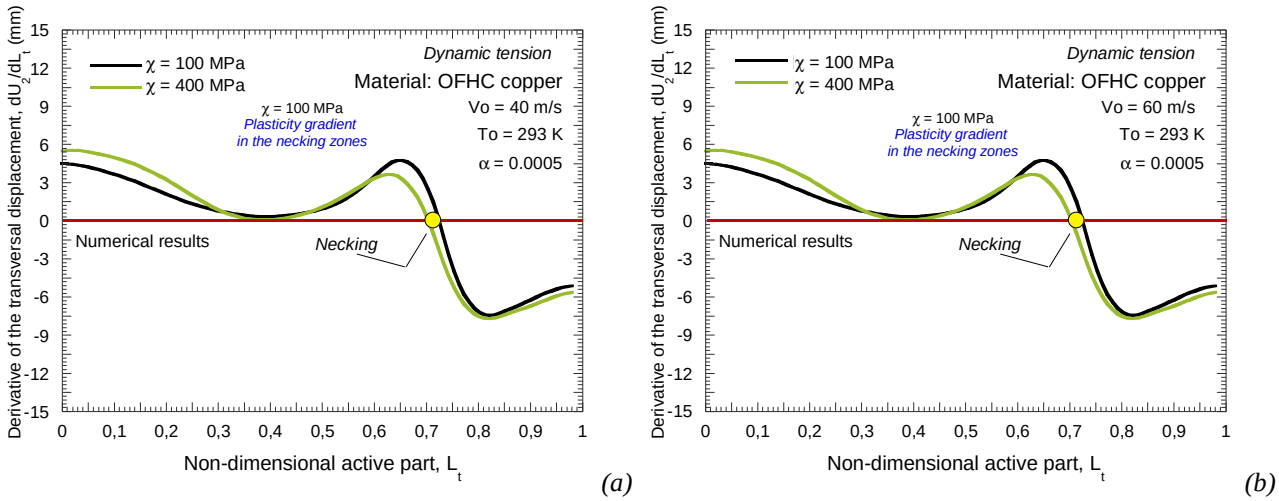

(a) *(b)*

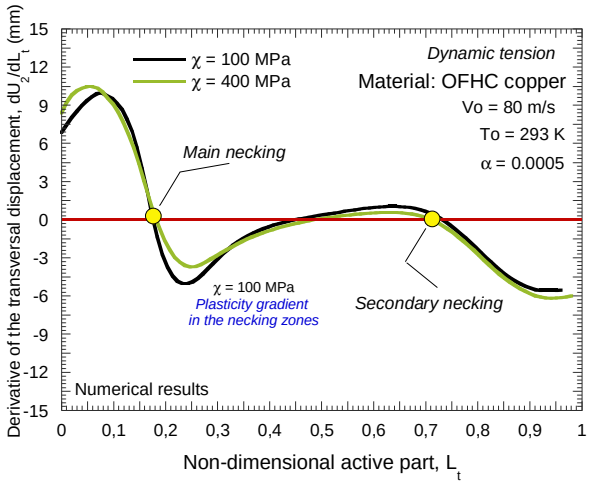

(c)

Fig. 3.44. Derivative of the transversal displacement of the active part of the specimen for different values of χ. (a) V_0=40 m/s, (b) V_0=60 m/s, (c) V_0=80 m/s.

Next is analyzed the influence of parameter α on flow localization for ring expansion and conventional dynamic tension configurations.

3.3.5.2 Influence of parameter α

In Fig. 3.45. is shown the evolution of the viscous drag stress versus strain rate for different values of α. The increase of α modifies the starting point where dislocations drag phenomenon takes place, Fig. 3.45. The plateau regime where no longer rate sensitivity is induced by the viscous drag term is modified too, Fig. 3.45. The slope of the rate sensitivity remains constant but shifted with strain rate, Fig. 3.45.

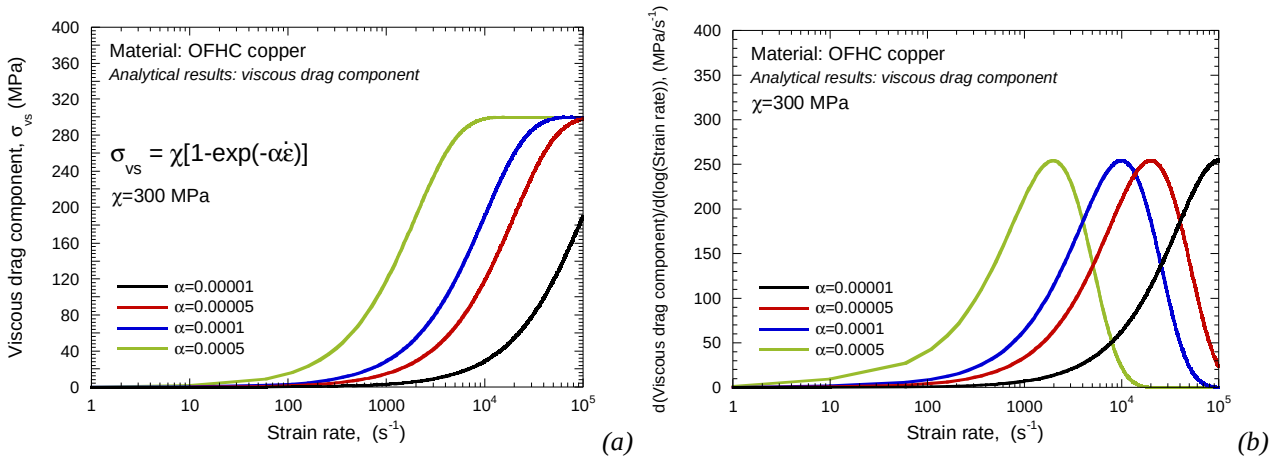

Fig. 3.45. (a) Viscous drag stress component as a function of the strain rate for different values of α. (b) Derivative of the viscous drag stress component as a function of strain rate for different values of α.

The flow stress evolution as a function of plastic strain for two values of α and different strain rate levels is plotted in Fig. 3.46-a-b. Although the variations of α conducted certainly modify the material flow stress level, its strain hardening *(plastic waves speed)* remains approximately invariable for the whole range of strain rates considered, Fig. 3.46-c-d. So, eventual differences in the adiabatic temperature increase due to variations of α will not change the analysis conducted subsequently.

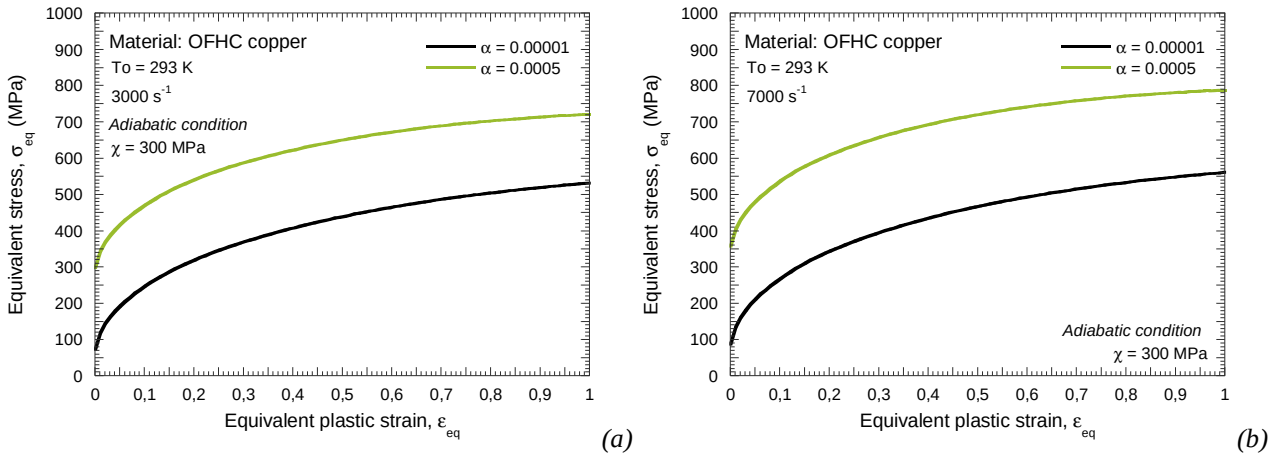

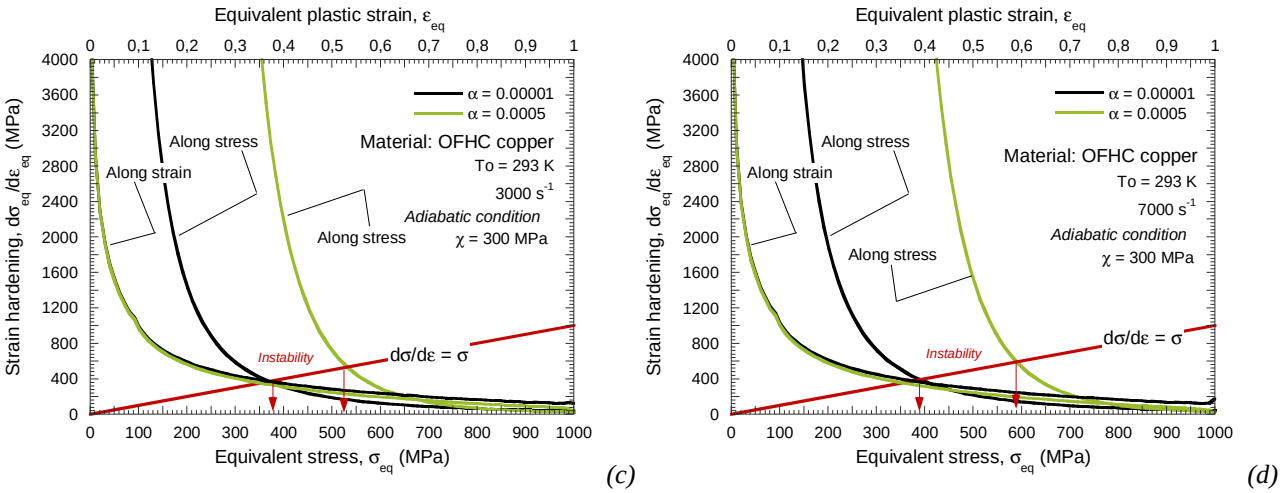

Fig. 3.46. (a)-(b) Flow stress evolution as a function of the plastic strain for different values of α. (c)-(d) Strain hardening evolution as a function of plastic strain and stress for different values of α.

In the following section of the document is examined the influence of the parameter α on the formation of plastic instabilities using ring expansion configuration.

3.3.5.2.1 The ring expansion test

In Fig. 3.47. is analyzed the evolution of the local plastic strain *(in the necking)* with the global plastic strain *(of the whole specimen)* for all the values of α considered and different impact velocities.

In the case of V_0 = 50 m/s, Fig. 3.47-a. as the value of α increases, the strain of instability value also does it *(in the case of α=0.00001 the viscous drag term is not even operative)*. However, different trend concerning the strain of instability evolution with α is observed for V_0 = 100 m/s, Fig. 3.47-b. In this case, the largest value of α does not match with the most stabilized material. Such behaviour is repeated for higher impact velocities, Fig. 3.47-c. This observation is of main interest. It occurs because the strain rate level for *α=0.0005 (homogeneous strain rate level)* is already close to the starting point of the plateau regime of the viscous drag component. The strain rate applied to the sample has exceeded the maximum rate sensitivity of the material. The increasing strain rate does not involve a remarkable stress increase. The physical interpretation to such phenomenon is that the relativistic effects have already taken place. The rate sensitivity of the material is basically due to the thermally activated mechanisms *(thermal stress component)*. In our particular case this rate sensitivity is quite reduced *(before the viscous drag regime, most **FCC** metals show reduce rate sensitivity [Follansbee 1986, Voyiadjis and Abed 2005, Rusinek and Rodríguez-Martínez 2009, Rusinek et al. 2010])* and the material becomes prone to instabilities formation.

Opposite behaviour is observed when the lowest value of α is applied to the viscous drag term. In this case, the increase of rate sensitivity caused by the viscous drag term is considerably delayed Fig. 3.47. For the range of impact velocities analyzed in this work, the material hardly get the benefits of the increasing strain rate provided by the viscous drag effect, Fig. 3.47.

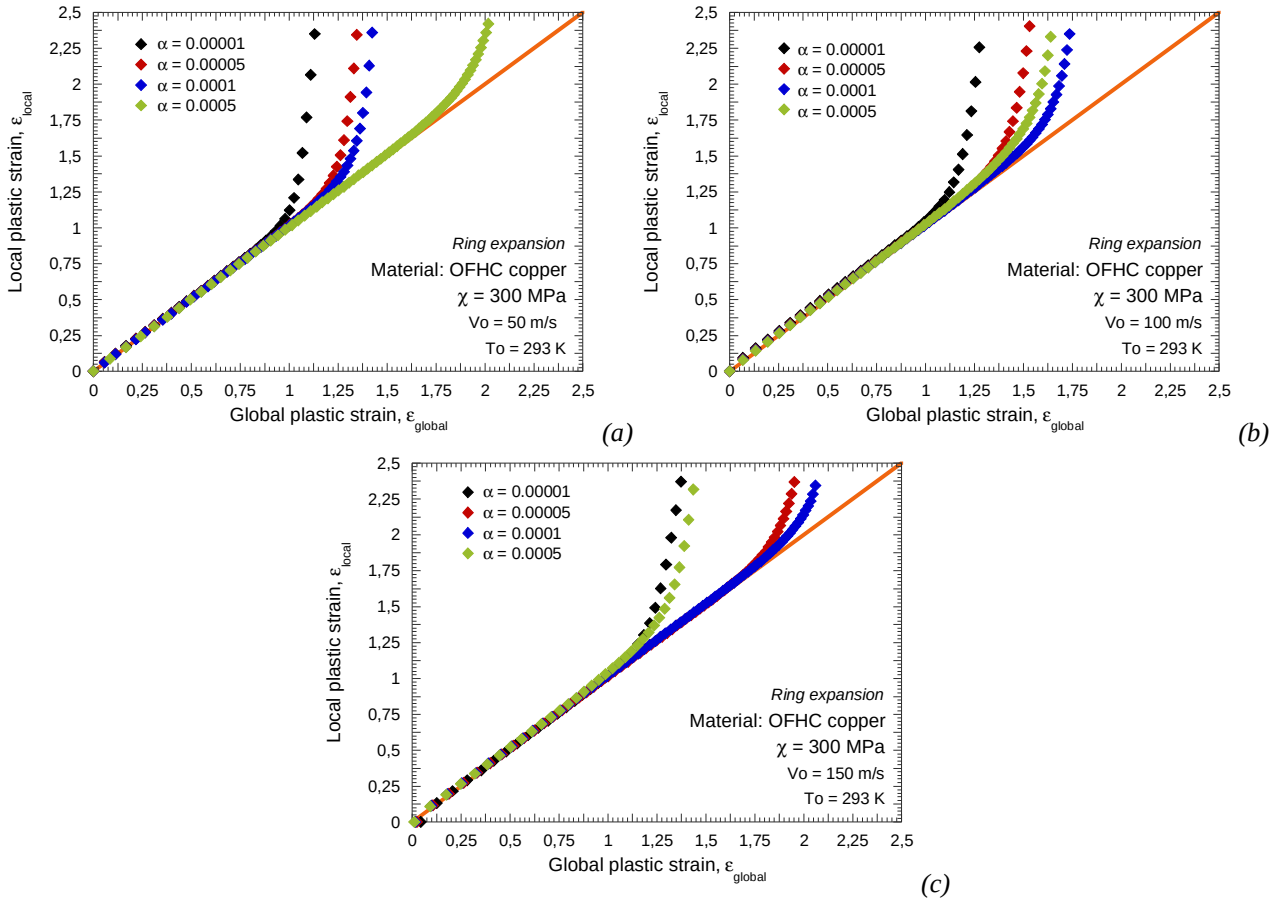

Fig. 3.47. Evolution of the local plastic strain as a function of the global plastic strain for different values of α. (a) V_0=50 m/s, (c) V_0=100 m/s, (c) V_0=150 m/s.

The strain of instability is increasing with impact velocity for all the values of α considered but for α=0.0005. In this last case, once the maximum rate sensitivity provided by the viscous drag formulation is overcome, the strain of instability is quickly reduced, Fig. 3.48.

Such behaviour is of main importance. It seems to probe that the rate sensitivity by itself is the main responsible of the increasing ductility of most metals under dynamic loading.

It must be noticed that beyond a certain value of impact velocity, intermediate values of α are more effective in order to stabilize the material behaviour, Fig. 3.48. However, it is expected that with increasing velocity the strain of instability in the cases of α=0.00005 and α=0.0001 will suffer a decrease *(when the reduction of the material rate sensitivity will take place)* as reported for α=0.0005.

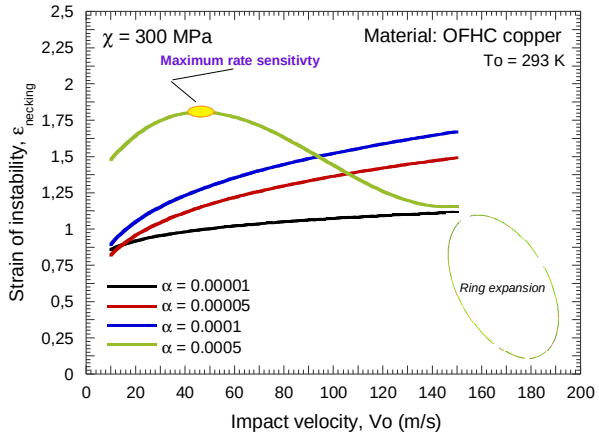

Fig. 3.48. Strain of instability as a function of the impact velocity for different values of α.

In Fig. 3.49. is analyzed the strain rate evolution in the necking versus plastic the strain in the cases of α=0.0001 and α=0.0005 for V_0 = 50 m/s and V_0 = 150 m/s. At low impact velocity, V_0 = 50 m/s, the strain rate in the necking bifurcates before from the theoretical one in the case of the lowest value of α analyzed, Fig. 3.49-a. Opposite behaviour is found for V_0 = 150 m/s, Fig. 3.49-b.

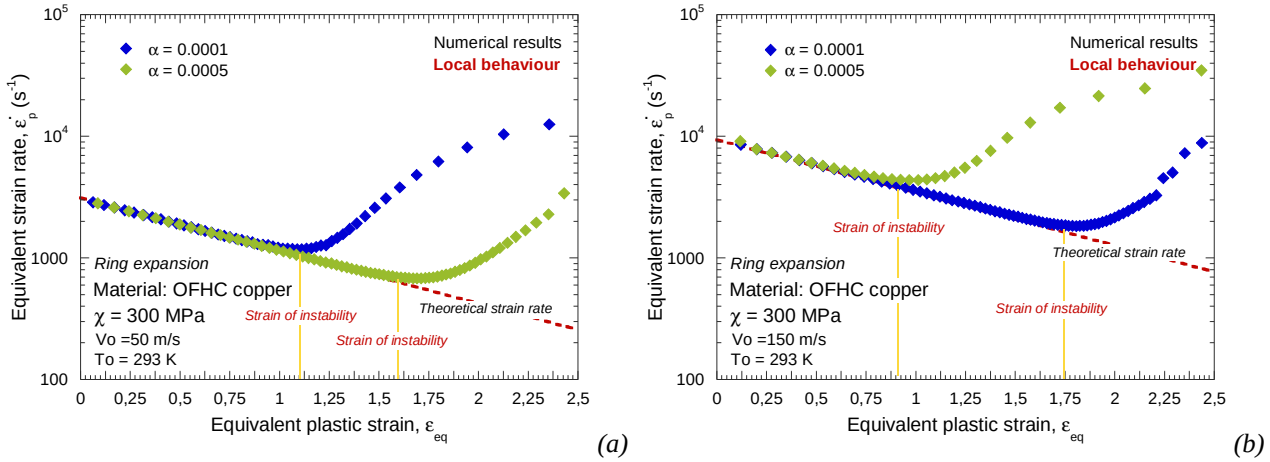

Fig. 3.49. Strain rate in the necking versus plastic strain in the necking in the case of α=0.0001 and α=0.0005. (a) V_0=50 m/s, (b) V_0=150 m/s.

Then, it is possible to understand the evolution of the local stress reported in Fig. 3.50. In the case of V_0 = 50 m/s the stress level for α = 0.0001 drastically increases after instability formation and overpasses the flow stress predicted in the case of α = 0.0005, Fig. 3.50-a. This behaviour is not repeated if higher impact velocity is applied V_0 = 150 m/s, Fig. 3.50-b.

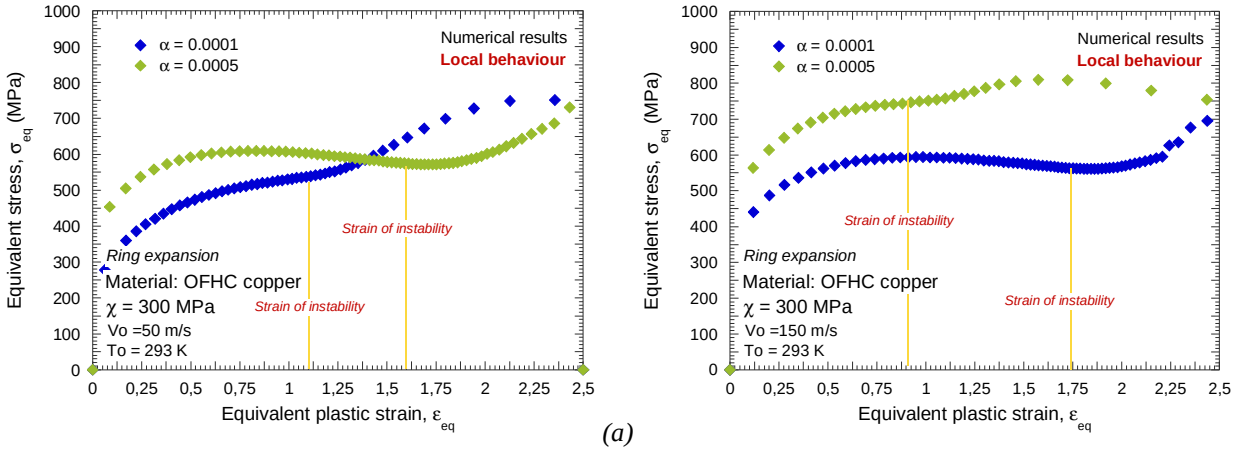

Fig. 3.50. Strain rate in the necking versus plastic strain in the necking in the case of α=0.0001 and α=0.0005. (a) V_0=50 m/s, (b) V_0=150 m/s.

Thus, in the case of α=0.0005 the number of fragments is no longer monotonically increasing with the applied velocity. The maximum number of pieces into which the ring is fragmented occurs for the maximum rate sensitivity of the material, Fig. 3.51. As the rate sensitivity due to the viscous drag term decreases the number of fragments also does it, Fig. 3.51. Such trend is clearly visible in Fig. 3.51. up to a plateau in the relation fragments/impact velocity takes place. At that point the viscous drag term does not longer provide rate sensitivity. The deformation mechanism thermally activated is the only one component of the flow stress providing of rate sensitivity to the material. From this analysis can be concluded that the rate sensitivity is one of the main mechanisms involved in the material fragmentation.

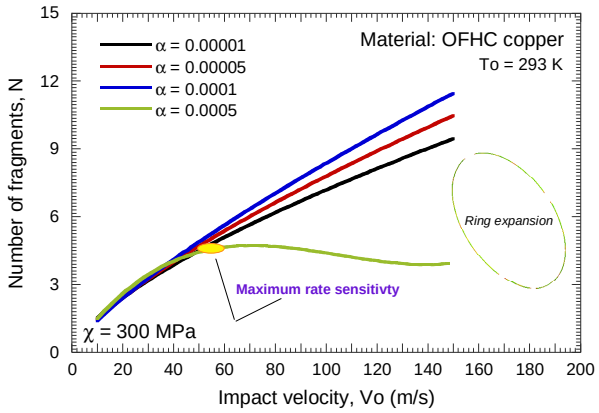

Fig. 3.51. Number of fragments as a function of the impact velocity for different values of α.

Thus in Fig. 3.52. is shown that the increasing rate sensitivity delays localization spreading plasticity along the ring. At high rate sensitivity condition, Fig. 3.52-b-c., the complete failure of the sample takes place in a very short period of time which generates large number of fragments of short length, Fig. 3.52.

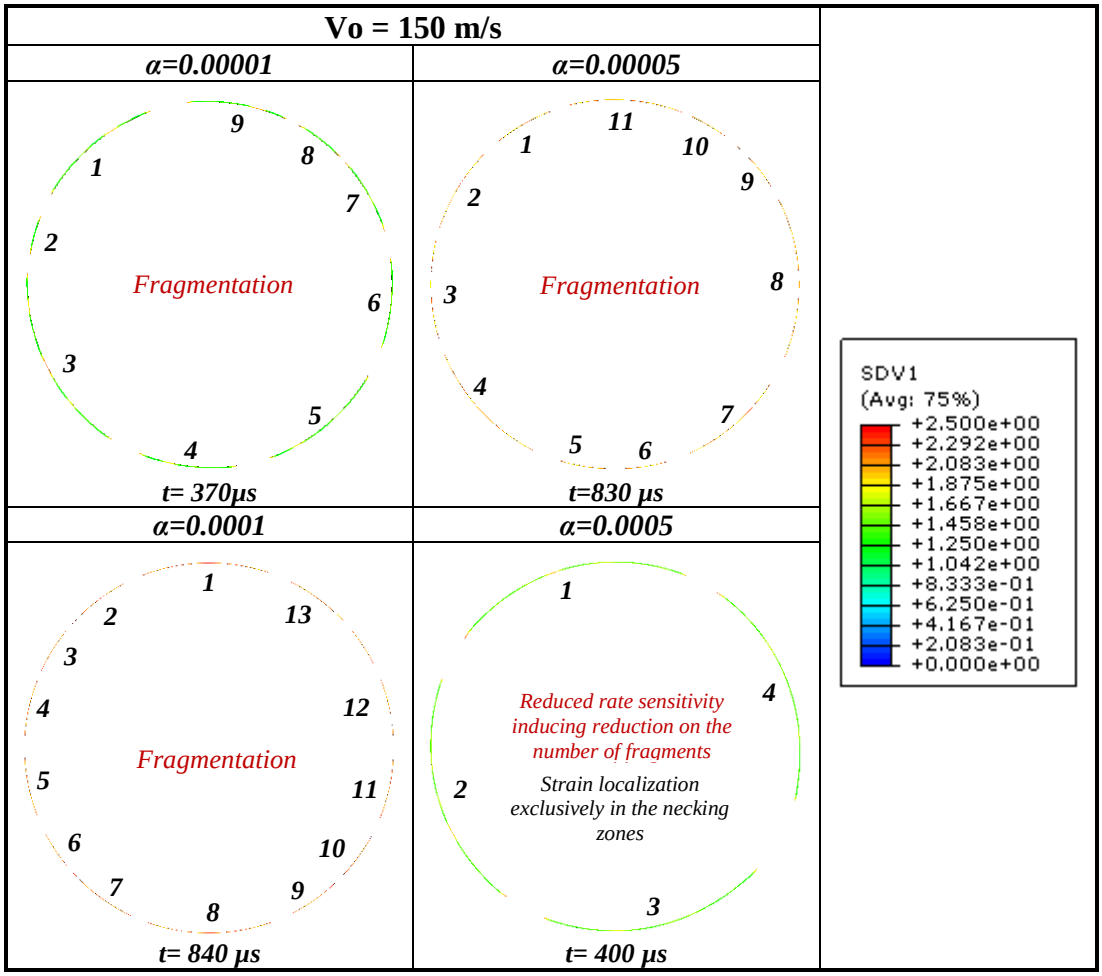

Fig. 3.52. Plastic strain contours at failure time and ring fragmentation for different values of α and V_0=150 m/s.

Subsequently, the effect of parameter α on the strain localization for the conventional dynamic tension test configuration is analyzed.

3.3.5.2.2 The conventional dynamic tension test

In Fig. 3.53. is illustrated the evolution of the local plastic strain as a function of the global plastic strain for all the values of α considered and different impact velocities. The influence of α in the strain of instability is analogous to that reported for the ring expansion case. Beyond a certain impact velocity the largest value of α does not correspond with the most stabilized material, Fig. 3.53.

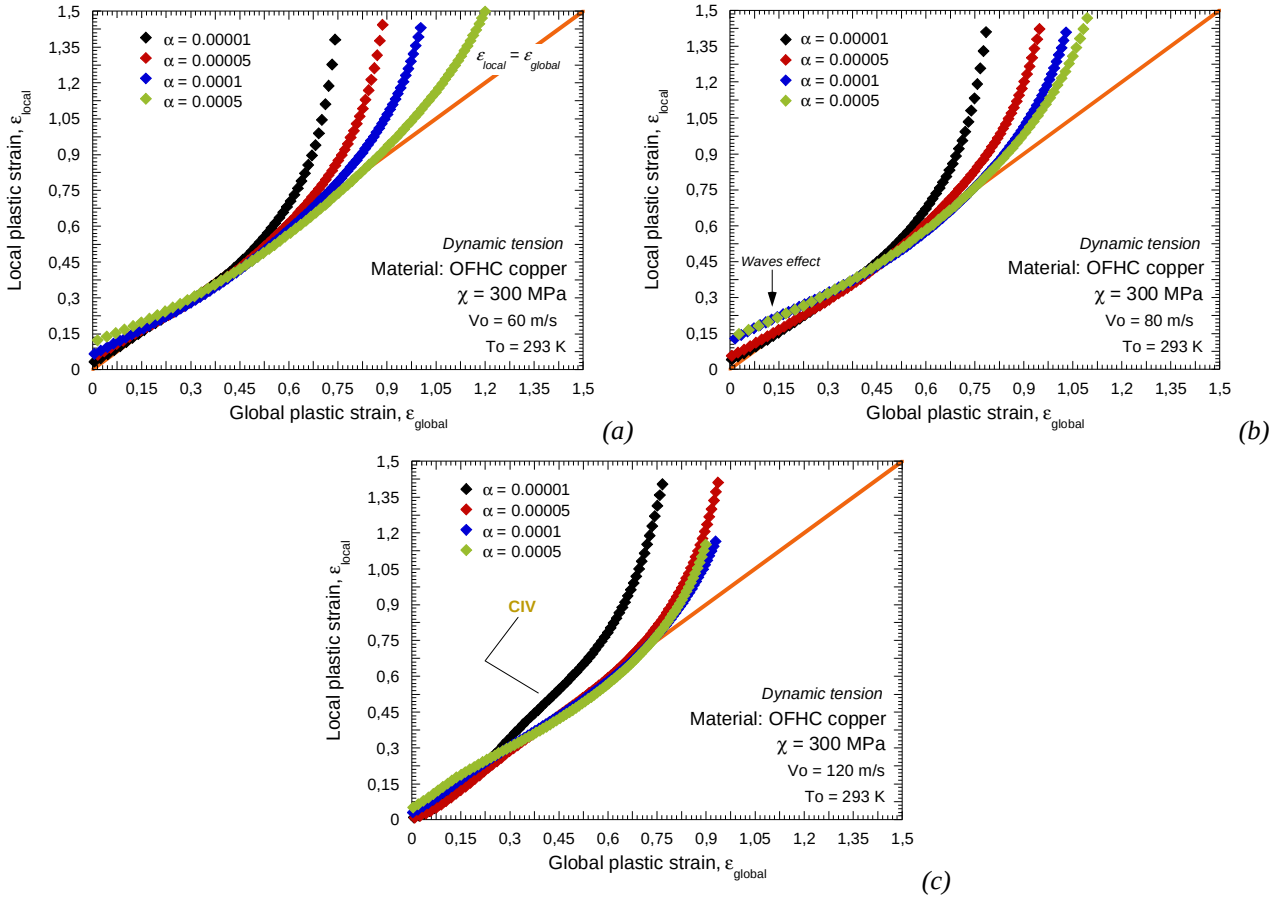

Fig. 3.53. Evolution of the local plastic strain as a function of the global plastic strain for different values of α. (a) V_0=60 m/s, (b) V_0=80 m/s, (c) V_0=120 m/s.

It must be noticed that in the case of α = 0.0005 the maximum strain of instability does not match with the proximity of the **CIV** appearance but with the maximum rate sensitivity of the material, Fig. 3.54.

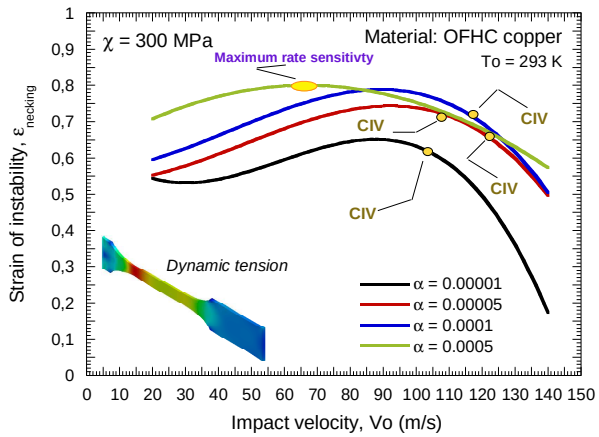

Fig. 3.54. Strain of instability as a function of the impact velocity for different values of α.

Such observation is confirmed in Fig. 3.55. where input and out forces are compared for all the values of α considered and two different impact velocities. In the case of V_0 = 60 m/s the sample behaviour is stable for all the cases analyzed, Fig. 3.55. In the case of V_0 = 100 m/s and α = 0.00001 the **CIV** has already started, for the rest of α values the specimen response is stable, Fig. 3.55. Specially for α = 0.0005 equilibrium between output and input forces is easily achieved, Fig. 3.55-h.

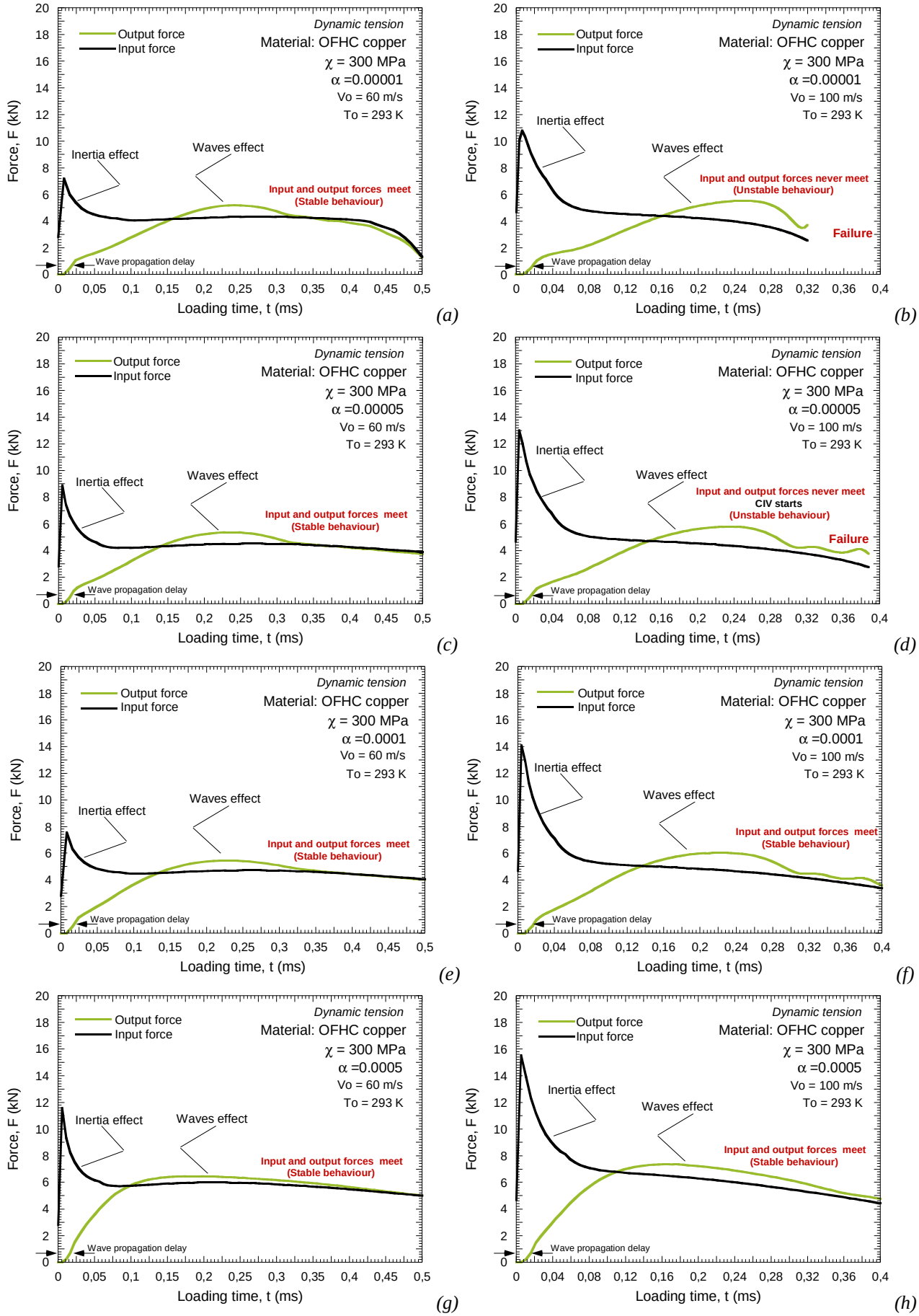

Fig. 3.55. Output and input forces for different values of α and two impact velocities, V_0=60 m/s and V_0=100 m/s.

Next is depicted the evolution of strain rate and flow stress versus plastic strain in the necking for $\alpha = 0.00001$ and $\alpha = 0.0001$ at $V_0 = 100$ m/s, Fig. 3.56. At the beginning of loading the difference takes place in the strain rate level, Fig. 3.56-a. Such change in the deformation rate modifies the material flow stress, Fig. 3.56-b.

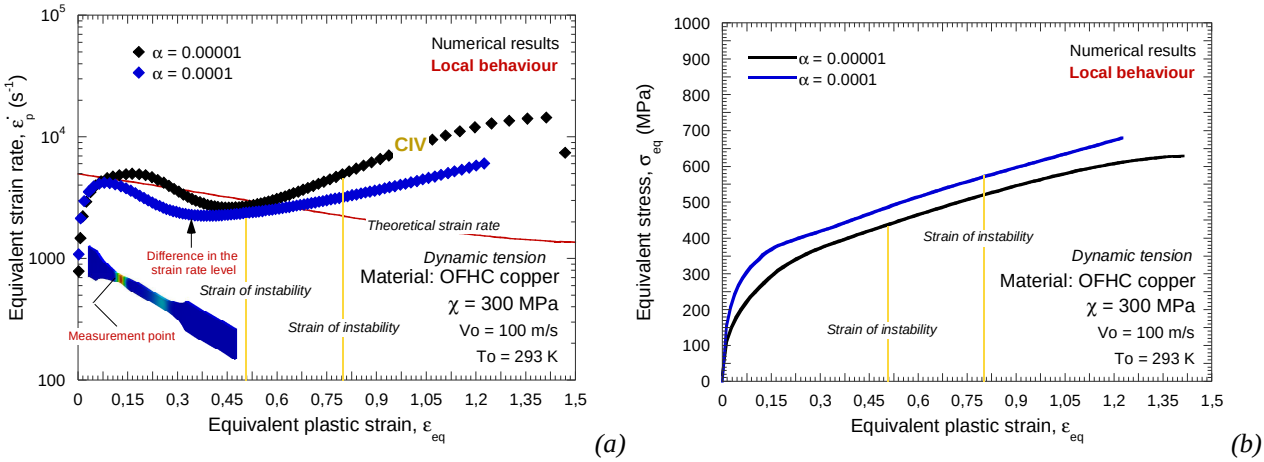

Fig. 3.56. Evolution (a) of strain rate and (b) stress versus plastic deformation in the necking for α=0.0001 and α=0.00001 at V_0=100 m/s.

Consequently, the strain hardening rate and therefore the plastic wave celerity are affected, Fig. 3.57. modifying the **CIV** value as previously reported.

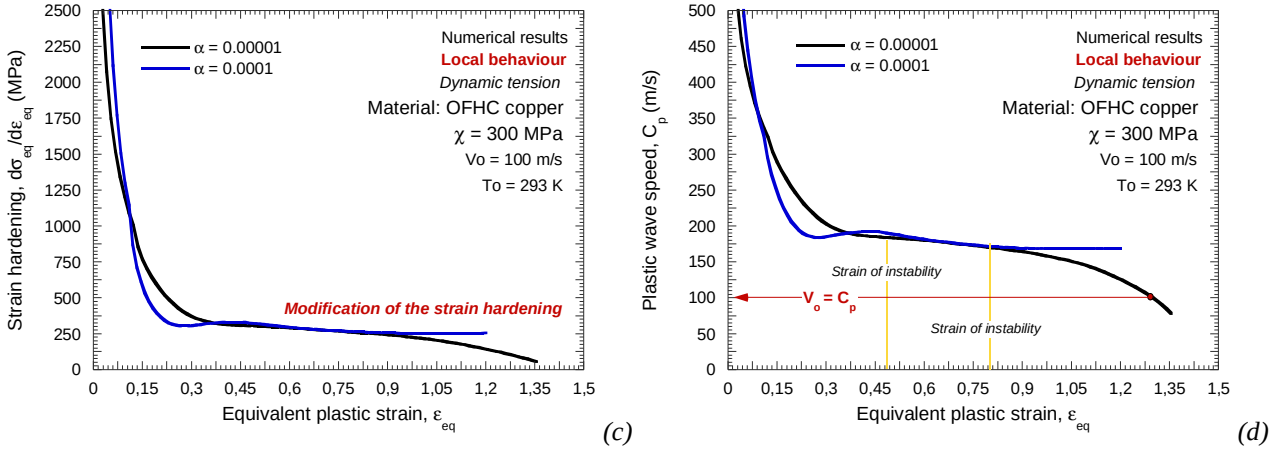

Fig. 3.57. (a) Strain hardening and (b) plastic wave celerity evolution versus plastic deformation in the necking for α=0.0001 and α=0.00001 at V_0=100 m/s.

Previous considerations concerning the local behaviour of the material depending on the value of α introduced into the drag formulation have their reflection on the global specimen response. Thus, at low impact velocities, $V_0 = 60$ m/s, the maximum elongation of the sample corresponds to the maximum value of α, Fig. 3.58. On the contrary, in the case of $V_0 = 120$ m/s and greatest value of α necking is brought forward and elongation of the specimen reduced, Fig. 3.58. Smallest elongation always corresponds to the lowest value of α.

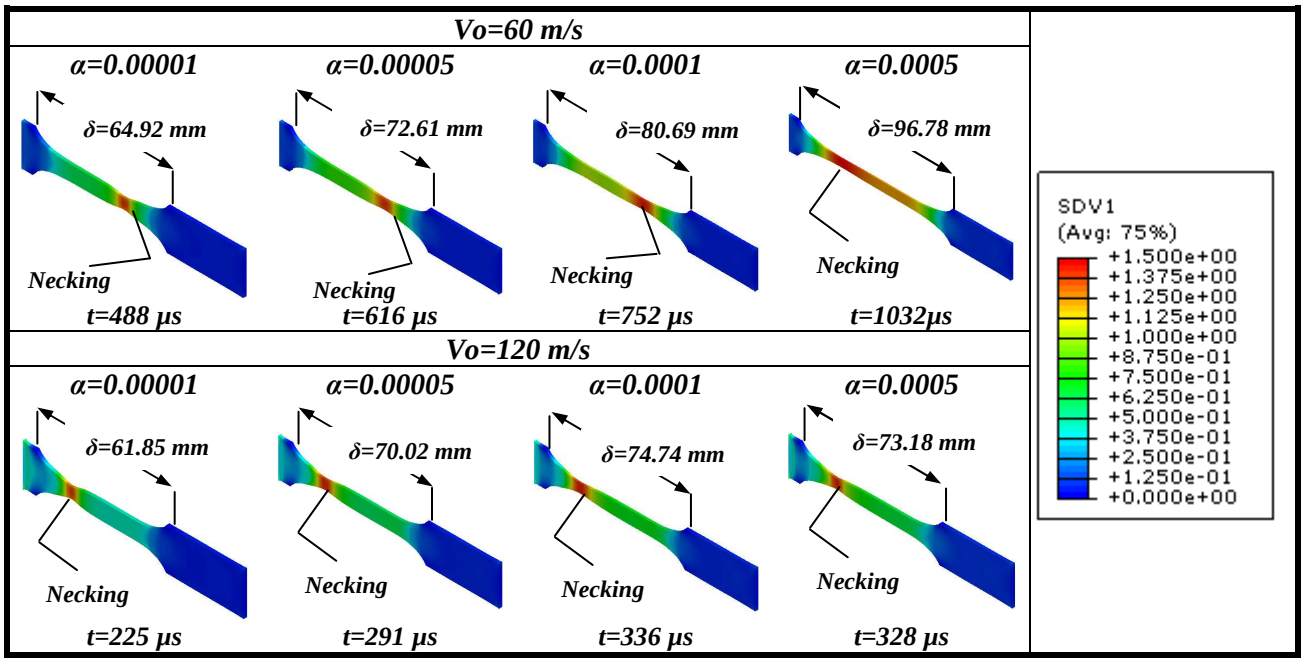

Fig. 3.58. Plastic strain contours at failure time for different values of α and two impact velocities, V_0=60 m/s and V_0=120 m/s.

From the analysis conducted in this part of the document it has been revealed the influence that rate sensitivity has on controlling instabilities formation under dynamic loading. Next, our attention will be focused on the role played by the strain hardening.

3.4 Influence of strain hardening on flow localization under dynamic tension

Let us go through the effect that strain hardening has on flow localization. For it, the extended **RK** model to *martensitic* transformation is applied. The first step concerns to the methodology developped to examine the influence of strain hardening on flow localization under dynamic tension

3.4.1 Methodology

The steps followed are described below:

1. The extension of the **RK** model to *martensitic* transformation introduced in **Section 2.6.** is used. Its strengths lie on a simple formulation facilitating its implementation into **FE** code.

2. The **AISI 301 Ln2B** is choosen as reference material to analyze the effect that the stain hardening has on the formation of plastic instabilities. This material shows marked increase of strain hardening due to *martensitic* transformation allowing for a proper analysis of the problem.

3. Next, the numerical models developed are validated for the ring expansion case and for the conventional dynamic tension case.

4. An analysis of the influence of the strain hardening on the formation of instabilities is conducted using both, the ring expansion configuration and the conventional dynamic tension configuration. Comparison between both configurations is indispensable in order to determine the effect of the boundary conditions on the flow localization. The analysis is expressed in the following terms:

    a. Ring expansion test
        i. Influence of the strain hardening on the strain of instability.
        ii. Influence of the strain hardening on the number of pieces into which the ring is fragmented.
        iii. Influence of the strain hardening on the failure time.

    b. Conventional dynamic tension test
        i. Influence of the strain hardening on the strain of instability.
        ii. Influence of the strain hardening on the **CIV**.
        iii. Influence of the strain hardening on the input and output forces registered in the sample.
        iv. Influence of the strain hardening on the position where the necking takes place
        v. Influence of the strain hardening on specimen elongation at failure

5. In order to provide of generality to the analysis, it is conducted a parametric study on the influence of the parameters of the extra strain hardening function on the flow localization.

3.4.2 Theoretical considerations

Under determined loading conditions metallic alloys may exhibit a strong increase of strain hardening. For example, at low strain rates *austenitic* steels may show *martensitic* transformation within determined range of initial temperatures. In such a case, a drastic increase of the strain hardening may occur, Fig. 3.59-a. Moreover, in the case of metals having **FCC** and **HCP** crystal lattices twinning deformation mode may take place at high deformation rate. Low stacking fault energy ***(SFE)*** of these crystallographic structures enhances *twins* appearance which may lead to a sudden increase of the material strain hardening, Fig. 3.59-b.

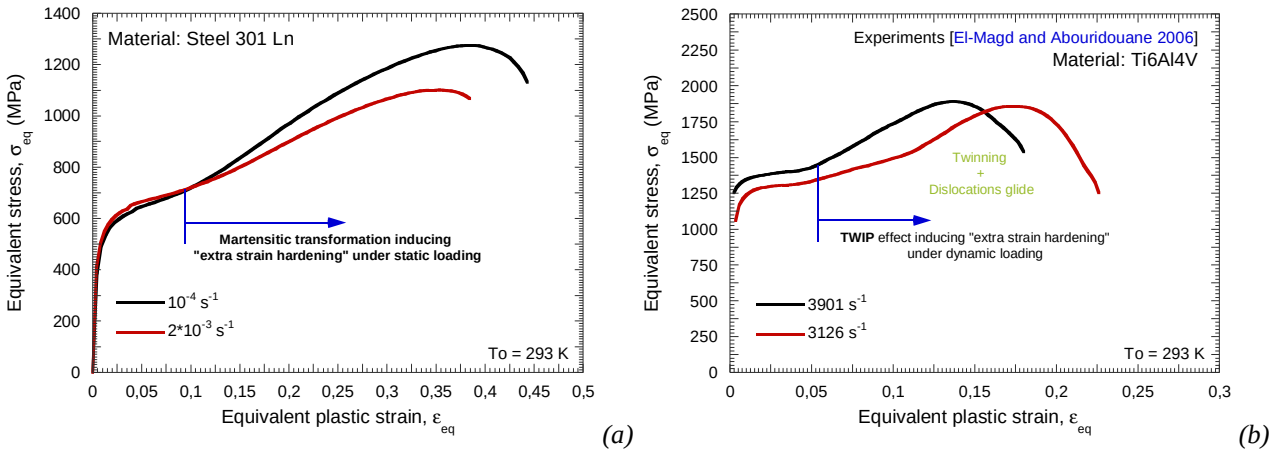

Fig. 3.59. (a) Extra strain hardening under static loading due to martensitic transformation. (b) Extra strain hardening under dynamic loading due to twinning [El-Magd and Abouridouane 2006].

Thus, in order to examine the influence of such processes of increasing strain hardening on the formation of instabilities under dynamic tension the formulation reported in Eq. 2.30., **Section 2.6**. has been used. Such formulation allows for defining *martensitic* transformation or *twinning* effect *(sudden increase of material strain hardening)* on the macroscopic behaviour of the material.

The material model corresponding to the steel **301 Ln2B** *(extended **RK** model to martensitic transformation)* has been chosen for this study, Tables 2.21-2.22. Temperature and strain rate sensitivities of the hardening function are neglected for the whole analysis conducted in the following sections of this work, $\bar{\sigma}_T = \bar{\sigma}_T\left(\bar{\varepsilon}^p, \dot{\bar{\varepsilon}}^p, T\right)\Big|_{\lambda=0}^{g(T)=1} \rightarrow \bar{\sigma}_T = \bar{\sigma}_T\left(\bar{\varepsilon}^p\right)$. It will allow us to isolate the effect of strain hardening, Eq. 3.7.

$$\bar{\sigma}_T\left(\bar{\varepsilon}^p\right) = \sigma_0 \cdot \left[1 - \exp\left(-\lambda_0 \cdot \bar{\varepsilon}^p\right)\right]^{\xi} \qquad (3.7)$$

In Fig. 3.60. the overall stress is decomposed into its respective stress components. The *extra strain hardening* operates beyond a certain value of plastic deformation. It drastically increases the material flow stress until saturation condition is reached, Fig. 3.60.

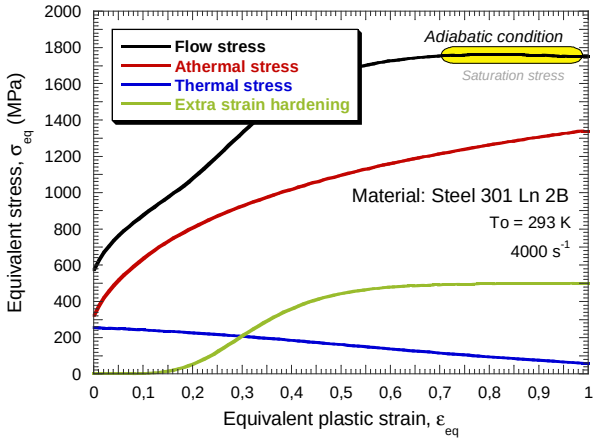

Fig. 3.60. Decomposition of the overall flow stress into its respective stress components.

The hardening function moves up the flow stress of the material from that predicted by the original **RK** formulation *(σ_T=0 MPa is the lower limit for our material configuration)* up to that corresponding to the value of the material constant σ_0 *(σ_T=500 MPa is the upper limit for our material configuration) (Eq. 3.7.)*, Fig. 3.61. These three material models will be used during the first part of the analysis in order to evaluate the influence of strain hardening on the formation of plastic instabilities, Table. 3.2.

Lower limit	**Strain hardening function**			**Upper limit**
σ_T=0 MPa	*σ_0 =500 MPa*	*ξ=17*	*λ_0=10*	*σ_T=500 MPa*

Table 3.2. Material configurations used to analyze the effect of strain hardening on the formation of plastic instabilities under dynamic loading.

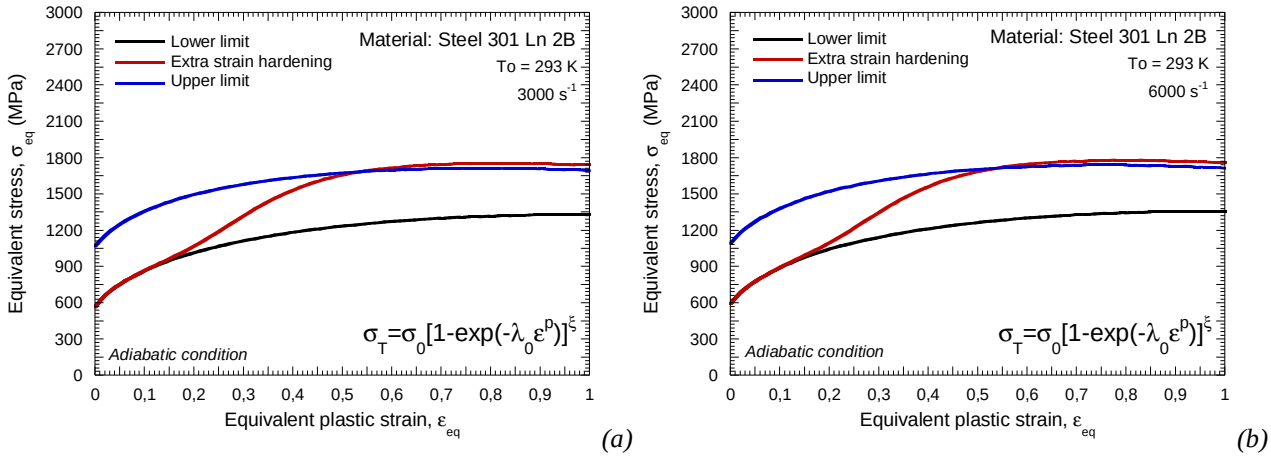

Fig. 3.61. Flow stress evolution versus plastic strain for the three material configurations analyzed and two strain rate levels.

The *strain hardening function* increases the plastic wave celerity. It is expected that it will delay instabilities formation in comparison with the *lower limit* and the *upper limit* configurations, Fig. 3.62. Moreover, it can be predicted that the *upper limit* configuration will be prone to instabilities formation. It shows the same strain hardening *(certain differences are reported due to the adiabatic heating)* than the *lower limit* configuration, but larger flow stress level. By means of the application of Considère criterion $(d\bar{\sigma}/d\bar{\varepsilon}^{p}=\bar{\sigma}$ *[Considère 1885])* to both material models such expectations seems to be confirmed, Fig. 3.62. This point will be matter of discussion along the following sections of the document when the numerical results will be presented.

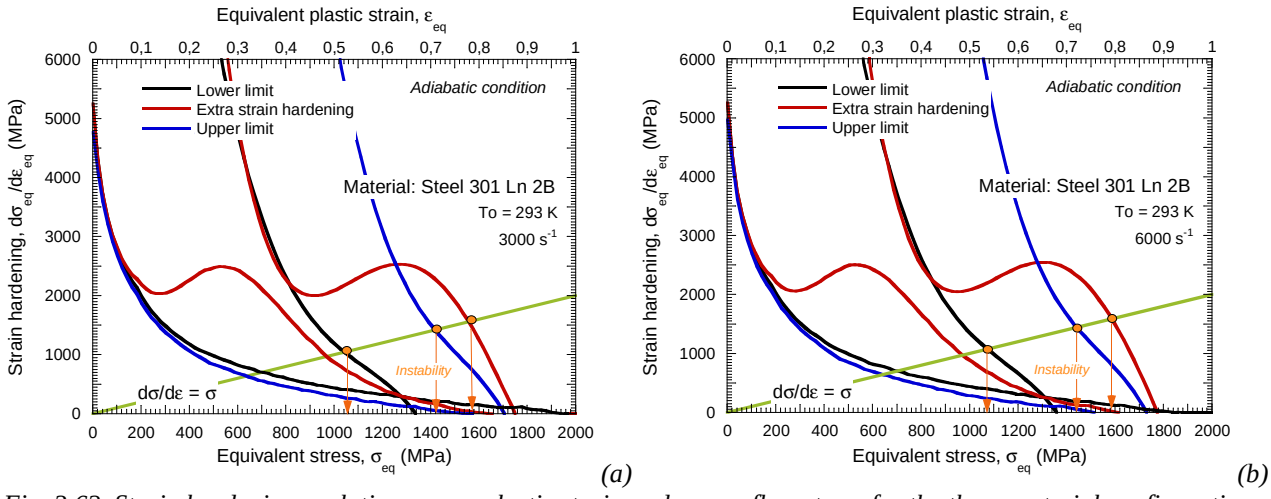

Fig. 3.62. Strain hardening evolution versus plastic strain and versus flow stress for the three material configurations considered and two different strain rate levels.

The analytical temperature increase during loading for the material configurations considered and two different strain rates is plotted in Fig. 3.63. Before the strain hardening function becomes active, the increase of temperature of the *lower limit* and the *strain hardening* configurations matches. When the hardening function becomes operative the adiabatic temperature drastically augments getting closer to the temperature increase predicted by the *upper limit* model.

During the analysis conducted in the following sections of the document it will be checked that potential modifications of the material response under loading will be intrinsically tied to the strain hardening effect and not to the differences in the adiabatic temperature increase predicted by each material model.

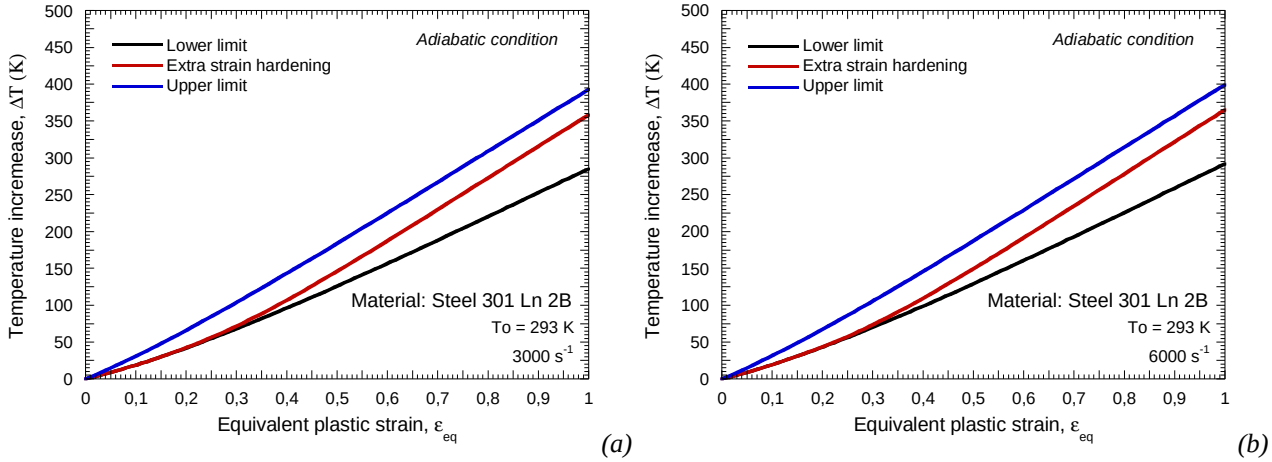

Fig. 3.63. Temperature evolution versus plastic strain for the three material configurations considered and two different strain rate levels.

It is important to notice the reduced rate sensitivity exhibited by all the material configurations considered, Figs. 3.64-3.65. Because of the strong influence of the strain hardening formulation on the material behavior, the effect of the rate sensitivity on the instabilities formation is expected to be relegated to a secondary role. This consideration will be confirmed along the following sections of this document.

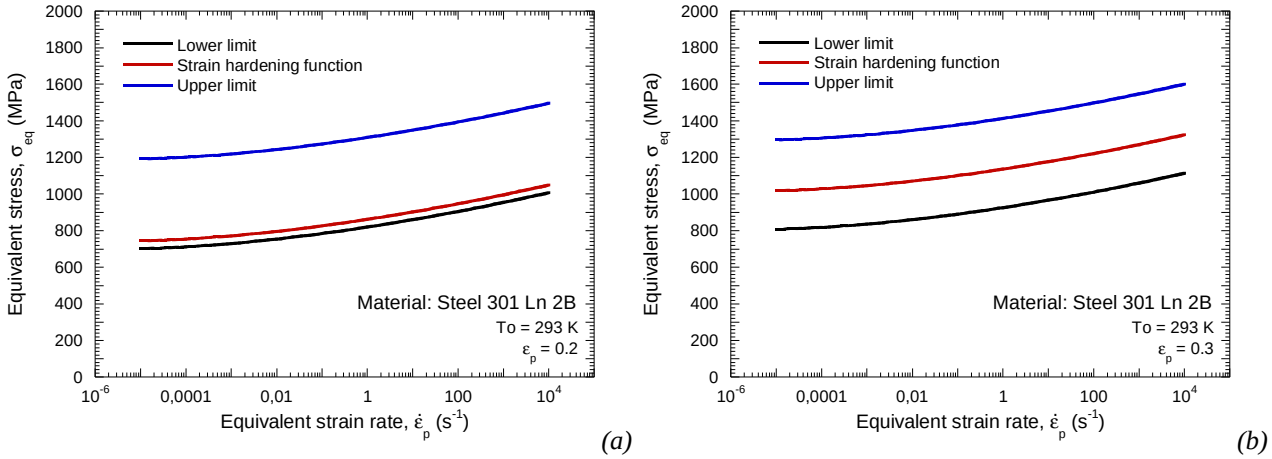

Fig. 3.64. Evolution of the flow stress versus strain rate for the three material configurations considered and different values of plastic deformation.

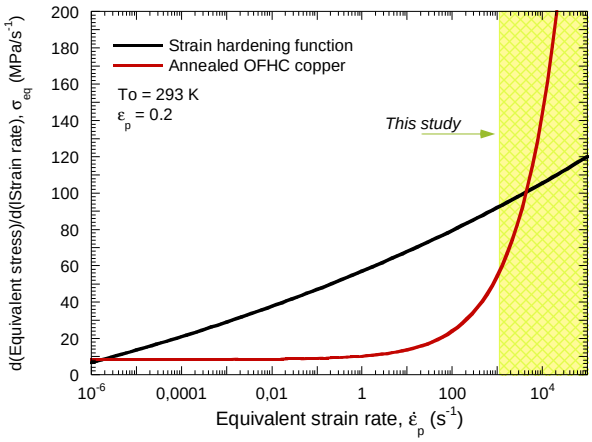

*Fig. 3.65. Evolution of the rate sensitivity versus strain rate for the extra strain hardening configuration at room temperature and ε_p=0.2. Comparison with annealed **OFHC** copper.*

3.4.3 Implementation of the extended RK model to martensitic transformation into FE code and validation of the numerical model

Following the same procedure reported in **Section 3.3.1**, the implementation into the **FE** code of the material models used to analyze strain hardening effect on flow localization is validated.

Perfect matching is observed between analytical predictions and simulation results for both numerical configurations, Fig. 3.66. It validates the implementation of the models.

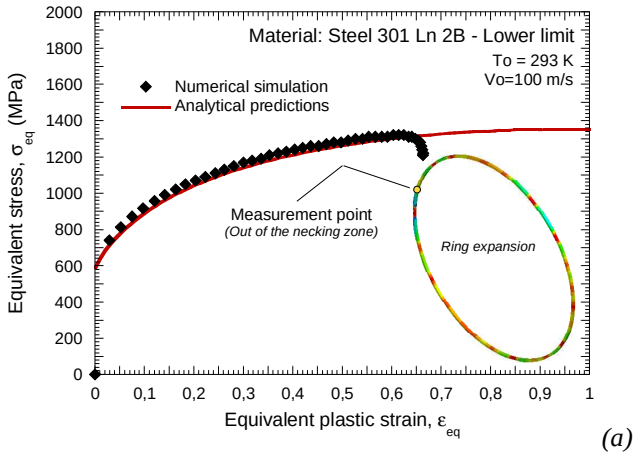

(a)

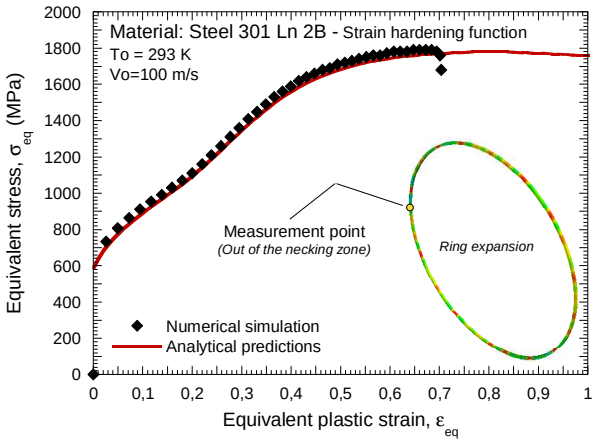

(b)

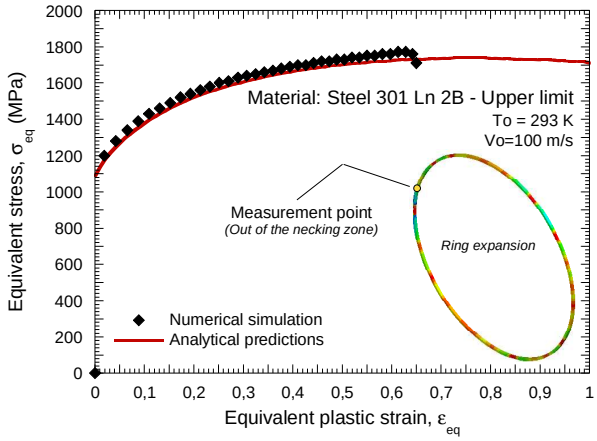

(c)

Fig. 3.66. Comparison between numerical results and analytical predictions for the material models considered. Ring expansion test, V_0=100 m/s.

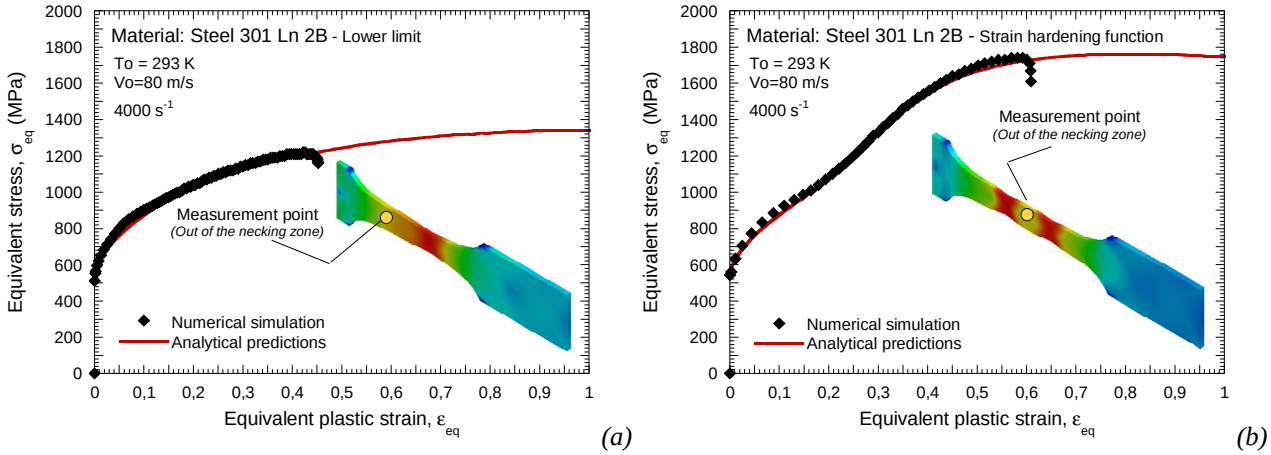

(a) *(b)*

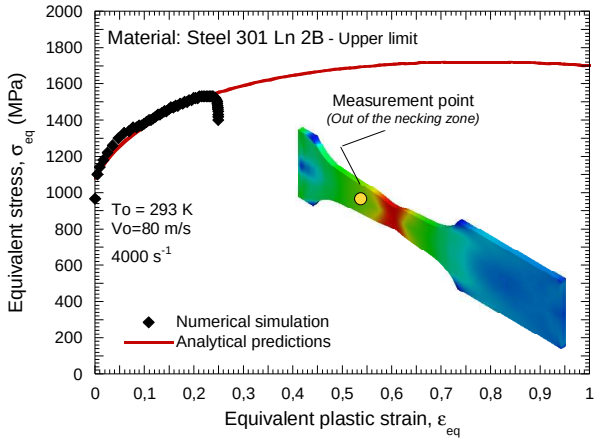

(c)

Fig. 3.67. Comparison between numerical results and analytical predictions for the material models considered. Conventional dynamic tension test, V_0=80 m/s.

3.4.4 Analysis and results for reference material

The next step is to analyze the effect of strain hardening on the flow localization for the ring expansion configuration. *Lower limit*, *upper limit* and *strain hardening function* material models are used for that task.

3.4.4.1 The ring expansion test

In the ring expansion case numerical simulations within the range of impact velocities 10 m/s ≤ V_0 ≤ 150 m/s have been carried out.

In Fig. 3.68. is shown the evolution of the local plastic strain versus the global plastic deformation for different impact velocities and the three material configurations considered. For the whole range of impact velocities the maximum strain of instability is reached by application of the *strain hardening function*, Fig. 3.68. As it was expected the *upper limit* configuration becomes prone to instabilities formation, Fig. 3.68. In comparison with the other material models, it shows a quite reduced strain of instability within the whole range of impact velocities, Fig. 3.68.

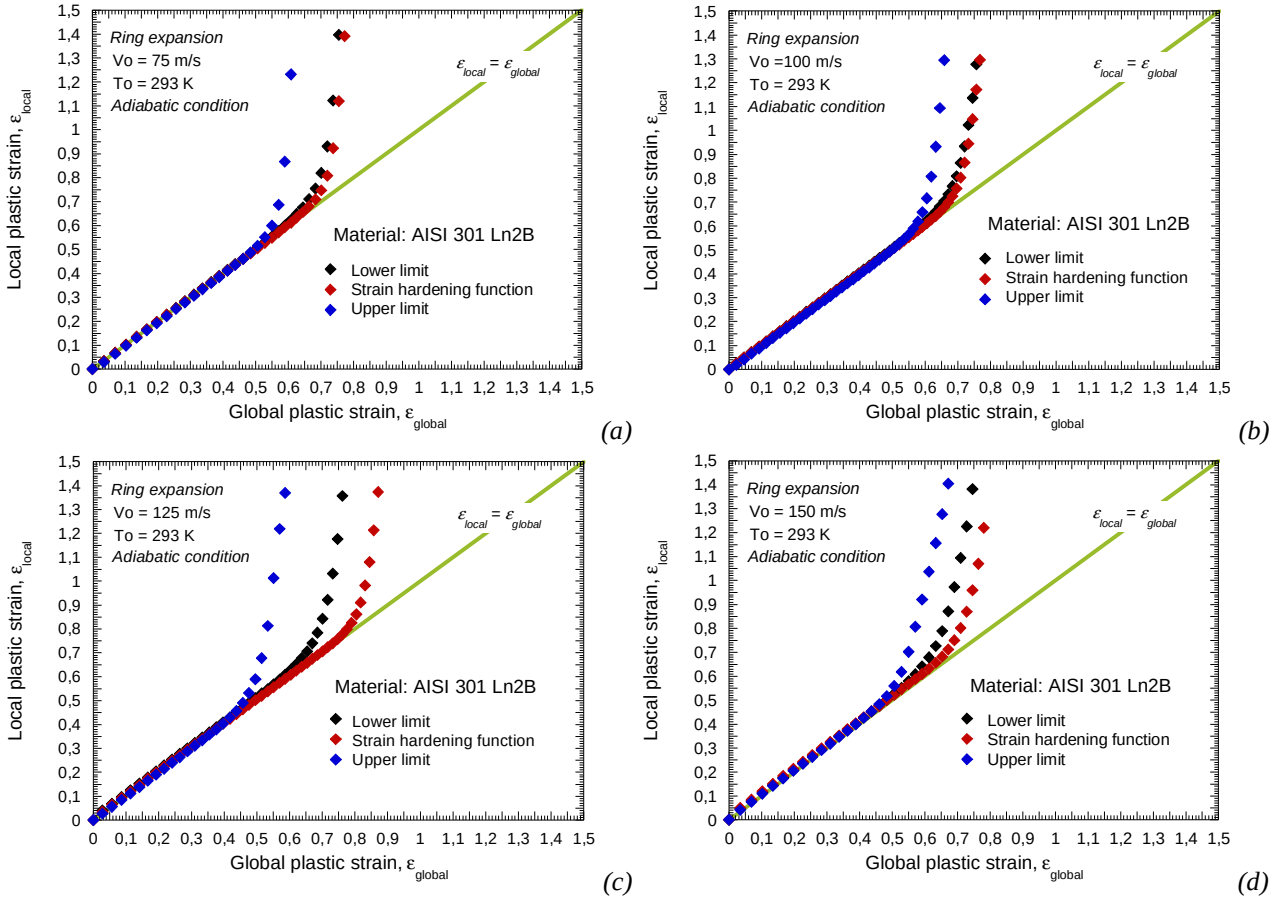

Fig. 3.68. Evolution of the local plastic strain versus the global plastic strain for the configurations analyzed (a) V_0=75 m/s, (b) V_0=100 m/s, (c) V_0=125 m/s, (d) V_0=150 m/s.

For the cases of *lower limit* and *upper limit* configurations, the strain of instability shows the expected increase with impact velocity, Fig. 3.69. However, it must be noticed that if the *strain hardening function* is applied, the strain of instability does not exhibit relevant changes with impact velocity *(so, with material rate sensitivity)*, Fig. 3.69-a. In Fig. 3.69-b. is proven that such effect is not related to differences in the temperature increase predicted by each constitutive relation. If isothermal conditions of deformation are applied the strain of instability is just moved up for the whole range of impact velocities, Fig. 3.69.

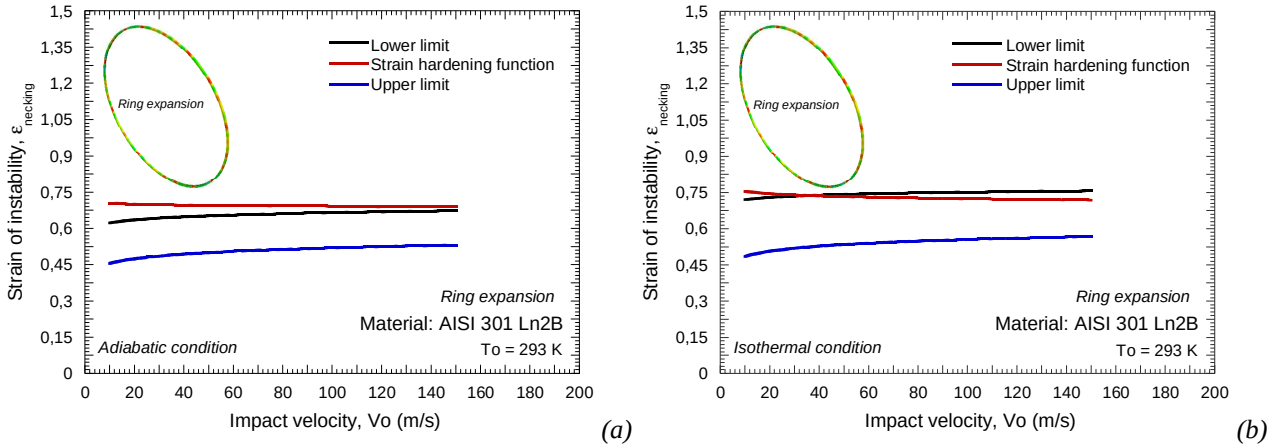

Fig. 3.69. Strain of instability as a function of impact velocity.
(a) Adiabatic conditions of deformation. (b) Isothermal conditions of deformation.

Previous considerations are of main interest. If the *hardening function* is applied, instability takes always place for approximately the same stress level, once the maximum hardening rate is overcome, close to the saturation stress condition, Fig. 3.70. Thus, the effect of rate sensitivity on the material ductility seems to be hidden by the strong influence of strain hardening; which is controlling the localization process.

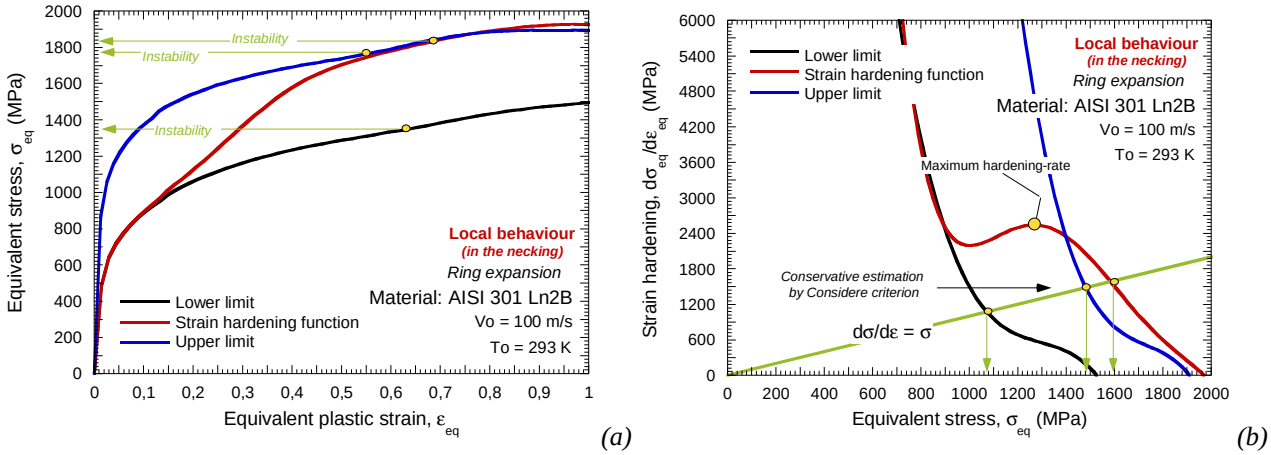

Fig. 3.70. (a) Flow stress evolution versus plastic strain and (b) evolution of the strain hardening versus stress in the necking for the three material configurations analyzed.

In Fig. 3.71. is depicted the evolution of the strain rate and the stress in the necking as a function of the plastic strain. If the *hardening function* is applied the bifurcation of the local deformation rate from the theoretical one is delayed until the hardening rate of the material starts to decrease. However, in the case of application of the *lower limit* and the *upper limit* models strain localization seems to be also influenced by the rate sensitivity of the material *(that in this particular case is quite reduced)*, Fig. 3.71.

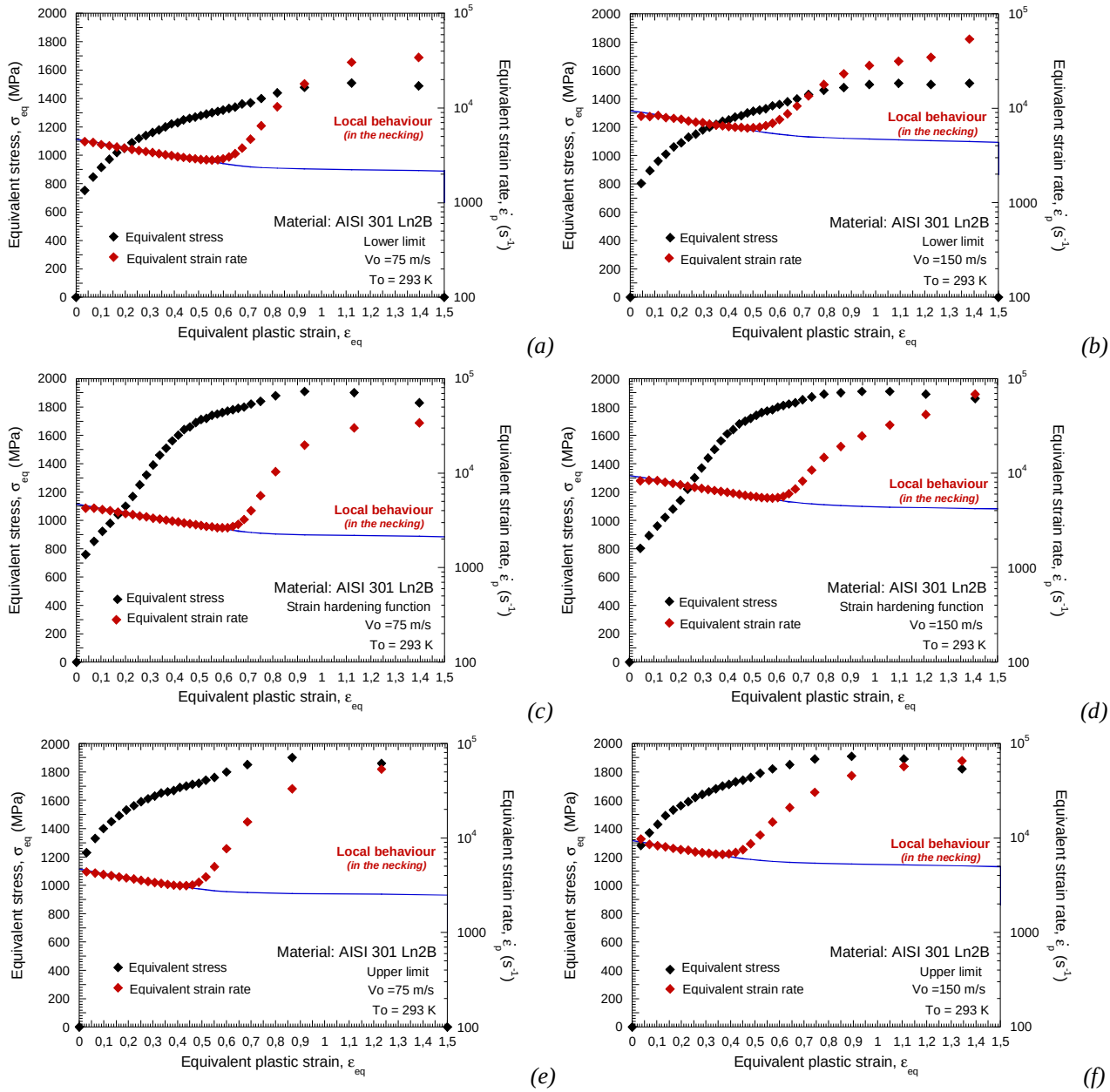

Fig. 3.71. Evolution of the stress and strain rate in the necking as a function of plastic strain for the three material configurations considered and different impact velocities.

It seems that for certain value of strain hardening rate *(in absence of material damage, wave propagation or any other disturbance mechanism)* strain localization may not take place. In following sections of the document this matter will be extensively discussed.

Next the dynamic tension test is analyzed.

3.4.4.2 The conventional dynamic tension test

In the case of the conventional dynamic tension test numerical simulations within the range of impact velocities 10 m/s $\leq V_0 \leq$ 240 m/s have been conducted.

For this configuration is clear that the largest strain of instability corresponds to the application of the *strain hardening function* for the whole range of impact velocities considered, Fig. 3.72.

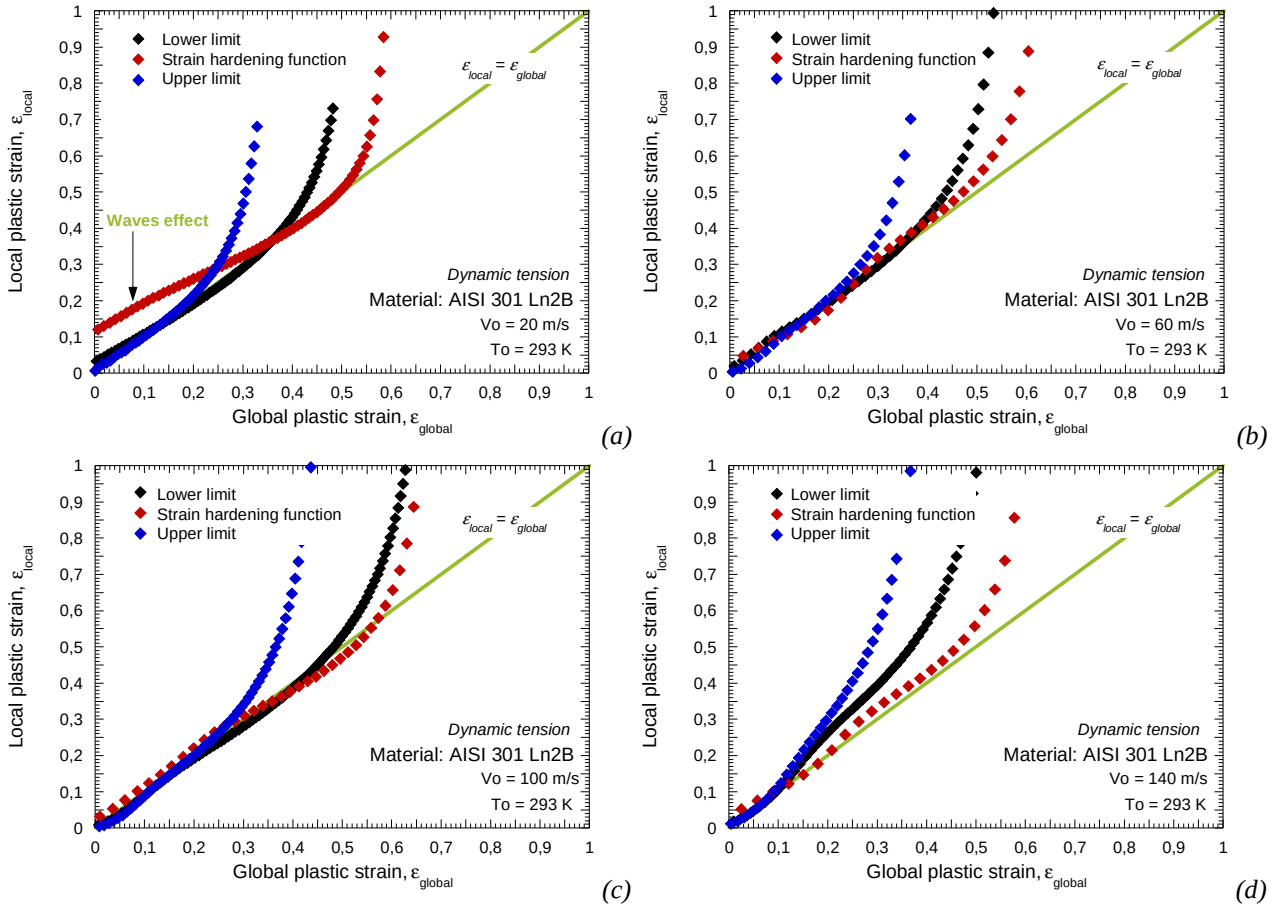

Fig. 3.72. Evolution of the local plastic strain versus the global plastic strain for the three configurations analyzed (a) V_0=60 m/s, (b) V_0=80 m/s, (c) V_0=100 m/s, (d) V_0=140 m/s.

In Fig. 3.73. is reported the evolution of the strain of instability versus the impact velocity for the three material configurations analyzed under adiabatic and isothermal conditions of deformation. Strain of instability values predicted by the three models seem not to be strongly affected by the adiabatic heating, Fig. 3.73.

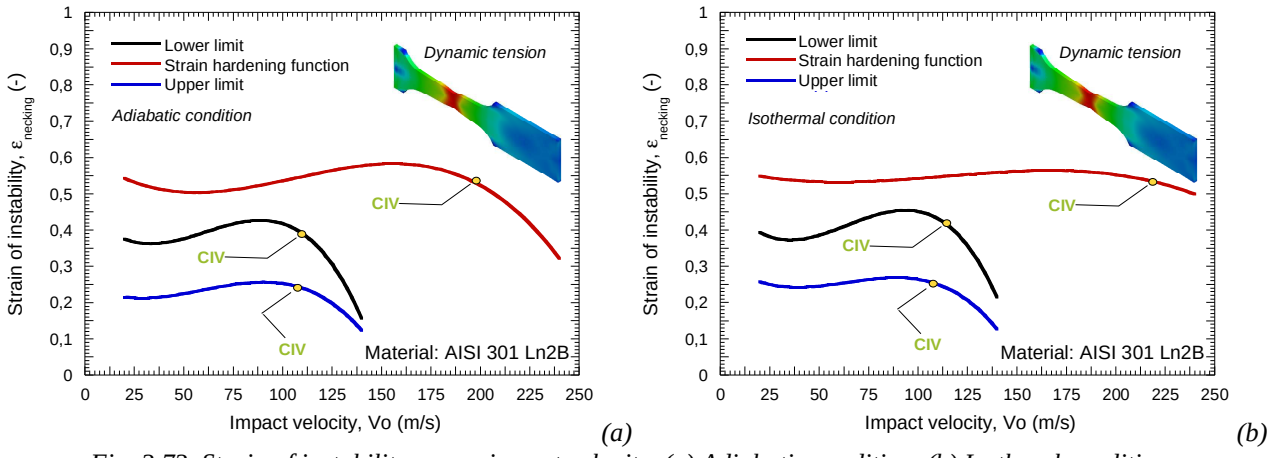

Fig. 3.73. Strain of instability versus impact velocity. (a) Adiabatic condition. (b) Isotheral condition.

In the case of application of the *strain hardening function*, before the **CIV** is reached, localization of deformation only takes place once the maximum hardening rate is overcome, Fig. 3.74. For this material configuration, as it was observed in the ring expansion case, strain localization is controlled by the material hardening rate.

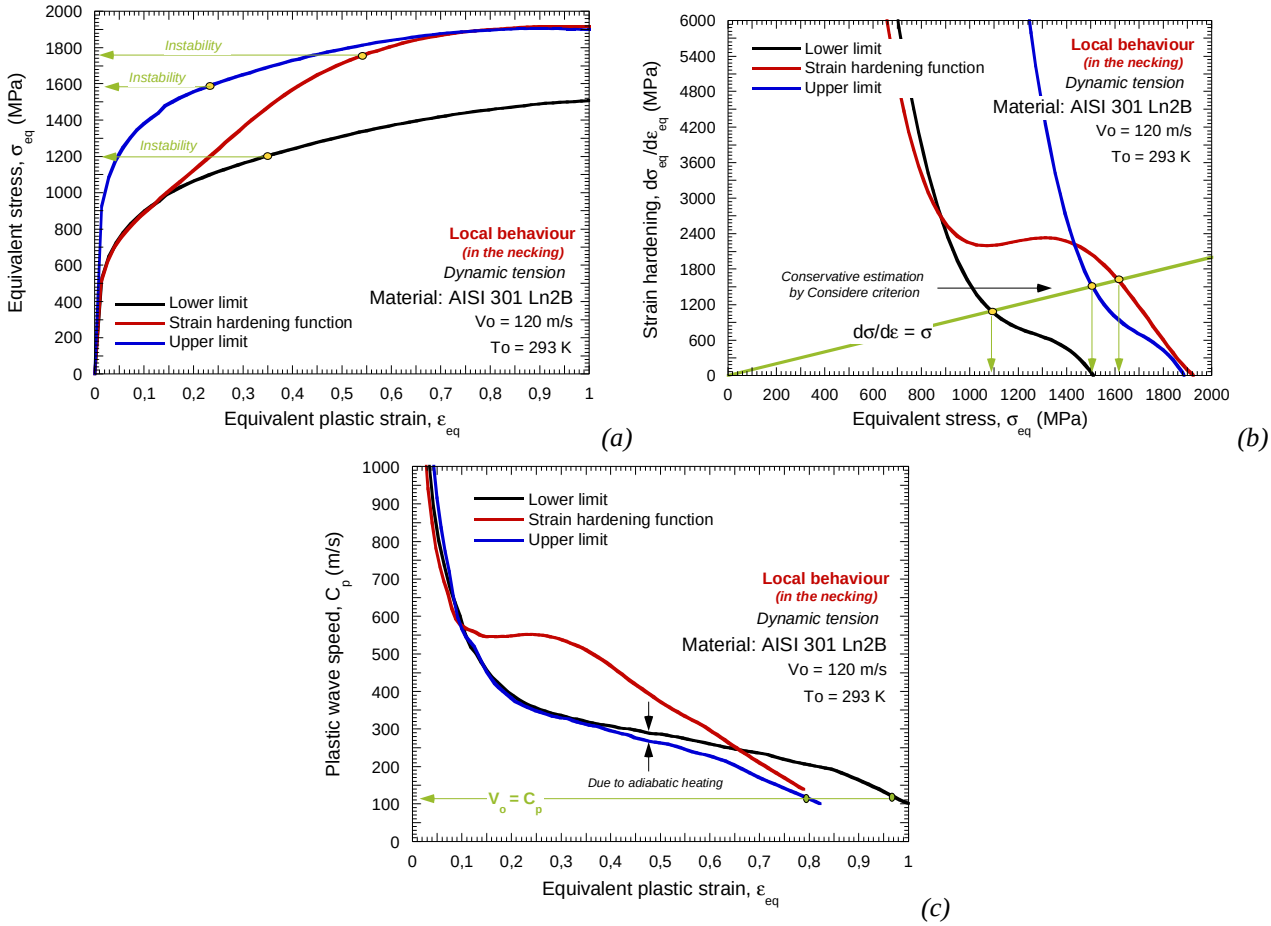

Fig. 3.74. (a) Flow stress evolution versus plastic strain in the necking, (b) evolution of the strain hardening versus stress in the necking and (c) evolution of the plastic wave speed versus plastic strain in the necking for the three material configurations analyzed.

The **CIV**-starts for *lower limit* and *upper limit* models is $\mathrm{CIV}\big|_{\text{lower limit}}^{\text{upper limit}} = \mathrm{V}_0 \approx 120\ \mathrm{m/s}$, Figs. 3.73-3.75. Slightly larger value of the plastic waves speed defined by the *lower limit* configuration *(certain differences in the plastic wave speed for both models are observed caused by the adiabatic heating, Fig. 3.74-c)* is balanced by the larger contribution of elasticity to the **CIV** value in the case of *upper limit* configuration, Eq. 3.5. In the case of *strain hardening function* application, the **CIV** is considerably delayed due to the large increase of the plastic wave speed predicted by the model, $\mathrm{CIV}\big|_{\text{strain hardening}} = \mathrm{V}_0 \approx 200\ \mathrm{m/s}$, Fig. 3.75-b.

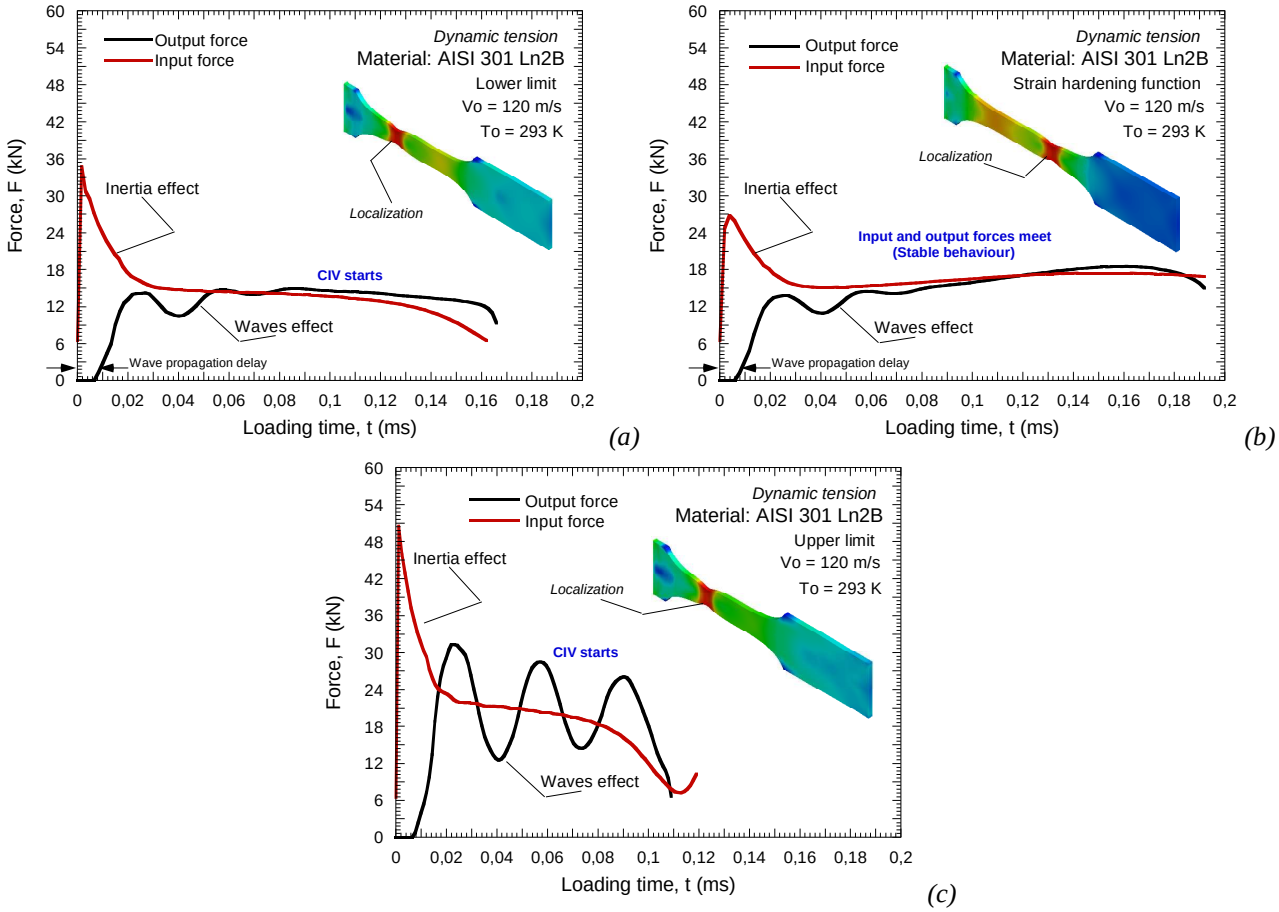

Fig. 3.75. Output and input forces for the material configurations considered at V_0=120 m/s.

Previous considerations are revealed analyzing the evolution of the strain rate in the necking as a function of the plastic strain, Fig. 3.76. If *lower limit* or *upper limit* configurations are used the strain rate in the necking quickly overpasses the theoretical one at the beginning of loading, leading to early strain localization *(strain of instability represented in Fig. 3.76 comes from Fig. 3.72)*, Fig. 3.76. If the *strain hardening function* is considered, the rate of deformation in the necking is controlled and restricted to values under the theoretical one until the maximum hardening-rate of the material is overcome, Fig. 3.76.

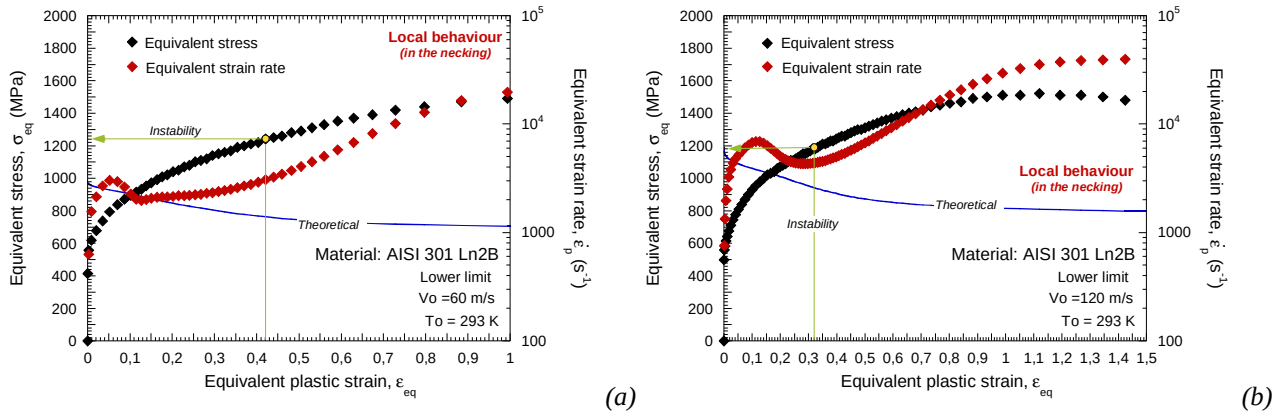

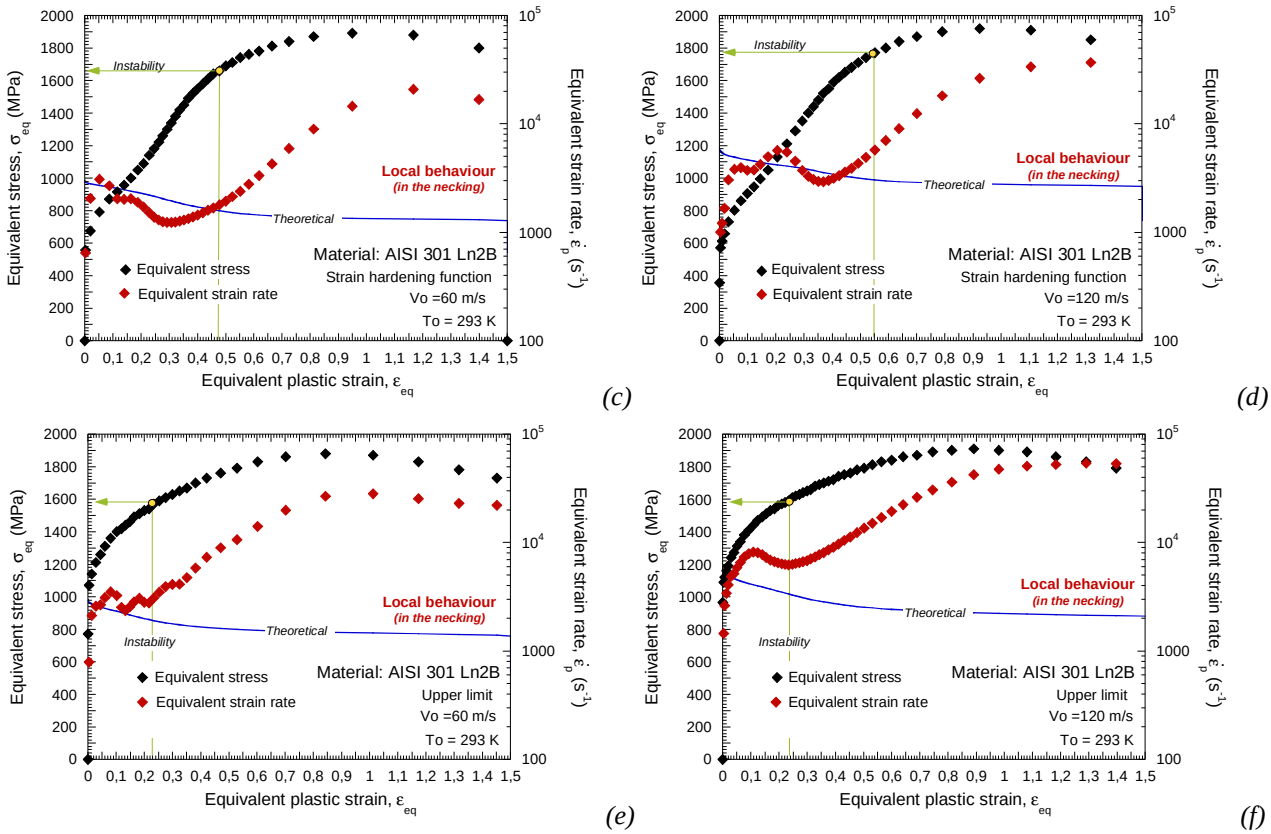

Fig. 3.76. Evolution of the strain rate and the flow stress in the necking as a function of plastic strain for the three material configurations considered and different impact velocities.

Finally, is necessary to check that the considerations reported for the local material behaviour are reflected in the global specimen response. At failure *(a constant failure strain is imposed* $\bar{\varepsilon}_f^p = 1.5$*)*, the sample elongation is much larger when the *strain hardening function* is applied, Fig. 3.77., improving the capability of the material for absorbing energy. Smallest specimen elongation corresponds to the *upper limit* configuration, Fig. 3.77.

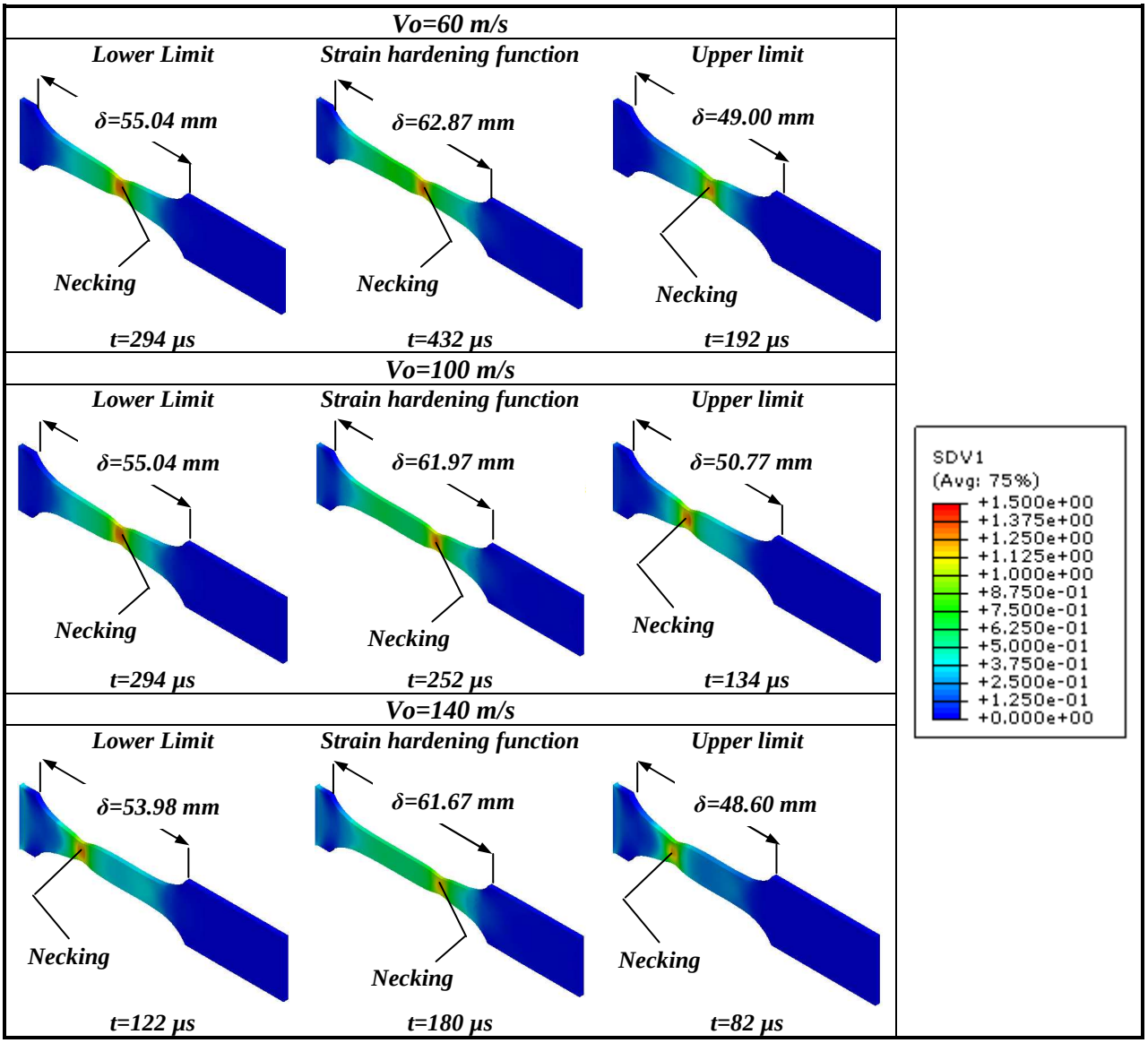

Fig. 3.77. Plastic strain contours at failure for the three material configurations analyzed and different impact velocities.

The position where necking takes place is coincident for the *lower limit* and the *upper limit* configurations, Fig. 3.78. It was expected since, as it was introduced previously, the wave propagation process for these two material models does not exhibit notable differences.

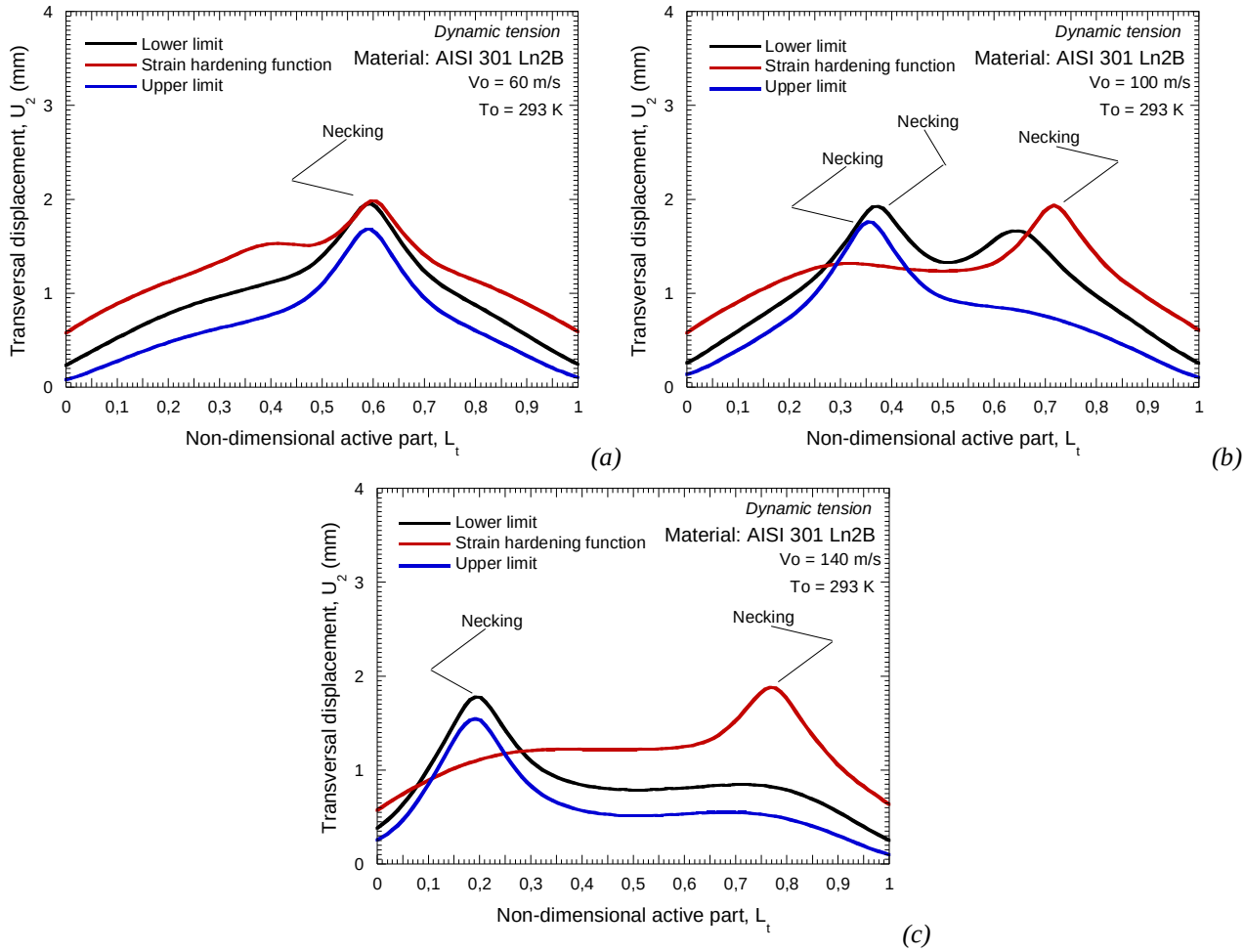

Fig. 3.78. Transversal displacement of the specimen at failure for the three material configurations analyzed and different impact velocities.

In order to go further in this investigation, a parametric study on the influence of *strain hardening function* parameters on the material response when it is subjected to dynamic tension is conducted in the following sections of the document.

3.4.5 Influence of strain hardening formulation parameters on the flow localization

Let us maintain the constants of the original **RK** formulation as those corresponding to steel **301 Ln2B**, Table 2.21. The constants of the strain hardening function will be varied using the values listed in Table 3.3. The values in bold will be kept as the reference values *(when varying one parameter the other one will take the value in bold).*

ξ (MPa)				λ_0 (-)			
10	*50*	*200*	*1000*	*3*	*5*	***10***	*15*

Table 3.3. Value of the strain hardening function constants used for the parametric study.

Next, the effect of parameter ξ on the flow localization under dynamic tension is analyzed.

3.4.5.1 Influence of parameter ξ

In Fig. 3.79-a. is depicted the evolution of the strain hardening function versus strain for different values of ξ. The increase of ξ delays both the plastic strain where the extra strain hardening becomes operative and the plastic strain where the extra strain hardening reaches saturation. However, the hardening rate remains unaltered but shifted along strain, Fig. 3.79-b.

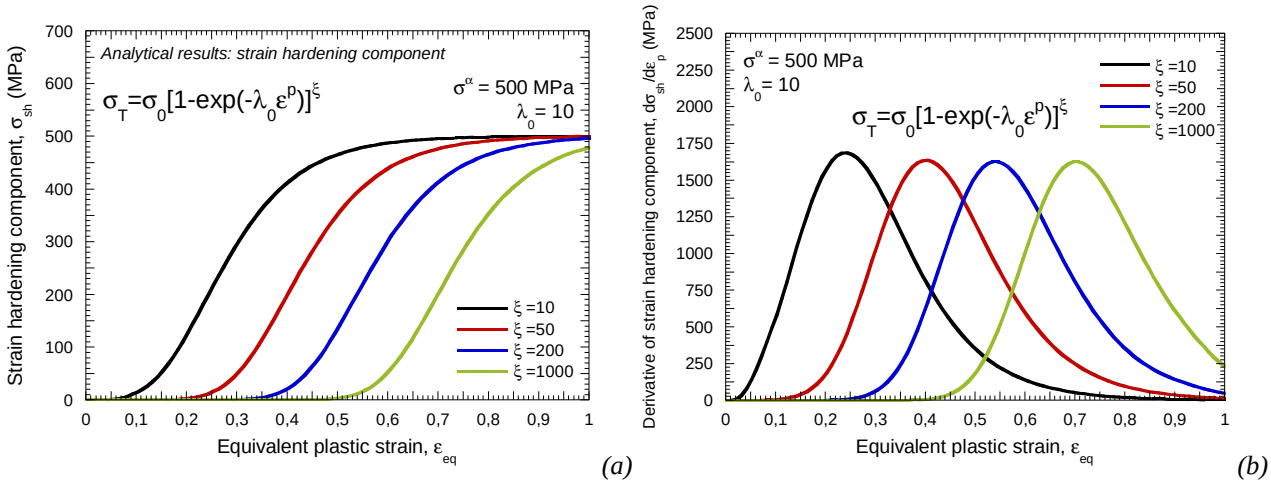

Fig. 3.79. (a) Flow stress predicted by the strain hardening function versus plastic strain. (b) Derivative of the strain hardening function versus plastic strain.

In the following section of the document is examined the influence of parameter ξ on the formation of plastic instabilities using ring expansion configuration.

3.4.5.1.1 The ring expansion problem

For the whole range of initial impact velocities considered as the value of ξ increases the strain of instability also does it, Fig. 3.80. All the material configurations analyzed get the benefits of the strain hardening function *(it might have been possible that instability would have taken place before the strain hardening function becomes operative if larger values of ξ would have been considered)* and the instability takes place close to the saturation stress condition, once the maximum hardening rate is overcome, Fig. 3.81.

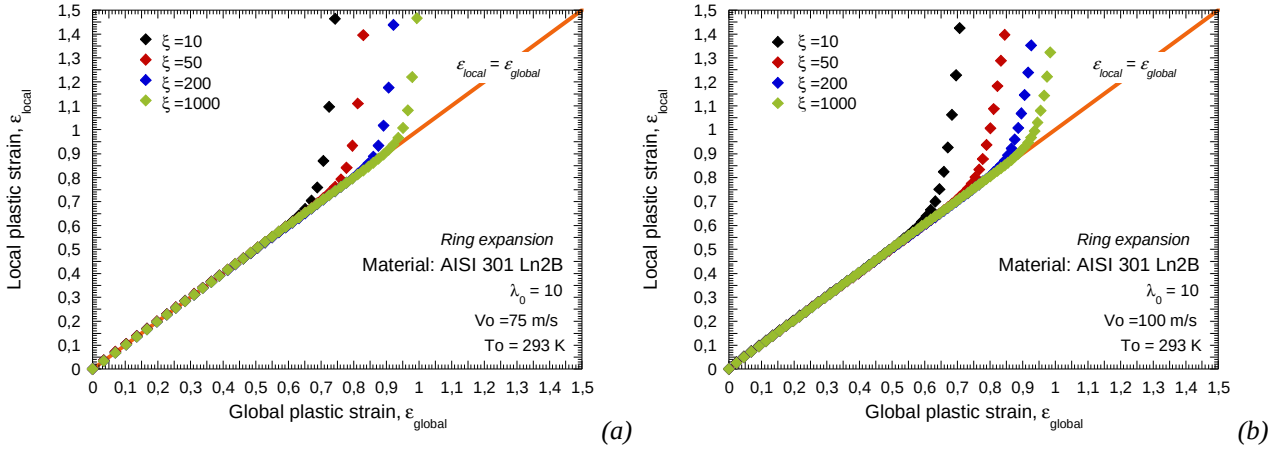

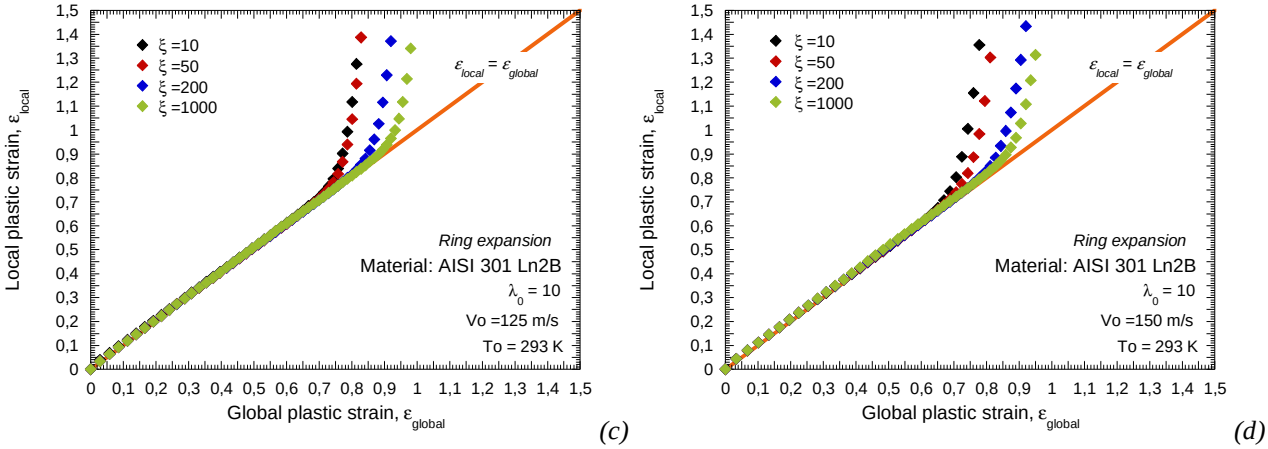

Fig. 3.80. Evolution of the local plastic strain with the global plastic strain for the configurations analyzed (a) V_0=75 m/s, (b) V_0=100 m/s, (c) V_0=125 m/s, (d) V_0=150 m/s.

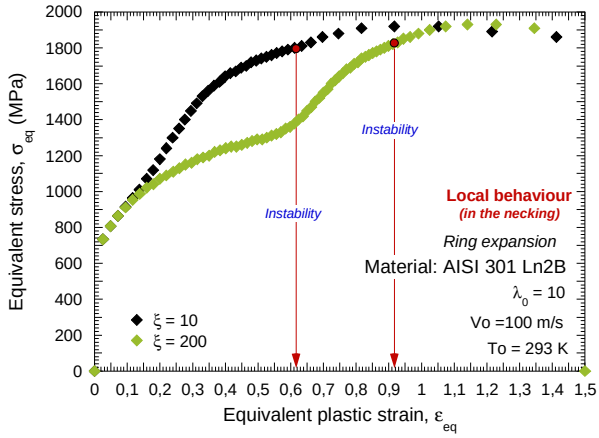

Fig. 3.81. Evolution of stress versus plastic strain in the necking for different values of ξ at V_0=100 m/s.

Thus, the strain of instability remains approximately constant for the whole range of impact velocities considered under both adiabatic and isothermal conditions of deformation *(in the case of isothermal conditions of deformation the strain of instability is slightly moved up in comparison with adiabatic conditions of deformation)*, Fig. 3.82.

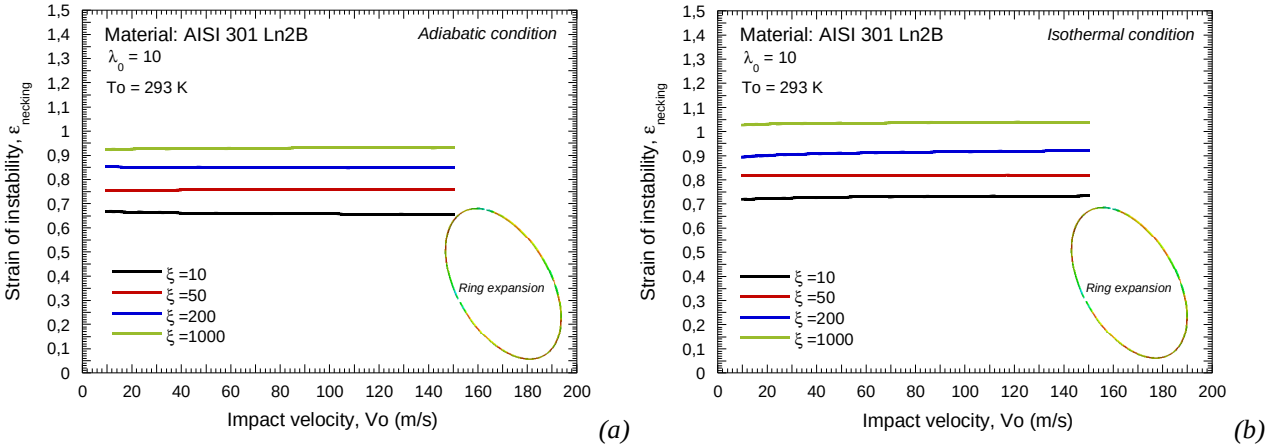

Fig. 3.82. Strain of instability as a function of impact velocity under (a) adiabatic and (b) isothermal conditions of deformation.

Next, it is shown the evolution of strain rate and stress in the necking for different impact velocities and all the values of ξ considered, Fig. 3.83. The deformation rate in the necking follows the theoretical one until, as previously commented, the maximum hardening rate is overcome. It seems to be confirmed that in an idealized material configuration free of disturbances there is certain value of hardening rate for which localization may not take place, Fig. 3.83.

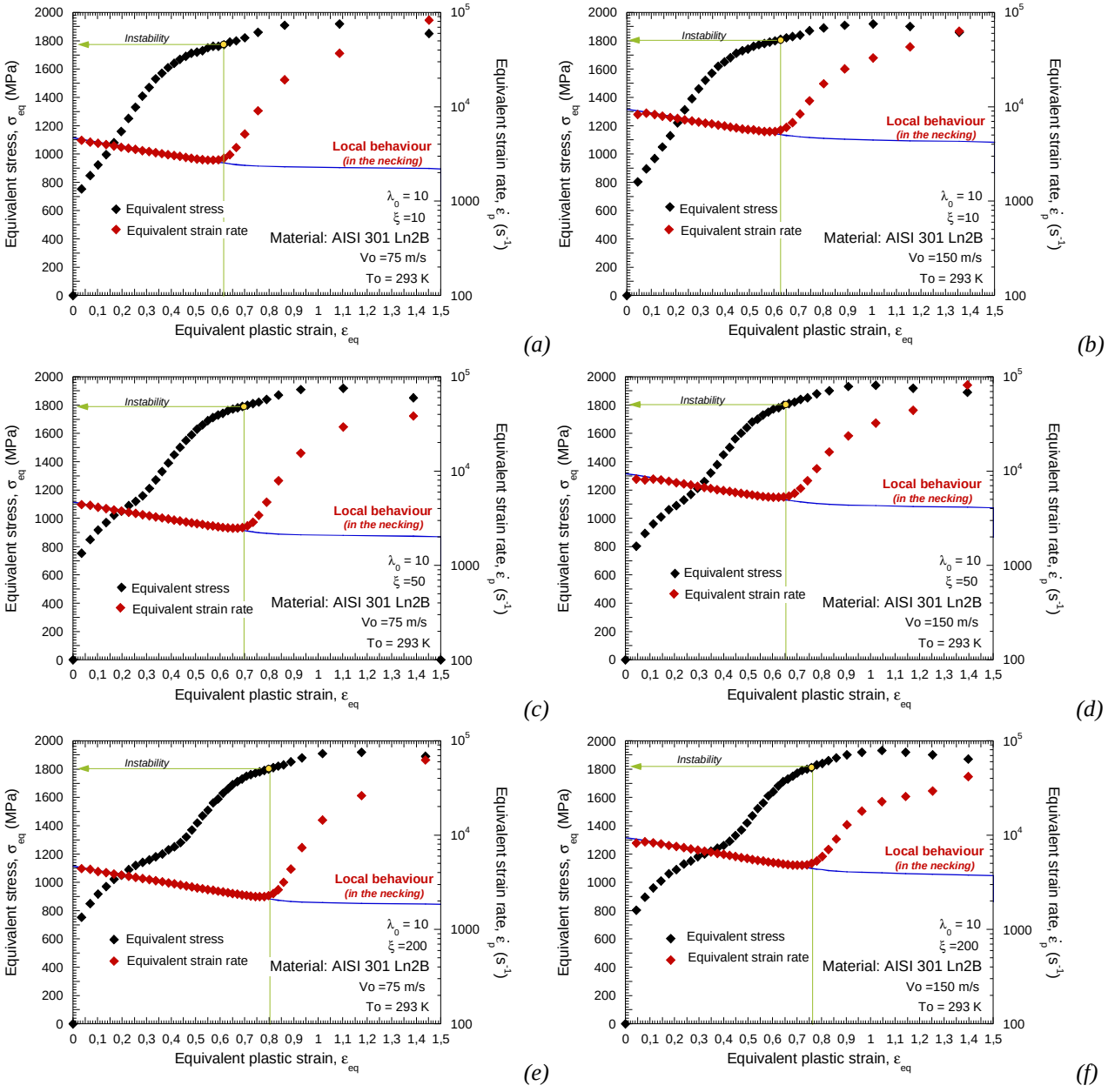

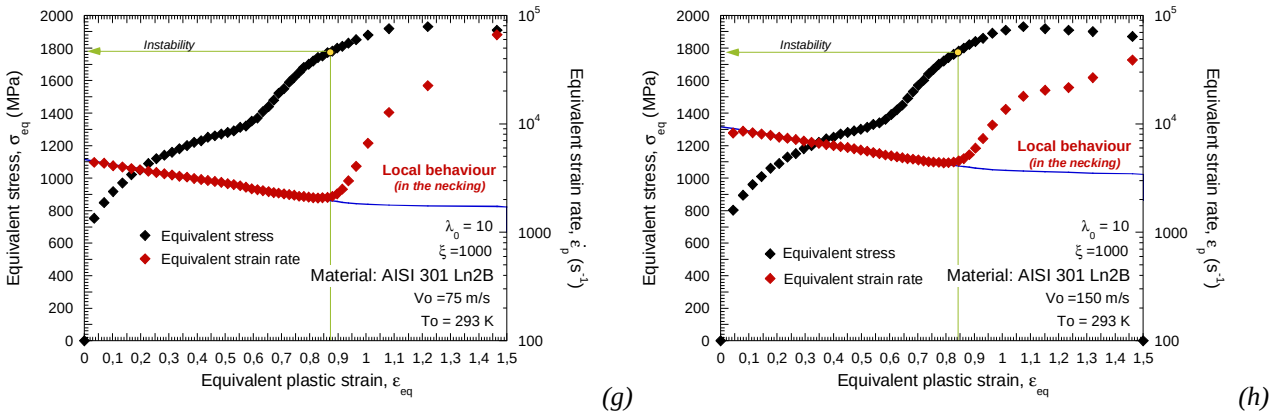

Fig. 3.83. Evolution of the strain rate and flow stress in the necking as a function of plastic strain for all the values of ξ considered and different impact velocities.

Finally, in Fig. 3.84. is shown the number of fragments as a function of the impact velocity for the material configurations analyzed in this section of the document *(a constant failure strain is imposed* $\bar{\varepsilon}_f^p = 1.5$*)*. It seems that the increase of ξ leads to larger number of fragments. Such is consistent with the observations reported along this document since augmenting the value of ξ the material ductility is increased too. However, the low rate sensitivity of the material configuration used provokes that the number of pieces into which the ring is fragmented is quite reduced *(at least in comparison with the number of fragments reported in previous sections of this document when the viscous drag stress term was analyzed)* , Fig. 3.84. Therefore, it becomes difficult to evaluate with precision the influence of ξ on the number of fragments.

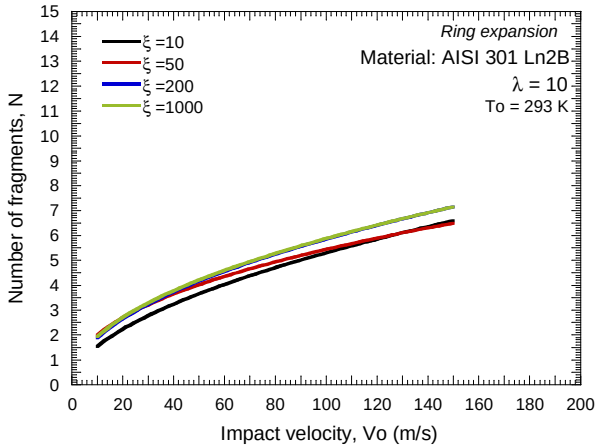

Fig. 3.84. Number of fragments as a function of the impact velocity for different values of ξ.

Next the conventional dynamic tension test is analyzed.

3.4.5.1.2 The conventional dynamic tension test

In Fig. 3.85. is depicted the evolution of the local plastic strain as a function of the global deformation of the sample. In the case of ξ=10 the local strain and the global strain match until instability takes place, Fig. 3.85-a. Up to here there are not differences in comparison with any other material configuration analyzed in this document.

However as the value of ξ increases the difference takes place. In the case of ξ=1000 is clearly visible that for a certain value of global deformation the local strain bifurcates, but, instead of

following an uncontrolled increasing it gets a second stage of stable behaviour, Fig. 3.85-a. Then, the local plastic deformation follows the global strain but moved up, Fig. 3.85. Depending on the impact velocity such behaviour is also repeated for ξ=50 and ξ=200, Fig. 3.85.

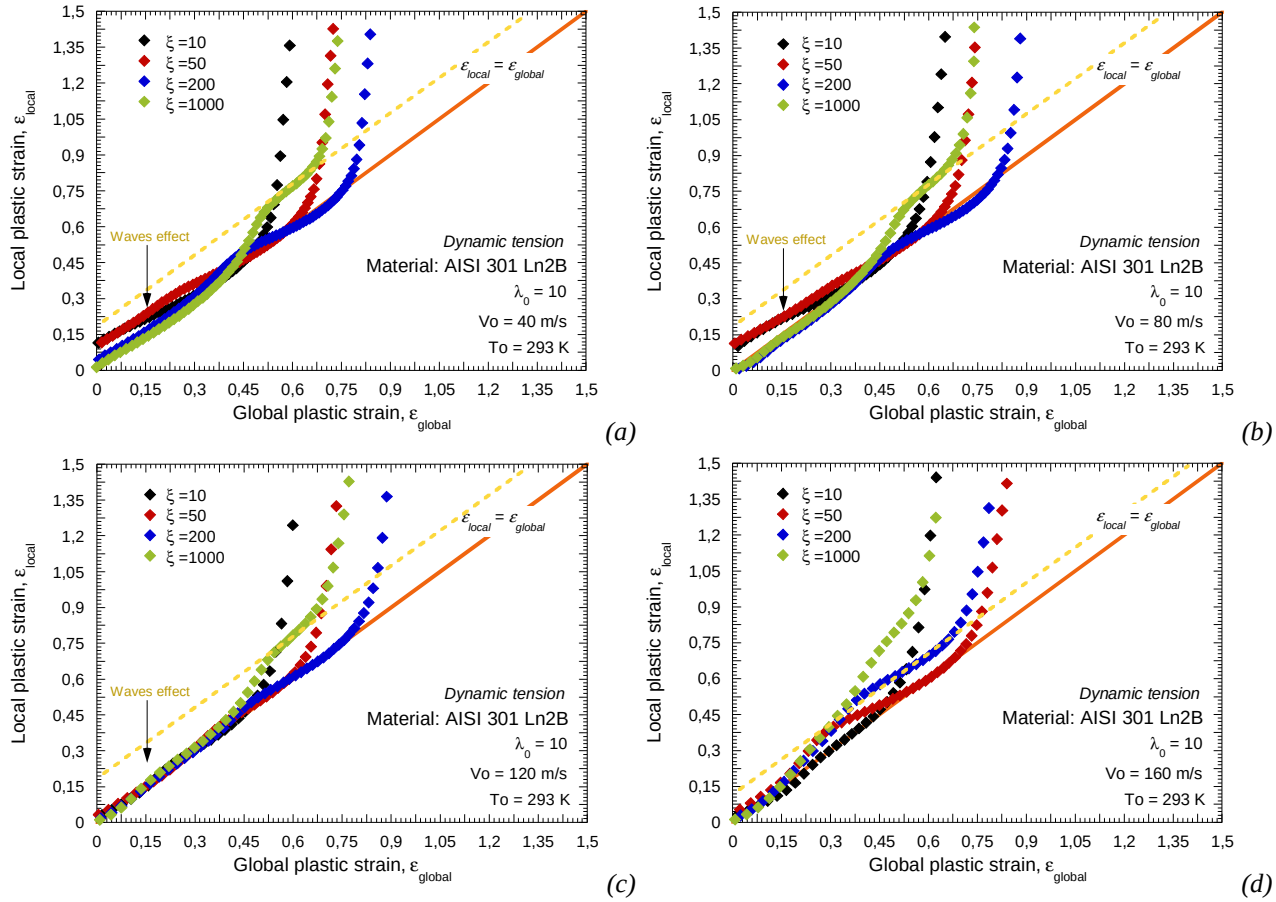

Fig. 3.85. Evolution of the local plastic strain versus the global plastic strain for all the values of ξ analyzed. (a) V_0=40 m/s, (b) V_0=80 m/s, (c) V_0=120 m/s, (d) V_0=140 m/s.

The explanation for such behaviour can be deduced from the following graphs, Fig. 3.86. If ξ=10 is applied the strain rate in the necking is continuously decreasing and going under the theoretical value until the strain of instability is reached, Fig. 3.86. If ξ=1000 is applied the strain rate in the necking starts to increase since the beginning of loading and instability is reached before the strain hardening function becomes operative. Due to instability progression the local strain quickly augments and the strain hardening function becomes operative, then the strain hardening of the material drastically increases, Fig. 3.86. It leads to the reduction of the local strain rate and the instability progression is stopped until the maximum hardening rate of the material is overcome, Fig. 3.86. Then, the instability starts to progress again, Fig. 3.86.

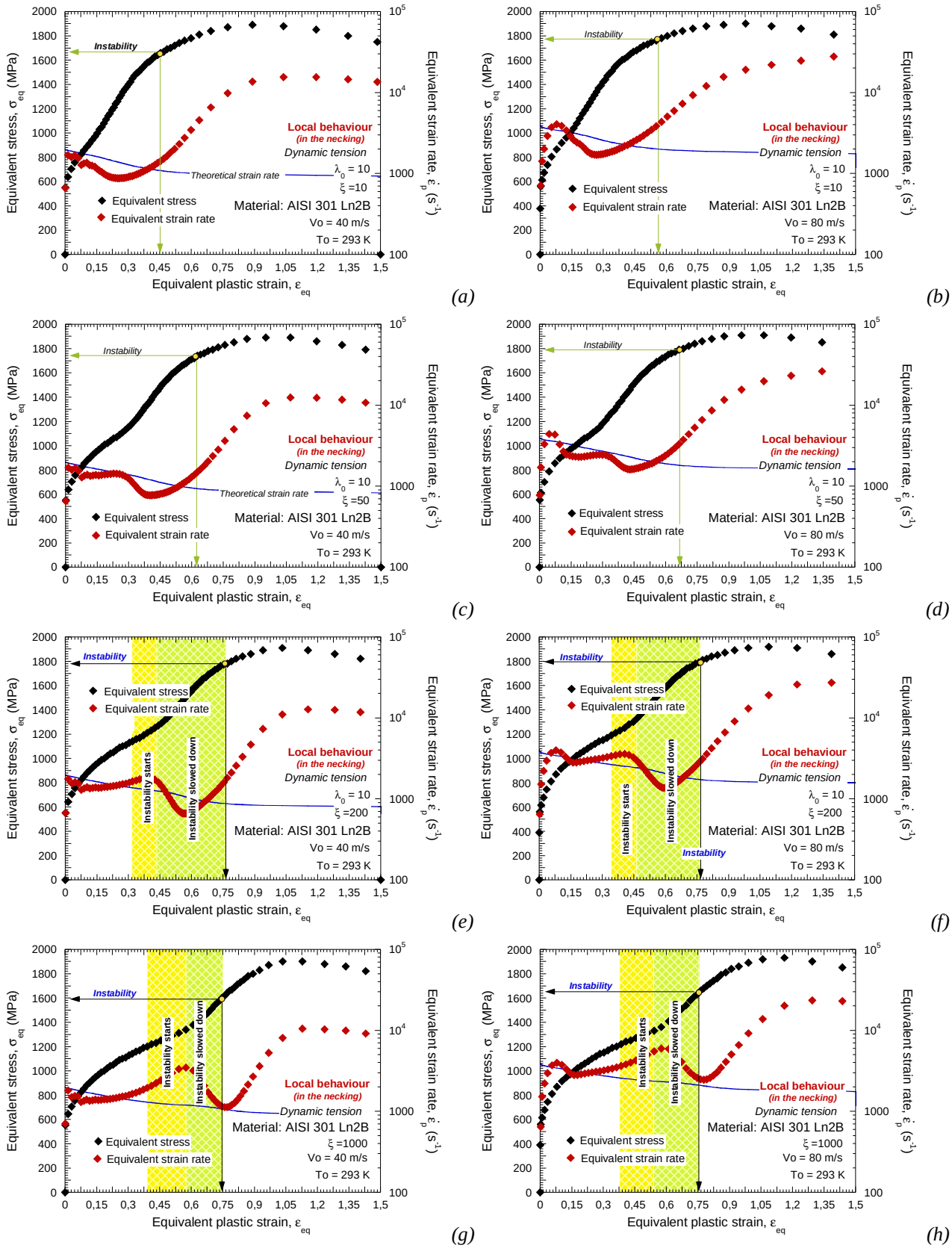

Fig. 3.86. Evolution of the strain rate and the flow stress in the necking as a function of plastic strain for all the values of ξ considered and different impact velocities.

This phenomenon is another proof for concluding that for certain value of strain hardening rate the instability may not take place.

On contrary to the ring expansion case, the increasing order of ξ does not match with the increasing strain of instability, Fig. 3.87. Due to the wave disturbances determined values of ξ are more effective at low impact velocities and some other at high impact velocities, Fig. 3.87. At low impact velocity, the material takes advantage of using large values of ξ. Instability does not propagate before the maximum hardening rate of the material is overcome, Fig. 3.87. However at high impact velocities, is possible that the **CIV** was reached before the strain hardening became operative. In such a case, the material ductility becomes drastically reduced, Fig. 3.87.

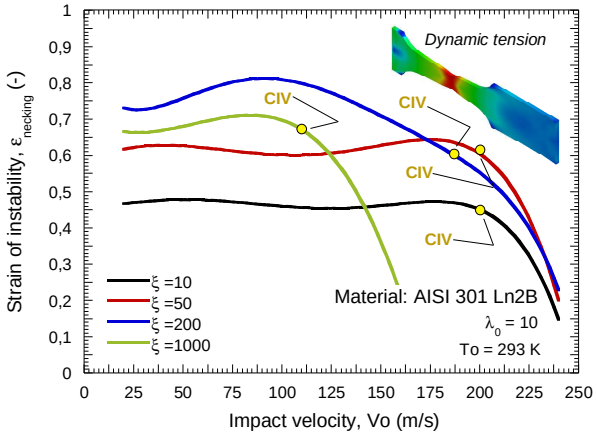

Fig. 3.87. Strain of instability as a function of impact velocity.

Previous considerations can be observed in Fig. 3.88. where input and output forces for the material configurations analyzed are shown for $V_0 = 180\ m/s$. In the case of ξ=1000 the sample behaviour is unstable. The **CIV** has been overcome. However in the case of ξ=200 output and input forces meet, the **CIV** is still not reached.

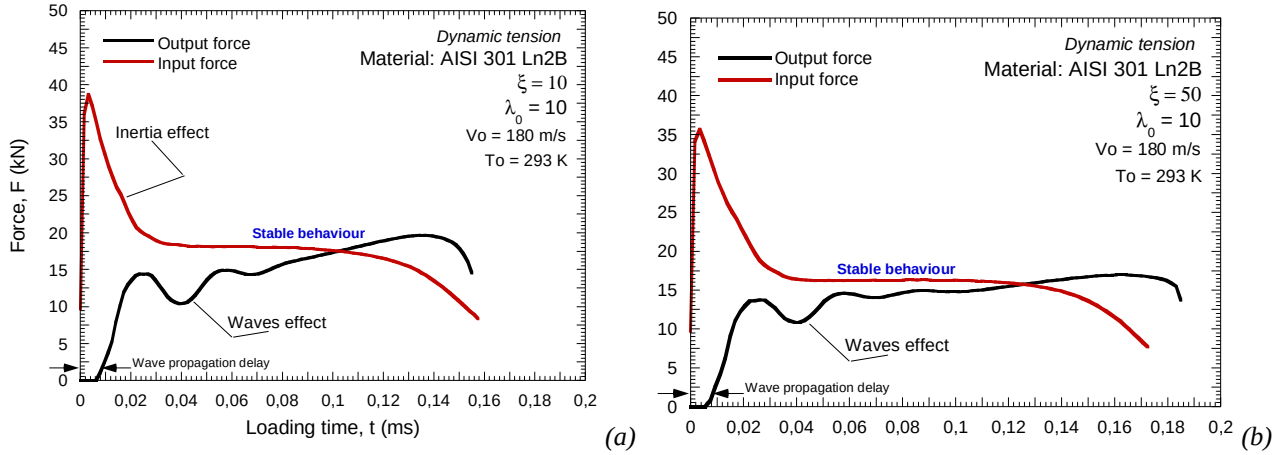

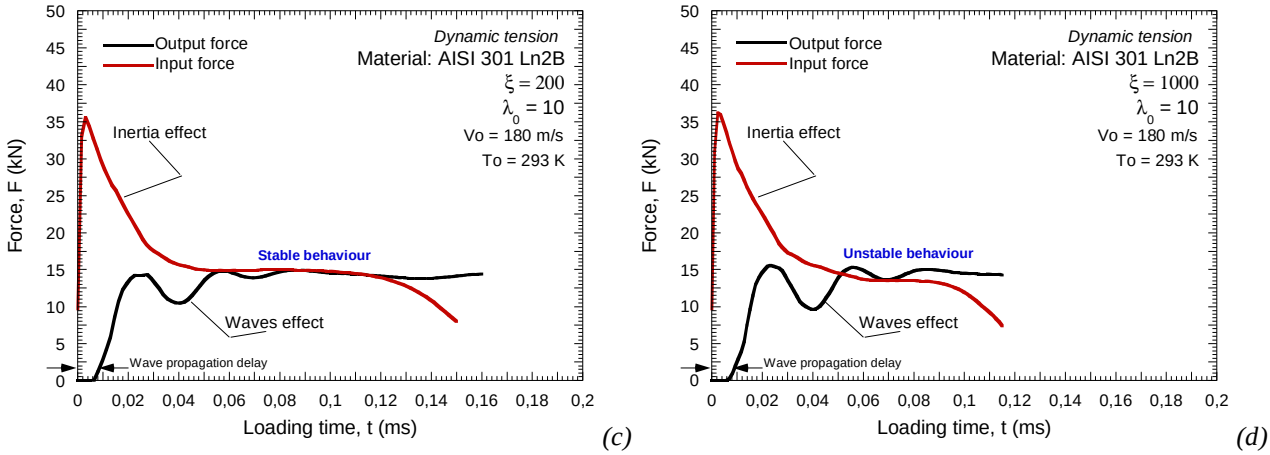

Fig. 3.88. Output and input forces for the material configurations considered, V_0=180 m/s.

From previous analysis is demonstrated that the potential benefits of increasing strain hardening are subordinated to the boundary value problem approached. Wave interactions are able to annihilate the beneficial effect of the strain hardening on the material ductility. The suitability of a material for absorbing energy under dynamic loading is dependent on the boundary value problem approached.

Next is discussed the effect of the parameter λ_0 on the flow localization.

3.4.5.2 Influence of parameter λ_0

In Fig. 3.89-a. is depicted the strain hardening function versus plastic strain for different values of λ_0. The increase of λ_0 augments the hardening rate of the material. In addition it moves forward both the plastic strain where the strain hardening function becomes operative and the plastic strain where the strain hardening function reaches saturation, Fig. 3.89-b.

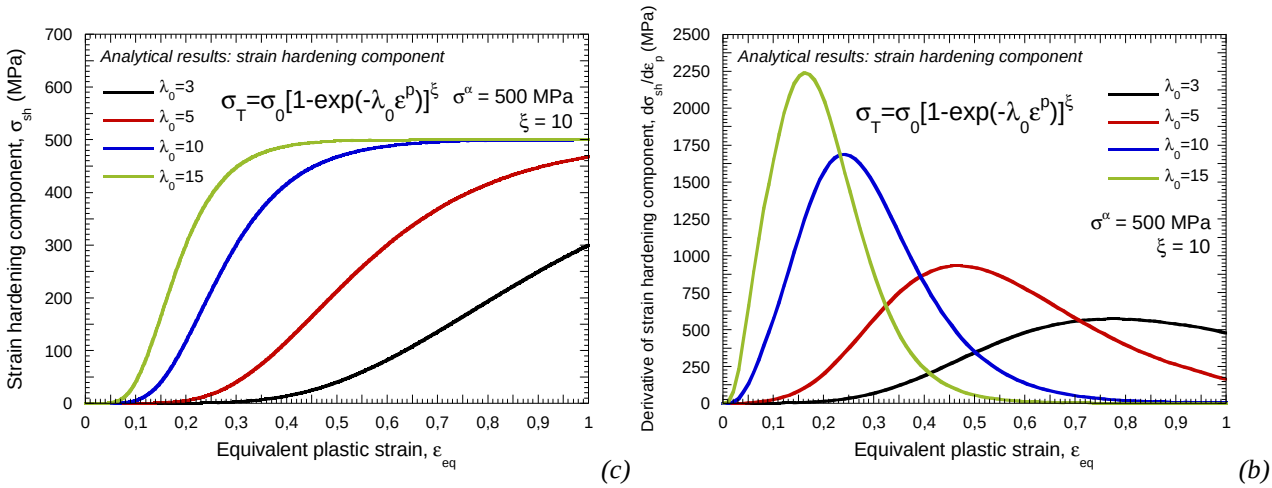

Fig. 3.89. (a) Flow stress predicted by the strain hardening function versus plastic strain for different values of λ_0. (b) Derivative of the strain hardening function versus plastic strain for different values of λ_0.

In the following section of the document is examined the influence of parameter λ_0 on the formation of plastic instabilities using ring expansion configuration.

3.4.5.2.1 The ring expansion test

In Fig. 3.90. is depicted the evolution of the local plastic strain versus the global deformation of the sample for different values of λ_0 within a wide range of impact velocities. Low values of λ_0 delay flow localization increasing the ductility of the material. In the cases of λ_0=5, λ_0=10 and λ_0=15 the strain localization is induced for, approximately, the same stress level, close to the saturation of the hardening function, Fig. 3.90. This agrees with previous considerations reported along this document.

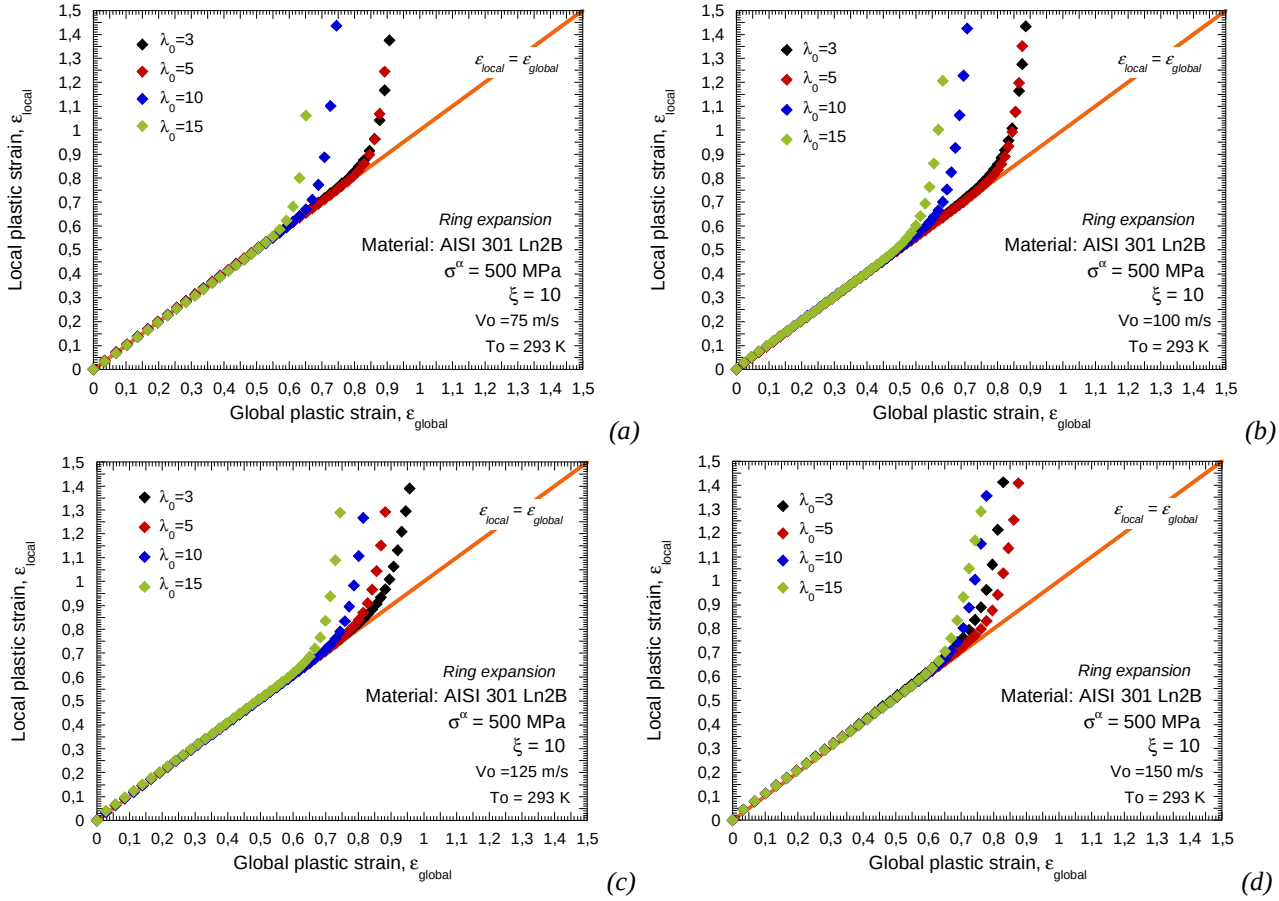

Fig. 3.90. Evolution of the local plastic strain as a function of the global plastic strain for the configurations analyzed (a) V_0=75 m/s, (b) V_0=100 m/s, (c) V_0=125 m/s, (d) V_0=150 m/s.

However in the case of λ_0=3 the instability takes place just after the maximum hardening rate is overcome, far from the saturation stress level, Fig. 3.91. This consideration is very interesting since it reveals the role that the hardening rate plays by itself, Fig. 3.91.

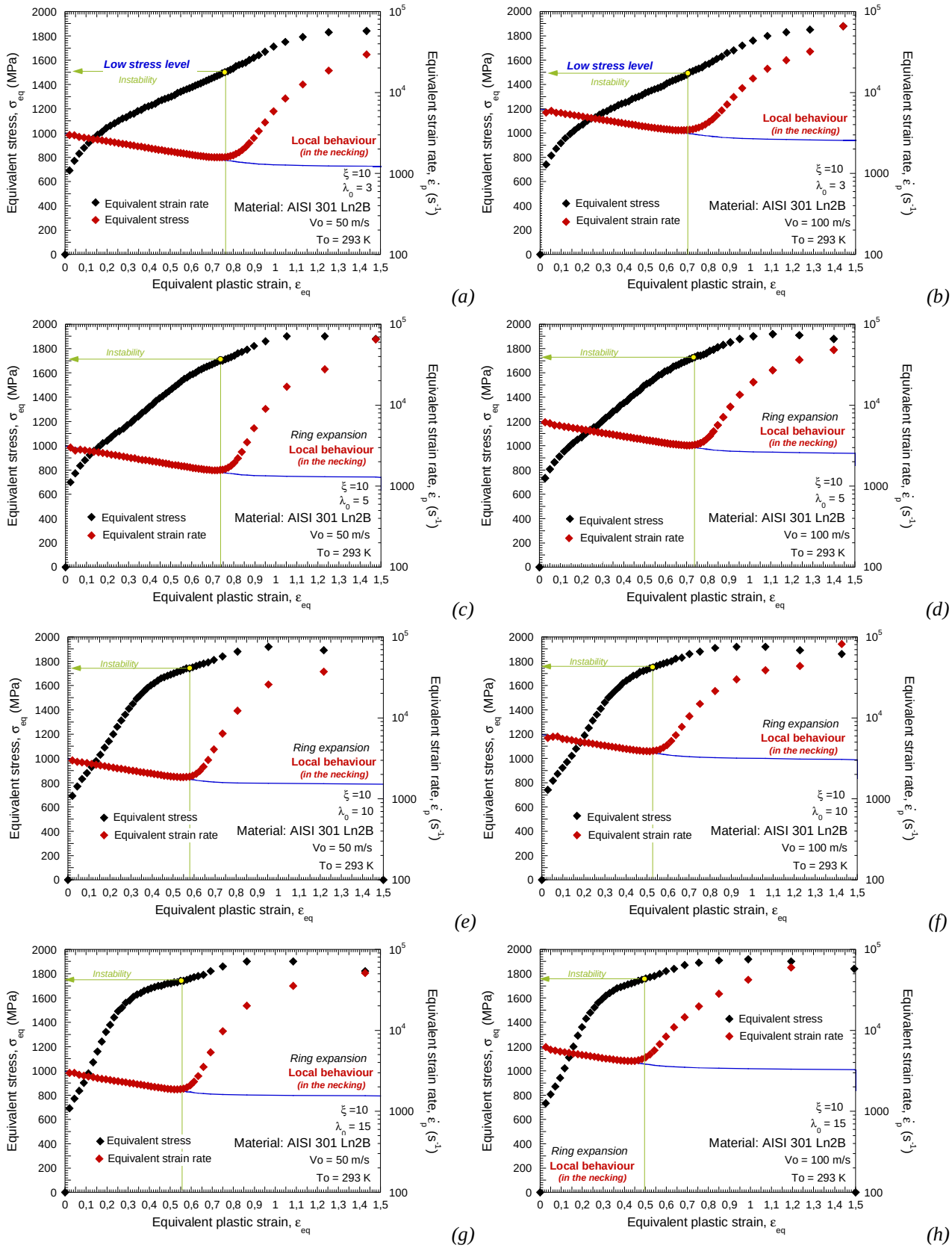

Fig. 3.91. Evolution of the strain rate and the flow stress in the necking as a function of plastic strain for all the values of λ_0 considered and different impact velocities.

Thus, the strain of instability in the cases of λ_0=3 and λ_0=5 is quite similar for the whole range of impact velocities. The strain hardening finds an optimum configuration depending on the value of λ_0

which enhances ductility of the material improving its capability for absorbing energy under dynamic solicitations, Fig. 3.92.

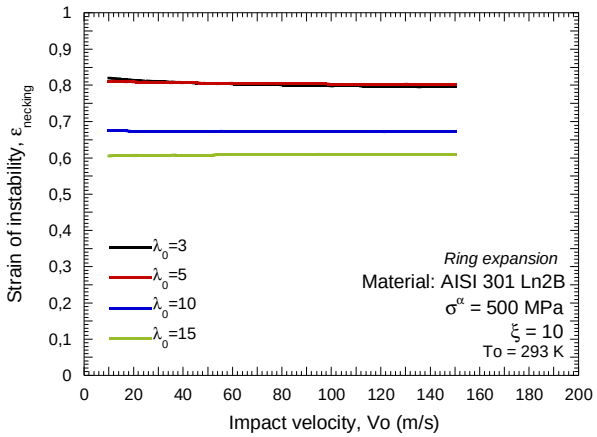

Fig. 3.92. Strain of instability as a function of impact velocity

Finally the number of fragments as a function of the impact velocity is shown in Fig. 3.93. It seems that the material configurations which showed the largest values of ductility are those exhibiting the greatest number of fragments, Fig. 3.93. Such behaviour agrees with the considerations reported along this document. However, the low rate sensitivity of the material configuration used provokes that the number of pieces into which the ring is fragmented is quite reduced *(at least in comparison with the number of fragments reported in previous sections of this document when the viscous drag stress term was analyzed)*, Fig. 3.93. Therefore, it becomes difficult to evaluate with precision the influence of λ_0 on the number of fragments

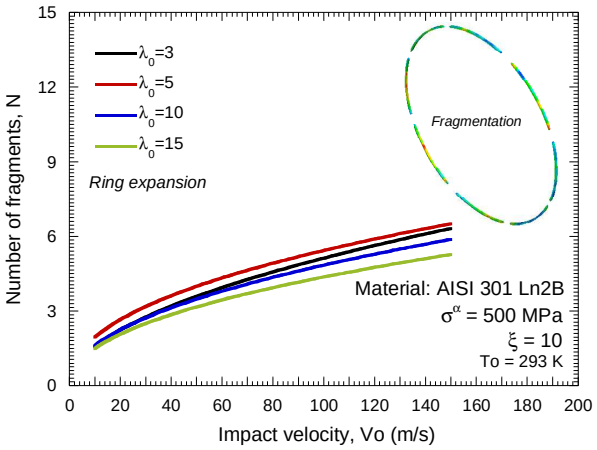

Fig. 3.93. Number of fragments as a function of the impact velocity for all the material configurations analyzed.

Next the conventional dynamic tension test is analyzed.

3.4.5.2.2 The conventional dynamic tension test

The first step is to compare the local plastic strain in the necking versus the global plastic strain for the material configurations considered and different initial impact velocities, Fig. 3.94. It can be observed that the decreasing order of λ_0 does not lead to increasing strain of instability as it was reported in the ring expansion case, Fig. 3.94. The value λ_0=3 leads to early strain localization, Fig. 3.94. As it was mentioned before, λ_0 finds an optimal value for enhancing the ductility of the material.

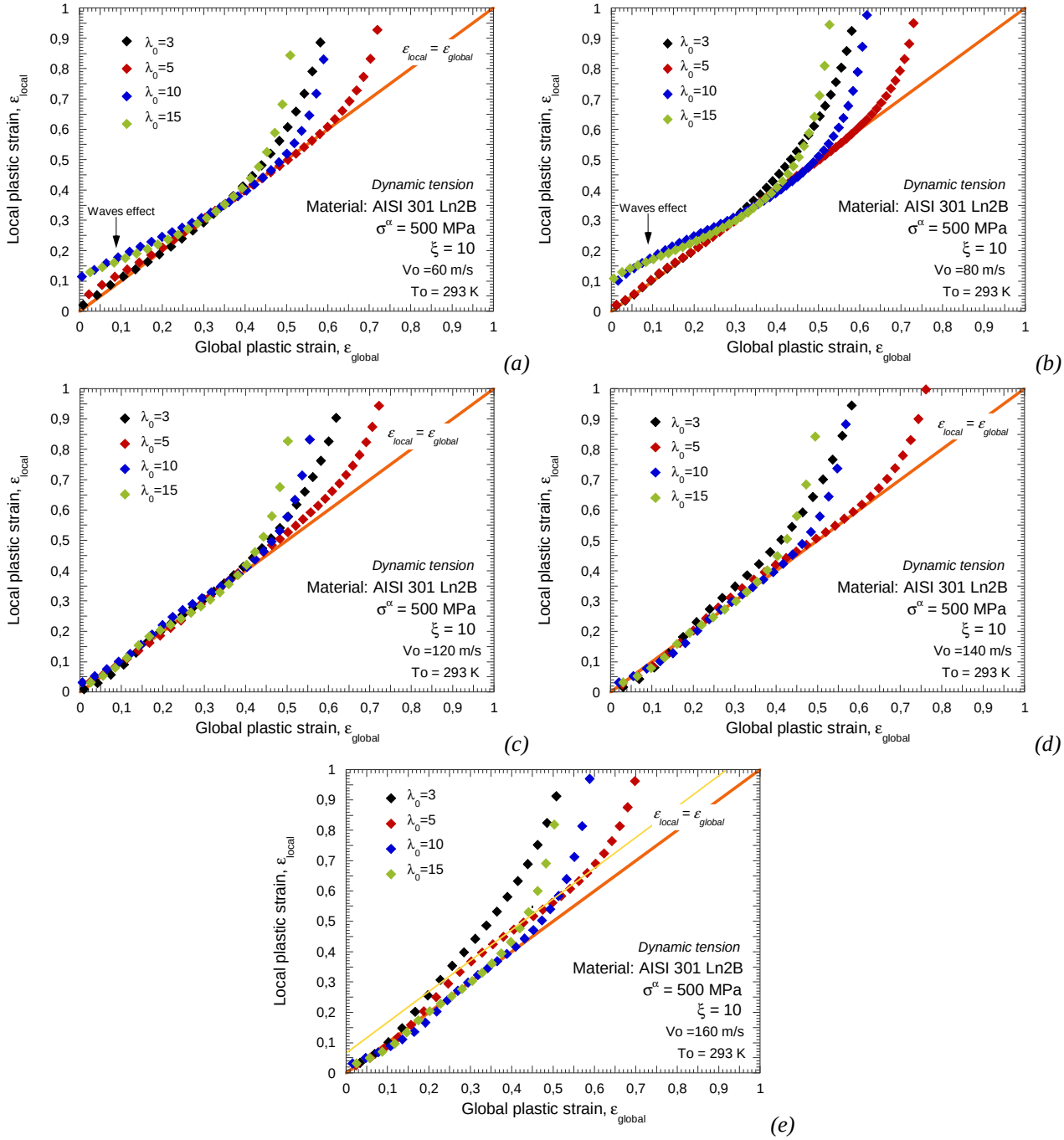

Fig. 3.94. Evolution of the local plastic strain as a function of the global plastic strain for the material configurations analyzed. (a) V_0=60 m/s, (b) V_0=80 m/s, (c) V_0=120 m/s, (d) V_0=140 m/s, (e) V_0=160 m/s.

It can be observed in Fig. 3.95. that if λ_0=3 the strain of instability is far from the saturation stress of the material. The flow stress level corresponding to instability in this material configuration is much lower than the one reported for the other material configurations. If $\lambda_0 \neq 3$ instability takes place close to stress saturation; once the maximum hardening rate has been overcome, Fig. 3.95.

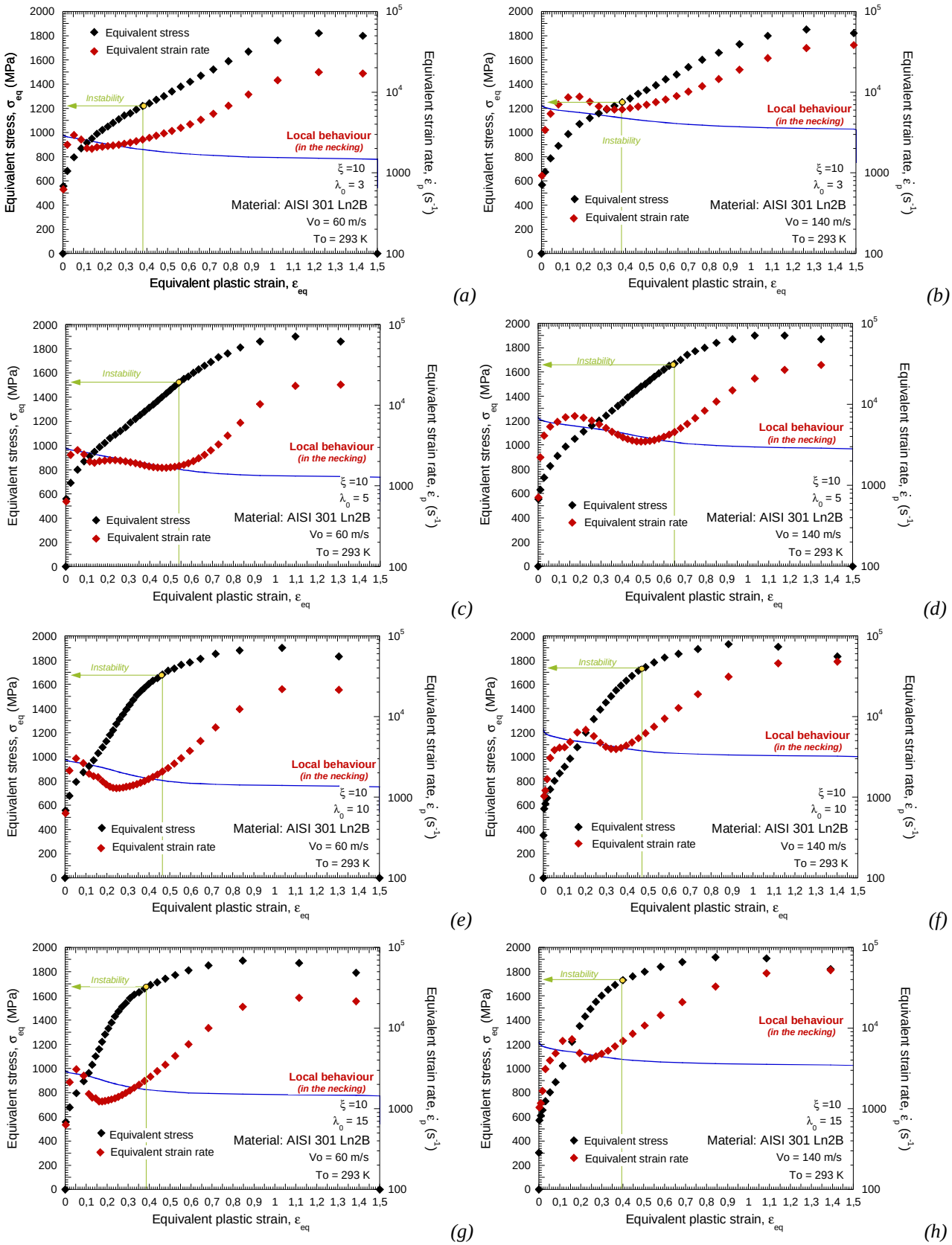

Fig. 3.95. Evolution of the strain rate and the flow stress in the necking as a function of plastic strain for all the values of λ_0 considered and different impact velocities.

In addition, the **CIV** is strongly influenced by the value of λ_0. In the case of λ_0=3 the **CIV** is early reached, $\mathrm{CIV}\big|_{\lambda_0=3} = V_0 \approx 120 \mathrm{m/s}$, Fig. 3.96. However for the rest of the material configurations checked the **CIV** takes much larger values, Fig. 3.96.

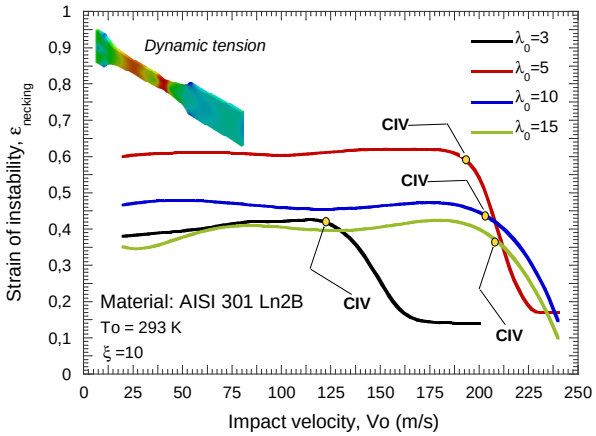

Fig. 3.96. Strain of instability as a function of impact velocity

Previous considerations can be observed by the comparison of the input and output forces reported in Fig. 3.97. At $V_0 = 80 \mathrm{m/s}$ Fig. 3.97-a-c., output and input forces meet in time for both values of λ_0 considered. However at higher impact velocity $V_0 = 160 \mathrm{m/s}$ the specimen behaviour in the case of λ_0=3 becomes unstable whereas in the case of λ_0=5 both forces still find agreement, Fig. 3.97.

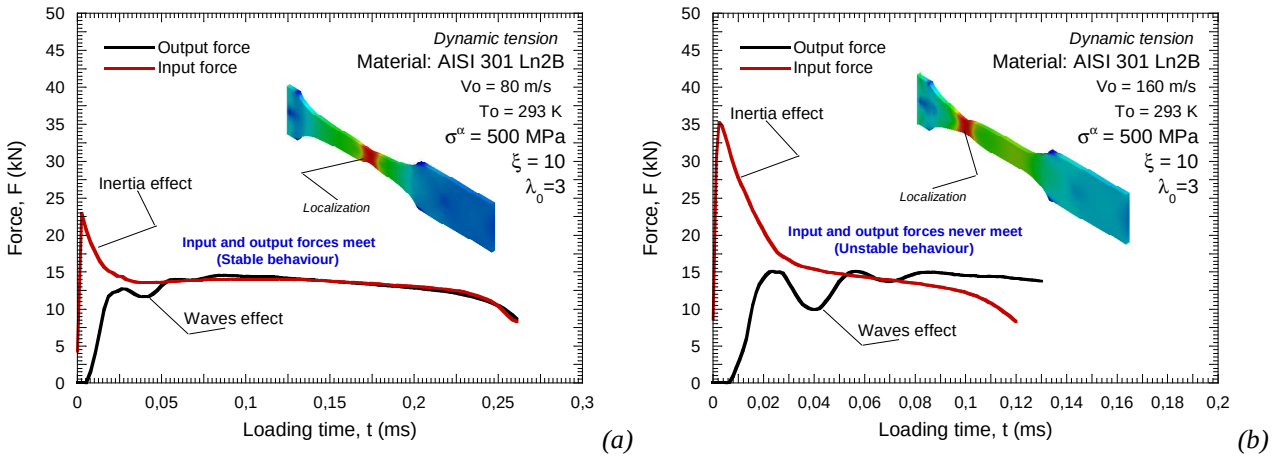

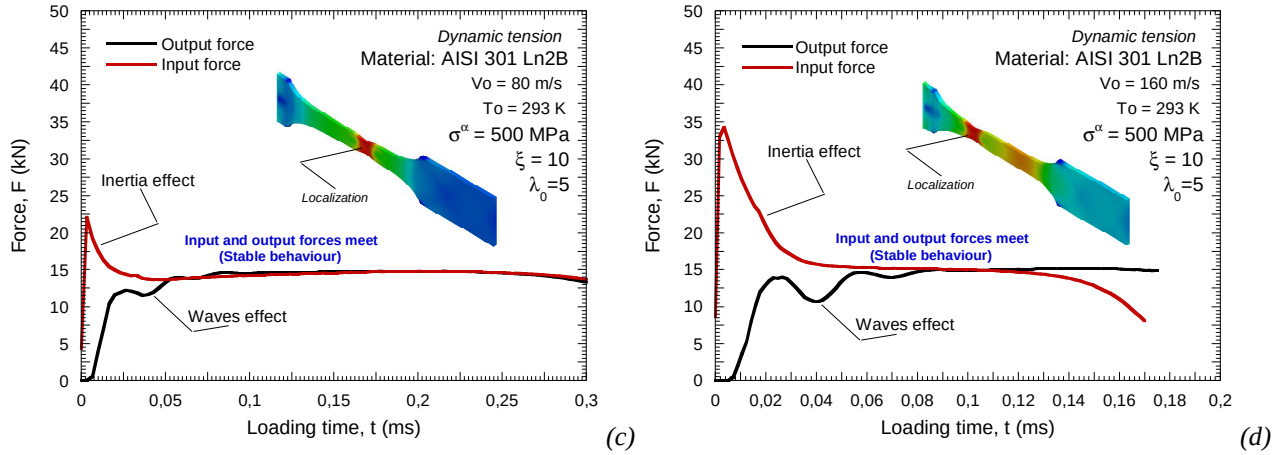

Fig. 3.97. Output and input forces for λ_0=3, λ_0=5 and different initial impact velocities.

Moreover, previous observations have their influence on the sample response during loading. At failure *(a constant failure strain is imposed* $\bar{\varepsilon}_f^p = 1.5$*)*, maximum specimen elongation is reached in the case λ_0=5. Intermediate values of λ_0 become more effective in order to increase the material ductility, Fig. 3.98.

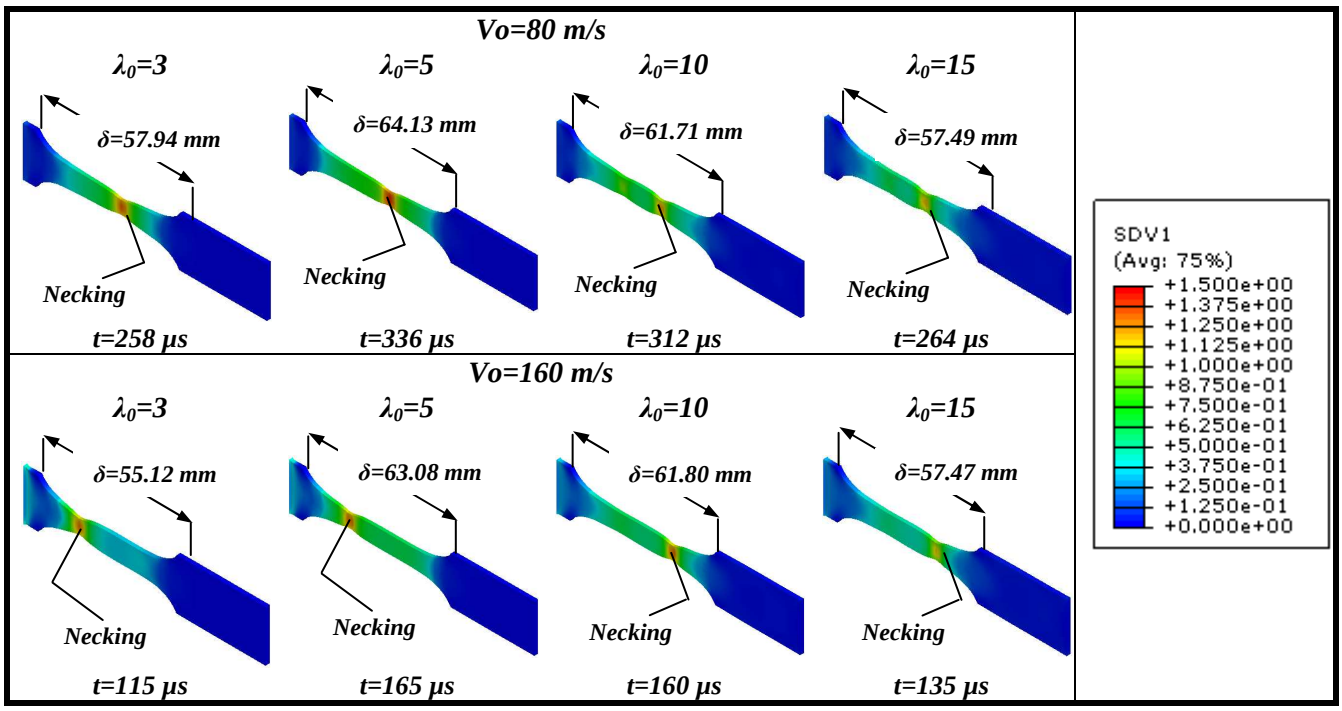

Fig. 3.98. Plastic strain contours at failure for different values of α and two impact velocities, V_0=60 m/s and V_0=120 m/s.

Based on the thermo-viscoplastic behaviour of metals described in the previous chapter, it has been developed a numerical methodology to analyze the material mechanisms responsible for absorbing energy under dynamic loading. It has been demonstrated that an accurate description of the strain hardening and strain rate sensitivity of metallic alloys is indispensable in order to evaluate their suitability for bearing hard mechanical solicitations. Application of such knowledge to study the behaviour of metallic sheet subjected to impact by non-deformable projectiles is conducted in the next chapters of the Thesis.

CHAPTER 4

IMPACT BEHAVIOUR OF METALLIC ALLOYS FOR PROTECTION APPLICATIONS

Abstract

In this chapter of the Thesis the thermo-mechanical behaviour of two metallic alloys is examined, the mild steel **ES** and the **AA 2024-T3**. The thermo-viscoplastic characterization of the materials is conducted and discussed. They have interest for many application fields like automotive or aeronautical industries. Different experimental setups for perforation of metallic sheets have been used in order to provide a proper description of the thermo-mechanical processes taking place under impact loading. Infrared thermography technique is used to determine the role that plastic instabilities formation have on their performance under perforation. It is developed a methodology which combines advanced measuring techniques with numerical simulations supported by the accurate description of the material behaviour. The role that adiabatic heating, strain hardening, strain rate sensitivity and temperature sensitivity play in the absorption of energy during perforation is extensively discussed.

4 CHAPTER 4. IMPACT BEHAVIOUR OF METALLIC ALLOYS FOR PROTECTION APPLICATIONS

4.1 Introduction

Among impact and impact related problems, perforation and penetration of thin metallic plates by non-deformable projectiles has long been of interest, and several studies on the subject are available in literature [Honda et al. 1930, Masket 1949, Nishiwaki 1951, Zaid and Paul 1958, Backman and Goldsmith 1978, Zukas et al. 1990, Zukas et al. 1992, Corbett et al. 1996, Borvik et al. 1999, Piekutowski 1999, Piekutowski 2001, Borvik et al. 2002a, Borvik et al. 2002b, Borvik et al. 2004, Gupta et al. 2006, Gupta et al. 2007, Gupta et al. 2008, Arias et al. 2008, Rusinek et al. 2008b, Rusinek et al. 2009a]. So far, most progress has been made during experimental investigations of the normal perforation of metal plates, and a large number of studies can be found in the literature most of them tied to the failure mode mechanisms. During such kind of impact loading, petalling as a failure mode commonly appears when ogival, conical or hemispherical projectiles are applied [Edwards and Mathewson 1997, Atkins et al 1998, Borvik et al. 2002a, Shen et al. 2002, Gupta et al. 2008, Rusinek et al. 2009a]. The failure mode seems to be strongly dependent on the impact velocity. Petalling can be replaced by failure mode of crack opening when impact velocity is close to the ballistic limit. In this situation a decrease of the circumferential strain during loading slows the crack progression [Shen et al. 2002]. Moreover, when the impact velocity is very high, the perforation process is governed by inertia effects and the failure mode changes from petalling to complete fragmentation of the zone affected by impact, inducing appearance of debris cloud as final stage of the process [Piekutowski 1993, Piekutowski 2001].

Substantial efforts have been invested in order to physically understand and mathematically describe the phenomena taking place during ordnance penetration. A number of analytical models have been proposed over the years [Forrestal et al. 1994, Ben-Dor 1998, Forrestal and Warren 2008, Ben-Dor 2009, Ben-Dor 2009], but the complexity of perforation events often limits the general use of closed-form analytical solutions. The information obtained from such analytical models becomes limited. Thus, advances are still required on the understanding of the deformation behaviour of the material during perforation.

For such goal, in this document is developed a methodology which combines advanced measuring techniques with numerical simulations supported by the accurate description of the material behaviour. This section is devoted to the analysis of the complex phenomena which take place during perforation processes. The goal of this investigation is not restricted to a description of the failure mode of impacted plates. The deformation mechanisms of materials which reside behind the absorption of energy under perforation have to be identified. Such determination will allow us to optimize materials in charge of bearing dynamic solicitation during their service life.

Two metallic alloys are examined, the mild steel **ES** and the aluminium alloy **2024-T3**. They have interest for many application fields like automotive and aeronautical industries. The thermo-mechanical characterization of the materials is conducted and discussed. Their thermo-viscoplastic behaviour is described by the constitutive descriptions developed in chapter 1. Different experimental setups for perforation of metallic sheets have been used in order to provide a proper description of the thermo-mechanical processes taking place under impact loading. The role that adiabatic heating, strain hardening, strain rate sensitivity and temperature sensitivity play in the absorption of energy during perforation is extensively discussed.

4.2 Impact behaviour of steel ES

It has been conducted an experimental and numerical analysis on the impact behaviour of **ES** mild steel sheets subjected to perforation by non-deformable hemispherical projectiles. Experiments have been carried out using pneumatic cannon within the range of impact velocities 5 m/s $\leq V_0 \leq$ 60 m/s. The tests were recorded using infrared high speed camera. It allowed obtaining temperature contours during impact. Assuming adiabatic conditions of deformation, temperature increase ΔT may be related to plastic deformation. It makes possible to evaluate the critical failure strain $\overline{\varepsilon}_f^p$ that leads to the collapse of the target. For that task, the temperature measurements are coupled with numerical simulations and with analytical predictions of the material behaviour obtained by means of the **RK** constitutive description [Rusinek and Klepaczko 2001].

4.2.1 Thermo-viscoplastic behaviour of the mild steel ES

Mild steel **ES** has considerable relevance since it is widely used in several engineering fields as for example in automotive industry for building structural elements responsible for absorbing energy under crash or impact. The application field of this material makes relevant to understand its response under impact loading. The **ES** steel has been frequently studied and a significant number of works dealing with the thermo-viscoplastic behaviour of this metal can be found in the literature [Zhao and Gary 1996, Klepaczko et al. 1999, Mouro et al. 2000, Rusinek et al. 2005, Larour et al. 2005, Haugou 2006, Rusinek and Zaera 2007, Rusinek et al. 2007, Rusinek et al. 2009a]. Mild steel **ES** consists of a *ferrite–pearlitic* (**BBC**) structure, where layers of *pearlite* lie between whole grains of *ferrite*. Its average grain size is $\phi = 16\ \mu m$. The chemical composition of the mild steel **ES** *(% of weight)* is reported in Table 4.1.

Mn	**Al**	**Cr**	**C**	**Ni**	**S**	**Cu**	**Si**	**P**	**N**	**Ti**
0.203	0.054	0.041	0.03	0.018	0.011	0.009	0.009	0.008	0.0063	0.002

*Table 4.1. Chemical composition of the mild steel **ES** (% of weight) [Rusinek et al. 2007, Rusinek et al. 2009a].*

In agreement with experimental evidences reported in [Rusinek and Klepaczko 2001, Rusinek et al. 2007] the **ES** steel behaviour can be considered isotropic. The isotropic behaviour showed by this material make it attractive for analyzing dynamic processes. It is widely accepted that material modeling can be conducted using **J2** theory facilitating the implementation of its constitutive equations into **FE** code.

4.2.1.1 Literature review

The thermo-viscoplastic characterization of the mild steel **ES** has been subjected to investigation by different laboratories during the last decades [Zhao and Gary 1996, Klepaczko et al. 1999, Mouro et al. 2000, Rusinek et al. 2005, Larour et al. 2005, Haugou 2006, Rusinek and Zaera 2007, Rusinek et al. 2007, Rusinek et al. 2009a].

Special relevance has gathered the works due to Rusinek and co-workers [Rusinek 2000, Rusinek and Klepaczko 2001, Rusinek et al. 2005, Rusinek et al. 2007]. Based on those investigations a brief review of the thermo-viscoplastic behaviour of this material is presented in this section of the document.

In Fig. 4.1. is analyzed the flow stress evolution as a function of plastic strain for different strain rates at room temperature. It can be observed that this material shows important ductility but reduced flow stress and strain hardening, Fig. 4.1.

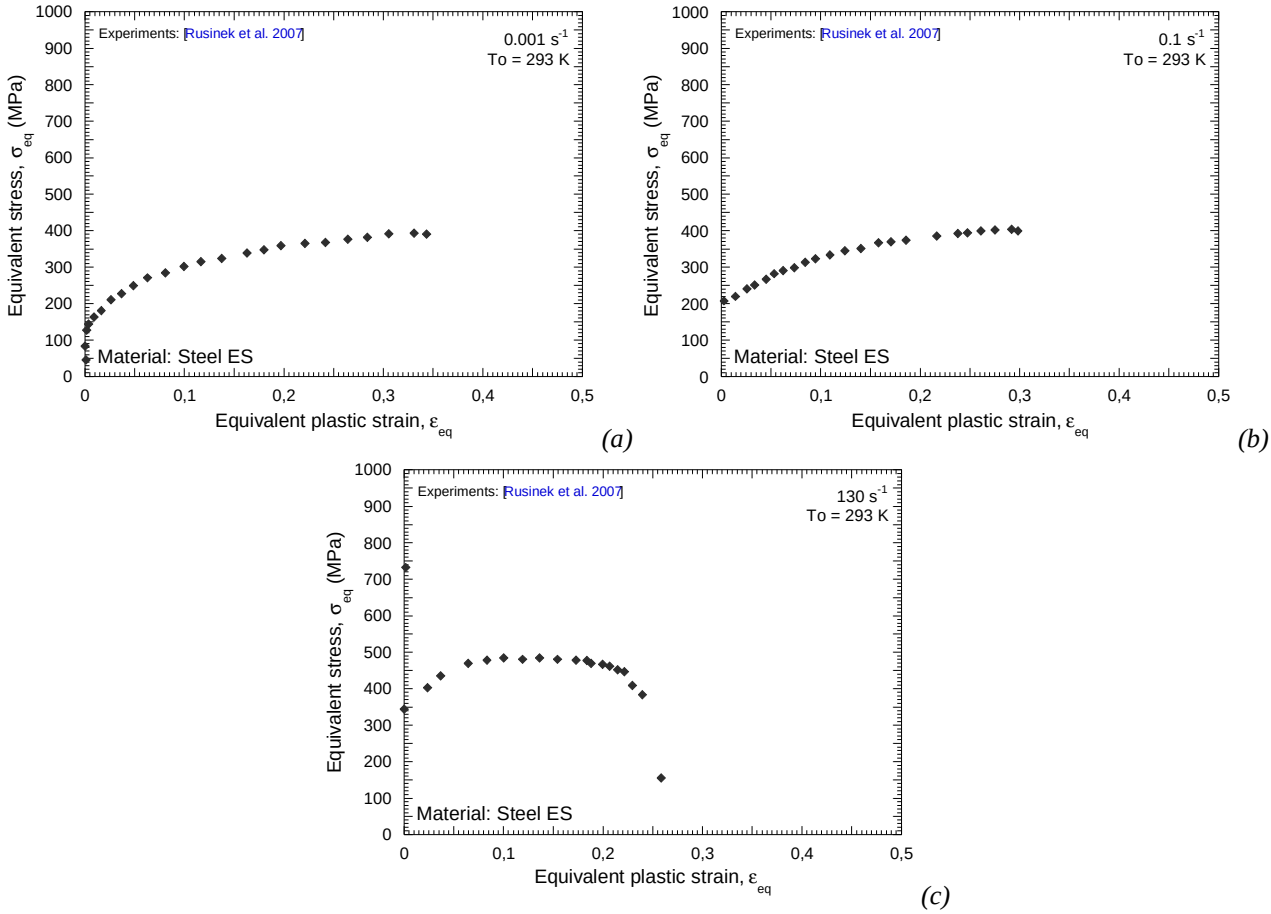

Fig. 4.1. Flow stress versus plastic strain for different strain rate values at room temperature [Rusinek et al. 2007].

Low strain hardening makes this material prone to instabilities formation, especially under dynamic solicitation [Rusinek et al. 2005, Rusinek and Zaera 2007] as can be observed in Fig. 4.2.

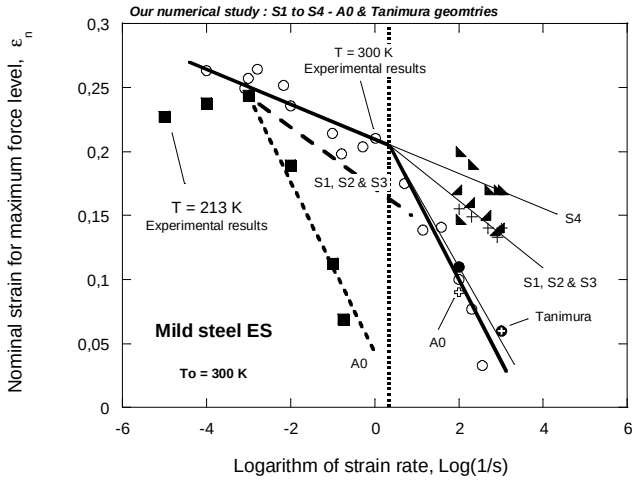

Fig. 4.2. Evolution of failure strain versus strain rate at different initial temperatures [Rusinek et al. 2005].

Moreover, mild steel **ES** possesses high strain rate and temperature sensitivities as reported in Figs. 4.3-4.4. Such observations agree with the theoretical considerations for **BCC** metals reported in chapter I of this Thesis.

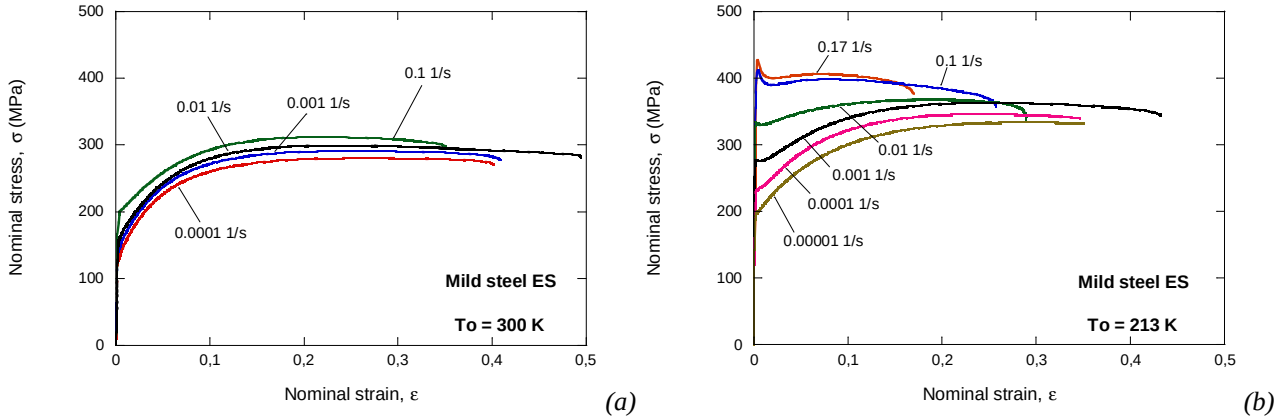

Fig. 4.3. Strain rate effects on the material flow stress. (a) T_0= 300 K, (b) T_0= 213 K [Rusinek et al. 2005].

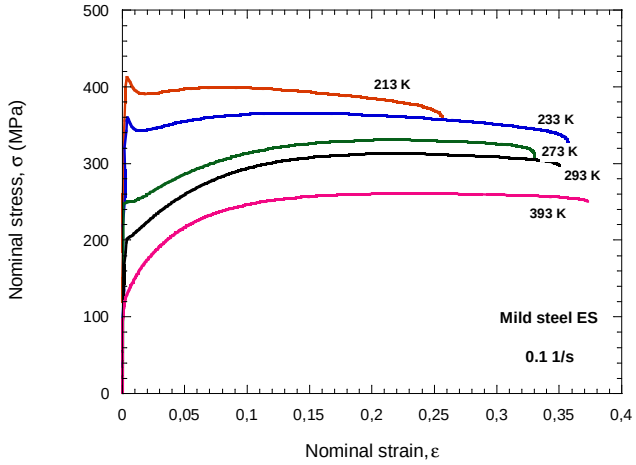

Fig. 4.4. Temperature effect on flow stress for mild steel ES at 0.1 s^{-1} [Rusinek et al. 2005].

Moreover, tensile tests at room temperature for different strain rates have been performed in order to complement the mechanical characterization of the material conducted by Rusinek and co-workers [Rusinek 2000, Rusinek and Klepaczko 2001, Rusinek et al. 2005, Rusinek et al. 2007].

4.2.1.2 Temperature measurements on ES steel samples subjected to tensile testing

The tensile tests have been recorded using infrared high speed camera, and the temperature increase in the material during loading has been obtained. It means the major contribution of this work to the characterization of this material. Due to the relation existing between material temperature increase and plastic deformation, infrared measurements provide valuable information of the deformation field of the material during loading. It allows estimating the susceptibility of the material for instabilities formation. Therefore, it will help to determine the suitability of the material for absorbing energy under impact loading.

The geometry and dimensions of the tensile specimens are reported in Fig. 4.5.

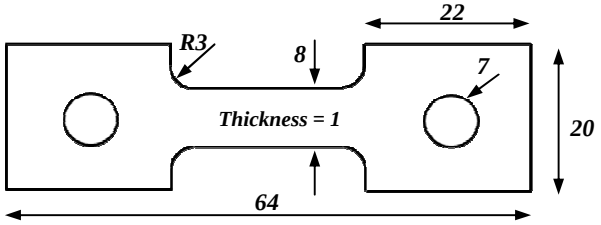

Fig. 4.5. Geometry and dimensions of the tensile specimens (mm).

The infrared camera used for measuring temperature contours features variable "snap shot" integration from 10 μs to 10 ms and frame rates up to 200 FPS *(Frames per Second)* in full frame mode and 6000 FPS in sub-windowing mode. Such features allow having high definition and elevated frame-rates [Rodríguez-Martínez et al. 2010a].

In order to get the maximum emissivity from the target, the steel sheets were covered with soot whose emissivity was estimated $\eta = 0.95$ *(before loading, the temperature registered by the camera on the soot-coated sample-surface must fit the room temperature)* [Guzman et al. 2008, Guzman et al. 2009, Rodríguez-Martínez et al. 2009].

The equation of energy balance provides the relationship between strain and temperature variation during loading. Assuming hypo-elastic plastic material behaviour is possible to set Eq. 4.1.

$$\lambda \cdot \nabla^2 T - \dot{T} = -\frac{\beta}{\rho \cdot C_p} \cdot \sigma_{ij} : \dot{\varepsilon}_{ij}^{p} + \frac{\alpha}{\rho \cdot C_p} \cdot \frac{E}{(1-2\cdot\nu)} \cdot T \cdot \mathrm{tr}\left(\dot{\varepsilon}_{ij}^{e}\right) \qquad (4.1)$$

Where λ is the coefficient of diffusivity, T is the absolute temperature, $\dot{T}$ is the temporal temperature variation, β is the Taylor-Quinney coefficient, ρ is the material-density, C_P is the specific heat at constant pressure, σ_{ij} is the stress tensor, $\dot{\varepsilon}_{ij}^{p}$ is the plastic strain rate tensor, α is the coefficient of thermal expansion, E is the Young's modulus, ν is the Poisson's coefficient and $\mathrm{tr}\left(\dot{\varepsilon}_{ij}^{e}\right)$ is the trace of the elastic strain rate tensor.

In the following graphs, Fig. 4.6, is reported the maximum variation of temperature during loading in the case of $\dot{\bar{\varepsilon}}^{p} = 0.01\ s^{-1}$. A small decrease of temperature is found at the beginning of loading. That corresponds to the elastic regime, Eq. 4.2., that under uniaxial tension leads to temperature decrease *(due to material volume variation).*

$$-\dot{T} = -\lambda \cdot \nabla^2 T + \frac{\alpha \cdot E}{\rho \cdot C_p \cdot (1-2\cdot\nu)} \cdot T \cdot \mathrm{tr}\left(\dot{\varepsilon}_{ij}^{e}\right) \qquad (4.2)$$

In the plastic range, the temperature is uniformly *(and approximately linearly)* increasing with stress and strain until necking takes place, Fig. 4.6. Then, a sudden increase of temperature leads to the failure of the sample. Maximum temperature recorded during the test is close to $\Delta T = 6\ K$, Fig. 4.6.

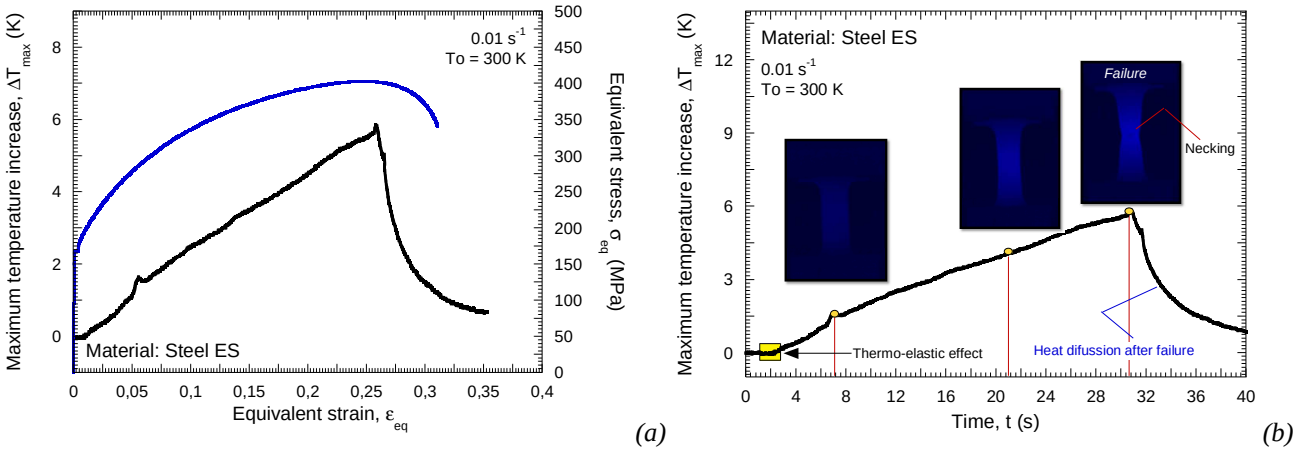

(a) *(b)*

Fig. 4.6. (a) Maximum temperature increase versus plastic strain and flow stress evolution versus plastic strain. (b) Maximum temperature increase versus time.

The temperature contours during loading are shown in Fig. 4.7. The increase of temperature is focused around the central part of the specimen where instability will take place. It seems that even for such global low loading rate the local effects play a role in the material behaviour. Beyond a certain loading level, the strain and strain rate fields seem not to be uniformly distributed along the active part of the specimen. It leads to the heterogeneous distribution of temperature reported in Fig. 4.7. After sample failure temperature recorded starts to decrease due to heat transfer and the material reaches thermal equilibrium with surrounding environment.

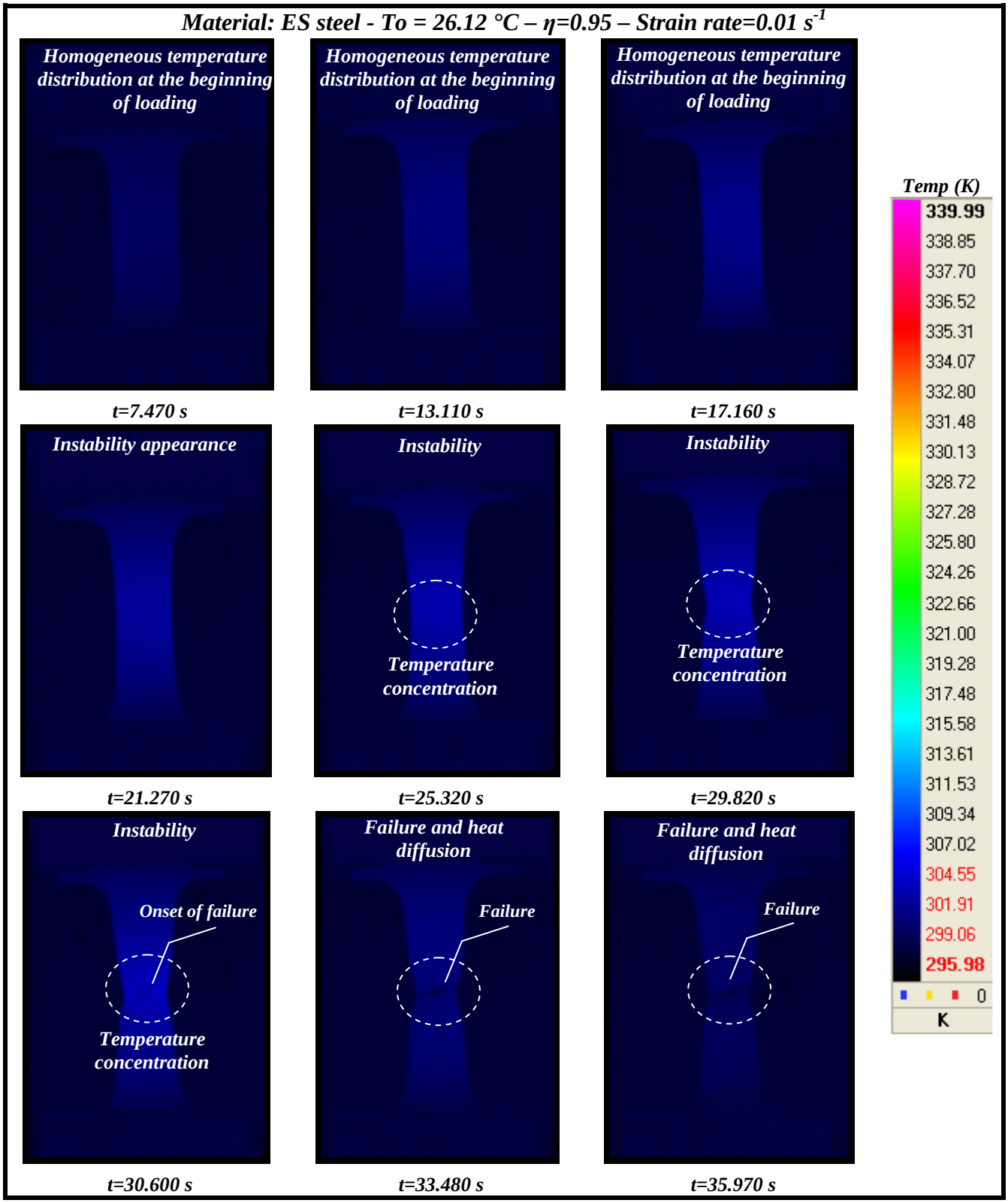

Fig. 4.7. Temperature contours during loading. Picture resolution 320×256 pixels.

Tests at higher strain rates have been performed. At $\dot{\bar{\varepsilon}}^{p} = 0.05\ s^{-1}$ the maximum temperature during the test reaches ΔT = 27 K, Fig. 4.8.

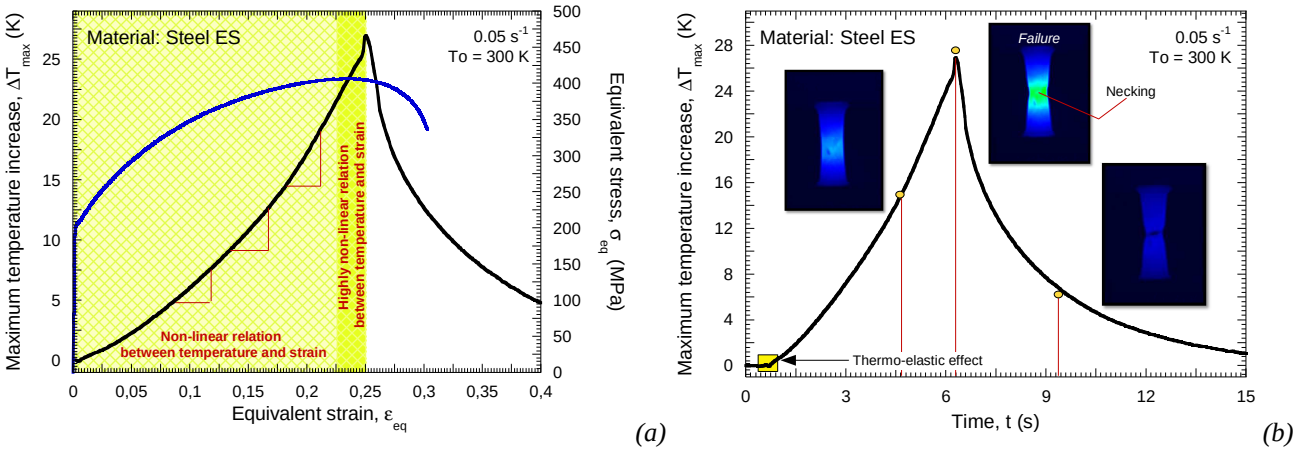

Fig. 4.8. (a) Maximum temperature increase versus plastic strain and flow stress evolution versus plastic strain. (b) Maximum temperature increase versus time.

In Fig. 4.8-a. it can be observed that the relation between temperature increase and plastic strain is not linear. According to Eq. 2.9., such non-linearity may come from the dependence that the inelastic heat fraction posseses on plastic strain, $\beta \rightarrow \beta\left(\overline{\varepsilon}^{p}\right)$.

Moreover, it has to be noted that the local effects in the necking zone become of main relevance, Fig. 4.8. In fact, the heat generated in the centre of the specimen is not being diffused *(at least not in a relevant way), Fig. 4.9.* In the necking zone the material seems to behave under adiabatic conditions of deformation. It means that when instability takes place, the strain rate is considerably increased *(in comparison with that corresponding to the global sample deformation [Borvik et al. 2003a])*, leading to local dynamic behaviour of the material. It agrees with the observations reported in Fig. 4.8-a. Before failure of the specimen the increase of temperature versus plastic strain is highly non-linear, Fig. 4.8.

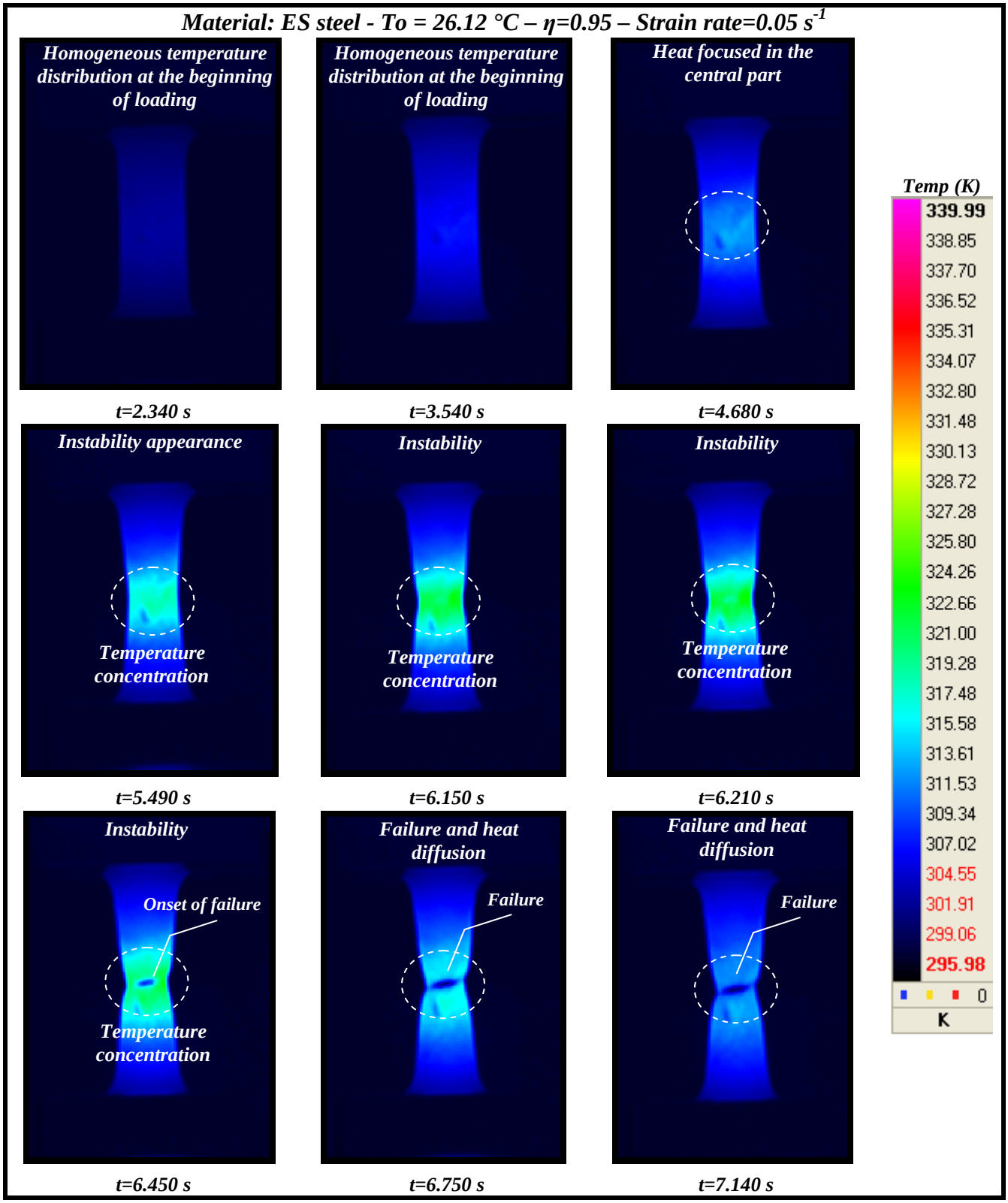

Fig. 4.9. Temperature contours during loading. Picture resolution 320×256 pixels.

At higher loading rate, $\dot{\bar{\varepsilon}}^{p} = 0.1\ s^{-1}$ the heat generation in the necking zone is much higher than in the rest of the specimen, Fig. 4.10. Maximum temperature increase in the necking reaches $\Delta T = 40$ K. It is reasonable to suppose adiabatic conditions of deformation in the necking zone. Instability formation and progression causes the peak of temperature reported in Fig. 4.10.

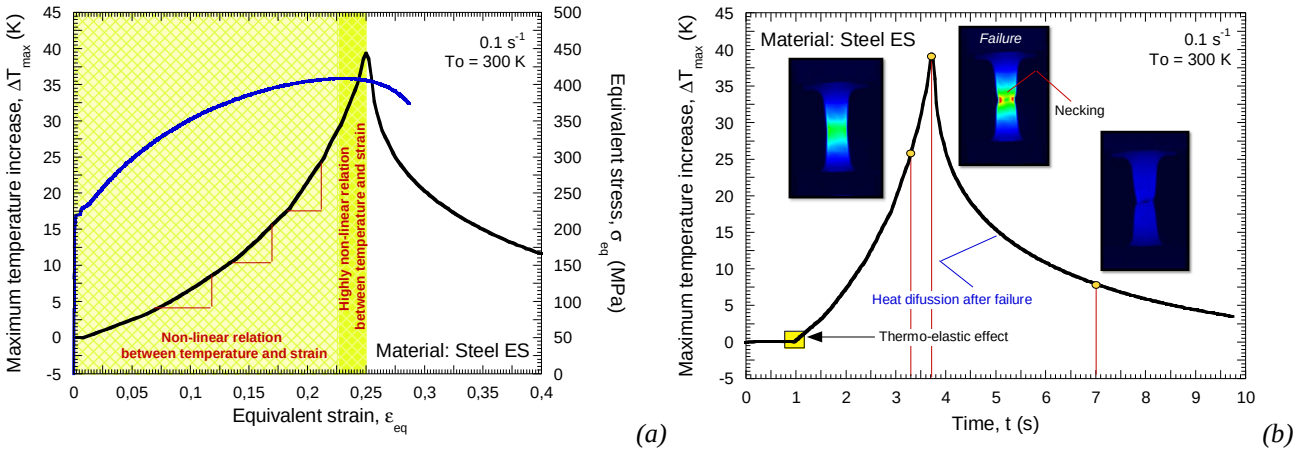

Fig. 4.10. (a) Maximum temperature increase versus plastic strain and flow stress evolution versus plastic strain. (b) Maximum temperature increase versus time.

As it was reported for $\dot{\bar{\varepsilon}}^p = 0.05\ s^{-1}$, in the case of $\dot{\bar{\varepsilon}}^p = 0.1\ s^{-1}$ the relation between temperature increase and plastic strain is not linear, Fig. 4.10-a. In fact, comparing Figs. 4.6-4.8-4.10 it seems that such non-linearity increases with strain rate. It seems to probe that the inelastic heat fraction may have also certain dependence on strain rate $\beta\left(\bar{\varepsilon}^p\right) \rightarrow \beta\left(\bar{\varepsilon}^p, \dot{\bar{\varepsilon}}^p\right)$. Interesting considerations concerning the dependence of β on the loading conditions are reported in [Macdougall 2000, Guzmán et al. 2008, Rusinek and Klepaczko 2009, Guzmán 2009, Guzmán et al. 2009]. A strong influence of the testing loading rate on the increase of temperature is then observed. Local rate and temperature effects in the necking govern the failure of the material even at low loading rates; Fig. 4.11.

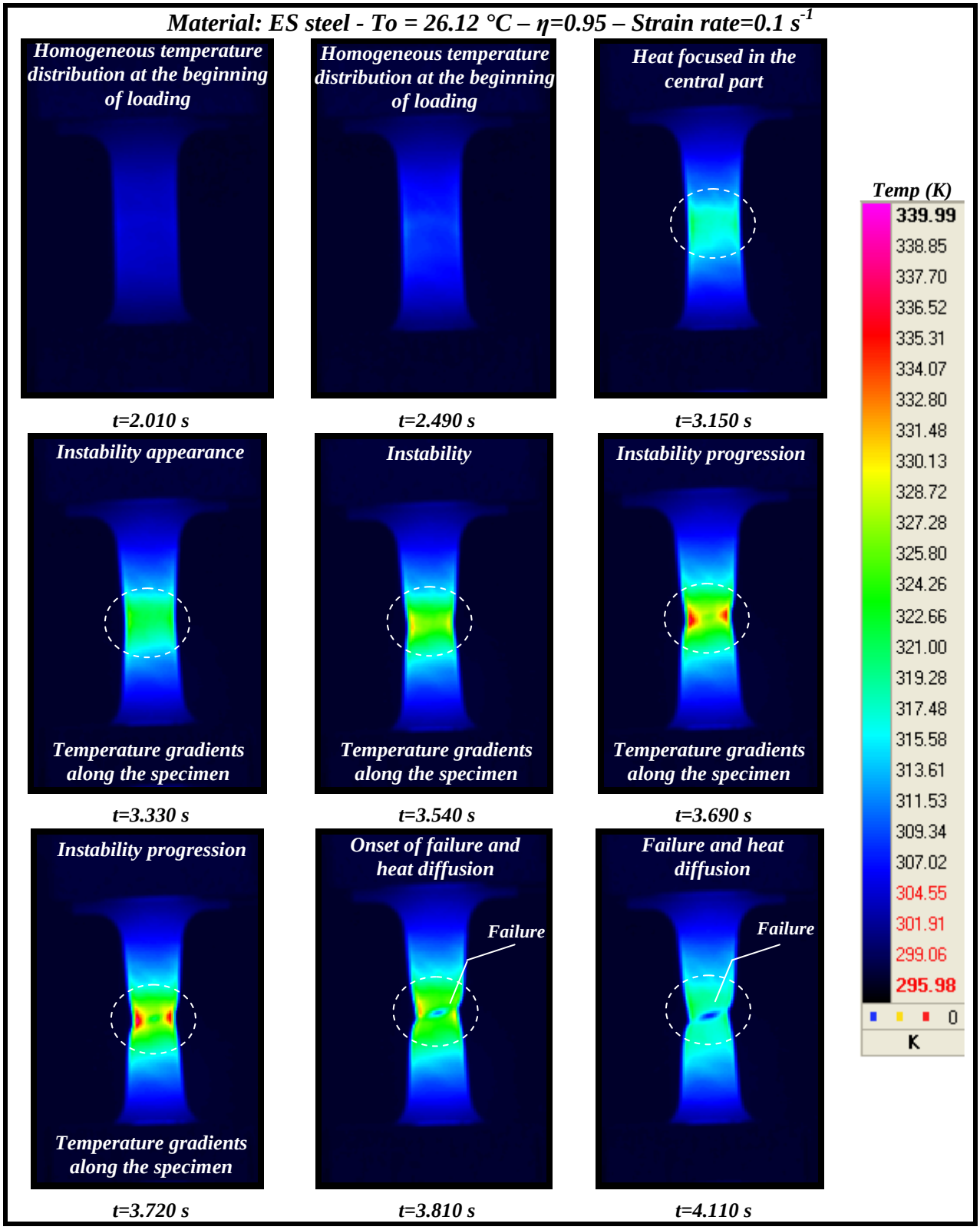

Fig. 4.11. Temperature contours during loading. Picture resolution 320×256 pixels.

Next, the behaviour of the mild steel **ES** is defined using the **RK** model

4.2.2 Constitutive relation for the ES steel

The suitability of the original **RK** formulation for describing the thermo-viscoplastic behaviour of the **ES** steel was already demonstrated in the works [Rusinek 2000, Rusinek and Klepaczko 2001, Rusinek et al. 2005, Rusinek et al. 2007]. Therefore, in this section of the document only a brief corroboration of such agreement between experiments and model predictions is shown.

The material constants for calibration of the **RK** model are listed in Table 4.2.

B_0 (MPa)	ν (-)	n_0 (-)	D_2 (-)	ε_0 (-)	σ_0^* (MPa)	m^* (-)	D_1 (-)	T_m (K)	$\dot{\varepsilon}_{min}$ (s^{-1})	$\dot{\varepsilon}_{max}$ (s^{-1})	θ^*
591.6	0.2	0.2852	0.19	0.018	406.3	2.8	0.48	1600	10^{-5}	10^{7}	0.59

*Table 4.2. Constants determined for mild steel **ES** for **RK** model [Rusinek 2000, Rusinek and Klepaczko 2001, Rusinek et al. 2005, Rusinek et al. 2007].*

In Fig. 4.12. is shown the satisfactory description of the flow stress and of the strain hardening of the material provided by the **RK** constitutive description.

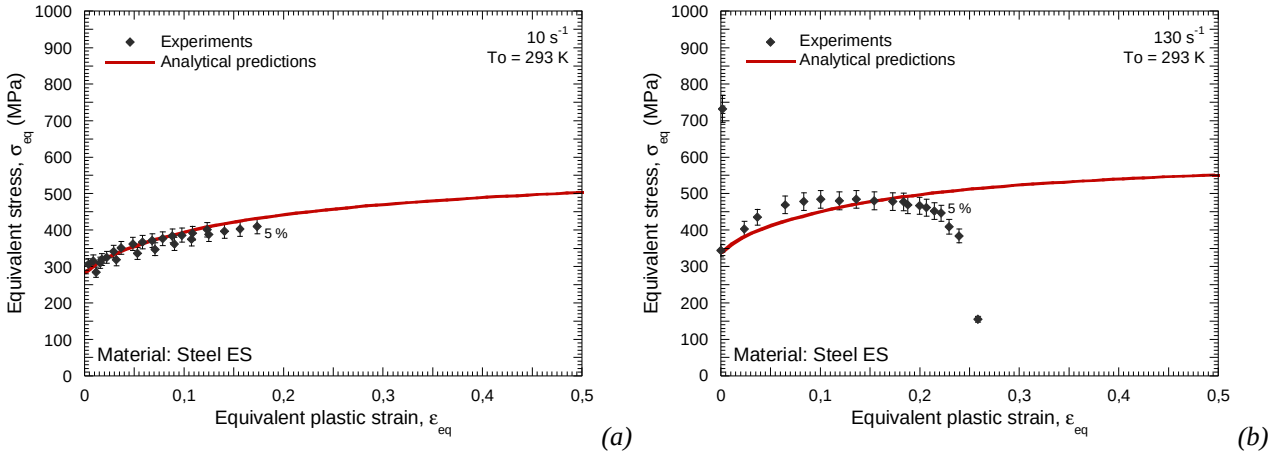

Fig. 4.12. Flow stress versus plastic strain for different strain rates at room temperature. Comparison between analytical predictions and experiments [Rusinek et al. 2007].

In addition it must be noticed the proper definition of the material rate sensitivity predicted by the **RK** model, Fig. 4.13

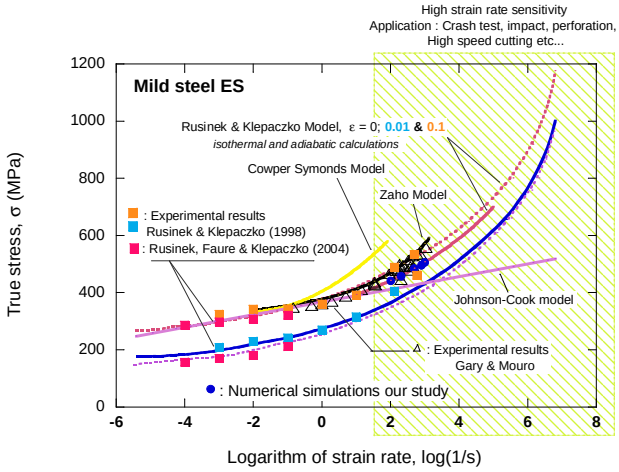

*Fig. 4.13. Strain rate sensitivity definition of mild steel **ES** provided by the **RK** model and comparison with other constitutive descriptions [Rusinek et al. 2007, Klepaczko et al. 2009].*

Next, the experimental setup used for perforation of the **ES** steel sheets is introduced.

4.2.3 Experimental procedure for perforation of metallic sheets

A scheme of the sample used for the perforation tests is shown in Fig. 4.14. The thickness of the specimen is h = 1 mm and its surface is $A_t = 140 \times 140$ mm^2. The active part of the sample after it is screwed and clamped on the support is $A_f = 100 \times 100$ mm^2.

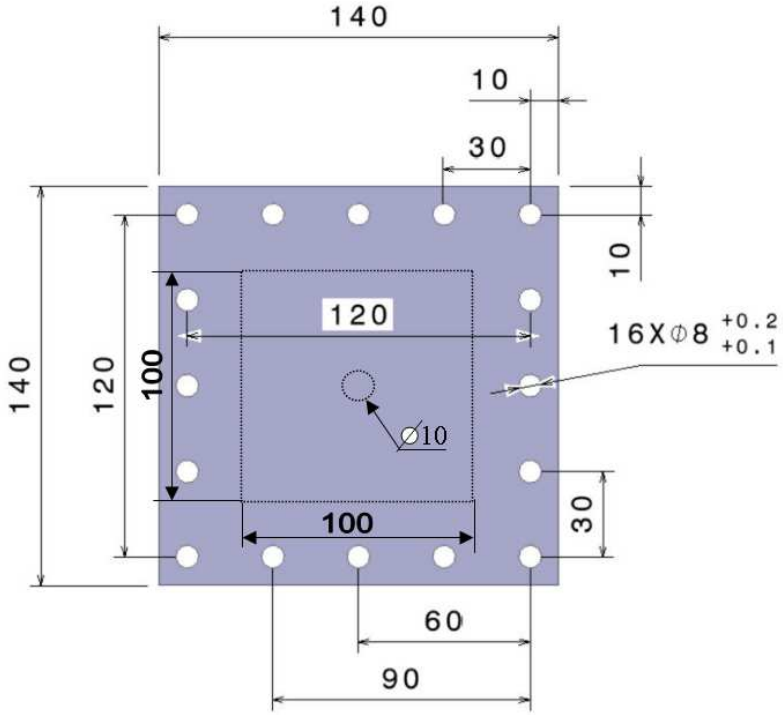

Fig. 4.14. Dimensions and geometry of the specimens used in the experiments (mm). (Design R. Bernier)

Several screws symmetrically placed are used to attach the steel sheet to the clamping support, Fig. 4.14. It allows eliminating potential sliding effect during the tests. Moreover, the mass of the hemispherical projectile used is $M_p = 0.063$ kg and its dimensions are shown in Fig. 4.15.

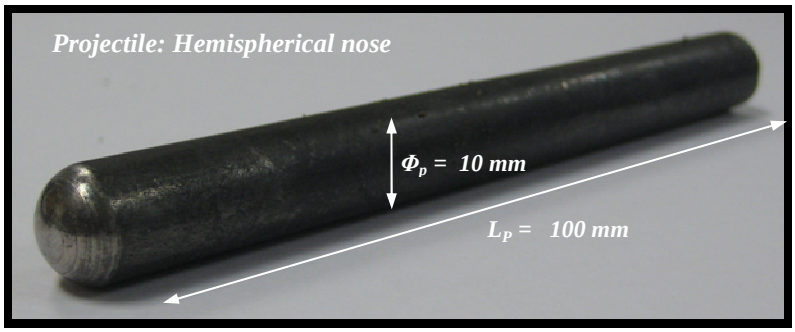

Fig. 4.15. Projectile used in the perforation tests. (Design R. Bernier)

The projectiles were made of *Maragin* steel which exhibits high yield stress $\sigma_y > 1$ GPa, much higher than that corresponding to the **ES** steel under dynamic conditions of deformation. In addition, the projectiles underwent a heat treatment in order to increase their hardness. A foam sabot was used in order to get the perpendicularity of the impact during the tests. It allowed launching these

projectiles whose diameter was considerably smaller than the diameter of the barrel, $\varphi_p < \varphi_b = 22$ mm.

4.2.3.1 The pneumatic cannon

In order to analyze the mechanical behaviour of the steel sheets within the impact velocity range 5 m/s $\leq V_0 \leq$ 60 m/s, a gas cannon has been used [Segreti et al. 2004, Rusinek et al. 2009a], Fig. 4.16-b. This technique allows measuring the initial velocity just before the impact takes place. Such measurement is carried out using 3 sources of light B_i coupled to 3 laser diodes C_i and 3 time counters, Fig. 4.16-a. When the projectile passes through a source of light, Fig. 4.16-a, a time counter is trigged. This procedure is repeated 3 times defining two time intervals Δt_{12} and Δt_{23}, Fig. 4.16-a. With knowledge of the distance between the 3 sources of light it is possible to measure two instantaneous projectile-velocities V_0^{ij}. Their average $\bar{V}_0$ was used to define the impact velocity values reported along this document.

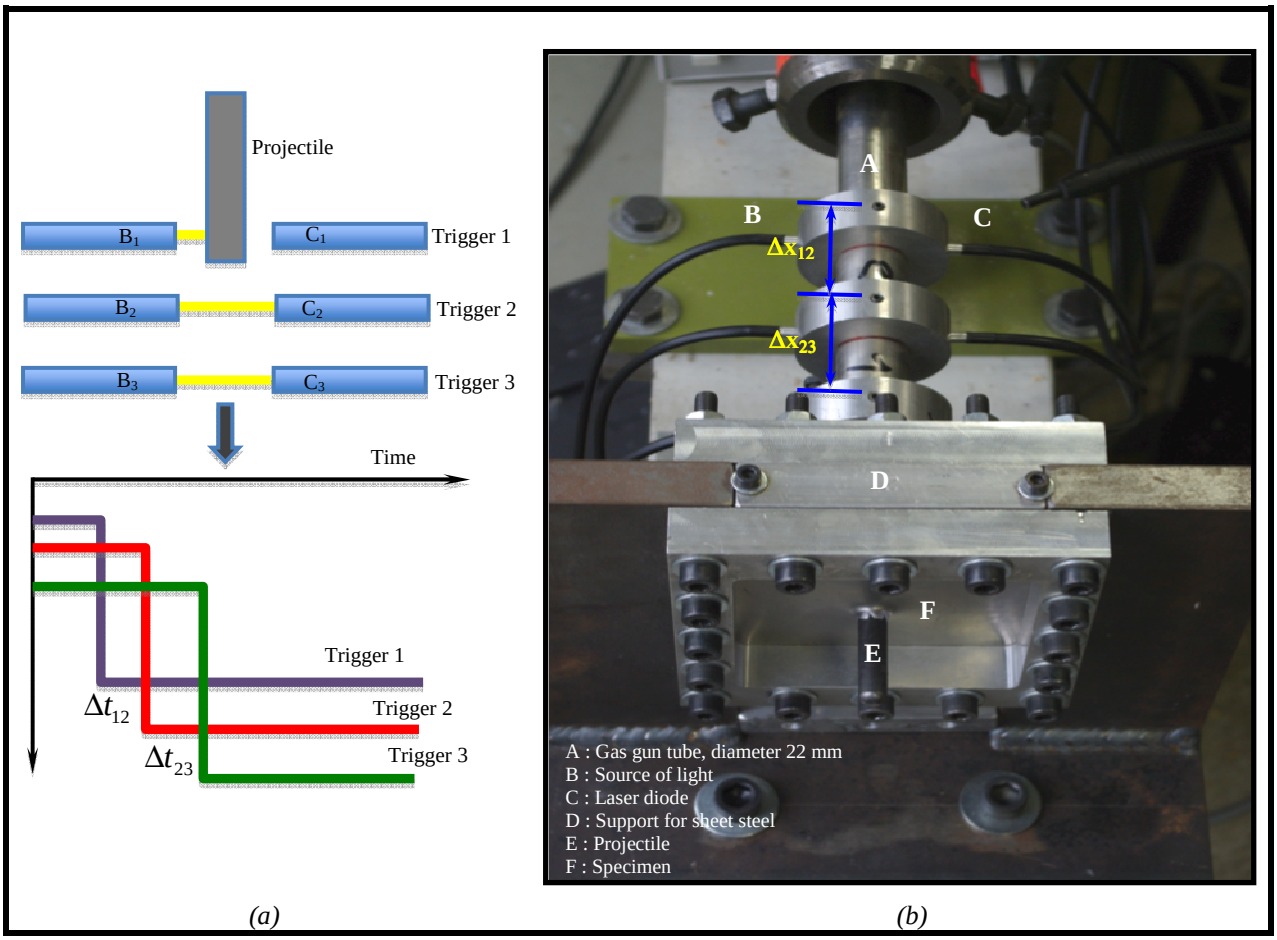

*Fig. 4.16. (a) Scheme of the facility used for measurement of the impact velocity. (b) Description of the experimental setup (**LPMM**).*

This experimental technique allows for an accurate definition of the ballistic limit V_{bl} for the boundary value problem examined in this work.

Post-mortem measurement of the targets-deflection was conducted using a 2D-profilometer, Fig. 4.17-a. It allowed measuring the profiles of the impacted plates with an accuracy of 3 µm ± 1 µm. Since the measurements are carried out after impact, the displacement of the steel sheets comes

exclusively from plastic deformation, Fig. 4.17-b. Elastic recovery cannot be taken into consideration.

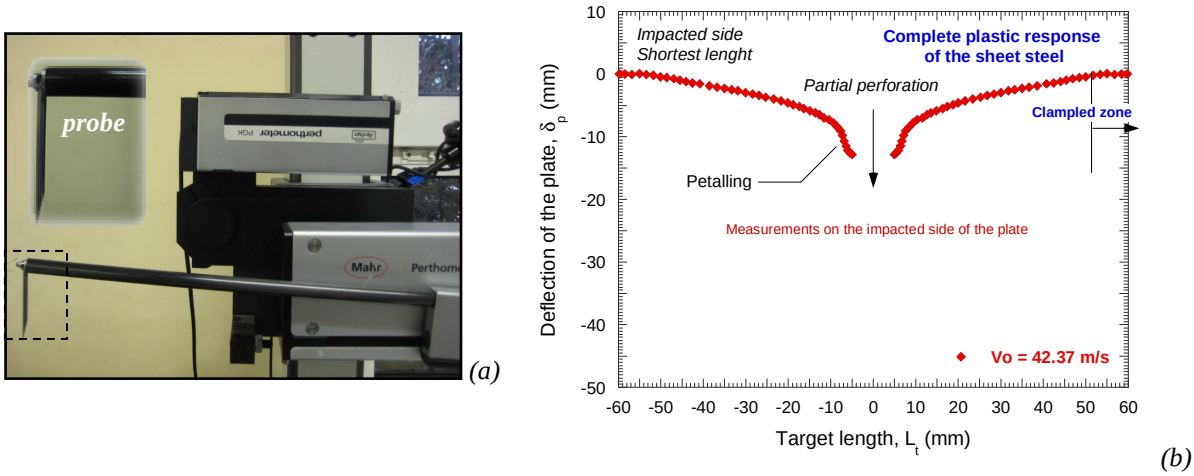

Fig. 4.17. (a) Profilometer used to measure the permanent deflection of the plates. (b) Measurement of the post-mortem deflection of the target.

Additionally, the perforation tests were recorded using an infrared high-speed camera.

4.2.3.2 Experimental temperature measurements using infrared camera

The infrared camera was placed in different positions depending on the impact velocity. In the case of initial velocity below the ballistic limit, the camera was placed on the impact axis, on the back of the sheet steel, *(Position 1)*. In the case of impact velocity above ballistic limit, the camera was placed with a small angle θ≈15°, in relation to the impact axis in order to guarantee the safety of the device, *(Position 2)* Fig. 4.18. The distance from the camera to the target remained approximately constant for both camera placements. During the tests it was checked that such camera angle *(θ≈15°)* allowed for a complete view of the rear side of the target during the impact process; temperature contours recorded during perforation were well defined. It is feasible to assume that the position of the camera during the tests involving perforation did not affect the temperature measurements.

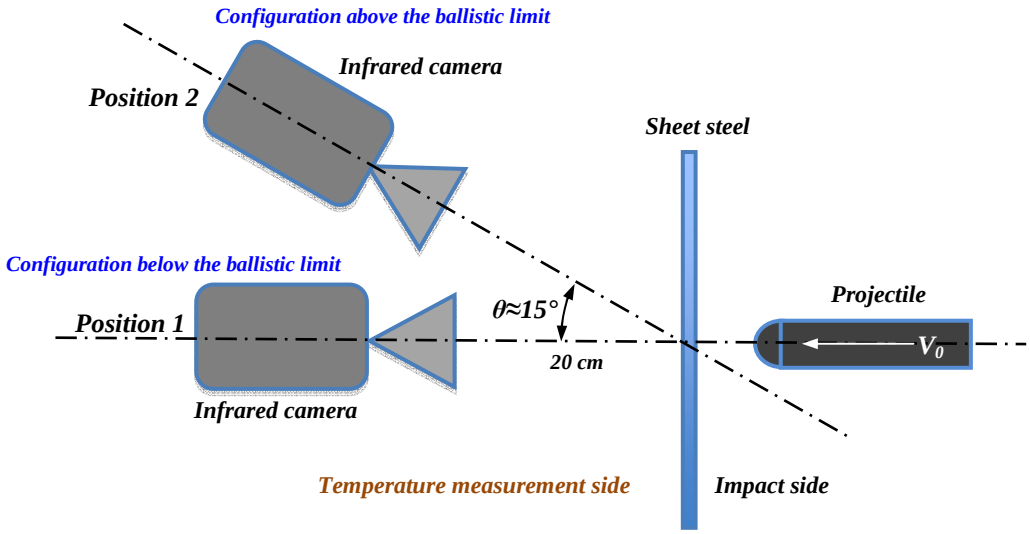

Fig. 4.18. Placements of the infrared camera during the tests depending on the impact velocity.

It must be noticed that in the area surrounding the projectile impact, the soot coating was ejected during the high velocity tests and the emissivity was reduced to η=0.64. This last value was obtained from the original target-surface *(before loading, the temperature registered by the camera on the original target-surface must fit the room temperature)*, Fig. 4.19. Therefore, after recording the impact, the video images must be properly interpreted using the camera-software. Suitable emissivity value is assigned to the images depending on the target-zone analyzed, Fig. 4.19. Assuming η=0.64 and η=0.95 as limiting values for the emissivity of the target during perforation, the maximum discrepancy in the temperature measurement is close to 15%.

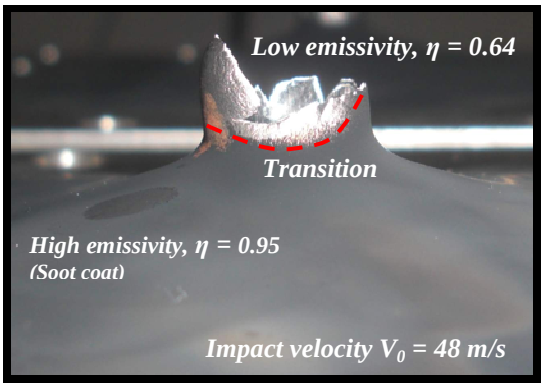

Fig. 4.19. Post-mortem estimation of the emissivity value depending on the target zone.

Measurements of the temperature increase in the material-target during impact ΔT(t) were obtained, Figs. 4.20-4.21.

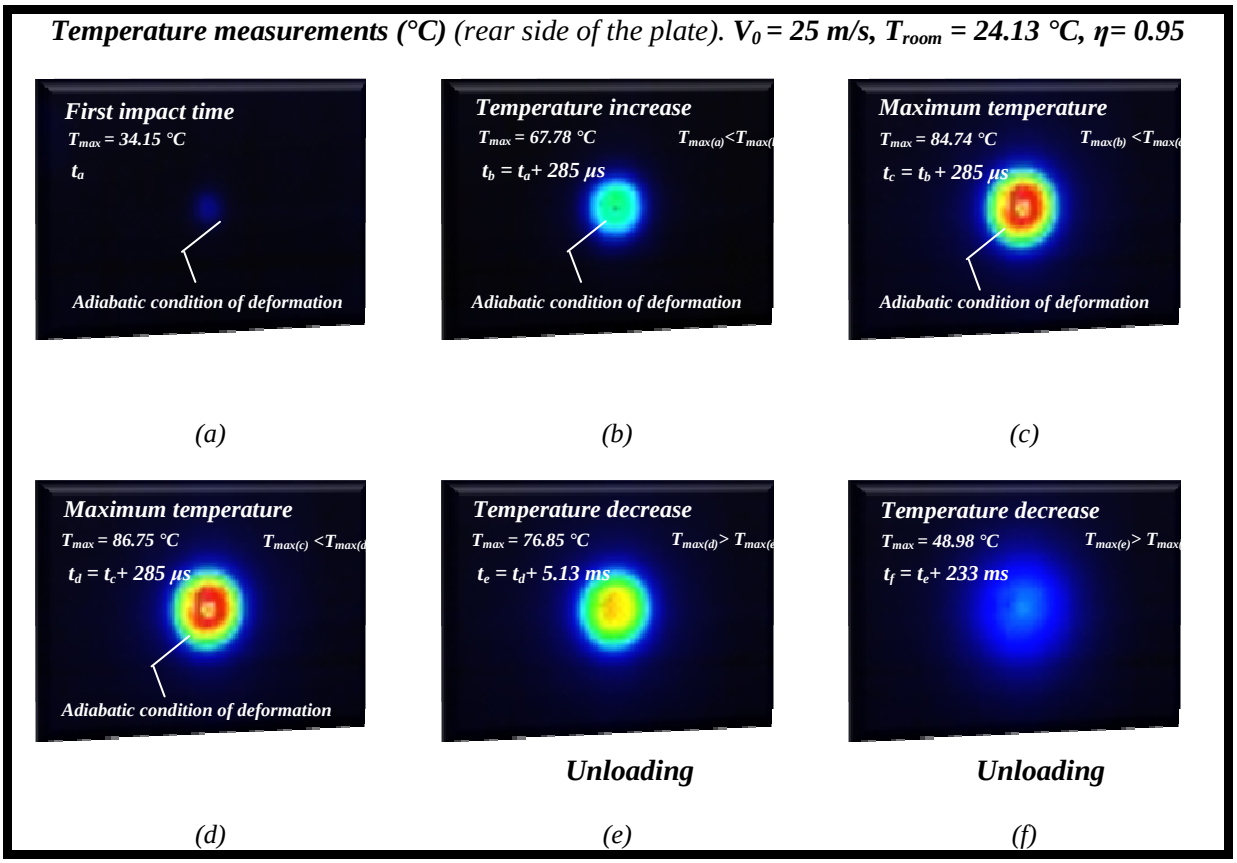

Fig. 4.20. Temperature in the rear side of the target for different stages of the impact process. V_0= 25 m/s and T_{room} = 24.13 °C. (a) T_{max}= 34.15°C ;(b) T_{max}=67.78°C ; (c) T_{max}=84.74°C ;(d) T_{max}=86.75°C ; (e) T_{max}=76.85°C ; (f) T_{max}=48.98°C. Picture resolution 80×64 pixels.

In view of Figs. 4.20-4.21., is possible to set two well differentiated stages during the impact. A drastic increase of temperature in a short period of time takes place at the beginning of loading. During this period let us assume adiabatic conditions of deformation in the target-zone affected by the impact. This first stage is followed by an exponential decrease of temperature *(slower)* due to heat transfer, Figs. 4.20-4.21. Finally, the material reaches thermodynamic equilibrium with the surrounding-environment Fig. 4.20-4.21.

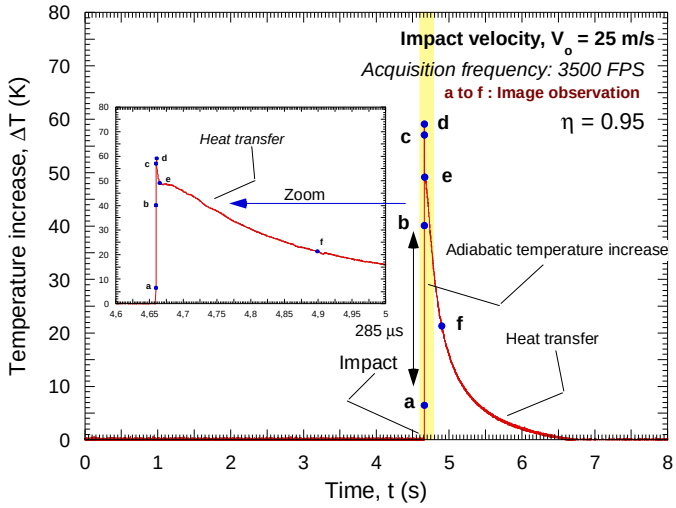

Fig. 4.21. Evolution of the maximum increase of temperature in the target as a function of time, V_0= 25 m/s.

The analysis of the experiments and the estimation of the critical failure strain leading to the target collapse are conducted along the following sections of the document.

4.2.4 Analysis of the perforation process

In this section of the document is analyzed the impact behaviour of the **ES** steel.

4.2.4.1 Study of the perforation mechanisms

The ballistic limit value found from experiments is $V_{bl} \approx 45$ m/s. In Fig. 4.22. are shown final stages of the impact process for different initial impact velocities. In the case of impact velocity above the ballistic limit $V_0 \approx 48$ m/s, well developed *petalling* is observed, Fig. 4.22-a. A small decrease of the initial velocity, $\Delta V_0 = -6$ m/s, strongly modifies the final stage of the impact process, Fig. 4.22-b. In Fig. 4.22-b the cracks generated at the dome of the contact projectile/plate did not have sufficient energy to progress *(local deformation induced by the projectile in the target did not allow for crack propagation).* Cracks were quickly arrested and the projectile was stopped before reaching complete perforation of the steel sheet. In the case of initial velocity under the ballistic limit, Fig. 4.22-c. is observed a zone affected by severe plastic deformation in absence of cracks *(Zone I).* It corresponds to the contact projectile/sheet steel. Outside of *Zone I*, large permanent bending takes place *(Zone II).*

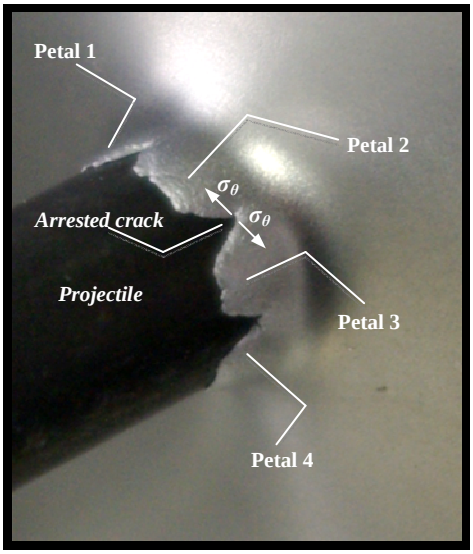

Projectile diameter: 10 mm
Mass: 0.063 kg
Impact velocity 48 m/s

(a)

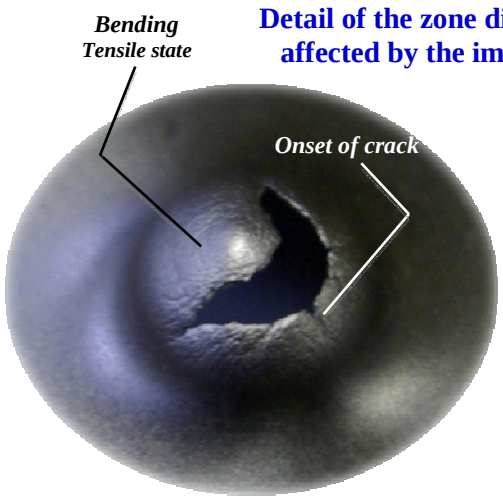

Projectile diameter: 10 mm
Mass: 0.063 kg
Impact velocity 42.5 m/s

(b)

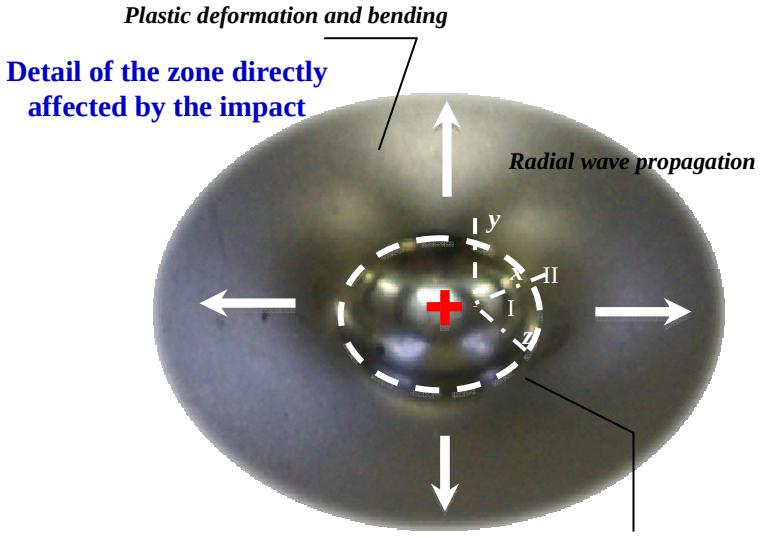

Projectile diameter: 10 mm
Mass: 0.063 kg
Impact velocity=37.60 m/s

(c)

Fig. 4.22. Final stage of the impact process for initial velocities close to the ballistic limit.

It has been observed a global response of the target during the perforation tests. The impact velocity range applied during the tests allows to the stress-waves generated by the impact to cover the whole steel sheet before rebounding of the projectile *(in the case of impact velocity below the ballistic limit)* or perforation of the target *(in the case of impact velocity above the ballistic limit)* . Deflection of the plate starts just beside the embedded perimeter, Fig. 4.23. Bending effect is enhanced by the small thickness of the target. Close to the ballistic limit the deflection of the plates reaches δ_p=10 mm in the zone directly affected by the impact. Large bending allows for radial sliding along the contact-zone projectile/plate leading to *necking* formation close to the dome of the contact zone projectile/plate [Rusinek et al. 2009a, Rodríguez-Martínez et al. 2010a]. *Necking* involves

localization of deformation acting as precursor of the onset of cracks, large plasticity values are expected in the *necking* zone [Rusinek et al. 2009a, Rodríguez-Martínez et al. 2010a]. When cracks are formed, they propagate radially leading to a *(approximately)* symmetric failure mode of the target.

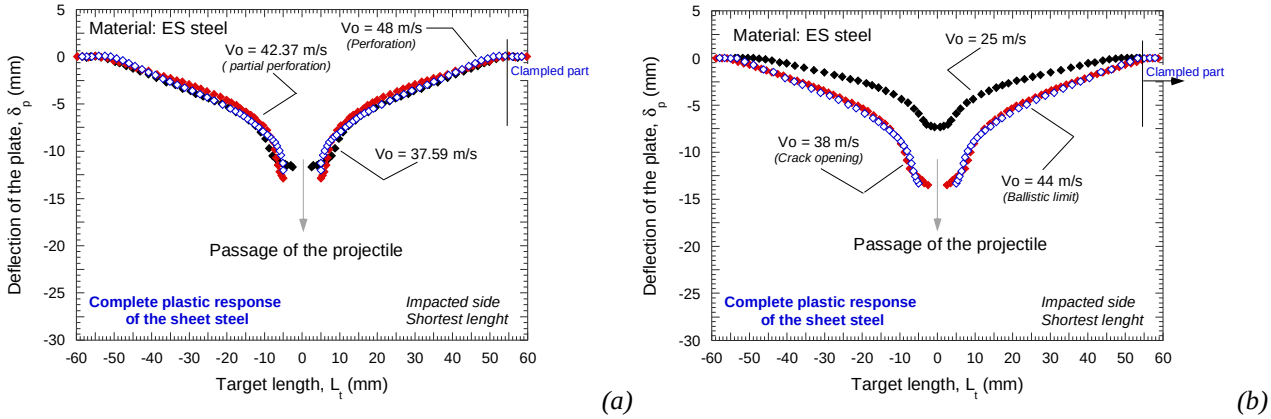

Fig. 4.23. Post-mortem deflection of the target for different initial impact velocities.

According to the previous considerations, cracks have long distance to cover until they are arrested on the rear side of the plate. It causes formation of long petals as final stage of the perforation process [Rusinek et al. 2009a]. No plug ejection was observed during the tests *(due to formation of cracks at the dome of the contact zone projectile/plate)*.

4.2.4.2 Analysis of the temperature fields during perforation

By using infrared recording is possible to analyze localization of deformation *(plastic instabilities appearance: necking formation, onset of cracks and their subsequent propagation)* which is responsible for target-failure during perforation.

In the zone directly affected by the impact, from the first contact until the onset of cracks takes place, the temperature is continuously increasing, Fig. 4.24. Maximum temperature increase, $\Delta T_{max} \approx$ 160 K if $\eta = 0.64$ *($\Delta T_{max} \approx 135$ K if $\eta = 0.95$)*, corresponds to the loading-time involving *necking* development and onset of cracks, Fig. 4.24-b-c. Such temperature level strongly reduces the strain hardening of the **ES** steel [Rusinek et al. 2005], promoting crack propagation.

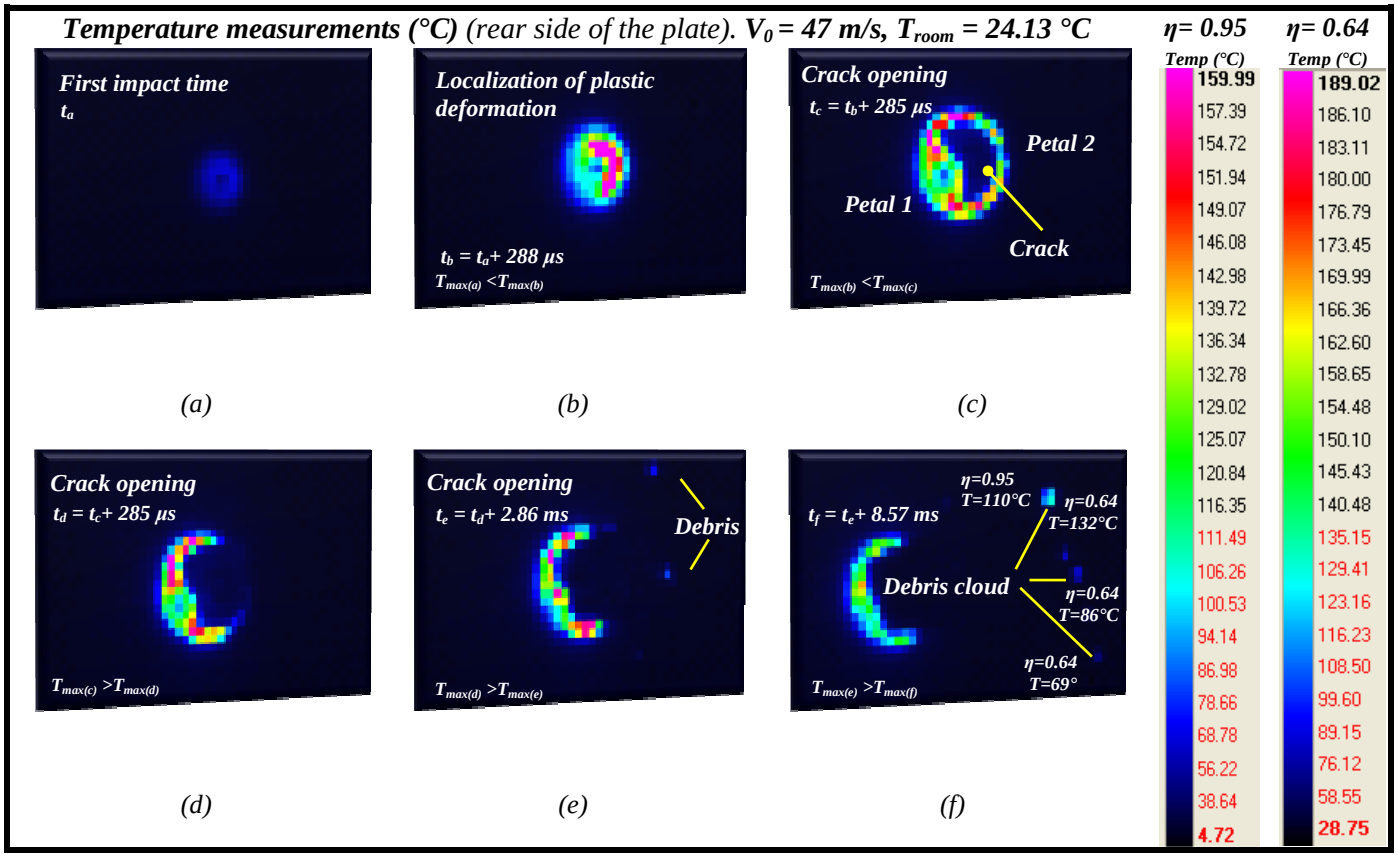

Fig. 4.24. Temperature level (°C) along the impact process for an impact velocity leading to target-perforation, observation of debris cloud, V_0 = 47 m/s and T_{room} = 24.13 °C. Picture resolution 80×64 pixels.

Measuring the temperature level on the impact zone *(on the rear side of the plate)* the following curves are obtained for different loading times, Fig. 4.25-a-b *(six stages of Fig. 4.24. correspond to six stages depicted in Fig. 4.25-a-b.)*. It can be observed that the temperature increase is not symmetrically distributed around the centre of the target, Fig. 4.25. Such phenomenon could be attributed to intrinsic material defects which induce certain asymmetry (*quite reduced in agreement with Fig. 4.22)* in the distribution of plastic deformation around the impact zone. Material defects become influential on the target failure at low impact velocities, close to the ballistic limit value. At high impact velocities *(much higher than the range of impact velocities covered in the experiments of the present work)* initial material defects have not time to growth due to fast failure of the target. Then it is expected that such asymmetry in the temperature field will not take place. Maximum temperature level is located on the petals-edge *(cracking interface).*

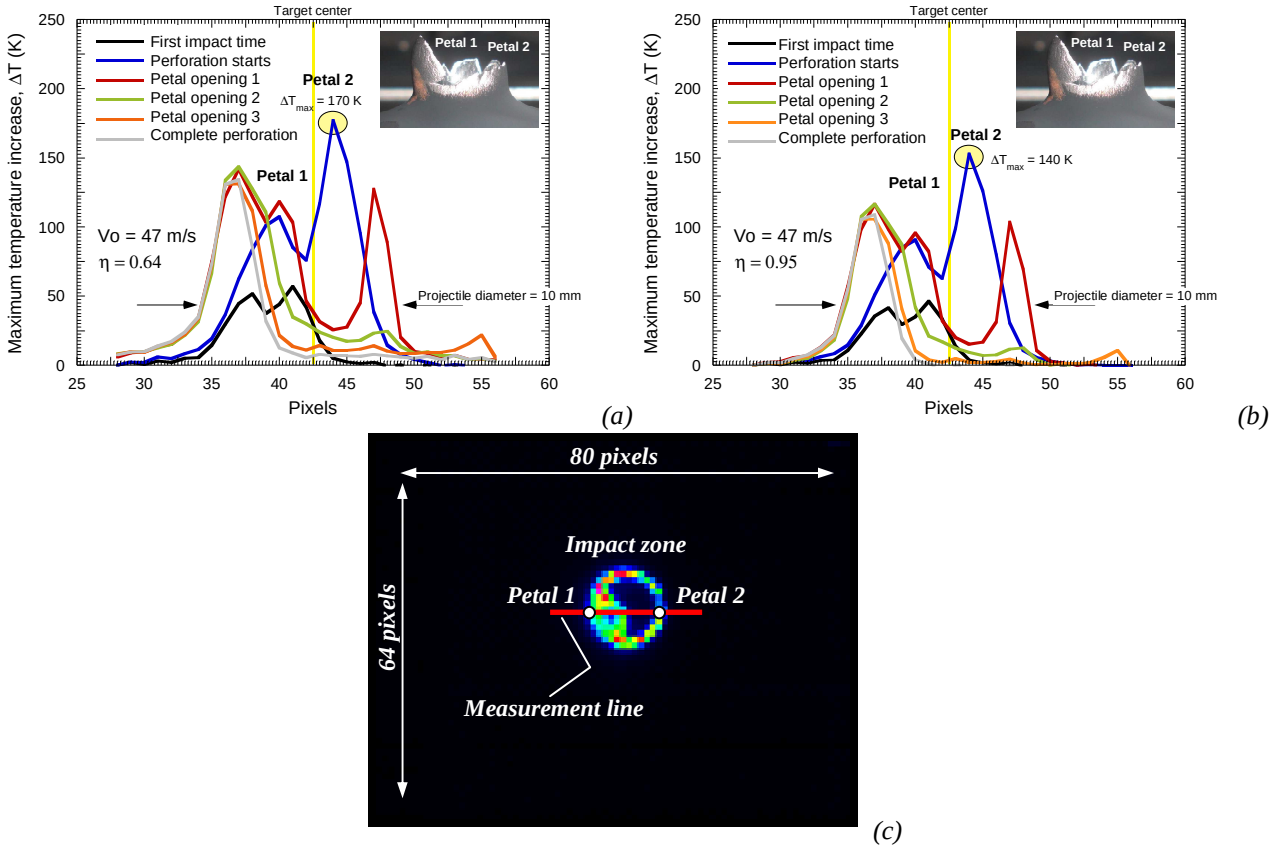

Fig. 4.25. Maximum temperature increase in the impact zone at V_0 = 47 m/s (a) η=0.64 and (b) η=0.95. (c) Measurement points of the temperature increase.

Out of the cracking interface, temperature increase is much more reduced, Figs. 4.24-4.25. In Fig. 4.26. is shown the temperature increase inside a circular surface centred on the impact-point as a function of time. Radius of the circular surface corresponds approximately to the projectile-radius; measurement zone includes the cracking interfaces. Maximum temperature level *(it corresponds to the cracking interfaces)* is much greater than the average temperature of the whole area. Strong temperature gradients take place surrounding the cracks, Figs. 4.24-4.25-4.26.

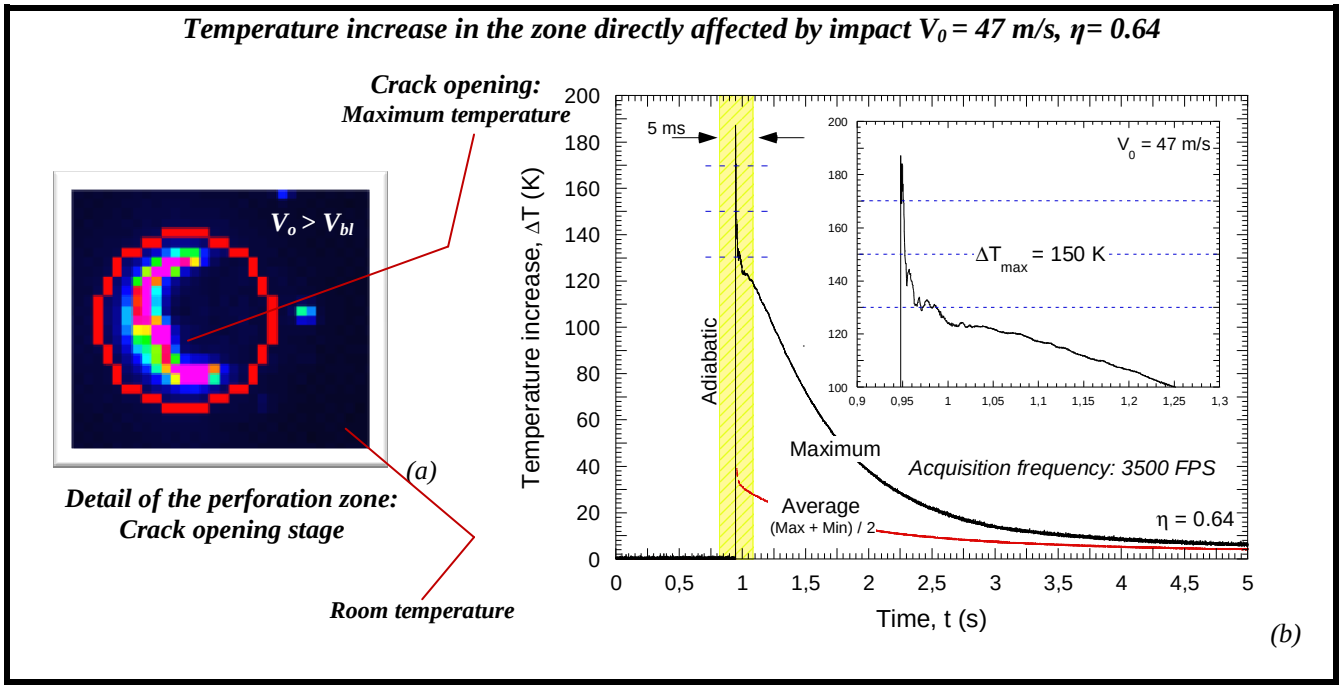

Fig. 4.26. Temperature increase in the impact zone. V_0 = 47 m/s.

Temperature-increase is found to be dependent on the impact velocity. For the whole range of impact velocities tested, as the initial velocity increases the maximum temperature recorded also does it, Fig. 4.27-a. Moreover, in Fig. 4.27-a. is observed an important gap between the maximum temperature registered in the case of impact velocity under or above the ballistic limit. In the range of 37 m/s ≤ V_0 ≤ 42 m/s *(in that range of impact velocities the projectile starts to pierce the target)* the slope of the curve $\Delta T_{max}/V_0$ is maximum, Fig. 4.27-b. For such a range of impact velocities, small increments on the impact energy lead to large increments on the local temperature.

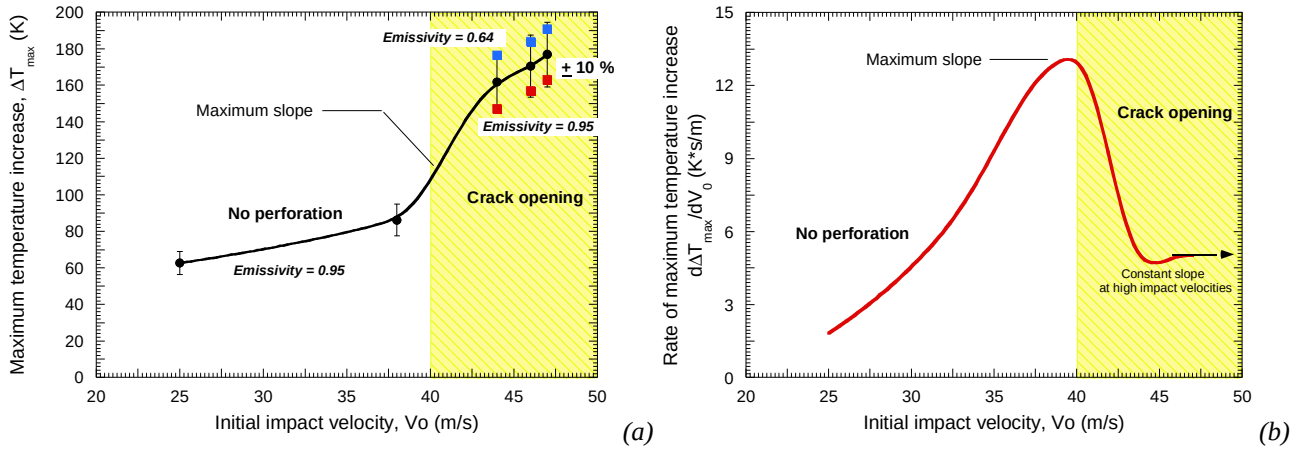

Fig. 4.27. (a) Maximum temperature increase and (b) rate of maximum temperature increase as a function of initial impact velocity.

Previous observations may be tied to the role that deformation rate has on the material behaviour [Hu and Daehn 1996, Altynova et al. 1996]. Therefore, in order to provide a proper interpretation of the experimental temperature-dependent measurements, it is necessary to estimate the strain rate level induced in the target-material by the impact. It will allow for estimation of the critical strain leading to material-failure.

4.2.4.3 Estimation of the critical failure strain leading to target failure

For this task, let us carry out the procedure described along the following sections of this document.

4.2.4.3.1 Considerations on dissipative effects

Although it is known that potential damage mechanisms taking place during perforation generate dissipative effects [Abu Al-Rub and Voyiadjis 2006, Perzyna 2008], let us assume their role negligible in comparison with the effect due to viscoplastic homogeneous flow stress. Moreover, **ES** steel is not susceptible of strain-induced *martensitic* transformation during loading unlike other steels such as the *austenitic* ones. Thus, no effect related to potential phase transformation processes has to be taken into account in the heat generation [Rusinek and Klepaczko 2009]. In the plastic range, at high rate of deformation the material behaves under adiabatic conditions of deformation. In such a case, the contributions to Eq. 4.1. due to the heat conduction and due to the elastic range *(it was shown in Figs. 4.6-4.8-4.10. the small contribution of the thermo-elastic effects)* can be neglected. Thus, the following expression can be derived Eq. 4.3.

$$\dot{T} = \frac{\beta}{\rho \cdot C_p} \cdot \sigma_{ij} : \dot{\varepsilon}_{ij}^{p} \qquad (4.3)$$

As it was previously reported, mild steel **ES** can be assumed as an isotropic material. In such a case, by integration of the previous expression, temperature increase is defined by Eq. 2.9'.

$$\Delta T\left(\bar{\varepsilon}^{p}, \bar{\sigma}\right) = \frac{\beta}{\rho C_p} \int_{\varepsilon^e}^{\bar{\varepsilon}^{p}} \bar{\sigma}\left(\bar{\varepsilon}^{p}, \dot{\bar{\varepsilon}}^{p}, T\right) d\bar{\varepsilon}^{p} \qquad (2.9')$$

Where $\bar{\sigma}\left(\bar{\varepsilon}^{p}, \dot{\bar{\varepsilon}}^{p}, T\right)$ is the equivalent stress (*considered dependent on plastic strain, strain rate and temperature),* $\bar{\varepsilon}^{p}$ is the current equivalent plastic strain, $\dot{\bar{\varepsilon}}^{p}$ is the equivalent plastic strain rate and ε^{e} is the elastic strain corresponding to the initial yield stress.

Under these assumptions there is a univocal relation between temperature increase and equivalent plastic strain for an imposed deformation rate. In order to take advantage of such consideration, a proper definition of the material behaviour $\bar{\sigma}\left(\bar{\varepsilon}^{p}, \dot{\bar{\varepsilon}}^{p}, T\right)$ is necessary.

4.2.4.3.2 Analytical description of the temperature increase

Using flow stress definition provided by the **RK** relation now it is possible to particularize Eq. 2.9'. to **ES** steel. Thus, the temperature increase is decomposed into the contributions due to the internal stress $\sigma_{\mu}\left(\bar{\varepsilon}^{p}, \dot{\bar{\varepsilon}}^{p}, T\right)$ and due to the effective stress $\sigma^{*}\left(\dot{\bar{\varepsilon}}^{p}, T\right)$, Eq. 4.4.

$$\Delta T\left(\bar{\varepsilon}^{p}, \bar{\sigma}\right) = \Delta T_{\text{internal stress}} + \Delta T_{\text{effective stress}} \qquad (4.4)$$

By integration of Eq. 4.4, the following expression is derived, Eq. 4.5

$$\Delta T\left(\bar{\varepsilon}^{p},\bar{\sigma}\right)=\frac{\beta}{\rho\cdot C_{p}}\int\frac{E(T)}{E_{0}}\cdot\bar{\sigma}(\bar{\varepsilon}^{p},\dot{\bar{\varepsilon}}^{p},T)\cdot d\bar{\varepsilon}^{p}=\frac{\beta}{\rho\cdot C_{p}}\int\frac{E(T)}{E_{0}}\cdot\left[\sigma_{\mu}(\bar{\varepsilon}^{p},\dot{\bar{\varepsilon}}^{p},T)+\sigma^{*}(\dot{\bar{\varepsilon}}^{p},T)\right]\cdot d\bar{\varepsilon}^{p} \qquad (4.5)$$

However, under adiabatic conditions of deformation, temperature is strain dependent $T=f(\bar{\varepsilon}^{p})$. The previous expression, Eq. 4.5. is solved numerically in order to obtain the temperature increase. Coupling Eq. 4.5. with experiments and with numerical simulations an *inverse method* for estimating the failure strain of the material-target during the perforation tests is proposed in the following sections of the document. However, it must be noticed that fracture models based on a constant strain value are a simplification for defining ductile failure. In further investigations it would be advisable to develop a methodology to gather explicitly the potential influence of the stress state and the strain rate on the material failure definition.

4.2.4.3.3 FE simulation of the impact process in order to estimate the strain rate level in the target during perforation.

Once it is possible to obtain the temperature increase depending on strain *(for an imposed deformation rate)* using Eq. 4.5., it is necessary to get an estimation of the strain rate level in the target-material during perforation.

For that task, numerical simulations of the perforation process have been conducted using the **FE** code **ABAQUS/Explicit**.

According to the observations reported in [Rusinek et al. 2009], the numerical simulations have been conducted using a fully **3D** description of the problem. The mesh used for the target is shown in Fig. 4.28. It presents radial symmetry to avoid appearance of spurious generation of cracks. The zone directly affected by the impact has been meshed with 222.400 8-node tri-linear elements with reduced integration (**C3D8R** in **ABAQUS** notation). In this zone ten elements are placed along the thickness. In order to reduce the computational time, beyond the zone directly affected by the impact is defined a transition zone using 50.413 tetrahedral elements. This technique allows decreasing the number of elements along the thickness of the plate. In this transition zone the amount of elements along thickness is varied from ten to two. After the transition zone, the mesh is defined using **C3D8R** elements until getting the perimeter of the target. This optimum configuration has been obtained from a convergence study using different mesh densities.

Since the experimental observations revealed absence of erosion on the projectile-surface after the impact *(the projectile was not deformed plastically in any test)*, the projectile has been defined as rigid body, Fig. 4.28. It enables to reduce the computational time required for the simulations. A constant friction coefficient value $\mu=0.1$ has been used to define the contact projectile/plate [Rusinek et al. 2008b].

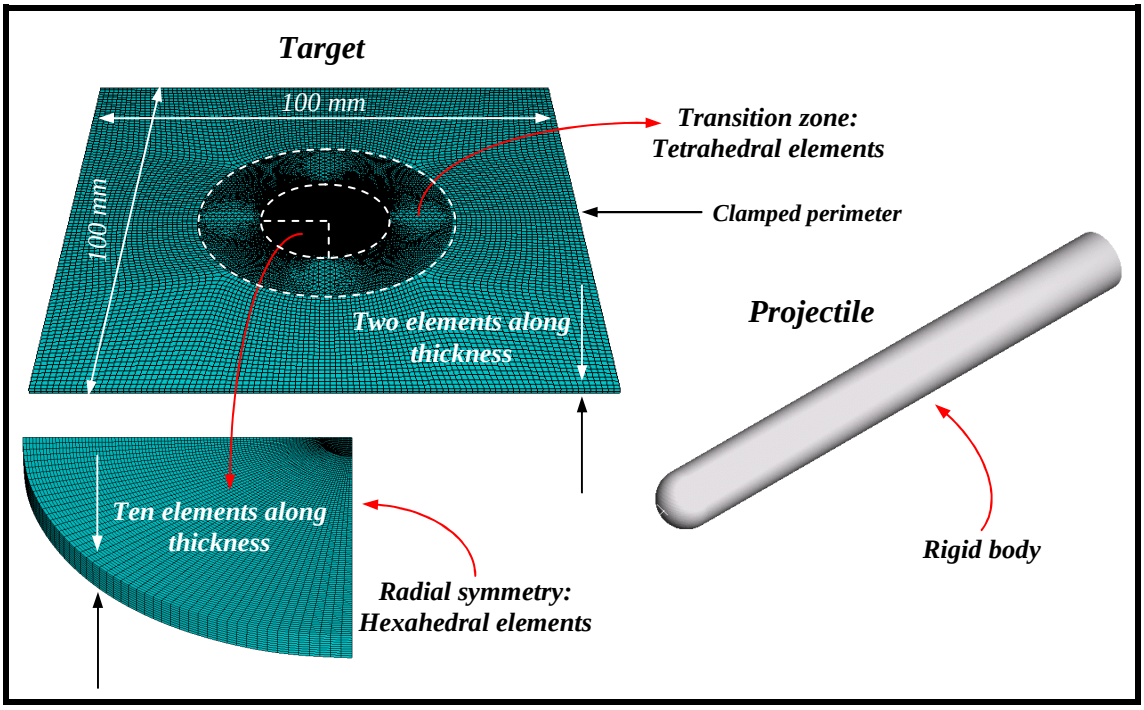

Fig. 4.28. Numerical configuration used in the simulations.

The impact velocities applied in the numerical simulations are those covered during the experiments.

The procedure for estimation of the strain rate level during perforation is the following:

- Maximum material-deformation allowed during the simulations is $\bar{\varepsilon}^p = 1.5$. Let us assume that during the experiments the local strain is lower than that value *(such assumption will be verified in the next section of the document when analytical predictions and experiments will be compared).*

- As soon as deformation reaches $\bar{\varepsilon}^p = 1.5$ in one integration point, the simulation is stopped *(It could be automatically stopped before reaching such a condition if the elements distortion becomes excessive).*

- Finally, the strain rate contours predicted by the simulations are analyzed as a function of the loading time.

In Figs. 4.29-4.30. are shown deformation rate fields for two initial velocities *(V_0 = 25 m/s and V_0 = 50 m/s)* and different stages of the impact process. They correspond approximately to the maximum and to the minimum of the impact velocities covered during the experiments. Maximum strain rate values are located along the contact-zone projectile/target, where localization of deformation takes place *(In Figs. 4.29-4.30. is visible the onset of necking precursor of failure).* For all the loading conditions shown in Figs. 4.29-4.30. the maximum strain rate level is varying within the range $10^3 s^{-1} \leq \dot{\bar{\varepsilon}}^p < 10^4 s^{-1}$. Such values are within the range of strain rates where the **RK** model defines properly the behaviour of the **ES** steel as previously reported in Fig. 4.12-4.13.

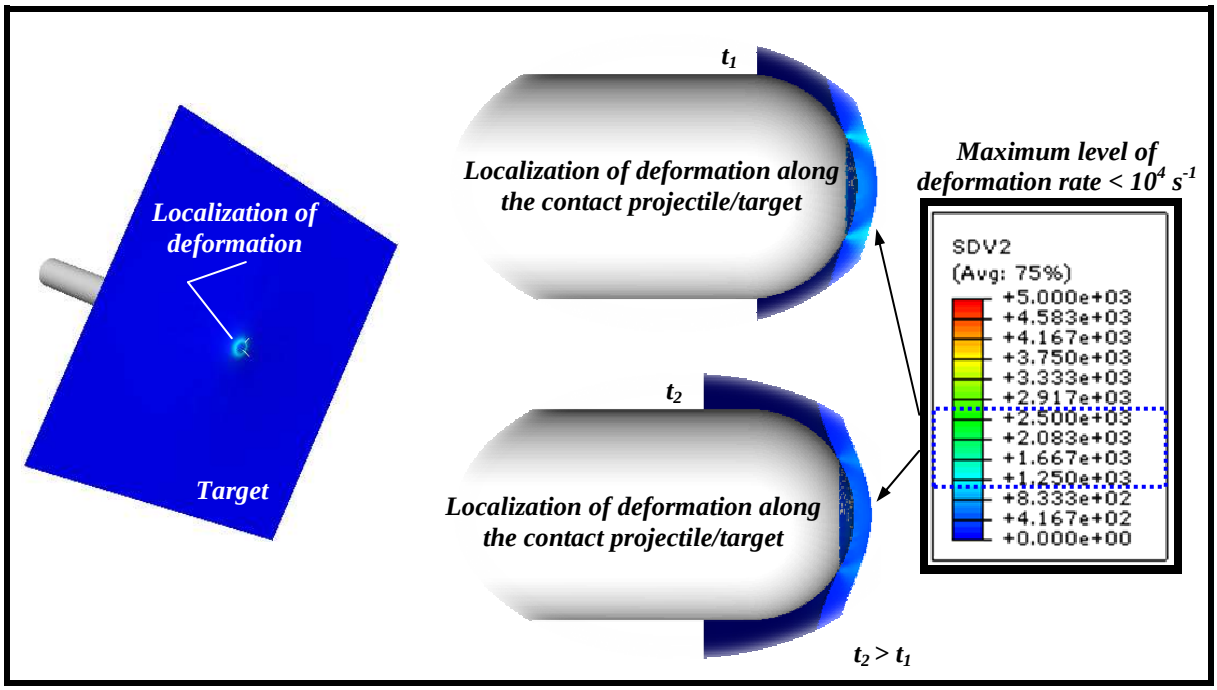

Fig. 4.29. Numerical estimations of strain rate contours during perforation, V_0 = 25 m/s.

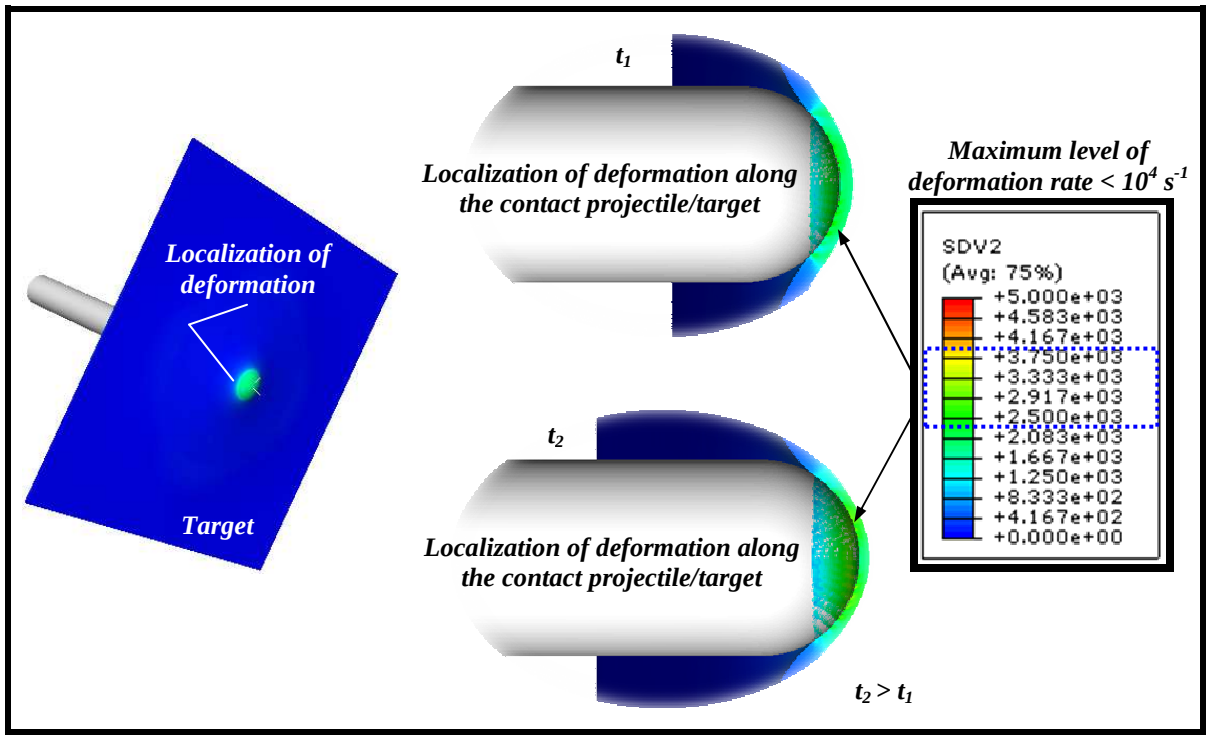

Fig. 4.30. Numerical estimations of strain rate contours during perforation, V_0 = 50 m/s.

Thus, let us assume that range of strain rate, $10^3\ s^{-1} \le \dot{\bar{\varepsilon}}^p < 10^4\ s^{-1}$, for coupling the experimental temperature measurements with the analytical predictions of the **RK** model. It will allow for estimation of a lower and an upper limit of the critical failure strain of the material during the perforation tests.

4.2.4.3.4 Coupling of experimental temperature measurements with analytical predictions of RK model and results obtained from numerical simulations

In Fig. 4.31. is depicted the temperature increase predicted by the **RK** model versus plastic strain for different strain rates Fig. 4.31-a, and versus strain rate for different deformation levels Fig. 4.31-b. Let us tie the maximum temperature measured during experiments $\Delta T_{max} \approx 150$ K *(which corresponds to target failure condition using $\eta = 0.64$ as it was previously reported)* to the critical failure strain, $\bar{\varepsilon}_f^p$. To obtain such a value of temperature $\Delta T_{max} \approx 150$ K for the range of strain rates estimated *($10^3\ s^{-1} \leq \dot{\bar{\varepsilon}}^p < 10^4\ s^{-1}$)* is necessary at least $\bar{\varepsilon}^p = 0.95$ in the case of $\dot{\bar{\varepsilon}}^p = 10^4\ s^{-1}$ or $\bar{\varepsilon}^p = 1.15$ in the case of $\dot{\bar{\varepsilon}}^p = 1000\ s^{-1}$, Fig. 4.31. This range for the critical failure strain $0.95 \leq \bar{\varepsilon}_f^p \leq 1.15$ *(values considerably lower than that used to estimate the strain rate level during perforation, $\bar{\varepsilon}_f^p = 1.5$)* is in agreement with experimental results and analytical predictions reported for steels for example in [Pandolfi et al. 1999, Triantafyllidis and Waldenmyer 2004, Borvik et al. 1999].

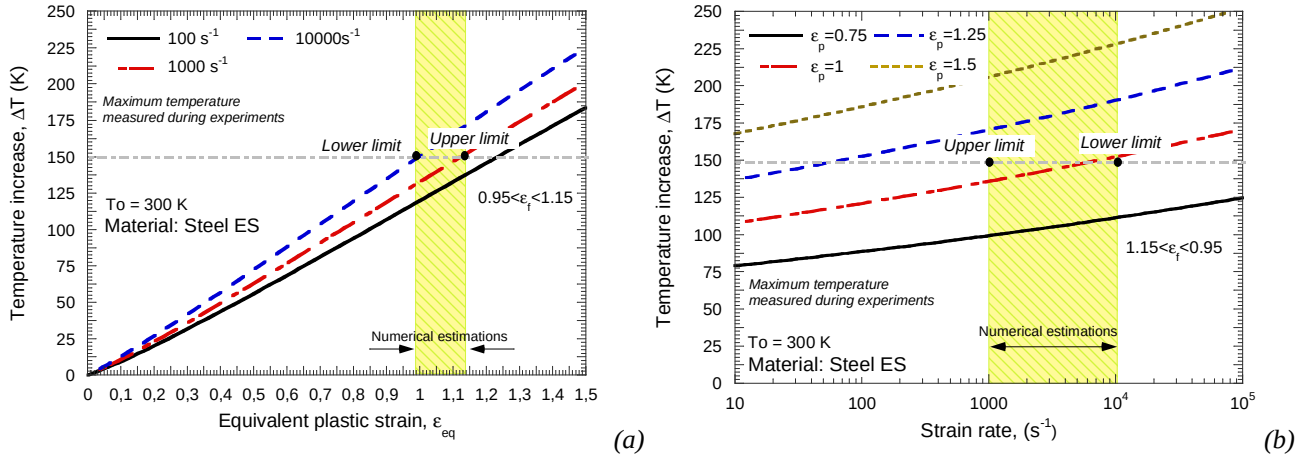

*Fig. 4.31. Analytical predictions of the **RK** model for the temperature increase in **ES** steel. (a) Temperature increase as a function of plastic deformation, (b) temperature increase as a function of strain rate*

Numerical simulations of the impact process are conducted using the critical failure strain previously estimated. Next, they are compared with experiments.

4.2.4.4 Comparison between experiments and numerical simulations

Numerical simulations of the perforation process using $\bar{\varepsilon}_f^p = 1$ *(average value of those obtained previously*) as failure criterion *(erosive failure criterion involving element deletion)* are conducted. In Fig. 4.32. it is observed that the numerical estimation of the ballistic limit matches with that obtained from experiments *($V_{bl\text{-}numerical} \approx V_{bl\text{-}experimental} \approx 50$ m/s).* In addition, the numerical prediction of the failure mode of the specimen fits properly the experimental observations, Fig. 4.32. Radial cracks take place at the dome of the interface projectile/target, Fig. 4.32. Petalling development and large bending effect are in agreement with Fig. 4.32. Finally, it must be noted that the maximum temperature increase registered during the simulations agrees with the experimental temperature measurements reported in previous sections of this document, Fig. 4.32.

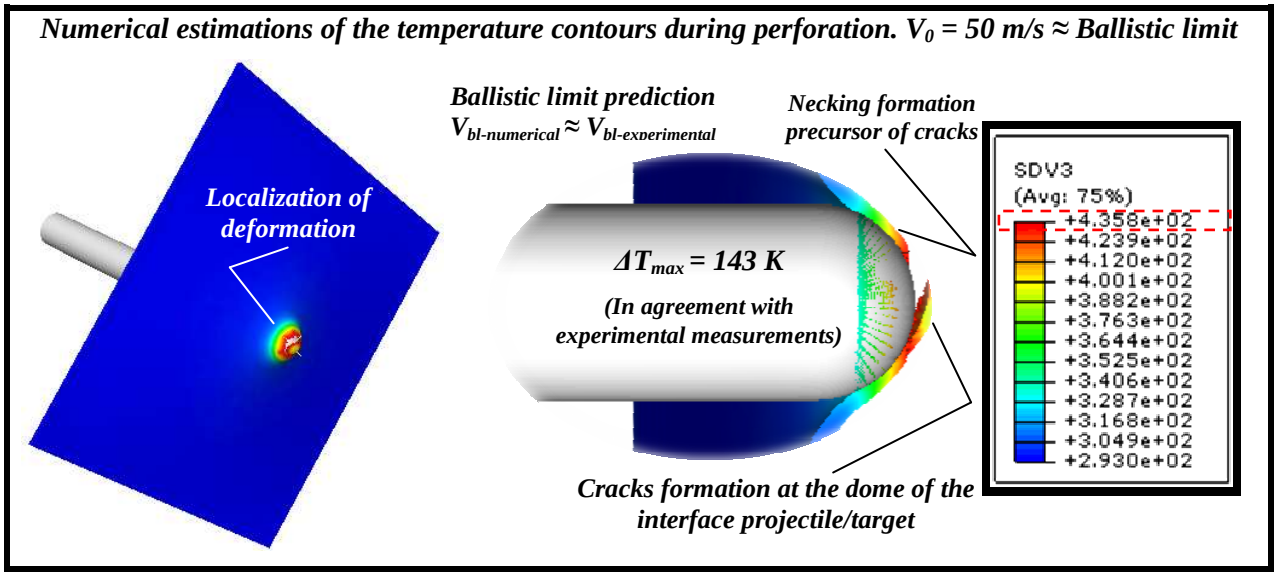

Fig. 4.32. Numerical estimations of temperature contours during perforation, V_0 = 50 m/s

It must be noticed that this simplified failure criterion allows obtaining numerical results in agreement with experiments due to the particularities of the boundary value problem approached. Since the target is very thin, the stress field along the thickness of the plate is rather constant during the perforation process *(plane stress state)*, Fig. 4.33.

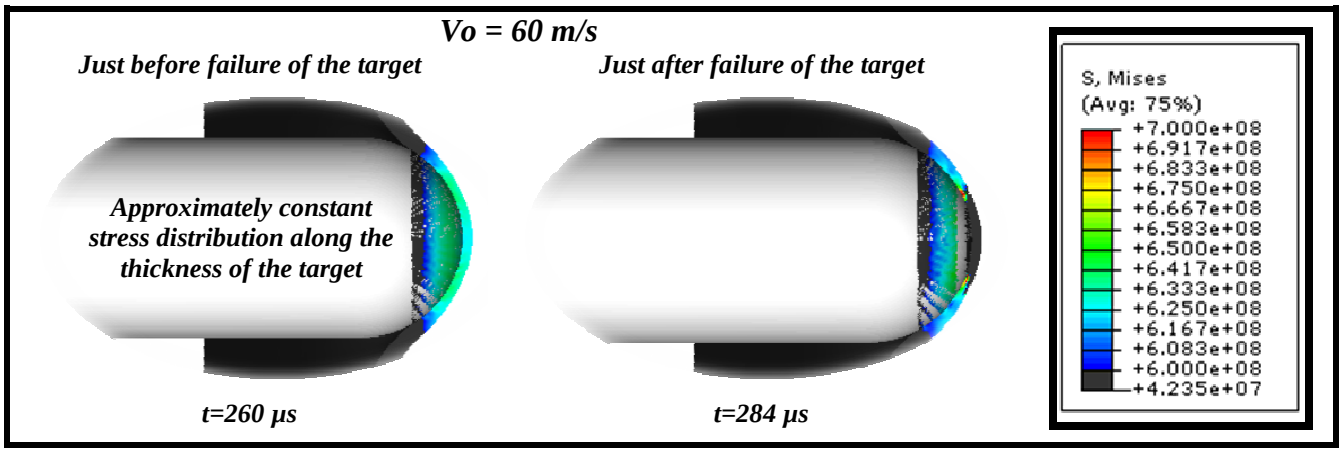

Fig. 4.33. Numerical estimation of stress contours during perforation. V_0 = 60 m/s

Moreover, failure of the target is due to ductile hole enlargement and subsequent necking which involves stress triaxiality values $\sigma^* \geq 1/2$, Fig. 4.34.

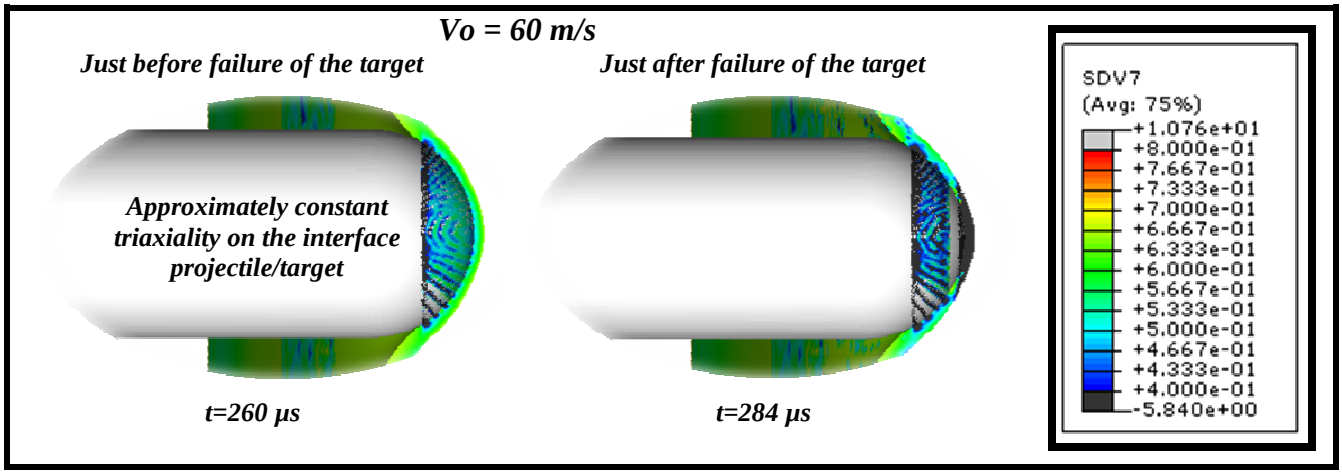

Fig. 4.34. Numerical estimation of triaxiality contours during perforation. V_0 = 60 m/s

For ductile metals, within that range of stress states, the failure strain becomes rather independent of triaxiality as reported for example in Dey et al. [Dey et al. 2004], Fig. 4.35.

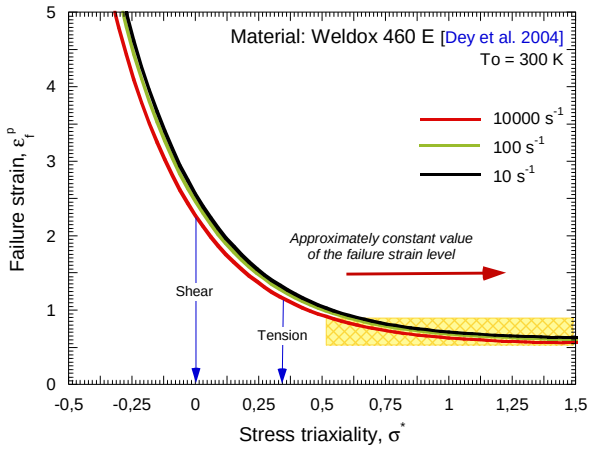

*Fig. 4.35. Estimation of the failure strain versus triaxiality by the Johnson-Cook failure criterion for **Weldox 460-E** ferritic steel [Dey et al. 2004].*

Thus, following an *inverse methodology* of analysis an estimation of the critical strain leading to material-failure during the perforation tests has been derived. In addition, the procedure followed in this study shows up the role played by the local phenomena that, in impact problems, lead to plastic instabilities appearance and subsequent material failure.

Next, the impact behaviour of the **AA 2024-T3** is examined.

4.3 Impact behaviour of aluminium alloy 2024-T3

In this part of the document the impact behaviour of the **AA 2024-T3** is examined. First, the thermo-mechanical characterization of the material is conducted. Then, it is modeled using the extended **MRK** model to viscous drag effects. Based on such understanding of the material behaviour, perforation tests of **AA 2024-T3** sheets are conducted. For that task two different experimental setups are used, a drop weight tower and a pneumatic gun. The results are compared with those previously reported for the mild steel **ES**.

4.3.1 Thermo-viscoplastic behaviour of the aluminium alloy 2024-T3

The **AA 2024-T3** is an aluminium alloy, with **Cu** and **Mg** as the alloying elements. It shows good machinability and surface finish capabilities. It is a high strength **AA** of adequate workability. It is widely used in aircraft structures where stiffness, fatigue performance and good strength are required. Other applications comprise hydraulic valve bodies, missile parts, munitions, nuts or pistons. The application fields of the **AA 2024-T3** make relevant to analyze and understand its behaviour under impact loading. The chemical composition of the **AA 2024-T3** *(% of weight)* is reported in Table 4.3.

Mn	**Si**	**Cr**	**Ti**	**Fe**	**Mg**	**Zn**	**Cu**
0.6	0.5	0.1	0.15	0.5	1.5	0.25	4.3

*Table 4.3. Chemical composition of the **AA 2024-T3** (% of weight).*

The thermo-viscoplastic behaviour of the material has been characterized in tension under wide ranges of strain rate and temperature. The tensile specimens used for this task are analogous to those used in the case of **ES** steel, Fig. 4.36.

In Fig. 4.36. is shown the flow stress evolution as a function of plastic strain under quasi-static loading. This alloy shows high yield stress and strain hardening which enhances ductility and toughness, Fig. 4.36.

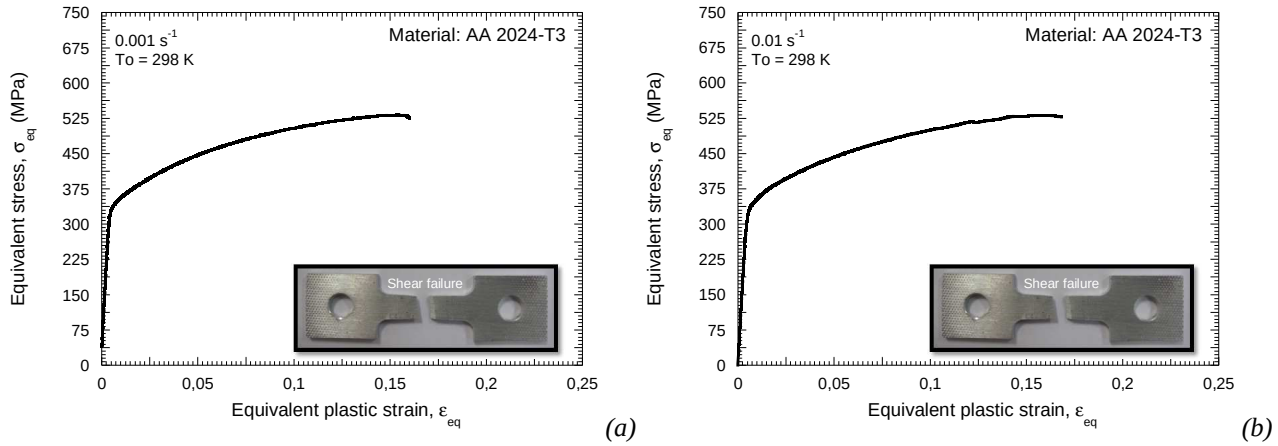

Fig. 4.36. Flow stress evolution versus plastic strain for different strain rates at room temperature.

Quasi-static tensile tests have been recorded using infrared camera, Fig. 4.37. Due to the relation existing between material temperature increase and plastic deformation, infrared measurements provide valuable information of the deformation field of the material during loading. It allows estimating the susceptibility of the material for instabilities formation. Therefore, it will help to determine the suitability of materials for absorbing energy under impact loading.

In the case of $\dot{\bar{\varepsilon}}^{p} = 0.001\ s^{-1}$ is observed that before instability takes place, the maximum increase of temperature in the specimen is quite reduced *(and approximately constant during the whole test)*, $\Delta T_{max} \leq 1$ K, Fig. 4.37. Such value is much more reduced than that observed for the **ES** steel under the same loading conditions *(and than that observed for steel **AISI 304** and steel **TRIP 1000** as it will be discussed later on this document)*. This behaviour is certainly caused by the high thermal conductivity of **AA,** K_{AA} = 237 W/(m·K), which leads to homogenous temperature field during loading, Fig. 4.38. The heat generated in the **AA** samples is quickly diffused and the material is deformed under thermodynamic equilibrium with the surrounding environment. Only when necking takes place is observable a relevant increase of temperature *(transient adiabatic conditions of deformation during necking formation and progression)*, Fig. 4.38. After failure, temperature rapidly decreases until reaching the environmental temperature, Fig. 4.37-4.38.

In Fig. 4.37. is illustrated the thermo-elastic effect, Eq. 4.2., occurring at the beginning of loading, $\Delta T_{AA}^{Elasticity} = -0.1$ K .

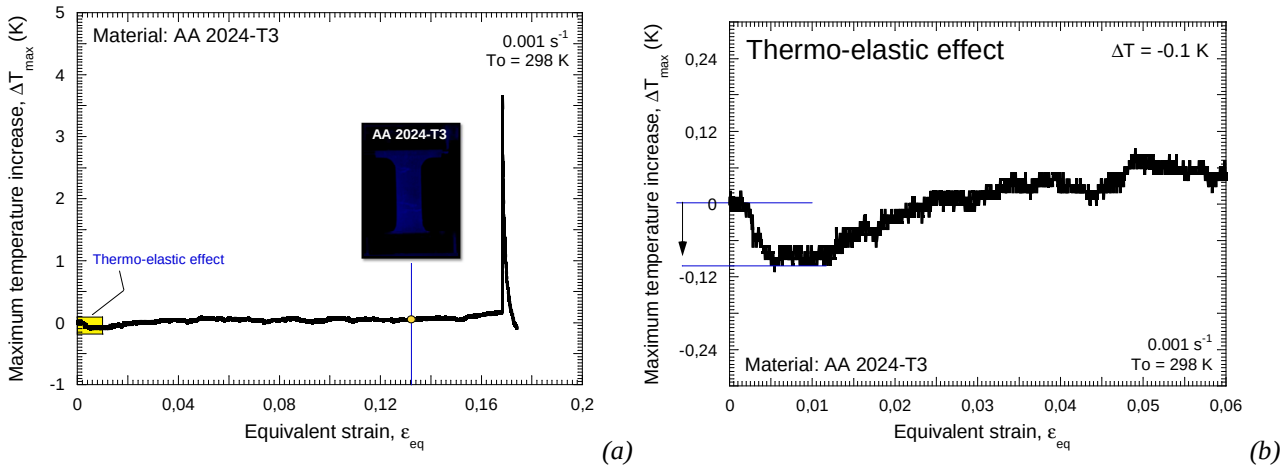

(a) *(b)*

*Fig. 4.37. (a) Temperature variation as a function of strain for **AA 2024-T3** and steel **AISI 304**. (b) Temperature decrease due to thermo elasticity.*

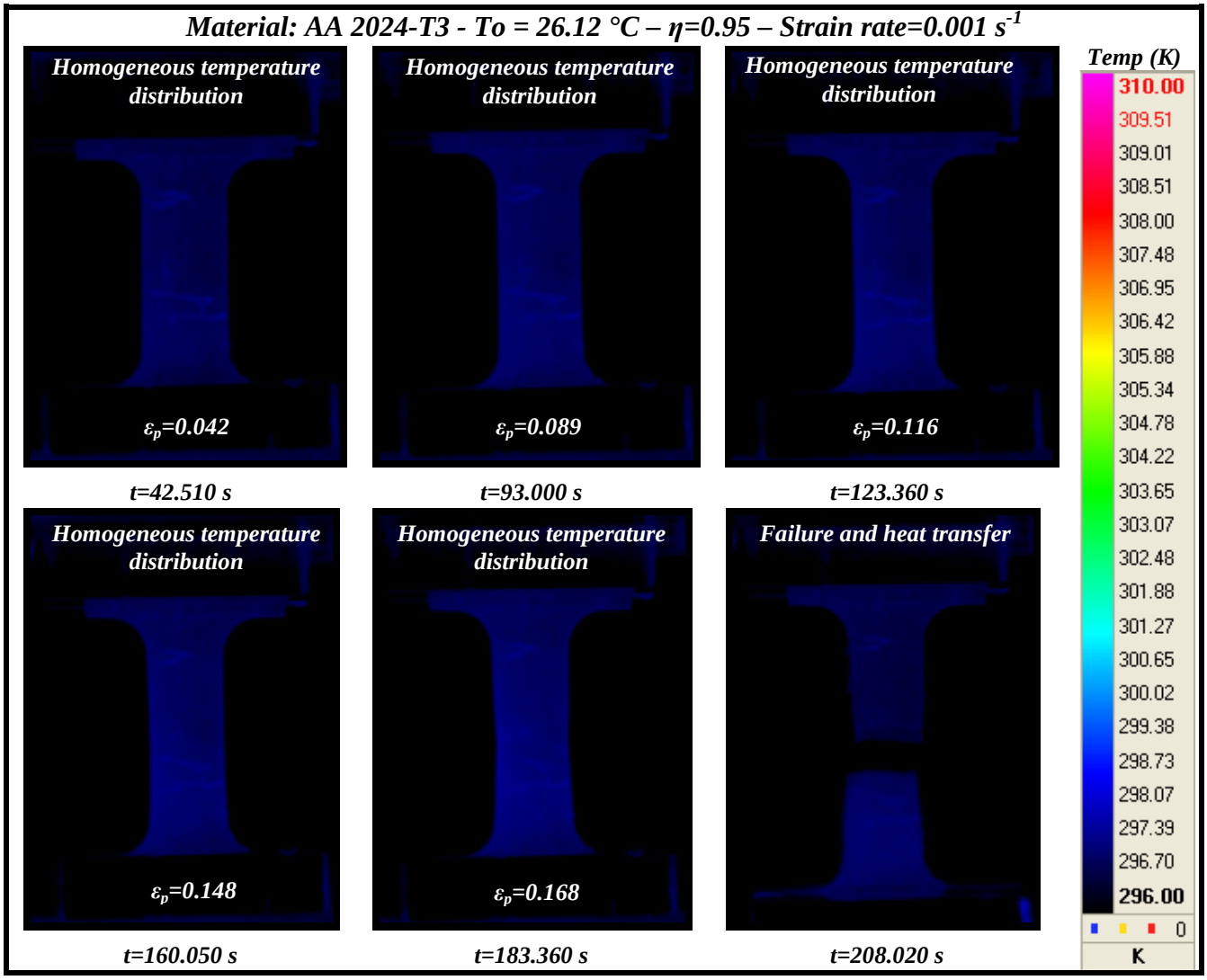

Fig. 4.38. Temperature contours during loading. Picture resolution 320×256 pixels.

Next, is shown the evolution of the material flow stress versus strain under different high loading rates, Fig. 4.39. It has to be highlighted that the material strain hardening is not being diminished with the deformation rate increase. Such characteristic is expected to provide to this alloy of good performance under dynamic events like crash or impact as it will be analyzed later in this document.

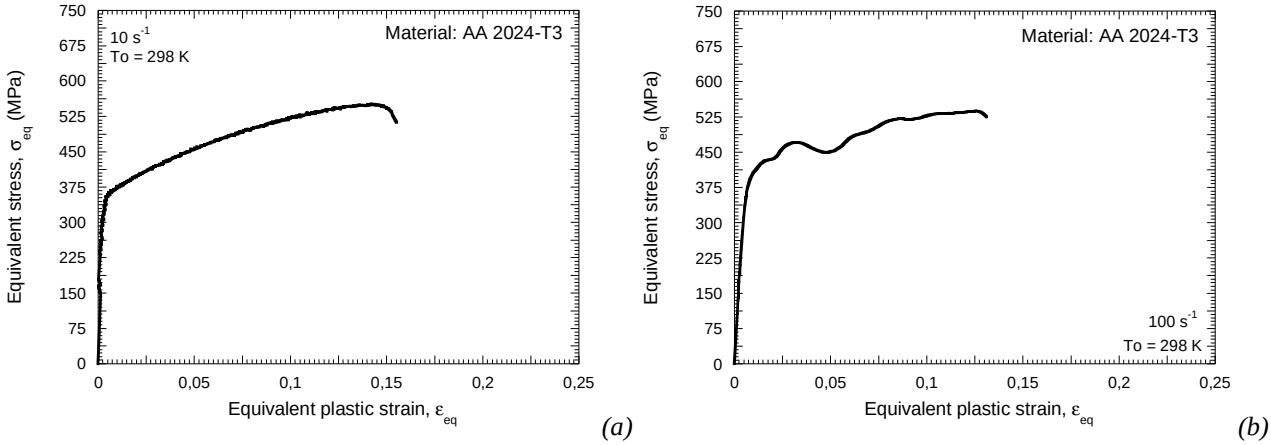

Fig. 4.39. Flow stress evolution versus plastic strain for different strain rates at room temperature.

In Fig. 4.40. is illustrated the flow stress evolution as a function of strain rate for different plastic strain values. The **AA 2024-T3** shows quite reduced *(and almost linear)* rate sensitivity in the range $0.001\ s^{-1} \leq \dot{\bar{\varepsilon}}^p \leq 10\ s^{-1}$. Such behaviour is in agreement with the observations reported in [Kumar et al. 1968, Follansbee 1986, Regazzoni et al. 1987, Rusinek and Rodríguez-Martínez 2009, Rusinek et al. 2010] for **FCC** metals. Beyond that rate level the flow stress rate starts to increase, Fig. 4.40. As it was discussed in **Section 2.4.1.**, such behaviour is certainly related to the viscous drag effects. In **AA** drag regime uses to become operative within the range $100\ s^{-1} \leq \dot{\bar{\varepsilon}}^p \leq 1000\ s^{-1}$. Unfortunately during testing it was not possible to go beyond $\dot{\bar{\varepsilon}}^p = 200\ s^{-1}$. Due to low density and stiffness of the material *(in comparison with other metals like steel, copper or tantalum widely analyzed in the international literature)*, the recorded force/displacement signal was subjected to strong disturbances. It made impossible to obtain a proper description of the material behaviour within the range $\dot{\bar{\varepsilon}}^p \geq 200\ s^{-1}$. In future works it would be advisable to provide an accurate definition of the drag regime using, for example, direct impact shear tests [Klepaczko 1994].

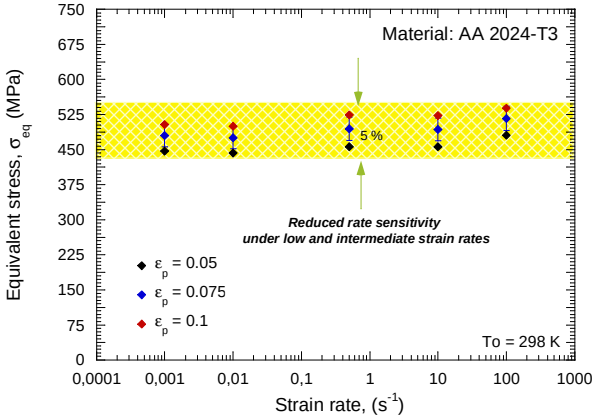

Fig. 4.40. Flow stress evolution versus strain rate for different plastic strain levels.

A remarkable characteristic of this alloy is the strong increase of the strain hardening with the temperature decrease, Fig. 4.41. It means that the temperature sensitivity is dependent on plastic strain *(and therefore the rate sensitivity is dependent on plastic strain)*. Because of that, the ductility of the material seems to be improved at low initial temperatures *(within the range of temperatures considered in this work, 223 K < T_0 < 373 K)*, Fig. 4.41. It is obvious that such behaviour makes this alloy of main interest for aeronautical applications in which the service temperature is usually within the range $213\ K \leq T_0 \leq 293\ K$.

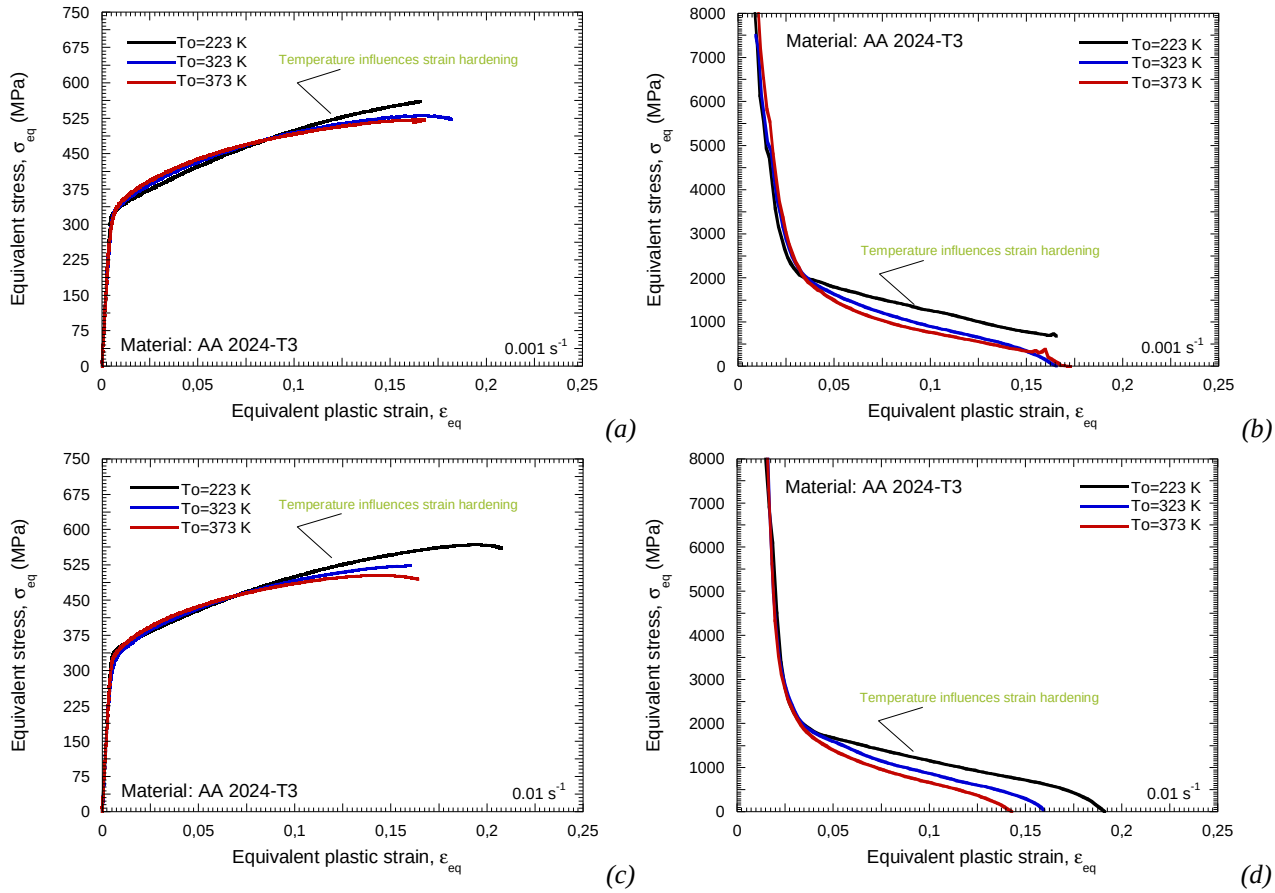

Fig. 4.41. (a) – (c) Flow stress evolution versus plastic strain for different strain rates and initial temperatures. (b) – (d) Strain hardening evolution versus plastic strain for different strain rates and initial temperatures

Based on previous considerations, the thermo-viscoplastic behaviour of the **AA 2024-T3** is modeled using the extended **MRK** model to viscous drag effects.

4.3.2 Constitutive relation for the aluminium alloy 2024-T3

Following the procedure detailed in **Section 2.3.2** and **Section 2.4.2.2** the following material constants for calibration of the extended **MRK** model to dislocations drag effects are obtained, Tables 4.4-4.5.

Y (MPa)	B_0 (MPa)	ν (-)	n_0 (-)	D_2 (-)	ξ_2(-)	ξ_1(-)	T_m (K)	$\dot{\varepsilon}_{min}$ (s^{-1})	$\dot{\varepsilon}_{max}$ (s^{-1})	θ^* (-)
300	1000.2	0.07023	0.4805	0.0292	0.00845	0.001159	900	10^{-5}	10^{7}	0.9

*Table 4.4. Constants determined for **AA 2024-T3** for thermal and athermal components of the **MRK** model.*

χ (MPa)	α (-)
286.7	0.00005368

*Table 4.5. Constants determined for **AA 2024-T3** for the viscous drag component of the **MRK** model.*

The predictions of the constitutive description fit properly flow stress and material strain hardening from low to high loading rates, Fig. 4.42.

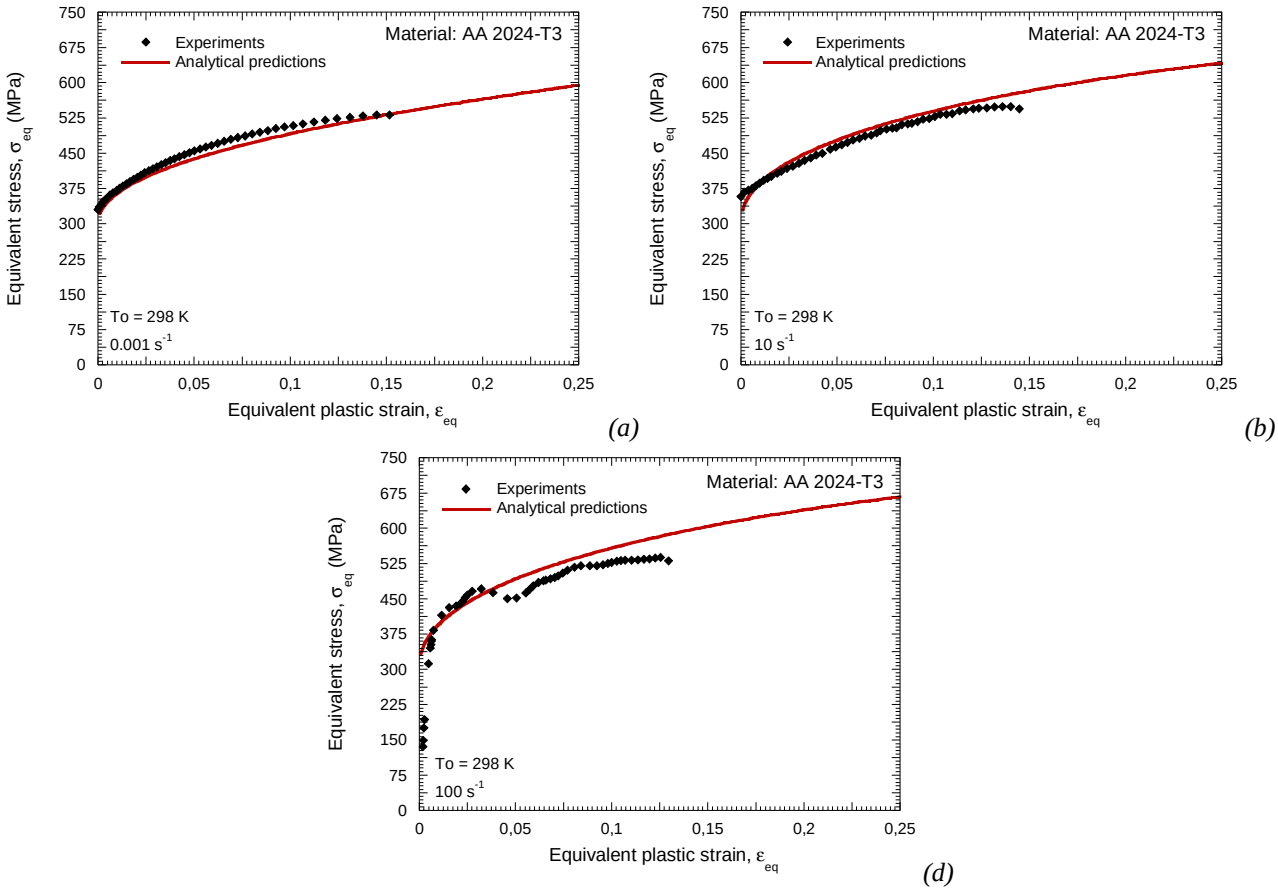

Fig. 4.42. Flow stress evolution versus plastic strain for different strain rates at room temperature and comparison with analytical predictions.

Moreover, the rate sensitivity of the material is also well described by the model and only some uncertainties may take place at very high strain rates in the drag regime definition, Fig. 4.43. However, let us assume that well developed viscous drag effect takes place in this material in agreement with the considerations reported for **AA** in [Kumar et al. 1968, El-Magd 1994, El-Magd and Abouridouane 2006].

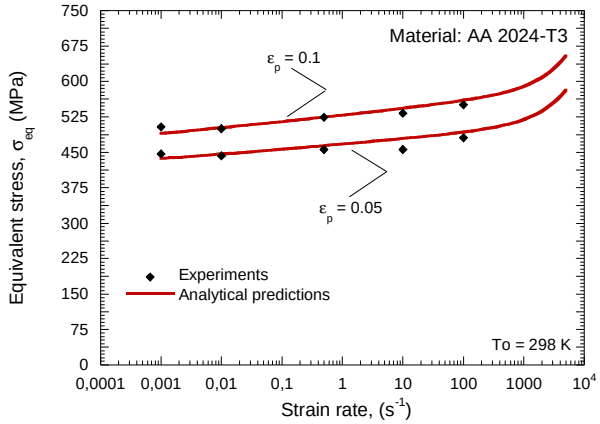

Fig. 4.43. Flow stress evolution versus strain rate for different plastic strain levels at room temperature and comparison with analytical predictions.

Moreover, it is remarkable that the model exhibits the capability for describing the strain hardening variations due to initial temperature effect, Fig. 4.44. As it was previously mentioned, this fact is of main relevance for aeronautical applications where this alloy is widely used.

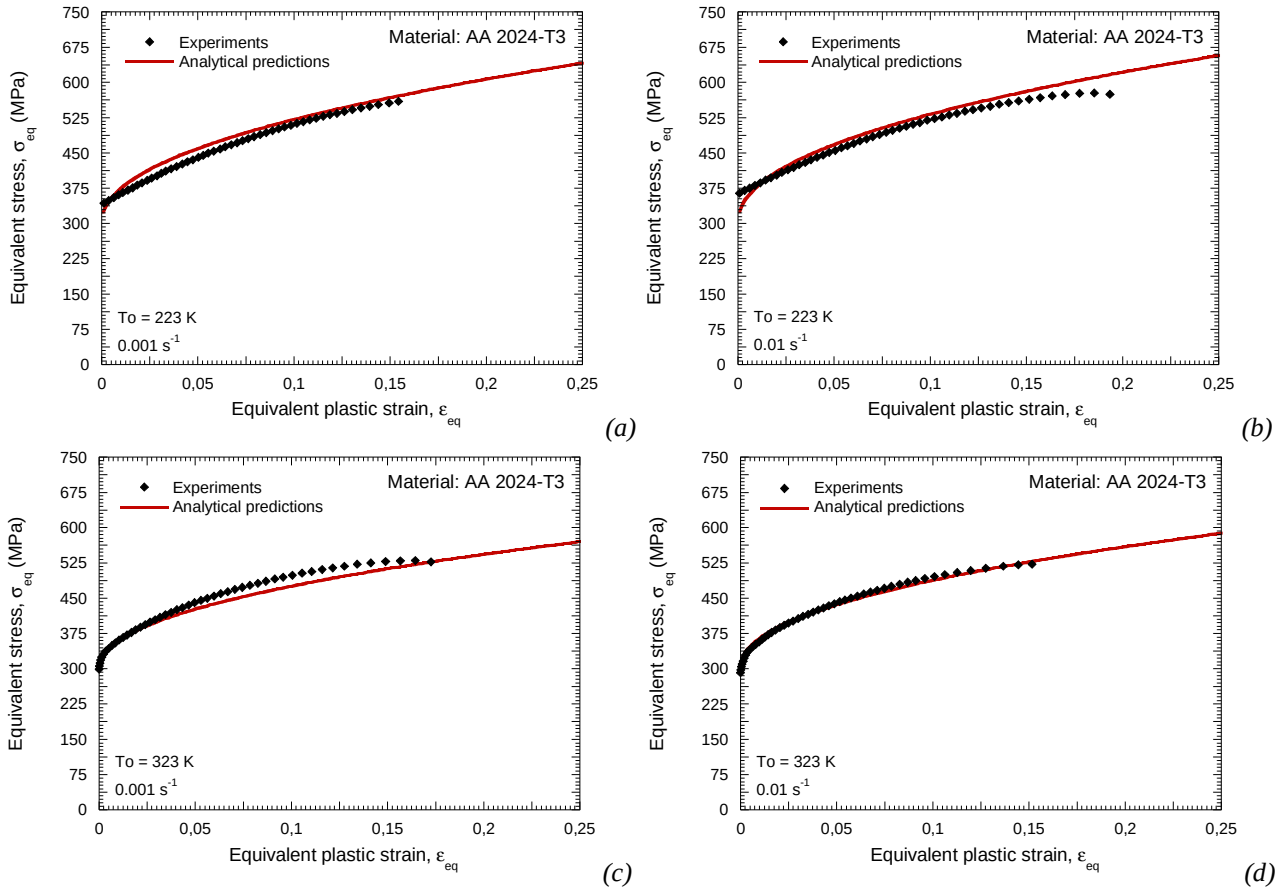

Fig. 4.44. Flow stress evolution versus plastic strain for different strain rates and temperatures and comparison with analytical predictions.

The experimental facilities used to conduct the perforation tests are described below.

4.3.3 Experimental procedure for perforation of metallic sheets

Two different experimental setups have been used for analyzing the impact behaviour of **AA 2024-T3** sheets. High velocity impact tests were conducted using the experimental technique described in **Section 4.2.3.1** Additionally; low velocity impact tests were conducted using a drop weight tower. It allows for low temperature testing, which is consistent with the application field of this alloy.

4.3.3.1 The drop weight tower

In order to conduct low velocity perforation tests a drop weight tower has been used [Sánchez-Sáez et al. 2007], Fig. 4.45. It allows for perpendicular impact on the metallic sheets within the range of impact velocities 0.5 m/s $\leq V_0 \leq$ 4.5 m/s. Since the mass of the impactor is chosen by the user, a wide range of impact energies can be covered. The drop weight tower has a climatic chamber, allowing variation of the testing temperature, T_0 = 288 K and T_0 = 213 K. A thermocouple was connected to a temperature controller regulating the opening of an electrovalve, which allowed a controlled volume of liquid nitrogen to enter the chamber. Thus, the testing temperature can be accurately defined by the user.

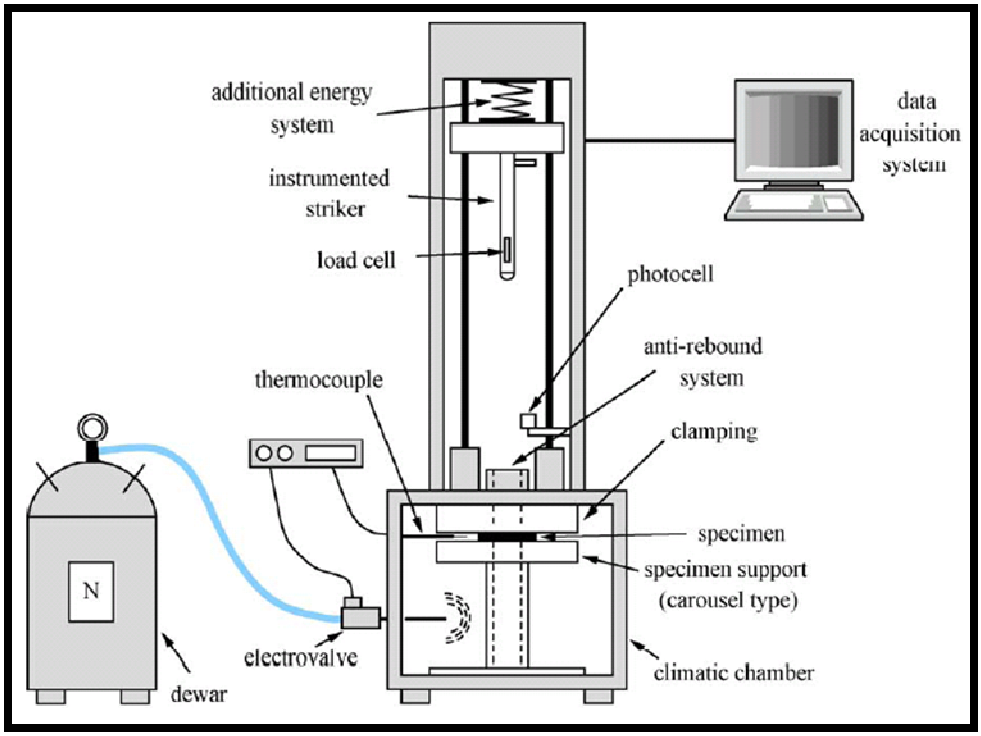

*Fig. 4.45. Schematic representation of the drop weight tower (**UC3M**) [Gomez-del Río et al. 2005].*

The tested square specimens presented a size of $A_t = 100\times100$ mm^2 and a thickness of h = 1 mm. They were clamped by screws all around the active surface of $A_a = 80\times80$ mm^2. The screws were symmetrically fixed in order to not disturb the test, Fig. 4.46. The device used to clamp the metallic sheets had a transparent side made of **PMMA.** Such an arrangement allowed filming the perforation process using a high speed camera.

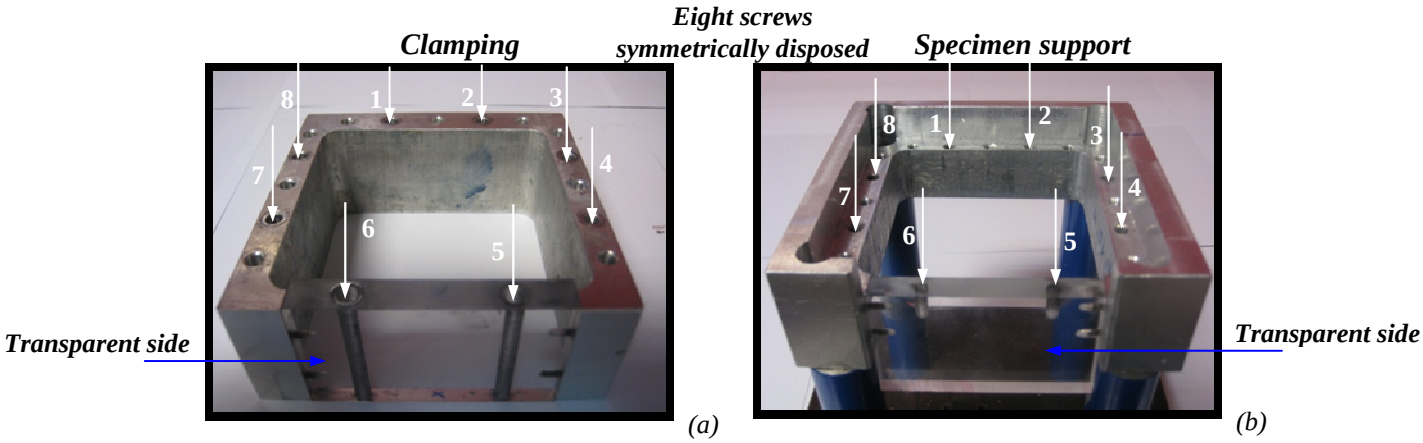

Fig. 4.46. Experimental device used to clamp the specimen during perforation tests (Design: S. Puerta and J. Puerta). (a) Clamping, (b) Specimen support.

The steel striker used has a conical shape, Fig. 4.47., its larger diameter is φ_p = 20 mm and its mass M_{imp} = 0.105 kg. After machining, the striker was oil quenched, thereby increasing the yield stress of the material up to $\sigma_y \approx 1.0$ GPa. It permitted to avoid its damage or erosion during perforation, Fig. 4.47.

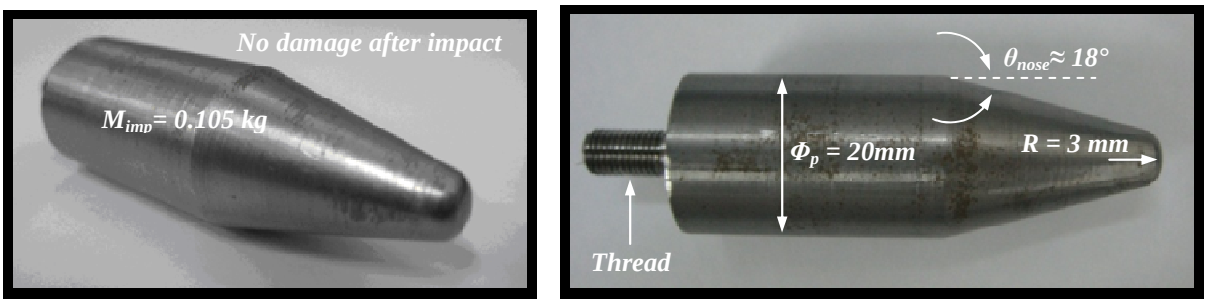

Fig. 4.47. Conical striker used during perforation tests (Design: S. Puerta and J. Puerta).

The striker was attached to the instrumented bar of the drop weight tower, whose mass was M_{bar} = 0.761 kg. Additional mass was added to the setup for a final value M_{total} = 18.787 kg *(for a final range of impact energy 59 J ≤ E_i ≤ 190 J).* A load cell placed on the striker enabled to record the force versus time signal. The velocity and the displacement of the striker during perforation can be obtained by integration of the force-time history [Santiuste et al. 2010]. After impact *(if there was no perforation of the plate),* an anti-rebound system held the striker to avoid multi-hits on the specimen.

The post-mortem measurement of the targets-deflection was conducted using a laser device following the experimental technique developed by Varas [Varas 2009]. The laser is coupled to an articulated beam which is aligned with the plates. Then the laser is connected to a voltmeter which provides a voltage depending on the distance laser/plate. Taking as reference the undeformed border of the metallic sheet is possible to know the displacement suffered by the target due to the impact. Details of this technique are given in [Varas 2009].

4.3.3.2 The pneumatic cannon

The description of the facilities used to conduct *(and analyze)* the high velocity impact tests was already carried out in **Section 4.2.3.1**

4.3.4 Analysis of the perforation process

Next the impact behaviour of the **AA 2024-T3** sheets is examined.

4.3.4.1 The drop weight tower tests

In this section of the document are presented the results obtained using the drop weight tower setup.

4.3.4.1.1 Test at room temperature

In order to estimate accurately the ballistic limit value, the residual velocity is compared to the initial velocity, Fig. 4.48. Residual velocity value is assumed as the speed of the striker corresponding to the failure time. Failure time is considered as the velocity for which the projectile pierces the target and ballistic limit is taken as the maximum speed of the striker for which no crack is generated in the plate. The fitting of the data depicted in Fig. 4.48. exhibits the characteristic shape of the curves obtained from perforation processes [Borvik et al. 1999, Borvik et al. 2002a, Gupta et al. 2006, Gupta et al. 2007, Gupta et al. 2008, Arias et al. 2008, Rusinek et al. 2008b, Klepaczko et

al. 2009]. The ballistic limit value obtained from the experiments performed at room temperature is $V_{bl}\big|_{T_0=288\ K} \approx 0.8$ m/s , Fig. 4.48.

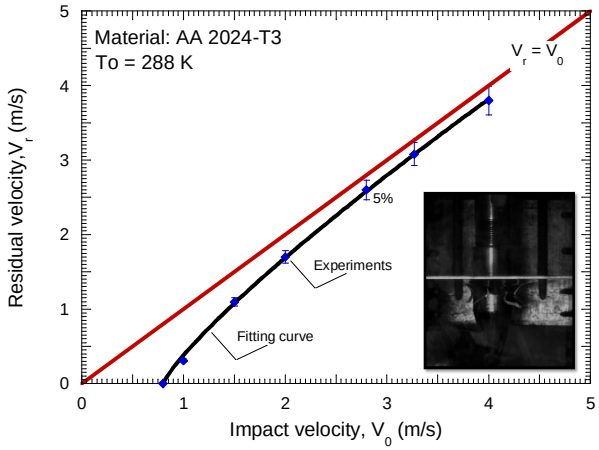

Fig. 4.48. Residual velocity versus impact velocity at room temperature.

For the range of impact velocities considered, the mechanisms involved in the perforation process do not vary with the initial velocity in a relevant way. The slope of the curve force/striker displacement $\partial F/\partial \delta_s$ remains approximately constant regardless of the impact velocity, Fig. 4.49. However the failure of the target $\partial F/\partial \delta_s = 0$ takes place for larger striker displacement as the impact velocity increases, Fig. 4.49.

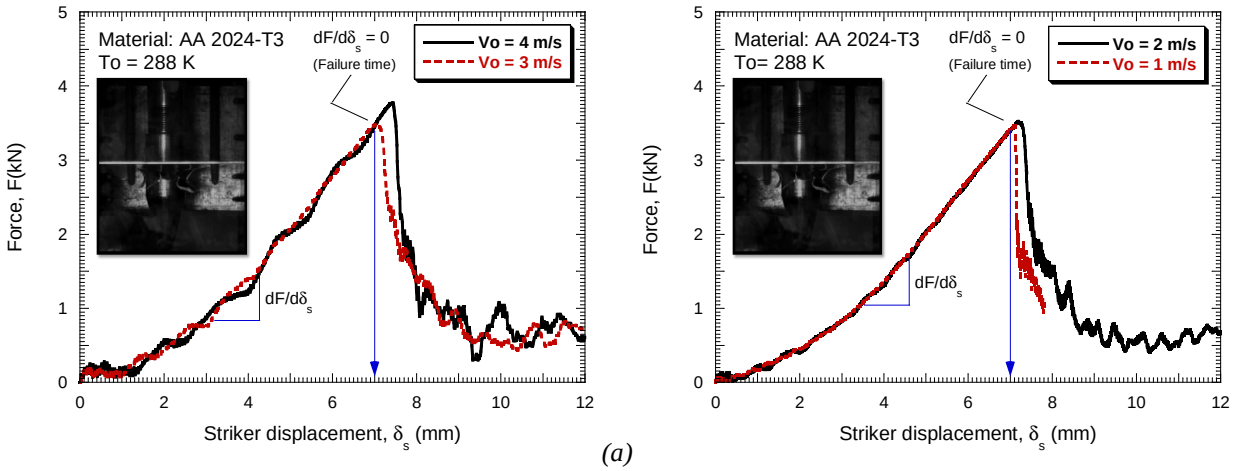

Fig. 4.49. Evolution of the impact force as a function of the striker displacement for different impact velocities at room temperature.

The material increases its capability of absorbing energy with the augment of the impactor velocity. Such effect of the impact velocity *(and therefore of the increasing strain rate)* on the energy absorbed by the target enhances the applicability of this material for building structures in charge of bearing dynamic solicitations. Larger bending effect is observed with the impact velocity increase, Fig. 4.50.

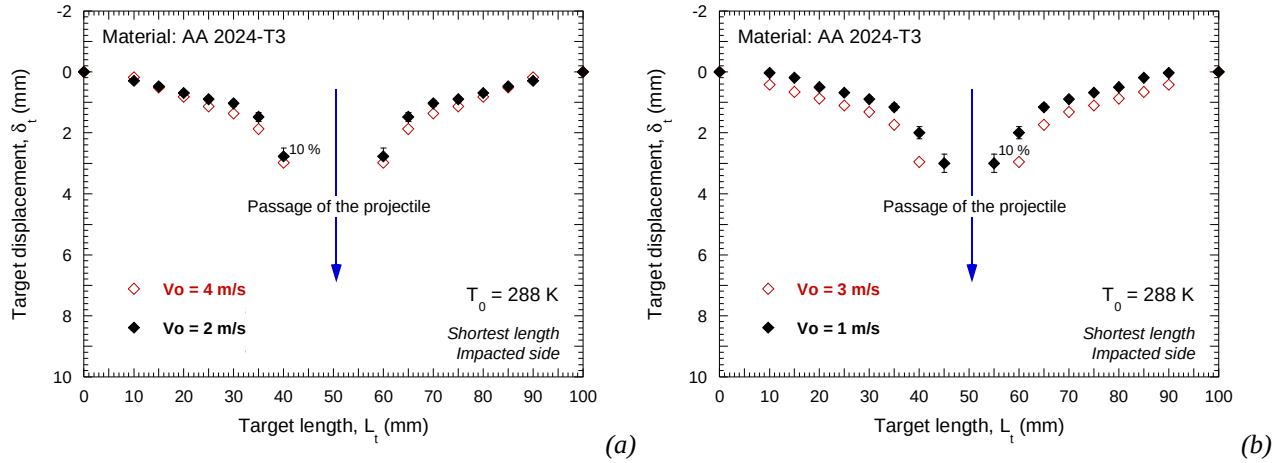

Fig. 4.50. Permanent bending of the target for different impact velocities at room temperature.

The analysis of the post-mortem specimens reveals that *petalling* is the recurring failure mode for all the perforation tests, Figs. 4.51-4.52. It has been noticed that neither the rolling direction nor boundary conditions influence the initiation or the propagation of cracks. The number of main petals occurring for each test oscillates between four and five, Figs. 4.51-4.52. The appearance of four or five petals is consistent with the observations reported in [Landkof and Goldsmith 1993, Wierzbicki 1999]. This number corresponds to a minimum of total rate of energy dissipation. A larger number of petals would be expected for initial velocities out of the range of impact velocities applied in the present study, [Rodríguez-Martínez et al. 2008, Rusinek et al. 2009a]. For impact velocities higher than a specific value, the energy lost by a projectile quickly increases. This is a consequence of the influence of inertia effects in the mechanisms of perforation. The perforation process becomes less efficient.

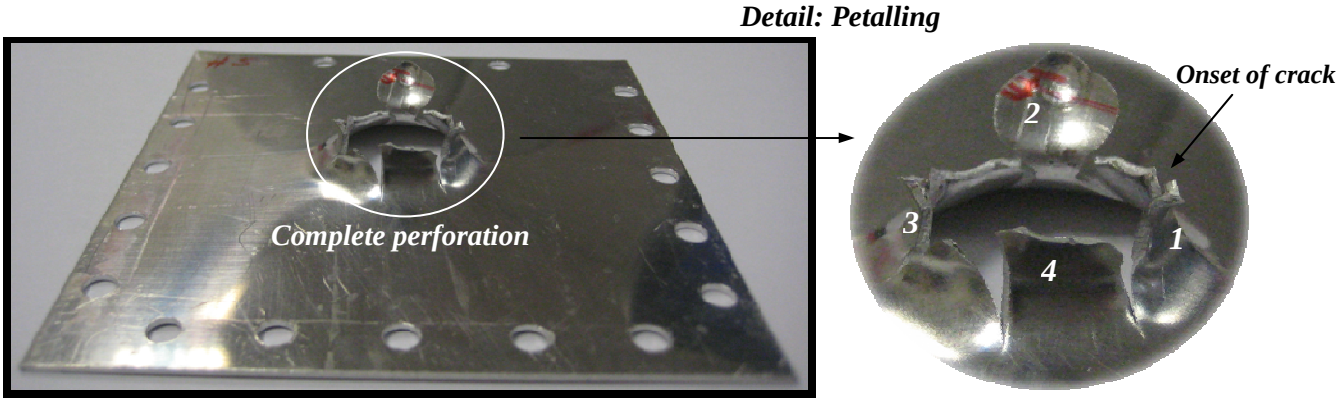

Fig. 4.51. Petalling failure mode for V_0 = 2.0 m/s and T_0 =288K.

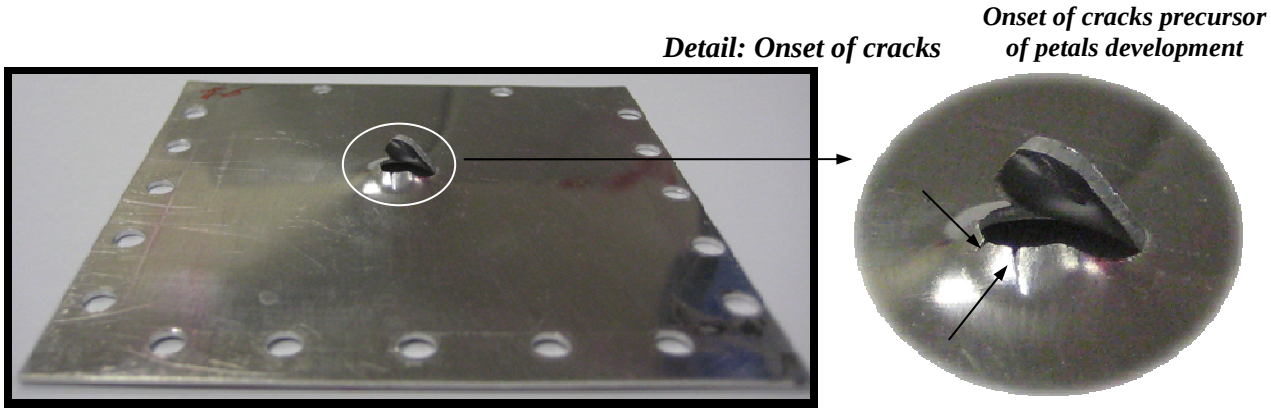

Fig. 4.52. Petalling failure mode for V_0 = 1.0 m/s and T_0 =288K.

Petalling is caused by the reduced thickness of the target and by the conical shape of the striker [Landkof and Goldsmith 1993, Wierzbicki 1999, Rodríguez-Martínez et al. 2008, Rusinek et al. 2009a]. At the beginning of loading, the deformation is localized in the small area corresponding to the interface projectile/plate, Fig. 4.54-a. That area of the target is strongly deformed and bent until failure time, Fig. 4.54-a. When the failure time is reached, several small cracks are generated at the dome of the interface projectile/plate, Fig. 4.53 - 4.54-b. Those cracks propagate until they reach the rear side of the plate due to the circumferential strain induced in the target by the passage of the striker, Fig. 4.53-4.54-c-d.

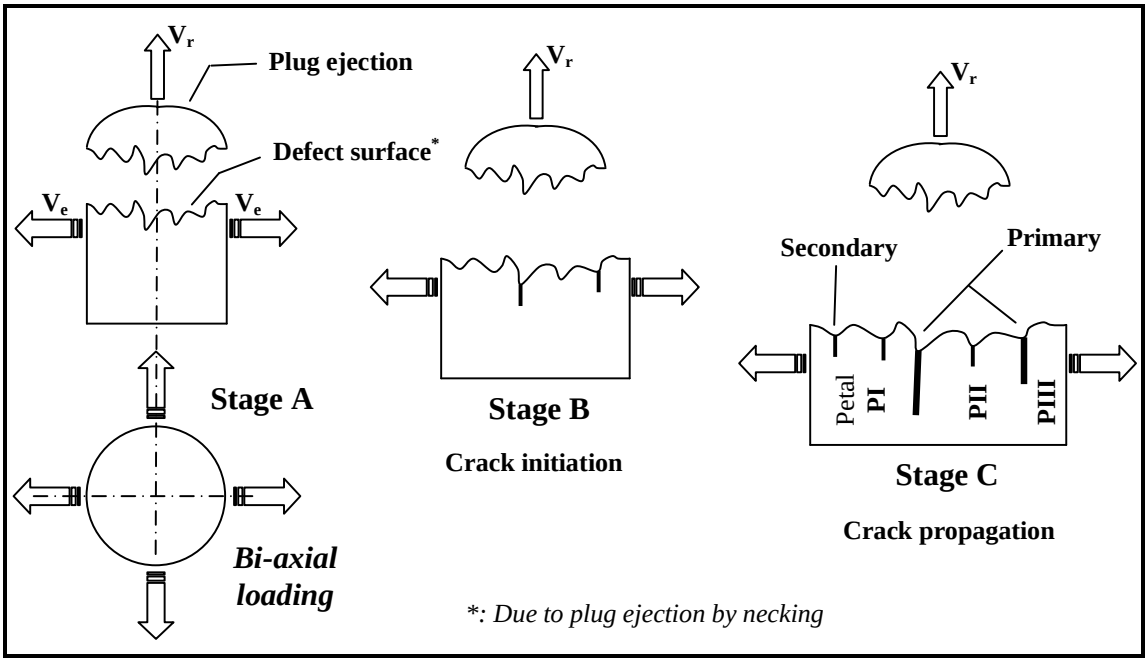

Fig. 4.53. Schematic representation of petalling formation during perforation of metallic sheets by hemispherical projectiles [Rusinek et al. 2009a].

As a consequence, several petals are formed, Figs. 4.53-4.54. These observations are in agreement with the experimental evidences and the numerical estimations reported by [Landkof and Goldsmith 1993, Wierzbicki 1999, Lee and Wierzbicki 2005, Rodríguez-Martínez et al. 2008, Rusinek et al. 2009a, Rodríguez-Martínez 2010].

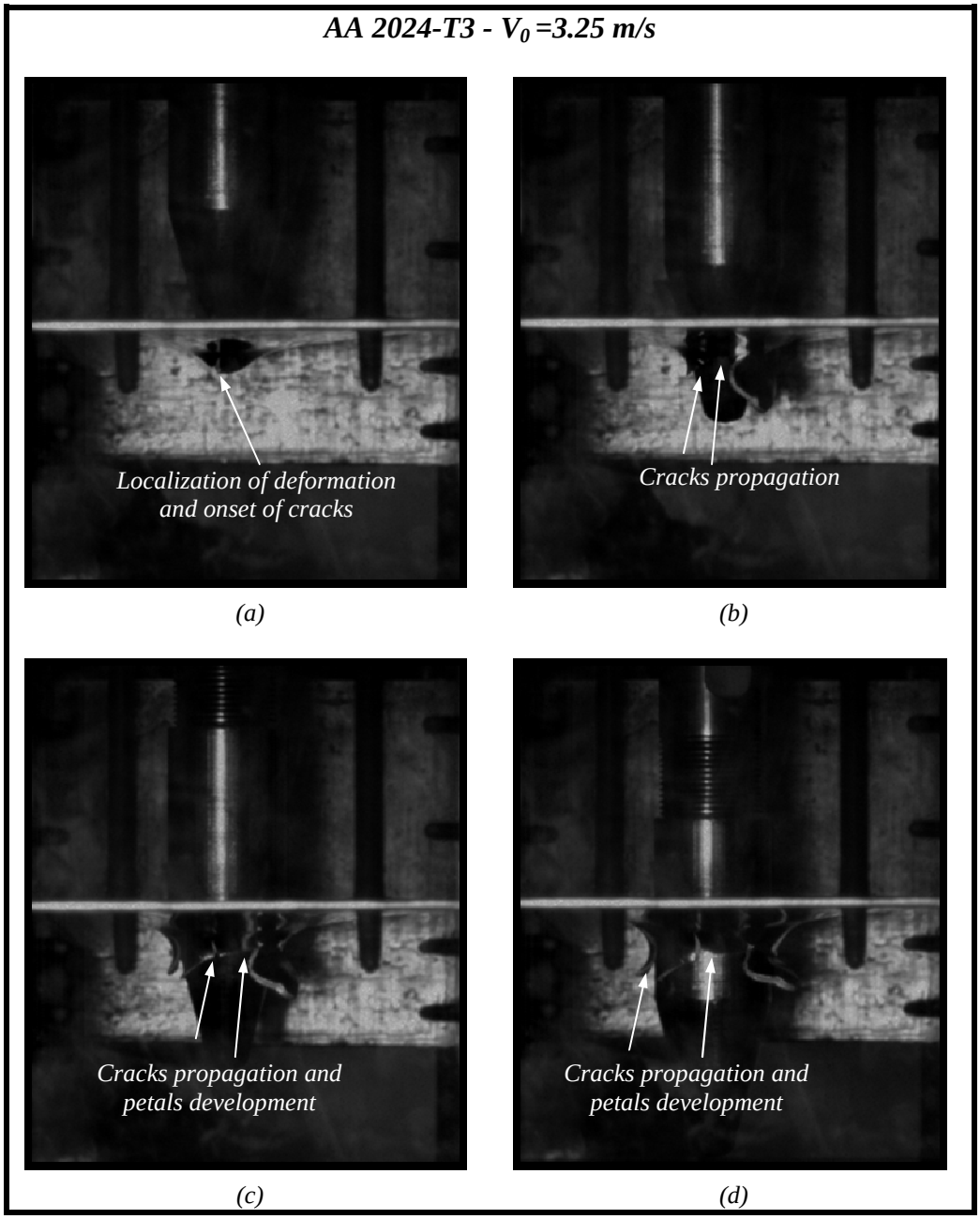

Fig. 4.54. Different stages of the perforation process for V_0=3.25 m/s and T_0=288K. (a) Localization of deformation and onset of cracks. (b) Cracks progression and generation of petals. (c) Development of petalling. (d) Complete passage of the impactor and petalling failure mode.

Next, it is analyzed the effect of testing temperature in the material response.

4.3.4.1.2 Test at low temperature

In this section of the document the effect of the initial temperature on the perforation process is studied. The tests performed at T_0 = 288 K are compared to those conducted at T_0 = 213 K. It must be noted that before testing at low temperature, the aluminium sheets *(already clamped and screwed)* were subjected to the testing temperature for 20 minutes *(as mentioned before, high thermal conductivity of the material leads to small exposition time for achieving thermal equilibrium with surrounding temperature)*. Such a period of time was considered as suitable in order to reach thermodynamic equilibrium material-target/testing-temperature.

The first observation concerns the failure mode of the target. No influence of the initial temperature on the perforation mechanisms has been observed for the whole range of impact velocities considered. The final stage of the perforation process is the development of petals, Figs. 4.55-4.56.

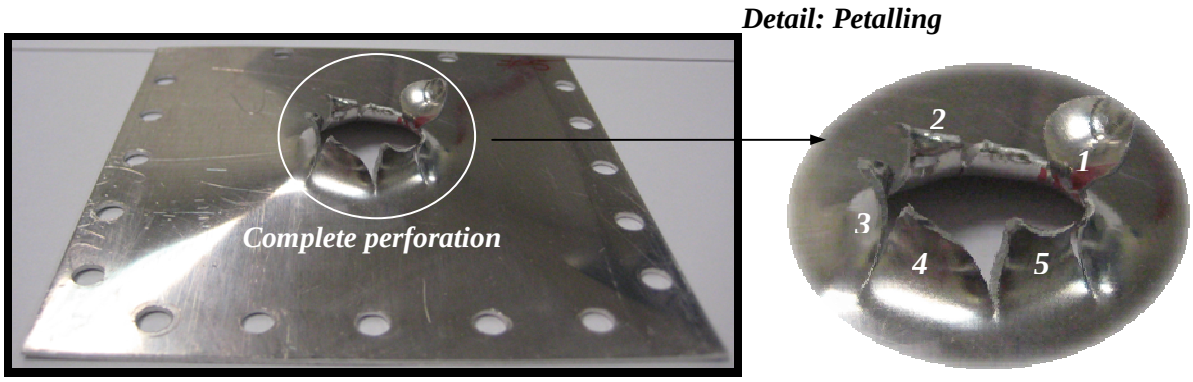

Fig. 4.55. Petalling failure mode for V_0 = 4.0 m/s and T_0 =213K.

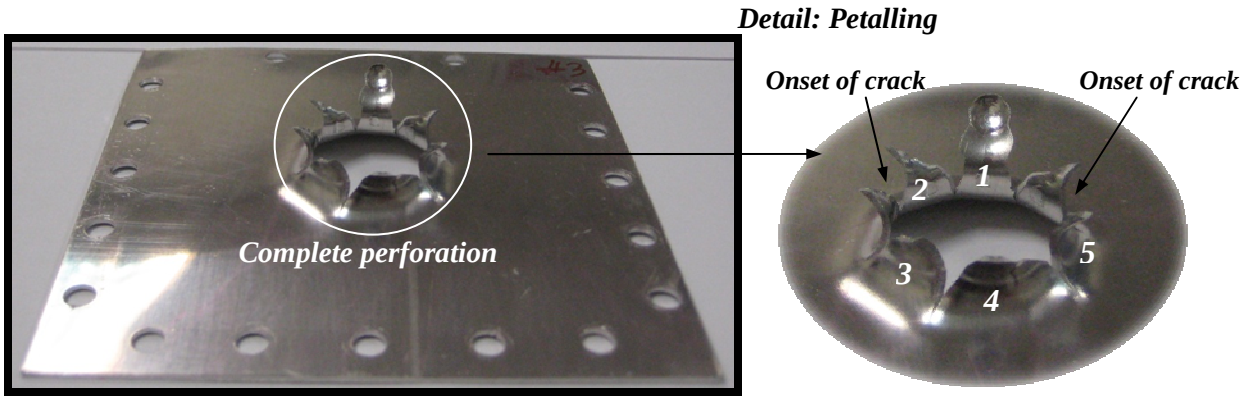

Fig. 4.56. Petalling failure mode for V_0 = 2.0 m/s and T_0 =213K.

However, the difference occurs with the energy absorbed by the target, Fig. 4.57. At low temperature the target absorbs approximately 20 % more of energy than at room temperature, Fig. 4.57.

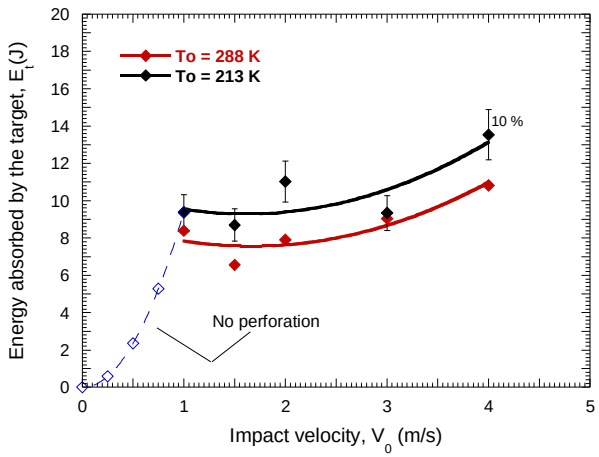

Fig. 4.57. Energy absorbed by the target as a function of the impact velocity for different initial temperatures.

At low temperature the ballistic limit is increased from $V_{bl}\big|_{T_0=288\ K} \approx 0.8$ m/s to $V_{bl}\big|_{T_0=213\ K} \approx 1.1$ m/s . In the case of V_0 = 1 m/s and T_0 = 213 K the striker does not generate any crack in the target, Fig. 4.58. However, it was observed in Fig. 4.52. that for the same impact velocity and T_0 = 288 K several cracks, precursor of *petalling*, took place.

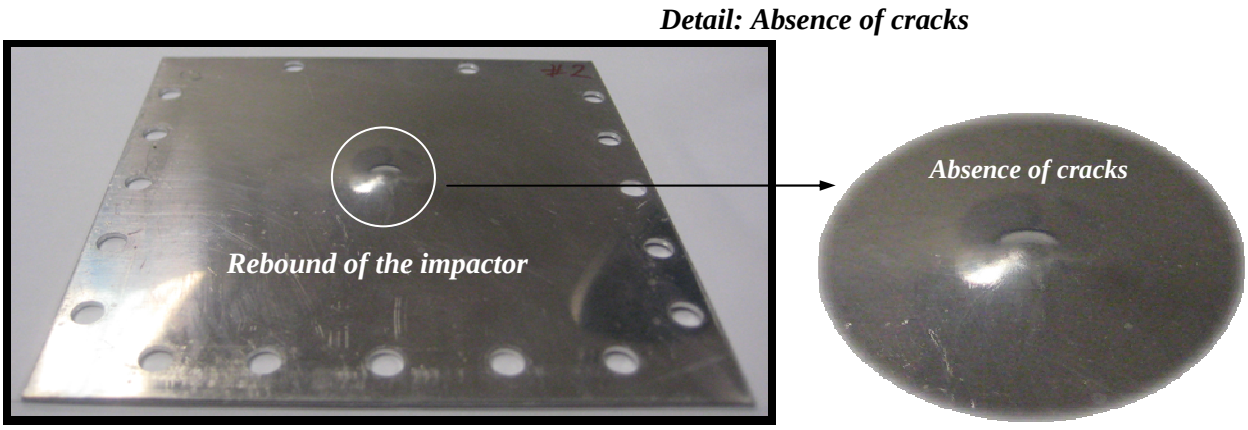

Fig. 4.58. Absence of cracks for V_0 = 1.0 m/s and T_0 =213K.

Permanent bending of the impacted specimens is greater at low temperature for the whole range of impact velocities tested, Fig. 4.59. In the case of T_0 = 213 K the target absorbs a larger amount of energy in the form of plastic work. The material seems to increase its ductility with the decrease of the initial temperature as it was already mentioned *(at least for this range of testing temperatures)*, Fig. 4.59. Such observation is reflected in the force/striker displacement evolution.

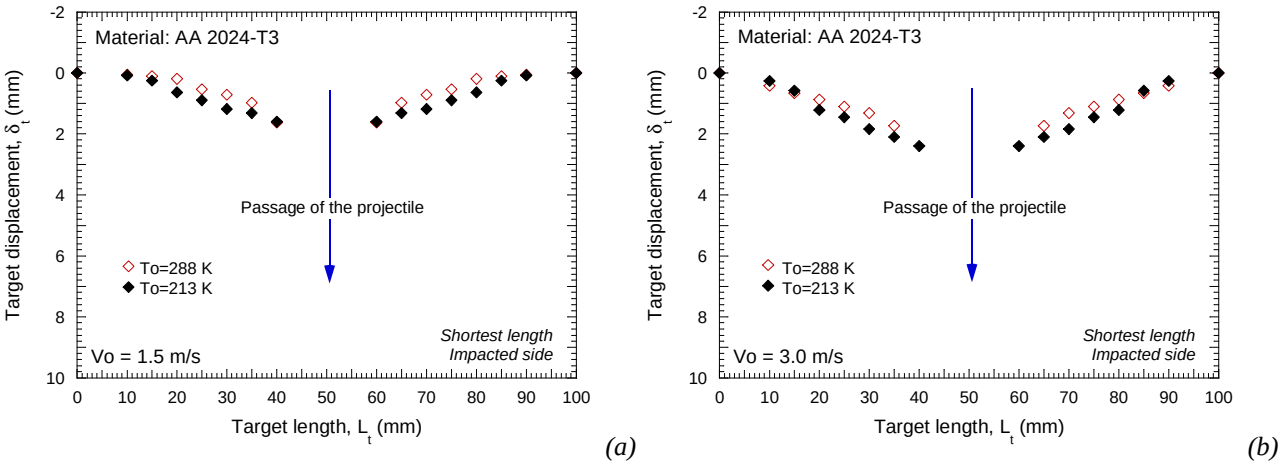

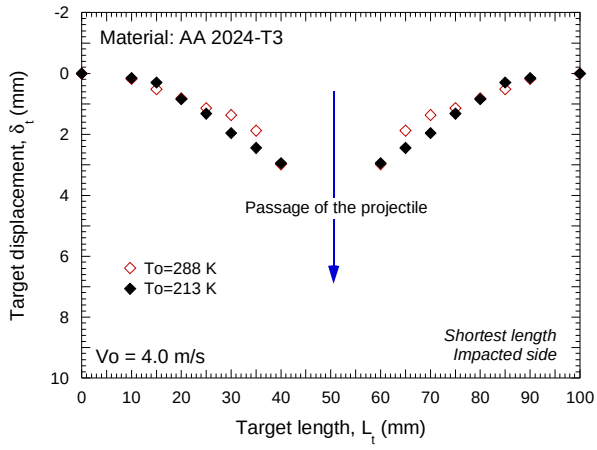

(c)

Fig. 4.59. Permanent bending of the target for different impact velocities and initial temperatures

For the highest impact velocities, Fig. 4.60-a-b, the force level for both initial temperatures is superimposed until target failure in the case of T_0 = 288 K takes place. As the impact velocity gets closer to the ballistic limit, in the case of T_0 = 213 K the slope of the curve force/striker displacement becomes reduced delaying target failure, Fig. 4.60-c.

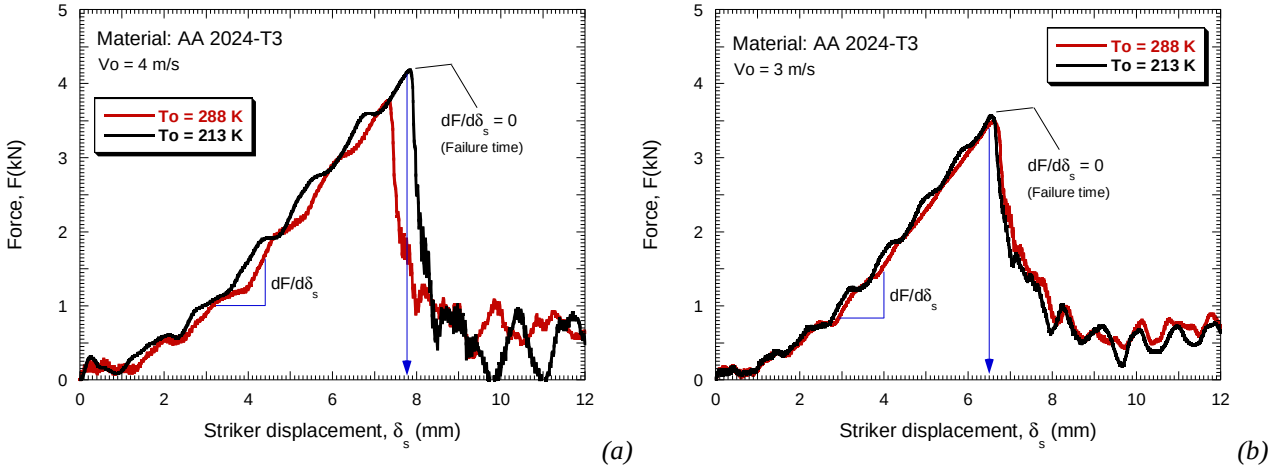

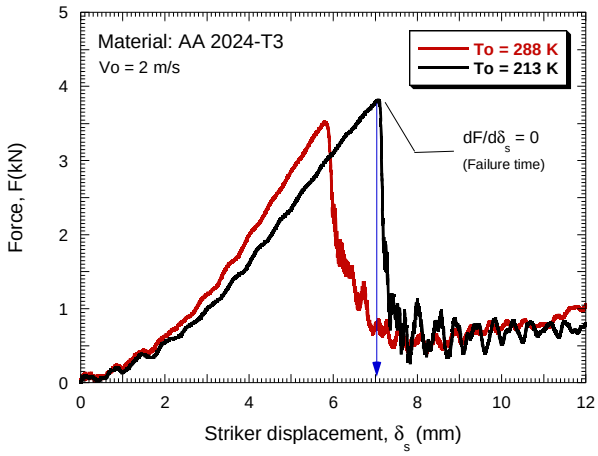

(c)

Fig. 4.60. Evolution of the force as a function of the striker displacement for different impact velocities and initial temperatures.

From this analysis seems clear the suitability of **AA 2024-T3** for mechanical applications requiring of service conditions at low temperature.

Next, it is examined the behaviour of this alloy under perforation at higher impact velocities using the pneumatic cannon configuration already introduced in **Section 4.2.3.1.**

4.3.4.2 The pneumatic cannon tests

Experiments within the range of impact velocities 10 m/s < V_0 < 45 m/s are conducted. The ballistic limit found from the tests is $V_{bl} \approx 25$ m/s. This value is quite lower than that reported for the steel **ES** *($V_{bl\text{-}ES} \approx 40$ m/s)*. However it must be taken into account that the **AA 2024-T3** plates absorb more energy than the **ES** steel sheets per unit of material density, $V_{bl\text{-}AA\ 2024\text{-}T3}/\rho > V_{bl\text{-}ES}/\rho$.

In Fig. 4.61. are shown final stages of the impact process for different initial impact velocities. Necking failure is visible in the case of impact velocities close to the ballistic limit Figs. 4.61-a-b. Onset of cracks takes place along the necking zone, Fig. 4.61-a-b. In the case of impact velocity well above the ballistic limit, Fig. 4.61-c. those cracks have propagated radially resulting in petals formation, Fig. 4.61.

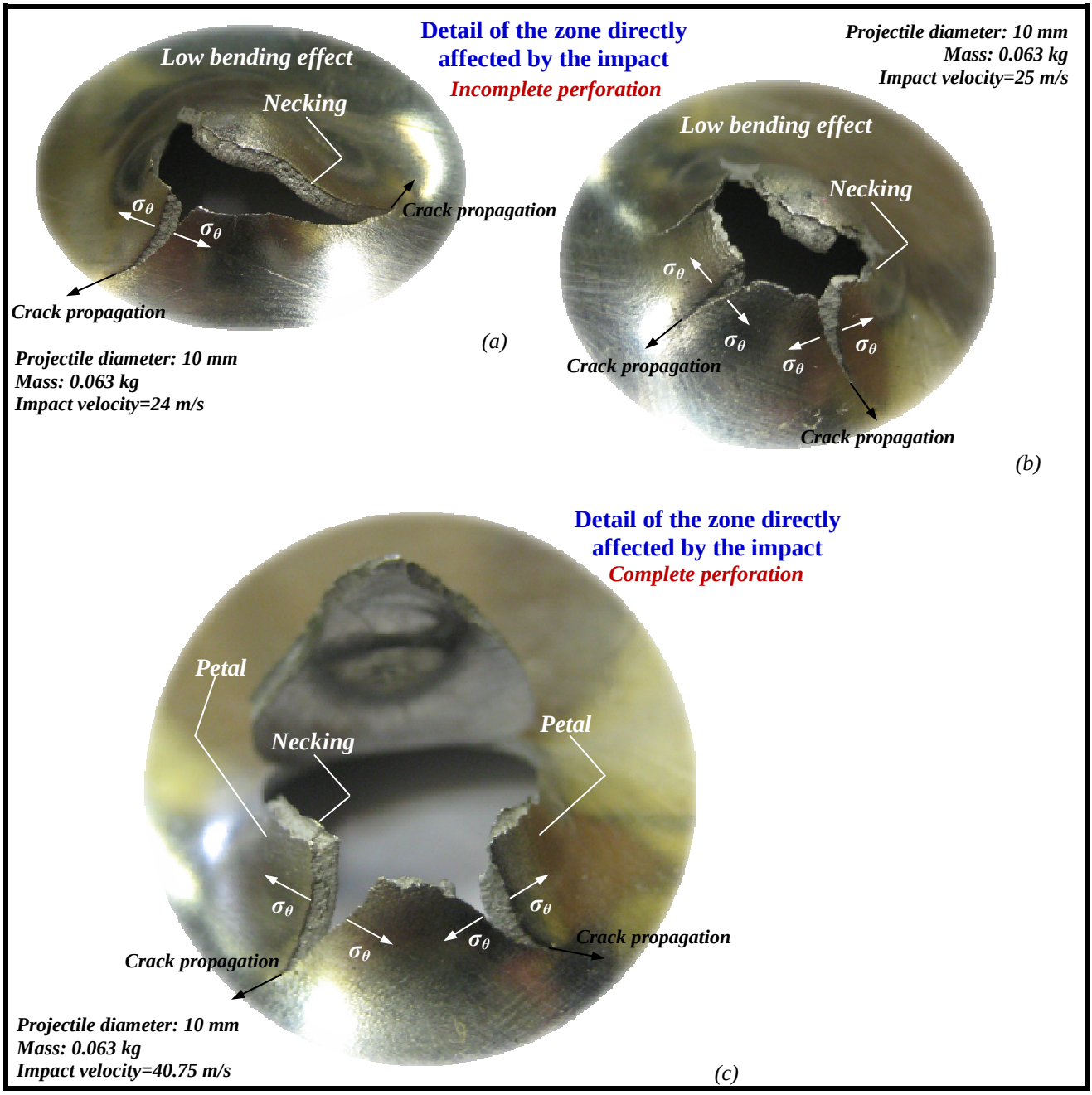

Fig. 4.61. Final stage of the impact process for initial velocities above the ballistic limit.

However differences with the failure mode observed for the **ES** steel sheets are reported. In the case of **AA 2024-T3** deflection of the sheets at failure is much more reduced, Figs. 4.62-4.63. Such behaviour limits the radial sliding along the contact-zone projectile/plate during perforation. Material stretching and subsequent necking takes place far from the dome of the contact projectile/target. Thus, the cracks ocurring in the necking zone have short distance to cover until they are arrested on the rear side of the target. Petals formed have limited length.

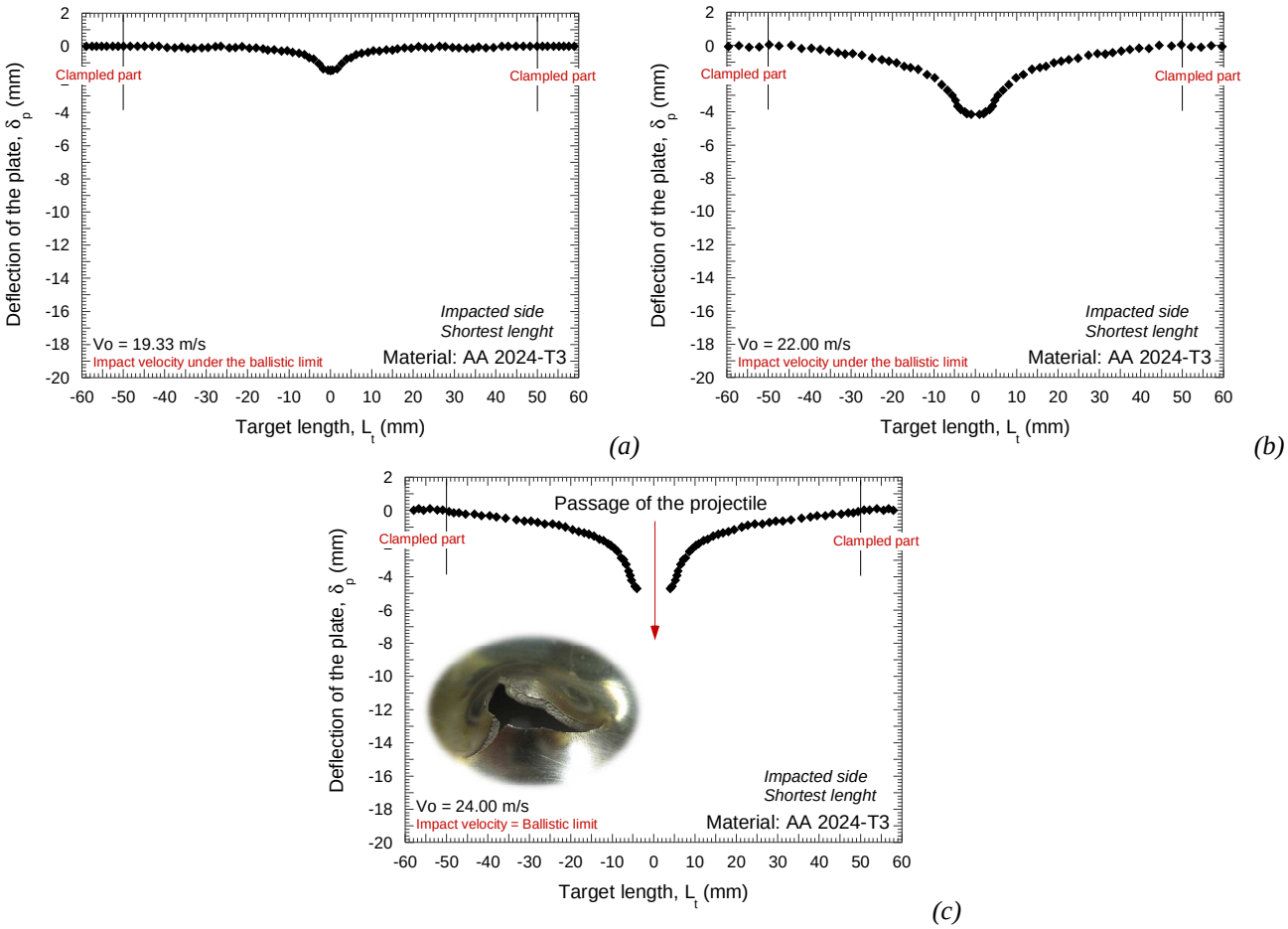

Fig. 4.62. Post-mortem deflection of the target for different initial impact velocities.

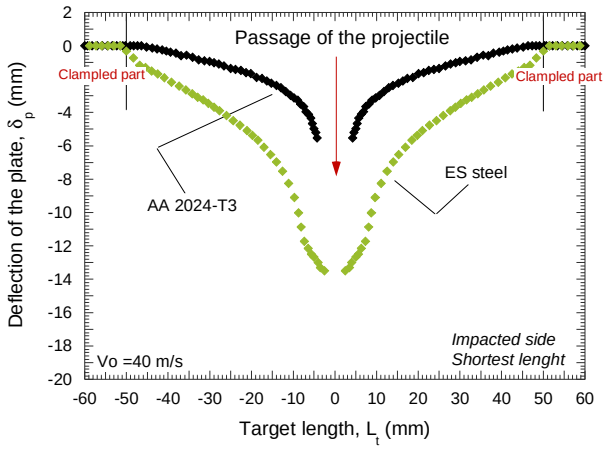

*Fig. 4.63. Post-mortem deflection of the target for **AA 2024-T3** and steel **ES** for $V_0 \approx 40$ m/s.*

Next, numerical simulations of the impact process are conducted.

4.3.4.2.1 Numerical analysis of the impact process

The numerical configuration used is that already presented in **Section 4.2.4.3.3.** The failure strain of the material has been estimated in $\varepsilon_f^p = 0.4$. Such value is obtained following the procedure reported in [Rusinek and Zaera 2007] and according to the experimental observations reported by [Bao and Wierzbicki 2004] for similar a **AA**.

From the numerical estimations the ballistic limit found is $V_{bl} \approx 27$ m/s, Figs. 4.64-4.65. Such value is a bit larger than that obtained from experiments. However the difference $\Delta V_{bl} = V_{bl\text{-numerical}} - V_{bl\text{-experimental}} \approx 2$ m/s can be assumed in complex dynamic events like high velocity perforation.

Moreover, the failure mode of the target predicted by the simulations is in agreement with the experimental observations. The localization process takes place since the beginning of loading along the whole contact-area projectile/plate, Figs. 4.64-4.65. Petals development is the final stage of the perforation process.

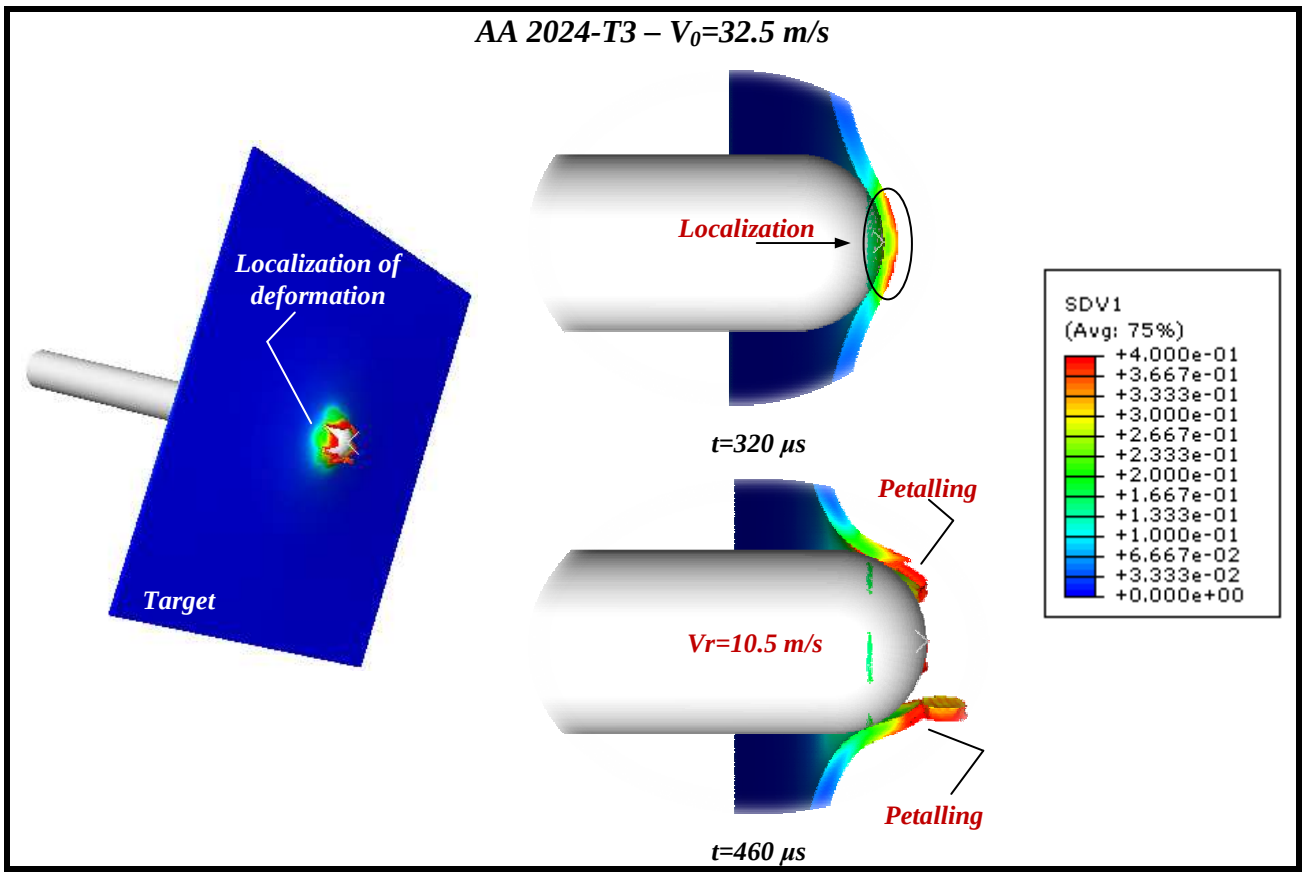

Fig. 4.64. Numerical estimations of plastic strain contours during impact, V_0 = 32.5 m/s.

From the simulations it has been observed that the maximum temperature increase in the material is approximately $\Delta T_{max} \approx 90$ K, Fig. 4.65. It is located in the petals zone. Such value is much lower than that experimentally measured *(and numerically predicted)* in the case of the **ES** steel. That is consistent with the different behaviours of both metals.

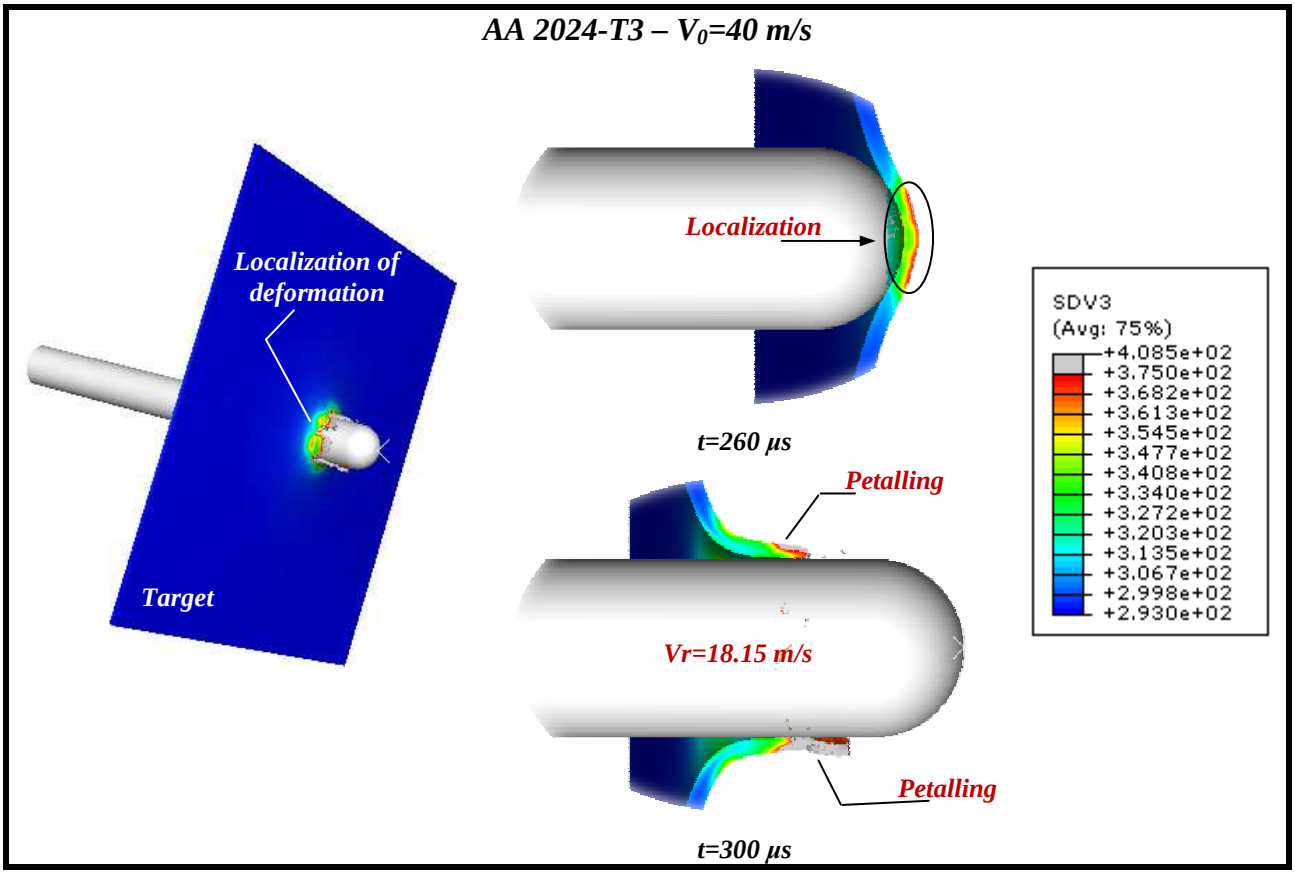

Fig. 4.65. Numerical estimations of temperature contours during impact, V_0 = 40 m/s.

The suitability of the numerical model used *(constitutive relation, failure criterion mesh configuration)* has to be highlighted.

This chapter dealt with the impact-perforation behaviour of two metallic alloys used for protection applications, mild steel **ES** and steel **AA 2024-T3**. These materials are thermo-mechanically characterized, analytically modeled and subjected to perforation by non-deformable projectiles. Their deformation mechanisms are tied to their answer under impact-perforation. Based on the constitutive relations developed in chapter 1, numerical models of the perforation test have been built. The numerical results obtained are in agreement with the experiments in terms of ballistic limit prediction and failure mode definition. Plastic instabilities formation and progression is revealed as the mechanism behind material failure in the impact tests.

CHAPTER 5

IMPACT BEHAVIOUR OF METALLIC ALLOYS WITH MARTENSITIC TRANSFORMATION FOR PROTECTION APPLICATIONS

Abstract

In this chapter of the Thesis the thermo-mechanical behaviour of two metallic alloys is examined, the steel **AISI 304** and the steel **TRIP 1000**. These metals show *martensitic* transformation under determined loading conditions. It makes them attractive for many engineering applications, especially for building structural elements responsible for absorbing energy under impact loading. The thermo-viscoplastic characterization of the materials is conducted and discussed. In addition, different experimental setups for perforation of metallic sheets have been used in order to provide a proper description of the thermo-mechanical processes taking place under impact. X-ray diffraction technique is used to determine the potential *martensitic* transformation taking place during loading.

5 CHAPTER 5. IMPACT BEHAVIOUR OF METALLIC ALLOYS WITH MARTENSITIC TRANSFORMATION FOR PROTECTION APPLICATIONS

5.1 Introduction

In the last decades, manufacturers have tried to minimize the production time and costs, while improving the properties and the quality of the products. This is also the case for important economic sectors like the automobile, naval or civil industries, which have invested substantial efforts in developing new generations of steels for light-weight structures capable of bearing strong mechanical and thermomechanical loading. In order to fulfil these objectives, new alloys with high strength, ductility and toughness have been developed. Among them, the high strength **TRIP** steels have become of great relevance.

As discussed in **Section 2.6.** and **Section 3.4.** this type of steels show *martensitic* transformation from **FCC** *austenite (γ)* to **BCC** *martensite (α')* under determined loading conditions strongly dependent on strain, strain rate and temperature. This transformation phenomenon is desirable during impact loading since it increases the strength and ductility of the material retarding plastic localization as described by [Fischer et al. 2000, Delannay et al. 2008, Curtze et al. 2009, Da Rocha and Silva de Oliveira 2009, Jiménez et al. 2009] and extensively discussed in chapter 3 of this Thesis.

Thus, the **TRIP** steels are nowadays in widespread use in the automotive industry, for example in crash-box structures, bumpers or side pannels. These components are responsible for absorbing the kinetic energy during a crash or accident and may be subjected to dynamic loading during their service life. However, most of the works available in the open literature are restricted to the study of *martensitic* transformation phenomenon under quasi-static loading [Bouaziz and Guelton 2001, Al-Abbasi and Nemes 2003, Bouaziz et al. 2008, Curtze et al. 2009]. The transformation mechanisms under high strain rate have been rarely studied. The potential appearance of *martensitic* transformation under real service conditions is not clear in many cases.

In this chapter of the Thesis the thermo-mechanical behaviour of two metallic alloys is examined, the steel **AISI 304** and the steel **TRIP 1000**. These metals show strain induced *martensitic* transformation under determined loading conditions. It makes them attractive for many engineering applications, especially for building structures responsible for absorbing energy under impact loading. The thermo-viscoplastic characterization of the materials is conducted and discussed. In addition, different experimental set-ups for perforation of metallic sheets have been used in order to provide a proper description of the thermo-mechanical processes taking place under impact. X-ray diffraction technique is used todetermine the potential *martensitic* transformation taking place during loading. The role that *martensitic* transformation plays in the absorption of energy during the perforation process is extensively discussed.

5.2 Impact behaviour of steel AISI 304

In this part of the document the impact behaviour of the steel **AISI 304** is examined. First, it is conducted a thermo-mechanical characterization of the material. Then, it is modelled using the extended **RK** model to viscous drag effects. Based on such understanding of the material behaviour, perforation tests of **AISI 304** sheets are conducted. For that task two different experimental setups are used, a drop weight tower and a pneumatic gun. The results are compared with those previously reported for mild steel **ES** and **AA 2024-T3**.

5.2.1 Thermo-viscoplastic behaviour of the steel AISI 304

Steel **AISI 304** is the most versatile and most widely used stainless steel. It has excellent forming and welding characteristics. Extensively used in a variety of industries, its typical applications include pipelines, heat exchangers railings, springs or threaded fasteners. The application fields of the **AISI 304** make relevant the understanding of its thermo-viscoplastic behaviour under wide ranges of strain rate and temperature. The chemical composition of the material is given in Table 5.1.

C	**Mn**	**Cr**	**Ni**	**Mo**	**Cu**	**Si**	**Nb**
0.06	*1.54*	*18.47*	*8.3*	*0.30*	*0.37*	*0.48*	*0.027*

*Table. 5.1. Chemical composition of steel **AISI 304** (% weight) [De et al. 2006]*

On undeformed state its microstructure is constituted by 100 % of *austenite (it is not magnetic in the as-received state)*. **AISI 304** belongs to the type called high-alloy **TRIP** steels. They are *austenitic* steels containing large amount of alloying elements as **Cr** and **Ni**, improving pitting and corrosion resistance and controlling *martensitic* transformation. The *martensitic* transformation is basically ruled by the "Magee effect" [Magee 1966] as reported in [Delannay et al. 2008, Fischer et al. 2000, Leblond et al. 1989].

By means of dilatometry, the *martensite* starts temperature of this material has been determined lower than that corresponding to liquid nitrogen temperature, $M_s < 77$ K *(Unfortunately it was not possible to determine the value with precision for $T_0 < 77$ K)*. The *martensitic* transformation may take place under determined loading conditions. Identification of such loading conditions will provide valuable information for evaluation of the suitability of this material for absorbing energy under dynamic events. For that task the procedure outlined in the next section of the document is followed.

5.2.1.1 X-ray diffraction technique

X-ray diffraction technique **(XRD)** has been used in order to examine the potential *martensitic* transformation taking place in this material. It is a very efficient non-destructive technique that enables to determine accurately the volume fraction of each phase as well as the average stress in each one. Thus, two different goals are pursued:

- Measurement of the stress of the phases both during loading *(in situ tensile test are performed for that task)* and in the post-mortem specimens.

- Measurement of the *martensite* volume fraction in the post-mortem specimens.

XRD is based on Bragg's law that provides the condition for a plane wave to be diffracted by a family of lattice planes, Eq. 5.1.

$$2d_{hkl}.\sin\theta = n\lambda \qquad (5.1)$$

where d_{hkl} is the lattice plane spacing (*interreticular distance)* of a {hkl} plane family, θ is the incident Bragg angle, λ is the wavelength of the incident X-ray beam and *n* is an integer corresponding to the order of reflection, Fig. 5.1.

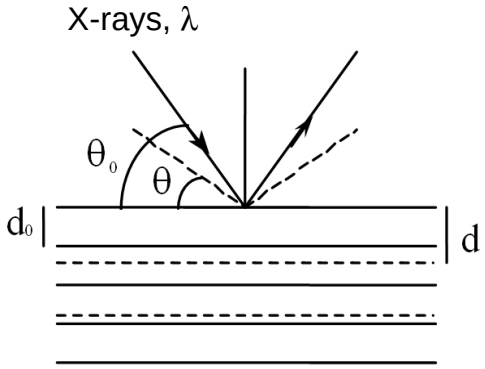

Fig. 5.1. Principle of X-ray diffraction (d_0 and θ_0 are respectively the lattice spacing and the Bragg angle corresponding to a stress free state).

When Bragg's law is satisfied, diffraction occurs and peaks of scattered intensity are observed.

5.2.1.1.1 Measurement of the stress of the phases

For stress determination, the classical $\sin^2\psi$ method has been used considering the lattice plane spacing d_{hkl} of a {hkl} plane family as an internal strain gauge [Hauk 1997, Inal et al. 2006]. Stress of the phases is determined on the surface of the specimens using a portable **PROTO** goniometer. It enables to analyze elaborately shaped parts since the sample stays fixed during the whole analysis *(the beam is moving around the specimen)*, Fig. 5.2.

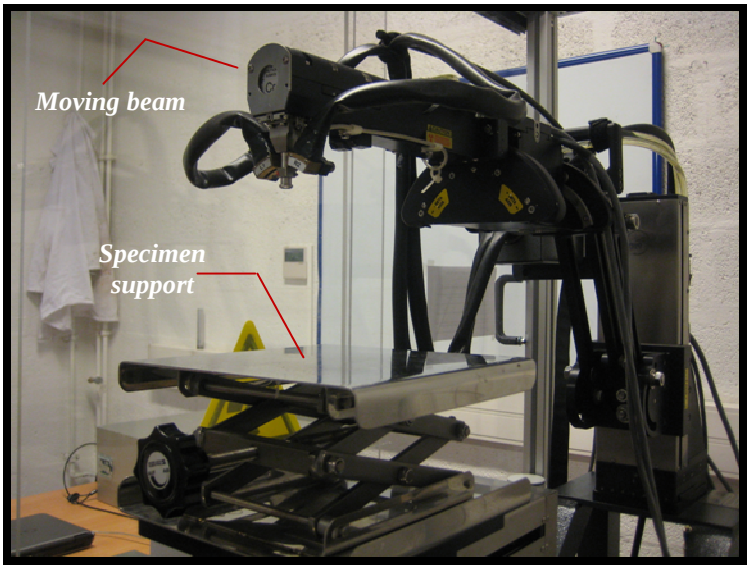

*Fig. 5.2. Portable **PROTO** goniometer used for **XRD** measurement (**ENSAM Metz**).*

The **BCC** phase *(martensite in **AISI 304**)* is analyzed by using a chromium anticathode (λ=2.2897Å); in order to obtain optimum results *(best accuracy)*, the analysis of the planes {211} corresponding to an angle 2θ =156.1° has been conducted.

The **FCC** phase *(austenite)* is analyzed by using a manganese anticathode (λ=2.102 Å); in order to obtain optimum results, the analysis of the planes {311} corresponding to an angle 2θ =151.0° has been conducted.

5.2.1.1.2 Measurement of the martensite volume fraction in the post-mortem specimens

The volume fraction of each phase has been calculated using a **SEIFERT XRD 3003 PTS** goniometer, Fig. 5.3., taking into account the intensity of diffraction peaks for both phases, *martensite* and *austenite*.

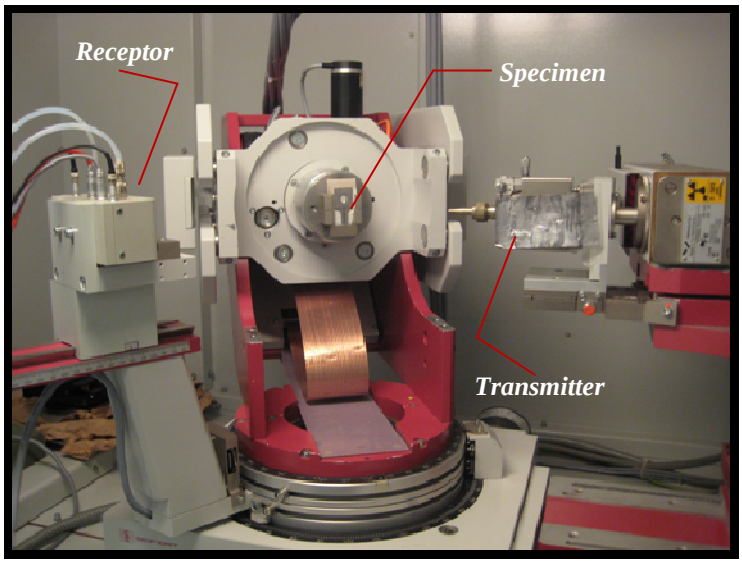

Fig. 5.3. Goniometer used for calculation of the martensite volume fraction (ENSAM/Metz).

In the case of **AISI 304**, a material containing two phases, the volume fraction of *martensite* is obtained from Eq. 5.2.

$$V_{\alpha'} = 1 \Big/ \left[1 + \left(I_{\gamma} / I_{\alpha'} \right) \cdot \left(\left(R_{\alpha'} / R_{\gamma} \right) \right) \right] \qquad (5.2)$$

where $I_{\alpha'}$ and I_{γ} are the intensity of the diffraction peaks for *martensite* and *austenite* respectively, $R_{\alpha'}$ and R_{γ} are coefficients depending on several parameters such as the absorption factor, the Lorentz polarisation factor, the multiplicity factor of the analysed planes families, the volume of the crystal lattices and others [Hauk 1997]. Furthermore, $V_{\alpha'} + V_{\gamma} = 1$. Both phases *(austenite and martensite)* were analyzed by using an iron anticathode (λ=1936 Å).

In the following section is conducted the thermo-mechanical characterization of this material. Two different experimental setups have been used for characterization of the thermo-viscoplastic behaviour of the material. Regular tensile tests under wide ranges of strain rate and temperature.

Unconventional in situ tensile tests for examination of the *martensitic* transformation under static loading at room temperature.

5.2.1.2 Tensile in-situ tests

In situ tensile tests are performed under quasi-static loading at room temperature. The specimen geometry and dimensions used during the tests are depicted in Fig. 5.4.

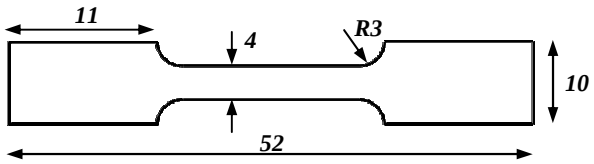

Fig. 5.4. Geometry and dimensions of the in situ tensile specimens.

The sample is mounted in a micro tensile machine originally developed in **ENSAM/Metz**, Fig. 5.5. Such reduced dimensions of the sample answer to the space constraints imposed by the testing technique. The testing machine is placed under the range of the **PROTO** goniometer. The longitudinal direction of the active part of the sample is aligned with the direction of the movement of the **PROTO** goniometer beam.

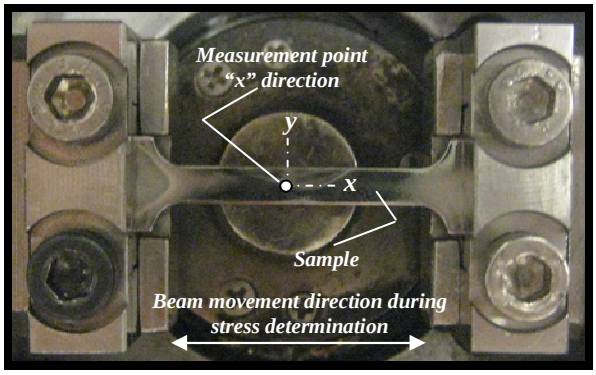

Fig. 5.5. Experimental setup for in situ test (ENSAM/Metz).

The first step is to compare the macroscopic stress-strain curve obtained from the experiments with results provided in the literature [Hecker et al. 1982, Tomita and Iwamoto 2001]. Satisfactory agreement is found from the comparison, Fig. 5.6. At room temperature and low loading rate the **AISI 304** shows an initial yield stress close to $\sigma\big|_{\bar{\varepsilon}^p=0} \approx 300\,\text{MPa}$, Fig. 5.6-a. This material possesses notable strain hardening which enhances material ductility. Strain hardening keeps approximately constant until determined value of plastic deformation is reached, $\bar{\varepsilon}^p \approx 0.25$, Fig. 5.6-b. Beyond that point the material flow stress sharply increases, Fig. 5.6-a.

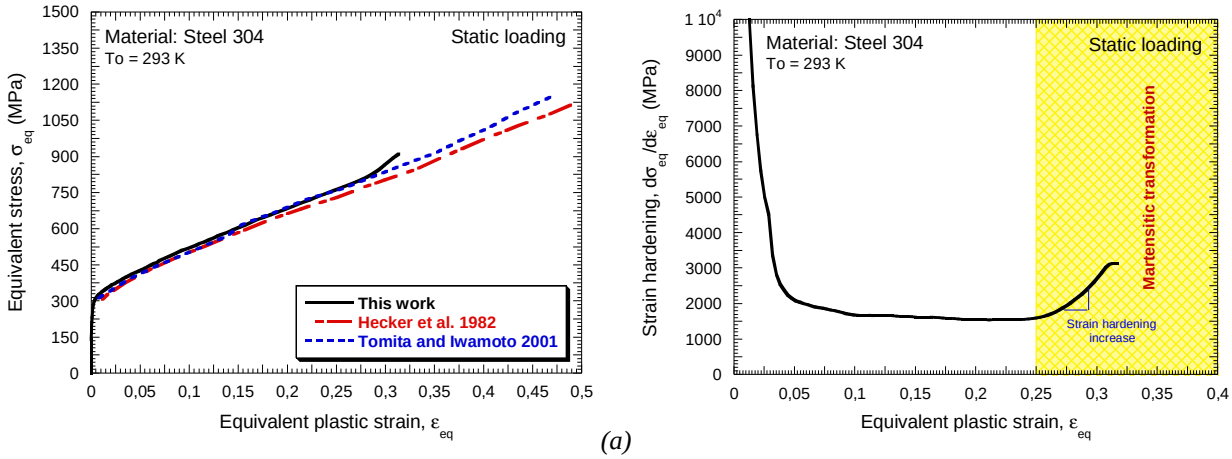

Fig. 5.6. (a) Flow stress evolution versus strain and comparison between our experiments and those reported in [Hecker et al. 1982, Tomita and Iwamoto 2001]. (b) Strain hardening evolution versus strain under static loading at room temperature.

From the in situ stress measurements conducted it is revealed that such strain hardening increase is caused by *martensitic* transformation, Fig. 5.7. Beyond $\bar{\varepsilon}^p > 0.27$ the volume fraction of *martensite* starts to be relevant and the *martensite* stress can be determined *(volume fractions $V_{\alpha'}$<10% do not allow for a proper stress determination using **XRD**).*

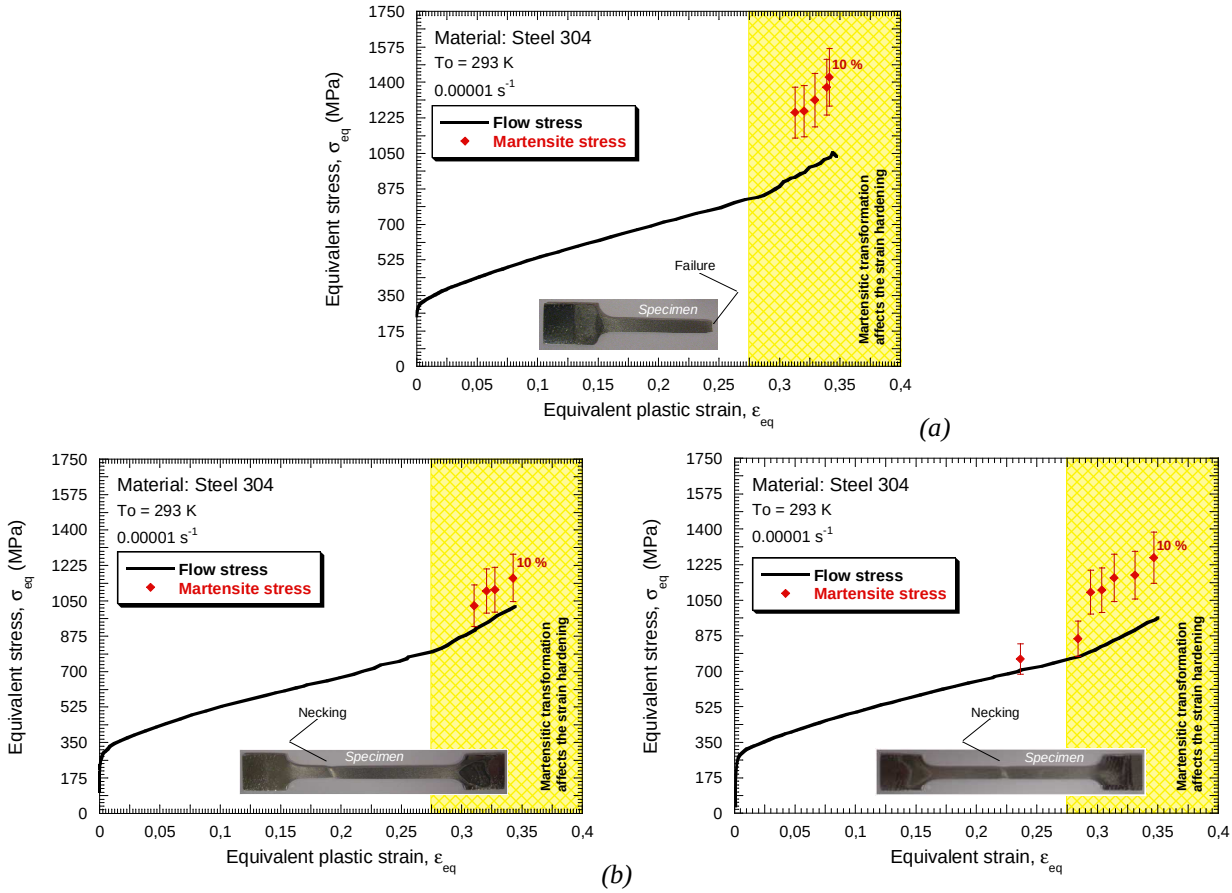

Fig. 5.7. Overall flow stress evolution and martensite stress evolution as a function of plastic strain under static loading at room temperature.

The stress in *austenite* during loading has also been determined. For all the tests conducted *austenite* acts as the soft phase of the material, Fig. 5.8. Repeatability of the measurements must be

highlighted. It was previously mentioned that the volume fraction of *martensite* was not relevant until $\bar{\varepsilon}^p \approx 0.27$, however in Fig. 5.8. it can be seen that *martensite (at least an small amount $V_{\alpha'}$<10%)* appears since the beginning of loading *(the overall flow stress is larger than the austenite stress from very low values of plastic deformation)*. In order to induce the visible extra strain hardening reported in Fig. 5.6-a. large volumes of *martensite* is required, $V_{\alpha'} > 10$ %.

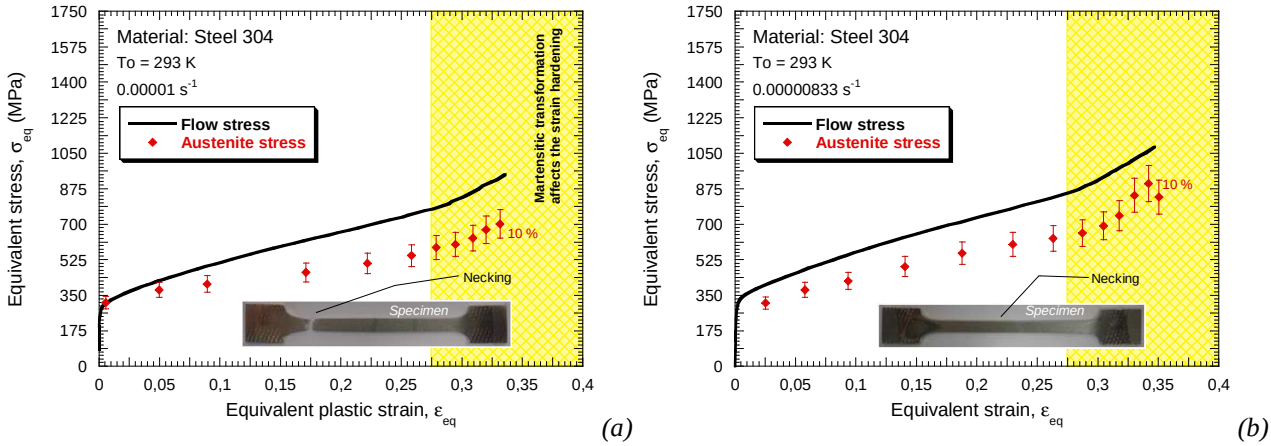

Fig. 5.8. Overall flow stress evolution and austenite stress evolution as a function of plastic strain under static loading and room temperature.

The volume fraction in the specimens tested has been determined, Fig. 5.9. The amount of *martensite* varies between $V_{\alpha'} \approx 55$ % in both ends of the active part of the specimen and $V_{\alpha} \approx 70$ % in the necking zone, Fig. 5.9. It has to be noted that such amount of *martensite* is larger than that determined in the literature by means of magnetic techniques, Fig. 5.10. The accuracy of the latter method has been recently questioned by the scientific community.

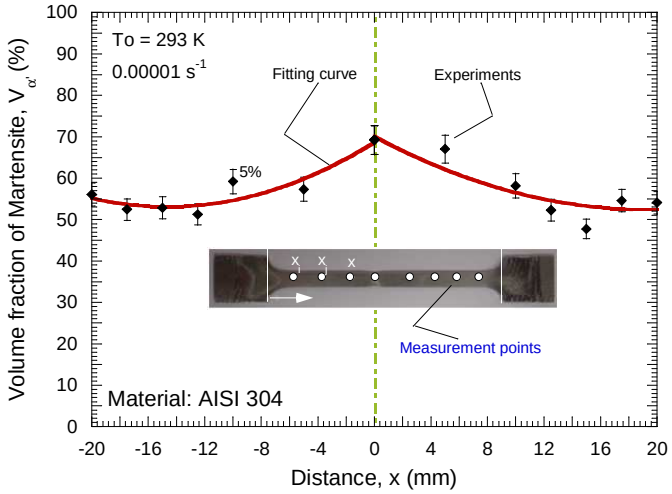

Fig. 5.9. Volume fraction of martensite after testing along the active part of the specimen.

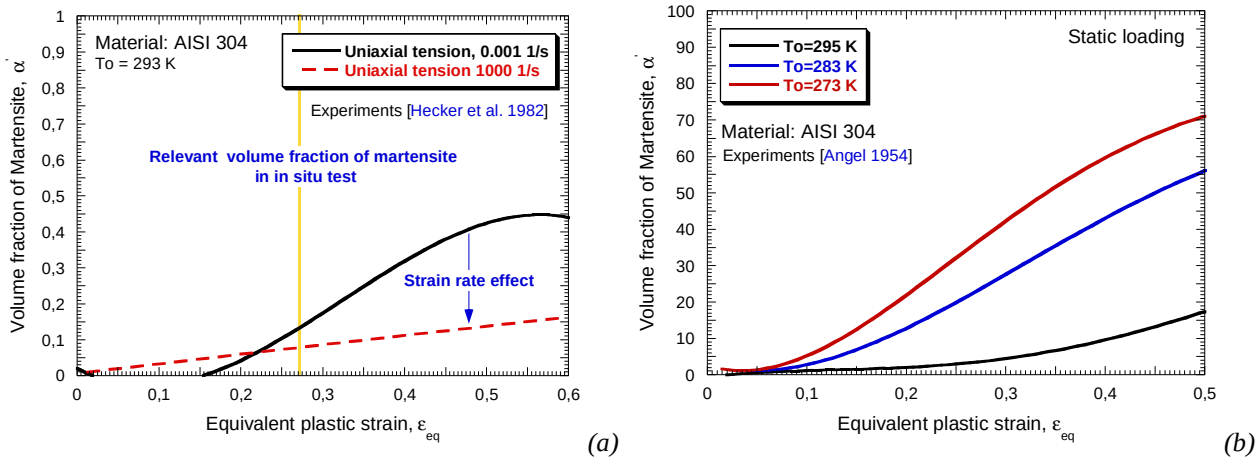

Fig. 5.10. (a) Actual volume fraction of martensite formed during straining at room temperature in tension at low and high strain rate at room temperature [Hecker et al. 1982]. (b) Formation of martensite by tensile plastic strain at various deformation temperatures [Angel 1954].

Since the greatest volume fraction of *martensite* is located in the necking it seems that plastic deformation is the dominant mechanism which resides behind the transformation phenomenon in this material. The free energy supplied by the material straining relegates to a secondary role the increase of temperature *(inhibitor of martensitic transformation)* due to conversion of plastic work into heat *(and due to martensitic transformation by itself which is an exothermic process [Rusinek and Klepaczko 2009]).* Then it is necessary to investigate the temperature increase in the material during loading. This point is discussed in the following section of the document.

5.2.1.3 Regular tensile tests

The specimens used during regular tensile tests are analogous to those used in the case of **ES** steel and **AA 2024-T3**, Fig. 4.5. For determination of the temperature increase during loading, low rate tensile tests have been recorded using infrared camera, Fig. 5.11. The experimental procedure followed for the temperature increase determination is analogous to that reported for **ES** steel in **Section 4.2.1.2.**

In Fig. 5.11. is illustrated the temperature increase taking place at $\dot{\bar{\varepsilon}}^{p} = 0.01\ s^{-1}$ for the steel **AISI 304** and the **AA 2024-T3** *(materials having similar flow stress level within the range $\bar{\varepsilon}^{p} < 0.1$, Fig. 5.11-c).* For the **AISI 304** the temperature is increasing during the whole test whereas in the case of **AA 2024-T3** it remains constant and close to the environmental temperature. As it was previously mentioned, this behaviour is certainly caused by the lower thermal conductivity of steel in comparison with **AA** *($K_{AA} = 237\ W/(m \cdot K) \gg K_{SA} = 80\ W/(m \cdot K)$)*.

In comparison with the **AA**, the thermo-elastic effect, Eq. 4.2., is more noticeable in the case of the steel **AISI 304**, $\Delta T_{SA}^{Elasticity} = -0.32\ K > \Delta T_{AA}^{Elasticity} = -0.1\ K$. Such observation is certainly tied to the larger Young's modulus of steel alloys in comparison with aluminium alloys, $\frac{E_{SA}}{E_{AA}} \approx 3$.

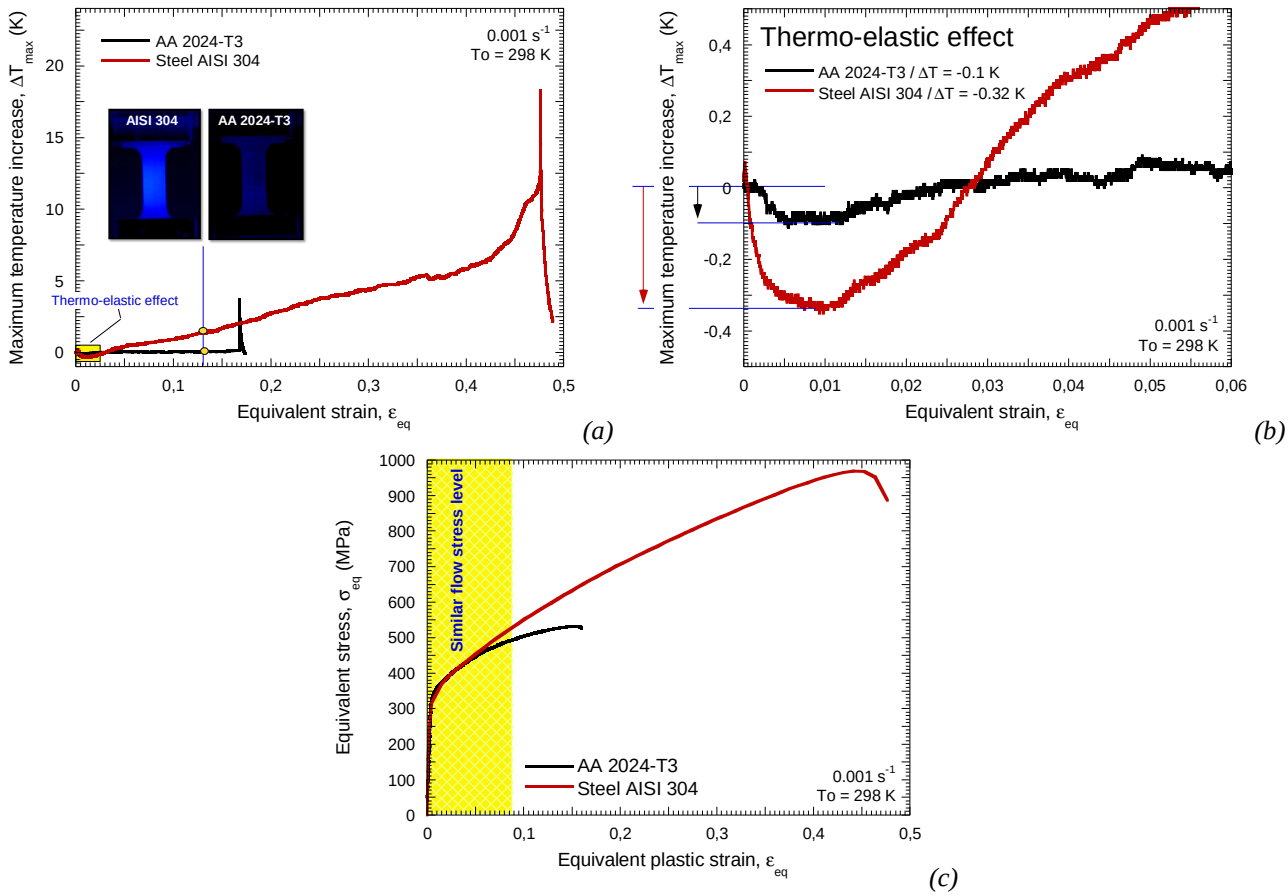

*Fig. 5.11. (a) Temperature variation as a function of strain for **AA 2024-T3** and steel **AISI 304**. (b) Temperature decrease due to thermo elasticity. (c) Flow stress evolution as a function of plastic strain for **AA 2024-T3** and steel **AISI 304**under static loading at room temperature.*

In the following graphs, Fig. 5.12, is reported for the **AISI 304** the maximum increase of temperature during loading in the case of $\dot{\bar{\varepsilon}}^{p} = 0.01\,s^{-1}$. The material temperature is continuously increasing with stress and strain, Fig. 5.12. Non-linear relation between temperature increase and plastic deformation, Fig. 5.12., is due to both the dependence of the inelastic heat fraction on plastic strain *(as previously discussed for mild steel **ES**)* and the *martensitic* transformation [Rusinek and Klepaczko 2009].

When instability takes place, a sudden increase of temperature is observed, Figs. 5.12-5.13. At that moment high strain rate level is reached in the necking, the deformation process seems to become adiabatic. The heat generated in the instability is hardly diffused to the rest of the sample, Fig. 5.13. Maximum temperature recorded during the test is close to $\Delta T_{max} \approx 110$ K, Fig. 5.12.

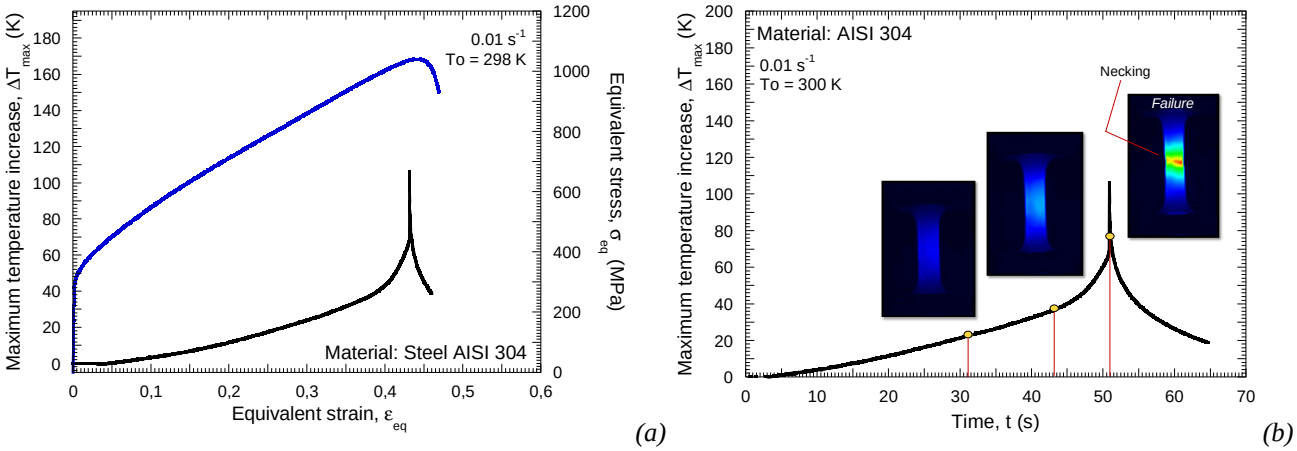

Fig. 5.12. (a) Maximum temperature increase versus plastic strain and flow stress evolution versus plastic strain. (b) Maximum temperature increase versus time.

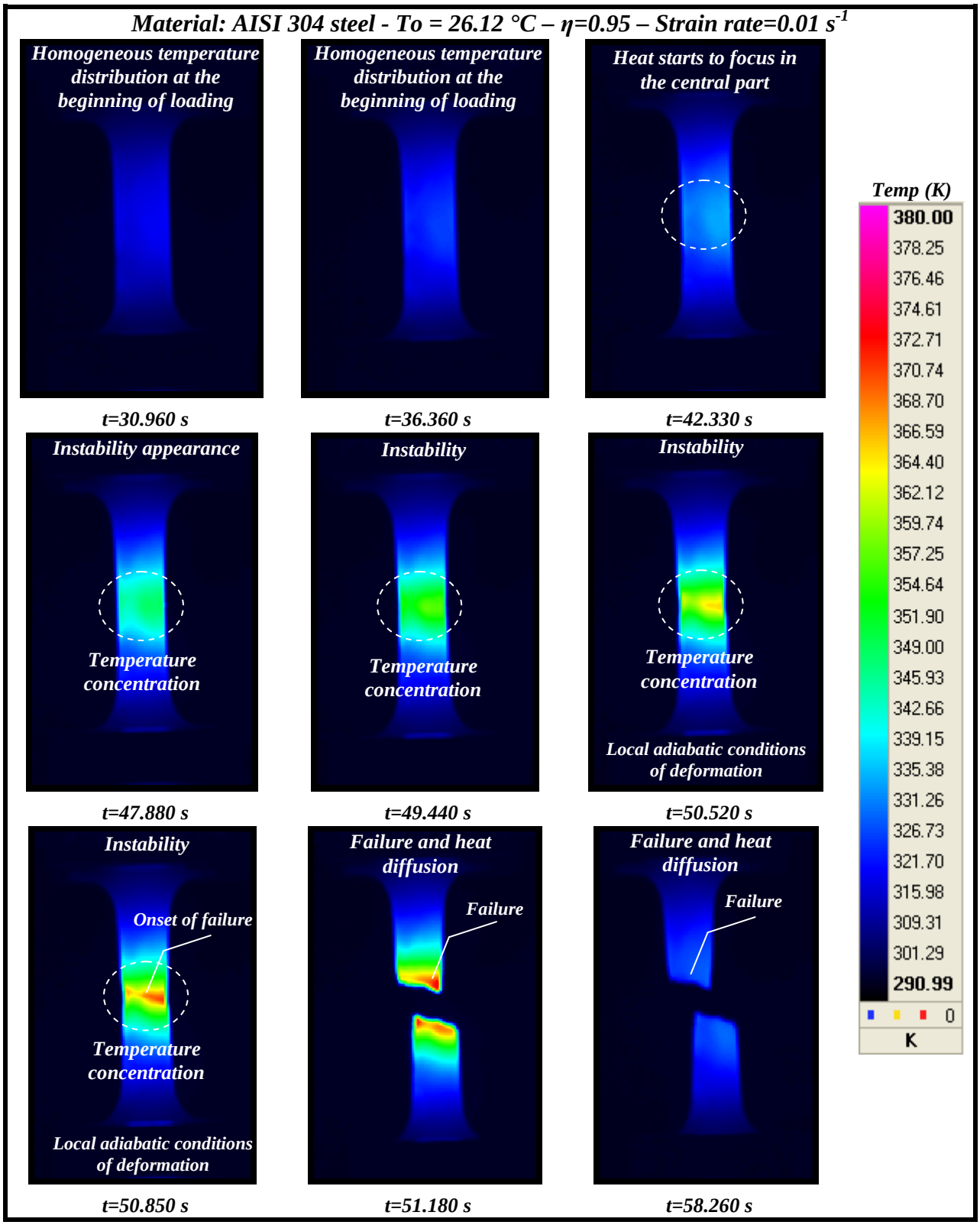

Fig. 5.13. Temperature contours during loading. Picture resolution 320×256 pixels.

Tests at higher strain rates have been performed. At $\dot{\bar{\varepsilon}}^{p} = 0.05\ s^{-1}$ the maximum temperature during the test reaches $\Delta T_{max} \approx 140$ K, Fig. 5.14.

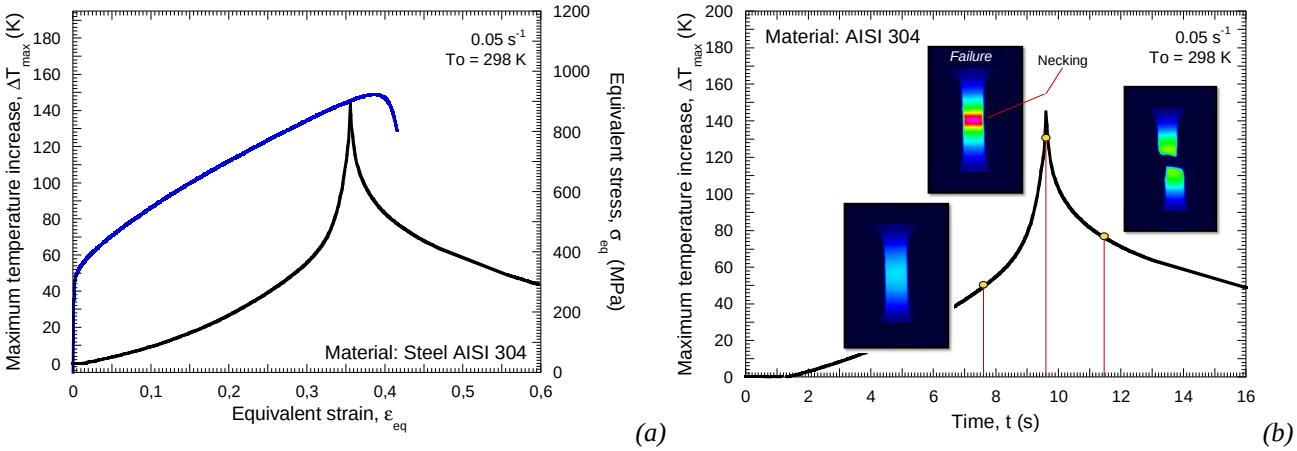

Fig. 5.14. (a) Maximum temperature increase versus plastic strain and flow stress evolution versus plastic strain. (b) Maximum temperature increase versus time.

An heterogeneous distribution of temperature is reached since the first stages of the deformation process, Fig. 5.15. Temperature increase is early concentrated in the central part of the specimen, Fig. 5.15. There, in the necking, the material behaves under adiabatic conditions of deformation. Once instability takes place the evolution of temperature with global deformation goes steep, almost following a vertical asymptote, Fig. 5.14. Therefore, strong gradients of deformation rate are expected in the necking zone.

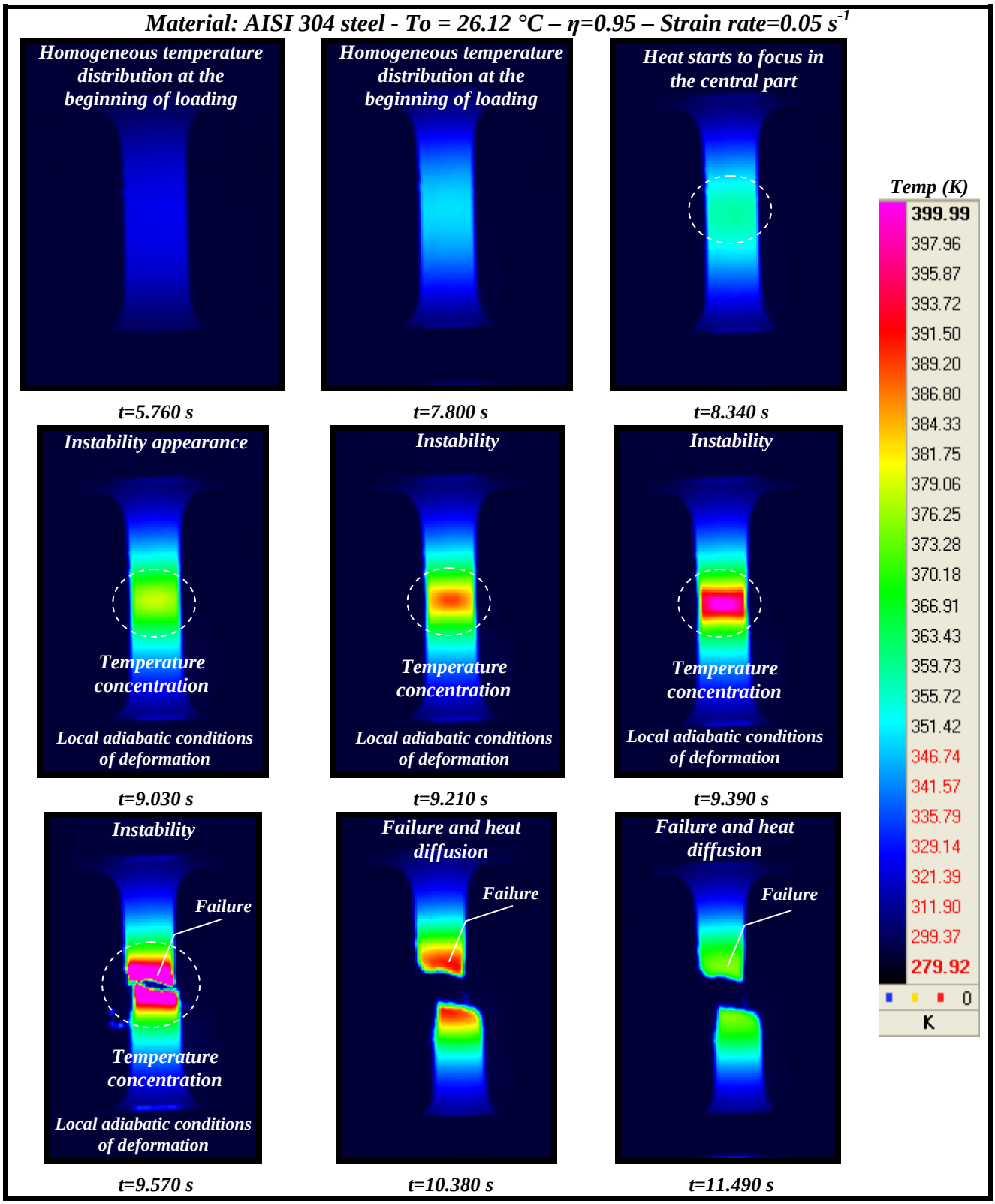

Fig. 5.15. Temperature contours during loading. Picture resolution 320×256 pixels.

Previous considerations are patently clear when the testing strain rate is increased up to $\dot{\varepsilon}^{p} = 0.1\ s^{-1}$, Fig. 5.16.

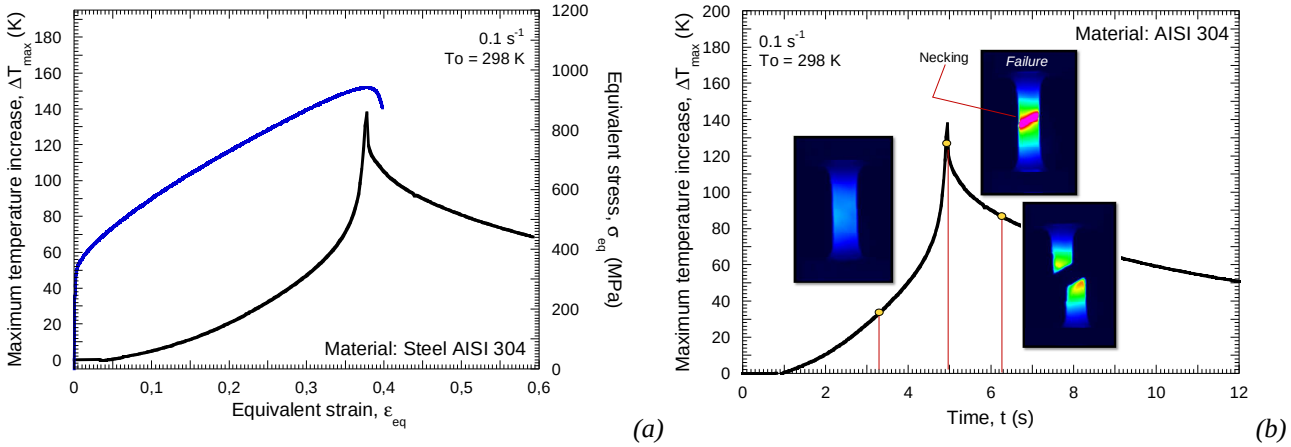

Fig. 5.16. (a) Maximum temperature increase versus plastic strain and flow stress evolution versus plastic strain. (b) Maximum temperature increase versus time.

In this case flow localization involves a maximum temperature increase of $\Delta T \approx 140$ K, Fig. 5.16. Heterogeneous temperature distribution along the sample is observed during, almost, the whole test, Fig. 5.17. It has to be remarked that in this material transition between isothermal and adiabatic conditions of deformation seems to take place for very low values of global testing rate *(at least in comparison with **ES** steel and **AA 2024-T3**)*.

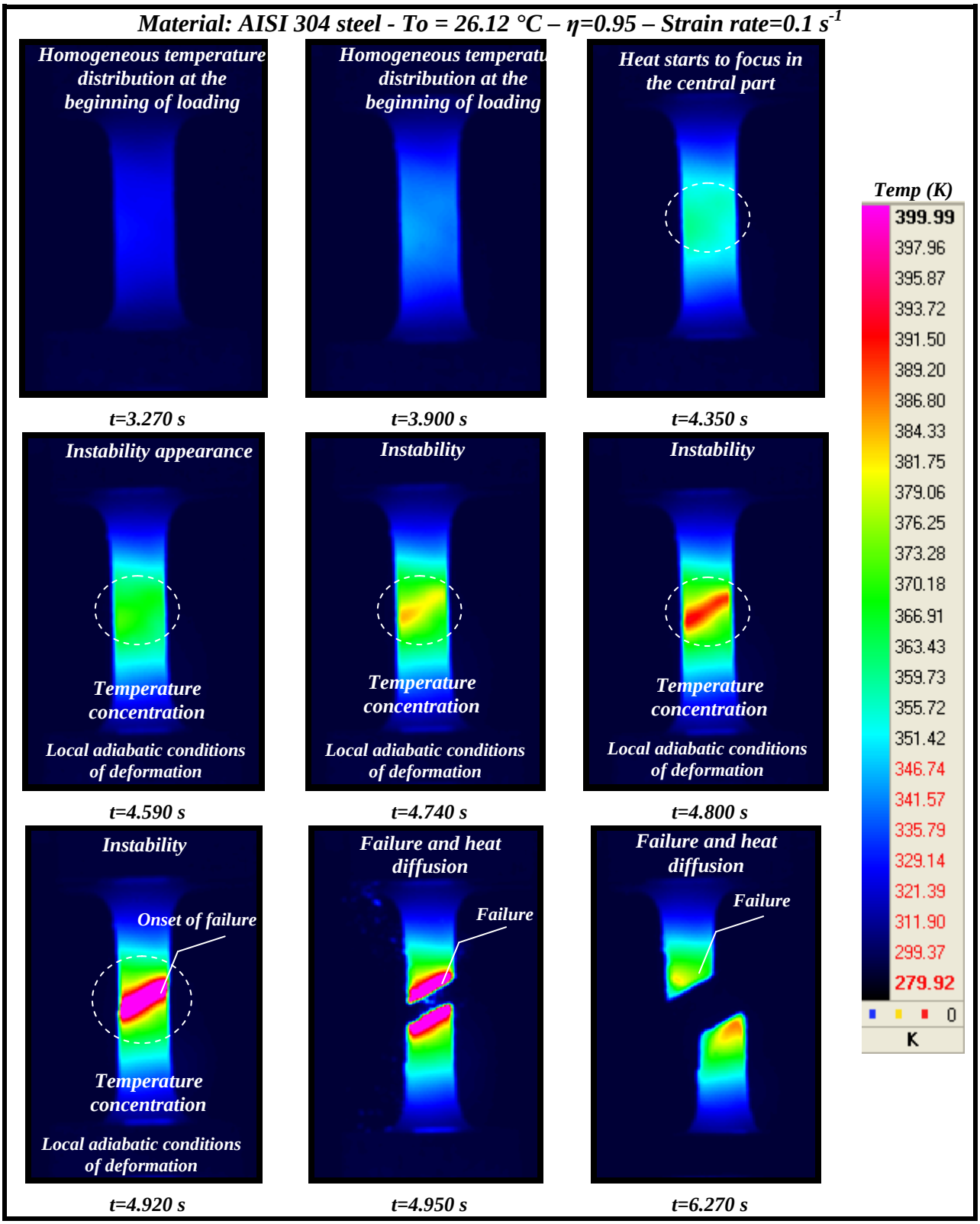

Fig. 5.17. Temperature contours during loading. Picture resolution 320×256 pixels.

Then, the *martensite* stress distribution and the volume fraction of *martensite* are obtained along the active part of the tested samples, Fig. 5.18. It is of main relevance to highlight that in **AISI 304** *martensitic* transformation takes place for temperature increase over $\Delta T > 140$ K, Fig. 5.18-a. This revelation is reported for the first time in the open literature. Even at 100 s^{-1} it is found $V_{\alpha'} \approx 30$ % in

the necking of the tested sample, Fig. 5.18. Under highly dynamic loading *martensitic* transformation takes place in steel **AISI 304**.

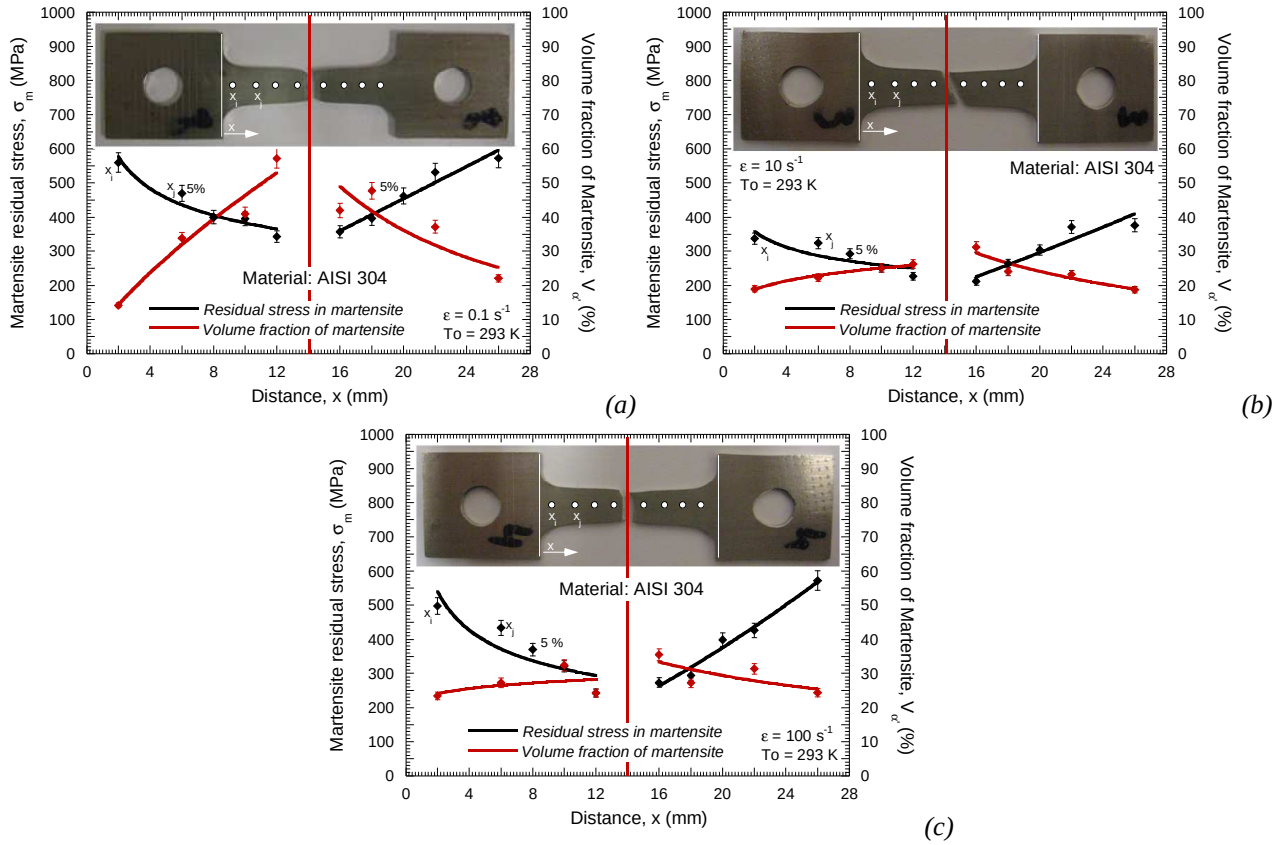

Fig. 5.18. Residual stress in martensite and volume fraction of martensite in tensile specimens tested at different strain rates

The measured volume fraction of *martensite* increases as one move from the ends of the active part to the necking zone. Thus, the *martensite* stress becomes reduced close to the necking since Eq. 5.3. must be fulfilled.

$$0 = \sigma_{\alpha'} \cdot V_{\alpha'} + \sigma_{\gamma} \cdot V_{\gamma} \qquad (5.3)$$

Flow stress evolution versus plastic strain for high loading rates is depicted in Fig. 5.19. Under such loading conditions the material keeps elevated work hardening enhancing ductility. It is proven the role played by *martensite* in such behaviour.

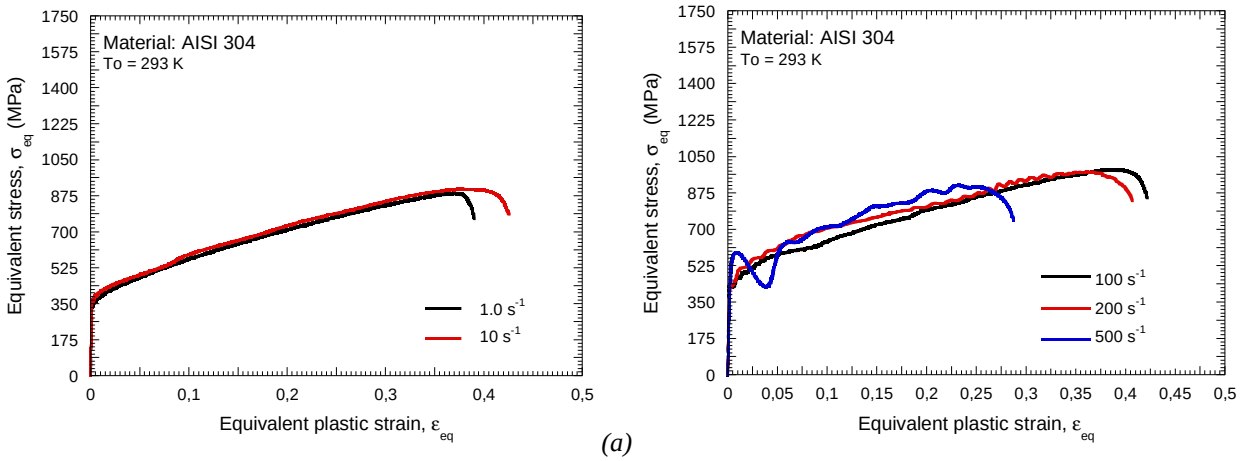

Fig. 5.19. Flow stress evolution as a function of the plastic strain for different strain rate levels at room temperature.

Finally it is examined the effect of temperature in the material behaviour under static loading. Two different initial temperatures are checked T_0 = 77 K and T_0 = 193 K, Fig. 5.20. For both cases, the macroscopic strain-stress evolution finds agreement with the results reported in [Tomita and Iwamoto 2001, Hecker et al. 1982, Huang et al. 1989].

For the test at T_0 = 193 K the specimen was placed inside a bath of solid carbon dioxide guarantying a constant temperature during loading. At this temperature the **AISI 304** shows an initial yield stress $\sigma\big|_{\bar{\varepsilon}^p=0} \approx 400\,\text{MPa}$. At the beginning of loading the stress does not increase with plastic deformation in a relevant way, however for a certain value of plastic deformation $\bar{\varepsilon}^p \approx 0.125$ the stress level dramatically augments, Fig. 5.20-a. It is caused by large *martensitic* transformation. It proofs that in **AISI 304** the *martensitic* transformation is strain induced for the whole range of initial temperatures.

For the test at T_0 = 77 K the specimen was placed inside a bath of liquid nitrogen guarantying a constant temperature during loading. The increase of strain hardening takes place for $\bar{\varepsilon}^p \approx 0.075$. The post-mortem analysis revealed $V_{\alpha'}$=100 % along the whole active part of the sample, Fig. 5.20-b.

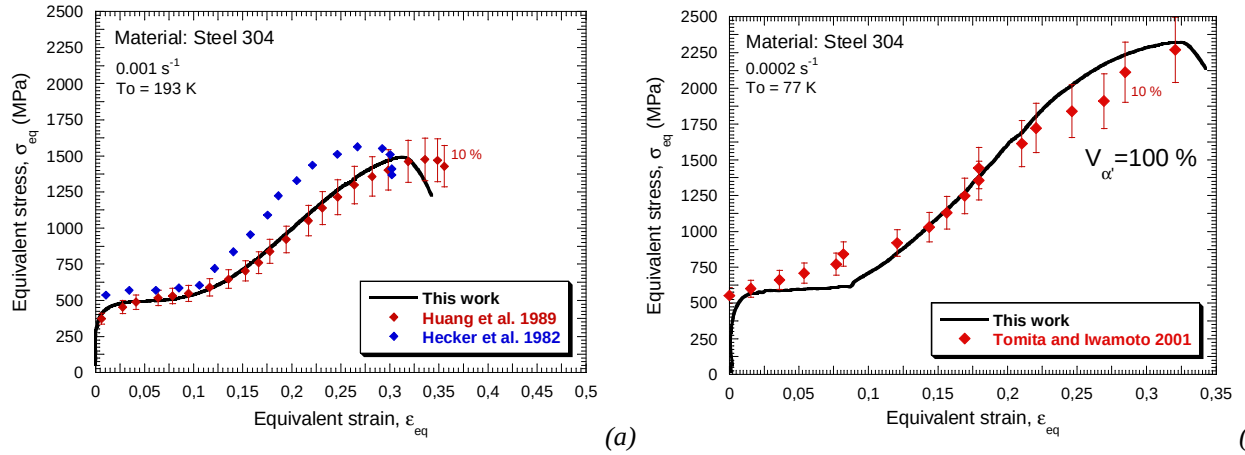

Fig. 5.20. Flow stress evolution versus plastic strain at low strain rates. (a) T_0=193 K, (b) T_0=77 K. Comparison with experimental results [Huang et al. 1989, Hecker et al. 1992, Tomita and Iwamoto 2001]

It has to be noted that extra strain hardening behaviour only takes place in **AISI 304** at very low initial temperatures or very low strain rates. However the phase transformation is proven to occur under wide ranges of loading conditions improving material performance under dynamic solicitation.

In order to analyze the suitability of this material for absorbing energy under impact in the following section of the document is conducted the macroscopic modelling of the thermo-viscoplastic material behaviour.

5.2.2 Constitutive relation for the steel AISI 304

At room temperature the material does not exhibit effect of strain on the rate sensitivity. Therefore the extended **RK** model to viscous drag effects [Rusinek and Rodríguez-Martínez 2009] has been used for modeling the thermo-viscoplastic behaviour of the material. It is assumed that using such formulation it is not possible to define the extra strain hardening observed at low temperatures. However, let us considered the modeling reported below as suitable for description of the material behaviour under dynamic loading at room temperature.

Thus, by means of the calibration procedure reported in **Section 2.2.1** and **Section 2.4.2** the following set of material constants has been found, Tables 5.2-5.3.

B_0 (MPa)	ν (-)	n_0 (-)	D_2 (-)	ε_0 (-)	σ_0^* (MPa)	m^* (-)	D_1 (-)	T_m (K)	$\dot{\varepsilon}_{min}$ (s^{-1})	$\dot{\varepsilon}_{max}$ (s^{-1})
1243.6	0.001	0.36	0.035	0.0118	117.72	1.29	0.55	1600	10^{-5}	10^{7}

*Table 5.2. Constants determined for the steel **AISI 304** for the **RK** model*

χ (MPa)	α (-)
200.83	0.0009774

*Table 5.3. Constants determined for the steel **AISI 304** for the viscous drag component of the extended **RK** model.*

It is observed that in Fig. 5.21. the analytical predictions of the constitutive description fit properly the experimental results within wide ranges of strain rate at room temperature. Flow stress level and material strain hardening are satisfactorily defined, Fig. 5.21.

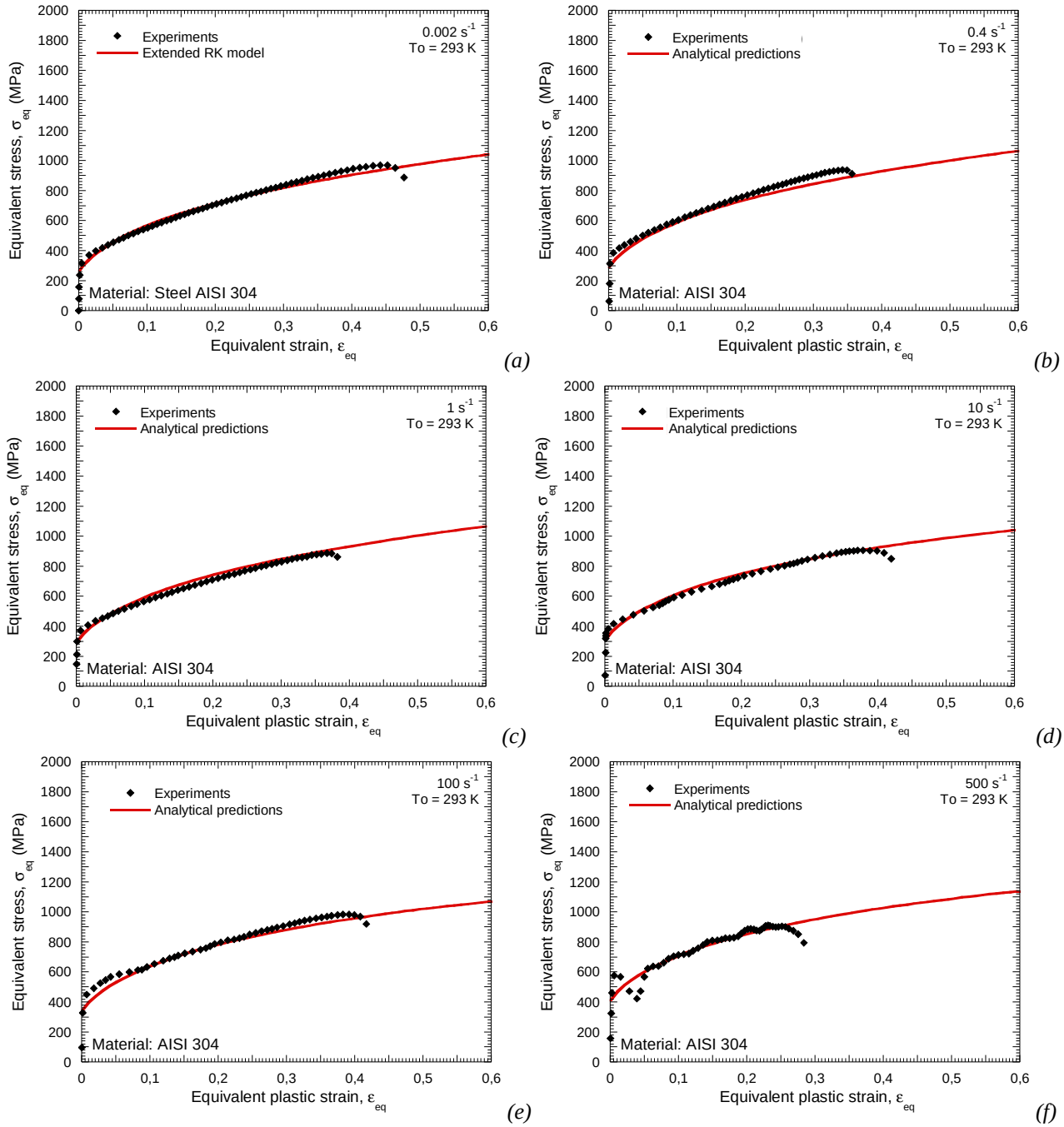

Fig. 5.21. Flow stress evolution versus plastic strain for different strain rates at room temperature and comparison with analytical predictions.

The model describes the reduced rate sensitivity characteristic of **FCC** metals at low strain rates [Kumar et al. 1968, Follansbee 1986, Regazzoni et al.1987, Rusinek and Rodríguez-Martínez 2009, Rusinek et al. 2009a] as well as the flow stress increase due to dislocations drag at high strain rates, Fig. 5.22.

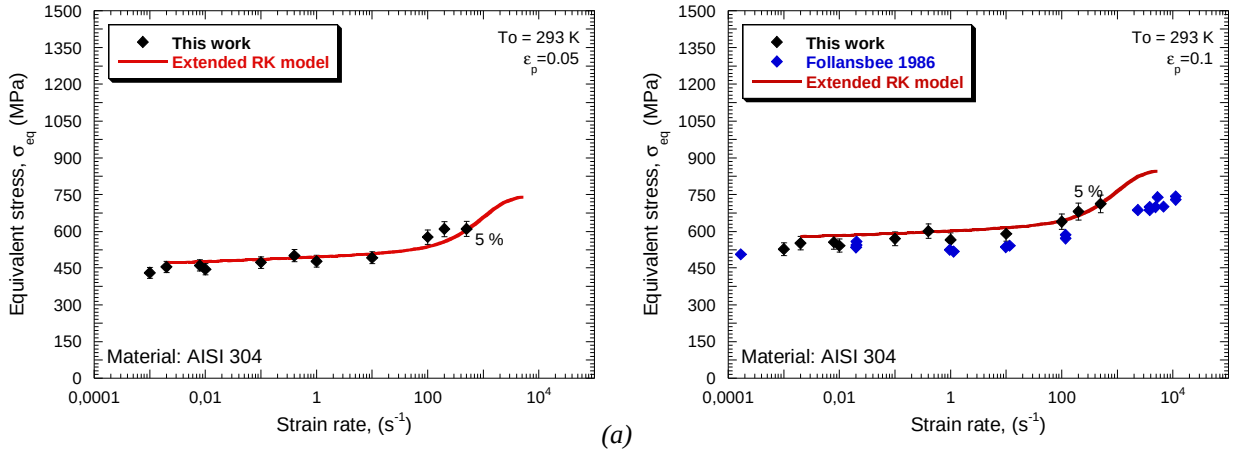

Fig. 5.22. Flow stress evolution versus strain rate for different plastic strain levels at room temperature and comparison with analytical predictions. Comparison with experiments reported in [Follansbee 1986].

Next, perforation tests on **AISI 304** sheets are conducted using the experimental facilities reported in **Section 4.2.3.1** and **Section 4.3.3.1** The results are compared with those previously reported for steel **ES** and **AA 2024-T3**. The goal is to examine the suitability of **AISI 304** for absorbing energy under dynamic solicitation and to determine if *martensitic* transformation still occurs under impact loading.

5.2.3 Experimental procedure for perforation of metallic sheets

Two different experimental setups have been used for analyzing the perforation behaviour of the **AISI 304** sheets.

5.2.3.1 The drop weight tower

The description of the facilities used to conduct *(and analyze)* the low velocity impact tests was already carried out in **Section 4.3.3.1**

5.2.3.2 The pneumatic cannon

The description of the facilities used to conduct *(and analyze)* the high velocity impact tests was already carried out in **Section 4.2.3.1**

5.2.4 Analysis of the perforation process

First, the results obtained using the drop weight tower are reported.

5.2.4.1 The drop weight tower tests

The first step is to obtain the ballistic curve residual velocity versus impact velocity, Fig. 5.23. following the procedure detailed in **Section 4.3.4.1**. The ballistic limit for **AISI 304** at room temperature is $V_{bl} \approx 2.9$ m/s *(much larger than that corresponding to **AA 2024-T3**)*, Fig. 5.23. For that velocity the impact does not lead to any crack in the target, Fig. 5.23. In Figs. 5.24-5.25-5.26. can be observed that small increments in the impact velocity involve a progressive appearance of

necking and failure in the interface projectile/target. That necking is precursor of crack generation and subsequent petalling development.

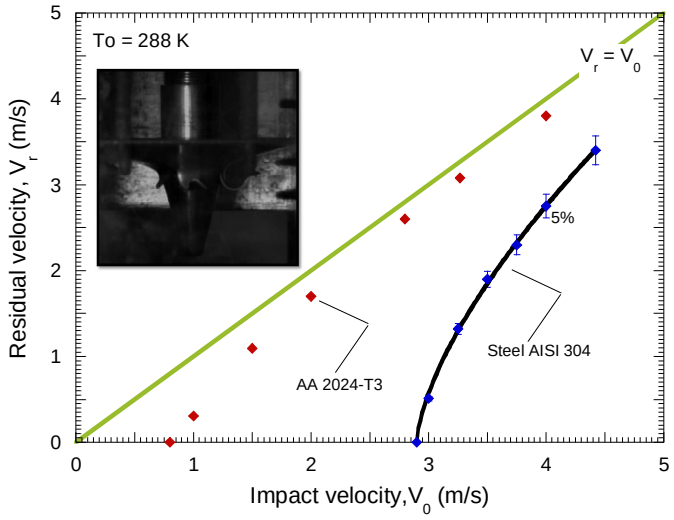

Fig. 5.23. Residual velocity versus impact velocity at room temperature.

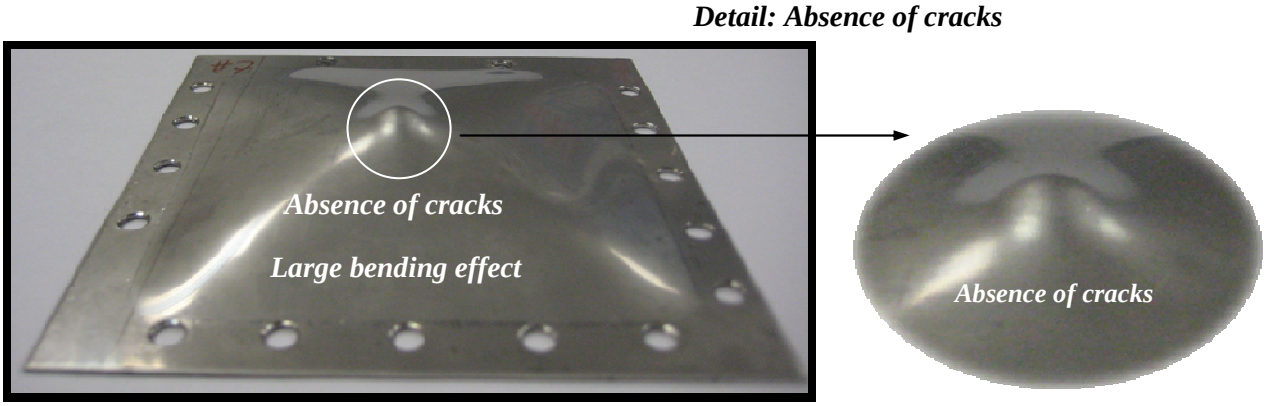

*Fig. 5.24. Absence of cracks, steel **AISI 304**, V_0=2.9 m/s at room temperature.*

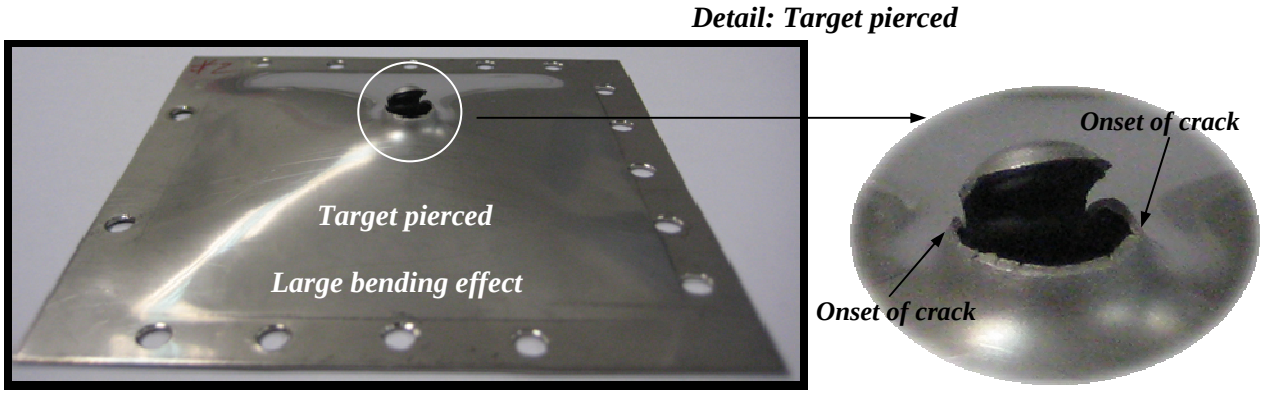

*Fig. 5.25. Pierced target, steel **AISI 304**, V_0=3.0 m/s at room temperature.*

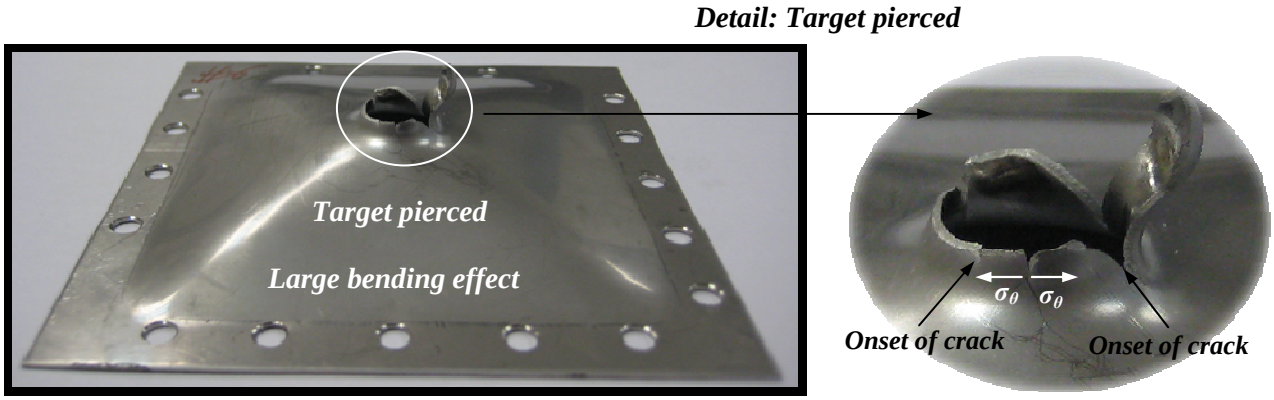

*Fig. 5.26. Pierced target, steel **AISI 304**, V_0=3.25 m/s at room temperature.*

It has to be highlighted the good performance of the steel **AISI 304** under impact, at least in comparison with **AA 2024-T3**. For both materials, let us calculate the ratio of the energy absorbed by the target per unit of material density, Fig. 5.27. From that comparison the **AISI 304** comes clearly benefited, it absorbs more than double energy than the **AA 2024-T3**, Fig. 5.27. It has to be noted that in the case of **AISI 304** the amount of energy absorbed by the target *(beyond the ballistic limit)* decreases with the impact velocity, within the range of impact velocities tested, Fig. 5.27. It is a transient trend due to proximity of the impact velocity to the ballistic limit *(optimum perforation)* [Landkof and Goldsmith 1993, Wierzbicki 1999, Rusinek et al. 2009a]. It is expected that for larger impact velocities the energy absorption will increase as reported in [Borvik et al. 2002b, Arias et al. 2008, Rusinek et al. 2009a].

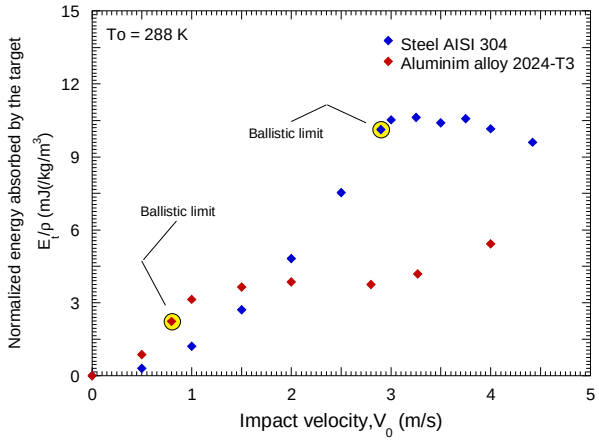

Fig. 5.27. Energy absorbed by the target as a function of the impact velocity at room temperature.

Such good performance of the **AISI 304** under impact is enhanced by the *martensitic* transformation which takes place during perforation. The impacted plates have been cut; petals and cracking interfaces have been examined using **SEM**, Fig. 5.28. For the whole range of impact velocities covered, *martensite* has been found in the tested specimens, Fig. 5.28.

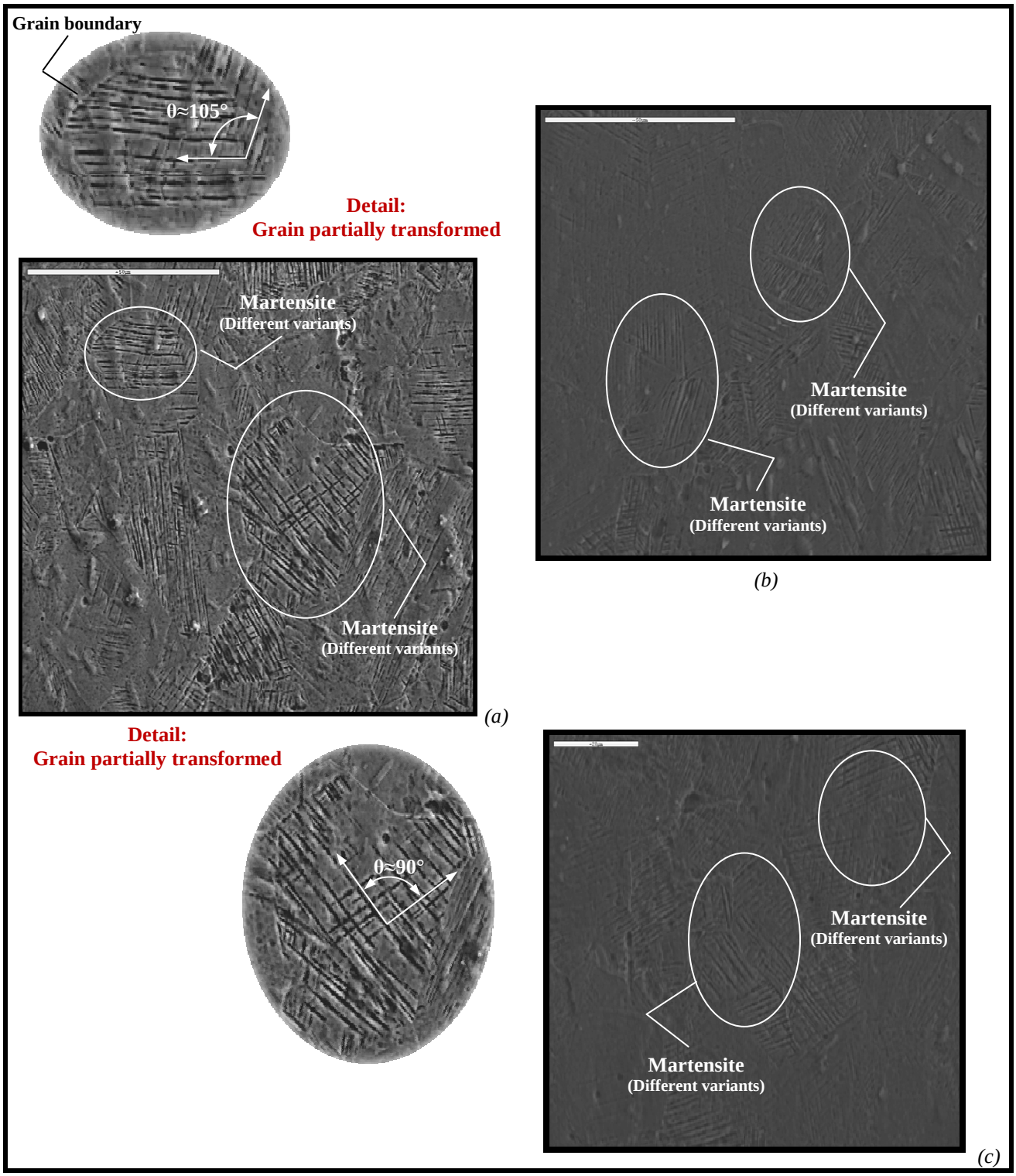

Fig. 5.28. ***SEM*** *micrographies of petals in* ***AISI 304*** *impacted plates.(a) V_0=4.4 m/s, (b)-(c) V_0=3.5 m/s.*

Unfortunately, due to complicated shape of the plates after impact, the exact volume fraction of *martensite* could not be accurately quantified. In addition, *martensitic* transformation seemed to be heterogeneously distributed showing strong dependence on grains orientation *(material strongly deformed which makes difficult the observation of the microstructure),* Fig. 5.28. However, it is assumed that the *martensite* found in the specimen may have an important role on the perforation process, enhancing material strain hardening *(at least locally in the proximity of the cracks where the*

maximum concentration of martensite was found) and therefore improving the capability of the **AISI 304** for absorbing energy in form of plastic work *(cracks are demanding larger amount of energy to progress)*.

Next, the force/striker displacement evolution for different initial impact velocities is depicted, Fig. 5.29. The slope of the curve force/striker displacement $\partial F / \partial \delta_s$ remains constant regardless of the impact velocity *(such behaviour was also observed in the case of **AA 2024-T3**)*, Fig. 5.29. The maximum force recorded is rather independent of impact velocity, Fig. 5.29.

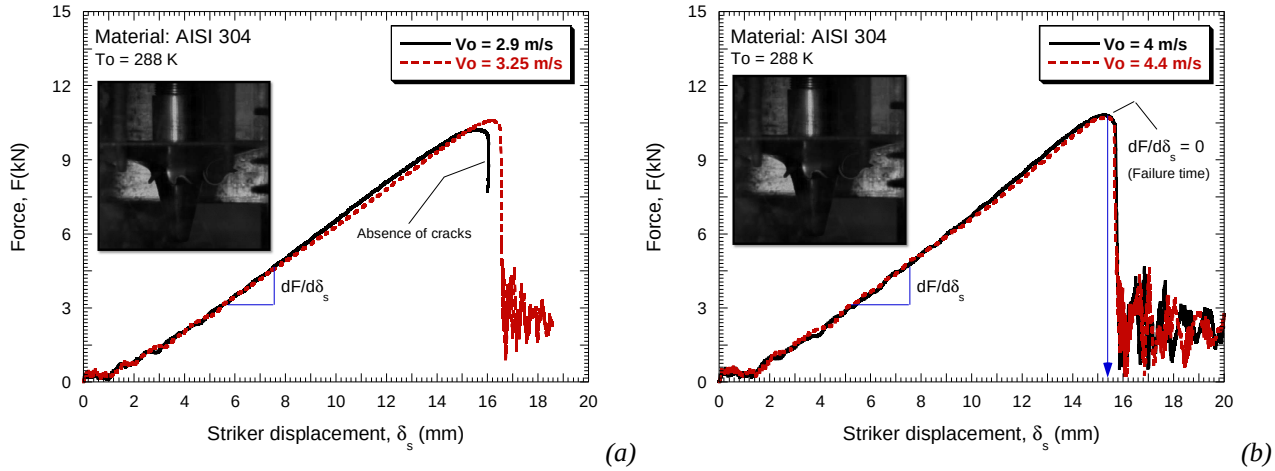

Fig. 5.29. Evolution of the impact force as a function of the striker displacement for different impact velocities at room temperature.

Thus, in the case of those tests leading to complete perforation of the target, the recurrent failure mode is petalling *(as it was observed for **AA 2024-T3**)*, Figs. 5.30-5.31. Neither the rolling direction nor boundary conditions influence the initiation or the propagation of cracks. Within the range of impact velocities considered, the number of petals varies between three and five [Landkof and Goldsmith 1993, Wierzbicki 1999].

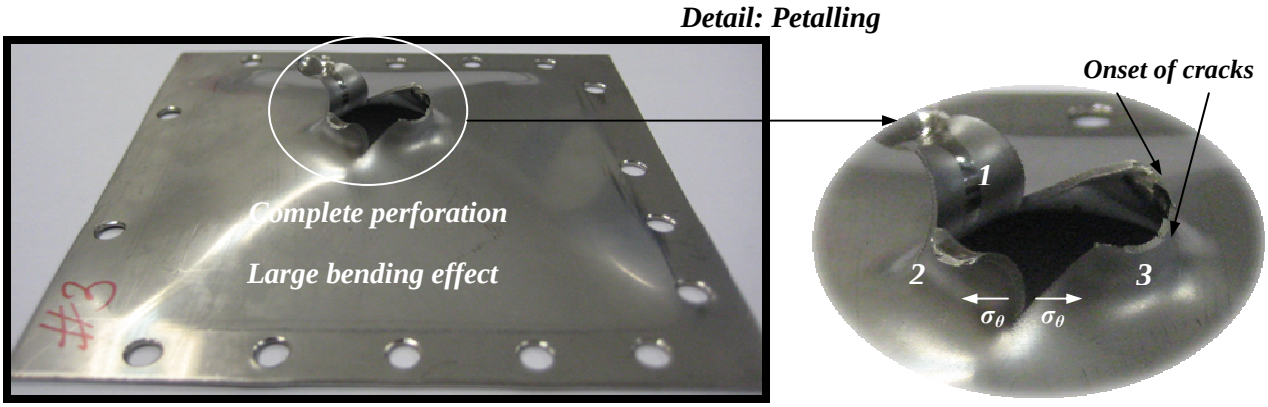

*Fig. 5.30. Petalling failure mode, steel **AISI 304**, V_0=3.5 m/s and room temperature.*

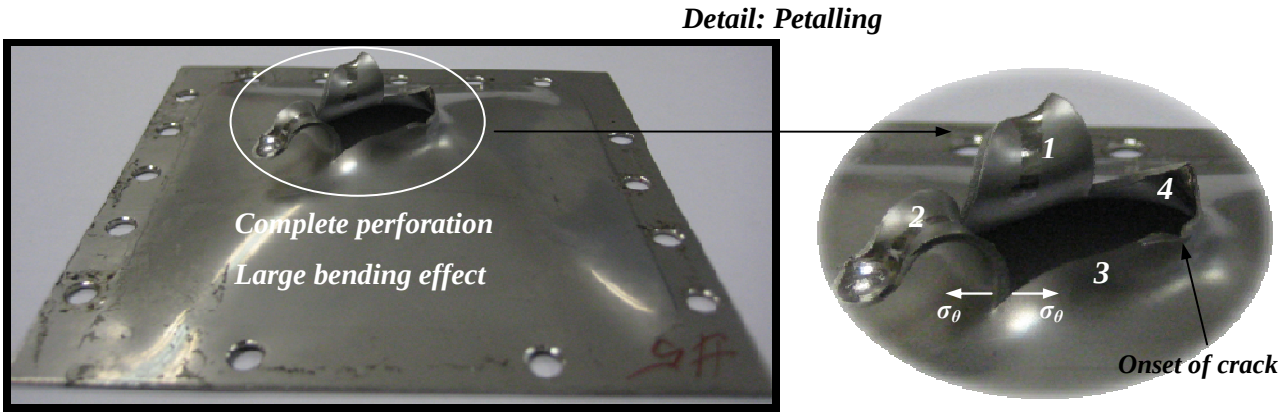

*Fig. 5.31. Petalling failure mode, steel **AISI 304**, V_0=4.4 m/s and room temperature.*

Large permanent bending can be observed in the impacted plates *(much larger than that reported for **AA 2024-T3**)*, Figs. 5.32-5.33.

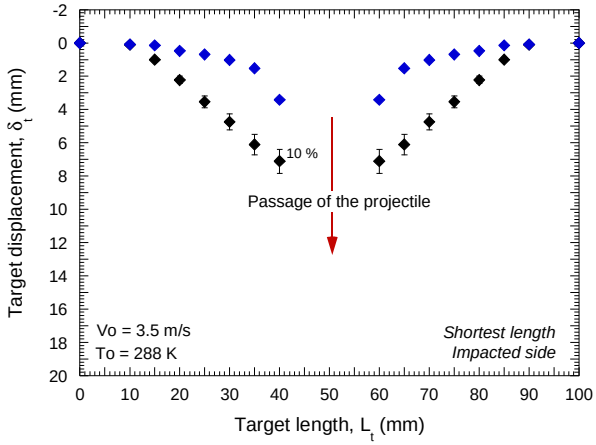

*Fig. 5.32. Permanent bending of the target for **AISI 304** and **AA 2024-T3** for V_0=3.5 m/s at room temperature.*

Plastic work *(enhanced by martensitic transformation)* in form of bending acts as the main mechanism for absorption of energy during perforation. High work hardening exhibited by this material spreads plasticity along the samples during perforation *(high velocity of the plastic waves)*. It homogenizes material behaviour leading to a global response to the impact by the whole plate, Fig. 5.33.

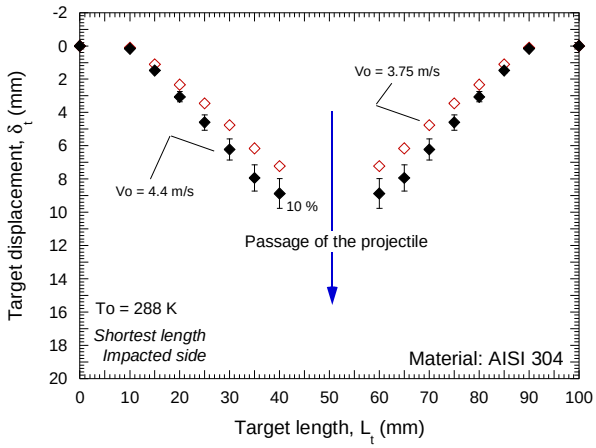

Fig. 5.33. Permanent bending of the target for different impact velocities at room temperature.

In Fig. 5.34. is shown a sequence of images of the perforation process for $V_0 = 4.4$ m/s. It is visible that before the onset of cracks take place the plate is strongly bent and deformed from the clamped perimeter up to the contact zone projectile/plate, 5.34-a. Failure occurs and cracks quickly propagate until the rear side of the target leading to petalling formation as final stage of the perforation process, 5.34-b-c-d.

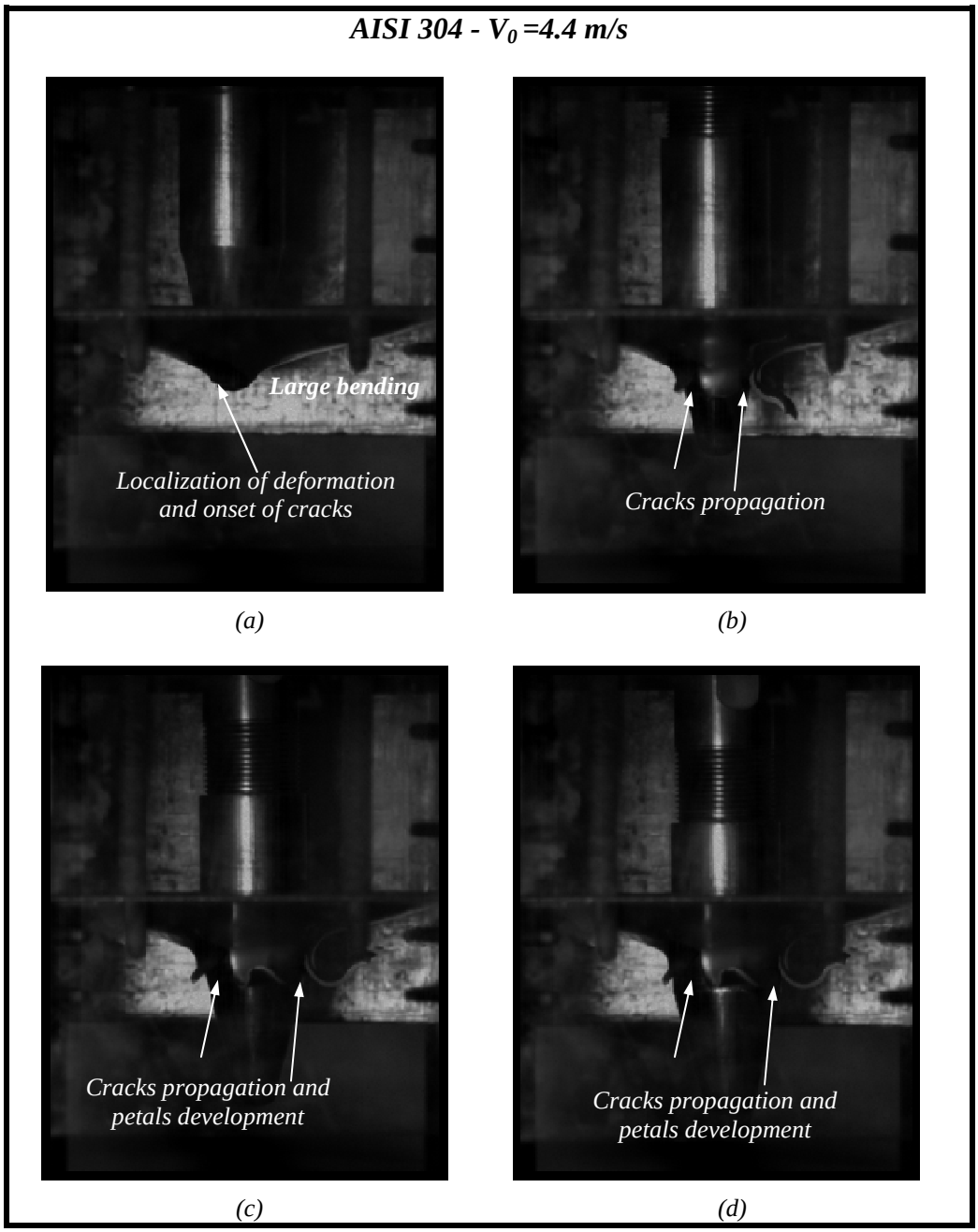

Fig. 5.34. Different stages of the perforation process for V_0=4.4 m/s at room temperature. (a) Localization of deformation and onset of cracks. (b) Cracks progression and generation of petals. (c) Development of petalling. (d) Complete passage of the impactor and petalling failure mode.

Next, the results obtained using the gas cannon are reported.

5.2.4.2 The pneumatic cannon tests

Experiments within the range of impact velocities 25 m/s ≤ V_0 ≤ 85 m/s are conducted. The ballistic limit found from the tests is $V_{bl} \approx 75$ m/s. It is necessary to highlight that in comparison with steel **ES** and **AA 2024-T3**, steel **AISI 304** shows the largest ratio ballistic limit/material density $V_{bl\text{-}AISI\ 304}/\rho_{AISI\ 304} > V_{bl\text{-}2024\text{-}T3}/\rho_{2024\text{-}T3} > V_{bl\text{-}ES}/\rho_{ES}$. This material possesses excellent mechanical properties for the absorption of energy under dynamic solicitations.

In Fig. 5.35. is shown the final stage of the impact process for different initial impact velocities. Failure by necking and subsequent propagation of cracks is the recurrent failure mode of the plates. Large bending effect leads to radial sliding projectile/plate. Necking appears close to the dome of the contact projectile/plate and large petals are formed, Fig. 5.35.

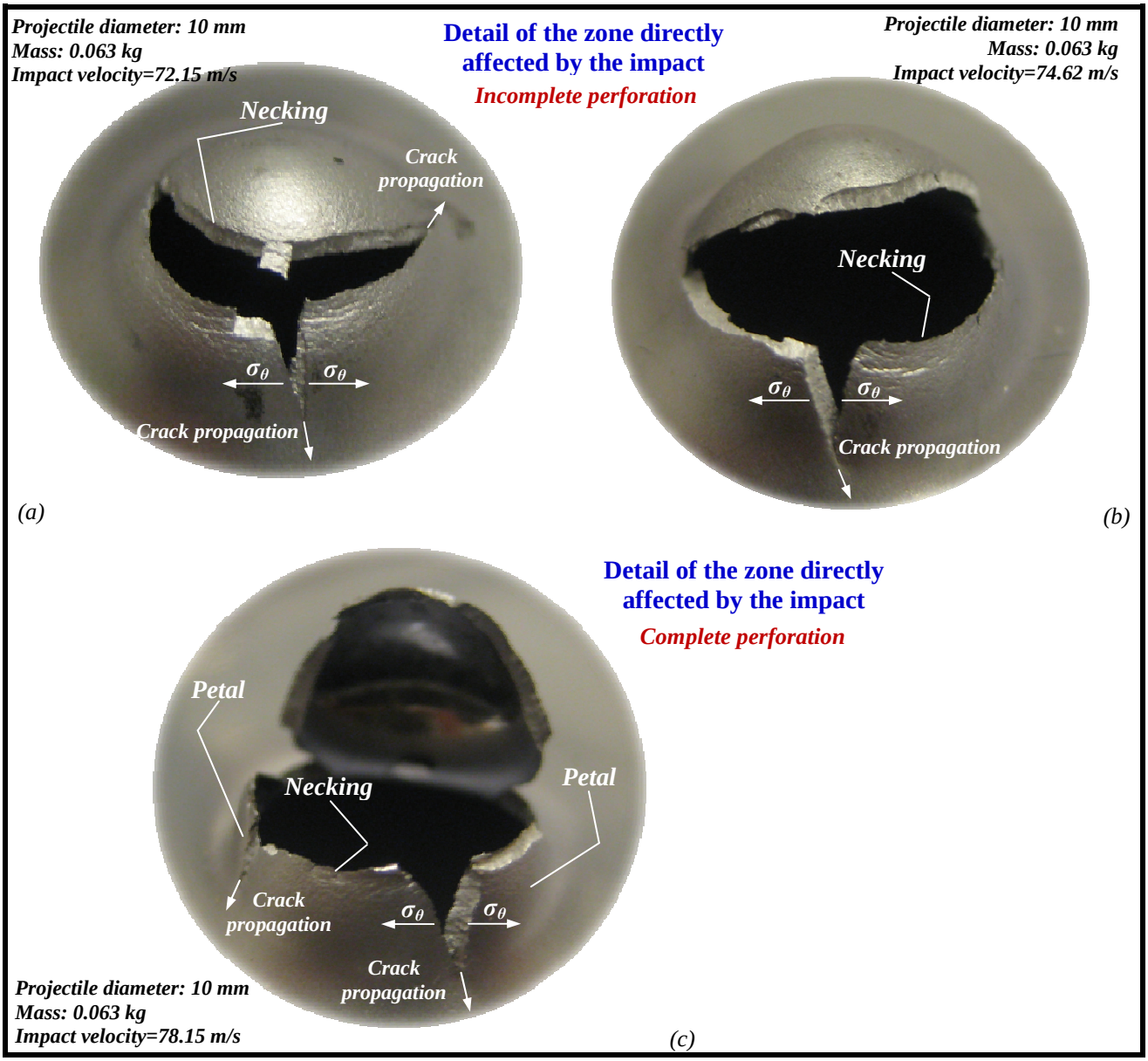

Fig. 5.35. Final stage of the impact process for different initial velocities.
(a) V_0 = 72.15 m/s, (b) V_0 = 74.62 m/s, (c) V_0 = 78.15 m/s.

Such a large bending of the plates is enhanced with increasing impact velocity, Fig. 5.36. For a given impact velocity, $V_0 \approx 48$ m/s **AISI 304** and **ES** steel sheets show quite similar permanent deflection. In the case of **ES** steel such loading condition corresponds to maximum bending, however in the case of **AISI 304** bending in still much more increased until ballistic limit is reached, Fig. 5.37.

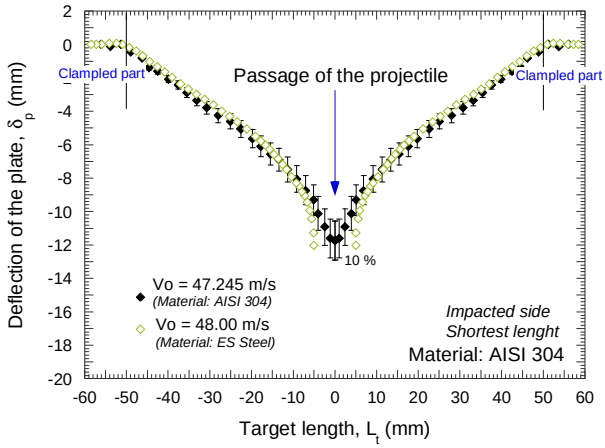

*Fig. 5.36. Post-mortem deflection of the target for **AISI 304** and steel **ES** for $V_0 \approx 48$ m/s.*

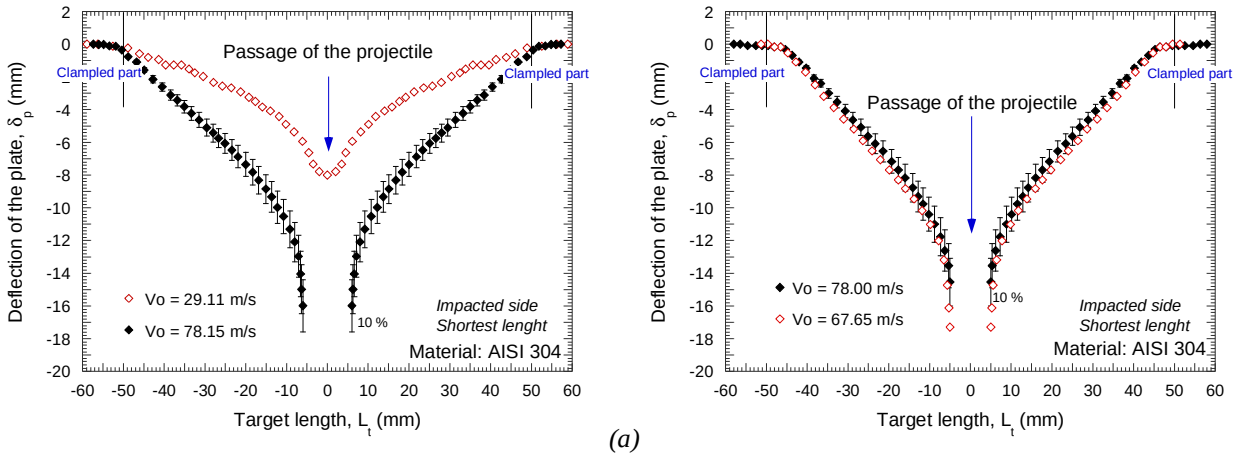

(a) *(b)*

Fig. 5.37. Post-mortem deflection of the target for different initial impact velocities.

Thus, in order to understand such good performance of the **AISI 304** under the gas cannon tests the procedure followed for analyzing the *martensite* transformation in the drop weight tower tests has been repeated. Again, *martensite* has been found for the whole range of impact velocities, especially in the petals and around the cracks *(strong material deformation makes difficult the observation of the microstructure, however traces of martensite are visible in all cases)*, Fig. 5.38. It is clear that for **AISI 304**, *martensite* is induced by material straining even under impact events. It makes this material propitious for bearing dynamic solicitations.

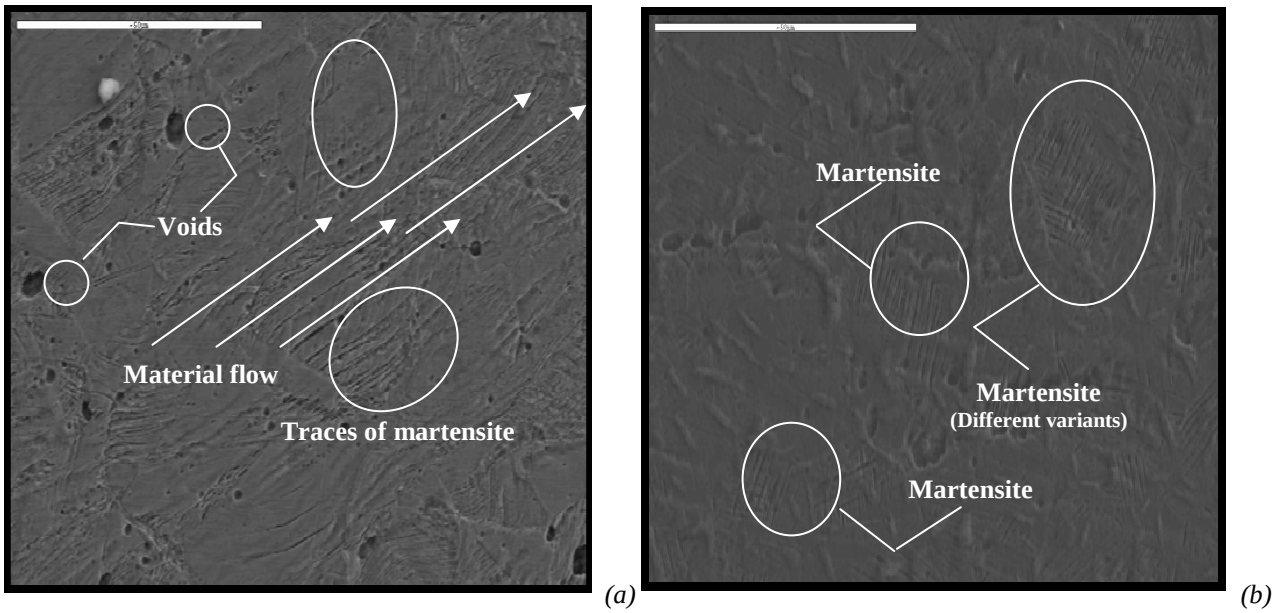

(a) *(b)*

*Fig. 5.38. **SEM** micrographies of petals in **AISI 304** impacted plates, V_0=78.15 m/s.*

Next, numerical simulations of the gas cannon tests are conducted. Such procedure will allow for estimation of the strain rate and temperature levels reached during the tests. It will provide useful information to analyze the loading conditions in which *martensitic* transformation is occurring.

5.2.4.2.1 Numerical analysis of the impact process

For the simulations of the impact on the **AISI 304** sheets the numerical configuration already introduced in **Section 4.2.4.3.3** has been used. Moreover, let us assume the same simplified failure criterion estimated for **ES** steel, $\overline{\varepsilon}_f^p = 1$.

From the numerical estimations the ballistic limit found is $V_{bl} \approx 85$ m/s, Figs. 5.39-5.40-5.41. Such value is a bit larger than that obtained from experiments. However the difference $\Delta V_{bl} = V_{bl\text{-}numerical} - V_{bl\text{-}experimental} \approx 10$ m/s can be assumed in complex dynamic events like high velocity perforation. The suitability of the numerical model used *(constitutive relation, failure criterion mesh configuration)* has to be highlighted.

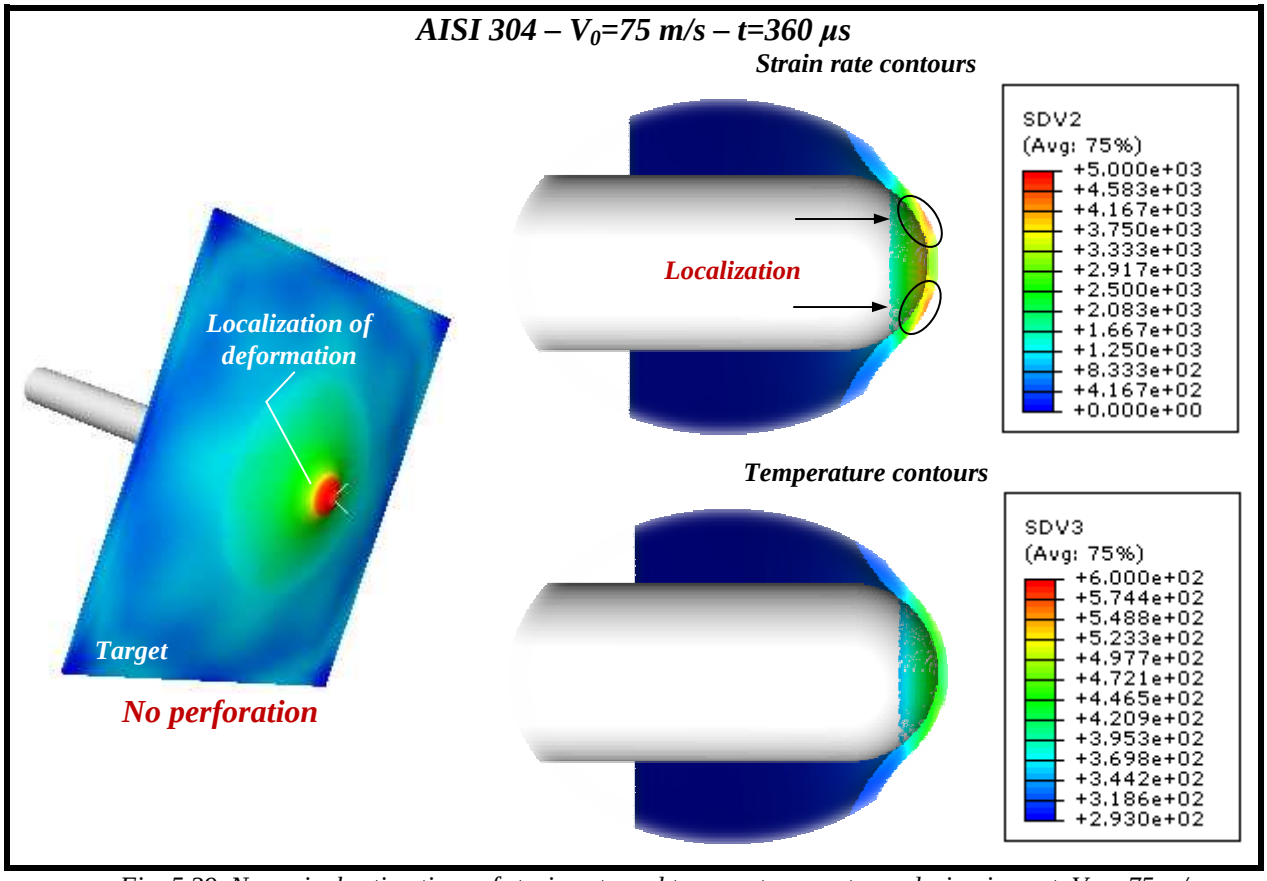

Fig. 5.39. Numerical estimations of strain rate and temperature contours during impact, V_0 = 75 m/s.

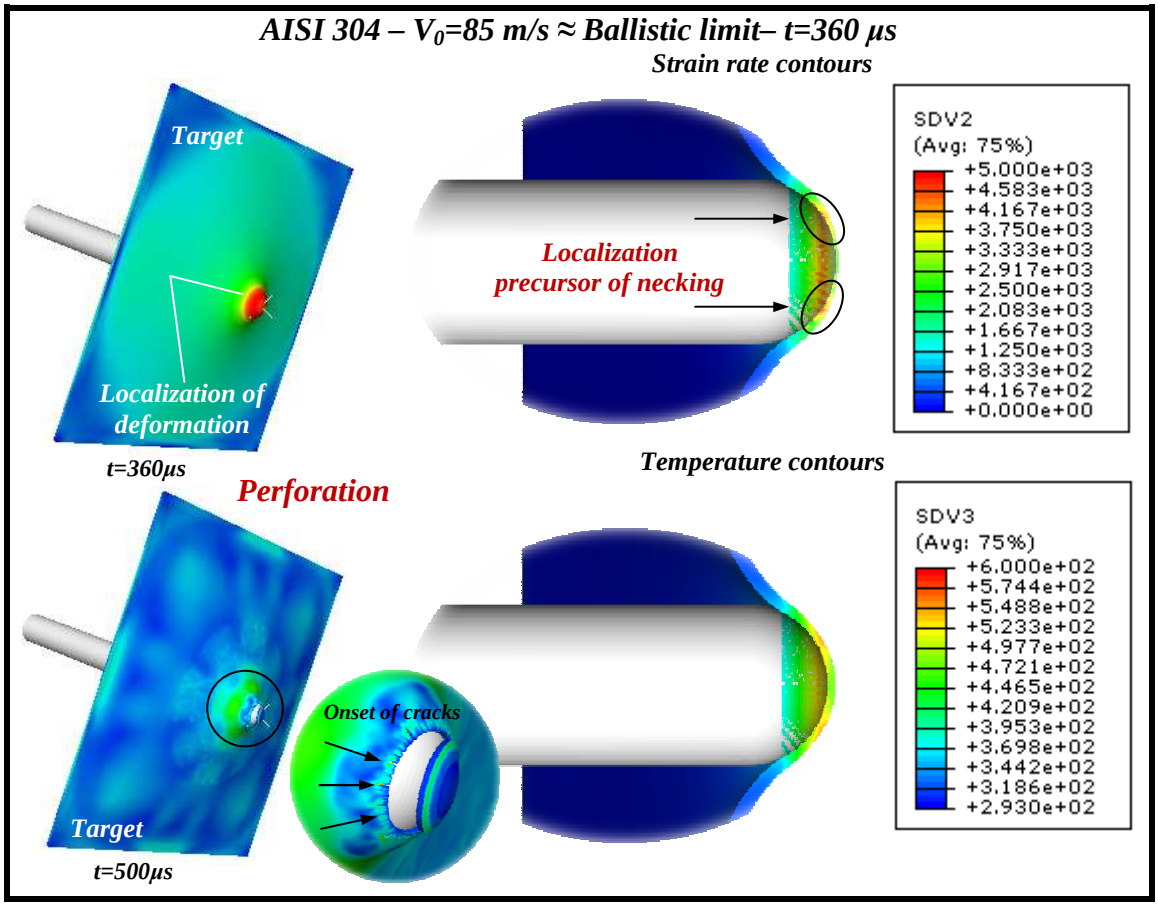

Fig. 5.40. Numerical estimations of strain rate and temperature contours during impact, V_0 = 85 m/s.

From the simulations it has been observed that the maximum strain rate in the material is within the range $1000\ s^{-1} \leq \dot{\bar{\varepsilon}}^p \leq 5000\ s^{-1}$, Figs. 5.39-5.40-5.41. It leads to a maximum increase of temperature within the range $200\ K \leq \Delta T \leq 300\ K$, Figs. 5.39-5.40-5.41. Such values are consistent with the experimental observation reported for **ES** steel if we take into consideration the larger flow stress level of the **AISI 304**. It can be concluded that even under very high temperature increase *martensitic* transformation occurs in this material, improving its performance under fast solicitations.

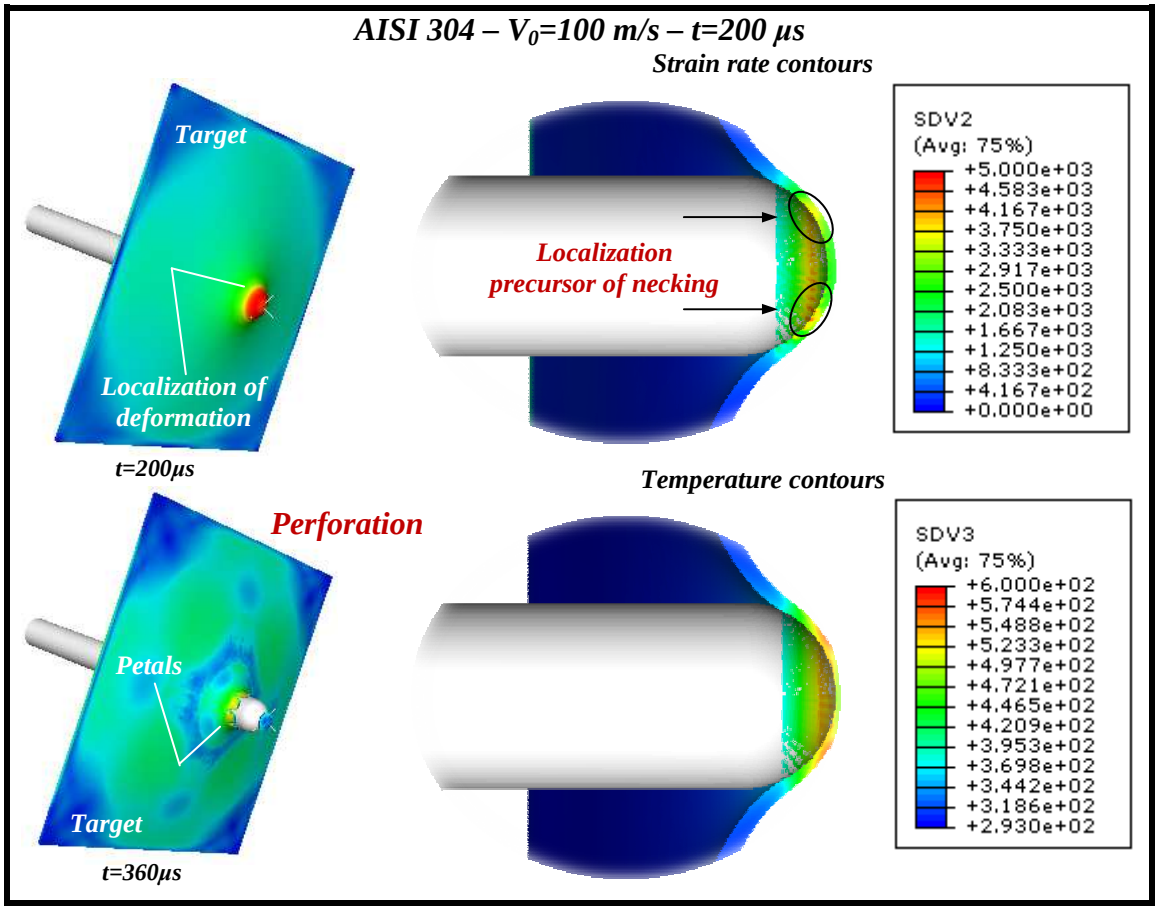

Fig. 5.41. Numerical estimations of strain rate and temperature contours during impact, V_0 = 100 m/s

5.3 Impact behaviour of steel TRIP

In this part of the document the impact behaviour of steel **TRIP 1000** is examined. First, it is discussed the thermo-mechanical characterization of the material conducted by Rusinek and Klepaczko [Rusinek and Klepaczko 2009]. Then perforation tests using the drop weight tower are carried out. Experiments at different initial temperatures T_0 = 213 K and T_0 = 288 K were conducted. The main goal is to examine the potential *martensitic* transformation taking place in **TRIP 1000** under dynamic loading. A comparison with those results reported for the **AISI 304** is conducted. Optimization of materials for absorbing energy under dynamic solicitations is pursued.

5.3.1 Thermo-viscoplastic behaviour of the TRIP 1000 steel

TRIP 1000 multiphase steel belongs to the type called low-alloy **TRIP** steels. This sort of steels is nowadays in widespread use in automotive industry, for example in crash-box structures construction. Such mechanical components are responsible for absorbing energy during crash or accident. The goal is to have advantage of the potential *martensitic* transformation taking place in this kind of material for increasing its strength and ductility during loading.

Low-alloy **TRIP** steels present a microstructure consisting of *ferrite*, *bainite* and retained *austenite* at room temperature. They use to contain low amount of *austenite* stabilisers which promote the phase transformation [Fischer et al. 2000, Liu et al. 2008]. Generally, in low alloy **TRIP** steels the retained *austenite* represents less than 20 % of the total volume, Fig. 5.42., and just a fraction of that *austenite* may be transformed during a mechanical solicitation.

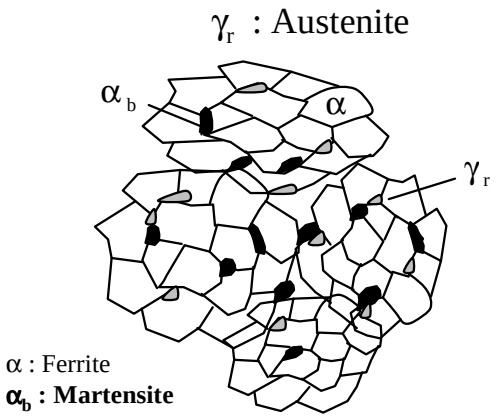

*Fig. 5.42. Scheme of the microstructure of **L-TRIP** steel*

These multiphase steels can be treated, up to a certain point, as composite materials where the retained *austenite* acts as inclusions embedded in a *ferrite-bainite* matrix. The *martensitic* transformation is basically controlled by the "Greenwood- Johnson effect" as reported in [Delannay et al. 2008].

The chemical composition of the **TRIP 1000** multiphase steel is given in Table 5.4 [Oliver et al. 2007].

C	Mn	Si	Cr	P	Al	Ni
0.16	1.58	1.47	0.20	0.087	0.048	0.04

*Table 5.4. Chemical composition of **TRIP 1000** (% of weight) [Oliver et al. 2007].*

It underwent several heat treatments. After being rolled, it first was annealed in the **AC1-AC3** *(beginning AC1≈1023 K and ending of austenitization AC3≈1113 K)* austenitization temperature range, in order to obtain a maximum amount of retained *austenite*. Then, it was quickly cooled down to T ≈ 670 K, when it underwent a tempering for the formation of some *bainite*. It makes the carbon issued from the *ferrite* migrate to the *austenite (carbon enrichment and stabilization of this last phase).* The resulting microstructure is a multiphased material constituted of *ferrite*, *bainite* and about 8% of retained *austenite (less than 2% on the surface and about 15% in the core: this gradient of composition along the thickness has been shown after a series of electropolishings every 50µm),* Fig. 5.43. The volume fraction of each phase has been quantified using picture correlation techniques *(**S**canning **E**lectron **M**icroscope (**SEM**) observations)* as well as **XRD**.

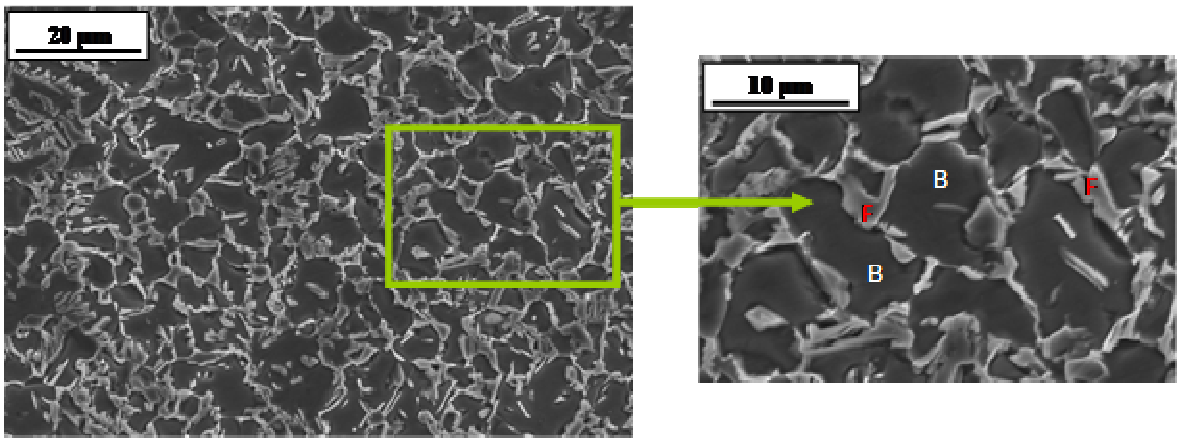

*Fig. 5.43. **SEM** micrograph of the **TRIP 1000** steel showing mainly bainite (B) and ferrite (F) on the surface.*

Moreover, the *martensite* starts temperature of this material, M_S = 135 K, has been determined by dilatometry *(cooling rate of 20°C/s).*

The surface roughness of the material has been analyzed. A mechanical treatment called *"skin pass"* is applied to the **TRIP 1000** steel during manufacturing process. It generates micro-plasticity on the surface of the sample, Fig. 5.44.

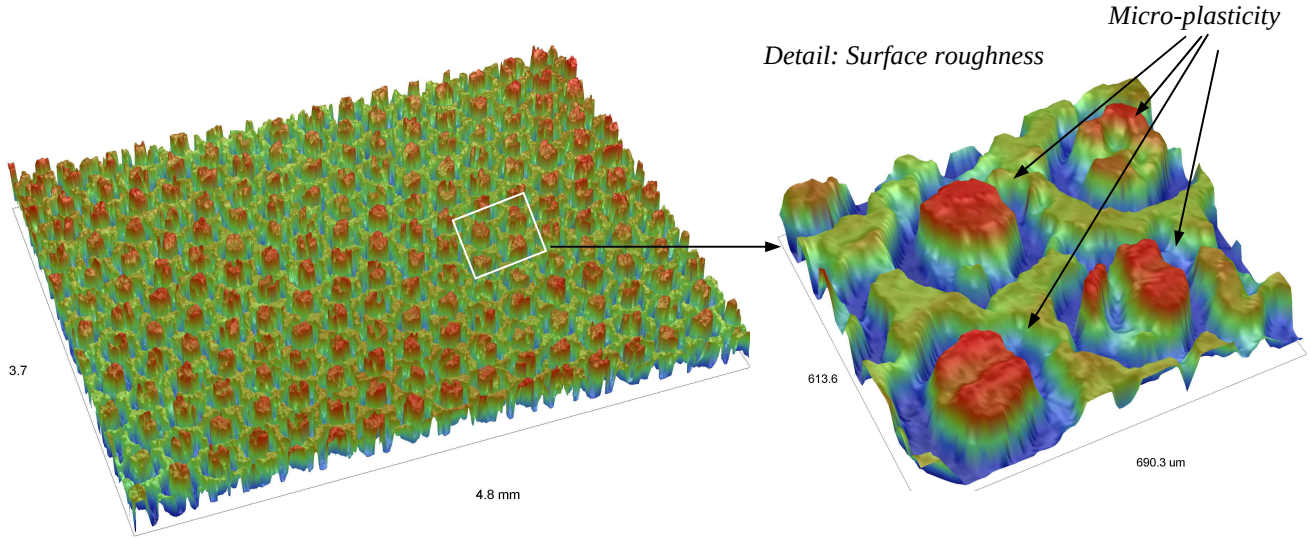

*Fig. 5.44. Surface roughness of **TRIP 1000** steel.*

The induced local plasticity acts as preferred place for the localization of deformation [Rusinek and Klepaczko 2009].

Moreover, **XRD** has enabled to determine the residual stress in the *ferritic* phase in the initial state of the material: 25 MPa in the rolling direction ***(LD)*** and -70 MPa in the transverse direction ***(TD)***. These values of residual stresses are negligible in the case of a **H**igh **S**trength **S**teel (**HSS**) like **TRIP 1000**. Such reduced residual stress level has been induced by the previously mentioned mechanical treatment *("Skin pass")* which, after rolling, has been applied to the material.

Next, it is discussed the thermo-viscoplastic behaviour of the **TRIP 1000**. The tests were originally performed by Rusinek and Klepaczko [Rusinek and Klepaczko 2009].

5.3.1.1 Literature review

In order to characterize the material behaviour, tensile tests were conducted at different loading rates [Rusinek and Klepaczko 2009]. The specimen geometry and dimensions are analogous to those used in the case of **ES** steel, **AA 2024-T3** and **AISI 304**, Fig. 4.5.

The evolution of the flow stress as a function of plastic strain for different rates of deformation is shown in Fig. 5.45-a. The **TRIP 1000** steel has reduced strain rate sensitivity *(in the range of strain rates covered during the tests)*, Fig. 5.45-a. Such an observation is in agreement with experimental data reported in the literature for other **HSS**, [Larour et al. 2007, Rusinek et al. 2009a]. In Fig. 5.45-b [Rodríguez-Martínez et al. 2010b] is depicted how the logarithmic rate sensitivity decreases with the initial static yield stress.

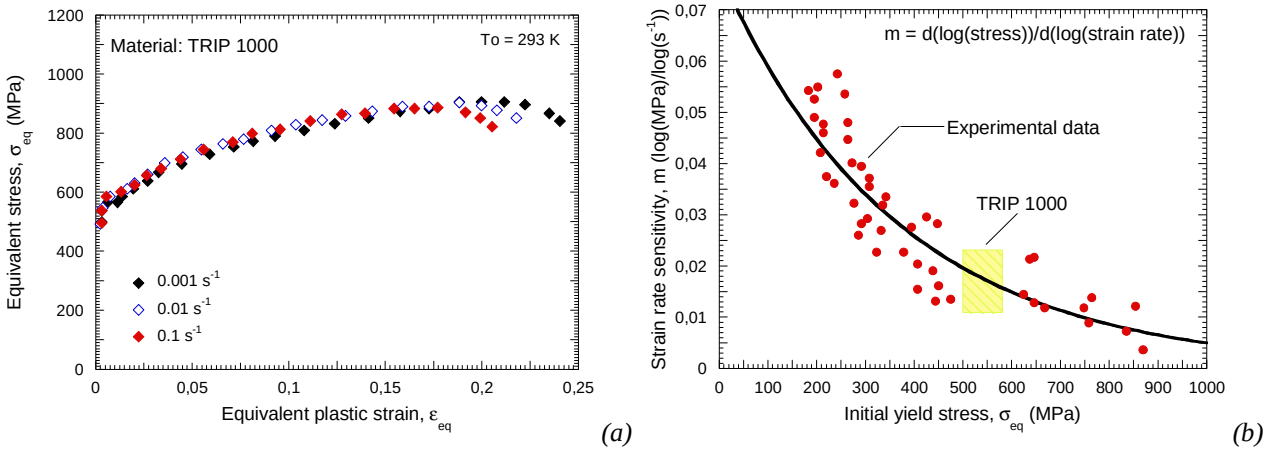

(a) *(b)*

*Fig. 5.45. (a) Flow stress of **TRIP 1000** as a function of plastic strain for different loading rates. (b) Evolution of the logarithmic strain rate sensitivity as a function of the initial static yield stress for different steel alloys [Rodríguez-Martínez et al. 2010b].*

Under quasi-static loading, the material exhibits important temperature sensitivity, Fig. 5.46-a. Temperature decrease leads to greater strain hardening, Fig. 5.46-b. Such behaviour comes from the straining of *austenite* and subsequent *martensitic* transformation [Rusinek and Klepaczko 2009]. Temperature sensitivity is revealed as plastic strain dependent, Fig. 5.46-c.

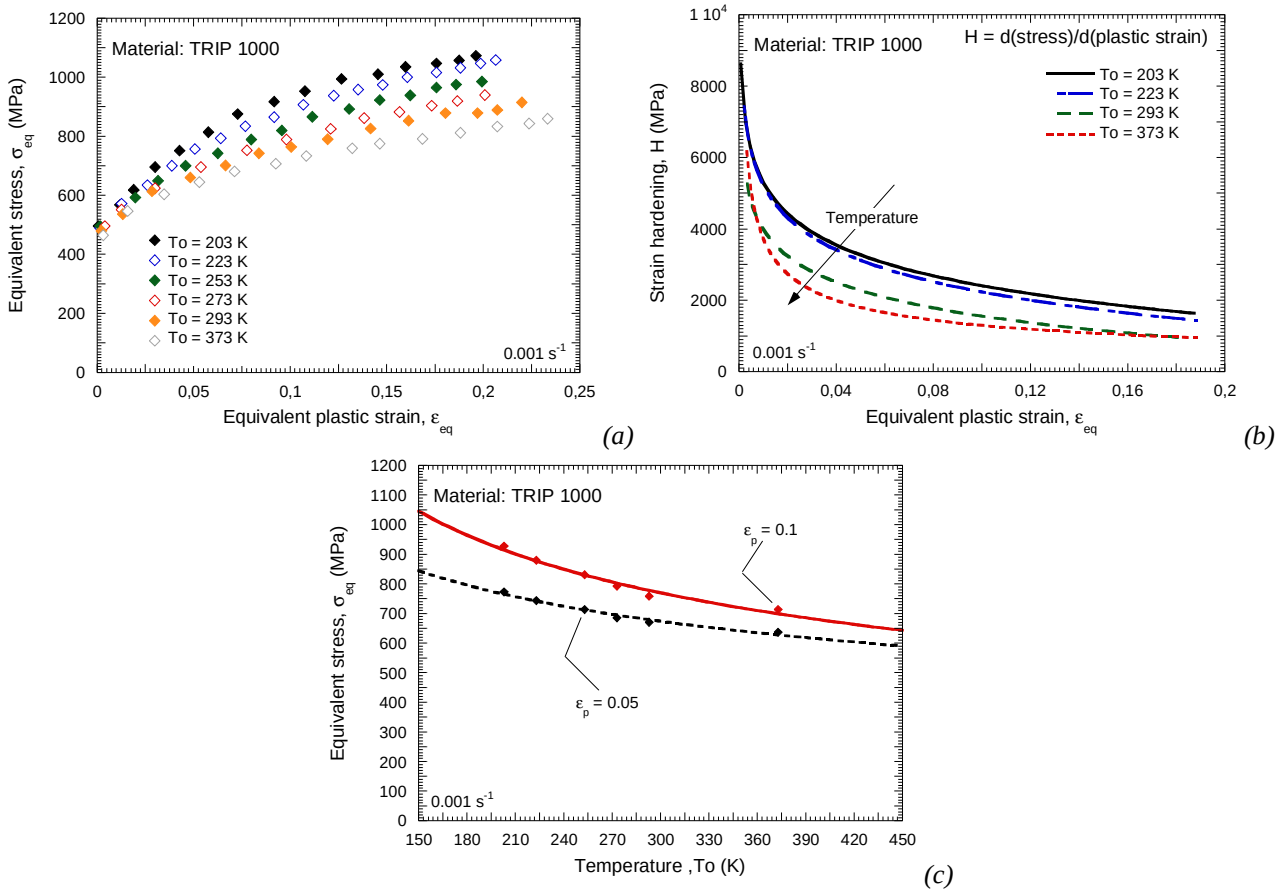

*Fig. 5.46. (a) Flow stress of **TRIP 1000** as a function of plastic strain for different initial temperatures. (b) Strain hardening of **TRIP 1000** as a function of plastic strain for different initial temperatures. (c) Evolution of the flow stress as a function of temperature for different plastic strain values.*

Temperature contours during loading at $\dot{\bar{\varepsilon}}^p = 0.01\ s^{-1}$ are shown in Fig. 5.47. At the beginning of testing is observed Lüder's band propagation along the active part of the specimen, Fig. 5.47. Beyond certain value of straining Lüder's band phenomenon vanishes and strain hardening of the material starts to increase. Then, enhanced by the high flow stress level of **TRIP 1000** *(and by the phase transformation which is an exothermic process as previously discussed in the present document)*, the material temperature strongly increases. Thus, when instability takes place the increase of temperature is clearly focused around the central part of the specimen. The heat generated in the necking zone is hardly being diffused to the rest of the sample, Fig. 5.47. Transient adiabatic conditions of deformation take place. Maximum temperature recorded during the test at $\dot{\bar{\varepsilon}}^p = 0.01\ s^{-1}$ was $\Delta T_{max} \approx 75$ K, Fig. 5.47. and in the case of $\dot{\bar{\varepsilon}}^p = 0.1\ s^{-1}$ was $\Delta T_{max} \approx 130$ K as discussed in [Rusinek and Klepaczko 2009]. It must be noted that such values are quite similar to those reported previously for the **AISI 304**.

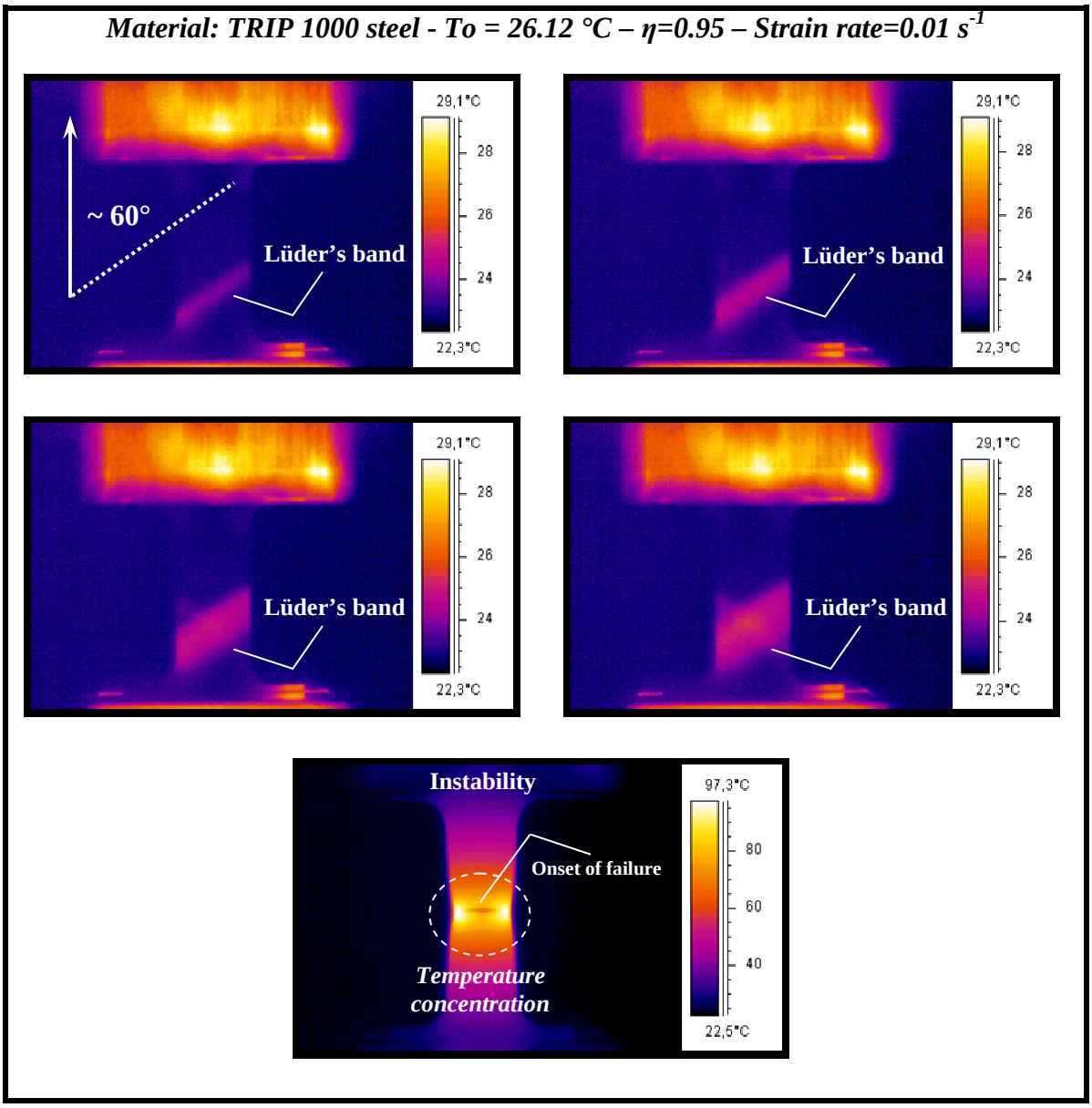

Fig. 5.47. Temperature contours during loading [Rusinek and Klepaczko 2009].

Next, perforation tests of **TRIP 1000** sheets are conducted using the experimental facilities reported in **Section 4.3.3.1.** The results are compared with those previously reported for steel **AISI 304.** The goal is to examine the **TRIP 1000** performance for absorbing energy under impact loading.

5.3.2 Experimental procedure for perforation of metallic sheets

5.3.2.1 The drop weight tower

The drop weight tower was used to conduct the perforation tests. It is considered as suitable for the comparison between **TRIP 1000** and **AISI 304** impact behaviours *(better than the gas gun setup also used to conduct perforation tests in this investigation)* since considerable amount of information can be obtained from the tests *(force history evolution, residual velocity, failure time...).*

The description of the facilities used to conduct *(and analyze)* the low velocity impact tests was already carried out in **Section 4.3.3.1.**

5.3.3 Analysis of the perforation process

Throughout this section of the document, the effects of impact velocity and initial temperature on the perforation process are analyzed.

5.3.3.1 Tests at room temperature

As it was observed for **AA 2024-T3** and **AISI 304** *petalling* is the recurring failure mode for all the perforation tests, Figs. 5.48-5.49. Neither the rolling direction nor boundary conditions influence the initiation or the propagation of cracks. The number of main petals occurring for all the tests performed also oscillates between four and five, Figs. 5.48-5.49.

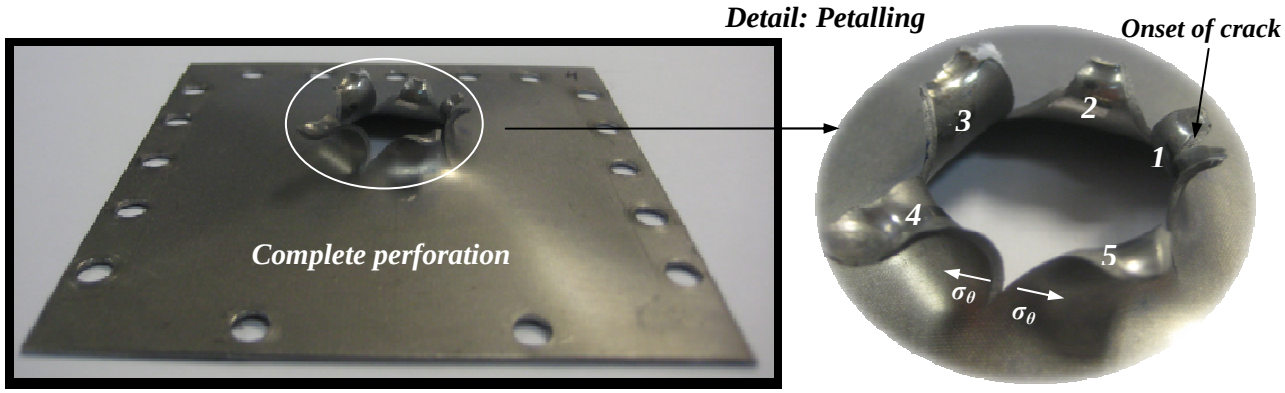

*Fig. 5.48. Petalling failure mode, steel **TRIP 1000**, V_0=4.4 m/s at room temperature.*

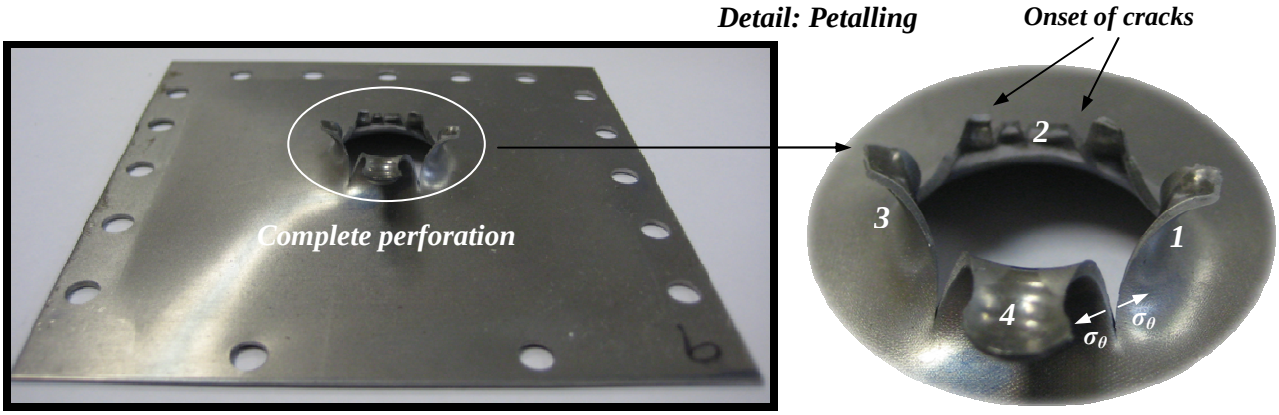

*Fig. 5.49. Petalling failure mode, steel **TRIP 1000**, V_0=3.5 m/s at room temperature.*

In Fig. 5.50. is shown a sequence of images of a test performed at V_0 = 4.4 m/s. The different stages of the perforation process are clearly visible; bending of the plate, localization of deformation, onset and progression of cracks.

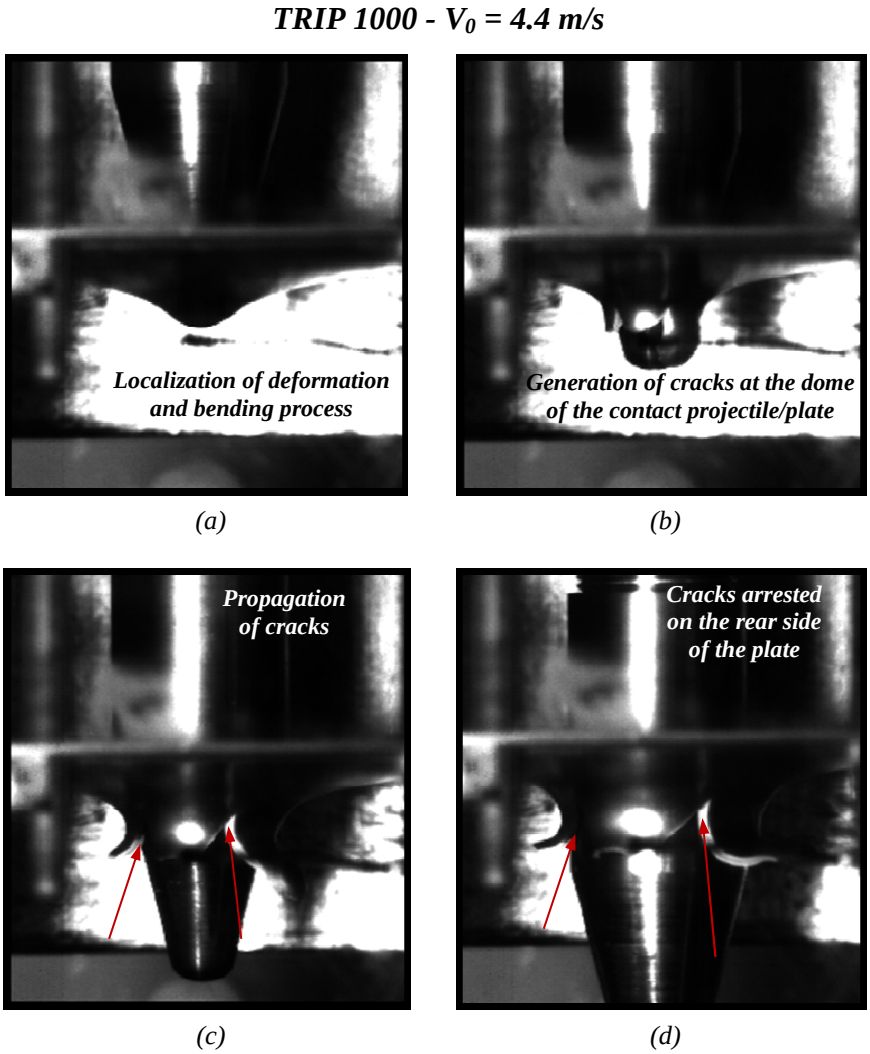

Fig. 5.50. Different stages of the perforation process for Vo=4.4 m/s at room temperature. (a) Localization of deformation and bending process. (b) Generation of cracks at the dome of the contact projectile/plate. (c) Propagation of cracks. (d) Cracks arrested on the rear side of the plate.

In Fig. 5.51. the residual velocity is compared to the initial velocity. The ballistic limit value obtained from the experiments performed at room temperature is V_{bl} = 2.6 m/s, Fig. 5.51. Such value is lower than that obtained for **AISI 304**, Fig. 5.51.

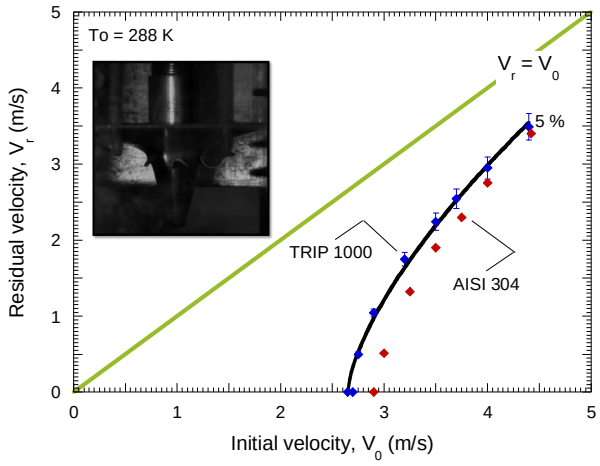

Fig. 5.51. Residual velocity versus initial impact velocity at room temperature.

Thus, it is revealed that the **TRIP 1000** sheets absorb between 10 % and 15% less energy than the **AISI 304** sheets for the whole range of impact velocities tested, Fig. 5.52. The causes which reside behind such difference must be identified.

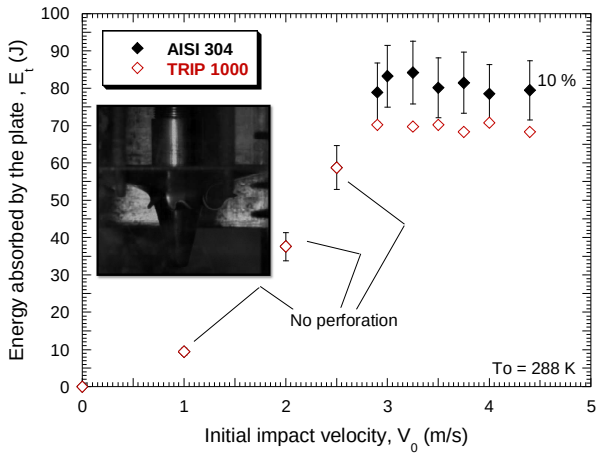

*Fig. 5.52. Energy absorbed by the target as a function of the impact velocity for **AISI 304** and **TRIP 1000**.*

Let us analyze the force evolution versus striker displacement for different impact velocities and both materials **TRIP 1000** and **AISI 304**, Fig. 5.53. In the case of the **TRIP 1000** sheets the slope of those curves $\partial F/\partial \delta_s$ is larger than in the case of **AISI 304**, however the striker displacement until failure is much reduced, Fig. 5.53. Maximum force recorded during perforation is quite similar for both materials within the whole range of impact velocities analyzed, Fig. 5.53.

Those observations can be explained in the following way. **TRIP 1000** shows larger flow stress level than **AISI 304** at the beginning of loading, it involves the larger value of the slope of the curves reported in Fig. 5.53. At the same time **TRIP 1000** shows much reduced strain hardening than **AISI 304** *(bainite and ferrite commonly have lower strain hardening than austenite)* which acts as limiting factor for **TRIP 1000** ductility *(and therefore acts as limiting factor for the striker displacement at failure)*. However both materials show similar maximum strength $(\sigma_{max} \approx 1\,GPa)$ leading approximately the same maximum force during the test.

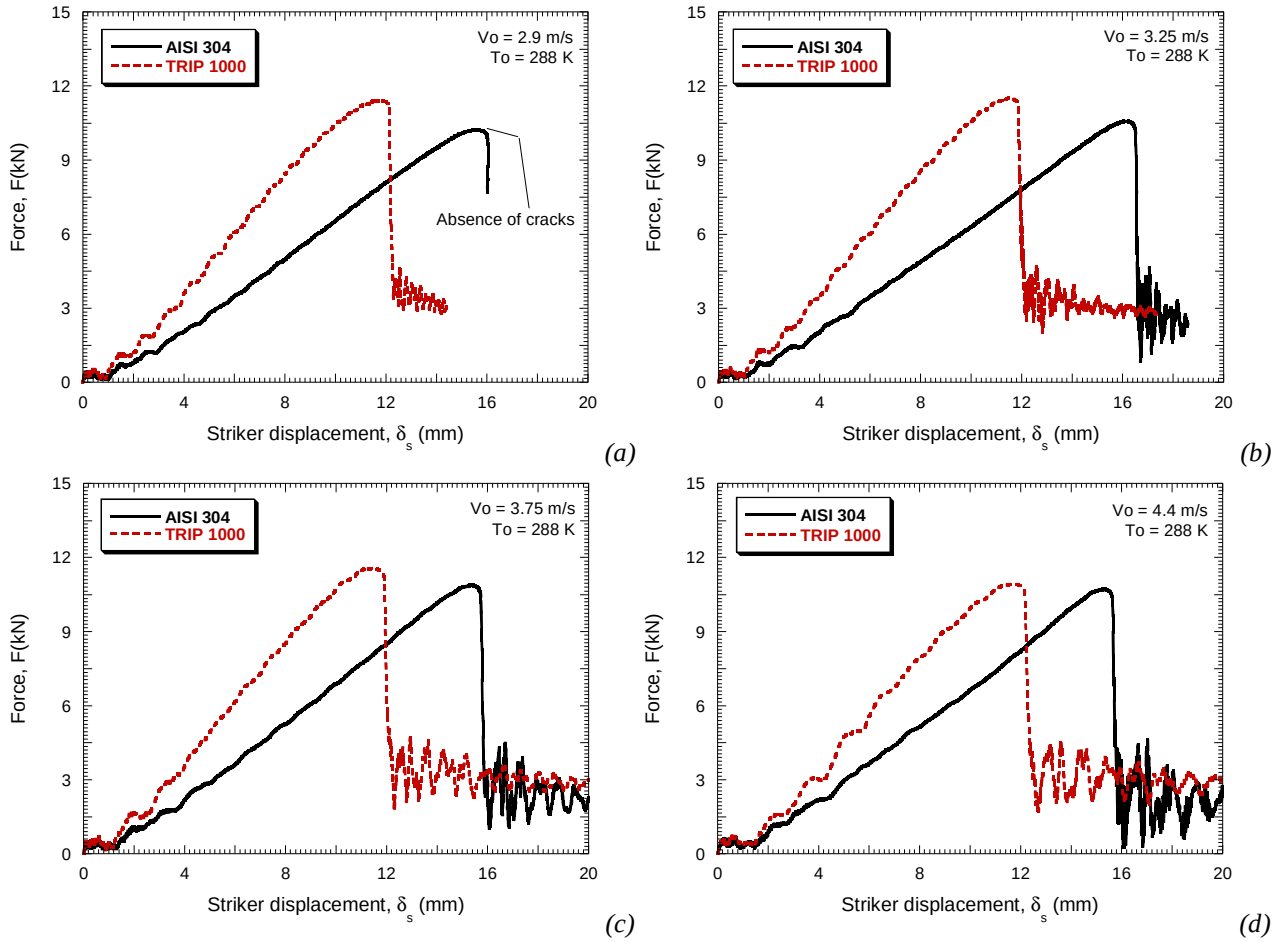

*Fig. 5.53. Force evolution as a function of the striker displacement. Comparison between **AISI 304** and **TRIP 1000** for different impact velocities.*

It can be assumed that in this particular boundary value problem *(and for these two materials)* material strain hardening controls the perforation process. Plastic work is revealed as the main mechanism for absorption of energy. That can be also observed by analyzing the post-mortem bending of the impacted plates, Fig. 5.54. Permanent deflection of the target *(so plastic work)* is much larger in the case of **AISI 304** for the whole range of impact velocities considered, Fig. 5.54.

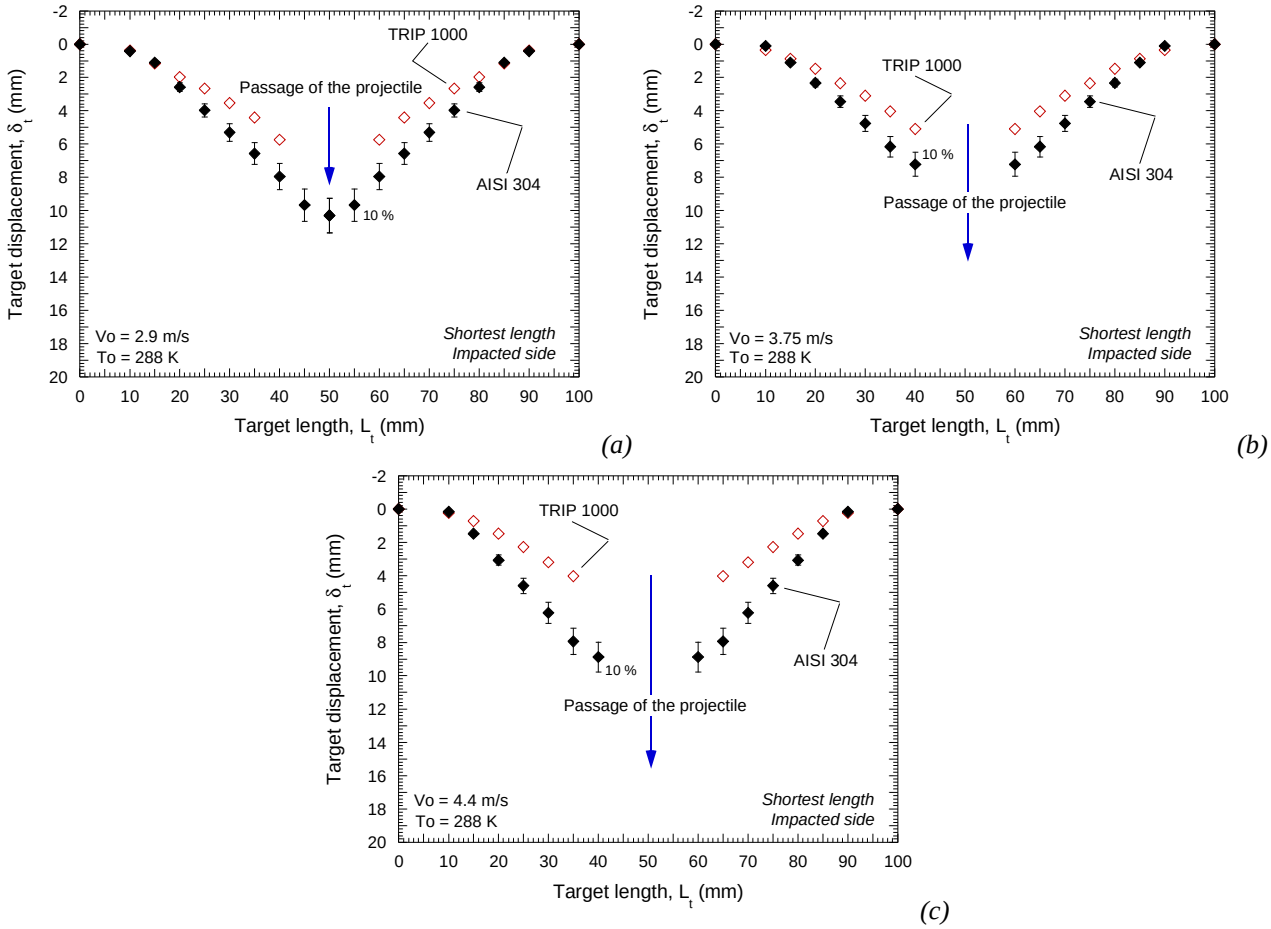

*Fig. 5.54. Permanent bending of the target. Comparison between **AISI 304** and **TRIP 1000** for different impact velocities.*

After such analysis is clearly proven the improved behaviour under low velocity perforation exhibited by **AISI 304** in comparison with **TRIP 1000**. However, is **TRIP 1000** and not **AISI 304** the material specially developed for absorbing energy under such loading conditions. The *martensitic* transformation process is expected to provide to **TRIP 1000** of improved ductility during dynamic solicitations.

Thus, in order to check if such *martensitic* transformation occurs during the perforation process of the **TRIP 1000** sheets **XRD** was used. The main problem induced by this technique is the difficulty in differentiating the *martensite* diffraction peaks from the *ferrite* ones, since these two phases have very similar crystallographic parameters. It was therefore impossible to detect *martensite* and to quantify its volume fraction directly. However, since **TRIP 1000** is a *martensite* free steel in its initial state, it was possible to carry out relevant analyses by calculating precisely the amount of *austenite* in the plates after testing. Subsequently, the possible decrease of its volume fraction was associated to the appearance of a similar volume fraction of *martensite*.

Thus, the volume fraction of retained *austenite* has been determined in different points of the impacted specimens, especially close to the cracking interfaces. Flat petals have also been tested after cutting. The results always revealed a volume fraction of *austenite* close to 2% on the surface of the specimens after failure. The gradient observed along the thickness was still the same, at least in the 300µm analyzed. It is the same amount of *austenite* observed before testing the samples. Therefore, it seems that there is not *martensitic* transformation during perforation.

Close to the zone directly affected by the impact this absence may be explained by the increase of temperature during dynamic loading. As it was previously reported, in **TRIP 1000** the temperature increase is already important under quasi-static loading. Let us assume that during perforation local temperature *(close to the zone directly affected by the impact austenite may be deformed)* deviates too much from the $\mathbf{M_S}$ temperature of this material. It makes the *austenite* phase stable even under potential large *austenite* deformation. Far from the zone directly affected by the impact this absence may be explained by reduce straining of *austenite*. The mechanical energy supplied to this phase may not be enough to promote the *martensitic* transformation. A combination of both effects may be also a plausible explanation.

In order to go further in this investigation let us perform drop weight tower tests at low temperature, T_0 = 213 K. Such experiments are carried out in order to promote *martensite* formation during loading. In adittion, T_0 = 213 K may be assumed as the minimum temperature of interest for automotive applications.

5.3.3.2 Tests at low temperature

Thus, in this section of the document the effect of the initial temperature on the perforation process is studied. The tests performed at T_0 = 288 K are compared to those conducted at T_0 = 213 K. Before testing at low temperature, the steel sheets *(already clamped and screwed)* were subjected to the testing temperature for approximately one hour *(longer time time than that used for the **AA 2024-T3** tets because of the lower conductivity of steel)*. Such a period of time was considered as suitable in order to reach thermodynamic equilibrium material target/testing temperature *(perfect thermodynamic equilibrium plate/environment was pursued in order to not disturb potential phase transformation during loading).*

The first observation concerns the failure mode of the target. No influence of the initial temperature on the perforation mechanisms has been observed for the whole range of impact velocities considered. The final stage of the perforation process is the development of *petals*, Fig. 5.55.

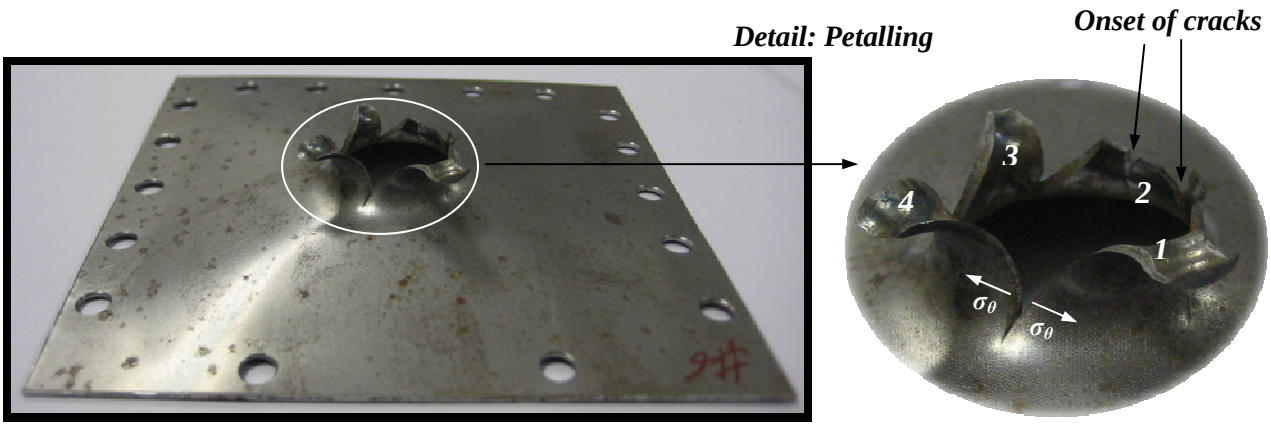

*Fig. 5.55. Petalling failure mode, steel **TRIP 1000**, V_0 = 3.7 m/s and T_0=213K.*

However, the difference occurs with the energy absorbed by the target. At low temperature the ballistic limit is increased from $V_{bl}\big|_{T_0=213\ K} = 2.6\ m/s$ to $V_{bl}\big|_{T_0=288\ K} = 3.1\ m/s$. In the case of V_0 = 2.9 m/s and T_0 = 213 K the striker does not generate any cracks in the target, Fig. 5.56. However, for the same impact velocity and T_0 = 288 K several cracks, precursor of *petalling*, took place.

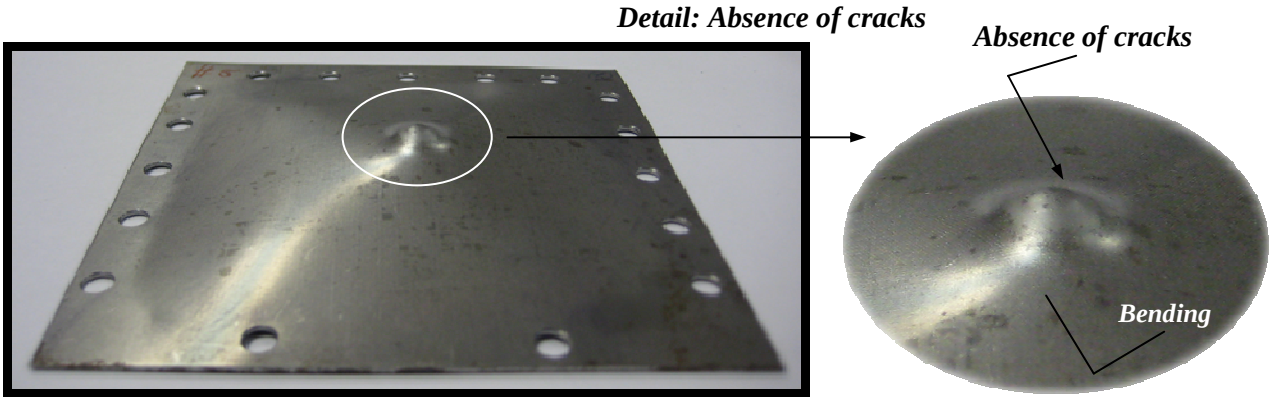

*Fig. 5.56. Petalling failure mode, steel **TRIP 1000**, V_0=2.9 m/s and T_0=213K.*

Permanent bending of the impacted specimens is greater at low temperature, Fig. 5.57. In the case of T_0 = 213 K the target absorbs a larger amount of energy in the form of plastic work.

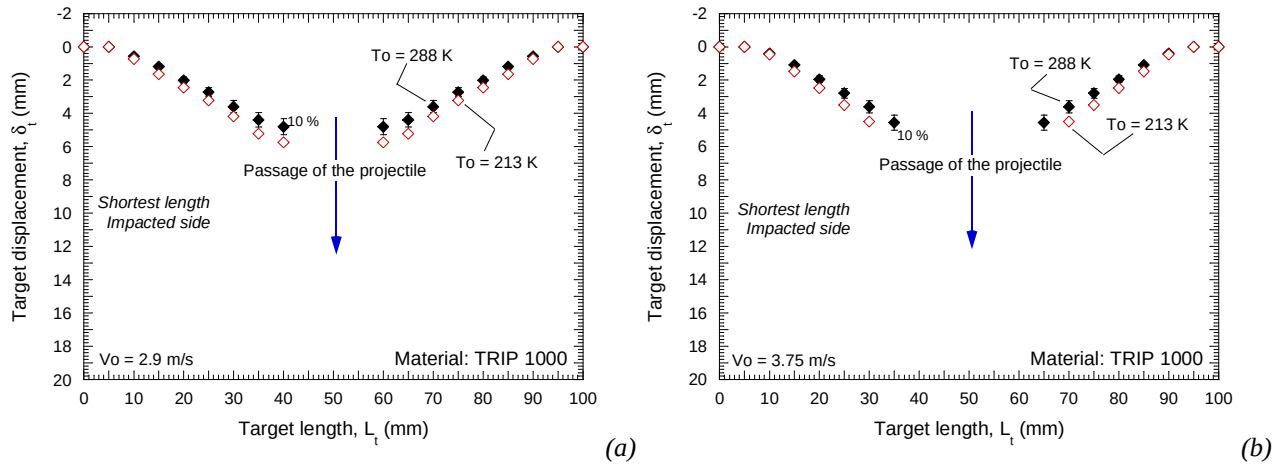

(a) *(b)*

Fig. 5.57. Permanent bending of the target for both initial temperatures. (a) V_0= 2. 9 m/s, (b) V_0 = 3.75 m/s.

The evolution of the force in relation to the striker displacement is shown in Fig. 5.58. for different initial impact velocities. The force level for both initial temperatures is superimposed up to a determined value of striker displacement. The testing temperature only affects the perforation process beyond certain deflection of the plate. Then, the difference resides in the slope of the curve force/striker displacement, Fig. 5.58.

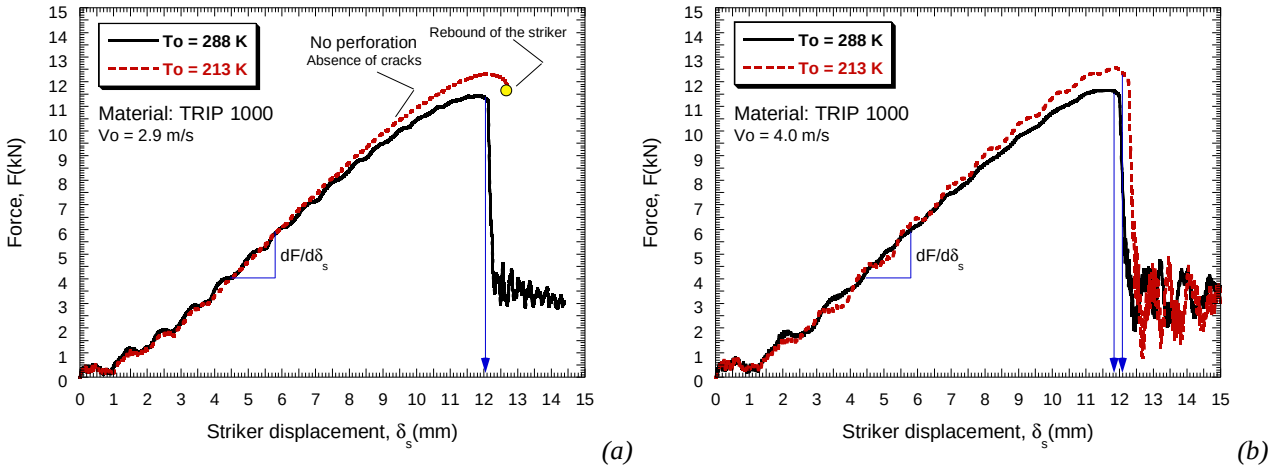

Fig. 5.58. Evolution of the force versus the striker-displacement for both initial temperatures. (a) V_0 = 2.9 m/s, (b) V_0 = 4.0 m/s.

It is necessary to investigate if such differences in the material response are due to *martensitic* transformation or they are simply related to the temperature sensitivity of the material.

Following the procedure reported in the previous section it was concluded that there was not *martensite* in the impacted plates at low temperature. From these results it is assumed that the temperature increase during loading may not be the only one responsible for the absence of *martensitic* transformation during loading. In order to check such assumption let us carry out the following analysis.

A complete residual stress profile has been conducted in the *ferritic* phase, in the two directions, **LD** and **TD**, of the impacted plates (*both radial and circumferential stresses*), Fig. 5.59.

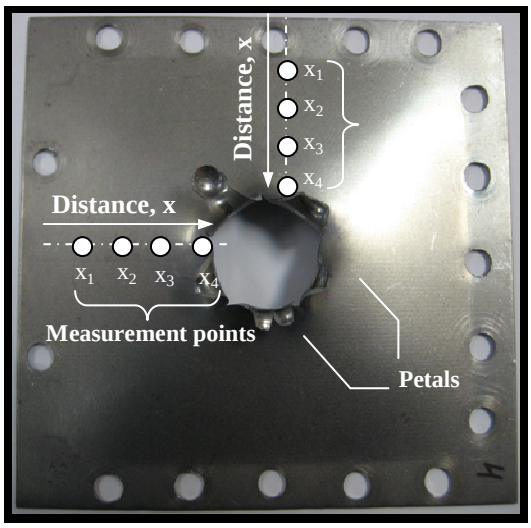

*Fig. 5.59. Measurement points where the **XRD** technique was applied.*

The stress values obtained for two impact velocities, V_0 = 4 m/s and V_0 = 4.4 m/s, are presented in Fig. 5.60. The results are introduced as a function of the distance from the border of the specimen. This distance can slightly vary in both directions (***LD*** *and* ***TD***) depending on the shape of the perforated zone (*in the same way, some points close to the impacted zones could not be analysed because petals constituted an obstacle to X-rays*).

Negative values of the residual stress in *ferrite* are illustrated in Fig. 5.60. It indicates that this phase is in compressive state in **TRIP 1000** *(soft phase). Cementite (present in bainite)* and *austenite* play the role of hard phases in this steel. During loading, the stress in *ferrite* is therefore inferior to the macroscopic stress of the material. An important part of the plastic strain required by *austenite* for the *martensitic* transformation is localized in the *ferrite*. Reduced deformation of the *austenite* phase seems to prevent *martensitic* transformation. The radial stress is maximum in *ferrite* close to the impacted zones. There, the discrepancy between the macroscopic stress and the one in *ferrite* is the greatest. The level of strain in *ferrite* is greater in the zone directly affected by the impact.

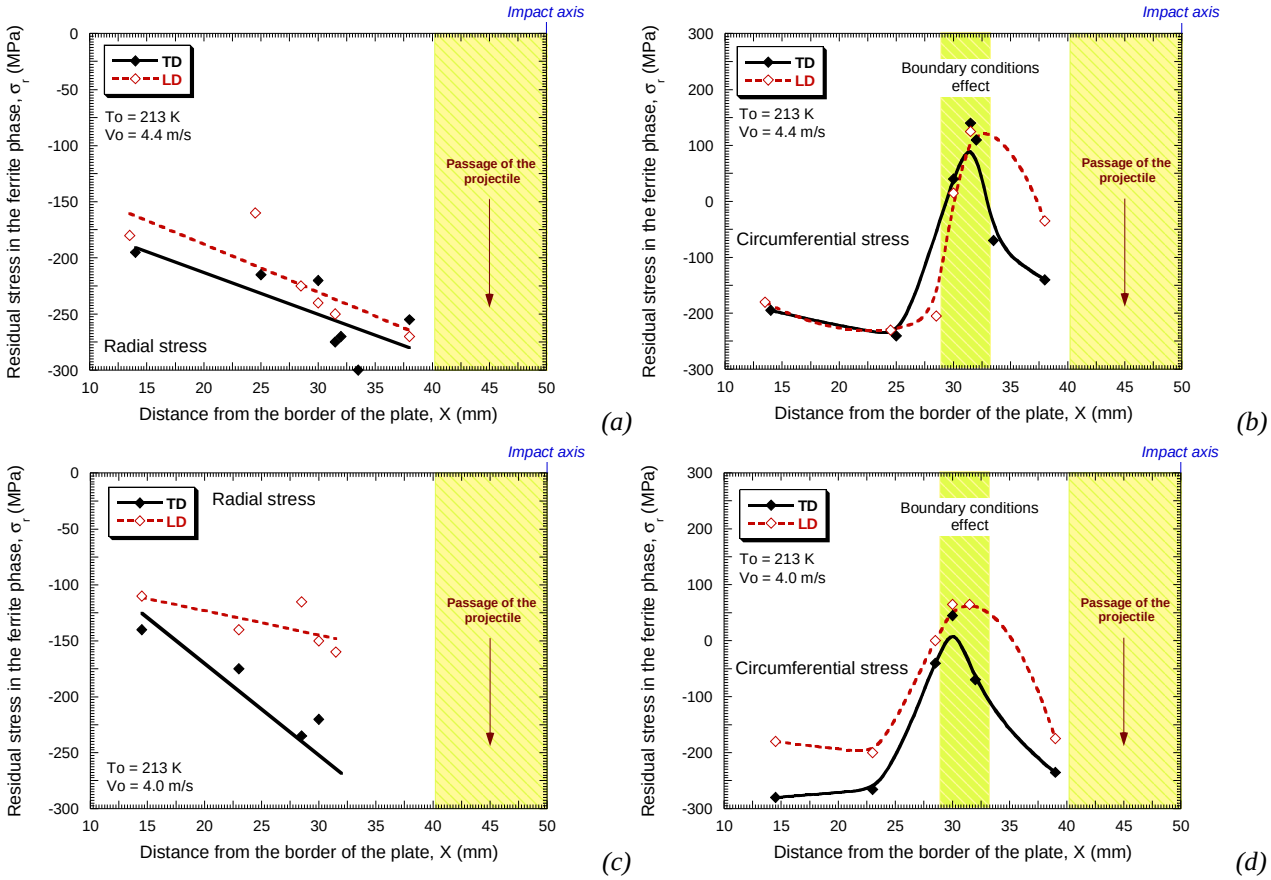

Fig. 5.60. Residual stress in ferrite along the distance from the border to the center of the plate for different initial impact velocities at T_0= 213 K. (a)-(b) V_0= 4.4 m/s, (c)-(d) V_0=4.0 m/s.

It must be noted that positive stress values in *ferrite* are observed for the circumferential stress in the reduced range 28 mm ≤ X ≤ 32 mm, Fig. 5.60-b-d. Such local behaviour may be associated to the curvature changes in the profiles of the impacted plates. Since the samples tested have a square shape, the bending effect is not symmetric, either in the radial, or in the circumferential direction *(impact induces radial wave propagation; however, the distance to the clamped perimeter is not the same in all directions).* In order to accommodate plastic deformation, the samples tested exhibit local tensile state *(in the circumferential direction)* in the previously mentioned target zone, 28 mm ≤ X ≤ 32 mm.

This chapter dealt with the impact-perforation behaviour of two metallic alloys, steel **AISI 304** and steel **TRIP 1000**. These materials are thermo-mechanically characterized, analytically modeled and subjected to perforation by non-deformable projectiles. Their deformation mechanisms are tied to their answer under impact-perforation. The potential martenstic transformation occurring during dynamic loading has been analyzed. Based on the constitutive relations developed in chapter 1, numerical models of the perforation test have been built. The numerical results obtained are in agreement with the experiments in terms of ballistic limit prediction and failure mode definition. Plastic instabilities formation and progression is revealed as the mechanism behind material failure in the impact tests.

CHAPTER 6

CONCLUSIONS AND FUTURE WORK

6 CHAPTER 6. CONCLUSIONS AND FUTURE WORK

6.1 Concluding and remarks

Below are summarized the main findings and conclusions arising from this doctoral Thesis:

- To complement the **RK** model, the **MRK** constitutive description has been proposed. The former is suitable for describing the behaviour of metals whose rate sensitivity in independent of plastic strain. The latter is suitable for defining the behaviour of metals showing dependence of strain on the volume thermally activated. Extensions to viscous drag effects, negative strain rate sensitivity and phase transformation phenomena are derived for both, **RK** and **MRK** models. It has been proven the suitability of the constitutive relations developed for defining the thermo-viscoplastic behaviour of both **BCC** and **FCC** metallic alloys. Such a range of strain hardening laws is indispensable for conducting a proper analysis of the plastic behaviour of metals under transient loadings.

- The constitutive relations developed have been implemented into the **FE** code **ABAQUS/Explicit**. It made possible to conduct a broad campaign of numerical simulations in order to analyze the impact of wave propagation, rate sensitivity and strain hardening on the formation of instabilities under dynamic loading. Both, ring expansion test and conventional dynamic tension test have been examined under wide ranges of impact velocities. It has been demonstrated that rate sensitivity and strain hardening rate determine ductility of metals. Therefore, they are main responsible for the capability of metallic materials for absorbing energy under dynamic events.

- It has been analyzed the thermo-viscoplastic behaviour of steel **ES** under impact/perforation. Experiments were conducted with a gas gun within the range of impact velocities 25 m/s $\leq V_0 \leq$ 60 m/s. The tests were recorded using high speed infrared camera. Assuming adiabatic conditions of deformation along the contact-interface projectile/plate, the increase of temperature is related to the plastic deformation. The critical failure-strain leading to target-collapse is evaluated coupling temperature-measurements with numerical simulations and with analytical predictions of the material behaviour obtained using the **RK** model. Following such procedure it has been estimated that the process of localization of deformation which is precursor of target-failure involves local plasticity values close to $\bar{\varepsilon}^p \approx 1$. The application of such value of failure strain to numerical simulations of the perforation tests provides results in agreement with experiments.

- The thermo-viscoplastic behaviour of **AA 2024-T3** has been characterized in tension under wide ranges of strain rate and temperature. The material shows high strain hardening and elevated ductility. A remarkable characteristic of this alloy is the increase of the strain hardening with the temperature decrease. The temperature sensitivity is dependent on plastic strain. Thus, the ductility of the material is increased at low initial temperatures. Such behaviour makes this alloy of main interest for aeronautical applications. The thermo-viscoplastic behaviour of **AA 2024-T3** has been modeled using the extended **MRK** model to viscous drag effects. Satisfactory agreement between experiments and analytical predictions of the constitutive relation are reported. Based on

such understanding of the material behaviour, perforation tests of **AA 2024-T3** sheets are conducted using both a gas cannon and a drop weight tower. High velocity impact tests were conducted within the range 10 m/s $\leq V_0 \leq$ 45 m/s. Drop weight tower experiments were carried out within the range 0.5 m/s $\leq V_0 \leq$ 4.5 m/s under different initial temperatures, T_0 = 213 K and T_0 = 288 K. As it was expected the **AA 2024-T3** exhibited a good performance under low testing temperatures. Numerical simulations of the high velocity impact tests were conducted. The numerical model developed allowed for a proper description of the perforation process in terms of ballistic limit prediction and failure mode.

- The thermo-viscoplastic behaviour of the steel **AISI 304** is examined. Two different experimental setups have been used for characterization of the thermo-mechanical behaviour of the material. First, unconventional in situ tensile tests were carried out for examination of the *martensitic* transformation under static loading at room temperature. The flow stress evolution as a function of plastic strain has been determined for both the *austenite* and *martensite* phases. It was revealed that *martensitic* transformation takes place from very low straining values. In the post mortem specimens it was measured the *martensite* volume fraction, $V_{\alpha'} \approx 60$ %. Second, regular tensile tests were conducted under wide ranges of strain rate and temperature. Such tests were recorded using high speed infrared camera. The volume fraction of *martensite* in the post-mortem specimens was determined. It was revealed that the phase transformation occurs even under a temperature increase above $\Delta T > 140$ K. The thermo-viscoplastic behaviour of the material has been defined using the extended **RK** model to viscous drag effects. Satisfactory agreement between experiments and analytical predictions of the constitutive relation are reported. Moreover perforation tests at room temperature using drop weight tower and gas cannon are conducted. The drop weight tower tests are carried out within the range of impact velocities 2.5 m/s $\leq V_0 \leq$ 4.5 m/s. The high impact velocity tests are conducted within the range 25 m/s $\leq V_0 \leq$ 85 m/s. The **AISI 304** showed very good performance under impact loading. The cause which resides behind such behaviour seems to be the *martensitic* transformation taking place during the perforation tests. The impacted plates were subjected to observation using **SEM**. Notable amount of *martensite* was found for all the tests performed. Finally numerical simulations of the impact process were conducted. The numerical model developed allowed for a proper description of the perforation process in terms of ballistic limit prediction and failure mode.

- The thermo-mechanical behaviour of the steel **TRIP 1000** under perforation has been examined. The relevance of this material resides in the potential transformation of residual *austenite* into *martensite* under straining. In order to study the material behaviour under fast loading, perforation tests have been performed using a drop weight tower. Experiments at different initial temperatures, T_0 = 213 K and T_0 = 288 K, and impact velocities, 5 m/s $\leq V_0 \leq$ 4.5 m/s, were carried out. **XRD** method allowed measuring the *austenite* content of the samples before and after impact. The results always revealed the same volume fraction of *austenite*. The absence of *martensitic* transformation may be explained by the increase of temperature during loading in the zone directly affected by the impact *(close to the zone directly affected by the impact austenite may be deformed)*. Moreover, residual stress analysis of *ferrite* showed that it plays the role of the soft phase during plastic deformation of the material. An important part of the plastic strain required by *austenite* for the *martensitic* transformation is localized in *ferrite*. In the target zones where an increase of temperature was not

noticeable *(far from the zone directly affected by the impact)*, reduced deformation of the *austenite* phase prevents *martensitic* transformation. Under these considerations *(and loading conditions)* **TRIP 1000** steel seems to behave as a regular **H**igh **S**trength **S**teel with an absence of *martensitic* transformation.

In this Thesis it has been demonstrated the necessity of providing an integrated view to the impact processes in order to understand the mechanisms for absorption of energy that, under dynamic loading, are showed by metallic alloys. For that task, an original methodology has been developed. This procedure combines advanced measuring techniques like infrared recording or X-ray diffraction with numerical simulations supported by the accurate description of the material behaviour. Thus, this investigation led to the main findings outlined above which are of relevant for different industrial applications.

6.2 Future work

Some of the future researching lines are outlined below:

- **RK** and **MRK** constitutive descriptions take into account only the instantaneous rate sensitivity of the material. Instantaneous strain rate sensitivity describes the rate-dependent behaviour of metals during continuous loading condition *(current value of flow stress is an instantaneous function of strain, strain rate and temperature)*. Many of the constitutive descriptions reported in the literature *(physical-based models as well as phenomenological models)* are usually restricted to such application fields. However, it is known that strain rate history effects are present in the material deformation behaviour. Historical effects may be of relevance for modeling the material behaviour when it is subjected to an abrupt increase of applied deformation rate or to a cycling loading process. In order to take into account such considerations, definitions of internal state variables in the formulation of the constitutive description are necessary. It will allow gathering information concerning the microstructure evolution suring plastic deformation.

- In this doctoral Thesis the **Huber-Misses** yield function has been used to describe the thermo-viscoplastic behaviour of metals. **J2** plasticity involves an isotropic definition of the material behaviour. In order to analyze metallic alloys with dependence of pressure on the yield condition, it would be helpful to combine the constitutive relations here proposed with advanced plasticity criteria like those due to **Gurson** or **Burzyński**.

- Moreover, it is known that damage softening may play an important role on the behaviour of certain metals under determined loading conditions. Damage is known as dependent on strain, strain rate and temperature as well as on stress state. Thus, a description of damage phenomenon gathering such dependences has to be derived and combined with the constitutive relations introduced in this work. For such a goal, it is required a rigorous experimental methodology which allow us to identify accurately the loading conditions under which damage softening in metals is developed.

- In order to complement the analysis conducted in this work for uniaxial stress state, in forthcoming studies it will be necessary to identify the role of strain rate and strain hardening on the formation of instabilities under other stress states like for example pure shear. Adiabatic shear bands formed under dynamic loading are responsible for material failure in industrial processes like high speed machining of fast cutting. The advanced constitutive descriptions developed in this work may be applied for such goal.

- It is revealed necessary to conduct an experimental campaign in order to go further in the understanding of the mechanisms responsible for absorbing energy under dynamic solicitation. Special interest must be focused on the new generations of **H**igh **S**trength **S**teels, like for example **TRIP** and **TWIP** steels. Classical testing methods must be combined with advanced measuring techniques like infrared thermography, image correlation and X-ray diffraction in order to examine the causes of strain localization. As it was described in this work, such experimental campaign has to cover from the uniaxial characterization of the material behaviour up to the structural response of the material under impact/perforation. The efforts may be centered on:

  - Application of image correlation technique to impact events like fast tension, compression and shear tests, perforation processes or impact of crash box structures. It will allow us to know the role played by strain and strain rate on the generation of plastic instabilities and failures under dynamic loading.

  - Infrared recording of dynamic events like fast tension, compression and shear tests, perforation processes or impact of crash box structures. It will allow us to measure the role played by thermal softening on the generation of plastic instabilities and failures under dynamic loading

6.3 Publications

Below are listed the publications related to this doctoral Thesis.

International Papers

AUTHORS: A. ARIAS, **J. A. RODRÍGUEZ-MARTÍNEZ,** A. RUSINEK
TITLE: NUMERICAL SIMULATIONS OF IMPACT BEHAVIOUR OF THIN STEEL PLATES SUBJECTED TO CYLINDRICAL, CONICAL AND HEMISPHERICAL NON-DEFORMABLE PROJECTILES
YEAR: 2008
VOLUME, PAGES: 75; 1635-1656
JOURNAL: ENGINEERING FRACTURE MECHANICS
JCR: 1.713

AUTHORS: A. RUSINEK, **J. A. RODRÍGUEZ-MARTÍNEZ,** A. ARIAS, J. R. KLEPACZKO, J. LÓPEZ-PUENTE
TITLE: INFLUENCE OF CONICAL PROJECTILE DIAMETER ON PERPENDICUALR IMPACT OF THIN STEEL PLATE
YEAR: 2008
VOLUME, PAGES: 78; 2946-2967
JOURNAL: ENGINEERING FRACTURE MECHANICS
JCR: 1.713

AUTHORS: A. RUSINEK, **J. A. RODRÍGUEZ-MARTÍNEZ,** R. ZAERA, J. R. KLEPACZKO, A. ARIAS, C. SAUVELET
TITLE: EXPERIMENTAL AND NUMERICAL ANALYSIS ON FAILURE PROCESS OF MILD STEEL SHEETS SUBJECTED TO PERPENDICUALR IMPACT BY HEMISPHERICAL PROJECTILES
YEAR: 2009
VOLUME, PAGES: 36; 565-587
JOURNAL: INTERNATIONAL JOURNAL OF IMPACT ENGINEERING
JCR: 1.398

AUTHORS: A. RUSINEK, **J. A. RODRÍGUEZ-MARTÍNEZ,** J. R. KLEPACZKO, R. B. PECHERSKI
TÍTULO: ANALYSIS OF THE THERMO-VISCOPLASTIC BEHAVIOUR OF HIGH SIX STRENGTH STEELS
YEAR: 2009
VOLUME, PAGES: 30; 1748-1761
JOURNAL MATERIALS AND DESIGN
JCR: 1.107

AUTHORS: A. RUSINEK, **J. A. RODRÍGUEZ-MARTÍNEZ,** J. R. KLEPACZKO, R. B. PECHERSKI, A. ARIAS
TITLE: MODELLING OF THERMO-VISCO-PLASTIC BEHAVIOUR OF DH-36 AND WELDOX-460-E STRUCTURAL STEELS AT WIDE RANGES OF STRAIN RATES AND TEMPERATURES, COMPARISON OF CONSTITUTIVE RELATIONS AND APPLICATION FOR IMPACT PROBLEMS
YEAR: 2009
VOLUME, PAGES: 41; 599-621
JOURNAL: MECHANICS OF MATERIALS
JCR: 2.374

AUTHORS: J. A. RODRÍGUEZ-MARTÍNEZ, A. RUSINEK, J. R. KLEPACZKO, R. B. PECHERSKI
TITLE: EXTENSION OF RUSINEK-KLEPACZKO CONSTITUTIVE RELATION TO PHASE TRANSFORMATION PHENOMENA
JOURNAL: MATERIALS AND DESIGN
YEAR: 2009
VOLUME, PAGES: 30; 2513-2520
JCR: 1.107

AUTHORS: J. A. RODRÍGUEZ-MARTÍNEZ, A. RUSINEK, J. R. KLEPACZKO
TITLE: CONSTITUTIVE RELATION FOR STEELS APPROXIMATING QUASI-STATIC AND INTERMEDIATE SRAIN RATES AT LARGE DEFORMATION
YEAR: 2009
VOLUME, PAGES: 36; 419-427
JOURNAL: MECHANICS RESEARCH COMMUNICATIONS
JCR: 1.045

AUTHORS: A. RUSINEK, **J. A. RODRÍGUEZ-MARTÍNEZ**
TITLE: THERMO-VISCOPLASTIC CONSTITUTIVE RELATION FOR ALUMINIUM ALLOYS, MODELING OF NEGATIVE STRAIN RATE SENSITIVITY AND VISCOUS DRAG EFFECTS
JOURNAL: MATERIALS AND DESIGN
YEAR: 2009
VOLUME, PAGES: 30; 4377-4390
JCR: 1.107

AUTHORS: J. A. RODRÍGUEZ-MARTÍNEZ, A. RUSINEK, A. ARIAS
TITLE: RELATION BETWEEN STRAIN HARDENING OF STEEL AND CRITICAL IMPACT VELOCITY IN TENSION
JOURNAL: JOURNAL OF THEORETICAL AND APPLIED MECHANICS
YEAR: 2009
VOLUME, PAGES: 47; 645-665

AUTHORS: A. RUSINEK, **J. A. RODRÍGUEZ-MARTÍNEZ**, A. ARIAS
TITLE: A THERMO-VISCOPLASTIC CONSTITUTIVE MODEL FOR FCC METALS WITH APPLICATION TO OFHC COPPER (IN PRESS)
JOURNAL: INTERNATIONAL JOURNAL OF MECHANICAL SCIENCES
JCR: 1.077

AUTHORS: J. A. RODRÍGUEZ-MARTÍNEZ, A. RUSINEK, P. CHEVRIER, R. BERNIER, A. ARIAS
TITLE: TEMPERATURE MEASUREMENTS ON ES STEEL SHEETS SUBJECTED TO PERFORATION BY HEMISPHERICAL PROJECTILES (IN PRESS)
JOURNAL: INTERNATIONAL JOURNAL OF IMPACT ENGINEERING
JCR: 1.398

AUTHORS: J. A. RODRÍGUEZ-MARTÍNEZ, R. PESCI, A. RUSINEK, A. ARIAS, R. ZAERA, D. A. PEDROCHE
TITLE: ON THE THERMO-MECHANICAL BEHAVIOUR OF TRIP 1000 STEEL SHEETS SUBJECTED TO LOW VELOCITY PERFORATION AT DIFFERENT TEMPERATURES BY CONICAL PROJECTILES (IN PRESS)
JOURNAL: INTERNATIONAL JOURNAL OF SOLIDS AND STRUCTURES
JCR: 1.809

International Conferences

AUTHORS: A. ARIAS, A. RUSINEK, **J. A. RODRÍGUEZ-MARTÍNEZ,** J. LÓPEZ-PUENTE, C. NAVARRO
TITLE: NUMERICAL MODELLING OF THE DYNAMIC BEHAVIOUR OF CLAMPED STEEL PLATES UNDER HIGH VELOCITY NORMAL IMPACT
CONFERENCE: MCMAT 2007. ASME. APPLIED MECHANICS AND MATERIALS CONFERENCE
LOCATION: AUSTIN (TEXAS) EEUU
YEAR: 2007

AUTHORS: A. RUSINEK, **J. A. RODRÍGUEZ-MARTÍNEZ,** R. ZAERA, C. SAUVELET, A. ARIAS, J. R. KLEPACZKO
TITLE: INVESTIGATION OF THE FAILURE MODE OF MILD STEEL SHEETS SUBJECTED TO PERPENDICULAR IMPACT BY HEMISPHERICAL PROJECTILES
CONFERENCE: LPMM-WORKSHOP 2007
LOCATION: METZ (FRANCE)
YEAR: 2007

AUTHORS: J. A. RODRÍGUEZ-MARTÍNEZ, A. RUSINEK, A. ARIAS, J. R. KLEPACZKO
TITLE: ANALYSIS OF PLASTIC INSTABILITIES FOR METALLIC SHEETS DURING PERFORATION: EFFECT OF PROJECTILE SHAPE, IMPACT VELOCITY, INITIAL TEMPERATURE AND FRICTION CONDITIONS.
CONFERENCE: POZNAN-WORKSHOP 2008
LOCATION: POZNAN (POLAND)
YEAR: 2008

AUTHORS: J. R. KLEPACZKO**, J. A. RODRÍGUEZ-MARTÍNEZ,** A. RUSINEK, A. ARIAS
TITLE: CRITICAL IMPACT VELOCITY IN TENSION AND SHEAR
CONFERENCE: POZNAN-WORKSHOP 2008
LOCATION: POZNAN (POLAND)
YEAR: 2008

AUTHORS: J. A. RODRÍGUEZ-MARTÍNEZ, A. RUSINEK, D. A. PEDROCHE, A. ARIAS, J. R. KLEPACZKO
TITLE: MECHANICAL BEHAVIOUR OF TRIP STEELS SUBJECTED TO LOW IMPACT VELOCITY AT WIDE RANGE OF TEMPERATURES
CONFERENCE: SOLID MECHANICS CONFERENCE 2008
LOCATION: GDANSK (POLAND)
YEAR: 2008

AUTHORS: J. R. KLEPACZKO, A. RUSINEK, **J. A. RODRÍGUEZ-MARTÍNEZ**
TITLE: ADVANCES CONSTITUTIVE RELATION FOR NUMERICAL APPLICATIONS: MODELLING OF STEELS IN A WIDE RANGE OF STRAIN RATES AND TEMPERATURES
CONFERENCE: SOLID MECHANICS CONFERENCE 2008
LOCATION: GDANSK (POLAND)
YEAR: 2008

AUTHORS: J. A. RODRÍGUEZ-MARTÍNEZ, A. RUSINEK, P. CHEVRIER, A. ARIAS
TITLE: NUMERICAL SURVEY ON THE PERFORATION PROCESS OF ES STEEL SHEETS SUBJECTED TO IMPACT BY HEMISPHERICAL PROJECTILES
CONFERENCE: COMPUTER METHODS IN MECHANICS
LOCATION: ZIELONA GORA (POLAND)
YEAR: 2009

AUTHORS: J. A. RODRÍGUEZ-MARTÍNEZ, A. RUSINEK, A. ARIAS
TITLE: THERMO-VISCOPLASTIC MODELLING OF METALLIC ALLOYS
CONFERENCE: JANUSZ ROMAN KLEPACZKO WORKSHOP
LOCATION: METZ (FRANCE)
YEAR: 2009

AUTHORS: A. RUSINEK, **J. A. RODRÍGUEZ-MARTÍNEZ,** A. ARIAS
TITLE: THERMO-VISCOPLASTIC MODELLING OF ALUMINIUM ALLOYS FOR AERONAUTICAL APPLICATIONS
CONFERENCE: MADRID-WORKSHOP 2009
LOCATION: LEGANES (SPAIN)
YEAR: 2009

AUTHORS: J. A. RODRÍGUEZ-MARTÍNEZ, A. RUSINEK, A. ARIAS, E. DOSSOU
TITLE: ON THE PERFORATION PROCESS OF 2024-T3 ALUMINIUM SHEETS SIBJECTED TO LOW IMPACT VELOCITY: EFFECTS OF FRICTION CONDITION AND INITIAL TEMPERATURE
CONFERENCE: DYMAT CONFERENCE
LOCATION: BRUSSELS (BELGIUM)
YEAR: 2009

AUTHORS: A. RUSINEK, J. R. KLEPACZKO, **J. A. RODRÍGUEZ-MARTÍNEZ**, A. ARIAS
TITLE: ADVANCED CONSTITUTIVE RELATIONS FOR STEEL ALLOYS: STRAIN HARDENING AND PHASE TRANSFORMATION EFFECTS
CONFERENCE: DYMAT CONFERENCE
LOCATION: BRUSSELS (BELGIUM)
YEAR: 2009

AUTHORS: J. A. RODRÍGUEZ-MARTÍNEZ, A. RUSINEK, A. ARIAS
TITLE: INFLUENCE OF FLOW STRESS AND STRAIN HARDENING OF HIGH STRENGHT STRUCTURAL STEEL ON THE NECK FORMATION UNDER DYNAMIC TENSION
CONFERENCE: DYMAT CONFERENCE
LOCATION: BRUSSELS (BELGIUM)
YEAR: 2009

National Conferences

AUTHORS: J. A. RODRÍGUEZ-MARTÍNEZ, A. RUSINEK, R. ZAERA, A. ARIAS, J. R. KLEPACZKO,
TITLE: ESTUDIO EXPERIMENTAL Y NUMÉRICO DEL COMPORTAMIENTO DE LÁMINAS DE ACERO SOMETIDAS A IMPACTO DE MEDIA Y ALTA VELOCIDAD
VOLUME, PAGES: 25; 211-216
LOCATION: SIGUENZA (SPAIN)
YEAR: 2008
CONFERENCE: ANALES DE MECÁNICA DE LA FRACTURA

AUTHORS: J. A. RODRÍGUEZ-MARTÍNEZ, A. RUSINEK, A. ARIAS, J. R. KLEPACZKO, J. FERNÁNDEZ-SÁEZ
TITLE: MECANISMOS DE FALLO EN PLACAS DE ACERO SOMETIDAS A IMPACTO DE PROYECTILES CILÍNDRICOS, CÓNICOS Y HEMISFÉRICOS.
VOLUME, PAGES 25; 217-223
LOCATION: SIGUENZA (SPAIN)
YEAR: 2008
CONFERENCE: ANALES DE MECÁNICA DE LA FRACTURA

Invited Seminars

AUTHORS: J. A. RODRÍGUEZ-MARTÍNEZ, A. RUSINEK
TITLE: EXPERIMENTAL AND NUMERICAL ANALYSIS OF FAILURE PROCESS USING DIFFERENT KINDS OF SHEET MATERIAL SUBJECTED TO PERPENDICULAR IMPACT
LOCATION: POLYTECHNICAL UNIVERSITY OF POZNAN. POZNAN (POLAND)
YEAR: FEBRUARY-2008

AUTHORS: A. RUSINEK, **J. A. RODRÍGUEZ-MARTÍNEZ**, J. R. KLEPACZKO, A. ARIAS
TITLE: EXPERIMENTAL AND NUMERICAL ANALYSIS OF METALLIC PLATES: EFFECT OF CONSTITUTIVE RELATION
LOCATION: INSTITUTE OF TECHNOLOGICAL FUNDAMENTAL RESEARCH. POLISH ACADEMY OF SCIENCES. WARSAW (POLAND)
YEAR: FEBRUARY-2008

AUTHORS: A. RUSINEK, **J. A. RODRÍGUEZ-MARTÍNEZ**
TITLE: RECENT ADVANCES IN CONSTITUTIVE RELATIONS: APPLICATION TO PERFORATION
LOCATION: AKADEMIA GORNICZO HUTNICZA CRACOVIA. KRAKOW (POLAND)
YEAR: MAY-2008

AUTHORS: J. A. RODRÍGUEZ-MARTÍNEZ, A. RUSINEK
TITLE: EXPERIMENTAL AN NUMERICAL TECHNIQUES FOR PERFORATION PROCESSES
LOCATION: COLUMBIA UNIVERSITY. NEW YORK (USA)
YEAR: JANUARY-2009

AUTHORS: J. A. RODRÍGUEZ-MARTÍNEZ, A. RUSINEK,
TITLE: EXPERIMENTAL AN NUMERICAL TECHNIQUES FOR PERFORATION PROCESSES PERFORATION
LOCATION: WEIDLINGER ASSOCIATES. NEW YORK (USA)
YEAR: JANUARY-2009

.

APPENDIX A

THE MECHANICAL TRESHOLD STRESS MODEL

APPENDIX A – The mechanical threshold stress model

The constitutive relations reported along this document are derived from the **M**echanical **T**hreshold **S**tress (**MTS**) model reported in [Kocks et al. 1975, Goto et al. 2000, Kocks and Mecking 2003, Banerjee 2007]. The formulation of the model is described below. It has to be noted that such complete constitutive formalism is complicated to be implemented directly into **FE** codes due to the complexity of each equation coupled with the great number of physical constants. That caused the derivation of the simplified constitutive descriptions proposed along this doctoral thesis.

The thermo-viscoplastic flow stress is defined by Eq. A-1:

$$\bar{\sigma}\left(\bar{\varepsilon}^{p},\dot{\bar{\varepsilon}}^{p},T\right)=\left[\bar{\sigma}_{a}\left(\bar{\varepsilon}^{p}\right)+\left(S_{i}\left(\dot{\bar{\varepsilon}}^{p},T\right)\cdot\bar{\sigma}_{i}+S_{\varepsilon}\left(\dot{\bar{\varepsilon}}^{p},T\right)\cdot\bar{\sigma}_{\varepsilon}\left(\bar{\varepsilon}^{p}\right)\right)\right]\cdot\frac{\mu(T)}{\mu_{0}} \qquad (A\text{-}1)$$

Where $\bar{\sigma}_{a}\left(\bar{\varepsilon}^{p},T\right)$ is the athermal stress component, $\bar{\sigma}_{i}$ is the intrinsic component of the flow stress due to barriers to thermally activated dislocation motion, $\bar{\sigma}_{\varepsilon}\left(\bar{\varepsilon}^{p}\right)$ describes the strain hardening component of the flow stress, $S_{i}\left(\dot{\bar{\varepsilon}}^{p},T\right)$ and $S_{e}\left(\dot{\bar{\varepsilon}}^{p},T\right)$ are rate and temperature dependent scaling factors and $\frac{\mu(T)}{\mu_{0}}$ defines the temperature dependent shear modulus [Varshni 1970, Chen and Gray 1996], Eq. A-2.

$$\mu(T)=\mu_{0}-\frac{D}{\exp\left(T_{0}/T\right)-1} \qquad (A\text{-}2)$$

Where μ_{0} is the shear modulus at $T=0$ K and D and T_{0} are material constants.

The athermal stress component of the constitutive description is given by Eq. A-3.

$$\bar{\sigma}_{a}\left(\bar{\varepsilon}^{p}\right)=\sigma_{0}+C_{1}\cdot\left(\bar{\varepsilon}^{p}\right)^{n}+\frac{K}{\sqrt{d}} \qquad (A\text{-}3)$$

Where σ_{0} is a material constant tied to long-range obstacles. The second term defines dependence of athermal stress on dislocations density where C_{1} and n are empirical material constants. The third term inside the brackets defines the Hall-Petch effect where K is a material constant and d is the grain size.

The thermal stress component of the constitutive description is derived by combination of an Arrhénius type equation, Eq. A-4. and the existing relation between free energy and mechanical threshold stress, Eq. A-4.

$$\begin{cases} \dot{\bar{\varepsilon}}^{p} = \dot{\bar{\varepsilon}}_{0j} \cdot \exp\left(\dfrac{-\Delta G_j}{k \cdot T} \right) \\ \Delta G_j = g_{0j} \cdot \mu \cdot b^3 \cdot \left(1 - \left(\dfrac{\sigma_j}{\hat{\sigma}_j} \right)^{p_j} \right)^{q_j} \end{cases} \tag{A-4}$$

Where $\dot{\bar{\varepsilon}}_{0j}$ is the pre-exponential term, ΔG_j is the free energy of thermal activation, k is the Boltzmann constant, g_{0j} is a normalized activation energy, b is the burgers vector, $\dfrac{\sigma_j}{\hat{\sigma}_j}$ is the ratio of temperature-dependent applied stress to the mechanical threshold stress, p_j and q_j are empirical constants defining the which describe the profile of energy barrier to dislocation motion.

In previous expressions, Eq. A-4, j enters as defined by Eq. A-5.

$$j = i \text{ if } S_i\left(\dot{\bar{\varepsilon}}^{p}, T\right) \text{ and } \begin{cases} j = i \text{ if } S_i\left(\dot{\bar{\varepsilon}}^{p}, T\right) \\ j = e \text{ if } S_e\left(\dot{\bar{\varepsilon}}^{p}, T\right) \end{cases} \tag{A-5}$$

Then, the scaling factors $S_i\left(\dot{\bar{\varepsilon}}^{p}, T\right)$ and $S_e\left(\dot{\bar{\varepsilon}}^{p}, T\right)$ read as follows, Eq. A-6.

$$S_i\left(\dot{\bar{\varepsilon}}^{p}, T\right) = \left[1 - \left(\frac{k_b \cdot T}{g_{0i} \cdot b^3 \cdot \mu(T)} \cdot \ln\left(\frac{\dot{\varepsilon}_{0i}}{\dot{\bar{\varepsilon}}^{p}} \right) \right)^{1/q_i} \right]^{1/p_i} \tag{A-6-a}$$

$$S_e\left(\dot{\bar{\varepsilon}}^{p}, T\right) = \left[1 - \left(\frac{k_b \cdot T}{g_{0e} \cdot b^3 \cdot \mu(T)} \cdot \ln\left(\frac{\dot{\varepsilon}_{0e}}{\dot{\bar{\varepsilon}}^{p}} \right) \right)^{1/q_e} \right]^{1/p_e} \tag{A-6-b}$$

Moreover, the strain hardening of the model $\bar{\sigma}_{\varepsilon}\left(\bar{\varepsilon}^{p}\right)$ is given by a modified Voce law, Eq. A-7.

$$\frac{d\sigma_e}{d\varepsilon_p} = \theta(\sigma_e) \tag{A-7}$$

Where the following empirical relation are defined, Eqs. A-8 – A-12.

$$\theta(\sigma_e) = \theta_0 \cdot \left[1 - F(\sigma_e) \right] + \theta_1 \cdot F(\sigma_e) \tag{A-8}$$

$$\theta_0 = a_{00} + a_{10} \cdot \ln\left(\dot{\bar{\varepsilon}}^{p}\right) + a_{20} \cdot \sqrt{\dot{\bar{\varepsilon}}^{p}} + a_{30} \cdot T \tag{A-9}$$

$$\theta_1 = a_{01} + a_{11} \cdot \ln\left(\dot{\bar{\varepsilon}}^{p}\right) + a_{21} \cdot \sqrt{\dot{\bar{\varepsilon}}^{p}} + a_{31} \cdot T \tag{A-10}$$

$$F(\sigma_e) = \frac{\tanh\left(\alpha \frac{\sigma_e}{\sigma_{es}}\right)}{\tanh(\alpha)} \qquad \textit{(A-11)}$$

$$\ln\left(\frac{\sigma_{es}}{\sigma_{0es}}\right) = \left(\frac{k_b \cdot T}{g_{0es} \cdot b^3 \cdot \mu(T)}\right) \cdot \ln\left(\frac{\dot{\bar{\varepsilon}}^p}{\dot{\varepsilon}_{0es}}\right) \qquad \textit{(A-12)}$$

Where θ_0 is the strain hardening rate due to dislocation accumulation, θ_1 is saturation hardening rate, $(a_{0j}, a_{1j}, a_{2j}, a_{3j}, \alpha)$ are material constants $(j = 0,1)$, σ_{es} is the saturation stress at zero strain hardening rate, σ_{0es} is the saturation threshold stress for deformation at $T = 0\ K$, g_{0es} is the associated normalized activation energy, and $\dot{\bar{\varepsilon}}_{0es}$ is the reference maximum strain rate.

APPENDIX B

THREE DIMENSIONAL MODEL

APPENDIX B – Three dimensional model

As reported, for example, in [Lubarda et al. 2003] particular relevance has the generalization of constitutive relations to three dimensional states of stress and strain. For it, the constitutive descriptions introduced in this document may be extended to **3D** modeling and implemented into **FE** code by means, for example, the integration scheme proposed in [Zaera and Fernández-Sáez 2006]. Such procedure was already applied to the formulation of the **RK** model [Rusinek and Zaera 2007]. Thus, the main features of the algorithm proposed by Zaera and Fernández-Sáez [Zaera and Fernández-Sáez 2006] are described below.

The yield condition is defined by Eq. B-1:

$$f = \bar{\sigma} - \sigma_y\left(\bar{\varepsilon}^p, \dot{\bar{\varepsilon}}^p, T\right) = 0 \qquad (B\text{-}1)$$

where $\bar{\sigma}$ is the equivalent stress, σ_y is the yield stress defined by the constitutive description, $\bar{\varepsilon}^p$ is the equivalent plastic strain, Eq. B-2, $\dot{\bar{\varepsilon}}^p$ is the equivalent plastic strain rate, Eq. B-3. and T is the temperature.

$$\bar{\varepsilon}^p = \int \dot{\bar{\varepsilon}}^p \cdot dt \qquad (B\text{-}2)$$

$$\dot{\bar{\varepsilon}}^p = \sqrt{\frac{2}{3} \cdot \dot{\varepsilon}_{ij}^{\ p} \cdot \dot{\varepsilon}_{ij}^{\ p}} \qquad (B\text{-}3)$$

Assuming additive decomposition of the deformation tensor *(hypoelastic-plastic approach)*, the tensor of total strain rate $\dot{\varepsilon}_{ij}$ is written as a sum of the elastic strain rate tensor $\dot{\varepsilon}_{ij}^e$, the plastic strain rate tensor $\dot{\varepsilon}_{ij}^p$ and the thermal strain rate tensor $\dot{\varepsilon}_{ij}^T$, Eq. B-4.

$$\dot{\varepsilon}_{ij} = \dot{\varepsilon}_{ij}^e + \dot{\varepsilon}_{ij}^p + \dot{\varepsilon}_{ij}^T \qquad (B\text{-}4)$$

Elastic strains are related to stress through an isotropic hypoelastic law, Eq. B-5.:

$$\dot{\sigma}_{ij} = C_{ijkl} \cdot \varepsilon_{kl}^e \qquad (B\text{-}5)$$

where C_{ijkl} is the stiffness tensor.

The thermal strains tensor is defined as follows, Eq. B-6:

$$\varepsilon_{ij}^T = \alpha \cdot \dot{T} \cdot \delta_{ij} \qquad (B\text{-}6)$$

where α is the coefficient of thermal expansion and δ_{ij} is the unit matrix $\left(\delta_{ij} = 1 \quad \text{if} \quad i = j\right)$

To define the plastic flow, the normality rule is used, Eq. B-7.

$$\varepsilon_{ij}^{p} = \dot{\lambda} \cdot \frac{\partial f}{\partial \sigma_{ij}} \qquad (B\text{-}7)$$

where $\dot{\lambda}$ is the rate plastic multiplier that, in **J2** plasticity, can be defined by Eq. B-8:

$$\dot{\lambda} = \frac{\Delta\lambda}{\Delta t} = \dot{\bar{\varepsilon}}^{p} \qquad (B\text{-}8)$$

And hence, the equivalency of the plastic multiplier and the equivalent plastic strain, Eq. B-9:

$$\bar{\varepsilon}^{p} = \lambda \qquad (B\text{-}9)$$

Assuming adiabatic conditions of deformation the material temperature increase is defined by the following relation, Eq. B-10:

$$\dot{T} = \frac{\beta}{\rho \cdot C_{p}} \cdot \sigma_{ij} \cdot \dot{\varepsilon}_{ij}^{p} \qquad (B\text{-}10)$$

Where β is the inelastic heat fraction and ρ is the material density.

The consistency model is used to integrate the thermo-viscoplastic rate equations, via the equality of equivalent stress and yield stress for updated values of plastic strain, plastic strain rate and temperature. In the frame of the return-mapping algorithms, the consistency condition, Eq. B-11, could be written in terms of the equivalent plastic strain increment corresponding to a time step, Eq. B-12:

$$\dot{\lambda} \cdot f = 0 \qquad (B\text{-}11)$$

$$f\left(\Delta\bar{\varepsilon}^{p}\right) = 0 \qquad (B\text{-}12)$$

Linearising the consistency condition, the following equation is found which allows us to iteratively obtain $\Delta\bar{\varepsilon}^{p}$, Eq. B-13:

$$f_{(k+1)} \approx f_{(k)} + \frac{\partial f}{\partial \sigma_{ij}}\left(-\delta\bar{\varepsilon}_{(k)}^{p} 2G \left.\frac{\partial f}{\partial \sigma_{ij}}\right|_{(k)}\right) + \left.\frac{\partial f}{\partial \bar{\varepsilon}^{p}}\right|_{(k)} \delta\bar{\varepsilon}_{(k)}^{p} + \left.\frac{\partial f}{\partial \dot{\bar{\varepsilon}}^{p}}\right|_{(k)} \frac{\delta\bar{\varepsilon}_{(k)}^{p}}{\Delta t} + \left.\frac{\partial f}{\partial T}\right|_{(k)} \frac{\beta}{\rho C_{p}}\left(\delta\bar{\varepsilon}_{(k)}^{p}\bar{\sigma}_{n+1}^{trial} - 6G\Delta\bar{\varepsilon}_{(k)}^{p}\delta\bar{\varepsilon}_{(k)}^{p}\right) = 0 \qquad (B\text{-}13)$$

where *k* is an iterative index. From the previous expression $\delta\bar{\varepsilon}_{(k)}^{p}$ can be calculated, Eq. B-14.

$$\delta\bar{\varepsilon}_{(k)}^{p} \approx \frac{f_{(k)}}{3G - \left.\frac{\partial f}{\partial \bar{\varepsilon}^{p}}\right|_{(k)} - \frac{1}{\Delta t}\left.\frac{\partial f}{\partial \dot{\bar{\varepsilon}}^{p}}\right|_{(k)} - \left.\frac{\partial f}{\partial T}\right|_{(k)} \frac{\beta}{\rho C_{p}}\left(\bar{\sigma}_{n+1}^{trial} - 6G\Delta\bar{\varepsilon}_{(k)}^{p}\right)} \qquad (B\text{-}14)$$

Then, $\Delta\lambda$ is updated after every iteration, Eq. B-15:

$$\Delta\lambda_{(k+1)} = \Delta\lambda_{(k)} + \delta\lambda_{(k)} \qquad (B\text{-}15)$$

All the variables could be determined from the final value of $\Delta\lambda$. A more detailed explanation of the integration procedure can be found in [Zaera and Fernández-Sáez 2006].

APPENDIX C

DERIVATIVES OF THE CONSTITUTIVE MODELS FOR IMPLEMENTATION INTO FE CODE

APPENDIX C – Derivatives of the constitutive models for implementation into FE code

If the integration scheme proposed in [Zaera and Fernández-Sáez 2006] is used for implementation into **FE** code of the constitutive descriptions reported in this document the first derivatives of the yield function *(of all arguments)* are required. They are reported below.

The Rusinek-Klepaczko constitutive description

$$\left.\frac{d\sigma_\mu\left(\bar{\varepsilon}^p,\dot{\bar{\varepsilon}}^p,T\right)}{d\bar{\varepsilon}^p}\right|_{\dot{\bar{\varepsilon}}^p,T}=B\left(\dot{\bar{\varepsilon}}^p,T\right)\cdot n\left(\dot{\bar{\varepsilon}}^p,T\right)\cdot\left(\bar{\varepsilon}^p+\varepsilon_0\right)^{n\left(\dot{\bar{\varepsilon}}^p,T\right)-1} \tag{C-1}$$

$$\left.\frac{d\sigma_\mu\left(\bar{\varepsilon}^p,\dot{\bar{\varepsilon}}^p,T\right)}{d\dot{\bar{\varepsilon}}^p}\right|_{\bar{\varepsilon}^p,T}=B\left(\dot{\bar{\varepsilon}}^p,T\right)\cdot\left(\bar{\varepsilon}^p+\varepsilon_0\right)^{n\left(\dot{\bar{\varepsilon}}^p,T\right)}\cdot\left[\frac{\nu\cdot\left(\bar{\varepsilon}^p+\varepsilon_0\right)}{\dot{\bar{\varepsilon}}^p\cdot\log\left(\frac{\dot{\varepsilon}_{max}}{\dot{\bar{\varepsilon}}^p}\right)}-\frac{n_0\cdot D_2\cdot\ln\left(\bar{\varepsilon}^p+\varepsilon_0\right)}{\dot{\bar{\varepsilon}}^p\cdot T_m}\right] \tag{C-2}$$

$$\left.\frac{d\sigma_\mu\left(\bar{\varepsilon}^p,\dot{\bar{\varepsilon}}^p,T\right)}{dT}\right|_{\bar{\varepsilon}^p,\dot{\bar{\varepsilon}}^p}=-B\left(\dot{\bar{\varepsilon}}^p,T\right)\cdot\left(\bar{\varepsilon}^p+\varepsilon_0\right)^{n\left(\dot{\bar{\varepsilon}}^p,T\right)}\cdot\left[\frac{\nu}{T}+\frac{n_0\cdot D_2}{T_m}\log\left(\frac{\dot{\bar{\varepsilon}}^p}{\dot{\varepsilon}_{min}}\right)\ln\left(\bar{\varepsilon}^p+\varepsilon_0\right)\right] \tag{C-3}$$

$$\left.\frac{d\sigma^*\left(\dot{\bar{\varepsilon}}^p,T\right)}{d\dot{\bar{\varepsilon}}^p}\right|_{T}=\frac{m\cdot D_1}{\dot{\bar{\varepsilon}}^p\cdot\ln(10)}\cdot\left(\frac{T}{T_m}\right)\cdot\sigma_0^*\cdot\left[1-D_1\cdot\frac{T}{T_m}\log\left(\frac{\dot{\bar{\varepsilon}}_{max}}{\dot{\bar{\varepsilon}}^p}\right)\right]^{m^*-1} \tag{C-4}$$

$$\left.\frac{d\sigma^*\left(\dot{\bar{\varepsilon}}^p,T\right)}{dT}\right|_{\dot{\bar{\varepsilon}}^p}=-\frac{m\cdot D_1}{T_m}\cdot\log\left(\frac{\dot{\bar{\varepsilon}}_{max}}{\dot{\bar{\varepsilon}}^p}\right)\cdot\sigma_0^*\cdot\left[1-D_1\cdot\frac{T}{T_m}\log\left(\frac{\dot{\bar{\varepsilon}}_{max}}{\dot{\bar{\varepsilon}}^p}\right)\right]^{m^*-1} \tag{C-5}$$

$$\frac{dE(T)}{dT}=-E_0\cdot\exp\left[\theta^*\left(1-\frac{T_m}{T}\right)\right]\cdot\left(\frac{1}{T_m}+\frac{\theta^*}{T}\right) \tag{C-6}$$

The Modified Rusinek-Klepaczko constitutive description

$$\left.\frac{d\bar{\sigma}^*\left(\bar{\varepsilon}^p,\dot{\bar{\varepsilon}}^p,T\right)}{d\bar{\varepsilon}^p}\right|_{\dot{\bar{\varepsilon}}^p,T}=B_0\cdot\left(\frac{T\cdot\log\left(\frac{\dot{\varepsilon}_{max}}{\dot{\bar{\varepsilon}}^p}\right)}{T_m}\right)^{-\nu}\cdot\left(\bar{\varepsilon}^p\right)^{n_0\left(1-\frac{D_2\cdot T\cdot\log\left(\frac{\dot{\bar{\varepsilon}}^p}{\dot{\varepsilon}_{min}}\right)}{T_m}\right)-1}\cdot n_0\cdot\left(1-\frac{D_2\cdot T\cdot\log\left(\frac{\dot{\bar{\varepsilon}}^p}{\dot{\varepsilon}_{min}}\right)}{T_m}\right)\cdot\left(1-\xi_1\cdot\left(\frac{T}{T_m}\right)\log\left(\frac{\dot{\varepsilon}_{max}}{\dot{\bar{\varepsilon}}^p}\right)\right)^{1/\xi_2} \tag{C-7}$$

$$\left.\frac{d\bar{\sigma}^{*}\left(\bar{\varepsilon}^{p},\dot{\bar{\varepsilon}}^{p},T\right)}{d\dot{\bar{\varepsilon}}^{p}}\right|_{\bar{\varepsilon}^{p},T}=\frac{B_0\cdot\left(\bar{\varepsilon}^{p}\right)^{n_0\left(1-\frac{D_2\cdot T\cdot\log\left(\frac{\dot{\bar{\varepsilon}}^{p}}{\dot{\varepsilon}_{min}}\right)}{T_m}\right)}\cdot\nu\cdot T\cdot\left(1-\frac{T\cdot\xi_1\cdot\log\left(\frac{\dot{\varepsilon}_{max}}{\dot{\bar{\varepsilon}}^{p}}\right)}{T_m}\right)^{1/\xi_2}\cdot\left(\frac{T\cdot\log\left(\frac{\dot{\varepsilon}_{max}}{\dot{\bar{\varepsilon}}^{p}}\right)}{T_m}\right)^{-1-\nu}}{\dot{\bar{\varepsilon}}^{p}\cdot T_m}$$

$$+\frac{B_0\cdot\left(\bar{\varepsilon}^{p}\right)^{n_0\left(1-\frac{D_2\cdot T\cdot\log\left(\frac{\dot{\bar{\varepsilon}}^{p}}{\dot{\varepsilon}_{min}}\right)}{T_m}\right)}\cdot T\cdot\xi_1\cdot\frac{1}{\xi_2}\cdot\left(1-\frac{T\cdot\xi_1\cdot\log\left(\frac{\dot{\varepsilon}_{max}}{\dot{\bar{\varepsilon}}^{p}}\right)}{T_m}\right)^{-1+\frac{1}{\xi_2}}\cdot\left(\frac{T\cdot\log\left(\frac{\dot{\varepsilon}_{max}}{\dot{\bar{\varepsilon}}^{p}}\right)}{T_m}\right)^{-\nu}}{\dot{\bar{\varepsilon}}^{p}\cdot T_m}$$

$$-\frac{B_0\cdot D_2\cdot\left(\bar{\varepsilon}^{p}\right)^{n_0\left(1-\frac{D_2\cdot T\cdot\log\left(\frac{\dot{\bar{\varepsilon}}^{p}}{\dot{\varepsilon}_{min}}\right)}{T_m}\right)}\cdot n_0\cdot T\cdot\log\left(\bar{\varepsilon}^{p}\right)\cdot\left(1-\frac{T\cdot\xi_1\cdot\log\left(\frac{\dot{\varepsilon}_{max}}{\dot{\bar{\varepsilon}}^{p}}\right)}{T_m}\right)^{1/\xi_2}\cdot\left(\frac{T\cdot\log\left(\frac{\dot{\varepsilon}_{max}}{\dot{\bar{\varepsilon}}^{p}}\right)}{T_m}\right)^{-\nu}}{\dot{\bar{\varepsilon}}^{p}\cdot T_m} \qquad \textit{(C-8)}$$

$$\left.\frac{d\bar{\sigma}^{*}\left(\bar{\varepsilon}^{p},\dot{\bar{\varepsilon}}^{p},T\right)}{dT}\right|_{\bar{\varepsilon}^{p},\dot{\bar{\varepsilon}}^{p}}=-\frac{B_0\cdot\left(\bar{\varepsilon}^{p}\right)^{n_0\left(1-\frac{D_2\cdot T\cdot\log\left(\frac{\dot{\bar{\varepsilon}}^{p}}{\dot{\varepsilon}_{min}}\right)}{T_m}\right)}\cdot\nu\cdot\left(1-\frac{T\cdot\xi_1\cdot\log\left(\frac{\dot{\varepsilon}_{max}}{\dot{\bar{\varepsilon}}^{p}}\right)}{T_m}\right)^{1/\xi_2}\cdot\log\left(\frac{\dot{\varepsilon}_{max}}{\dot{\bar{\varepsilon}}^{p}}\right)\left(\frac{T\cdot\log\left(\frac{\dot{\varepsilon}_{max}}{\dot{\bar{\varepsilon}}^{p}}\right)}{T_m}\right)^{-1-\nu}}{T_m}$$

$$-\frac{B_0\cdot\left(\bar{\varepsilon}^{p}\right)^{n_0\left(1-\frac{D_2\cdot T\cdot\log\left(\frac{\dot{\bar{\varepsilon}}^{p}}{\dot{\varepsilon}_{min}}\right)}{T_m}\right)}\cdot\xi_1\cdot\frac{1}{\xi_2}\cdot\log\left(\frac{\dot{\varepsilon}_{max}}{\dot{\bar{\varepsilon}}^{p}}\right)\cdot\left(1-\frac{T\cdot\xi_1\cdot\log\left(\frac{\dot{\varepsilon}_{max}}{\dot{\bar{\varepsilon}}^{p}}\right)}{T_m}\right)^{-1+1/\xi_2}\cdot\left(\frac{T\cdot\log\left(\frac{\dot{\varepsilon}_{max}}{\dot{\bar{\varepsilon}}^{p}}\right)}{T_m}\right)^{-\nu}}{T_m}$$

$$-\frac{B_0\cdot D_2\cdot\left(\bar{\varepsilon}^{p}\right)^{n_0\left(1-\frac{D_2\cdot T\cdot\log\left(\frac{\dot{\bar{\varepsilon}}^{p}}{\dot{\varepsilon}_{min}}\right)}{T_m}\right)}\cdot n_0\cdot\log\left(\bar{\varepsilon}^{p}\right)\cdot\left(1-\frac{T\cdot\xi_1\cdot\log\left(\frac{\dot{\varepsilon}_{max}}{\dot{\bar{\varepsilon}}^{p}}\right)}{T_m}\right)^{1/\xi_2}\cdot\left(\frac{T\cdot\log\left(\frac{\dot{\varepsilon}_{max}}{\dot{\bar{\varepsilon}}^{p}}\right)}{T_m}\right)^{-\nu}\cdot\log\left(\frac{\dot{\bar{\varepsilon}}^{p}}{\dot{\varepsilon}_{min}}\right)}{T_m} \qquad \textit{(C-9)}$$

The viscous drag stress term

$$\frac{d\sigma_{vs}\left(\dot{\bar{\varepsilon}}^{p}\right)}{d\dot{\bar{\varepsilon}}^{p}}=\alpha\cdot\chi\cdot\exp\left(-\alpha\cdot\dot{\bar{\varepsilon}}^{p}\right) \qquad \textit{(C-10)}$$

The negative strain rate sensitivity stress term

$$\left.\frac{d\sigma_{ns}\left(\dot{\bar{\varepsilon}}^{p},T\right)}{d\dot{\bar{\varepsilon}}^{p}}\right|_{T}=\frac{\sigma_{0}^{ns}\cdot\left(1-\frac{D_{3}\cdot T_{m}\cdot\log\left(\frac{\dot{\bar{\varepsilon}}^{p}}{\dot{\varepsilon}_{max}}\right)}{T}\right)}{\dot{\bar{\varepsilon}}^{p}}-\frac{D_{3}\cdot T_{m}\cdot\sigma_{0}^{ns}\cdot\log\left(\frac{\dot{\varepsilon}_{trans}}{\dot{\bar{\varepsilon}}^{p}}\right)}{\dot{\bar{\varepsilon}}^{p}\cdot T} \qquad (C\text{-}11)$$

$$\left.\frac{d\sigma_{T}\left(\dot{\bar{\varepsilon}}^{p},T\right)}{dT}\right|_{\dot{\bar{\varepsilon}}^{p}}=\frac{D_{3}\cdot\sigma_{0}^{ns}\cdot T_{m}\cdot\log\left(\frac{\dot{\bar{\varepsilon}}^{p}}{\dot{\varepsilon}_{max}}\right)\cdot\log\left(\frac{\dot{\varepsilon}_{trans}}{\dot{\bar{\varepsilon}}^{p}}\right)}{T^{2}} \qquad (C\text{-}12)$$

The strain hardening function

$$\left.\frac{df\left(\bar{\varepsilon}^{p},\dot{\bar{\varepsilon}}^{p}\right)}{d\bar{\varepsilon}^{p}}\right|_{\dot{\bar{\varepsilon}}^{p}}=\left[\xi\cdot\left[1-\exp\left(\lambda_{0}\cdot\dot{\bar{\varepsilon}}^{p}\cdot\exp\left(-\lambda\cdot\dot{\bar{\varepsilon}}^{p}\right)\right)\right]^{\xi-1}\right]\cdot\left[-\exp\left(-\lambda_{0}\cdot\bar{\varepsilon}^{p}\cdot\exp\left(-\lambda\cdot\dot{\bar{\varepsilon}}^{p}\right)\right)\right] \qquad (C\text{-}13)$$
$$\cdot\left[-\lambda_{0}\cdot\exp\left(-\lambda\cdot\dot{\bar{\varepsilon}}^{p}\right)\right]$$

$$\left.\frac{df\left(\bar{\varepsilon}^{p},\dot{\bar{\varepsilon}}^{p}\right)}{d\dot{\bar{\varepsilon}}^{p}}\right|_{\bar{\varepsilon}^{p}}=\left[\xi\cdot\left[1-\exp\left(-\lambda_{0}\cdot\bar{\varepsilon}^{p}\cdot\exp\left(-\lambda\cdot\dot{\bar{\varepsilon}}^{p}\right)\right)\right]^{\xi-1}\right]\cdot\left[-\exp\left(-\lambda_{0}\cdot\bar{\varepsilon}^{p}\cdot\exp\left(-\lambda\cdot\dot{\bar{\varepsilon}}^{p}\right)\right)\right] \qquad (C\text{-}14)$$
$$\cdot\left[-\lambda_{0}\cdot\bar{\varepsilon}^{p}\cdot\exp\left(-\lambda\cdot\dot{\bar{\varepsilon}}^{p}\right)\right]\cdot\left[-\lambda\right]$$

$$\frac{dg_{1}(T)}{dT}=\left[-\eta\cdot\left(\frac{T-M_{S}}{M_{D}-M_{S}}\right)^{\eta-1}\right]\cdot\left[\frac{1}{M_{D}-M_{S}}\right] \qquad (C\text{-}15)$$

$$\frac{dg_{2}(T)}{dT}=\left[\exp\left[-\left(\frac{T}{M_{D}-T_{0}}\right)^{\alpha}\right]\right]\cdot\left[-\alpha\cdot\left(\frac{T}{M_{D}-T_{0}}\right)^{\alpha-1}\right]\cdot\left[\frac{1}{M_{D}-T_{0}}\right] \qquad (C\text{-}16)$$

APPENDIX D

ANALYTICAL DERIVATION OF THE CRITICAL IMPACT VELOCITY IN TENSION

APPENDIX D – Analytical derivation of the critical impact velocity in tension

Let us consider the following boundary value problem where a semi-infinite slender bar extending from $x=-\infty$ to $x=0$ is impacted with a constant velocity V_0, Fig. D-1. Let us assume that the impact velocity V_0 is high enough to produce plastic deformation in the material.

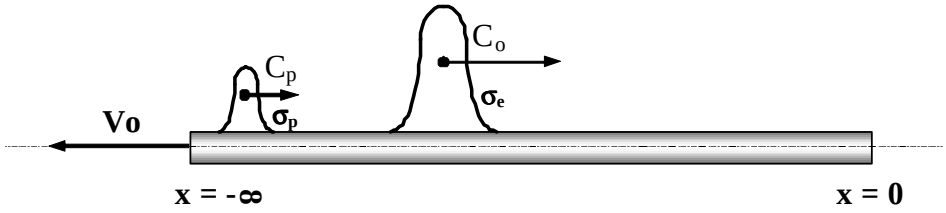

Fig. D-1. Schematic representation of the elastic and plastic wave propagation along a semi-infinite bar.

The constitutive behaviour of the material is assumed of the form $\sigma(\varepsilon)$ where σ and ε are the stress and the strain respectively. The relation $\sigma(\varepsilon)$ shows a smooth first derivative which is a decreasing function of strain.

The uniqueness of the relation $\sigma(\varepsilon)$ leads to the **rate-independent theory of plastic wave propagation**. A more general approach to the wave propagation phenomena in inelastic solids will lead to the **rate-dependent theory of plastic wave propagation** where rate and temperature effects are taken into consideration (*By now, let us assume the wave celerity only dependent on strain).* In addition, the radial contraction of the material is neglected. Under these assumptions, the equation of motion for an element of the bar reads as follows, Eq. D-1.

$$\frac{\partial^2 U_x}{\partial t^2} = C_i^2(\varepsilon)\frac{\partial^2 U_x}{\partial x^2} \qquad \textit{(D-1)}$$

The wave propagates in the longitudinal direction of the bar x, where U_x is the material particle displacement in that direction, t is time, C_i is the wave speed and ε is the strain that can be split into elastic ε_e and plastic ε_p terms. In the elastic range $C_0=(E/\rho)^{1/2}$ and in the plastic range $C_p(\varepsilon^p)=(d\sigma/\rho d\varepsilon^p)^{1/2}$. In the **isothermal rate-independent theory of wave propagation** the wave velocity is a constant in the elastic range, only dependent on Young's modulus and material density. In the plastic range it becomes a decreasing function of the plastic deformation.

Previous differential equation, Eq. D-1. can be solved by the method of characteristics. The definition of the characteristic line reads as follows, Eq. D-2

$$\frac{dx}{dt} = \pm C(\varepsilon) \qquad \textit{(D-2)}$$

Then, in the elastic range $dx/dt=\pm C_0$ and in the plastic range $dx/dt=\pm C_p(\varepsilon^p)$. Thus, Eq. D-2. satisfied along the characteristic lines gives Eq. D-3.

$$dv = \pm C(\varepsilon) \cdot d\varepsilon \qquad \textit{(D-3)}$$

Along two sets of characteristics the mass velocities in both elastic and plastic ranges are given Eq. D-4.

$$\begin{cases} v = \pm C_0 \varepsilon \\ v(\varepsilon^p) = \pm \int_0^{\varepsilon^p} C_p(\varepsilon^p)\, d\varepsilon^p \end{cases} \qquad \textit{(D-4)}$$

The first relation in Eq. D-4. takes place along the linear characteristics $dx/dt = \pm C_0$, so it corresponds to the elastic range. The second relation in Eq. D-4. occurs along the non-linear characteristics $dx/dt = \pm C_p(\varepsilon_p)$, so it corresponds to the plastic range.

Thus, Eq. D-4. defines the mass velocity which reaches a maximum at a specific value of total strain. Such value of strain is given by the condition $d\sigma/d\varepsilon^p = 0 \rightarrow C_p(\varepsilon) = 0$ which corresponds to saturation of the material. Higher mass velocities cannot propagate. It leads to the definition of the **C**ritical **I**mpact **V**elocity (**CIV**) in tension. Therefore the value of the **CIV** is the integral of the wave speed given by Eq. D-5.

$$CIV = \int_0^{\varepsilon_e} C_e \cdot d\varepsilon + \int_{\varepsilon_e}^{\varepsilon_{pm}} C_p(\bar{\varepsilon}^p) \cdot d\bar{\varepsilon}^p \qquad \textit{(D-5)}$$

The fist term of Eq. D-5 corresponds to the elastic range, where ε_e is the elastic deformation corresponding to the initial yield stress, $\varepsilon_e = \varepsilon_e|_{\varepsilon^p=0}$.

The second term corresponds to the plastic range. In that term ε_{pm} is the upper limit of integration defined as the plastic strain value for which the mass velocity *(in the plastic range)* equals the plastic wave speed leading to the **CIV** phenomenon.

In a more general case rate and temperature effects have to be taken into account, is the **rate-dependent theory of plastic wave propagation**.

Now, the elastic wave speed is defined as follows, Eq. D-6:

$$C_e(T) = \left(\frac{E(T)}{\rho(T)} \right)^{1/2} \qquad \textit{(D-6)}$$

Moreover, the material constitutive behaviour becomes of the form $\sigma\left(\bar{\varepsilon}^p, \dot{\bar{\varepsilon}}^p, T(\varepsilon^p)\right)$. A more complete, and closer to the reality of fast plastic deformation, is assumption of the adiabatic deformation. Then increase of material temperature is defined in a general case by, Eq. D-7.

$$\Delta T\left(\bar{\varepsilon}^{p},\bar{\sigma}\right)=\int_{0}^{\bar{\varepsilon}^{p}_{max}}\frac{\beta\left(\bar{\varepsilon}^{p},\dot{\bar{\varepsilon}}^{p}\right)}{\rho(T)\cdot C(T)}\cdot\bar{\sigma}\left(\bar{\varepsilon}^{p},\dot{\bar{\varepsilon}}^{p},T\left(\bar{\varepsilon}^{p}\right)\right)d\bar{\varepsilon}^{p} \qquad \textit{(D-7)}$$

where $\beta\left(\bar{\varepsilon}^{p},\dot{\bar{\varepsilon}}^{p}\right)$ is the Taylor-Quinney coefficient, $\rho(T)$ is the material density and $C(T)$ is the specific heat at constant pressure.

Then, the plastic wave celerity $C_{p}\left(\bar{\varepsilon}^{p},\dot{\bar{\varepsilon}}^{p},T\left(\bar{\varepsilon}^{p}\right)\right)$ dependent on plastic strain, strain rate and temperature is given by Eq. D-8.

$$C_{p}\left(\bar{\varepsilon}^{p},\dot{\bar{\varepsilon}}^{p},T\left(\bar{\varepsilon}^{p}\right)\right)=\left(\frac{1}{\rho}\cdot\frac{d\bar{\sigma}\left(\bar{\varepsilon}^{p},\dot{\bar{\varepsilon}}^{p},T\left(\bar{\varepsilon}^{p}\right)\right)}{d\bar{\varepsilon}^{p}}\right)^{1/2} \qquad \textit{(D-8)}$$

Then, the **CIV** definition becomes given by Eq. D-9.

$$CIV=\int_{0}^{\varepsilon_{e}}C_{e}(T)\cdot d\varepsilon+\int_{\varepsilon_{e}}^{\varepsilon_{pm}}C_{p}\left(\bar{\varepsilon}^{p},\dot{\bar{\varepsilon}}^{p},T\left(\bar{\varepsilon}^{p}\right)\right)\cdot d\bar{\varepsilon}^{p} \qquad \textit{(D-9)}$$

REFERENCES

REFERENCES

Abbadi M, Hahner P, Zeghloul A. On the characteristics of Portevin-Le Chatelier bands in aluminum alloy 5182 under stress-controlled and strain-controlled tensile testing. Mater Sci Eng A 2002;337:194–201.

Abed F. H., Voyiadjis G. Z. Plastic deformation modeling of AL-6XN stainless steel at low and high strain rates and temperatures using a combination of bcc and fcc mechanisms of metals. Int J Plasticity 2005; 21: 1618–1639.

Abramowicz W, Jones N. Dynamic axial crushing of square tubes. Int J Impact Eng 1984;2:179–208.

Abramowicz W, Jones N. Dynamic axial crushing of circular tubes. Int J Impact Eng 1984;2:263–281.

Abu Al-Rub R. K., Voyiadjis G. Z. A Finite Strain Plastic-damage Model for High Velocity Impact using Combined Viscosity and Gradient Localization Limiters: Part I – Theoretical Formulation. Int J Damage Mech. 2006; 15: 293-334.

Al-Abbasi F. M., Nemes J. A. Micromechanical modeling of dual phase steels. Int. J. Mech. Sci. 2003; 45: 1449-1465.

Allain S, Cugy P, Scott C, Chateau JP, Rusinek A, Deschamp A. The influence of the plastic instabilities on the mechanical properties of a high manganese austenitic FeMnC steel. Int J Mater Res 2008;99:734–8.

Alos S, Hopperstad O. S., Tomquist R., Amdahl J. Analytical and numerical analysis of sheet metal instability sing a stress based criterion. Int J Solids Struct 2008;45:2042–55.

Altynova M, Hu X, Daehn GS. Increased ductility in high velocity electromagnetic ring expansion. Metall Trans A 1996;27:1837–1844.

Angel T. Formation of martensite in austenitic stainless steels. Effects of deformation, temperature and composition. J Iron Steel Inst. 1954; 177:165-174

Arias A, Rodríguez-Martínez J. A., Rusinek A, 2008. Numerical simulations of impact behaviour of thin steel to cylindrical, conical and hemispherical non-deformable projectiles, Eng. Fract. Mech. 2008; 75: 1635–1656.

Armstrong R. W., Campbell J. D. The microstructure and design of alloys. Proceedings on the third international conference on the strength of metals and alloys. Vol. 1. Inst. Metals and the Iron and Steel Int. Cambridge; 1973 529.

Aravas N. On the numerical integration of a class of pressure-dependent plasticity models. Int J Numer Methods Eng 1987;24:1395–1416.

Atkins A. G., Afzal Khan M, Liu J. H. Necking and radial cracking around perforations in thin sheets at normal incidence. Int J Impact Eng 1998;21:521–539.

Ayisit O. The influence of asymmetries in shaped charge performance. Int J Impact Eng 2008;35:1399–404.

Backman M. E., Goldsmith W. The mechanics of penetration of projectiles into targets. Int J Eng Sci 1978;16:1–99.

Banerjee B. The Mechanical Threshold Stress model for various tempers of AISI 4340 steel International Journal of Solids and Structures 2007;44: 834–859.

Bao Y., Wierzbicki T. On fracture locus in the equivalent strain and stress triaxiality space Int J Mech Sci. 2004; 46:81–98.

Barsoum I., Faleskog J. Rupture mechanisms in combined tension and shear—Experiments. Int J Solids and Struc. 2007; 44: 1768–1786.

Basinski Z. S. Thermally activated glide in face-centred cubic metals and its application to the theory of strain hardening. Philosophical Magazine. 1959; 4:393-432.

Batra R. C., Kim C. H. Effect of viscoplastic flow rules on the initiation and growth of shear bands at high strain rate. J Mech Phys Solids. 1990; 6:859-874.

Batra R. C, Chen L. Effect of viscoplastic relations on the instability strain, shear band initiation strain, the strain corresponding to the minimum shear band spacing, and the band width in a thermoviscoplastic material. Int J Plasticity 2001; 17:1465–89.

Batra R. C., Wei Z. C. Instability strain and shear band spacing in simple tensile/ compressive deformations of thermoviscoplastic materials. Int J Impact Eng 2007; 34:448–463.

Becker R. Ring fragmentation predictions using the Gurson model with material stability conditions as failure criteria. Int J Solids Struct 2002; 39:3555–3580.

Benallal A, Berstad T, Børvik T, Hopperstad O. S, Koutiri I, Nogueira de Codes R. An experimental and numerical investigation of the behaviour of AA5083 aluminium alloy in presence of the Portevin-Le Chatelier effect. Int J Plasticity 2008;24:1916–1945.

Ben-Dor G., Dubinsky A., Elperin T. New area rules for penetrating impactors. Int J Impact Eng. 1998; 21:51-59.

Ben-Dor G., Dubinsky A., Elperin T. Engineering approach to penetration modeling. Eng Fract Mech. 2008; 75: 4279–4282

Ben-Dor G., Dubinsky A., Elperin T. Modeling of penetration by rigid impactors Mechanics Research Communications 2009; 36:625–629

Berbenni S., Favier V., Lemoine X., Berveiller N. Micromechanical modelling of the elastic–viscoplastic behaviour of polycrystalline steels having different microstructures. Mater Sci Eng 2004;372:128–136.

Bonora, N., Milella, P.P. Constitutive modeling for ductile behavior incorporating strain rate, temperature, and damage mechanics. Int. J. Impact Eng. 2001; 26, 53–64.

Borvik T, Langseth M, Hopperstad O. S., Malo K. A. Ballistic penetration of steel plates. Int J Impact Eng 1999;22:855–886.

Borvik T, Langseth M, Hoperstad O. S, Malo K. A. Perforation of 12 mm thick steel plates by 20 mm diameter projectiles with flat, hemispherical and conical noses Part I: Experimental study. Int. J. Impact. Eng. 2002; 27: 19-35.

Borvik T., Langseth M., Hoperstad O. S., Malo K. A. Perforation of 12 mm thick steel plates by 20 mm diameter projectiles with flat, hemispherical and conical noses. Part II: Numerical study. Int J Impact Eng 2002;27:37–64.

Børvik T., Hopperstad O. S., Berstad T. On the influence of stress triaxiality and strain rate on the behaviour of a structural steel. Part II. Numerical study. Eur J Mech A/Solids. 2003a; 22:15–32.

Borvik T, Hoperstad OS, Langseth M, Malo KA. Effect of target thickness in blunt projectile penetration of Weldox 460 E steel plates. Int J Impact Eng 2003b; 28:413–64.

Borvik T., Clausen A. H., Hopperstad O. S., Langseth M. Perforation of AA5083-H116 aluminium plates with conical-nose steel projectiles—experimental study. Int J of Impact Eng 2004; 30: 367–384

Bouaziz O., Guelton N. Modelling of TWIP effect on work-hardening. Materials Science and Engineering A. 2001; 319–321, 246–249.

Bouaziz O., Allain S., Scott C. Effect of grain and twin boundaries on the hardening mechanisms of twinning induced plasticity steels. Scripta Materialia. 2008; 58, 484–487.

Brechet Y, Estrin Y. On the influence of precipitation on the Portevin-Le Chatelier effect. Acta Metall Mater 1995;43:955–963.

Brooks J. A., Lippold J. C. Selection of wrought austenitic stainless steels. ASM handbook. ASM International; 1990; 6: 457–469.

Campbell J. D. The yield of mild steel under impact loading. J Mech Phys Solids 1954;3:54–62.

Campbell J. D, Ferguson W. G. The temperature and strain-rate dependence of the shear strength of mild steel. Philos Mag 1970; 81:63–82.

Chen, S.R., Gray, G.T. Constitutive behavior of tantalum and tantalum–tungsten alloys. Metall. Mater. Trans. 1996; 27 A: 2994–3006.

Cherkaoui M, Berveiller M, Sabar H. Micromechanical modelling of martensitic transformation induced plasticity (TRIP) in austenitic single crystals. Int J Plasticity 1998;14:597–626.

Cherkaoui M, Berveiller M, Lemoine X. Coupling between plasticity and martensitic phase transformation: overall behavior of polycrystalline TRIP steels. Int J Plasticity 2000;16:1215–1241.

Clark D. S., Wood D. S. The influence of specimen dimension and shape on the results in tension impact testing. T Am Soc Mech Eng 1957:577–85.

Clausen A. H., Børvik T, Hopperstad O. S., Benallal A. Flow and fracture characteristics of aluminium alloy AA5083-H116 as function of strain rate, temperature and triaxiality. Mater Sci Eng A 2004; 364:260–272.

Clifton R. J. Dynamic plasticity. J. Applied Mech. 1983; 50: 941-952

Clifton R. J., Duffy J., Hartley K. A., Shawki T. G. On the critical conditions for shear band formation at high strain rates. Scripta Metall 1984; 5:443-448.

Conrad, H., On the mechanism of yielding and flow in iron. J. Iron Steel Inst. 1961; 198-364.

Considère AG. L'emploi du fer de l'acier dans les constructions, Me´moire no. 34. Ann Ponts et Chaussées, Paris 1885:574–5.

Corbett G. G, Reid S. R, Johnson W. Impact loading of plates and shells by free-flying projectile. Int J Impact Eng 1996;18:141–230.

Cottrell A. H. A note on the Portevin-Le Chatelier effect. Phil Mag (seventh series) 1953;44:829–832.

Cottrell A. H. Dislocations and plastic flow in crystals. Oxford: University Press;1953.

Couque H. On the use of the symmetric Taylor test to evaluate dynamic ductile compression fracture properties of metals. In Proceedings of the 5th International Conference on Structures Under Shock and Impact, pages 579–589. Computational Mechanics Inc, Billerica, MA, USA, 1998.

Couque H., Lichtenberger A., Lach E., Salesse B. Study of dynamic plastic deformation of a nitrogen alloyed steel using single and symmetric Taylor testing. J Phys IV France 2000;10.

Cowper G. R., Symonds P. S. Strain hardening and strain rate effects in the impact loading of cantilever beams. Brown Univ., Div. of Appl. Mech., report no. 28; 1952.

Curtze S., Kuokkala V. T., Hokka M., Peura P. Deformation behavior of TRIP and DP steels in tension at different temperatures over a wide range of strain rates Materials Science and Engineering A. 2009; 507, 124–131.

Da Rocha M. R., Silva de Oliveira C. A. Evaluation of the martensitic transformations in austenitic stainless steels. Materials Science and Engineering A doi:10.1016/j.msea.2009.04.004.

De A. K., Speer J. G, Matlock D. K., Murdock D. C., Mataya M. C., Comstock R. J. Deformation-induced phase transformation and strain hardening in type 304 austenitic stainless steel. Metall and Mat Trans A 2006; 37 :1875-1886

Delannay L., Jacques P., Pardoen T. Modelling of the plastic flow of trip-aided multiphase steel based on an incremental mean-field approach. Int. J. Solids. and Struct. 2008; 45, 1825–1843.

Denhard EE, Espy RH. Austenitic stainless with unusual mechanical and corrosion properties. Metals Eng Quart 1972 (November):18–20.

Dey S., Børvik T., Hopperstad O. S., Leinum J. R., Langseth M. The effect of target strength on the perforation of steel plates using three different projectile nose shapes. Int J Impact Eng 2004; 8-9:1005-1038.

Diep Q. B., Moxnes J. F., Nevstad G. Fragmentation of projectiles and steel rings using numerical 3D simulations, In: The 21th International Symposium of Ballistics, April 2004, Adelaide, Australia.

Dorward R. C, Hasse K. R. Strain rate effects on tensile deformation of 2024-O and 7075-O aluminium alloy sheet. J Mater Eng Perform 1995; 4:216–220.

Drucker D. C. A definition of stable inelastic material. J Appl Mech, Trans ASME 1959; 81:101–106.

Durrenberger L, Even D, Molinari A, Rusinek A. Influence of the strain path on crash properties of a crash-box structure by experimental and numerical approaches. J Phys IV 2006; 134:1287–1293.

Durrenberger L., Klepaczko J. R., Rusinek A. Constitutive modeling of metals based on the evolution of the strain-hardening rate. Trans. ASME. 2007; 129:550–558.

Durrenberger L, Molinari A., Rusinek A. Internal variable modeling of the high strain-rate behavior of metals with applications to multiphase steels. Mat Sci and Eng A. 2008; 478: 297–304.

Duszek M. K., Perzyna P. The localization of plastic deformation in thermoplastic solids. Int J Solids and Struct. 1991;27:1419-1443

Eakins D., Thadhani N. N. Analysis of dynamic mechanical behavior in reverse Taylor anvil-on-rod impact tests. Int J Impact Eng 2007; 34:1821–1834.

Edwards M. R., Mathewson A. The ballistic properties of tool steel as a potential improvised armour plate. Int J Impact Eng. 1997;19:297–309.

El-Magd E. Mechanical properties at high strain rates. J Phys IV 1994; C8 (4):149–70.

El-Magd E. M., Abouridouane M. Characterization, modelling and simulation of deformation and fracture behaviour of the light-weight wrought alloys under high strain rate loading. Int J Impact Eng 2006; 32:741–58.

Fischer F. D. A micromechanical model for transformation plasticity in steels. Acta Metall Mater 1990;38:1535–1546.

Fischer F. D. Transformation induced plasticity in triaxiality loaded steel specimens subjected to a martensitic transformation. Eur J Mech A/Solids 1992;11:233–244.

Fischer F. D., Sun Q. P., Tanaka K. Transformation-induced plasticity (TRIP). Appl Mech Rev 1996;49:317–364.

Fischer F. D., Reisner G., Werner E., Tanaka K., Cailletaud G., Antretter T. A new view on transformation induced plasticity (TRIP) Int. J. Plasticity. 2000; 16: 723-748.

Follansbee, P.S. High-Strain-Rate Deformation of FCC Metals and Alloys**.** Metallurgical Applications of Shock-Wave and High-Strain-Rate Phenomena. 1986: 451-479.

Follansbee P. S., Kocks U. F. A constitutive description of the deformation of copper based on the use of the mechanical threshold stress as an internal state variable. Acta Metall. 1988; 1, 81-93.

Forrestal M. J., Altman B. S., Cargile J. D., Hanchak S. J. An empirical equation for penetration depth of ogive-nose projectiles into concrete targets. Int J Impact Eng. 1994; 15:395-405.

Forrestal M. J., Warren T. L. Penetration equations for ogive-nose rods into aluminum targets. Int J Impact Eng. 2008; 35:727–730.

Frechard S, Redjaimia A, Lach E, Lichtenberger A. Mechanical behaviour of nitrogen-alloyed austenitic stainless steel hardened by warm rolling. Mater Sci Eng A 2006; 415:219–224.

Frechard S, Redjaimia A, Lach E, Lichtenberger A. Dynamical behaviour and microstructural evolution of a nitrogen-alloyed austenitic stainless steel. Mater Sci Eng A 2008; 480:89–95.

Fressengeas C., Molinari A. Instability and localization of plastic flow in shear at high strain rates. J. Mech. Phys Solids. 1987; 2:185-211.

Fressengeas C., Molinari A. The time development of Eulerian/Lagrangian perturbations to simple shear and its applications to shear banding. J Mech Phys Solids 1992;8:1735-1756.

Ghosh A. K. Tensile instability and necking in materials with strain hardening and strain-rate hardening. Acta Metall. 1977; 25:1413-1424.

Glema A., Tomasz Łodygowski T., Perzyna P. Interaction of deformation waves and localization phenomena in inelastic solids. Comput. Methods Appl. Mech. Engrg. 2000;183:123-140

Goldsmith W. Non-ideal projectile impact on targets. Int J Impact Eng 1999;22:95–395.

Gomez-del Río T., Zaera R., Barbero E., Navarro C. Damage in CFRPs due to low velocity impact at low temperature. Composites: Part B. 2005; 36: 41–50.

Goto D. M., Bingert J. F., Chen S. R., Gray III G. T., Garrett Jr. R. K. The mechanical threshold stress constitutive-strength model description of HY-100 steel. Metall Metal Trans A. 2000; 31A:1985-1996

Grady D. E. Local inertia effects in dynamic fragmentation. J. Appl Phys 1982; 1:322-325

Grady D. E., Benson D. A. Fragmentation of metal rings by electromagnetic loading. Exp Mech 1983;12:393–400.

Greenwood, G.W., Johnson, R.H. The deformation of metals under small stresses during phase transformation. 1965; Proc. Roy. Soc. A283, 403.

Guduru P. R., Freund L. B. The dynamics of multiple neck formation and fragmentation in high rate extension of ductile materials. Int J Solids Struct 2002; 39:5615–5632.

Guo W. G., Nemat-Nasser S. Flow stress of Nitronic-50 stainless steel over a wide range of strain rates and temperatures. Mech Mater 2006; 38:1090–1103.

Gupta N. K., Iqbal M. A., Sekhon G. S. Experimental and numerical studies on the behaviour of thin aluminium plates subjected to impact by blunt- and hemispherical- nosed projectiles. Int J Impact Eng 2006; 32:1921–1944.

Gupta N. K, Iqbal M. A, Sekhon G. S. Effect of projectile nose shape, impact velocity and target thickness on deformation behaviour of aluminium plates. Int J Solids Struct 2007; 44:3411–3439.

Gupta N. K., Iqbal M. A., Sekhon G. S. Effect of projectile nose shape, impact velocity and target thickness on the deformation behaviour of layered plates. Int J Impact Eng 2008; 35:37–60.

Guzmán R. Obtención de leyes tensión – deformación de materiales viscoplásticos a partir de mediciones del incremento de temperature asociado a su deformación plástica. Doctoral Thesis. University Carlos III of Madrid, 2009.

Guzmán R., Essa Y. E, Meléndez J., Aranda J., López F., Pérez-Castellanos J. L. Measurement of temperature increment in compressive quasi-static and dynamic tests using the infrared thermography. Strain. 2008; doi:10.1111/j.1475-1305.2007.00384x.

Guzmán R., Meléndez J., Zahr J., Pérez-Castellanos J. L. Determination of the constitutive relation parameters of a metallic material by measurement of temperature increment in compressive dynamic tests. Exp. Mech. doi: 10.1007/s11340-009-9223-z.

Hähner P. On the critical conditions of the Portevin-Le Châtelier effect. Acta Mater 1997; 45:3695–3707.

Han J. B., Tvergaard V. Effect of inertia on the necking behaviour of ring specimens under rapid axial expansion. Eur J Mech A/Solids 1995; 14:287–307.

Haugou G., Markiewicz E., Fabis J. On use of the non direct tensile loading on a classical split Hopkinson bar apparatus dedicated to sheet metal specimen characterisation. International Journal of Impact Engineering 2006; 32:778–798.

Hauk V. Structural and Residual Stress Analysis by Nondestructive Methods, Elsevier 1997.

Hecker S. S., Stout M. G., Staudhammer K. P. Smith J. L. Effects of strain and strain rate on deformation-induced transformation in 304 stainless steel: Part I. Magnetic measurements and mechanical behaviour. Met Trans A. 1982; 13A: 619-626.

Higashi K, Mukai T, Kaizu K, Tsuchida S, Tanimura S. Strain rate dependence on mechanical properties is some commercial aluminium alloys. J Phys III 1991.

Hill R. Acceleration wave in solids, J. Mech. Phys. Solids. 1962;10:1-16.

Hirth, J. P., Lothe, J. Theory of Dislocations. 1982. John Wiley & Sons, New York.

Honda K, Takamae G, Watanabe T. On the measurement of the resistance of shield plates to penetration by a rifle bullet. In: Tohoku Imperial Univ, first Series. 1930; 19:703–725.

Hu X, Daehn GS. Effect of velocity on flow localization in tension. Acta Mater 1996;44:1021–1033.

Huang G. L., Matlock D. K., Krauss G. Martensite formation, strain rate sensitivity, and deformation behavior of type 304 stainless steel sheet. Metall. Trans. A, 1989; 20A:1239-1246.

Huang M., Rivera-Díaz-del-Castillo P. E. J., Bouaziz O., Van der Zwaag S. A constitutive model for high strain rate deformation in FCC metals based on irreversible thermodynamics. Mech Mat 2009; 41:982–988.

Huh H, Seok-Bong Kima S. B., Songa J. H., Lim J. H. Dynamic tensile characteristics of TRIP-type and DP-type steel sheets for an auto-body. Int J Mech Sci. 2009; doi:10.1016/j.ijmecsci.2007.09.004.

Hutchinson J. W., Neale K. W. Influence of strain rate sensitivity on necking under uniaxial tension. Acta Metall 1977; 25:839-846.

Inal K., Pesci R., Lebrun J. L., Diard O., Masson R. Grain and phase stress criteria for behaviour and damage in duplex and bainitic steels. Fat. & Frac. Eng. Mat. & Struc. 2006; 29 : 685-696.

Iwamoto T, Tsuta T, Tomita Y. Investigation on deformation mode dependence of strain-induced martensitic transformation in TRIP steels and modeling of transformation kinetics. Int. J. Mech. Sci. 1998; 40:173–182.

Iwamoto T., Tsuta T. Computational simulation of the dependence of the austenitic grain size on the deformation behaviour of TRIP steels. Int. J. Plasticity. 2000; 16: 791-804.

Jiménez J. A., Carsí M, Ruano O. A., Frommeyer G. Effect of testing temperature and strain rate on the transformation behaviour of retained austenite in low-alloyed multiphase steel. Materials Science and Engineering A. 2009; 508: 195–199.

Johnson, G. R., Cook, W. H. A constitutive model and data for metals subjected to large strains, high strain rates and high temperatures. In: Proceedings of Seventh International Symposium on Ballistics. 1983: 541–547.

Johnson G. R., Cook W. H. Fracture characteristics of three metals subjected to various strains, strain rates, temperatures and pressures. Eng Fract Mech 1985; 21:31–48.

Kapoor R., Nemat-Nasser S. Comparison between high strain-rate and low strain-rate deformation of tantalum. Metall Mater Trans 1999; 31 A: 815–823.

Klepaczko J. R. Generalized conditions for stability in tension test. Int J Mech Sci. 1968; 10, 297-313.

Klepaczko J. R. Thermally activated flow and strain rate history effects for some polycrystalline FCC metals. Mater Sci Eng. 1975; 18: 121–135.

Klepaczko J. R., Duffy J. Strain rate history effects in Body-Centered-Cubic metals. Mechanical Testing for Deformation Model Development, ASTM STP 765, R. W. Rohde and J. C. Swearengen, Eds., American Society for Testing and Materials, 1982; 251-268.

Klepaczko J. R. A practical stress–strain–strain rate–temperature constitutive relation of the power form. J Mech Work Technol 1987;15: 143–165.

Klepaczko J. R. The newest development on physically based constitutive modeling in dynamic plasticity. In: Mechanical behaviour of Materials, Eds M. Jono and T. Inone. Pergamon Press, Oxford, 1991; 235.

Klepaczko, J. R. An experimental technique for shear testing at high and very high strain rates. The case of a mild steel. Int. J. Impact Eng. 1994; 15, 25–39.

Klepaczko J. R. A general approach to rate sensitivity and constitutive modeling of FCC and BCC metals, in: Impact: Effects of Fast Transient Loadings, Rotterdam; 1998: 3-35.

Klepaczko J.R. Remarks on impact shearing, J. Mech. Phys. Solids.1998; 35 :1028-1042.

Klepaczko J. R., Viem Nguyen H., Nowacki W. K. Quasi-static and dynamic shearing of sheet metals. Eur J Mech 1999; 18:271–289.

Klepaczko J. R. Review on critical impact velocities in tension and shear, Int. J. Impact Eng. 2005; 32, 188-209.

Klepaczko J. R., Rusinek A., Rodríguez-Martínez J. A., Pęcherski R. B., Arias A. Modelling of thermoviscoplastic behaviour of DH-36 and Weldox 460-E structural steels at wide ranges of strain rates and temperatures, comparison of constitutive relations for impact problems. Mech. Mat. 2009; 41: 599–621.

Klose F. B, Ziegenbein A., Hagemann F., Neuhäuser H, Hähner P., Abbadi M, et al. Analysis of Portevin-Le Chatelier serrations of type Bin Al–Mg. Mater Sci Eng A 2004;369:76–81.

Kocks, U. F., Argon, A. S., Ashby, M. F. Thermodynamics and kinetics of slip. In: Chalmers, B., Christian, J.W., Massalski, T.B. (Eds.), Progress in Materials Science, 1975; vol. 19. Pergamon Press, Oxford.

Kocks U. F. Realistic constitutive relations for metal plasticity. Mat Sci and Eng A. 2001; 317: 181–187.

Kocks U. F., Mecking H. Physics and phenomenology of strain hardening: the FCC case Progress in Materials Science. 2003; 48: 171–273.

Koistinen D. P., Marburger R. E. A general equation prescribing the extent of the austenite–martensite transformation in pure iron–carbon alloys and plain carbon steels. Acta Mater 1959; 7:59–60.

Kubin L. P., Estrin Y. Portevin-Le Chatelier effect in deformation with constant stress rate. Acta Metall 1985; 33:397–407.

Kumar A, Hauser FE, Dorn JE. Viscous drag on dislocations in aluminum at high strain rates. Acta Metall 1968;9:1189–1197.

Kuroda M, Uenishi A, Yoshida H, Igarashi A. Ductility of interstitial-free steel under high strain rate tension: experiments and macroscopic modelling with a physically-based consideration. Int J Solids Struct 2006; 43:4465–4483.

Landkof B., Goldsmith W. Petalling of thin, metallic plates during penetration by cylindro-conical projectiles. Int J Solids Struct 1993; 21:245-266.

Larour, P., Baumer, A., Bleck, W. High strain rate tensile testing of modern car body steels. In: SCT05 Conference Proceeding, Wiesbaden, Germany; 2005: 1–8.

Larour P., Verleysen P, Bleck W. Influence of uniaxial, biaxial and plane strain pre-straining on the dynamic tensile properties of high strength sheet steels. J. Phys. IV. 2006; 134: 1085–1090.

Larour P., Rusinek A, Klepaczko J. R., Beck W. Effects of strain rate and identification of material constants for three automotive steels. Steel Res. Int. 2007; 78, 348–358.

Larson M., Needlemen A, Tvergaard V, Storakers B. Instability and failure of internally pressurized ductile metal cylinders. Internal report, Division of Engineering, Brown University, Providence, June 1981.

Lebedev A., Kosarchuk V. Infuence of phase transformations on the mechanical properties of austenitic stainless steels. Int. J. Plasticity. 2000; 16, 749-767.

Leblond J. B, Mottet G, Devaux J. C. A theoretical and numerical approach to the plastic behaviour of steels during phase transformations—I. Derivation of general relations. J Mech Phys Solids 1986;34:395–409.

Leblond J. B, Mottet G, Devaux J. C. A theoretical and numerical approach to the plastic behaviour of steels during phase transformations—II. Study of classical plasticity for ideal-plastic phases. J Mech Phys Solids 1986;34:410–432.

Leblond, J. B., Devaux, J., Devaux, J. C. Mathematical modelling of transformation induced plasticity in steels- I. Case of ideal-plastic phases; II. Coupling with strain hardening phenomena. Int. J. Plasticity. 1989; 5, 551-573.

Lee Y. W., Wierzbicki T. Fracture prediction of thin plates under localized impulsive loading. Part II: discing and petalling. Int J Impact Eng. 2005; 31:1277–1308.

Lennon A. M., Ramesh K. T. The influence of crystal structure on the dynamic behavior of materials at high temperatures. International Journal of Plasticity 2004; 20; 269–290.

Litonski, J. Plastic flow of a tube under adiabatic torsion. Bulletin of the Polish Academy of Sciences, 1977; 25, 7–14.

Liu J-Y, Lu H., Chen J-M., Jullien J-F, Wub T. Simulation of mechanical behavior of multiphase TRIP steel taking account of transformation-induced plasticity. Comp. Mat. Sci. 2008; 43: 646–654.

Łodygowski T., Lengnick M., Perzyna P., Stein E. Viscoplastic numerical analysis of dynamic plastic strain localization for a ductile material, Archives Mech. 1994; 46 :1-25.

Łodygowski T., Perzyna P. Numerical modeling of localized fracture of inelastic solids in dynamic loading processes, Int. J. Num. Meth. Eng. 1997; 40: 4137-4158.

Lubarda V. A., Benson D.J., Meyers, M. A. Strain-rate effects in rheological models of inelastic response. Int. J. Plast. 2003 ;19 :1097–1118.

Macdougall D. Determination of the plastic work converted to heat using radiometry. Exp Mech 2000; 40:298–306.

Magee, C.L. Transformation kinetics, micro-plasticity and aging of martensite in Fe-31 Ni. 1966; PhD Thesis, Carnegie Inst. Tech., Pittsburgh, PA.

Magness Jr L. S. High strain rate deformation behaviors of kinetic energy penetrator materials during ballistic impact. Mech Mater 1994;17:47–154.

Mahnken R, Schneidt A, Antretter T. Macro modelling and homogenization for transformation induced plasticity of a low-alloy steel. Int J Plasticity, in press. doi:10.1016/j.ijplas.2008.03.005.

Mann H. C. High-velocity tension-impact tests. Proc. ASTM. 1936; 36, 85.

Masket A. The measurement of forces resisting armor penetration. J Appl Phys 1949;20:132–140.

McCormick P. G. The Portevin-Le Châtelier effect in an Al–Mg–Si alloy. Acta Metall 1971; 19:463–471.

Meftah S., Barbe F., Taleb L., Sidoroff F. Parametric numerical simulations of TRIP and its interaction with classical plasticity in martensitic transformation. Eur. J. Mech. A Solids. 2007; 26, 688–700.

Mercier S., Molinari A. Analysis of multiple necking in rings under rapid radial expansion Int J Impact Eng, 2004; 4:403-419.

Molinari A., C. Musquar C., G. Sutter G. Adiabatic shear banding in high speed machining of Ti–6Al–4V: Experiments and modeling. Int J Plasticity 2002; 18: 443–459.

Molinari A, Ravichandran G. Constitutive modeling of high-strain-rate deformation in metals based on the evolution of an effective microstructural length. Mech Mat. 2005; 37: 737–752.

Mouro P., Gary G., Zhao H. Dynamic tensile testing of sheet metal. J Phys IV 2000; 10:149–154.

Mukai T, Higashi K, Tanimura S. Influence of the magnesium concentration on the relationship between fracture mechanism and strain rate in high purity Al– Mg alloys. Mater Sci Eng A 1994; 76:181–189.

Nemat-Nasser, S., Isaacs, J. Direct measurement of isothermal flow stress of metals at elevated temperatures and high strain rates with application to Ta and Ta–W alloys. Acta Metall, 1997; 45: 907–919.

Nemat-Nasser S., Li Y., Flow stress of FCC polycrystals with application to OFHC Copper. Acta Mater. 1998; 46, 565-577.

Nemat-Nasser S, Guo W. G, Kihl D. P. Thermomechanical response of AL-6XN stainless steel over a wide range of strain rates and temperatures. J Mech Phys Solids 2001; 49:1823–1846.

Nemat-Nasser, S., Guo, W.G. Thermomechanical response of DH-36 structural steel over a wide range of strain rates and temperatures. Mech. Mat. 2003; 35: 1023–1047.

Nemat-Nasser S., Guo W. G. Thermomechanical response of HSLA-65 steel plates: experiments and modelling. Mech Mater 2005; 37:379–405.

Niordson F. L. A unit for testing materials at high strain rates. Exp Mech 1965;5:29–32.

Nishiwaki J. Resistance to the penetration of a bullet through an aluminium plate. J Phys Soc Jpn 1951;5:374–378.

Odeshi A. G., Al-ameeri S., Mirfakhraei S., Yazdani F., Bassim M. N. Deformation and failure mechanism in AISI 4340 steel under ballistic impact. Theoretical and Applied Fracture Mechanics. 2006; 45:18–24

Oliver S., Jones T.B., Fourlaris G. Dual phase versus TRIP strip steels: microstructural changes as a consequence of quasi-static and dynamic tensile testing. Mat. Charac. 2007; 58: 390–400.

Olson G. B, Cohen M. Kinematics of strain-induced martensitic nucleation. Metall Trans A 1975; 6:791–795.

Oussouaddi O, Klepaczko JR. An analysis of transition from isothermal to adiabatic deformation in the case of a tube under torsion. Proceedings. conf. DYMAT 91. Journal de Physique IV 1991;Coll. C3 (Suppl. III):C3–323 [in French].

Pandolfi A, Krysl P, Ortiz M. Finite element simulation of ring expansion and fragmentation. Int J Fract 1999; 95:279–297.

Papatriantafillou I., Agoras M., Aravas N., Haidemenopoulos G. Constitutive modeling and finite element methods for TRIP steels Comput. Methods Appl. Mech. Eng. 2006; 195, 5094–5114.

Papirno R. P., Mescall J. F., Hansen A. M. Beyond the taylor test to fracture. In Designing for extremes: Environment, loading, and structural behavior, Proceedings of the Army Symposium on Solid Mechanics, pages 367–385,Watertown, MA, September 1980. Army Materials and Mechanics Research Center.

Pęcherski R. B. Macroscopic effect of micro-shear banding in plasticity of metals. Acta Mech 1998; 131:203–224.

Pęcherski R.B. Continuum mechanics description of plastic flow produced by micro-shear bands. Tech Mech 1998; 18:107–115.

Perzyna P. In: Fundamental problems in viscoplasticity, vol. 9. New York: Academic Press; 1966; 243–377.

Perzyna P. Instability phenomena and adiabatic shear band localization in thermoplastic flow processes. Acta Mechanica. 1994; 106:173-205.

Perzyna P. Application of the Thermodynamical Theory of Elasto–Viscoplasticity in Modern Manufacturing Processes. Course notes: Damage mechanics and micromechanics of localized fracture phenomena in inelastic solids. CISM. Udine, July 7 - 11, 2008.

Picu R. C. A mechanism for the negative strain-rate sensitivity of dilute solid solutions. Acta Mater 2004; 52:3447–3458.

Piekutowski A. J. Characteristics of debris clouds produced by hypervelocity impact of aluminum spheres with thin aluminum plates. Int J Impact Eng. 1993; 14: 573-586

Piekutowski A. J. Holes produced in thin aluminium sheets by the hypervelocity impact of aluminium spheres. Int J Impact Eng 1999; 23:71 l-722.

Piekutowski A. J. Debris clouds produced by the hypervelocity impact of nonspherical projectiles. Int J Impact Engng 2001; 26:613–624.

Rajendran A. M, Fyfe I. M. Inertia effects on the ductile failure of thin rings. Journal of Applied Mechanics. Transactions of the ASME. 1982; 49:31-36.

Rakhmatulin H. A. Mechanics of unloading waves. Prilkl Mat Meh 1945;9:91.

Regazzoni G., Kocks U. F, Follansbee P. S. Dislocation kinetics at high strain rates. Acta Metall 1987; 12:2865–2875.

Rice J. R. The localization of plastic deformation, in: W.T. Koiter (Ed.), Theoretical and Applied Mechanics, North-Holland, Amsterdam, 1976; 207-220.

Rittel D., Ravichandran G., Venkert A. The mechanical response of pure iron at high strain rates under dominant shear. Mat Sci Eng A. 2006; 1-2:191-201.

Rodríguez-Martínez J. A., Rusinek A., Zaera R., Arias A., Klepaczko J. R, 2008. Estudio experimental y numérico del comportamiento de láminas de acero sometidas a impacto de media y alta velocidad. Anales de Mecánica de la fractura – In spanish –

Rodríguez-Martínez J. A., Rusinek A., Arias A. Relation between strain hardening and critical impact velocity in tensión. J Theoretical and Applied Mech. 2009; 47:645-665.

Rodríguez-Martínez J. A., Rusinek A., Chevrier P., Bernier R., Arias A. Temperature measurements on ES steel sheets subjected to perforation by hemispherical projectiles. Int J Impact Eng DOI: 0.1016/j.ijimpeng.2010a.12.005.

Rodríguez-Martínez J. A., Pesci R., Rusinek A., Arias A., Zaera R., Pedroche D. A. On the thermo-mechanical behaviour of TRIP 1000 steel sheets subjected to low velocity perforation at different temperatures by conical projectiles. Int J Solids and Struc doi: 10.1016/j.ijsolstr.2010b.01.013.

Rosenberg Z, Ashuach Y, Yeshurun Y, Dekel E. On the main mechanisms for defeating AP projectiles, long rods and shaped charge jets. Int J Impact Eng 2009; 36:588–596.

Rusinek A. Modélisation thermo viscoplastique d'une nuance de tôle d'acier aux grandes vitesses de de´formation. Etude expérimentale et numérique du cisaillement, de la traction et de la perforation, PhD Thesis, University of Metz; 2000.

Rusinek, A., Klepaczko, J.R. Shear testing of sheet steel at wide range of strain rates and a constitutive relation with strain-rate and temperature dependence of the flow stress. Int J Plasticity. 2001; 17: 87–115.

Rusinek, A., Zaera, R., Klepaczko, J.R., Cheriguene, R. Analysis of inertia and scale effects on dynamic neck formation during tension of sheet steel. Acta Mater. 2005; 53: 5387–5400.

Rusinek, A., Zaera, R. Finite element simulation of steel ring fragmentation under radial expansion. Int J Impact Eng. 2007; 34, 799–822.

Rusinek A., Zaera R., Klepaczko J. R. Constitutive relations in 3-D for a wide range of strain rates and temperatures – Application to mild steels. Int J Solids Struct. 2007; 44:5611–5634.

Rusinek A., Zaera R., Forquin P., Klepaczko J. R. Effect of plastic deformation and boundary conditions combined with elastic wave propagation on the collapse site of a crash box. Thin-Walled Struct 2008a; 46:1143–1163.

Rusinek A., Rodríguez-Martínez J.A., Arias A., Klepaczko J. R., López-Puente J. Influence of conical projectile diameter on perpendicular impact of thin steel plate. Eng. Fract. Mech. 2008b; 75: 2946-2967.

Rusinek A, Klepaczko J. R. Experiments on heat generated during plastic deformation and stored energy for TRIP steels. Mater Design 2009; 30:35–48.

Rusinek A, Rodríguez-Martínez J. A. Thermo-viscoplastic constitutive relation for aluminium alloys, modeling of negative strain rate sensitivity and viscous drag effects. Mater Des 2009; 30:4377–4390.

Rusinek A., Rodríguez-Martínez J.A., Zaera R., Klepaczko J. R., Arias A, Sauvelet C. Experimental and numerical analysis of failure process of mild steel sheets subjected to perpendicular impact by hemispherical projectiles. Int. J. Impact Eng. 2009a; 36: 565–587.

Rusinek, A., Rodríguez-Martínez, J. A., Klepaczko, J. R., Pecherski, R. B. Analysis of thermo-visco-plastic behaviour of six high strength steels. Mater Design 2009b; 30:1748–1761.

Rusinek A, Cheriguene R., Bäumer A, Klepaczko J. R., Larour P. Dynamic behaviour of high-strength sheet steel in dynamic tension: experimental and numerical analyses J. Strain Analysis 2008c; 43: 37-53.

Rusinek A, Rodríguez-Martínez J. A., A. Arias. A thermo-viscoplastic constitutive model for FCC metals with application to OFHC copper. Int J Mech Sci. doi:10.1016/j.ijmecsci.2009.07.001.

Sánchez-Sáez S., E. Barbero E., Navarro C. Analysis of the dynamic flexural behaviour of composite beams at low temperature. Composites Science and Technology 2007; 67: 2616–2632.

Santiuste C., Sanchez-Saez S., Barbero E. Residual flexural strength after low-velocity impact in glass/polyester composite beams. Comp Struct 2010;92:25–30.

Seeger, A. The mechanism of glide and work-hardening in face centered cubic and hexagonal close-packed metal. 1957, In: Dislocations and Mechanical Properties of Crystals. J. Wiley, New York.

Segreti M, Rusinek A, Klepaczko JR. Experimental study on puncture of PMMA at low and high velocities, effect on the failure mode. Polym Test 2004; 23: 703–718.

Shen W. Q., Rieve R. O., Baharun B. A study on the failure of circular plates struck by masses. Part 1: experimental results. Int J Impact Eng 2002;27:399–412.

Sleeswijk A. W. Slow strain hardening of ingot iron. Acta Metall 1958; 6:598–603.

Sorensen N. J., Freund L. B. Unstable neck formation in a ductile ring subjected to impulsive radial loading. Int J Solids Struct 2000; 37:2265–83.

Steinberg DJ, Cochran SG, Guinan MW. Constitutive model for metals applicable at high strain rates. J Appl Phys. 1980;51:1498–1504.

Stringfellow R. G., Parks D. M., Olson G. B. A constitutive model for transformation plasticity accompanying strain-induced martensitic transformation in metastable austenitic steels. Acta Metall 1992;40:1703–1716.

Taleb L., Petit S. New investigations on transformation induced plasticity and its interaction with classical plasticity. Int. J. Plasticity. 2006; 22, 110–130.

Tanner A. B., McDowell D. L. Deformation, temperature and strain rates sequence experiments on OFHC Cu. Int J Plasticity 1999; 15:375–399.

Taylor G. I. Plastic wave in a wire extended by an impact load. Scientific papers, vol. 1 mechanics of solids. Cambridge: Cambridge University Press; 1958: 456.

Taylor G. Thermally-activated deformation of bcc metals and alloys. Progress in Materials Science. 1992; 36, 29-61.

Tomita Y, Iwamoto T. Constitutive modelling of TRIP steel and its application to the improvement of mechanical properties. Int J Mech Sci. 1995; 37, 1295–305.

Tomita Y., Iwamoto T. Computational prediction of deformation behavior of TRIP steels under cyclic loading. Int J Mech Sci 2001; 43: 2017–2034

Triantafyllidis N, Waldenmyer JR. Onset of necking in electro-magnetically formed rings. J Mech Phys Solids 2004; 52:2127–2148.

Uenishi A., Teodosiu C. Constitutive modelling of the high strain rate behaviour of interstitial-free steel. Int J Plasticity. 2004; 20: 915–936.

Varas D. Estudio experimental y numérico del comportamiento de tanques integrados de combustible frente a impacto de alta velocidad. 2009 Doctoral Thesis. University Carlos III of Madrid.

Varshni, Y. P. Temperature dependence of the elastic constants. Phys. Rev. B 2 1970;10:3952–3958.

Von Kàrman T., Duwez P. The propagation of plastic deformation in solids. J Appl Phys 1950;21:987.

Voyiadjis G. Z., Abed F. H. Microstructural based models for bcc and fcc metals with temperature and strain rate dependency. Mechanics of Materials 2005; 37: 355–378.

Voyiadjis G. Z., Almasri A. H., A physically based constitutive model for fcc metals with applications to dynamic hardness. Mech. Mat. 2008; 40: 549-563.

Weertman J. Metallurgical effects at high strain rates. 1973, 319. Plenum press, New York.

Wierzbicki T. Petalling of plates under explosive and impact loading. Int J Impact Eng 1999; 22:935–954.

Wierzbicki T., Bao Y., Lee Y. W., Bai Y. Calibration and evaluation of seven fracture models. Int J Mech Sci. 2005; 47:719–743.

Zaera R., Fernández-Sáez J. An implicit consistent algorithm for the integration of thermoviscoplastic constitutive equations in adiabatic conditions and finite deformations. Int. J. Solids Structures 2006; 43: 1594-1612.

Zaid M., Paul B. Mechanics of high speed projectile perforation. J Franklin Inst 1958;35:265–317.

Zerilli, F. J., Armstrong, R. W., 1987. Dislocation-mechanics-based constitutive relations for material Dynamics calculations. J Appl Phys. 1987; 61:1816–1825.

Zerilli F. J., Armstrong R. W. The effect of dislocation drag on the stress–strain behaviour of FCC metals. Acta Metall Mater 1992; 40:1803–1808.

Zhang S., McCormick P. G., Estrin Y. The morphology of Portevin–Le chatelier bands: finite element simulation for Al–Mg–Si. Acta Mater 2001; 49:1087–1094.

Zhang H, Ramesha K. T., Chin E. S. C. High strain rate response of aluminum 6092/ B4C composites. Mater Sci Eng A 2004;384: 26–34.

Zhao H., Gary G. The testing and behaviour modelling of sheet metals at strain rates from 10^{-4} to 10^{4} s^{-1}. Mater Sci Eng 1996;207: 46–50.

Zhou F., Molinari J. F., Ramesh K. T. An elasto-visco-plastic analysis of ductile expanding ring. Int J Impact Eng 2006; 33:880-891.

Zukas J. A. , Nicholas T. , Swift H. F. Impact dynamics. Florida: Krieger; 1992.

Zukas J. A., Hohler V., Jameson R. L., Mader C. L., Nicholas T., Rajendran M. A, et al. High velocity impact dynamics. New York: Wiley; 1990.

Zukas J. A., Scheffler D. R. Practical aspects of numerical simulations of dynamic events: effects of meshing. Int J Impact Eng 2000: 925–945.